Gary Foss · Christopher Niezrecki   *Editors*

Special Topics in Structural Dynamics, Volume 6

Proceedings of the 32nd IMAC, A Conference and Exposition on Structural Dynamics, 2014

SEM

Springer

Conference Proceedings of the Society for Experimental Mechanics Series

Series Editor

Tom Proulx
Society for Experimental Mechanics, Inc.,
Bethel, CT, USA

Gary Foss • Christopher Niezrecki
Editors

Special Topics in Structural Dynamics, Volume 6

Proceedings of the 32nd IMAC, A Conference and Exposition on Structural Dynamics, 2014

Springer

Editors
Gary Foss
Boeing Test and Evaluation
Seattle, WA, USA

Christopher Niezrecki
Department of Mechanical Engineering
University of Massachusetts Lowell
Lowell, MA, USA

Preface

Special Topics in Structural Dynamics, Volume 6 represents one of the eight volumes of technical papers presented at the 32nd IMAC, A Conference and Exposition on Structural Dynamics, 2014 organized by the Society for Experimental Mechanics, and held in Orlando, Florida, February 3–6, 2014. The full proceedings also include volumes on Dynamics of Coupled Structures; Nonlinear Dynamics; Model Validation and Uncertainty Quantification; Dynamics of Civil Structures; Structural Health Monitoring; Topics in Modal Analysis I; and Topics in Modal Analysis II.

Each collection presents early findings from experimental and computational investigations on an important area within structural dynamics. Special Topics in Structural Dynamics represents papers on enabling technologies for modal analysis measurements such as sensors and instrumentation, and applications of modal analysis in specific application areas. Topics in this volume include:

Aircraft/aerospace
Active control
Analytical methods
System identification
Sensors and instrumentation

The organizers would like to thank the authors, presenters, session organizers, and session chairs for their participation in this track.

Seattle, WA, USA Gary Foss
Lowell, MA, USA Christopher Niezrecki

Contents

Chapter 1
Vibration Class at GIST, Korea

Semyung Wang, Jongsuh Lee, Youngeun Cho, Homin Ryu, and Kihwan Park

Abstract Vibration class covers vibration phenomena of mechanical systems due to dynamic load is studied. It covers from single DOF to multi DOF and theory as well as numerical and experimental methods. It deals various subjects: Lagrange equation, Laplace transformation, Fourier transformation, mode superposition, finite element method, experimental modal analysis, random vibration, vibro-acoustics and model validation.

Keywords Laboratory • Structural dynamics • Numerical analysis • Experimental modal analysis • Model updating

1.1 Introduction

Advanced vibration course is intended for graduated students; its goal includes deep understanding and estimating the mechanism of how vibration takes place in a mechanical system as well as understanding the vibration theory [1–4]. The class begins with a detailed description of single degree of freedom (DOF) and two DOF systems for the underlying understanding of vibration. In these parts, the system responses, which are governed by differential equation, are investigated in time and frequency domain. These equations are used to explain the characteristics of response with respect to different damping ratio values (under, over and critical damping) and different kinds of damping (viscous, structural). For the case of multi DOF system which is represented by matrix, the system is analyzed based on the eigenvalue problem.

Especially, mode shape of the system which is represented by eigenvector is introduced, and it is described that the several characteristics (reciprocal theorem, modal matrix) caused by the orthogonal property between this vector and system matrix. In addition, it is introduced that the frequency response function (FRF), which is the response of the applied force in the frequency domain, can be described by mode summation approach. For continuous system, modal parameters of the system are investigated through the governing equation, and the form of FRF is examined in the same way to the previous one by mode summation approach.

In order to carry out experiments for vibration analysis, covers following contents are covered in the class [5].

1. Different signals of force and types of sensors
2. Fundamental understanding of digital signal (leakage, window, power spectra, coherence and etc.)
3. Modal parameter estimation methods (peak picking, circle fitting, etc.)

To relate the theory with the experiments and for students' better understanding of the knowledge delivered in the class, two projects are assigned. One, as a common project to every student, is for verifying the theory, which they have learned in the class, by implementing the simple model (beam, plate). The basic purpose is to obtain the dynamic characteristics (natural frequency, damping, mode shape and FRF) of the system through analytic approach and these obtained results are verified from numerical analysis and experimental results. The other project is chosen as an individual topic that should be related to individual research area.

S. Wang (✉) • J. Lee • Y. Cho • H. Ryu • K. Park
Gwangju Institute of Science and Technology (GIST), Gwangju 500-712, Republic of Korea
e-mail: smwang@gist.ac.kr

This paper is organized as follows. In Sect. 1.2, a brief description of the contents covered in the class is introduced, and in Sect. 1.3, the conducted projects are introduced as divided into common and individual topics. This paper is concluded in the Sect. 1.4. In addition, the detailed description of the commercialized non-contact sensor, i.e. laser scanning vibrometer (LSV), which is developed by this laboratory and is used in the common project, is attached as an Appendix.

1.2 Class Contents

1.2.1 Single Degree of Freedom

In this chapter, a single DOF system as shown in Fig. 1.1 is introduced. It begins with derivation of the equation of motion shown in Eq. (1.1) for the system using Newton's second law.

$$m\ddot{x} + c\dot{x} + kx = F(t) \tag{1.1}$$

Next, the explanation of the resonance and resonance frequency is introduced from the undamped free vibration case. The solution of the homogeneous differential equation is derived. Next, damping ratio is introduced followed by vibration characteristics according to the damping (underdamped, over damped, critical) and the types of damping (structural, coulomb, viscous damping) are presented to the students.

In the next problem, forced vibration is examined and shown through an example of vibration due to rotating unbalance under the harmonic excitation. The solution of forced vibration equation of motion composed of homogeneous solution and particular solution is shown, and the concept of frequency response function as shown in Eq. (1.2) is introduced.

$$\frac{X}{F} = \frac{1}{\sqrt{(k - m\omega)^2 + (c\omega)^2}} \tag{1.2}$$

Students can understand that the vibration frequency response is dominated by the stiffness term at lower frequency than resonance frequency, and by the mass term at frequencies higher than the resonance frequency, also by the damping term at near resonance frequency as shown in Eqs. (1.3)–(1.5). Then, structure modification using vibration frequency response characteristics and estimation of mass and stiffness based on an experiment are introduced.

$$\omega \ll \omega_n : \frac{X}{F} \approx \frac{1}{k} \tag{1.3}$$

$$\omega \gg \omega_n : \frac{X}{F} \approx -\frac{1}{m\omega^2} \tag{1.4}$$

$$\omega \approx \omega_n : \frac{X}{F} \approx \frac{1}{jc\omega} \tag{1.5}$$
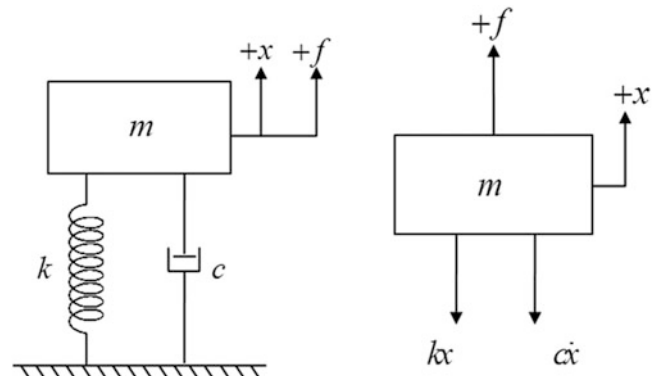
Fig. 1.1 Damped single degree of freedom system

Fig. 1.2 Half power points and Q-factor
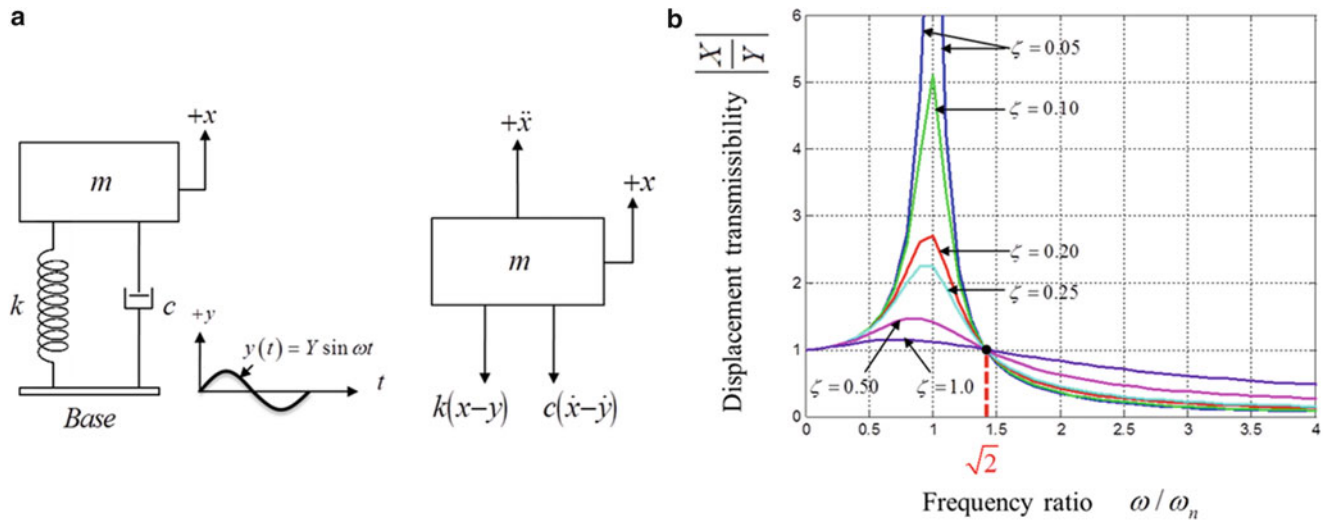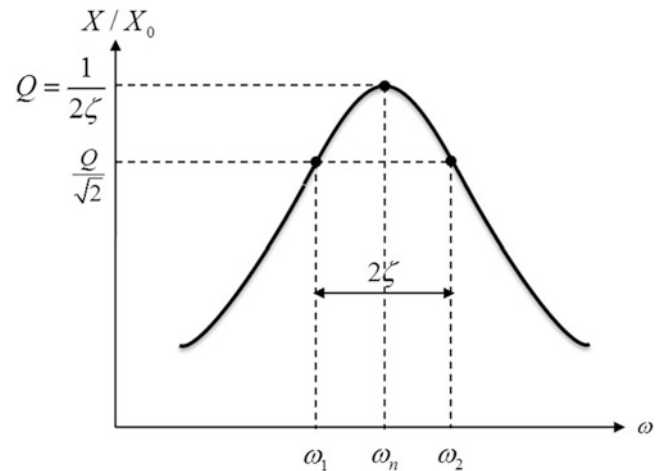
Fig. 1.3 (**a**) System excited by motion of support point (**b**) Transmissibility curve

The estimation of the damping ratio using Q-factor in FRF is offered to the students. Specifically, the process of calculating the Q-factor using half power points is explained and the equivalent viscous damping can be estimated from this process as shown in Eq. (1.6) and Fig. 1.2.

$$Q \approx \frac{1}{2\zeta} \approx \frac{\omega_n}{\omega_2 - \omega_1} \tag{1.6}$$

Next, support motion is introduced, and it leads to the explanation of transmissibility as shown in Fig. 1.3. It is shown that the principle of vibration isolation, and the transmissibility becomes smaller than 1 at the frequency range where the frequency ratio is larger than $\sqrt{2}$.

In addition, method of obtaining the transient response under non-periodic excitation is introduced. Transient vibration problem under impulse excitation is firstly introduced in order to convey the content to students successfully. Then, it is shown that vibration response under arbitrary excitation can be obtained using the combination of the impulse responses.

1.2.2 Multi Degree of Freedoms

Even though an actual structure is a continuous system, the continuous system is discretized and modeled as a multi degree of freedoms (MDOF) system (Fig. 1.4) for a practical sense. Finite element method, boundary element method, and transfer
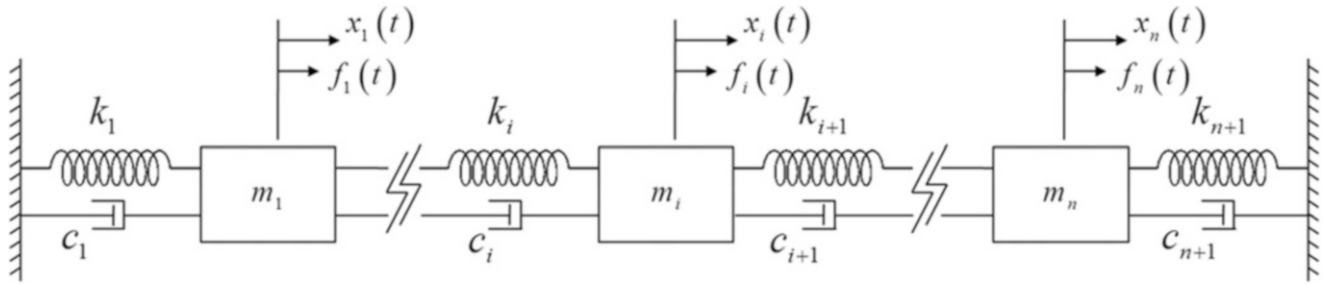
Fig. 1.4 Damped multi degree of freedoms system

matrix method are introduced as general discretization methods, and the discretization process of the vibration system is explained. The equation of motion in matrix form is derived as shown in Eq. (1.7).

$$\mathbf{M}\ddot{\underline{x}} + \mathbf{C}\dot{\underline{x}} + \mathbf{K}\underline{x} = \underline{F}(t) \tag{1.7}$$

The MDOF undamped free-vibration problem is switched to an eigenvalue problem, and the result shows that eigenvalues and eigenvectors can be equally considered as natural frequencies and mode shapes respectively. Also, the relationship between the number of the degree of freedom and the number of the natural frequencies and mode shapes can be explained. The eigenvectors of the system are shown to be orthogonal with respect to both mass and stiffness matrices. Modal matrix which assembles eigenvectors into a square matrix is introduced. By using the modal matrix, decoupling of the forced vibration terms and modal damping concept can be explained.

In forced vibration case, FRF as shown in Eq. (1.8) can be obtained using the orthogonality of eigenvectors. Additionally, Maxwell's reciprocity theorem states that $H_{ik} = H_{ki}$ for the linear system,

$$H_{ik}(\omega) = \sum_{r=1}^{N} \frac{\phi_r^i \phi_r^k}{(k_r - \omega^2 m_r) + j(\omega c_r)} \tag{1.8}$$

When the system becomes larger and more complex, DOF is increased. This leads to the difficulty of calculating the exact solution. To solve this kind of problem, an approximate solution is introduced. Mainly, superposition methods such as mode displacement method (MDM), mode acceleration method (MAM), load dependent Ritz vectors (LDRV) method, Krylov sequence, and Lanczos algorithm are explained, and the advantages and disadvantages of the each method are explained as well.

Newton's second law, energy method, and virtual work method are compared with each other so that the equation of motion is formulated. Consequently, Lagrange's equation as shown in Eq. (1.9) is introduced to formulate the large and complex system.

$$\frac{d}{dt}\left(\frac{\partial T}{\partial \dot{q}_i}\right) - \frac{\partial T}{\partial q_i} + \frac{\partial U}{\partial q_i} = Q_i \tag{1.9}$$

1.2.3 Experimental Modal Analysis

Experimental modal analysis (EMA) contains experimental measurement process for the FRF of the system; signal processing, and extracting the modal parameters (natural frequencies, mode shapes, and damping ratios) from measured FRF. Verifying a numerical model, determining dynamic durability by experiments, and machinery diagnostics for maintenance are possible by using the modal parameters.

The techniques needed to experimentally determine the FRF showing the relationship of response and excitation force are introduced. There are two kinds of methods to excite a structure. First case is supplying excitation force by attaching a vibration exciter as shown in Fig. 1.5a. In this case, in order to reduce the mass loading due to an attached vibration exciter, a stinger should be used. The type of signals that is applied to the vibration exciter is introduced,and the characteristics in the
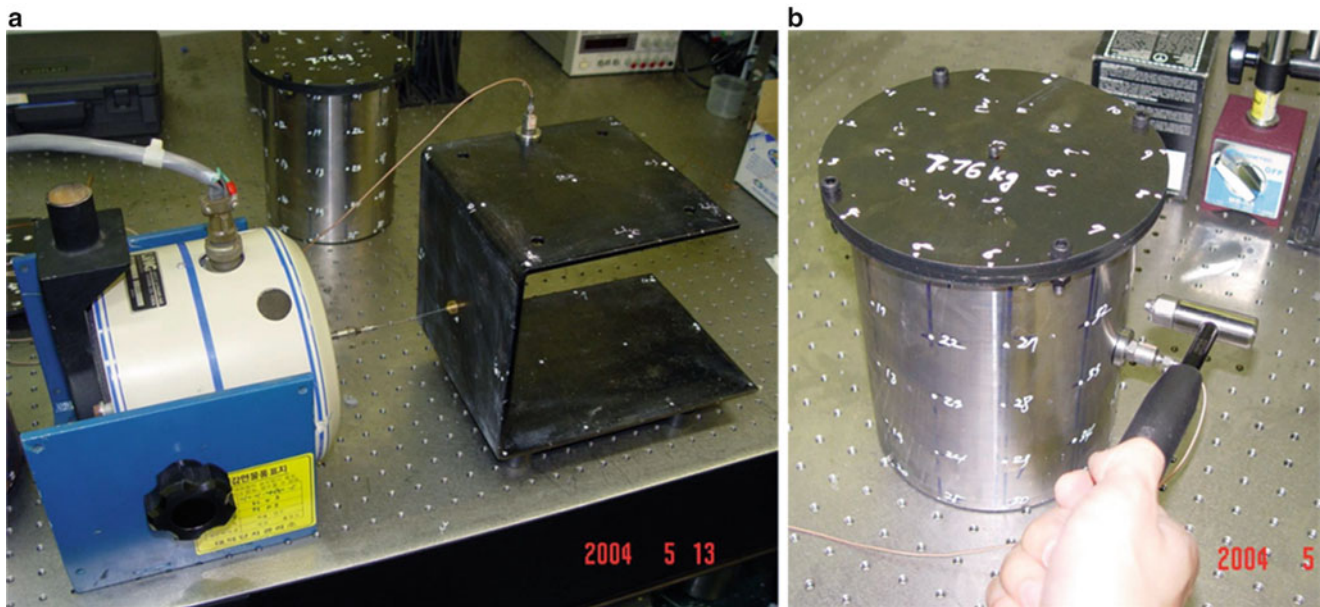
Fig. 1.5 Vibration excitation methods (**a**) Vibration exciter with a stinger (**b**) Impact hammer

frequency domain corresponding to each signal are described. Second case is to use an impact hammer as shown in Fig. 1.5b. In this case, the characteristics of excited force in the frequency domain are explained. Also, effects of the header and tip of the hammer corresponding to the frequency range of interest are discussed. Lastly, the advantages and disadvantages of both methods are compared.

The sensors for detecting a response and excitation force applied to the structure are explained. There are two kinds of sensors to measure vibration signal, which are contact and non-contact. The contact sensors are an accelerometer and a strain gauge. Because they are attached to the structure, there is a mass added effect. The non-contact sensors are a position sensitive detector (PSD) to measure displacement and a LSV to measure velocity. Because LSV can rapidly measure the vibration of several positions, it makes EMA easier. LSV is a device that was developed in this laboratory; a detailed description is attached in the Appendix.

Digital signal processing theory for obtaining FRF from measured data is introduced. Because EMA contains the sampling process which is converting an analog signal into a digital signal, Nyquist sampling theorem as shown in Eq. (1.10) should be described.

$$f_s \geq 2f_0 \qquad\qquad (1.10)$$

The aliasing phenomenon in which high-frequency component is detected in the low-frequency component occurs when the sampling rate is not enough. Hence, antialiasing filter is used to prevent the aliasing phenomenon. Fourier transform is explained because frequency conversion is needed to obtain FRF from the measured signal. Also, the leakage in which the frequency component power leaks to adjacent frequency component is explained. The window function which can reduce the leakage is shown and, its principle is explained.

In processing techniques of experimental measurement signal, correlation function and spectral density function can obtain the correlation between the two signals in time domain and frequency domain. The linear relationship between the input and output signals (FRF) can be expressed in the correlation function and the spectral density function. And the coherence function which may indicate the degree of noise mixed in the signal via the spectral density function is introduced. Therefore, a coherence function can show whether the characteristic values measured in the experiment are being measured correctly.

The peak picking and circle fitting which extracts the modal parameters from experimentally measured FRF are explained. And it is possible to observe the mode shapes using predicted values at some points, i.e. by the mode analysis method introduced.
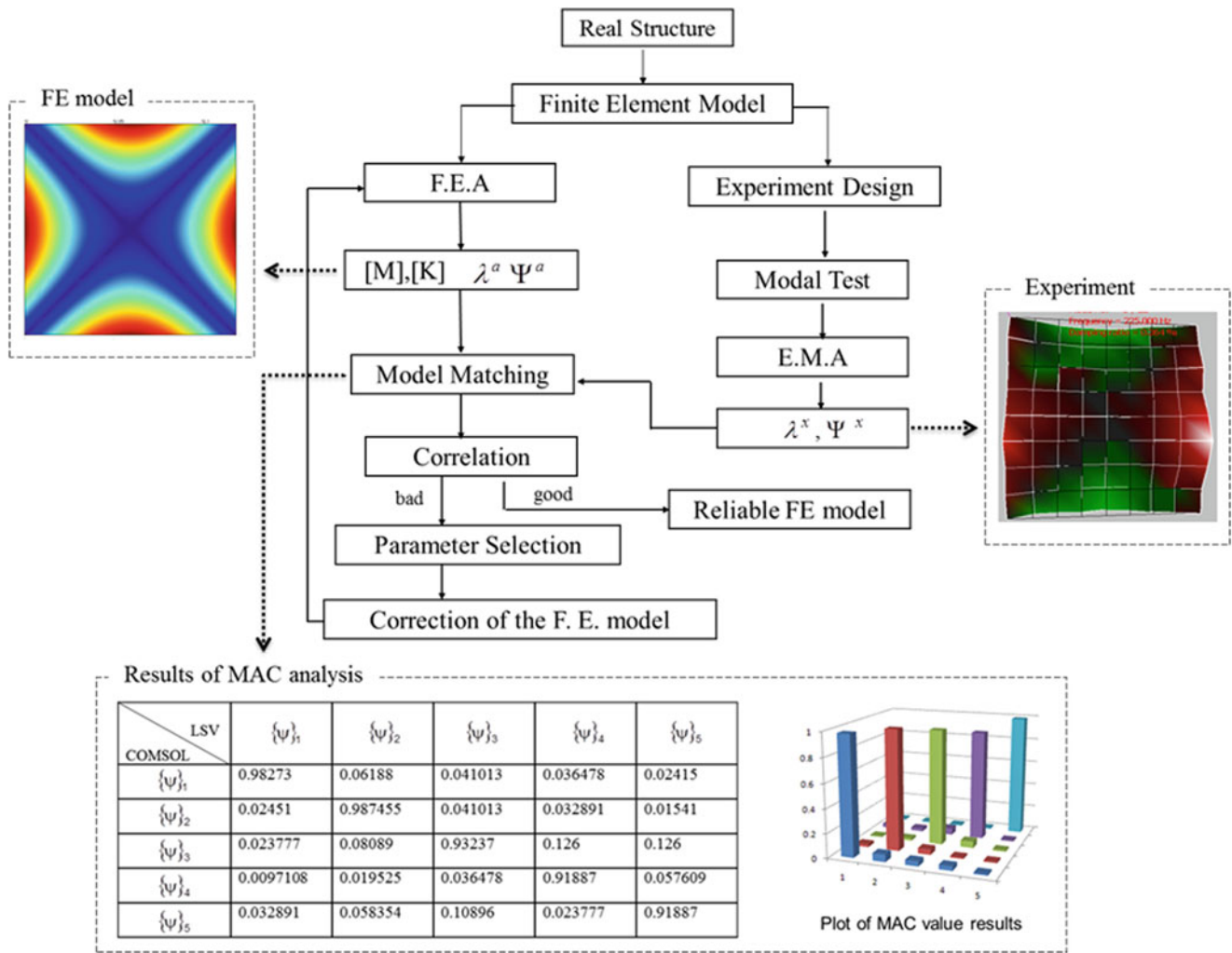
Fig. 1.6 Model updating process

1.2.4 Model Updating Process

It is possible to verify the numerical model using the modal parameters obtained by the EMA. However, since the error exists between FE model and EMA results, the need for reliable FE model should be explained. A model updating for matching between the dynamic characteristics of numerical model and modal parameters obtained via the EMA by changing the parameters of the numerical model is introduced. It is the required process to construct the FE model for the optimal design. Figure 1.6 is a flow chart showing the model updating process of a square steel plate.

1.3 Class Project

1.3.1 Midterm Project

Midterm project is assigned to offer an opportunity to recognize the relationship between vibration theory and experiment based on the class contents introduced in Sect. 1.2. Specifically, student should obtain modal parameters using the governing equation of the system through analytical, numerical and experimental approach. In this way, students can understand each process and the relationship between them. Finally, numerical model updating process based on the experimental results is conducted repeatedly for the numerical model validation. The following two application systems are considered.
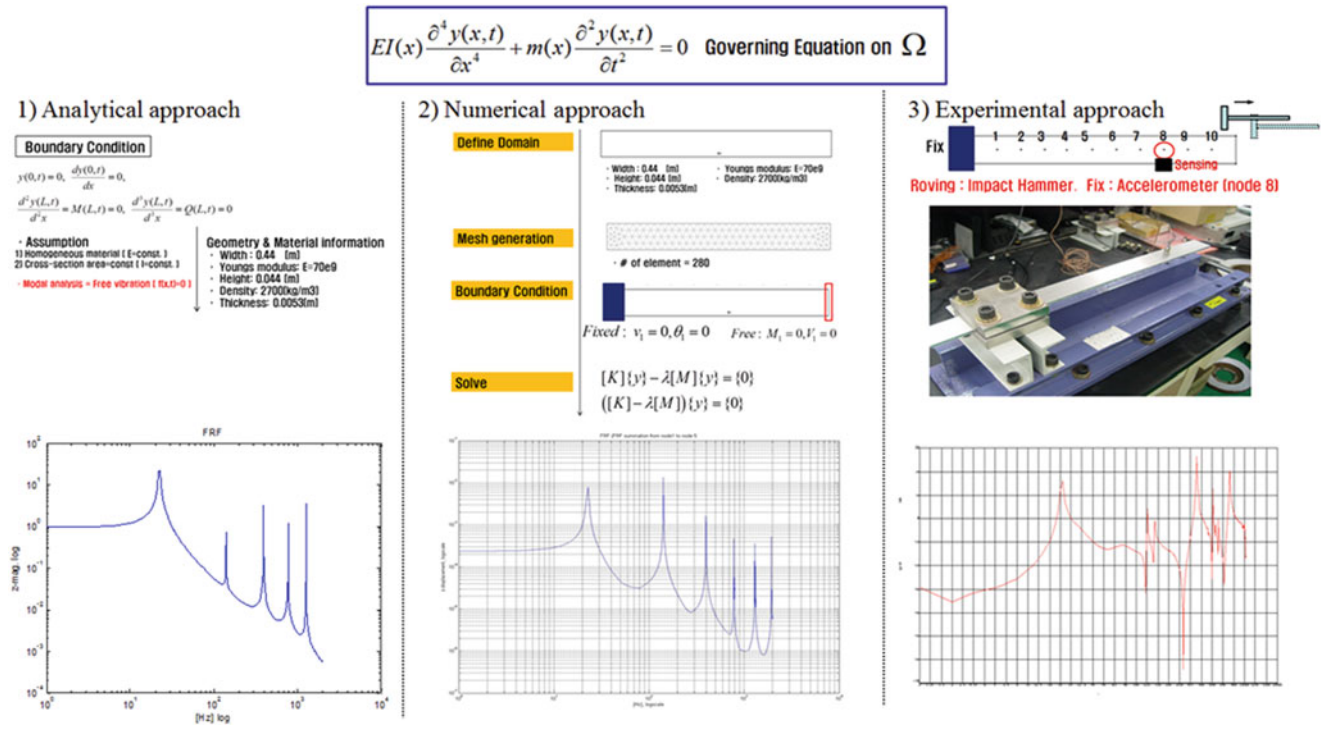
Fig. 1.7 Midterm project of a cantilever beam using analytical, numerical, experimental approach

1. Cantilever beam: Accelerometer and Impact hammer
2. Plate and Brake-disk: LSV and Vibration exciter

1.3.1.1   Cantilever Beam

Cantilever beam is given to the students for the experimental modal test using an impact hammer and an accelerometer. As mentioned previously, modal parameters using analytical and numerical approach are obtained using the governing equation and boundary condition of the system. Meanwhile, modal parameter using experimental approach is obtained through roving impact hammer test as shown in the experimental setup in Fig. 1.7. Student can verify the vibration theory of the cantilever beam by comparing the results from three different approaches.

1.3.1.2   Plate and Brake-Disk

Next, plate and brake-disk are given to the student for the experimental modal test using a laser scanning vibration rather than an impact hammer and an accelerometer. Analytical approach is based on a related reference paper [6]. COMSOL (commercial numerical analysis program) offered to students for finding the modal parameters of the structure numerically; material properties of the structure are given in Table 1.1. A laser scanning vibrometer is offered in experimental approach (non-contact sensor) for measuring the vibration response of the system under the excitation condition using a vibration exciter.

Tables 1.2 and 1.3 represent modal parameters of plate and brake-disk respectively obtained from student's midterm report.

Students can understand different facts from Tables 1.2 and 1.3. Firstly, modal parameter results of the plate using analytical approach and numerical approach are similar. On the other hand, modal parameter results using experimental approach has a little difference as compared with that of other two approaches. This result tells that the numerical model used in numerical approach has a little difference as compared to actual system. Finally, modal validation process is conducted while repeating the numerical model updating in order to reduce this difference.

Table 1.1 Description of plate and brake-disk and experimental setup
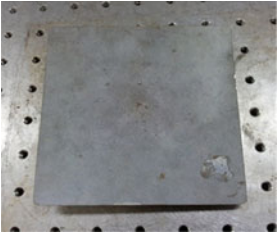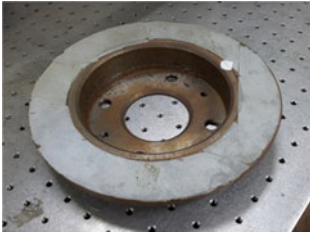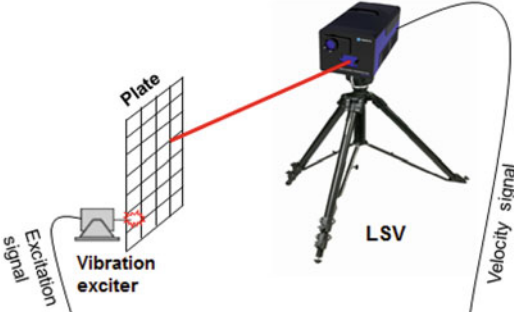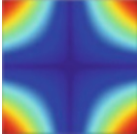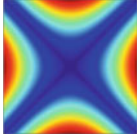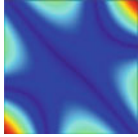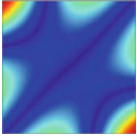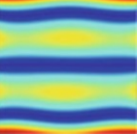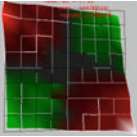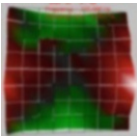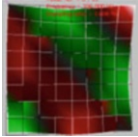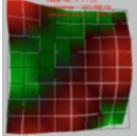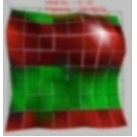
Objectives		
	Plate	Brake-disk
Material properties	1. Dimension: $0.119 \times 0.119 \times 0.0006$ (m^3) 2. Density: 2,700 (kg/m^3) 3. Young's Modulus: 75 (GPa) 4. Poisson's ratio: 0.3	1. Density: 7,450 (kg/m^3) 2. Young's Modulus: 115 (GPa) 3. Poisson's ratio: 0.33
Boundary condition	Free–free condition	
Experimental setup		

Table 1.2 Modal parameter results of a plate

	1	2	4	5	6
Analytical approach (Hz)	145.076	212.833	376.687	376.687	661.719
Numerical approach (Hz)	144.515	210.729	373.430	374.450	656.764
Experimental approach (Hz)	144	225	336	343	536

1.3.1.3   Conclusion of Midterm Project

Students have an opportunity to apply the vibration theory into the real system through a modal analysis using analytical, numerical and experimental approach. Moreover, students can understand the features and pros and cons of the each modal analysis approach. Lastly, they can learn the process of numerical model updating and validation based on the experimental result.

1.3.2   Individual Project

Individual project proceeds with proposal and presentation. First of all, the description of the project and the information regarding student final goal are presented in the proposal, the students have to show detail project overflow, as develop through discussion and brainstorming. The evaluation on the conducted individual project is carried out depending on the

Table 1.3 Modal parameter results of a brake-disk

	1	2	3	4
Numerical approach (Hz)	1,358.199	2,555.593	2,578.565	3,050.416
Experimental approach (Hz)	1,434	2,616	2,912	3,370
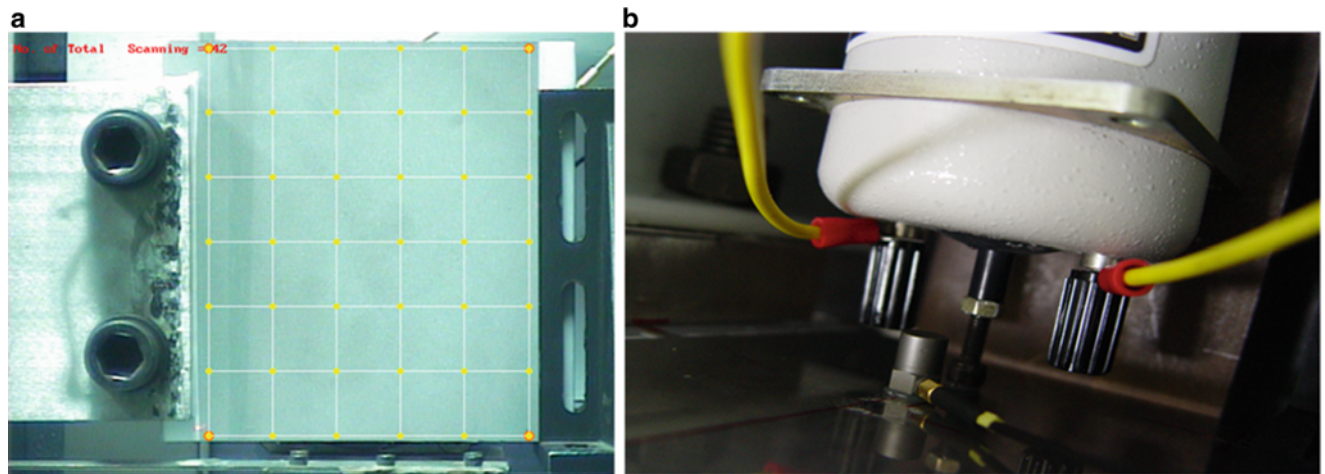
Fig. 1.8 (**a**) Experimental configuration and measured nodes using LSV (**b**) Attached vibration exciter and accelerometer on the backside of the plate as an operator and a reference

novelty, difficulty, degree of performance compared to the proposal, presentation material, etc. In this paper, a research on the damage detection by using operating deflection shape (ODS) is introduced, which is selected from the presented researches. Its purpose is to find out the location of damage or failure of a mechanical system by comparing [through Eq. (1.11)] the deflection shapes between un-damaged and damaged one. This project is briefly introduced in the following Figs. 1.8 and 1.9. This research performed in the class was published in the journal paper [7].

$$\text{Damage detection} = (\varphi_{h_i} - \psi_{u_i})^2 \qquad (1.11)$$

1.4 Conclusion

This paper is an introduction given to graduate students in vibration class at GIST, Korea. Vibration class contents and individual projects are introduced. These individual projects are assigned to the students for better understanding of vibration by applying the vibration theory that they learned in the class to the real mechanical system. Midterm project is used to familiarize the students with the vibration system using analytical numerical and experimental approach. Finally, validation of the numerical model is conducted using model updating procedure. Another individual project is assigned to combine the theory with the individual research topic of the respective student. Moreover, Appendix covers the syllabus of the vibration class and the explanation of the commercial non-contact sensor developed and used by this laboratory.
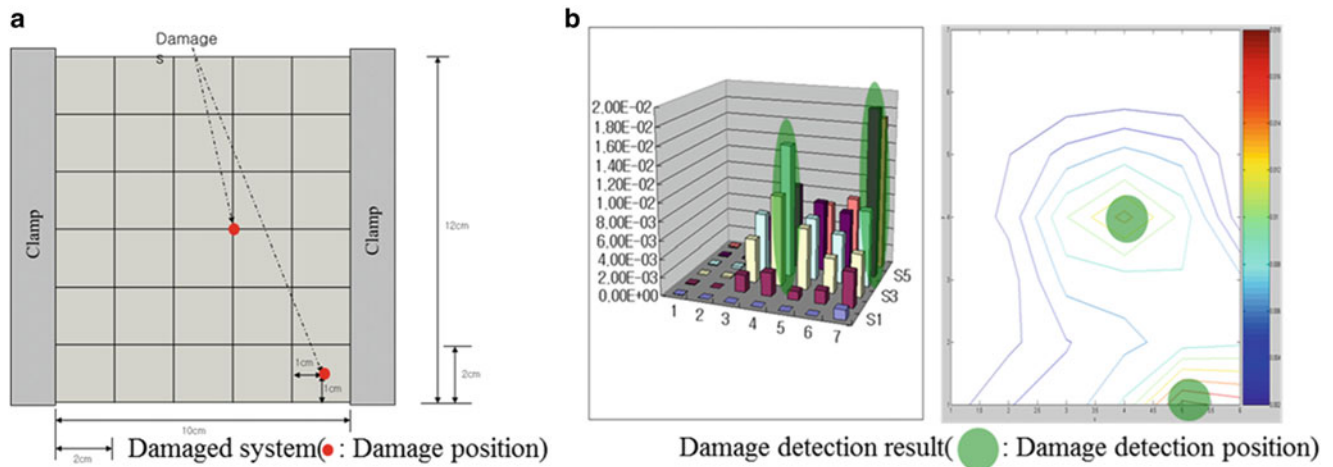
Fig. 1.9 (**a**) Locations of the damages (**b**) Comparison result between damaged ODS and un-damaged ODS bar and contour plot

A.1 Appendix

A.1.1 Syllabus

5603 Advanced Vibration Summary:
In this course, vibration phenomena of electro-mechanical systems due to dynamic load is studied. It covers from single DOF to multi DOF and theory as well as numerical and experimental methods. It deals various subjects: Lagrange equation, Laplace transformation, Fourier transformation, mode superposition, finite element method, experimental modal analysis, random vibration, mode component synthesis, rotor dynamics, vibro-acoustics.

Text:

1. *Theory of Vibration with Applications*, 5th ed., W. T. Thomson and M. D. Dahleh, Prentice Hall, 1998.

References:

2. *Vibration with Control*, D. J. Inman, Wiley, 2006.
3. *Structural Dynamics: An Introduction to Computer Methods*, R. R. Craig, John Wiley & Sons, 1981.
4. *Finite Element Procedures*, K.J.Bathe, Prentice Hall, 1996.

Prerequisites by Topics:
Engineering Mathematics
Fundamental Vibration
Tools Used:
Experimental Modal Analysis: Laser Scanning Vibrometer, Pulse Modal Test, LMS CADA-X
FEA codes: MSC/NASTRAN, ANSYS, COMSOL, SYSNOISE
Math tools: Matlab

Topics:
SDOF [1]
Free Vibration (damp free, damped)
Forced Vibration (unbalance, vibration isolation, damping)
Transient Vibration (impulse, arbitrary, shock)
MDOF [1]

(continued)

(continued)
MDOF (mode, forced harmonic vibration)
Properties of Vibration Systems (flexibility influence, stiffness influence, Castigliano's theorem, modal matrix)
Lagrange's Equation (virtual work, Hamilton's Equation)
Vibration Test [2]
Measurement Hardware
Digital Signal Processing
Random Signal
Mode Shape
Computational Methods [3]
Finite Element Method
Static Problem (Gaussian elimination, Cholesky decomposition)
Eigenvalue Problem (Rayleigh method, Lanczos)
Harmonic Problem (direct frequency, modal frequency)
Acoustics
Transient Problem (direct integration, mode superposition)
Component Mode Synthesis [2]
Static Condensation/Super Element
Component Mode Synthesis
Design Sensitivity Analysis
DSA of Static Problem
DSA of Eigenvalue Problem
DSA of Noise and Vibration
Random Vibration [1]
Vibro-acoustics
Rotor Dynamics

Exams: Midterm (35)
Projects: 2 (15, 30)
Homeworks: (20)

A.1.2 Introduction to the Development of Laser Scanning Vibrometer

A.1.2.1 Motivation of LSV Development

In general, vibration measurement equipment is essential in the development process of the structure system, which is used to identify the vibration characteristics of the structures including electric motors, automobiles, aircraft structures, nuclear reactors, towers, etc.

In the past, the contact sensor is mostly used in identifying vibration characteristics. However, the contact sensor can induce changes in the dynamics characteristics of the structure and has several limitations in vibration measurement due to its own features. For these reasons, the demand for the laser vibrometer is on the increase globally [8].

Currently, the most famous and expensive laser vibrometer has been developed by Polytec. However, as it is too expensive, intelligent system design laboratory (ISD) and venture company "EM4SYS" (www.em4sys.com) are collaborating for the development of the LSV (Fig. 1.10) in the School of Mechatronics of Gwangju Institute of Science and Technology.

A.1.2.2 Specification of LSV

Next is the specification of LSV as shown in Table 1.4 [9].
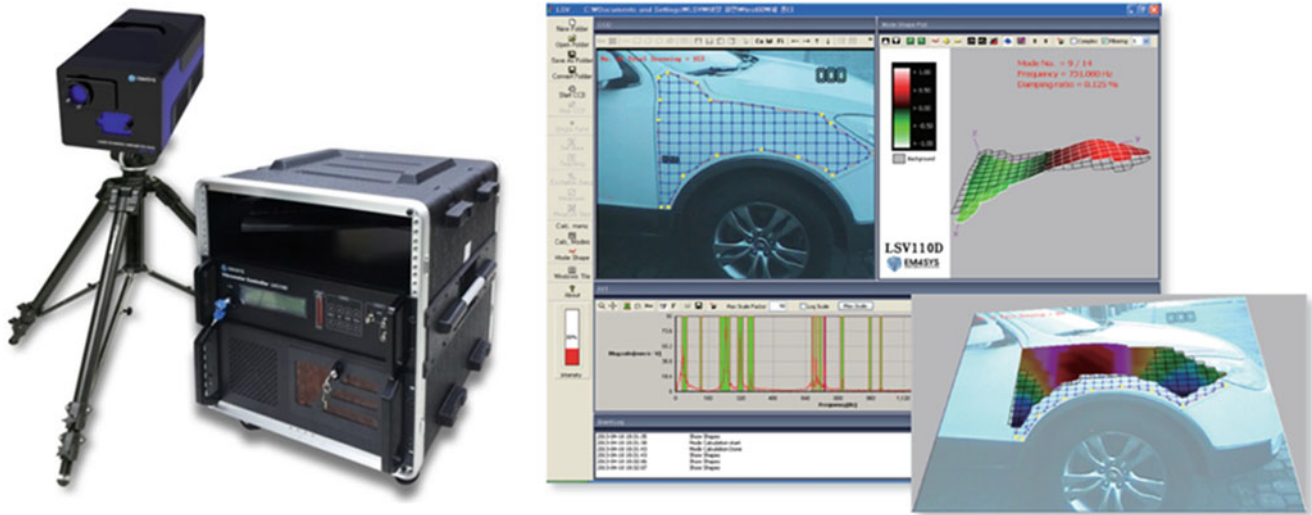
Fig. 1.10 Image of Laser Scanning Vibrometer (LSV)

Table 1.4 Specification of laser scanning vibrometer

ESV-200	Laser scanning vibrometer			
Laser wavelength	He–Ne laser 632.8 nm, Class II <1 mW, eye-safe			
Laser beam size	100 μm at 1 m distance			
Working distance	0.4–40 m (depending on reflection condition)			
Sample size	Several mm^2 up to m^2 range (depending on distance)			
Maximum velocity	2,530 mm/s			
Velocity output	$\pm$10 V (analog)			
Velocity gain	3 mm/s/V	15 mm/s/V	30 mm/s/V	120 mm/s/V	240 mm/s/V
Displacement gain	4 μm	20 μm	40 μm	160 μm	320 μm
Velocity resolution	0.5 μm/s			
Frequency range	2 Hz to 40 kHz			
Low pass filter	1 kHz	5 kHz	10 kHz	20 kHz	50 kHz
Scan grid	Multiple grid densities and coordinate systems			
Scan angle	25° $\times$ 25° scanning range			
Angular resolution	0.01°			
Scan speed	Up to 10 pts/s			
Power	220 V AC (50/60 Hz), 70 W			
Operating temperature	+5 $^\circ$C to +40 $^\circ$C			
Storage temperature	−10 $^\circ$C to +65 $^\circ$C			
Relative humidity	Max. 80 %, non-condensing			
Dimension (mm)	Head		Controller	
	305 $\times$ 200 $\times$ 160 (L $\times$ W $\times$ H)		360 $\times$ 435 $\times$ 132 (L $\times$ W $\times$ H)	
Weight	Head		Controller	
	10 kgf		11 kg	

A.1.2.3 Features of LSV

1. Noncontact vibration and displacement measurement
2. Quick and easy to setup
3. Time and cost saving with no transducer mounting, wiring, and signal conditioning
4. Modal analysis by measuring the complete spectra of all scanned points
5. Operational deflection shape (ODS) analysis by measuring the operating structural vibration
6. Dynamic displacement visualization of a vibrating object with an arbitrary shape
7. 3D vibration measurement using a single laser scanning vibrometer by moving to three different locations

Table 1.5 Software features of laser scanning vibrometer

Analysis	Modal Analysis (Peak-picking method) and operational deflection shape (ODS) Analysis
Versatile mesh generation	Line, rectangle, circle, polygon, copy and delete and rotate and resize
Excitation signal	Random, sine-sweep, hammering
Data analysis	Data export to universal file format (UFF) for Me'scopeImport to MATLAB/ MS EXCEL
Time data	Measured time data is saved automatically in the setup folder
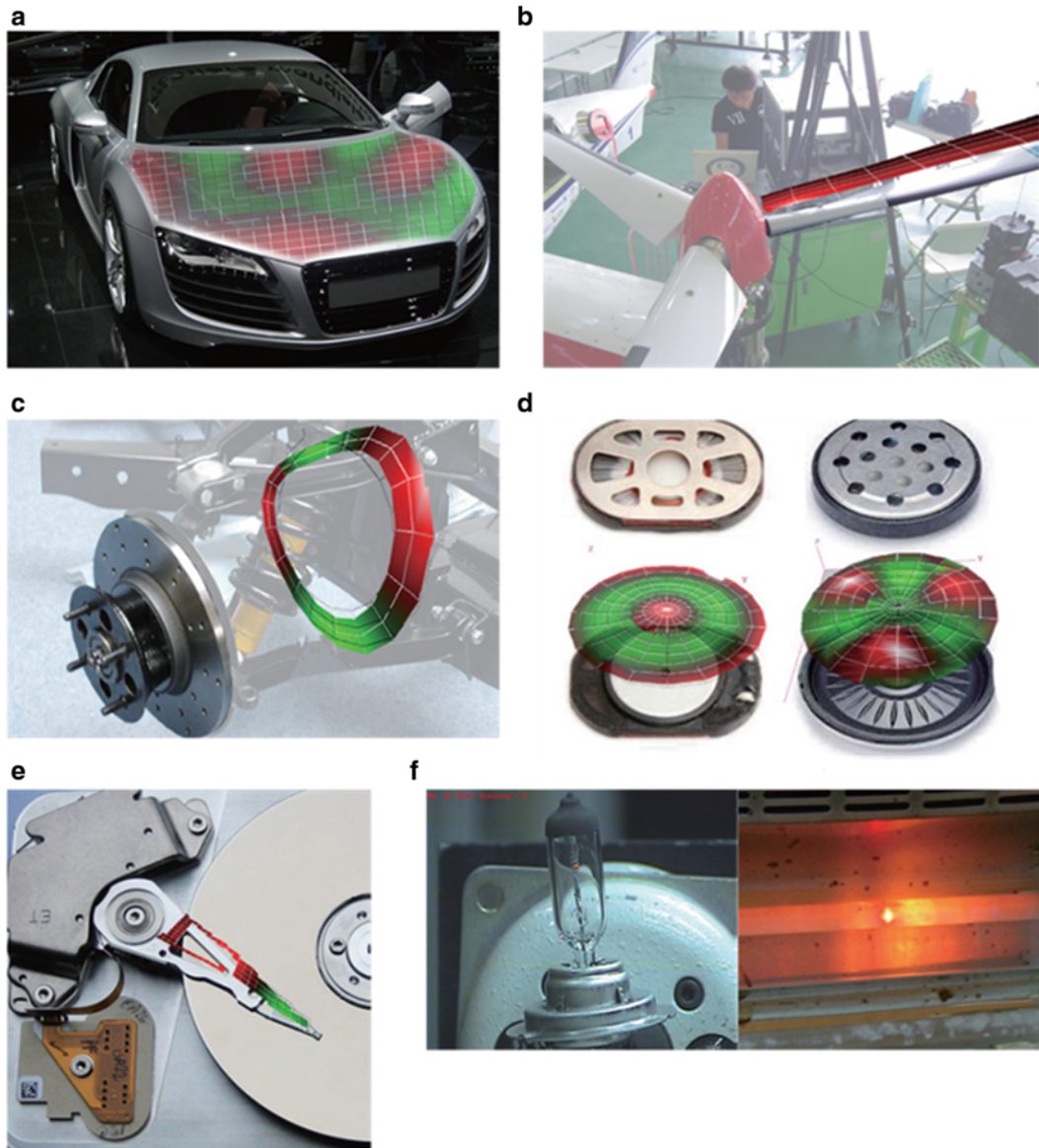
Fig. 1.11 Applications of Laser Scanning Vibrometer (**a**) automobile (**b**) aircraft (**c**) brake-disk (**d**) micro-speaker (**e**) hard disk (**f**) small scale and heated object

A.1.2.4 Software Features of LSV

Next are software features of LSV as shown in Table 1.5.

A.1.2.5 Applications of LSV

There are a lot of applications of laser scanning vibrometer as shown in Fig. 1.11.

References

1. Thomson WT, Dahleh MD (1998) Theory of vibration with applications, 5th edn. Prentice Hall, Englewood Cliffs, NJ
2. Inman DJ (2007) Engineering vibration, 3rd edn. Prentice Hall, Englewood Cliffs, NJ
3. Craig RR (1981) Structural dynamics: an introduction to computer methods. Wiley, New York
4. Bathe KJ (1996) Finite element procedures. Prentice Hall, Englewood Cliffs, NJ
5. Ewins DJ (2000) Modal testing: theory, practice and application, 2nd edn. Research Studies Press, Baldock, Hertfordshire, England
6. Leissa AW (1973) The free vibration of rectangular plates. J Sound Vib 31(3):257–293
7. Bae WK, Kyong YS, Park KH, Dayou J, Wang SM (2011) Scaling the operating deflection shapes obtained from scanning laser Doppler Vibrometer. J Nondestruc Eval 30(2):91–98
8. SPIE Annual Report, 2000
9. Catalog of 'Laser Scanning Vibrometer, VIXCEL Series', EM4SYS, 2013

Chapter 2
Lab Exercises for a Course on Mechanical Vibrations

Anders Brandt

Abstract This paper presents some exercises designed to teach fundamental aspects of mechanical vibrations in general, and experimental techniques for vibration measurements in particular. Teaching students to become good experimentalists is a very difficult task, and is perhaps not even possible inside standard curricula. However, some fundamental aspects of experimental work must be taught, and can be included in a course on vibrations as well as in other courses. The first exercise is designed to teach the student how careful one has to be when applying vibration sensors to a structure, and is based on the repeatability of mass calibration measurements. This makes it a good exercise to base a discussion on experiment setup and repeatability issues etc. The second exercise is an exercise where an approximate single-degree-of-freedom (SDOF) system is investigated by some simple analytical calculations as well as by an experimental measurement. This exercise serves to demonstrate the rather abstract notion of SDOF, and also illustrate the applicability of a simplified model in a limited frequency range. Finally, a third exercise is made where modal analysis of a slalom ski using impact testing is used as a demonstration of more advanced vibration analysis.

Keywords Vibration measurement • Teaching vibration • Mass calibration • Accelerometer mounting • Experimental modal analysis

2.1 Introduction

Making accurate vibration measurements is known to be rather difficult due to the many challenges of sensor choice, sensor mounting, and, in the case of investigation of eigenfrequencies (modal analysis), for example, the problems of suspending the structure properly. As this paper describes some exercises designed to teach students some good practice for vibration measurements, additional difficulties for students are often that they are not yet mature when it comes to perform good measurements; i.e. they have not yet learnt to be patient, to double check everything, etc.

The course, for which the exercises described in the present paper are used, is a graduate (master) level course of a third semester length. The students have had a course on general signal processing, but are unfamiliar with the particular measurement and analysis techniques for vibration analysis. In the course, both wave theory of continuous structures and discrete mechanical systems are taught; the exercises covered in the present paper, however, focuses on the discrete system description of mechanical systems.

The particular difficulties of vibration measurements addressed by the exercises described here are

- to learn some experimental methodology to ensure good experimental results, such as checking repeatability, double checking everything that could potentially affect the measurement, etc.,
- to yield respect for the particular difficulties of applying accelerometers correctly, and
- to correctly suspend a structure under free–free conditions for experimental modal analysis

An additional point which is very important for these exercises is, of course, to tie the theory taught in the course to experimental results.

A. Brandt (✉)

Department of Technology and Innovation, University of Southern Denmark, Campusvej 55, 5230 Odense M, Denmark
e-mail: abra@iti.sdu.dk

Perhaps a good way to summarize the spirit of the exercises described here is to use the famous quote by Albert Einstein; "A theory is something nobody believes, except the person who made it. An experiment is something everybody believes, except the person who made it." The exercises described in this paper, addresses first and foremost the second part of this quote; the importance of being in constant doubt over ones experimental results. The exercises are, however, also touching on the essence of also questioning *theoretical results*, and the importance of verifying ones theories (which in our engineering terminology are, of course, usually called *models*).

2.2 Exercises

The exercises we are about to describe here, require some basic vibration measurement equipment and sensors. The measurement hardware and software can be essentially any vibration measurement system. We are using a National Instruments 9234 USB box, driven by homemade MATLAB software using the Data Acquisition Toolbox, and the free ABRAVIBE [1] toolbox for the analysis. This means that the students record time data, for subsequent analysis in MATLAB. We have found that this ensures that the students understand every step in the processing of the data; something more "automatic" commercial systems often make more difficult.

On the sensor side, in the exercises we use two accelerometers, a force sensor, an impact hammer, and a shaker with amplifier and random noise generator. Which particular sensors used are not particularly important, although the accelerometers should weigh less than 10 g, the force sensor should be of suitable sensitivity, and the same is true for the impact hammer. We currently use Dytran 3097A2T accelerometers with a sensitivity of 100 mV/g and mass of 4.3 g. The force sensor is a Kistler 9712B50 with a sensitivity of approximately 20 mV/N, and the impulse hammer is a Dytran 5800B3T with a sensitivity of approximately 10 mV/N.

In addition to this, some relatively inexpensive measurement objects are needed, which will be described in conjunction with each exercise. The first three exercises described in Sects. 2.2.1–2.2.3 are made at one instance in the laboratory, in approximately 2 h, followed by 4–6 h of analysis and report writing. The last exercise, described in Sect. 2.2.4, is accomplished in a second laboratory session, in approximately 4 h, followed by 6–8 h of analysis and report writing.

2.2.1 Mass Calibration

The first exercise we present, is based on calibration of an accelerometer (or a force sensor in an impact hammer) using a simple mass, as depicted in Fig. 2.1. This well-known technique, see for example [2], should be familiar to everyone making vibration measurements. It is a good technique not only for calibration, but also for checking that accelerometers are functional through the full frequency range, and for checking which frequency range a particular accelerometer can be used for (see Sect. 2.2.2), etc.

The calibration procedure is simple; the accelerometer is attached to a mass, typically a piece of round rod of steel. The weight of the mass is accurately measured, and should be different depending on the impact hammer used, so that a soft hit with the hammer produces a suitable acceleration level. For this exercise we use a weight of approximately 1 kg, made of a piece of rod with approximately 40 mm diameter. The mass is hanging in two strings from a supporting rig, so that it can
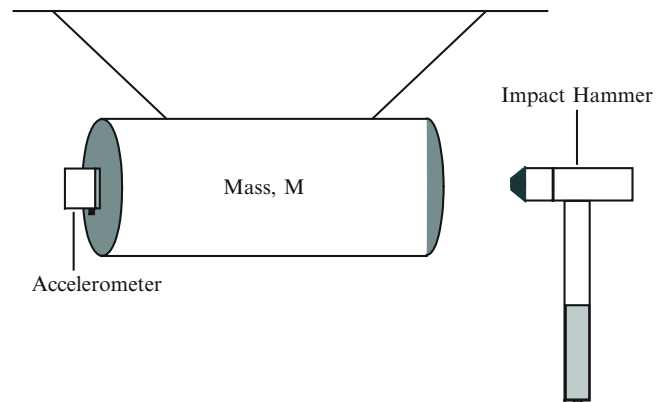
Fig. 2.1 Setup for mass calibration for the exercise described in Sect. 2.2.1

move as a pendulum in the direction of the accelerometer as illustrated in Fig. 2.1, or alternatively placed on a soft foam pad. The mass is then excited by the impact hammer, while the force and accelerometer signals are recorded. The hardest tip for the hammer is chosen, to yield a frequency range as high as possible, typically up to 10 kHz. To give better accuracy, several impacts can be averaged, although this is generally not necessary if the sensitivities of the force sensor in the impact hammer and the accelerometer are appropriate, so that the measurement noise is minimal.

After the time signals with the impact force and resulting acceleration are recorded, the students calculate the frequency response (FRF) of acceleration with force. Since Newton's well-known formula for a mass is $F = Ma$, this FRF should be a constant $H = A/F = 1/M$, i.e. the FRF forms a straight line, independent of frequency. The exercise is made so that the students are given the sensitivity of the force sensor in the impact hammer, but not the sensitivity of the accelerometer: They are then asked to calculate the sensitivity of the accelerometer, given the measured frequency response at, for example, 159.2 Hz, which is equal to 1,000 rad/s, a common frequency for this purpose.

2.2.2 Accelerometer Mounting

The next exercise is using the mass calibration method described in Sect. 2.2.2 to investigate the effects of different mounting techniques for mounting accelerometers. This exercise has several important objectives; first of all it obviously discusses different means of attaching an accelerometer to the test structure and, as we will see, what performance these mounting techniques result in. Second of all, it demonstrates the difficulty of getting repeatable measurements, as in most cases the students do not get the same result even if they use the same mounting technique twice. This also makes a good point of discussing the concept of repeatability, and the importance of this concept in engineering (or science in general). Third, I am using this exercise to teach the students not to trust their measurements, until they have investigated that the accelerometer they use with a particular mounting technique, actually has a frequency range high enough for the measurements they want to make; this is very easily investigated by using the mass calibration method. Fourth, this exercise also illustrates that accelerometers, like all measurement sensors, are not perfect, but vary rather much with frequency.

In this exercise, the students use some different techniques to mount an accelerometer on the calibration mass, and perform measurements as described in Sect. 2.2.2. For each measurement the FRF is calculated and stored. In our case we mount the accelerometer with the following techniques:

- a thin layer of wax,
- a thick layer of wax,
- a thin layer of hot glue (hot melt adhesive, using a "hot glue gun"), and
- super glue (cyanoacrylate adhesive)

Other techniques such as screw mount and magnetic base could also be used. They are, however, somewhat difficult to make identical to the techniques above, as they change the mass of the accelerometer unit.

Since the students already have made a measurement with a thin layer of wax in the first exercise, this means that they obtain a total of five different FRFs, of which the two first should be identical (or very similar). These two FRFs based on a thin layer of wax are first compared. Regardless of whether they are identical or not (often they are not; usually because of too much wax) a fruitful discussion on repeatability issues is held, and the students who gets almost identical results are told that they have applied a sufficiently thin layer of wax. Many students are surprised how thin this layer has to be to yield identical FRFs.

As the next step in this exercise, the students are asked to plot all five FRFs in one plot, and determine which of the mounting techniques works best. This produces a plot similar to Fig. 2.2, where the FRFs have first been normalized to have the same value at 159.2 Hz, and limits of ± 5 % around this value are plotted, to indicate the accuracy limits specified by the sensor manufacturer. Note that only one of the two thin wax measurements is included in the figure, which is for clarity only. The students are finally asked to find the frequency where the error reaches 5 % for all mounting techniques, and find the technique giving the highest frequency limit. This often results in a dead-end between superglue and wax.

It should be stressed, and we do this during the lab exercise, that the frequency range obtained by the method described here, is not necessarily the frequency range obtained when the accelerometer is mounted in a point with less stiffness, such as on a lightly damped structure. It is therefore necessary to consider the obtained frequency range found on the calibration mass as a maximum frequency range, and to use some margin when using the accelerometer on a real structure.

Fig. 2.2 Comparison of the
FRFs from four measurements on
a mass, using four different
mounting techniques as described
in Sect. 2.2.2. The FRFs are
normalized to the same value at
159.2 Hz (1,000 rad/s) (from [2],
Copyright 2011, John Wiley and
Sons; reprinted with permission)
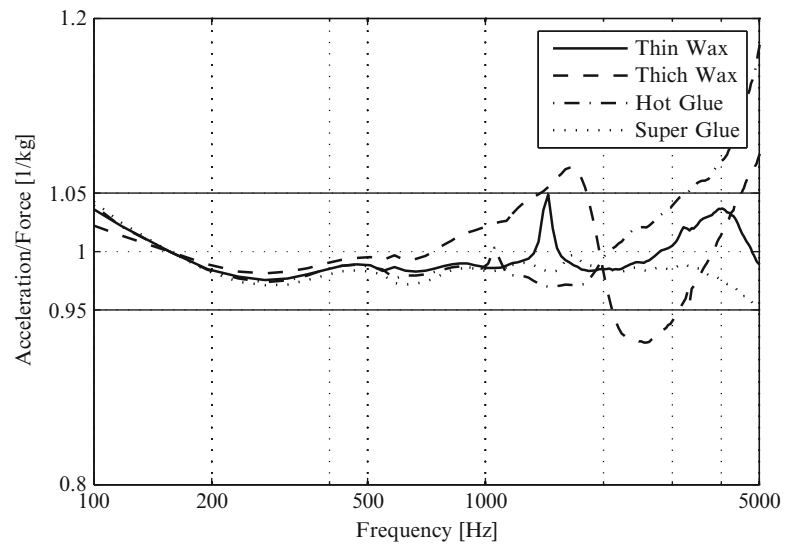
Fig. 2.3 Schematic illustration
of the approximate SDOF system
used for the exercise described in
Sect. 2.2.3
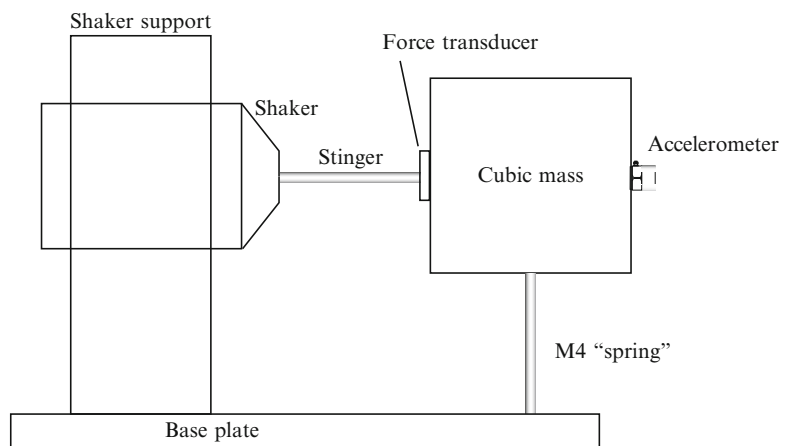
2.2.3 SDOF Measurement and Analysis

The single degree of freedom (SDOF) system is a key component in vibrations and structural dynamics. In this exercise, a simple system behaving as an approximate SDOF system is investigated, and used to illustrate the connection between theory and real world to the students. The system used is shown schematically in Fig. 2.3, and consists of a base plate of steel, approximately $100 \times 300 \times 10$ mm; a steel cube with 30 mm side length; and a M4 bolt, approximately 50 mm long. There are two locking nuts locking the M4 bolt against the base plate and the mass. The mass is excited by a random force applied by a shaker through a stinger and a force sensor, and an accelerometer is mounted on the opposite to the force sensor. The FRF between the force and the acceleration is measured and compared to analytical results.

This exercise has several objectives; first it illustrates that the SDOF system used in theory can, at least in a limited frequency range, be found in "real life". Second, it allows for discussion between model and reality, since the results obtained are rarely identical to the analytical results calculated by the students.

The stiffness of the M4 bolt is readily calculated using known formulas for moment of inertia and stiffness of a beam, and is omitted here so that professors can include this step as an exercise for the students with having direct access to the answer. The students are asked to measure the various components, and estimate the mass of the cube, including the accelerometer, and the stiffness, and from this estimate the "SDOF" natural frequency.

From the measured FRF, the students are asked to approximately estimate the natural frequency and damping (through the -3 dB bandwidth and natural frequency). Once these parameters are obtained, the students should calculate the mass, stiffness, and damping coefficients of the system. The mass and stiffness coefficients thus obtained are compared with the mass calculated from the measurements of the cube, and the stiffness calculated for the beam. Since the results rarely compare particularly closely due to the lack of "precision" in the setup, it forms a good discussion point for differences between model and reality.

2.2.4 Full-Scale Modal Analysis Test

After the initial exercises described in Sects. 2.2.1–2.2.3, the students are well suited for the second exercise; a full experimental modal analysis test of a slalom ski using impact excitation with roving hammer. The students are asked to read the text [3] prior to the lab exercise, so that they are acquainted with the theory, and particularly with the practical aspects of an experimental modal analysis test.

The choice of the slalom ski is, of course, rather arbitrary, and almost any linear structure could be used. The idea with using the slalom ski instead of a more simple beam or plate, is that the students, in our experience, find it more interesting to measure a "real" object. Therefore an automotive component or any other simple structure would work equally well.

The exercise is rather straight forward. First, the structure is suspended, and a discussion is held on how to best suspend this long, slender, structure. The "correct" answer is, that it should be suspended hanging vertically, as this ensures the rotational rigid body mode is low, which is very difficult to obtain if it is supported horizontally. This is the case for all long, slender structures with small moments of inertia around the long axis. In our case, the ski has a small drilled hole in the back end, in the center of the ski in the "short" direction. Through this hole, a fishing line is threaded, forming a loop, to which a rubber cord is attached. The reason for this is that the rubber cord could add damping to the ski if it was in direct contact with the ski. Second, the ski is instrumented with accelerometers in two corners, for a minimum multi-reference test. We thus discuss the potential use of even more sensors, and the advantages with that. Third, the impact hammer tip, suitable frequency range, etc. are investigated by some rough measurements. Proper FRF estimation settings such as trigger level, pretrigger condition, block size, and force and exponential windows, are then obtained by the procedures laid out in [2, 4], which are supported by the command `impsetup` in the ABRAVIBE toolbox [1].

After these optimal settings are obtained, the experimental setup is investigated for two things: (1) is the suspension affecting the structure?, and (2) are the measurements free from mass loading effects from the accelerometers? The first point, the suspension effects, are investigated by changing the suspension, which in this case is a rubber cord, by extending the length so as to almost double it (or some sufficient change). FRFs measured before and after this change are compared, and if they differ in the frequency range of interest, the reasons for this are discussed; obviously the suspension is then wrong (Is it too short? Or is there friction between the ski and the fishing line? Or are the cables for the accelerometers "pulling" the structure, adding damping? Etc.) The second point, mass loading, is investigated by mounting an additional accelerometer right next to one of the existing accelerometers, and making a new measurement. If the new FRF is different from the previous without the extra mass next to the accelerometer, there is apparently mass loading with the double mass of two accelerometers. The risk of having mass loading even when using a single accelerometer is then imminent. Actually, avoiding mass loading on the slalom ski requires very low weight accelerometers, due to the low damping, so with the 4.3-g accelerometers used in this exercise there is some mass loading, affecting the frequency range of the higher modes. This becomes a point of discussion, and I still have not had a single student who has thought that mass loading would occur with this small light sensor on this ski.

Finally, when everything is checked and the students are satisfied that everything is in order, the ski is excited in all points, one by one, in a 3×7 grid, and time data are stored at each point for later processing by the ABRAVIBE command `impproc` [1, 4]. Before leaving the lab, the students are encouraged to post process all their time data and make a first curve fitting using a MATLAB script given to the students prior to the lab exercise, to ensure that they get some reasonable good looking stabilization diagrams. This step only takes 10–15 min, and ensures that the students leave with good data that allows for the rest of the analysis to be performed outside the lab.

2.3 Conclusions

We have described four exercises whereof three fundamental exercises which teach students some good experimental practices as applied to vibration measurements, and illustrate the concept of model versus reality. The three exercises comprises an exercise to learn to apply mass calibration using and impact hammer and an accelerometer, and an exercise to compare different mounting techniques such as wax, hot glue, and super glue. The third exercise is demonstrating measurements on an approximate single degree of freedom (SDOF) system, and to identify the mechanical properties of this system using an experimentally obtained frequency response function (FRF). A fourth exercise, a complete experimental modal analysis of a slalom ski, is then performed using impact testing, giving the students experience of this important measurement technique, and some of the issues one has to watch for applying it. The exercises are suitable for students which have had some introduction to signal processing, but not necessarily vibration analysis procedures.

Although it is difficult, if not impossible, to teach students to be good vibration experimentalists in a few hours of lab exercises, some key points can surely be taught. The main points thus taught in the exercises presented in this paper are

- Summarizing the message, it is: do not "trust" anything that can be tested easily. This applies for example to

    - if the useful frequency range of your accelerometer is sufficient, using the same mounting technique you are going to use in your experiment; do not trust the data sheet frequency range!
    - if there are mass loading effects from your accelerometers; do not trust your intuition!
    - if the suspension affects your measured FRFs, do not believe it does not—investigate it!
    - if there are effects, on damping for example, from accelerometer cables; again—investigate it!

- A model is always limited and should be verified by experiments
- Measuring FRFs with impact testing, the measurement settings need to be optimized to ensure best possible FRFs

References

1. Brandt A (2011) ABRAVIBE – A MATLAB toolbox for noise and vibration analysis and teaching. http://www.abravibe.com
2. Brandt A (2011) Noise and vibration analysis: signal analysis and experimental procedures. Wiley, Chichester
3. Brandt A (2013) Notes on using the ABRAVIBE toolbox for experimental modal analysis. http://www.abravibe.com
4. Brandt A, Brincker R (2011) Impact excitation processing for improved frequency response quality. In: Proceedings of 28th international modal analysis conference, Jacksonville

Chapter 3
Variational Foundations of Modern Structural Dynamics

Robert N. Coppolino

Abstract The foundations of modern structural dynamic analysis are presented from a historical perspective. Underlying variational principles due to d'Alembert, Hamilton and Lagrange are reviewed, followed by subsequent key contributions to approximate analysis. Closely related procedures introduced by Ritz, Galerkin and Trefftz are described in terms of their original application to continuum boundary value problems. The role these procedures played in the development of the Finite Element Method and Matrix Structural Analysis is described. Finally, the continuing influence of variational principles in structural dynamics and mathematical physics in general is outlined.

Nomenclature

$[A_p]$	Acoustic surface area matrix
$[C]$	Damping matrix
$[C_p]$	Acoustic compliance matrix
E	Elastic stiffness property
F	Force
$[G]$	Transformation matrix
$[K]$	Stiffness matrix
L	Lagrangian
$[M]$	Mass matrix
N.B.C	Natural boundary condition
$[P]$	Modal participation factor matrix
P.D.E	Partial differential equation
$\{Q\}$	Modal generalized forces
S	Surface area
S_p	Acoustic susceptance matrix
T	Kinetic energy
U	Potential or strain energy
V	Volume
W	Work
m	Mass
$\{p\}$	Acoustic pressure array
q	Generalized coordinate (displacement)
t	Time
u	Displacement
x, y, z	Position
$[\Phi]$	Modal matrix

R.N. Coppolino (✉)

Measurement Analysis Corporation, 23850 Madison Street, Torrance, CA 90505, USA

e-mail: bobcoppolino@gmail.com

$[\Gamma]$	Force allocation matrix
$[I]$	Identity matrix
Ψ	Shape function
α, β	Proportional damping constants
δ	Variation
ϵ	Strain
λ	Eigenvalue
ρ	Mass density
ω_n	Natural frequency
ζ_n	Critical damping ration

3.1 Introduction

The development of mathematical physics, of which structural dynamics is a branch, owes its present state to two general viewpoints. The first viewpoint due to Newton [1] sees nature following postulates describing the dynamic equilibrium of interacting bodies. The second viewpoint, due to d'Alembert [2], Hamilton [3] and Lagrange [4], sees nature following postulates describing efficient organization of energies (variational principles). The variational viewpoint, specifically Hamilton's principle, has guided the development of partial differential equations and natural boundary conditions for technical structural theories [5, 6].

Difficulties encountered in the quest for exact solutions of partial differential equations, subjected to natural boundary conditions, led to the introduction of approximate techniques based on Hamilton's principle. Ritz [7] employed assumed shape functions and generalized coordinates to deduce mass and stiffness matrices, which are foundational to the Finite Element Method [8] and Matrix Structural Analysis [9]. Galerkin [10] similarly applied assumed functions to a variational integral associated with a system's partial differential equations; his formulation, while influential in development of the Finite Element Method, has also been applied to solve nonlinear dynamic problems [11]. Trefftz [12] introduced a novel variational technique focusing on approximate satisfaction of natural boundary conditions, which are a byproduct of Hamilton's principle; his employment of shape functions that automatically satisfy the system's partial differential equations forms a basis of the boundary element method [13].

Hamilton's principle and the Ritz method, in particular, have been instrumental in the development of both the Finite Element Method and Matrix Structural Analysis. The basic building blocks of the Finite Element Method are most often developed on the basis of assumed boundary displacement referenced and optional interior displacement shape polynomials, which are used to define element mass and stiffness matrices based on the Ritz method. Assembly and analysis of structural system models falls in the category of Matrix Structural Analysis, which for a time before general acceptance of the Finite Element Method employed a force (degree of freedom) method. The force method was based on a complementary variational principle introduced by Castigliano [14].

Free vibration analysis of a matrix structural system is typically performed on an undamped system, for which the modes or real eigenvectors satisfy a mass weighted orthogonality relationship. Free vibration analysis of a damped structural system is rarely performed due to difficulties associated with theoretical damping matrices that do not relate to empirical modal damping. An alternative to the explicit damping matrix, namely a complex structural damping constant, is often employed in aeroelastic analysis [15]. The more widely used description of damping is based on critical damping ratio factors assigned to a truncated set of undamped system modes.

Several strategies for (a) computation of system modes and natural frequencies, and (b) accurate computation of system responses are consequences of Mach's interpretation of d'Alembert's principle [16]. In particular the iterative modal analysis procedures due to Vianello [17], Stodola [18] and Bathe [19] successively update inertial forces initially described by assumed mode shapes. Accuracy of computed system dynamic response associated with a truncated set of modes was greatly enhanced by a mode acceleration method introduced by Williams [20], which automatically accounts for the quasi-static response of higher frequency modes without explicitly solving for them.

During the 1960s the complexity of finite element models outpaced the development of digital computers and several authors developed procedures to treat system models piecemeal. Hurty [21] and Craig and Bampton [22] developed equivalent techniques known as component mode synthesis that described major structural components in terms of (a) generalized modal coordinates, and (b) physical boundary (interface) degrees of freedom. The Ritz-based building blocks (sometimes called substructures or superelements) associated with component mode synthesis exhibit the same features as finite elements.

Mathematical formulations and procedures based on variational principles continue to influence developments both in structural dynamics and other branches of applied physics. The complementary viewpoint introduced by Castigliano in 1873 was generalized for dynamics by Toupin [23]. Toupin's variational principle was found to be quite useful in fluid–structure interaction studies [24]. In addition, variational formulations that are direct consequences of Galerkin's method have been introduced by Biot [25] for heat transfer and MacNeal et al. [26] for electromagnetics.

3.2 Economy in Nature and Basic Variational Formulations

Philosophers of antiquity, well before the advent of modern science initiated by Newton [1], believed that nature operated in accordance with a rule of economy as noted by Aristotle (d. 312 BC), "Nature follows the easiest path that requires the least amount of effort". In the medieval era, William of Ockham (1347) suggested an economic principle for human reasoning with his famous saying, "It is futile to employ many principles when it is possible to employ fewer" (popularly known as Ockham's razor). It is fascinating that Newton's second law may be used as a postulate to deduce variational formulations of mechanics [2–4] (as theorems). Moreover, when the variational principle due to Hamilton [3], is postulated, Newton's second law follows as a theorem.

The postulate-theorem interrelationship is demonstrated below for a mechanical system composed of a single particle restricted to motion along one direction. Newton's second law [1] states the postulate,

$$F = \frac{d}{dt}\left(m\frac{du}{dt}\right) \tag{3.1}$$

D'Alembert [2] claimed that the system follows an "economy" in variational terms that

$$\left(F - \frac{d}{dt}\left(m\frac{du}{dt}\right)\right) \cdot \delta u = 0 \tag{3.2}$$

where "δu" is defined as a variation off the true path of "u". Hamilton [3] added to D'Alembert's principle by claiming that the following time integral is true:

$$\int_{t_1}^{t_2}\left(F - \frac{d}{dt}\left(m\frac{du}{dt}\right)\right) \cdot \delta u \cdot dt = 0 \tag{3.3}$$

After rearranging terms and integrating by parts, the above integral is expressed as

$$\int_{t_1}^{t_2}\left(\delta\left(\frac{1}{2}m\left(\frac{du}{dt}\right)^2\right) + F \cdot \delta u\right) \cdot dt - \left(m\frac{du}{dt}\right) \cdot \delta u\Big|_{t_1}^{t_2} = 0 \tag{3.4}$$

This variational integral is more compactly expressed as

$$\int_{t_1}^{t_2} (\delta T + \delta W) \cdot dt = 0 \text{ subjected to the end conditions } \left(m\frac{du}{dt}\right) \cdot \delta u\Big|_{t_1}^{t_2} = 0 \tag{3.5}$$

$T = \frac{1}{2}m\left(\frac{du}{dt}\right)^2$ is the system's kinetic energy and $\delta W = F\delta u$ is the system's virtual work. In addition, in order to curtail mathematical imposition of "Calvinist" predestination doctrine, we avoid imposition of the initial and final time constraints by extending t_2 to infinity and enforce two initial (state) conditions, namely that $u(0)$ and $\dot{u}(0)$ are specified. The variational integral defined in Eq. (3.5) is known as Hamilton's principle. A more familiar form of Hamilton's principle results from dividing the total applied force into two components, namely (a) a conservative potential energy (U) based force, and (b) a non-conservative component, which are expressed as

$$F = -\frac{dU}{du} + F_e \tag{3.6}$$

Thus the variational integral becomes

$$\int_{t_1}^{t_2} (\delta T - \delta U + \delta W) \cdot dt = \int_{t_1}^{t_2} (\delta L + \delta W) \cdot dt = 0 \tag{3.7}$$

where $L = T - U$ is known as the Lagrangian function.

The postulate-theorem relationship may be reversed by starting with Hamilton's principle as a postulate. Two consequences follow from this starting point in mechanics of distributed as well as single degree of freedom systems, namely, (a) Lagrange's equations [4], and (b) Newton's second law; both may be viewed as theorems resulting from the starting postulate.

3.3 Mathematical Physics and Hamilton's Principle

Much like the above discussion on dynamics of a particle, the partial differential equations of mathematical physics (in particular mechanics) may be derived on the basis of dynamic equilibrium (Newton's laws and free body diagrams) or on the basis of Hamilton's principle (energy and virtual work). Results of both approaches produce the same description. Application of Hamilton's principle to a dynamic system described as a continuum yields a volume integral of the type

$$\int_{t_1}^{t_2} \int_V (\delta T_V - \delta U_V + \delta W_V) \cdot dV \cdot dt = 0, \tag{3.8}$$

where T_V, U_V, and δW_V are the kinetic energy, potential (or strain) energy, and virtual work functions per unit volume, respectively. Analysis of any particular dynamic system, described in terms of displacement variables, $u(x, y, z, t)$, which may be vectors, results in the following type of functionals

$$\int_{t_1}^{t_2} \int_V (P.D.E) \cdot \delta u \cdot dV \cdot dt + \int_{t_1}^{t_2} \int_S (N.B.C) \cdot \delta u \cdot dS \cdot dt = 0 \tag{3.9}$$

"P.D.E" represents the particular partial differential equation(s) within the system's volume. "N.B.C" represents the natural boundary conditions, which are mathematically and physically admissible on the system's boundary surface(s). The general process for derivation of a system's partial differential equations and natural boundary conditions has provided a consistent basis for the development of technical structural theories for prismatic bars, beams, rings, plates and shells [5, 6].

3.4 The Contributions of Ritz, Galerkin, and Trefftz

Three outstanding contributions that led to the development of approximate analysis techniques date back to the early part of the twentieth century. The methods bearing the names of Ritz, Galerkin and Trefftz are all consequences of Hamilton's principle and the assumption of approximate solution functions.

3.4.1 The Ritz Method

A monumental contribution to approximate analysis was introduced by Ritz [7], who described the displacement field in variable separable terms

$$u\,(x, y, z, t) = \sum_{n=1}^{N} \Psi_n\,(x, y, z) \cdot q_n\,(t)\,, \tag{3.10}$$

where $\Psi_n(x, y, z)$ are assumed shape functions and $q_n(t)$ are temporal generalized coordinates (displacements). In addition, the strain field,

$$\varepsilon\,(x, y, z, t) = \sum_{n=1}^{N} \Psi_{\varepsilon,n}\,(x, y, z) \cdot q_n\,(t)\,, \tag{3.11}$$

is linearly related to the assumed displacement field employing the appropriate partial derivatives. It should be noted that exact closed form solutions of partial differential equations are often expressed in variable separable form, whenever such solutions are possible. By assuming a series of functions that satisfy particular boundary conditions (or generally permit solution of natural boundary conditions), substitution of Eq. (3.10) into Hamilton's principle (Eq. 3.8), the following symmetric matrix equations are deduced

$$[M]\,\{\ddot{q}\} + [K]\,\{q\} = [\Gamma]\,\{Q\} \tag{3.12}$$

where the positive semi-definite, symmetric mass and stiffness matrix terms are

$$M_{mn} = \int_V "\rho" \cdot \Psi_m \Psi_n dV, \; K_{mn} = \int_V "E" \cdot \Psi_{\varepsilon,m} \Psi_{\varepsilon,n} dV \tag{3.13}$$

[Note: "ρ" and "E" are representative of mass density and elastic stiffness material properties]. In addition, the generalized forcing terms are governed by volume and surface integrals associated with applied body forces and surface loads, respectively.

The Ritz method, outlined above, was initially employed to approximately solve difficult problems described by partial differential equations and associated natural boundary conditions. Ultimately, it was extensively applied in development of the Finite Element Method [8] and Matrix Structural Analysis [9].

3.4.2 Galerkin's Method

Galerkin [10] defined an approximate method using the variable separable displacement field and associated generalized coordinates (Eqs. 3.10 and 3.11) by substitution of the assumed functions into Eq. (3.9) where the boundary conditions are automatically satisfied by choice of an appropriate set of spatial functions. The general statement of Galerkin's method is

$$\int_V (P.D.E) \cdot \delta u \cdot dV = 0 \tag{3.14}$$

An appealing aspect of Galerkin's method is that it can be applied to any set of partial differential equations (even if a suitable variational formulation is unknown). The method has been successfully applied in the study of nonlinear dynamic systems [11].

3.4.3 Trefftz's Method

Trefftz [12] proposed an approximate method that employs a set of assumed functions that automatically satisfy the partial differential equations. Therefore the form of Eq. (3.9) that must be satisfied is

$$\int_S (N.B.C) \cdot \delta u \cdot dS = 0 \tag{3.15}$$

This method was generally ignored for about three decades until its advantage in the approximate solution of infinite domain problems was recognized. Trefftz's method has been instrumental in the development of the boundary element method [13].

3.5 Automated Formulations in Structural Dynamics

Among the methodologies that owe their foundations to Hamilton's principle and the contributions of Ritz, Galerkin and Trefftz, two leading techniques are of prominence, namely (a) the Finite Element Method [8], and (b) systematic Matrix Structural Analysis [9]. Discussion of these two topics will be limited to linear systems.

3.5.1 The Finite Element Method

The Finite Element Method encompasses three mathematical disciplines, namely (1) definition of building blocks (finite elements), (2) assembly of structural system models, and (3) solution of structural system equations. The third discipline is addressed by systematic Matrix Structural Analysis.

3.5.1.1 Finite Elements: The Building Blocks

The basic building block, a finite element, is generally derived as a specialized application of the Ritz Method. The displacement field associated with a single element is most generally described in terms of the following family of shape functions:

$$u(x, y, z, t) = \sum_{n=1}^{N_h} \Psi_{h,n}(x, y, z) \cdot u_n(t) + \sum_{n=1}^{N_p} \Psi_{p,n}(x, y, z) \cdot q_n(t) \text{ or in matrix form,}$$
$$\{u\} = [\Psi_h]\{u_h\} + [\Psi_p]\{q_p\} \tag{3.16}$$

The "h" shape functions are referenced to physical displacements at specific grid points on the element's (boundary) surface and the "p" shapes are polynomial functions that have null value along the element's boundary surface. Substitution of the above shape family functions (and their appropriate strain partial derivatives) into Hamilton's principle (Eq. 3.8) results in positive semi-definite mass and stiffness matrices of the forms

$$[M]_{element} = \begin{bmatrix} M_{pp} & M_{ph} \\ M_{hp} & M_{hh} \end{bmatrix}_{element}, [K]_{element} = \begin{bmatrix} K_{pp} & K_{ph} \\ K_{hp} & K_{hh} \end{bmatrix}_{element} \tag{3.17}$$

It should be emphasized here that definition of well-posed and accurate finite elements depends upon expert selection of shape functions and numerical integration schemes. To be sure, development of advanced finite elements is a very important engineering/mathematics specialty.

The most commonly employed finite elements in commercial finite element codes is the "h" element which does not include "p" generalized coordinates. The more general elements are often called "h-p" elements.

3.5.1.2 Assembly of Structural System Models

Assembly of a system structural dynamic model involves the allocation and superposition (overlapping) of individual finite elements onto a system degree-of-freedom map. This process defines sparse system mass and stiffness matrices that are positive semi-definite and symmetric. A system composed of an assembly of "h" elements is defined by "grid" set mass and stiffness matrices denoted by $[M_{gg}]$ and $[K_{gg}]$, respectively. Two other matrix quantities complete the ingredients for a structural dynamic model, namely (1) allocation of excitation forces to system grid points, and (2) formation of an assumed damping matrix (which unfortunately does not resemble physical reality in most commercial finite element codes). The grid set equations for the structural dynamic model are of the form

$$\left[M_{gg}\right]\{\ddot{u}_g\} + \left[C_{gg}\right]\{\dot{u}_g\} + \left[K_{gg}\right]\{u_g\} = \left[\Gamma_g\right]\{F\} \tag{3.18}$$

Constraints describing boundary conditions, described by transformations of the form

$$\{u_g\} = \left[G_{ga}\right]\{u_a\}, \tag{3.19}$$

are applied in a symmetric manner as a consequence of the quadratic forms and integrals defined by the Ritz method, resulting in the "analysis" set equations and matrices

$$\begin{aligned}&[M_{aa}]\{\ddot{u}_a\} + [C_{aa}]\{\dot{u}_a\} + [K_{aa}]\{u_{aa}\} = [\Gamma_a]\{F\}\\&[M_{aa}] = \left[G_{ga}\right]^T\left[M_{gg}\right]\left[G_{ga}\right], [C_{aa}] = \left[G_{ga}\right]^T\left[C_{gg}\right]\left[G_{ga}\right], [K_{aa}] = \left[G_{ga}\right]^T\left[K_{gg}\right]\left[G_{ga}\right], [\Gamma_a] = \left[G_{ga}\right]^T\left[\Gamma_g\right]\end{aligned} \tag{3.20}$$

3.5.2 Matrix Structural Analysis

Matrix Structural Analysis predates the Finite Element Method by several decades. Historically, matrix formulations for structural systems developed along two paths, namely (a) the force method, and (b) the displacement method. The force method owes its foundations to Castigliano [14], who introduced a complementary variational formulation for statics. The displacement method, based primarily on Hamilton's principle and the Ritz method, ultimately eclipsed the force method due to the advent of the Finite Element Method.

3.5.2.1 Free Vibration and Modal Analysis

Free vibration of a structural system generally relates to the undamped eigenvalue problem (dropping the "a" subscript in Eq. 3.20)

$$[M]\{\ddot{u}\} + [K]\{u\} = \{0\}, \tag{3.21}$$

which has solutions described by the (real) mode transformation,

$$\{u\} = [\Phi]\{q\} \tag{3.22}$$

Solutions of the resulting two matrix eigenvalue problem

$$[K]\{\Phi_n\} - [M]\{\Phi_n\}\lambda_n = \{0\} \quad \left(\lambda_n = \omega_n^2\right) \tag{3.23}$$

are expressed by symmetric transformations, dictated by Hamilton's principle and the Ritz method, which have the following mathematical properties (for unit mass normalized modes):

$$[\Phi]^T[M][\Phi] = [I], [\Phi]^T[K][\Phi] = [\lambda] \ \text{(where } [\lambda] \text{ is a diagonal matrix)} \tag{3.24}$$

These orthogonality properties are guaranteed by symmetries in the mass and stiffness matrices, which are consequences of the Ritz method.

It should be noted that inclusion of the damping matrix in the free vibration equations will generally result in complex modes and eigenvalues. Analysis of complex modes of structural systems, fortunately, is not often pursued. This is "fortunate" for two primary reasons, namely (a) experimental modal analysis generally indicates that "real" modes accurately fit measured data, and (b) popular damping matrix formulations generally do not relate to measured damping characteristics.

3.5.2.2 Proportional Damping Foolishness

Many texts in the field of mechanical vibration and structural dynamics (e.g., [6]) introduce the convenient notion of proportional damping, which assumes a physical damping matrix of the form

$$[C] = \alpha[M] + \beta[K] \qquad (3.25)$$

This assumption is mathematically convenient in that the undamped system modes define a decoupling transformation for the damping matrix, which is

$$[\Phi]^T[C][\Phi] = \alpha[I] + \beta[\lambda]. \qquad (3.26)$$

However, the on-diagonal terms must correspond to the following relationship for the critical damping ratio, ζ_n

$$\{\Phi_n\}^T[C]\{\Phi_n\} = 2\zeta_n\omega_n = \alpha + \beta\omega_n^2 \quad \text{or} \quad \zeta_n = \frac{\alpha + \beta\omega_n^2}{2\omega_n}, \qquad (3.27)$$

which is restrictive and does not relate to experimental reality for many structural systems displaying relatively uniform critical damping ratios.

There are two practical alternatives to proportional damping "foolishness". The first alternative, namely complex proportional damping, is widely used in aeroelasticity [15]. The second, more widely used alternative circumvents the explicit damping matrix altogether and inserts assumed (or experimentally determined) modal critical damping ratios in truncated modal response analysis of structures.

3.5.2.3   Normal Modes and Mach's Interpretation of d'Alembert's Principle

Several iterative strategies developed for the computation of normal modes have, perhaps unconsciously, benefited from Ernst Mach's interpretation of d'Alembert's principle [16], which simply views inertia (the time derivative of momentum) as an equivalent "static" force. Therefore, the undamped modal problem (Eq. 3.21) is posed as

$$[K]\{\Phi\} = \{F_I\} \approx [M]\{\Psi\} \text{ (individual mode)}, \text{ or } [K][\Phi] = [F_I] \approx [M][\Psi] \text{ (mode subspace)} \qquad (3.28)$$

where $\{\Psi\}$ and $[\Psi]$ are individual and grouped subspace modal guesses, respectively, and $\{\Phi\}$ and $[\Phi]$ are corresponding iterated updates of the respective guesses. The single (fundamental) mode iteration method is attributed to Vianello [17] and Stodola [18], while the grouped mode "subspace iteration" method was more recently introduced by Bathe [19]. More recently introduced methods for treatment of very large order structural systems are now widely utilized.

3.5.2.4   Response to Dynamic Loads: Modal Truncation and d'Alembert's Remedy

Employment of a truncated modal transformation (modes with natural frequency below a threshold) results in a series of ordinary differential equations of the form

$$\ddot{q}_n + 2\zeta_n\omega_n\dot{q}_n + \omega_n^2 q_n = \left[\Phi_n^T \Gamma\right]\{F(t)\} \qquad (3.29)$$

Recovery of physical displacements and loads using the truncated modal transformation

$$\{u\} = [\Phi]\{q\}, \qquad (3.30)$$

in many applications is inaccurate because the quasi-static response of all higher frequency modes is ignored. A clever approach, that implicitly employs Mach's interpretation of d'Alembert's principle, known as the mode acceleration method was defined by Williams [20]. The method casts the matrix equations governing system dynamics (Eq. 3.20) as follows

$$[K]\{u\} = [\Gamma]\{F(t)\} - \{F_I(t)\} \approx [\Gamma]\{F(t)\} - [M]\{\ddot{q}\} \qquad (3.31)$$

where the damping forces are generally ignored. Solution of the above equation set (quasi-statically) at each time point automatically accounts for the quasi-static response of all higher frequency modes (without the need to explicitly know them!). This fact is mathematically provable.

3.5.2.5 Large Order Systems: Component Mode Synthesis

During the 1960s the complexity of finite element models outpaced the development of digital computers and several authors developed procedures to treat system models piecemeal. Hurty [21] and Craig and Bampton [22] developed equivalent techniques known as component mode synthesis that described major structural components in terms of (a) generalized modal coordinates, and (b) physical boundary (interface) degrees of freedom. The general approach is defined by partitioning of a structural component (in a state of free vibration) into "internal" or "i" degrees of freedom and "boundary" or "b" degrees of freedom, as follows:

$$\begin{bmatrix} M_{ii} & M_{ib} \\ M_{bi} & M_{bb} \end{bmatrix} \begin{Bmatrix} \ddot{u}_i \\ \ddot{u}_b \end{Bmatrix} + \begin{bmatrix} K_{ii} & K_{ib} \\ K_{bi} & K_{bb} \end{bmatrix} \begin{Bmatrix} u_i \\ u_b \end{Bmatrix} = \begin{Bmatrix} 0_i \\ 0_b \end{Bmatrix} \tag{3.32}$$

Ritz vectors are then computed as an assembly of (a) internal modes associated with a fixed boundary, and (b) static shapes (or constraint modes) relating internal displacements to boundary displacements, as follows:

$$\begin{Bmatrix} u_i \\ u_b \end{Bmatrix} = \begin{bmatrix} \Phi_{iq} & -K_{ii}^{-1}K_{ib} \\ 0_{bq} & I_{bb} \end{bmatrix} \begin{Bmatrix} q \\ u_b \end{Bmatrix} \tag{3.33}$$

By applying the above transformation in a symmetric manner (following the Ritz method), reduced order mass and stiffness matrices for the component are realized. The form of the matrices is

$$[M] = \begin{bmatrix} I_{qq} & P_{qb} \\ P_{bq} & M_{bb} \end{bmatrix}, [K] = \begin{bmatrix} \lambda_{qq} & 0_{qb} \\ 0_{bq} & \overline{K}_{bb} \end{bmatrix} \tag{3.34}$$

It is of significance to note that the description of the reduced order structural component is the same as that of a finite element of the h-p type described in Sect. 3.5.1.1, where (a) the internal modes serve as "p" functions, and (b) the constraint modes serve as "h" functions. Assembly of the large-order structural dynamic system then follows the overlapping procedure used for assembling an ordinary finite element model. Component mode synthesis procedures, which now include additional particular strategies beyond the Hurty–Craig–Bampton method, are widely used in the aerospace industry.

3.6 Additional Variational Principles and Applications

The complementary viewpoint introduced by Castigliano in 1873 was generalized for dynamics by Toupin [23]. The complementary form of Hamilton's principle, known as Toupin's principle, may be derived in a manner similar to the approach described in Chap. 3 of this paper.

The postulate-theorem interrelationship is demonstrated below for a mechanical system composed of a single particle restricted to motion along one direction. The time integral of Newton's second law states the postulate,

$$\widehat{F} = \int_{-\infty}^{t} F dt = m \frac{du}{dt} \text{ or } \frac{\widehat{F}}{m} = \frac{du}{dt} \tag{3.35}$$

A d'Alembert type variational statement is that the system follows an "economy" in variational terms such that

$$\left(\frac{\widehat{F}}{m} - \frac{du}{dt} \right) \cdot \delta\widehat{F} = 0 \tag{3.36}$$

where "$\delta\widehat{F}$" is defined as a variation off the true path of "$\widehat{F}$". The complementary form of Hamilton's principle is therefore

$$\int_{t_1}^{t_2} \left(\frac{\widehat{F}}{m} - \frac{du}{dt} \right) \cdot \delta\widehat{F} \cdot dt = 0 \tag{3.37}$$

This variational integral is more compactly expressed as

$$\int_{t_1}^{t_2} (\delta T_C + \delta W_C) \cdot dt = 0, \tag{3.38}$$

where $T_C = \dfrac{\widehat{F}^2}{m}$ is the system complementary kinetic energy and $\delta W_C = -\dfrac{du}{dt} \cdot \delta \widehat{F}$ is the system complementary virtual work. By introducing a complementary strain energy function (not described here), the variational principle takes the form

$$\int_{t_1}^{t_2} (\delta T_C - \delta U_C + \delta W_C) \cdot dt = 0 \tag{3.39}$$

This complementary variational principle was employed in the study and resolution of difficulties encountered with fluid–structure interaction models, which employed pressure as the physical variable for the fluid, by Coppolino [24]. One of the more interesting peculiarities of Toupin's principle is the role reversal of kinetic and strain energies in that the time derivative is associated with strain energy. As illustrated in the acoustic matrix equation

$$\left[C_p\right] \left\{ \ddot{\widehat{p}} \right\} + \left[S_p\right] \left\{ \widehat{p} \right\} = -\left[A_p\right]^T \left\{ \dot{u} \right\} \quad \text{or} \quad \left[C_p\right] \left\{ \ddot{p} \right\} + \left[S_p\right] \left\{ p \right\} = -\left[A_p\right]^T \left\{ \ddot{u} \right\}, \tag{3.40}$$

$[C_p]$ is the acoustic compliance (flexibility) matrix, $[S_p]$ is the susceptance (inverse mass) matrix, and $[A_p]$ is the surface area matrix. Toupin's principle, while mathematically curious, has not found many convenient applications to this date.

Additional variational formulations have been derived and employed for the study of other applications in applied physics. It appears that use of Galerkin's method as a starting point facilitates definition of novel versions of Hamilton's principle. Biot's variational principle [25] for heat conduction and Hamilton's principle for finite element solution of Maxwell's equations by MacNeal et al. [26], are just two examples of alternative expressions of Hamilton's principle.

3.7 Conclusions

This paper offers a historical thread tracing the development of modern structural dynamics, which owes much of its present state to variational principles. The foundational variational principles are presented as a logical progression stemming from (a) ancient and medieval notions of economy in nature and human reasoning, (b) Newton's laws, (c) d'Alembert's principle, and (d) Hamilton's principle. A fifth principle or consequence, (e) Lagrange's equations, is derivable from Hamilton's principle (in spite of the fact that it was introduced before Hamilton's principle). All of the variational principles were fully developed by the first half of the nineteenth century.

Three approaches to approximate analysis based on Hamilton's principle were introduced during the early part of the twentieth century by Ritz, Galerkin, and Trefftz. Each of the three approaches has led to significant progress in structural dynamics, which can be summarized as follows:

1. The Ritz method, which substitutes an assumed shape function series into Hamilton's principle, is responsible for definition of symmetric, positive semi-definite mass and stiffness matrices. Moreover, the Ritz method provides a foundation for generalized coordinates (displacements) and generalized forces. It forms the foundation for much of the Finite Element Method and Matrix Structural Analysis.
2. Galerkin's method substitutes an assumed shape series into a continuum mechanics statement of Hamilton's principle consisting of (a) a stationary integral with a partial differential equation kernel, and (b) a stationary integral with a natural boundary condition kernel. By selecting shape functions that automatically satisfy natural boundary conditions, Galerkin's method focuses on (a) and it is employed to treat a very wide range of problems in applied physics for which variational principles are not known or well understood. It has been employed in the study of nonlinear phenomena.
3. Trefftz's method takes on a complementary approach with respect to the Galerkin method in that the assumed functions automatically satisfy (a) the partial differential kernel, and it seeks a least squares solution to (b) the natural boundary condition kernel integral. This strategy is well-suited for problems related to unbounded media, and it forms much of the basis of the Boundary Element Method.

Two tasks in Matrix Structural Analysis have benefited from consequences of Mach's viewpoint of d'Alembert's principle, published near the end of the nineteenth century. They are as follows:

1. Computation of the lowest eigenvalues and eigenvectors for an undamped structural system is performed by (a) employing a single mode iteration procedure introduced by Vianello and Stodola by the first decade of the twentieth century, or (b) employing a modal block (subspace) iteration procedure introduced by Bathe in the early 1970s.
2. Accurate computation of structural dynamic response by treating a truncated set of modal accelerations as equivalent "static loads". The technique introduced by Williams in 1945 automatically accounts for the quasi-static response of all high frequency modes without explicitly solving for them.

The influence of variational principles reaches a much broader set of applications than structural dynamics based on (a) a complementary variational principle introduced by Toupin in 1952, and generalizations of Galerkin's method which resulted in (b) Biot's variational principle for heat transfer in 1957, and (c) a variational formulation for electromagnetics introduced by MacNeal et al. in 1987.

It is clear that progress in the development of variational principles, approximate methods, and practical applications has occurred in successive stages depending on prior contributions. There is a wisdom statement, generally attributed to Newton, "If I have seen further . . . ", which actually has more ancient roots. The Italian-Jewish sage, Isaiah di Trani (d. 1250) stated: "Who sees further a dwarf or a giant? Surely a giant for his eyes are situated at a higher level than those of a dwarf. But if the dwarf is placed on the shoulders of the giant, who sees further? So too we are dwarfs astride the shoulders of giants. We master their wisdom and move beyond it".

References

1. Newton I (1689) Philosophiæ naturalis principia mathematica. London
2. Jean le Rond d'Alembert (1743) Trait e de Dynamique. Paris
3. Hamilton WR (1835) On a general method in dynamics. Phil Trans R Soc
4. Lagrange JL (1788) Mechanique Analitique. Desaint, Paris
5. Timoshenko SP (1953) History of strength of materials. McGraw-Hill, New York
6. Piersol A, Paez T (eds) (2010) Harris' shock and vibration handbook, 6th edn. New York, McGraw-Hill
7. Ritz W (1909) Über eine neue Methode zur Lösung gewisser Variationsprobleme der mathematischen Physik. Journal für die Reine und Angewandte Mathematik
8. Zienkiewicz OC, Taylor RL, Zhu JZ (2005) The finite element method, its basis and fundamentals, 6th edn. Elsevier, Boston
9. Pipes LA (1961) Matrix methods for engineering. Prentice-Hall, Englewood Cliffs
10. Galerkin BG (1915) . . . Some questions of elastic equilibrium of rods and plates. Vestnik inzhenerov i tekhnikov 19
11. Nayfeh AH, Mook DT (1979) Nonlinear oscillations. Wiley, New York
12. Trefftz E (1926) Ein Gegenstuck zum Ritzschen Verfahren. In: Proceedings of the 2nd international congress of applied mechanics
13. Brebbia CA, Dominguez J (1992) Boundary elements an introductory course, 2nd edn. WIT Press, Boston
14. Castigliano A (1879) Theorie de l'equilibre des systemes elastiques. Turin
15. Rodden WP (2011) Theoretical and computational aeroelasticity. Crest Publishing, Burbank
16. Mach E (1883) The science of mechanics a historical account of its development. Open Court Publishing Co., Lasalle, IL USA
17. Vianello L (1898) Graphische Untersuchung der Knickfestigkeit gerarder Stabe. Z Ver Deut Ing 42
18. Stodola A (1905) Steam and gas turbines, 2nd edn. Van Nostrand Company, New York
19. Bathe K-J (1972) Large eigenvalue problems in dynamic analysis. ASCE J Eng Mech Div 98(6):1471–1485
20. Williams D (1945) Dynamic loads in aeroplanes under given impulsive load with particular reference to landing and gust loads on a large flying boat. Great Britain Royal Aircraft Establishment Reports SME 3309 and 3316
21. Hurty W (1965) Dynamic analysis of structural systems using component modes. AIAA J 3(4):678–685
22. Craig R, Bampton M (1968) Coupling of substructures for dynamic analysis. AIAA J 6(7):1313–1319
23. Toupin RA (1952) A variational principle for the mesh-type analysis of a mechanical system. J Appl Mech 74, 19:574
24. Coppolino RN (1975) A numerically efficient finite element hydroelastic analysis, volume 1: theory and results. NASA CR-2662, April 1975
25. Biot MA (1957) New methods in heat flow analysis with applications to flight structures. J Aeronaut Sci 24:857–873
26. MacNeal B, Bauer J, Coppolino R (1990) A general finite element vector potential formulation of electromagnetics using a time-integrated electric scalar potential. IEEE Trans Magn 26:1768–1770

Chapter 4
Some Cornerstones of Signal Analysis History

Anders Brandt

Abstract This brief paper contains a survey of some fundamental cornerstones to contemporary analysis of random signals. Being among the most important contributions to this field, the paper presents the background of the sampling theorem, as this is the foundation on which all modern data analysis rests. In addition, the background and history of the Fourier transform, the discrete Fourier transform (DFT), and, particularly, the fast Fourier transform (FFT) is given.

Keywords Signal processing • History • Sampling theorem • Spectrum analysis • FFT

4.1 Introduction

This brief paper will present some of the author's views on some important cornerstones of signal processing history, particularly as it is impacting the modal analysis community and our applications. As I am no historian, and the work mentioned in this paper is solely other people's work, I choose to only summarize very brief points, and point to sources of good reading. Hopefully I can tempt at least some interested readers to follow these references to find out much more. You will be on a very interesting journey! Of course, this text is extremely limited; it does not imply that there were not a vast number of other people contributing to develop the knowledge we have today. They will have to forgive me for omitting them.

4.2 Early Signal Processing History

As will be apparent in the next section, the fundamentals of what we use in signal analysis (and particularly the dynamics theory) today were discovered already in the eighteenth century. There are two particular giants of science that we rest upon for much of these discoveries; Laplace and Fourier.

To start with, we will have to note *Pierre-Simon Laplace* (1749–1827) [1], by many called the French Newton [2] and seen as one of the foremost scientists through all times. Laplace, who was an astronomer and mathematician, among many things made important contributions in calculus, probability theory [3], and physical mathematics. We are particularly interested in Laplace because he has given name to the *Laplace transform*, despite the fact that, technically speaking, he actually used the Z transform on finite difference equations himself [4]. Nevertheless, the Laplace transform is essential in the systems theory that we use widely today in order to explain input–output relationships of linear systems. This dynamic systems theory is considerably younger, however. Laplace would hardly have recognized much of today's ways of describing linear systems theory, being methods developed post WWII in the control engineering community.

Jean Baptiste Joseph Fourier (1768–1830) is, of course, also worth mentioning in this context. Fourier was a French mathematician and physicist, living in the same period as Laplace [5]. They were both members of the Academy of Sciences in Paris [6], and, interestingly, Fourier too was compared to Newton, even in his own lifetime; when applying to the military

A. Brandt (✉)
Department of Technology and Innovation, University of Southern Denmark, Campusvej 55, 5230 Odense M, Denmark
e-mail: abra@iti.sdu.dk

academy, Fourier was refuted with the words "Fourier," replied the minister, "Fourier, not being noble, could not enter the artillery, although he were a second Newton" [6]. He is most interesting to us because he invented the *Fourier Series* to describe periodic signals, which he applied to heat transfer and vibration problems. He has also given name to the continuous Fourier transform, and its discrete cousin, the DFT, see below. The theories named after Fourier are probably the most important contributions to signal analysis, because without them the spectrum analysis we use in modern signal analysis would not be available [7].

One of the very central theorems in linear systems theory is the *convolution theorem*; the output of a linear system is the input convolved by the impulse response of the system [8]. As we know so well today, the Laplace transform of the impulse response is the *transfer function*, and the Fourier transform of it is the often used *frequency response function*. Although the background to the convolution theorem goes all the way back to the time of Laplace and Fourier, the term convolution dates back only to the 1950s [9]; the convolution integral was probably first presented by *Jean-Baptiste le Rond d'Alembert* (1717–1783). It should also be mentioned that the convolution is often called the Duhamel integral in mechanics (perhaps unjustified [9] because Duhamel seems not to have been the first to publish this principle). From my point of view, the dynamic systems theory is much more general and should therefore be preferred; it is unfortunate that this theory is not considered necessary in the curricula of many mechanical and civil engineering programs.

4.3 Late Developments

As we saw in Sect. 4.2, some of the most important foundation of modern signal analysis was laid in the late eighteenth century, by what was to be the dynamic systems theory that we rely on today (using convolution in the time domain or multiplication in the frequency or Laplace domains to relate the input to the output of a linear system). This black box theory is standard textbook knowledge, so we will assume it is known here; otherwise see for example [7].

4.3.1 The Sampling Theorem

The modern methods for signal analysis are to a large extent based on *digital signal processing*. The theory of this part of engineering is relatively new, mostly developed in the twentieth century. Central to all digital signal processing is the *sampling theorem*, which states that, provided that the frequency content of a continuous signal, $x(t)$, is limited to a frequency range (bandwidth) $B < \frac{f_s}{2}$, where f_s is the sampling frequency, then a sampled version of the signal, $x(n)$, can be related to the original, continuous function by the *reconstruction formula*

$$x(t) = \sum_{n=-\infty}^{\infty} x(n) \frac{\sin \left(\pi f_s \left(t - n \Delta t \right) \right)}{\pi f_s \left(t - n \Delta t \right)}. \tag{4.1}$$

The sampled signal thus *exactly* represents the continuous signal in the case this signal is bandlimited. The importance of this theorem is great and its history is interesting [10]. The origin of the sampling theorem goes a long way back. The reconstruction formula in Eq. (4.1) is often attributed to Whittaker 1915 [11] under the name Whittaker's cardinal theorem [12]. It is, however, Shannon [13] that is (at least usually) now giving name to this theorem, despite the fact that he wrote, right under the line where he states the theorem, that "this is a fact which is common knowledge in the communication art." It was Shannon that named half the sampling frequency the *Nyquist frequency* after Nyquist [14], acknowledging the latter for important contributions in the development of the sampling theorem. Indeed, sometimes the theorem is denoted the Nyquist–Shannon sampling theorem. Sometimes, also Kotel'nikov [15] is attributed for discovering the sampling theorem independently in the Soviet Union.

As pointed out in [10], there is today in the telecommunication and signal processing fields a different view of the sampling theorem, not stressing the exact representation, but instead focusing on the sampling theorem of non-bandlimited signals, as essentially all signals we sample are indeed not bandlimited, so we have to deal with some approximation. I still dare to say that in mechanical engineering and the modal analysis community this has had little impact. We deal with the approximations in the sense of limited *dynamic range* in our measurements [7]. The importance of the sampling theorem is that it ensures that we can sample any analog signal and treat it with digital signal processing, without losing any information. In modal analysis applications, this is valid, since we are by nature, so to speak, interested in a limited frequency band where the structure response is modal (i.e. where the mode density is low).

4.3.2 *Random Data Theory*

The next important cornerstone is that of random data theory, or more precisely, how we deal with spectra of random processes. This theory is vital for spectrum analysis, and needs to be addressed before we can address spectrum analysis of general random vibrations. The first important contribution to this field was made by the math giant Wiener [16], and similar results were discovered by Khinchin (sometimes Khintchine) [17]. They both explained, that despite the fact that for wide-sense stationary signals, the Fourier transform does generally not exist, the *power spectral density* of the signals can still (often) be found by the Fourier transform of the autocorrelation function. The importance of this discovery cannot be overstated, as it added a very important piece to the theory of spectrum analysis of random signals. Recently [18] it has been found that actually Albert Einstein realized the connection between autocorrelation functions and spectral density already 1914 (although the terms autocorrelation and spectral density are much younger). The significance of this is quite extraordinary, since the whole theory of random variables (stochastic processes) is essentially a post WWII field [19], although the work by mathematicians like Wiener and Khinchin had paved the way.

On the more practical side of our current use of random data theory, Julius Bendat and his coauthor, Allan Piersol, made considerable contributions in the practical use of random data analysis [20–22]. Julius Bendat's first book was published already 1958, in a time where the foundation of the theory of random processes that we take for granted today was still not formed, although much of the knowledge was established in journal papers. Bendat and Piersol did substantial work in developing practical procedures for, and particularly explaining errors involved in, estimates based on random processes. When it comes to estimating frequency response functions from measured records of input and output signals, their work was vital. A humorous description of some of the achievements comes from Julius Bendat's own pen (computer?) [23].

4.3.3 *Spectrum Analysis*

The (re)-invention of the Fast Fourier Transform, FFT, in 1965 by Cooley and Tukey [24] is probably the most important cornerstone in twentieth century signal processing. This algorithm reduces the number of computations of the discrete Fourier transform, DFT, of length N, from proportional to N^2 arithmetic operations by direct computation, to proportional to $N \cdot \log_2(N)$ operations with the FFT algorithm. The FFT algorithm has revolutionized vibration analysis, and made very much of what we do routinely today possible. Today when it is not uncommon to make, for example, an FFT computation of signals of $1,024^2$ samples (1 Mega samples—this is not considered a large record today), the saving is in the order of 50,000 times. On my current laptop, the FFT of $1,024^2$ samples takes approximately 34 ms to compute, which means that the straight DFT computation would instead take half an hour, had I the patience to try! The importance of the FFT paper is shown, if nothing else, by the paper being the most cited paper of the Mathematics of Computation journal [25].

The previous paragraph starts by "the (re)-invention . . . " This is because it was soon discovered that algorithms very similar to the one published by Cooley and Tukey were already around [26], the earliest first thought to be an algorithm by Runge already 1903. It should be mentioned, however, that the Cooley–Tukey algorithm is more general than these algorithms, which are now called Prime Factor Algorithms (PFA), although the PFA algorithms are certainly sometimes to prefer. Relatively soon (1977) it was further discovered [27], that *Carl Friedrich Gauss* (1777–1855), the giant mathematician, had developed the FFT algorithm already in 1804 [28]. It is no exaggeration to say that this is quite remarkable, because Fourier published his work on the Fourier series only 1822, although his work was probably made around 1804 [29]. There were, however, around the time of these gentlemen many people who worked on formulations of periodic signals—quite natural considering the applications of astronomy, for example, of those days. This is probably a good illustration that science history, described as a series of developments, is deceiving; actual developments usually occur in parallel, of course, and attributing a discovery to a single person, as we are so keen to, many times means unnecessarily ignoring many other scientists with similar level discoveries.

The FFT paved the way to, or triggered, many developments in spectrum analysis, as it suddenly became practical to compute correlation functions and spectra in a fast way. The most popular such method for computing spectral densities is the one by Welch [30], which was published 1967, quickly becoming "industry standard" because of its easy implementation in processors with low memory capacity. Some methods were actually developed before the FFT was available, for example the method I personally prefer to call the *smoothed periodogram method* [7], which is also sometimes referred to as the Daniell method [31], although it should be attributed to Albert Einstein who seems to have discovered it first, already 1914 [18]. Sometimes this method is, somewhat deceivingly, referred to as the Blackman–Tukey method [32, 33], although the Blackman–Tukey method is not based on a smoothed periodogram but rather on the Fourier transform of a correlation function, albeit, mathematically, it is equivalent. By these last developments, the success of the modal analysis community was on its way; or, at least, the necessary tools were there. The rest, as they say, is history.

References

1. http://en.wikipedia.org/wiki/Pierre-Simon_Laplace. Last visited Oct 21, 2013
2. Gindikin S (2007) Pierre-Simon Laplace. In: Tales of mathematicians and physicists. Springer, New York, pp 247–262
3. Laplace P-S (1995) Philosophical essay on probabilities. Springer, New York
4. http://en.wikipedia.org/wiki/Laplace_transform#History. Last visited Oct 21, 2013
5. http://en.wikipedia.org/wiki/Joseph_Fourier. Last visited Oct 21, 2013
6. Arago F (2013) Biographies of distinguished scientific men, Project Gutenberg. http://www.gutenberg.org/ebooks/16775. Last visited Oct 21, 2013
7. Brandt A (2011) Noise and vibration analysis: signal analysis and experimental procedures. Wiley, Cichester
8. http://en.wikipedia.org/wiki/Convolution_integral. Last visited Oct 21, 2013
9. Dominguez-Torres A (2010) Origin and history of convolution. http://www.slideshare.net/Alexdfar/origin-adn-history-of-convolution. Retrieved Oct 21 2013, p 41
10. Unser M (2000) Sampling-50 years after Shannon. Proc IEEE 88:569–587
11. Whittaker E (1915) On the functions which are represented by the expansion of interpolating theory. Proc R Soc Edinburgh 35:181–194
12. Butzer P (1983) A survey of the Whittaker–Shannon sampling theorem and some of its extensions. J Math Res Exposition 3:185–212
13. Shannon CE (1998) Communication in the presence of noise. Proc IEEE 86:447–457 (Reprinted from the Proceedings of the IRE, vol 37, pp. 10–21, 1949)
14. Nyquist H (2002) Certain topics in telegraph transmission theory. Proc IEEE 90:280–305 (Reprinted from Transactions of the A. I. E. E., February, pp. 617–644, 1928)
15. Kotel'nikov VA (2006) On the transmission capacity of 'ether' and wire in electric communications. Physics-Uspekhi 49:736–744 (Reprint of Izd. Red. Upr. Svyazzi RKKA Moscow, 1933)
16. Wiener N (1930) Generalized harmonic analysis. Acta Math 55:117–258
17. Khintchine A (1934) Korrelationstheorie der stationären stochastischen Prozesse. Mathematische Annalen 109:604–615 (Springer)
18. Yaglom A (1987) Einstein's 1914 paper on the theory of irregularly fluctuating series of observations. ASSP Magazine IEEE 4:7–11
19. Meyer P-A (2009) Stochastic processes from 1950 to the present. Journal Électronique d'Histoire des Probabilités et de la Statistique 5, 42 p [electronic only]
20. Bendat J (1958) Principles and applications of random noise theory. Wiley, New York
21. Bendat J, Piersol AG (1966) Measurement and analysis of random data. Wiley, New York
22. Bendat J, Piersol AG (1971) Random data: analysis and measurement procedures. Wiley Interscience, New York (2nd ed. 1986, 3rd ed. 2000, 4th ed. 2010)
23. Bendat JS (2007) A personal history of random data analysis. Sound Vib 41:101–106
24. Cooley JW, Tukey JW (1965) An algorithm for machine calculation of complex Fourier series. Math Comput 19:297–301
25. Cooley JW, Tukey JW (1993) On the origin and publication of the FFT paper: a citation-classic commentary on an algorithm for the machine calculation of complex Fourier-series. In: Cooley JW, Tukey JW (eds) Current contents/physical chemical & earth sciences, (51–52), pp 8–9
26. Cooley J, Lewis P, Welch P (1967) Historical notes on the fast Fourier transform. IEEE Trans Audio Electroacoust 15:76–79
27. Goldstine H (1977) A history of numerical analysis from the 16th through the 19th century. Springer, New York, pp 249–253
28. Gauss C (1866) Nachlass: Theoria interpolationis methodo nova tractate, Carl Friedrich Gauss Werke, Band 3. Königlichen Gesellschaft der Wissenschaften, Göttingen, pp 265–303
29. Heidemann MT, Johnson DH, Burrus CS (1984) Gauss and the history of the fast Fourier-transform. IEEE ASSP Magazine 34:15–21
30. Welch P (1967) The use of fast Fourier transform for the estimation of power spectra: a method based on time averaging over short, modified periodograms. IEEE Trans Audio Electroacoust AU-15:70–73
31. Daniell PJ (1946) Discussion of 'on the theoretical specification and sampling properties of autocorrelated time-series'. J R Stat Soc 8(1):88–90
32. Blackman RB, Tukey JW (1958) The measurement of power spectra from the point of view of communications engineering, Part 1. Bell Syst Tech J 37:185–282
33. Blackman RB, Tukey JW (1958) The measurement of power spectra from the point of view of communications engineering, Part 2. Bell Syst Tech J 37:485–569

Chapter 5
Structural Dynamic Test-Analysis Correlation

Robert N. Coppolino

Abstract A historical perspective of structural dynamic test-analysis correlation is presented. Mathematical relationships for normal mode orthogonality and cross-orthogonality, which require use of a theoretical mass matrix, are described. The most demanding requirements for model fidelity, in launch vehicle and spacecraft applications, are specified in terms of correlation criteria defined by U.S. government agencies. Procedures developed to identify the primary physical locations of test-analysis differences are discussed. Alternative correlation metrics, which do not employ a theoretical model mass matrix, are reviewed.

Nomenclature

[A]	Flexibility matrix
C	Correlation scale factor
[C]	Damping matrix
[COR]	Cross-orthogonality matrix
[COH]	Modal coherence matrix
[E]	Error matrix
{F}	Force array
[K]	Stiffness matrix
[LTM]	Load transformation matrix
[M]	Mass matrix
MAC	Modal assurance criterion
$[M_{eff}]$	Modal effective mass matrix
[OR]	Modal orthogonality matrix
[P]	Modal participation factor matrix
{Q}	Modal generalized force array
[R]	Residual error matrix
[T]	Modal kinetic energy matrix
[U]	Modal strain energy matrix
f_n	Natural frequency (Hz)
{q}	Modal displacement array
t	Time
{u}	Physical displacement array
[Φ]	Modal matrix
[Γ]	Force allocation matrix
[l]	Identity matrix
[Ψ]	Displacement allocation matrix

R.N. Coppolino (✉)
Measurement Analysis Corporation, 23850 Madison Street, Torrance, CA 90505, USA
e-mail: bobcoppolino@gmail.com

$\{\varepsilon\}$	Strain array
$[\lambda]$	Eigenvalue matrix
ω_n	Natural frequency (rad.sec)
ζ_n	Modal critical damping ratio

5.1 Introduction

Developments in structural dynamic modeling and modal testing [1, 2] were strongly motivated by aircraft structural failures as early as the first decade of the twentieth century [3]. The space race, dating back to the 1950s, and its early failures resulted in the development of strict government modal test-analysis correlation standards [4–6] based on mass-weighted orthogonality and cross-orthogonality metrics. Widespread advances in structural dynamics and experimental modal analysis [7–12] experienced accelerated growth due to advances in computer science, applied mathematics and microelectronics . . . all motivated by cold war anxieties before 1990. Thanks to continued enthusiasm in the academic world, further advances are realized and shared on a regular basis at IMAC and other conferences during the past 30 years.

Introduction of a systematic procedure for model order reduction by Guyan in 1967 [12] led to meaningful and sometimes flawed reduced order mathematical models, which are employed in modal test planning and correlation efforts. Over enthusiasm and mindless computer automation results in model reductions (and accompanying sensor allocations) that obscure important dynamic responses (like those of passenger seats in a luxury automobile [13]). This deficiency has been addressed by many contributors [14, 15] who developed strategies for definition of adequate sensor mapping and reduced order mass matrices. The art and science of model order reduction for modal test planning and correlation recently hit a "road block" due to the popularization of 3-D solid elements in automated finite element codes. The fundamental operations implied in Guyan reduction [12] imply the imposition of concentrated unit loads, which is not a problem for technical theories (e.g., truss, beam, shell elements). However, concentrated loads lead to mathematically infinite displacements in 3-D elasticity. The system equivalent reduction-expansion process, SEREP [16], appears to provide an alternative path for definition of reduced order model correlations with modal test data [17]; developments along these lines require clearer guidelines and standards. In the meantime, it is prudent for those involved in the development of models for test-analysis correlation to restrict finite element model contents to elements based on technical theory.

Beyond satisfying well-defined correlation standards [4–6], localization of the sources of test-analysis discrepancy is a task undertaken by many investigators. While detailed review of test and model based mode pairs often provides clues to the discrepancy sources, a universal strategy based on mode-to-mode comparisons has not been identified. More fruitful strategies for discrepancy localization have been developed based the incomplete flexibility matrix, introduced by Rodden in 1967 [18]. Further developments, for example the incomplete flexibility method due to Lin [19], appear to clearly identify local discrepancy sources (provided the test deduced flexibility is of very good quality).

As noted in the first paragraph of this introduction, many recent advances in test-analysis correlation are the product of enthusiasm in academia. Methodologies and metrics [20, 21], not based on weighting (the mass matrix) are a source of controversy and disagreement. In its defense, however, employment of non-weighted metrics provides a path for test-analysis correlation in situations that do not enjoy the luxury of "complete" modal sensor arrays.

5.2 Relevant Finite Element Models

Definition of a structural dynamic model (specifically a finite element model) must follow a series of guidelines (see Ref. 1, Chap. 23), which assure its relevance. It must reflect the following considerations:

a. System Operations: The model must address its end purpose. Intense steady loading (e.g., shell subassembly pressurization) may strongly influence stiffness characteristics and immersion in a fluid and/or containment of a fluid may increase structural dynamic mass. Interaction of the structure with other phenomena and subsystems may lead to the need for additional model features (e.g., aeroelasticity (flutter) [3], structure-control interaction, launch vehicle structure-propulsion system instability a.k.a. POGO).
b. Dynamic Environments: The dynamic bandwidth (frequency range, $0 < f < f^*$) and intensity of an operational environment are estimated by shock response spectrum or power spectrum analysis [1]. Employing the estimated cut-off frequency, f^*, the shortest wavelengths of system structural members are estimated, from which grid spacing requirements are derived. High magnitude environments may suggest potentially complicating nonlinear effects.

c. Element Selection: Based on the above considerations, informed decisions are made regarding the type of finite element (truss, bar, beam, shell, 3-D solid, etc.) to be employed. Moreover, features, such as differential stiffness, added fluid mass, and joint flexibility (uncertainties) may be required.

Typical linear structural dynamic models have matrix forms associated with applied external loads and base motions, respectively:

$$[M]\{\ddot{u}\} + [C]\{\dot{u}\} + [K]\{u\} = [\Gamma]\{F(t)\} \quad \text{(Applied external loads)} \tag{5.1}$$

$$[M]\{\ddot{u}'\} + [C]\{\dot{u}'\} + [K]\{u'\} = -[\Psi]\{\ddot{u}_0(t)\} \quad \text{(Base motion excitations)} \tag{5.2a}$$

$$\{\ddot{u}\} = \{\ddot{u}'\} + [\Psi]\{\ddot{u}_0(t)\} \quad \text{(Absolute acceleration recovery)} \tag{5.2b}$$

Common to both of the above situations are structural dynamic mass and stiffness distributions that result from the finite element modeling process, applied excitation distributions ([Γ], [Ψ]) and associated time functions from the engineering development process. The damping matrix, [C], is almost never explicitly defined unless specific damping components are incorporated in the structure's design; it is generally described in "modal" terms as part of modal analysis.

5.3 Initial Model Verification

A vital preliminary step in model correlation is initial model verification. Over the past half century, rigid body checks have been a standard part of the verification process. The most demanding standards for model verification have been documented by the U.S. Air Force Space Command [4, 5] and less strictly by NASA [6]. Using a geometrically defined rigid body displacement matrix, [Ψ_{RB}], the rigid body mass properties of a structure (both the complete assembly and subassemblies in unconstrained form) defined by

$$[M_{RB}] = [\Psi_{RB}]^T[M][\Psi_{RB}], \tag{5.3}$$

are correlated with reference engineering properties (total mass, center of gravity, mass moments of inertia) of the designed system. It should be noted that aircraft and space system development organizations generally include weight engineering departments which manage system mass budgets throughout the development process. The Society of Allied Weights Engineers (SAWE) was established in the United States in 1939 to support the weights engineering community.

The companion initial model verification calculation

$$[K_{RB}] = [\Psi_{RB}]^T[K][\Psi_{RB}], \tag{5.4}$$

is employed on the structure (both the complete assembly and subassemblies in unconstrained form) to verify integrity of the modeling process. [K_{RB}] must be a null matrix for an unconstrained structure. It should be noted that in special situations involving structures with "mechanisms" additional unconstrained verification calculations are required on the assembled system model (i.e., more than six stiffness free "modes").

5.4 Structural Dynamic Response Analysis and Model Correlation Requirements

Linear structural dynamic models subjected to dynamic environments are defined by equation sets 1 and 2 for applied forces and base motions, respectively. Undamped modes are calculated over the relevant bandwidth ($0 < f < f^*$) by solution of the algebraic eigenvalue problem,

$$[K][\Phi] = [M][\Phi][\lambda], \tag{5.5}$$

for an appropriately constrained system. Note that the diagonal terms in the eigenvalue matrix are directly related to the system's natural frequencies,

$$\lambda_n = \omega_n^2 = (2\pi \cdot f_n)^2 \tag{5.6}$$

The system eigenvectors (or modes) have the mathematical properties

$$[\Phi]^T [M] [\Phi] = [I], [\Phi]^T [K] [\Phi] = [\lambda], \tag{5.7}$$

for unit-mass normalized eigenvectors.

The system modes define the truncated $(0 < f < f^*)$ modal displacement transformations,

$$\{u\} = [\Phi] \{q\} \quad \text{(Applied external loads)} \tag{5.8a}$$

$$\{u\} = [\Phi] \{q\} + [\Psi_R] \{u_0(t)\} \quad \text{(Applied base excitations)} \tag{5.8b}$$

yield the uncoupled modal response equations,

$$\ddot{q}_n + 2\zeta_n\omega_n\dot{q}_n + \omega_n^2 q_n = Q_n(t) = [\Phi_n^T \Gamma_e] \{F_e(t)\} \quad \text{(Applied external loads)} \tag{5.9a}$$

$$\ddot{q}_n + 2\zeta_n\omega_n\dot{q}_n + \omega_n^2 q_n = Q_n(t) = -[\Phi_n^T M\Psi_R] \{\ddot{u}_0(t)\} \quad \text{(Base excitations)} \tag{5.9b}$$

Recovery of physical displacements by substitution of modal displacement solutions (Eq. 9) into the truncated modal transformations (Eq. 8) produces results that tend to be inaccurate (with respect to direct integration solutions of system Eqs. 5.1 or 5.2).

Accurate recovery of physical displacements is realized by employment of the mode acceleration method, which was introduced by Williams in 1945 [7]. The mode acceleration method employs substitution of modal accelerations into Eq. (5.1) (applied external force case) resulting in

$$\{u\} = [K^{-1}\Gamma_e] \{F_e(t)\} - [K^{-1}M\Phi] \{\ddot{q}\} \tag{5.10}$$

where contributions associated with modal velocities are generally ignored. For the case of applied base motion accelerations (equation set 2), mode acceleration displacement recovery results in

$$\{u'\} = -[K^{-1}M\Psi_R] \{\ddot{u}_0(t)\} - [K^{-1}M\Phi] \{\ddot{q}\} \tag{5.11}$$

In many situations, base excitation distribution is approximated by a statically determinate allocation matrix, $[\Psi_R]$, and the relative displacements, $\{u'\}$, are sufficient for use in recovery of structural strains and stresses. It is mathematically provable that the mode acceleration method automatically accounts for the quasi-static response of all system modes (while mode displacement recovery is limited to the truncated mode subset). A persistent irony in modern engineering practice is that most commercial finite element codes employ the mode displacement method for dynamic data recovery.

The following additional matrix relationships are employed to recover structural system strains and stresses (or member loads):

$$\{\varepsilon\} = [K_\varepsilon] \{u\}, \{\sigma\} = [K_{\sigma\varepsilon}] \{\varepsilon\} = [K_{\sigma\varepsilon}] [K_\varepsilon] \{u\} = [K_\sigma] \{u\} \tag{5.12}$$

It should be noted that the strain-displacement matrix, $[K_\varepsilon]$, is governed by kinematics while the stress-displacement matrix, $[K_{\varepsilon\sigma}]$, is governed by material elastic properties.

Substitution of the mode acceleration displacement recovery relationships into the strain recovery equation yields the well-known load transformation matrix relationships shown below for applied external forces,

$$\{\varepsilon\} = [K_\varepsilon K^{-1}\Gamma_e] \{F_e(t)\} - [K_\varepsilon K^{-1}M\Phi] \{\ddot{q}\} = [LTM_F] \{F_e(t)\} + [LTM_a] \{\ddot{q}\} \tag{5.13}$$

and for applied base motions (statically determinate case),

$$\{\varepsilon\} = -[K_\varepsilon K^{-1}M\Psi_R] \{\ddot{u}_0(t)\} - [K_\varepsilon K^{-1}M\Phi] \{\ddot{q}\} = [LTM_R] \{\hat{u}_0(t)\} + [LTM_a] \{\ddot{q}\} \tag{5.14}$$

Similar load transformation relationships for stress recovery result from employment of $[K_\sigma]$ instead of $[K_\varepsilon]$. It should be noted that load transformation matrices take on more elaborate particular forms in situations involving evaluation of designated substructures or subassemblies.

It is important to note that accurate structural dynamic loads require correlation of the following information with respect to test data and system design data:

a. Modal frequencies, f_n, in the relevant frequency band ($0 < f < f^*$)
b. Mode shapes, $[\Phi_n]$ in the relevant frequency band ($0 < f < f^*$)
c. Structural system flexibility, $[K^{-1}]$
d. Structural system mass, $[M]$.

5.5   Target Modes

An important practical aspect of model correlation and modal test planning is designation of a target mode set within the relevant frequency band ($0 < f < f^*$).

In the case of applied force excitations, the most prominent modes producing physical stresses (or member loads) are those associated with "high" modal gain, $\{\Phi_n\}^T[\Gamma_e]$, (see Eq. 5.9a) and "high" $[LTM_a]$ terms. The process of target mode selection for the case of applied force excitations is often "risky" as the prominence of measured test modes may differ from corresponding model modes (especially for closely-spaced modes). However, in the case of structures composed of thin shells having many breathing modes with low modal gain, elimination of such modes from the target mode set reduces challenges for both the modal test and test-analysis correlation process.

In the case of applied base motions, the most prominent modes producing physical stresses (or member loads) are those associated with "high" modal participation factors (see Eq. 5.9b) or "high" modal effective mass which are defined as follows:

$$[P_n] = [\Phi_n]^T [M] [\Psi_R] \quad \text{(Modal participation factors for mode"n")} \tag{5.15}$$

$$[Meff_n] = [P_n] * [P_n] \quad \text{(Modal effective mass)} \tag{5.16}$$

In addition, the total reference mass (rigid body bass for statically determinate $[\Psi_R]$) is

$$[M_{RR}] = [\Psi_R]^T [M] [\Psi_R] \tag{5.17}$$

The accepted metric for judgment of completeness of a selected subset of system modes is the ratio of a partial sum of modal effective masses to the total system mass (diagonal terms in $[M_{RR}]$), which is

$$M_{Ratio,i} = 100 \sum_n [Meff_{i,n}]/M_{RR,i,i} \quad \text{(Percent units)} \tag{5.18}$$

The standard employed for U.S. Navy's Dynamic Design Analysis Process (DDAM) [8] for roughly the past 50 years requires that the terms of $M_{Ratio,j}$ be at least 80 % for a modal subset to be judged adequate. Similar standards of target mode completeness have been informally adopted for space and civil engineering applications. It should be noted that for many applications, the lowest frequency modes in each geometric direction are the highest contributors to $M_{Ratio,j}$.

5.6   Modal Kinetic and Strain Energy Distributions

Term-by-term deconstruction of mode orthogonality relationships (Eq. 5.7) provides insight into the distribution of structural system modal kinetic and strain energies. In particular,

$$2 [T_n] = [M\Phi_n] * [\Phi_n] \quad \text{(Modal kinetic energy distribution)} \tag{5.19}$$

$$2 [U_n] = [K\Phi_n] * [\Phi_n] \quad \text{(Modal strain energy distribution)} \tag{5.20}$$

The sums of the energy distributions are 1.0 and λ_n, respectively, when the modes are normalized to unit modal mass. It should also be noted that for an assembled structural system, modal kinetic and strain energy distributions are equivalent (other than the eigenvalue as a scale factor for strain energy). It is of great interest, however, that disassembly of the structural system into disconnected substructures produces dissimilar "substructure" kinetic and strain energy distributions (Again, it must be emphasized that substructure designations must not be defined on the basis of degree-of-freedom subsets of the assembled system model!).

The practice of calculation of (or accounting for) substructure modal kinetic and strain energy distributions has been commonplace in the aerospace industry for organizations employing the most prevalent component mode synthesis (CMS) methodologies [9–11]. An illustrative example of this process is as follows:

a. Assembled launch vehicle & spacecraft system:

$$2[T_n]_{total} = \sum_{dofs} [M\Phi_n] * [\Phi_n] = [\Phi_n]^T [M] [\Phi_n] = 1 \ \text{(Normalized kinetic energy)} \tag{5.21}$$

$$2[U_n]_{total} = \left(\sum_{dofs} [K\Phi_n] * [\Phi_n] \right) / \lambda_n = [\Phi_n]^T [K] [\Phi_n] / \lambda_n = 1 \ \text{(Normalized strain energy)}$$

b. Subsystem allocations (into partially overlapping component partitions)

$$[\Phi_n]_{stage1} = \left[\Gamma_{stage1}\right]^T [\Phi_n] , [\Phi_n]_{stage2} = \left[\Gamma_{stage2}\right]^T [\Phi_n] , [\Phi_n]_{spacecraft} = \left[\Gamma_{spacecraft}\right]^T [\Phi_n] \tag{5.22}$$

c. Subsystem kinetic and strain energies:

$$2[T_n]_{stage1} = [\Phi_n]_{stage1}^T \left[M_{stage1}\right] [\Phi_n]_{stage1} < 1 \ \text{(Stage 1 kinetic energy)} \tag{5.23}$$

$$2[U_n]_{stage1} = [\Phi_n]_{stage1}^T \left[K_{stage1}\right] [\Phi_n]_{stage1} / \lambda_n < 1 \ \text{(Stage 1 strain energy)}$$

(Similar relationships for other two components)

d. Subsystem energy properties:

$$2[T_n]_{stage1} + 2[T_n]_{stage2} + 2[T_n]_{spacecraft} = 1, 2[U_n]_{stage1} + 2[U_n]_{stage2} + 2[U_n]_{spacecraft} = 1 \tag{5.24}$$

$2[T_n]_{stage1} \neq 2[U_n]_{stage1}$, etc. for all components

Comparisons of component kinetic and strain energy distributions between analysis and test modal data may provide insight into the localized difference between test and analysis.

5.7 Modal Test Planning

As a general rule, the number of system model degrees-of-freedom is substantially greater than a practical number of acceleration sensor channels. Before 1965, allocation of a modal test accelerometer array was a task guided primarily by general understanding of the character of anticipated system modes. Moreover, the assembly of a system mass allocation matrix (corresponding to the test accelerometer array) was conducted on the basis of engineering experience and "expertise". The mass allocation matrix was deemed necessary for validation of test mode orthogonality, especially in aeronautical applications.

Introduction of a novel model order reduction technique, namely Guyan reduction [12], in 1965 offered a systematic strategy for definition of an appropriate test accelerometer array and system mass allocation matrix. The approximation suggested by Guyan divided the degrees of freedom of a structural system into two subsets, namely (1) the "analysis" set, $\{u_a\}$, and the "other" or "omit" set, $\{u_o\}$. An undamped system in a state of free vibration is therefore partitioned as,

$$\begin{bmatrix} \overline{M}_{aa} & M_{ao} \\ M_{oa} & M_{oo} \end{bmatrix} \begin{Bmatrix} \ddot{u}_a \\ \ddot{u}_0 \end{Bmatrix} + \begin{bmatrix} \overline{K}_{aa} & K_{ao} \\ K_{oa} & K_{oo} \end{bmatrix} \begin{Bmatrix} u_a \\ u_0 \end{Bmatrix} = \begin{Bmatrix} 0_a \\ 0_o \end{Bmatrix} \tag{5.25}$$

and it is assumed (based on engineering intuition) that the "omit" degrees of freedom (approximately) follow a static relationship with respect to the "analysis" set degrees of freedom,

$$
\begin{Bmatrix} u_a \\ u_o \end{Bmatrix} = \begin{bmatrix} I_{aa} \\ -K_{oo}^{-1}K_{oa} \end{bmatrix} \{u_a\}
\tag{5.26}
$$

Application of the above transformation to Eq. (5.25), results in the approximate reduced order equation set

$$
[M_{aa}]\{\ddot{u}_a\} + [K_{aa}]\{u_a\} = \{0_a\},
\tag{5.27}
$$

where the reduced order, approximate mass and stiffness matrices are

$$
[M_{aa}] = \begin{bmatrix} I_{aa} \\ -K_{oo}^{-1}K_{oa} \end{bmatrix}^T \begin{bmatrix} \overline{M}_{aa} & M_{ao} \\ M_{oa} & M_{oo} \end{bmatrix} \begin{bmatrix} I_{aa} \\ -K_{oo}^{-1}K_{oa} \end{bmatrix}
\tag{5.28}
$$

$$
[K_{aa}] = \begin{bmatrix} I_{aa} \\ -K_{oo}^{-1}K_{oa} \end{bmatrix}^T \begin{bmatrix} \overline{K}_{aa} & K_{ao} \\ K_{oa} & K_{oo} \end{bmatrix} \begin{bmatrix} I_{aa} \\ -K_{oo}^{-1}K_{oa} \end{bmatrix}
$$

Appropriateness of a selected "analysis" set may be verified by comparison of approximate modes and natural frequencies associated with the reduced eigenvalue problem (Eqs. 5.26–5.28) with the results for the exact eigenvalue problem (Eq. 5.25). The exact and approximate modal vectors (which use Eq. (5.26) as an expansion transformation) are

$$
[\Phi]_{exact} = \begin{bmatrix} \Phi_a \\ \Phi_o \end{bmatrix}_{exact}, [\Phi]_{Guyan} = \begin{bmatrix} I_{aa} \\ -K_{oo}^{-1}K_{oa} \end{bmatrix} [\Phi_a]_{Guyan}
\tag{5.29}
$$

The choice of a specific set of "analysis" degrees of freedom is acceptable if all "Guyan" approximate modes and natural frequencies are is "satisfactory" agreement with the "exact" system modes and natural frequencies. A very clear example of an inadequate selection of "analysis" set degrees of freedom is discussed in [13], which describes difficulties encountered in modal testing of a trim body automobile test article. In that experience, the front seats were not modeled or designated by "analysis" degrees of freedom and local seat flexing modes which coupled with overall body vertical bending motions were obscured. In response to this and other experiences, a variety of automated "analysis" degree of freedom selection algorithms were developed. Coppolino [14] describes one such strategy.

Utilization of Guyan reduction to designate (1) the "analysis" set degrees of freedom as the modal test accelerometer array and (2) the reduced mass matrix, $[M_{aa}]$, as the test-analysis model (TAM) mass (allocation) matrix is the most prevalent, contemporary test planning strategy in the U.S. aerospace industry. Allocation of force excitation resources on the basis of modal gains, $\{\Phi_n\}^T[\Gamma_e]$, complements the allocated accelerometer array. Additional strain gage sensor arrays have been successfully employed by NASA/JPL [15] since the 1980s as part of modal survey planning and execution. Such information provides a basis for correlation and validation of load transformation matrices (see Eqs. 5.13 and 5.14).

Finally, it should be pointed out that allocation of an accelerometer array may require special considerations to avoid the mapping of unwanted modes, specifically breathing modes of plate and shell subassemblies (that are not included in the target mode set). In such situations, accelerometers directed normal to a "breathing" surface should not be allocated. Moreover, if possible, tangentially oriented accelerometers should be allocated only at stiffening rings and spars to further suppress measurement of breathing modes.

In summary, the following data sets form the basis of modal test planning in the U.S. aerospace industry:

a. TAM mass matrix, $[M_{aa}]$, derived from appropriate application of the Guyan reduction process.
b. TAM predicted modes and natural frequencies based on solution of the exact (unreduced) eigenvalue problem. The accelerometer array modal partition represents the predicted test modes. *It should be noted that some organizations use the Guyan reduction solution as the predicted mode set*.
c. Applied force allocation, based on predicted mode gains to excite all target modes.
d. Additional designated strain gages at critical locations based on pre-test flight loads analyses (the "NASA/JPL" strategy [15]).

5.8 Test Planning Challenges Associated with Large-Order Models

At the present time, automated computer analysis technology has advanced to the point that very large order ($>10^5$ degree of freedom) models are commonplace. Moreover, models composed of 3-D solid elements are sometimes developed for structural dynamic analysis and modal test planning. In such situations, the Guyan reduction process is inherently inaccurate and inappropriate (in the limit, deflection due to point loading is infinite for a three-dimensional elastic solid). One way to avoid this difficulty is to build the system model with technical theory based elements (e.g., truss, bar, beam, shell). When this is not practical or possible, the SEREP [16] method provides a viable alternative for modal test planning.

An effort to define an approach for employment of a "sensitivity" vector enhanced SEREP transformation for modal test planning is described in [17]. Much additional work is required, however, to define clear and widely accepted standards for SEREP based test planning.

5.9 Correlation of Test and Analysis Modal Data (Cross-Orthogonality)

The relationship between target test modes, $[\Phi_t]$, and their analytical counterparts, $[\Phi_a]$, is described by the transformation,

$$[\Phi_t] = [\Phi_a][COR] + [R] \tag{5.30}$$

where [COR] is the cross-orthogonality matrix and [R] is the residual error matrix. Employing the TAM mass matrix, $[M_{aa}]$, as a weighting matrix, the least squares solution for cross-orthogonality is

$$[COR] = [OR_a]^{-1}\left[\Phi_a^T M_{aa} \Phi_t\right], \tag{5.31}$$

where the analysis mode orthogonality matrix is

$$[OR_a] = \left[\Phi_a^T M_{aa} \Phi_a\right] \approx [I] \tag{5.32}$$

It should be noted that $[OR_a]$ is exactly an identity matrix only if the "analysis" modes are the unit mass normalized modes of the Guyan reduced structural dynamic model.

An additional useful modal coherence matrix, [COH], is defined as follows

$$[COH] = \left([I] - [OR_t]^{-1/2}\left[R^T MR\right][OR_t]^{-1/2}\right) = [I] - [OR_t]^{-1/2}\left[COR^t OR_a COR\right][OR_t]^{-1/2} \tag{5.33}$$

The following standards are imposed on space systems contractors by U.S. government agencies:
Air Force Space Command [4, 5]
For all spacecraft modes up to 70 Hz, test mode orthogonality (unit mass normalized)
$|OR_{t,ij}| \leq 0.10$ (10 %) for $i \neq j$
Test-Analysis mode cross-orthogonality (both sets unit mass normalized)
$|COR_{ij}| \geq 0.95$ (95 %) for $i = j$
$|COR_{ij}| \leq 0.10$ (10 %) for $i \neq j$
Difference between corresponding test and analysis modal frequencies must be less than 3 %.
NASA [6]
For all significant modes, test mode orthogonality (unit mass normalized)
$|OR_{t,ij}| \leq 0.10$ (10 %) for $i \neq j$
Test-Analysis mode cross-orthogonality (both sets unit mass normalized)
$|COR_{ij}| \geq 0.90$ (90 %) for $i = j$
$|COR_{ij}| \leq 0.10$ (10 %) for $i \neq j$
Difference between corresponding test and analysis modal frequencies must be less than 5 %.
It should be noted that the stricter standards imposed by the U.S. Air Force Space Command, particularly for spacecraft, are suited for situations in which test data is employed directly to construct a hybrid test-analysis dynamic model [15], which circumvents an often lengthy model correlation and reconciliation process.

5.10   Correlation of Test and Analysis Modal Data (Localization of Differences)

A variety of strategies have been used by engineering organizations to localize discrepancies between test and analysis modes. The intentions of such efforts are to (a) identify measurement errors and/or (b) identify modeling errors (or sensitivities). The following metrics are typically employed:

Comparison of Modal Vectors

– Tabular and bar graph displays of correlating mode pair displacement vectors
– Tabular and bar graph displays of correlating mode pair kinetic energies
– Tabular and bar graph displays of correlating mode pair substructure kinetic energies
– Animated displays of corresponding mode pair displacement vectors

The tabular and bar graph displays often, but not always, provide indications of measurement and/or modeling errors. Animated displays (which become quite detailed if the Guyan reduction transformation is used for modal expansion) may be of utility for relatively simple structural systems.

An alternative set of strategies for localization of measurement and/or modeling errors is based on experimentally and analytically derived incomplete flexibility matrices (also called influence coefficient matrices). An early work (1967) describing definition and issues associated with experimentally derived incomplete flexibility matrices is due to Rodden [18]. The incomplete flexibilities associated with unit mass normalized test and analysis modes respectively are,

$$[A_t] = [\Phi_t]\,[\lambda_t]^{-1}[\Phi_t]^T, [A_a] = [\Phi_a]\,[\lambda_a]^{-1}[\Phi_a]^T \tag{5.34}$$

Both of the above flexibility matrices are singular and have rank equal to the number of modes.

One promising approach for localization of test-analysis differences, regardless of cause, was introduced by Lin in 1990 [19]. The error matrix, $[E_{ta}]$, is formed by the product,

$$[E_{ta}] = ([A_t] - [A_a]) \cdot [K] \tag{5.35}$$

The sum of the rows of $[E_{ta}]$ provides a simple focus on degrees of freedom affected by test and/or modeling errors in structural system stiffness.

5.11   Correlation of Test and Analysis Modal Data (Non-Weighted Metrics)

The introduction of minicomputers, PCs, and advanced digital processing software in the laboratory over the past 40 years has led to development and wide acceptance of "non-weighted" modal analysis procedures. A general result of these developments is experimental modal analysis and test-analysis correlation procedures, which do not rely on physics-based metrics (e.g. energy, orthogonality and cross-orthogonality). A thorough summary of both physics and non-physics based correlation metrics is provided in [20]. In addition, a historical perspective and critique of the modal assurance criterion (and its offspring) is provided in [21].

Definition of the modal assurance criterion (MAC) closely follows the process outlined in Sect. 9 of this paper. The relationship between a pair of corresponding test and analysis modes, $\{\Phi_t\}$ and $\{\Phi_a\}$, respectively, is described by,

$$\{\Phi_t\} = \{\Phi_a\}\,C + \{R\} \tag{5.36}$$

where C is the correlation scale factor and $\{R\}$ is the residual error vector. Employing un-weighted least squares,

$$C = \left(\Phi_a^T \Phi_t\right) / \left(\Phi_a^T \Phi_a\right), \tag{5.37}$$

The modal assurance criterion, MAC, is in actuality the following un-weighted coherence function:

$$MAC = \frac{\Phi_t^T \Phi_t - R^t R}{\Phi_t^T \Phi_t} = \frac{\left(\Phi_a^T \Phi_t\right)^2}{\left(\Phi_a^T \Phi_a\right) \cdot \left(\Phi_t^T \Phi_t\right)} \tag{5.38}$$

Review of the definition of modal coherence (Eq. 5.33) indicates that MAC is equivalent to modal coherence if the mass matrix is an identity matrix. For structural dynamic systems with non-uniform mass distribution, in general, MAC and it offspring are purely mathematical functions that (a) do not relate to physical energy distributions and (b) cannot be employed to indicate linear independence of dissimilar modes. This fact begs the question: *Of what use is MAC and its offspring?* The answer lies in the many situations for which relatively complete mapping of system is not practical or possible, including field (especially flight and civil structure) data analyses intended for condition monitoring and damage detection.

5.12 Illustrative Example

The one-dimensional structural dynamic system, described below in Fig. 5.1, is used to illustrate the correlation concepts described in the previous sections of this paper. Two complicating characteristics, namely (1) a branch substructure and (2) a redundantly attached substructure, are included in the example system (Note this example is not intended to resemble any real system).

Two classes of dynamic excitation are considered:

a. Base excitation motion at grid point "0"
b. Three independent applied force patterns (shown in Fig. 5.2)

Modal frequencies, modal effective masses, and modal gains for both the "model" and "test" data sets, and model-test cross-orthogonality are provided below in Table 5.1.

The modal frequencies indicate that the Air Force Space Command's 3 % frequency criterion is not satisfied by mode 3. Moreover, the 95 % on-diagonal and 10 % off-diagonal cross-orthogonality criterion is not satisfied by modal subsets 3–4 and 6–8. If the excitation environment is defined by base motion, the U.S. Navy's DDAM criterion for significant modes (80 % modal effective mass) indicates that only mode 1 is of significance; and test-model correlation could be judged adequate. On the contrary, if the excitation environment is defined by the three force patterns (shown in Fig. 5.2), most of the eight system modes are of significance; and test-model correlation must be judged inadequate.

While there is no accepted standard for modal coherence (Eq. 5.33), partial coherence within mode subsets 3–4 and 6–8, shown below in (Table 5.2) indicate that the "model" and "test" counterparts are linear combinations of one another.

A revealing exercise that demonstrates the significance of the U.S. Air Force Space Command's standard is carried out through study of the consequences of varying degrees of model-test correlation on system dynamic loads. To this end,

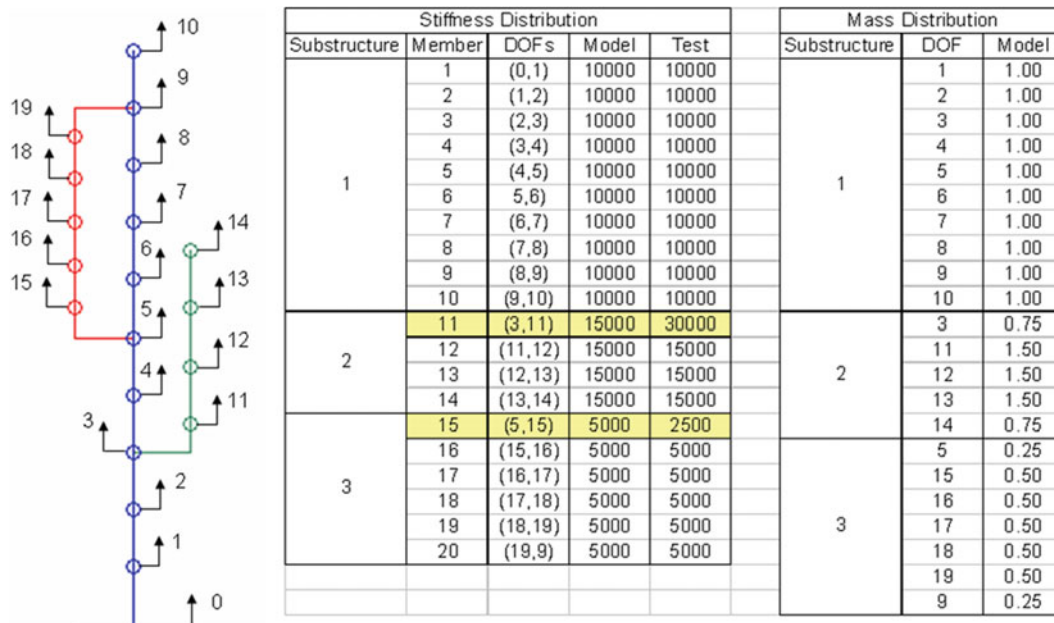|	Stiffness Distribution					Mass Distribution		
Substructure	Member	DOFs	Model	Test		Substructure	DOF	Model
	1	(0,1)	10000	10000			1	1.00
	2	(1,2)	10000	10000			2	1.00
	3	(2,3)	10000	10000			3	1.00
	4	(3,4)	10000	10000			4	1.00
1	5	(4,5)	10000	10000		1	5	1.00
	6	(5,6)	10000	10000			6	1.00
	7	(6,7)	10000	10000			7	1.00
	8	(7,8)	10000	10000			8	1.00
	9	(8,9)	10000	10000			9	1.00
	10	(9,10)	10000	10000			10	1.00
	11	(3,11)	15000	30000			3	0.75
2	12	(11,12)	15000	15000			11	1.50
	13	(12,13)	15000	15000		2	12	1.50
	14	(13,14)	15000	15000			13	1.50
	15	(5,15)	5000	2500			14	0.75
	16	(15,16)	5000	5000			5	0.25
3	17	(16,17)	5000	5000			15	0.50
	18	(17,18)	5000	5000			16	0.50
	19	(18,19)	5000	5000		3	17	0.50
	20	(19,9)	5000	5000			18	0.50
							19	0.50
							9	0.25

Fig. 5.1 One-dimensional structural dynamic system

Fig. 5.2 Applied force patterns
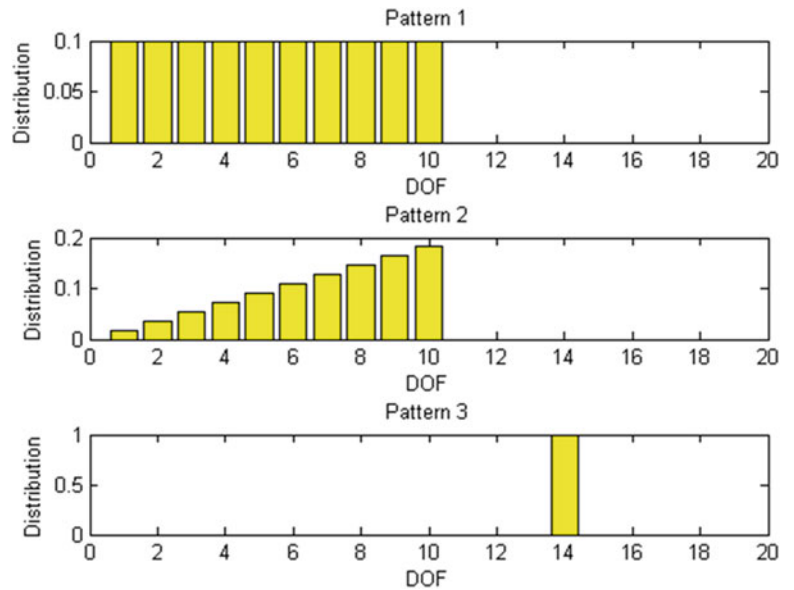
Table 5.1 "Model" and "Test" modal data sets

	Modal Frequency (Hz)			Meff (%)		Pattern 1 Modal Gain		Pattern 2 Modal Gain		Pattern 3 Modal Gain	
Mode	Model	Test	Δ (%)	Model	Test	Model	Test	Model	Test	Model	Test
1	1.87	1.86	-0.43	91	90	22	22	26	26	19	18
2	4.27	4.37	2.43	5	6	5	3	12	11	39	38
3	8.46	8.02	-5.16	0	0	1	11	10	17	21	3
4	9.22	9.06	-1.72	0	0	16	12	14	6	22	32
5	11.64	11.76	1.04	1	1	6	6	0	1	32	37
6	15.10	14.75	-2.30	0	0	1	1	3	5	5	2
7	16.61	16.14	-2.79	1	1	8	5	3	2	29	3
8	17.36	17.47	0.65	0	1	4	8	0	2	31	34

		Cross-Orthogonality (%)							
		Test							
	Mode	1	2	3	4	5	6	7	8
Model	1	100.0	1.9	-0.8	-0.7	0.1	0.3	-0.4	0.3
	2	-1.9	99.6	0.5	-7.0	-1.7	0.9	0.3	3.1
	3	1.1	4.2	80.1	58.2	1.1	-5.5	4.7	-8.1
	4	0.1	5.8	-59.1	79.6	-6.3	-3.3	5.8	-0.4
	5	-0.1	1.8	-4.3	3.9	99.6	-0.9	3.9	3.4
	6	-0.3	-1.1	4.4	9.5	0.7	93.9	-18.9	23.8
	7	0.3	0.9	-3.5	-7.9	-0.7	32.1	75.2	-54.8
	8	0.0	-2.2	4.2	0.6	-3.7	-8.7	60.9	74.7

consider a transient force (shown below in Fig. 5.3) applied to both the "model" and "test" (representing actual flight hardware) representations of the example system (load pattern 3). Note from the transient force's normalized SRS [1] that it dynamic bandwidth spans modes 1–8.

Results of the dynamic response sensitivity study, summarized below in Table 5.3, illustrate typical peak member load errors and correlation metrics as functions of the level of model stiffness correction.

Based on the above sensitivities, the consequences of enforcement of U.S. government imposed correlation criteria and adaptation of the standards for modal assurance criteria are provided below in Table 5.4.

For the illustrative example system, adherence to U.S. government imposed (cross-orthogonality) correlation criteria produce the most accurate member loads. Employment of "MAC" based correlation standards (tailored to conform to U.S. government correlation criteria) produce less accurate member loads, which are driven by modal frequency criteria.

Comparison of individually paired modes (and modal quantities such as kinetic and strain energy distributions), while utilized by many organizations, does not consistently and clearly highlight local test-model differences. The fact that cross-orthogonality and partial modal coherences (illustrated in Table 5.2) correlate "clusters" of modal subgroups points to the futility of difference localization based on individual test-model mode pairs (or coherent modal clusters). Note the modal kinetic energy provided in Table 5.5:

Table 5.2 Partial coherence of "Model" and "Test" modal data subsets

		Partial Coherences (%)							
		Test							
	Mode	1	2	3	4	5	6	7	8
Model	1								
	2								
	3			99.1	-0.5				
	4			-0.5	97.2				
	5								
	6						99.1	1.1	-1.7
	7						1.1	97.2	-0.2
	8						-1.7	-0.2	91.4
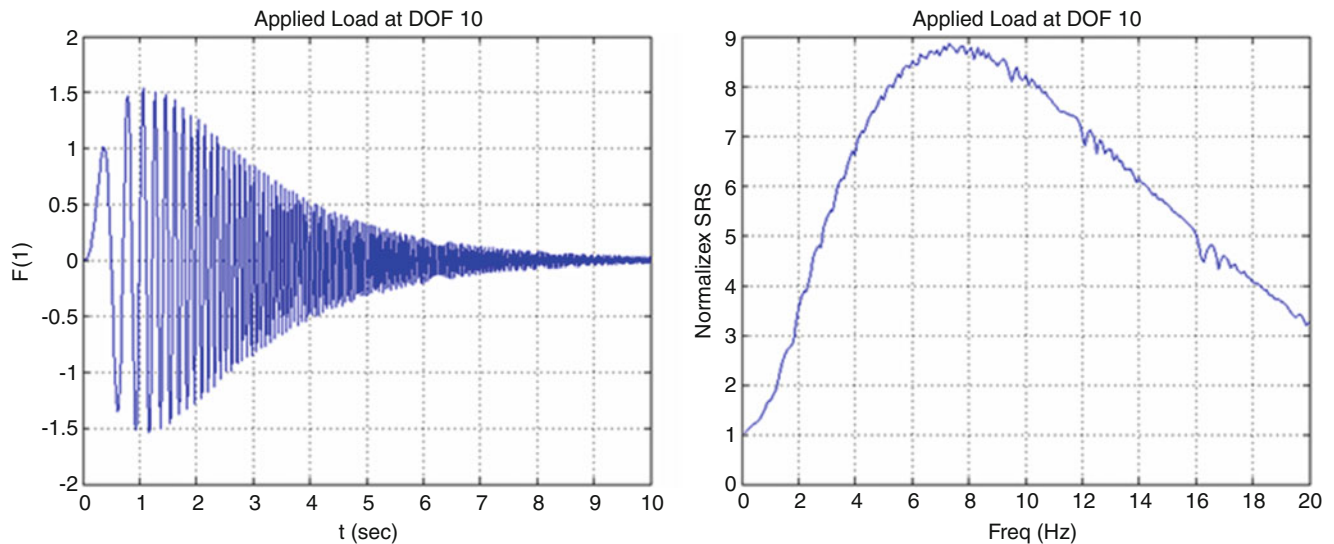
Fig. 5.3 Applied force time history and normalized SRS

Greater success in localization of test-model differences is achieved by analysis of incomplete flexibility matrices. In particular, the row sum of the metric described in Eq. (5.35) provides a very clear indication of local test-model differences as illustrated in Fig. 5.4. While attempts to localize test-analysis difference using unweighted metrics (based on MAC) are not shown in this paper, their futility is intuitively obvious.

5.13   Conclusions

This paper provides a historical perspective on structural dynamic test-analysis correlation from the viewpoint of its author and aerospace industry colleagues. As the perspective of several individuals, it should not be considered totally inclusive and unbiased. Nevertheless, the following conclusions are the result of our experiences.

(1) Structural dynamic models used in test-analysis correlation must be defined on the basis of rigorous criteria [e.g., focus on system operation (purpose), dynamic environments (especially the relevant frequency band), and sound modeling practices (element selection)].

(2) The model correlation process begins with initial model verification, which employs rigid body mass and stiffness checks that "correlate" the mathematical model to basic design data.

(3) The structural dynamic model plays a crucial role in modal test planning, especially in selection of sensor and excitation resources. Close attention must be paid to results of model simulations with regard to the issue of target modes and local dynamic responses (e.g., flexibility of car seats) that will produce much confusion and difficulty if not adequately addressed.

Table 5.3 Peak member load errors for various stiffness correction levels

Stiffness correction (%)	Peak member load error (%)			Air force space command standard			"MAC" standard	
	Tension	Compression	Max of both	Δ(Freq3) (%)	Min(COR$_{ii}$)	Max(COR$_{ij}$)	Δ(Freq3) (%)	Min(MAC$_{ii}$)
0	40.4	27.3	40.4	5.44	74.7	61.0	5.44	50.7
5	39.2	28.2	39.2	5.50	78.5	57.0	5.50	56.4
10	37.8	29.1	37.8	5.53	81.4	54.0	5.53	61.8
15	36.2	29.9	36.2	5.52	84.0	51.0	5.52	66.9
20	34.6	30.8	34.6	5.48	86.3	49.0	5.48	70.4
25	32.9	31.7	32.9	5.41	88.3	46.0	5.41	73.4
30	31.0	29.5	31.0	5.31	90.1	43.0	5.31	76.3
35	29.0	24.2	29.0	5.18	91.5	40.0	5.18	79.2
40	26.9	19.8	26.9	5.01	92.8	36.0	5.01	82.0
45	24.7	19.9	24.7	4.81	94.0	33.0	4.81	84.7
50	22.2	20.1	22.2	4.57	95.1	30.0	4.57	87.3
55	22.5	17.0	22.5	4.30	96.1	27.0	4.30	89.7
60	23.1	14.5	23.1	3.99	96.9	24.0	3.99	91.9
65	23.7	13.5	23.7	3.65	97.7	20.0	3.65	93.8
70	23.6	13.5	23.6	3.26	98.3	17.0	3.26	95.5
75	20.3	12.4	20.3	2.83	98.8	14.0	2.83	96.9
80	16.6	12.3	16.6	2.36	99.2	11.0	2.36	98.1
85	13.5	12.1	13.5	1.84	99.6	8.0	1.84	98.9
90	9.0	10.1	10.1	1.28	99.8	5.0	1.28	99.5
95	4.5	5.9	5.9	0.66	100.0	3.0	0.66	99.9
100	0.0	0.0	0.0	0.00	100.0	0.0	0.00	100.0

Table 5.4 Member load accuracies for various U.S. Govt. Standards

Standard	Criterion	Member load error (%)
Air force space command	Δf = 3 %	21.6
	Diagonal COR = 95 %	22.4
	Off-Diagonal COR = 10 %	15.6
NASA	Δf = 5 %	26.8
	Diagonal COR = 90 %	31.1
	Off-Diagonal COR = 10 %	15.6
"MAC"	Δf = 5 %	26.8
	(MAC)$^{1/2}$ = 90 %	27.7
	Δf = 3 %	21.6
	(MAC)$^{1/2}$ = 95 %	22.6

(4) Adherence to strict test-analysis correlation standards (based on orthogonality and cross-orthogonality metrics), such as those defined by U.S. government agencies, provides a well-developed framework for test-analysis correlation. When acceptable criteria are met, dynamic loads are accurately predicted. Alternative (non-weighted) metrics are in need of well-defined standards to gain broader acceptance.

(5) Localization of test-analysis discrepancies appears to benefit from utilization of test-based flexibility metrics, rather than mode-to-mode based review procedures.

Unweighted test-analysis metrics [based on the modal assurance criterion (MAC) and its offspring], and modal expansion strategies (based on the system equivalent reduction-expansion process) represent alternatives that may address difficulties associated with very large-order finite element models and measurement situations for which instrumentation arrays cannot completely map system modes. As alternative test-analysis correlation procedures gain maturity, well thought out standards analogous to U.S. government standards (developed for weighted orthogonality metrics) should be developed.

Table 5.5 Comparison of coherent modal cluster kinetic energy distributions

Modal cluster kinetic energies (%)

DOF	(Mode 1) Model	Test	Δ (%)	(Mode 2) Model	Test	Δ (%)	(Modes 3 + 4)/2 Model	Test	Δ (%)	(Mode 5) Model	Test	Δ (%)	(Modes 6 + 7 + 8)/3 Model	Test	Δ (%)
1	0.33	0.32	−0.01	0.47	0.65	0.17	0.53	0.27	−0.27	7.58	7.34	−0.24	10.58	12.79	2.21
2	1.29	1.26	−0.03	1.76	2.39	0.63	1.51	0.76	−0.75	16.27	15.52	−0.75	9.02	9.84	0.82
3	4.97	4.84	−0.13	6.13	8.26	2.13	3.13	1.54	−1.59	17.45	15.95	−1.49	0.60	1.77	1.18
4	4.25	4.16	−0.09	0.81	1.47	0.66	5.41	4.91	−0.50	1.15	1.32	0.17	5.94	5.01	−0.93
5	7.25	7.12	−0.12	0.02	0.03	0.01	8.53	9.63	1.10	3.15	2.27	−0.87	6.03	7.64	1.62
6	6.84	6.79	−0.05	0.71	0.35	−0.36	6.15	7.51	1.35	9.72	8.17	−1.55	0.77	0.93	0.16
7	7.77	7.78	0.01	2.20	1.68	−0.53	4.35	4.90	0.55	8.89	7.89	−1.01	5.76	5.89	0.13
8	8.53	8.61	0.08	4.09	3.62	−0.47	3.46	3.36	−0.09	1.57	1.50	−0.07	5.11	6.15	1.04
9	11.36	11.55	0.19	7.29	7.00	−0.29	6.18	6.30	0.13	1.65	1.32	−0.33	0.12	0.24	0.12
10	9.34	9.49	0.15	6.77	6.55	−0.22	9.61	9.82	0.22	6.09	5.12	−0.97	9.46	9.71	0.25
11	4.72	4.36	−0.35	11.14	10.19	−0.95	0.13	0.19	0.06	5.97	8.46	2.49	8.52	5.25	−3.27
12	5.06	4.68	−0.38	17.16	16.11	−1.05	1.24	1.26	0.02	0.08	0.07	−0.02	3.62	2.76	−0.86
13	5.28	4.88	−0.40	21.62	20.55	−1.07	4.78	5.39	0.62	8.20	10.79	2.58	1.69	0.94	−0.75
14	2.68	2.47	−0.20	11.63	11.10	−0.53	3.34	3.84	0.49	7.64	10.20	2.56	4.55	2.96	−1.58
15	3.39	3.76	0.37	0.30	0.63	0.33	5.52	8.47	2.95	1.48	1.31	−0.17	5.87	8.68	2.81
16	3.82	4.15	0.33	0.92	1.40	0.48	10.85	11.87	1.02	0.44	0.38	−0.06	7.32	4.24	−3.08
17	4.17	4.45	0.28	1.70	2.21	0.51	13.06	11.04	−2.02	0.06	0.06	0.00	0.75	0.89	0.14
18	4.41	4.63	0.22	2.41	2.81	0.40	9.06	6.55	−2.51	1.05	0.96	−0.09	7.12	8.46	1.34
19	4.54	4.69	0.15	2.86	3.03	0.17	3.17	2.38	−0.79	1.57	1.38	−0.20	7.19	5.84	−1.34
Total	100.00	100.00	0.00	100.00	100.00	0.00	100.00	100.00	0.00	100.00	100.00	0.00	100.00	100.00	0.00

Component	(Mode 1) Model	Test	Δ (%)	(Mode 2) Model	Test	Δ (%)	(Modes 3+4)/2 Model	Test	Δ (%)	(Mode 5) Model	Test	Δ (%)	(Modes 6+7+8)/3 Model	Test	Δ (%)
1	56.07	56.11	0.04	26.17	27.04	0.87	44.57	45.15	0.59	65.07	58.85	−6.22	51.90	57.63	5.73
2	19.87	18.47	−1.40	64.18	61.49	−2.69	10.83	11.35	0.52	29.37	36.35	6.98	18.62	12.67	−5.95
3	24.06	25.42	1.36	9.65	11.47	1.82	44.60	43.50	−1.10	5.56	4.80	−0.76	29.48	29.70	0.22
Total	100.00	100.00	0.00	100.00	100.00	0.00	100.00	100.00	0.00	100.00	100.00	0.00	100.00	100.00	0.00

Fig. 5.4 Localization of test-model differences using a modal flexibility metric

Localization of Test-Model Differences using a Modal Flexibility Metric
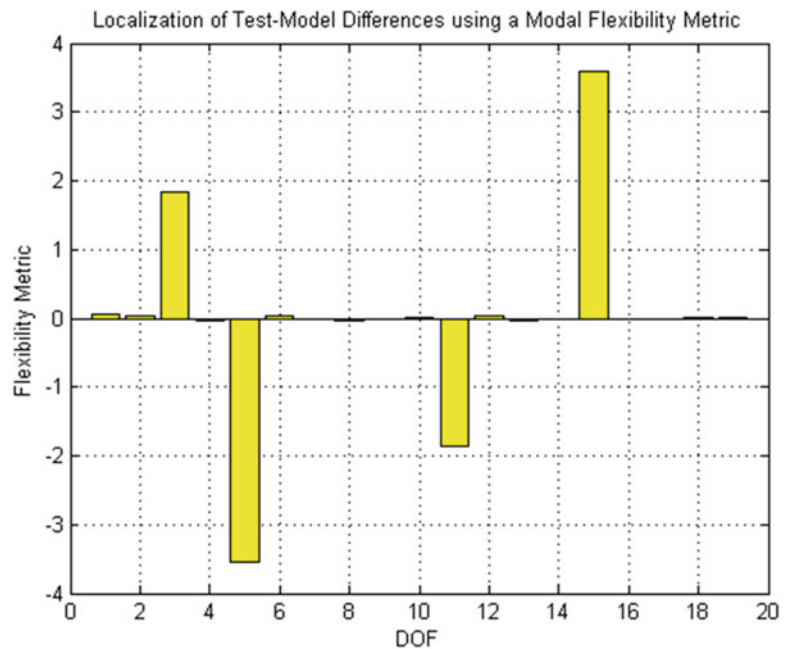
References

1. Piersol A, Paez T (2010) Harris' shock and vibration handbook, 6th edn. McGraw-Hill, New York
2. Zienkiewicz OC, Taylor RL, Zhu JZ (2005) The finite element method: its basis and fundamentals, 6th edn. Elsevier, Boston
3. Rodden WP (2011) Theoretical and computational aeroelasticity. Crest Publishing, Burbank
4. Independent structural loads analysis, Air Force Space Command, SMC-S-004, 13 June 2008
5. Test requirements for launch, Upper Stage and Space Vehicles, MIL-STD-1540C, 1994 (USAF)
6. Load analyses of spacecraft and payloads, NASA-STD-5002, 1996
7. Williams D (1945) Dynamic loads in aeroplanes under given impulsive load with particular reference to landing and gust loads on a large flying boat. Great Britain Royal Aircraft Establishment Reports SME 3309 and 3316
8. Shock design criteria for surface ships, NAVSEA 0908-LP-000–3010 Rev 1, 1995
9. Hurty W (1965) Dynamic analysis of structural systems using component modes. AIAA J 3(4):678–685
10. Craig R, Bampton M (1968) Coupling of substructures for dynamic analysis. AIAA J 6(7):1313–1319
11. Benfield W, Hruda R (1971) Vibration analysis of structures by component mode substitution. AIAA J 9(7):1255–1261
12. Guyan R (1965) Reduction of mass and stiffness matrices. AIAA J 3:380
13. Coppolino R, Borowski V (1997) Integrated modal testing and analysis of a body-on-frame automobile. In: Proceedings of IMAC XV, February 1997
14. Coppolino R (1998) Automated response DOF selection for mapping of experimental normal modes. In: Proceedings of the 16th international modal analysis conference (IMAC), February 1998
15. Martinez D, Miller A (1985) Combined experimental/analytical modeling of dynamic structural systems: ASME, AMD, vol 67, New Mexico, 1985
16. O'Callahan J, Avitabile P, Riemer R (1989) System equivalent reduction expansion process. In: Proceedings of the 7th international modal analysis conference (IMAC), 1989
17. Coppolino R (2013) FEM sensitivity vector basis for measured mode expansion. In: Proceedings of the 31st international modal analysis conference (IMAC), February 2013
18. Rodden W (1967) A method for deriving structural influence coefficients from ground vibration tests. AIAA J 5:991–1000
19. Lin C (1990) Location of modeling errors using modal test data. AIAA J 28(9):1650–1654
20. Avitabile P (1998) Overview of analytical and experimental modal model correlation techniques
21. Allemang R (2002) The modal assurance criterion (MAC): twenty years of use and abuse. In: Proceedings of the 16th international modal analysis conference (IMAC), 2002

Chapter 6
A Brief History of 30 Years of Model Updating in Structural Dynamics[*]

François M. Hemez and Charles R. Farrar

Abstract Since the development of the Finite Element (FE) method at the University of California Berkeley and the Boeing Company in the 1960s, the question of appropriateness of a model has always preoccupied developers and practicing engineers. Because of the early focus on predicting the linear vibrations of coupled systems for aerospace and civil engineering applications, test-analysis reconciliation initially consisted in updating the FE matrices such that their eigen-properties reproduce the identified resonant frequencies and mode shape vectors. As the FE method increased in sophistication in the following decades, and computational resources became widespread, test-analysis reconciliation evolved beyond optimal matrix updating to include sensitivity and residual-based methods that attempted to calibrate individual element matrices or design parameters. Fueled by an ever-increasing diversity of applications, FE model updating expanded beyond the correlation of modal response to handle frequency response functions, static deflections, and time-domain waveforms. Component mode synthesis concepts were progressively integrated to handle the spatial mismatch between measurement points of a structure and the FE discretization where the spatial information is predicted. This publication briefly overviews the first 30 years of FE model updating development, from the mid-1960s to the mid-1990s, because most of the technology currently available originates in this period. FE model updating methods are categorized into broad categories that each offer their own benefits and limitations. Potential growth areas, such as application to nonlinear dynamics, are discussed.

Keywords Finite element model updating • Calibration • Test-analysis correlation • Verification and validation • Uncertainty quantification

6.1 Introduction

Since it was first developed in the 1960s, Finite Element (FE) modeling has become an essential analysis method in computational physics and engineering. Areas of application range from disciplines of conventional mechanical engineering (solid mechanics, structural dynamics, fluid dynamics, etc.) to material science, the medical field, transport applications and problems featuring coupled physics. The desire to "validate" models and quantify the agreement between physical measurements and code predictions has paralleled the development of the FE method since its early beginnings. This chapter develops a brief discussion of techniques developed for test-analysis correlation in the context of FE modeling, also referred to as *model updating*.

Because the history of model updating is closely linked to the development of the FE method, Sect. 6.2 starts by overviewing how the idea of finite elements came about. This discussion is not meant to be an exhaustive history of the FE technology. A few ideas are presented that are useful to understand the potentials and limitations of FE model updating.

---

[*]This chapter is dedicated to Dr. David Zimmerman, great researcher and educator who made significant contributions to the discipline of finite element model updating.

F.M. Hemez (✉) • C.R. Farrar
Los Alamos National Laboratory, NSEC, 87545, Los Alamos, NM, USA
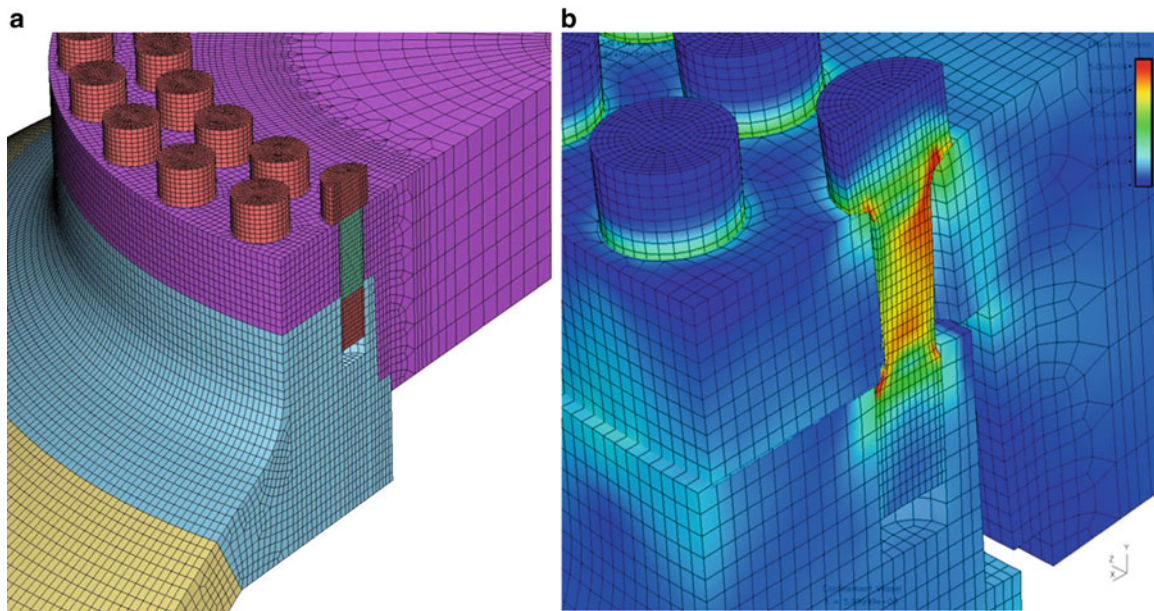e-mail: hemez@lanl.gov; farrar@lanl.gov

Fig. 6.1 Illustration of a FE mesh for the simulation of pressure vessel dynamics. (**a**) Finite element discretization. (**b**) Stress prediction in a bolt (credit: J. Pepin, LANL, and B. Thacker, Southwest Research Institute)

Section 6.3 organizes the vast landscape of model updating into broad categories, motivates each category and briefly presents their advantages and drawbacks. Again, the discussion is not meant to be exhaustive and the chapter is not attempting to fully review the discipline of model updating. Our intent, instead, is to promote a better understanding of why FE model updating has evolved as it has.

Figure 6.1 illustrates the FE method with a dynamic calculation of stress for a pressure vessel. The element discretization is shown in Fig. 6.1a, while the cut-away view of Fig. 6.1b illustrates the stress distribution of a bolt as well as the relative displacement between the vessel wall and top door.

A characteristic of the FE method, not always observed in other computational approaches, is that the physical interpretation is closely coupled to the mathematical theory. Indeed, the two have been developed in synergy. Literature on the subject parallels this observation. Oden [1], for example, discusses the finite element theory, while [2, 3] develop somewhat more practical-oriented explanations. Hughes [4] introduces the main techniques for analysis of linear problems, which currently still comprise the majority usage of the FE method.

The need to calibrate, or update, FE models stems from the desire to generate predictions that reproduce, to the extent possible, the available measurements. In linear mechanics, these are static deflections and vibration properties of structures (frequency response functions, resonant frequencies, mode shapes). Due to the prominence of experimental modal analysis in structural dynamics, these measurements represent the overwhelming majority of data used to update FE models today. However, we will discuss that the early focus of FE model updating was not so much to "validate" a model. It was to match the available measurements. Said differently, a model was found to be "validated" if its predictions were able to reproduce the measurements, which begs the first question: are the right answers obtained for the right reasons?

The second question is: what gets calibrated? Due to limited computing resources, the early developments of FE model updating emphasized optimal matrix updates to estimate mass and stiffness matrix corrections, ΔM and ΔK, for the free-vibration equation. With the arrival of more powerful computing resources, then, came the development of methods based on Taylor series expansion of the equation-of-motion, as well as iterative solvers and optimization algorithms. Combined with sensitivity analysis, these techniques made it possible to apply corrections to individual material properties or geometrical attributes of finite elements.

The third question, that we wish to briefly address in this chapter, is: to what extent is model updating able to handle the practical difficulties of engineering applications? Irrespective of how sophisticated, or elegant, a correction method might be, it remains an academic exercise if it cannot handle "real" situations. Engineering applications offer many complications, including the fact that nodes of a FE discretization have no reason to be collocated with measurement points, the fact that experimental variability needs to be accounted for in the updating process, and the potential for nonlinear dynamics. We will briefly discuss the extent to which the early FE model updating technology was able to meet these challenges.

The chapter is organized as follows. Section 6.2 discusses a few concepts of the FE method that are useful to understand the history of model updating. In Sect. 6.3, updating methods are organized in three broad categories. The logic behind each category is presented in order to explain their respective strengths and weaknesses. Section 6.4 discusses factors that complicate the development of model updating techniques, and their application to "real-life" problems.

6.2 Genesis and Concepts of the Finite Element Method

In this section, a few concepts of the FE method are briefly discussed. The discussion is not meant to provide a particularly complete overview of the technology; the aspects emphasized, instead, are useful to understand the history of model updating.

6.2.1 Early Genesis of the Finite Element Method

What marks the unofficial "birth" of the FE method in 1955, approximately, is the research performed at Boeing (Seattle, Washington) on "structural elements" to analyze the vibrations of large-aspect-ratio Delta wings. Two basic formulations are then studied, the first one based on the concept of stiffness, while the second one uses a flexibility approach. (For more about this, see Sect. 6.2.3). Prior to the 1960s, these analyses of vibration dynamics were performed "by hand" using back-of-the-envelope, 1D beam-like models. Despite being based on highly simplified models and somewhat crude approximations, this approach nevertheless provided accurate-enough predictions for design and analysis. So why seek a new approach?

New design concepts, such as Delta wings, make it necessary to develop a general-purpose capability for predictions because structural stress distributions can no longer be estimated with confidence from beam-like approximations. This lack-of-confidence prompts the paradigm shift from closed-form derivations to numerical methods. It coincides with the fast development of computer science that opens the door to novel and faster methods to assess prototype designs.

The work of Professor Edward Wilson, University of California Berkeley (Civil Engineering), makes him what many consider the "founding father" of the FE method [5–7]. Professor B. Fraeijs de Veubeke, University of Liège (Belgium), although not as well-known in the U.S., is the other key figure [8, 9]. In the early 1960s, applied mathematicians and engineers make the link between Boeing's "structural elements" and variational principles [10]. The original FE method is re-discovered as a Ritz-Galerkin weak formulation of the equations-of-motion using piece-wise linear shape functions. In 1966, Carlos Felippa, now Professor at the University of Colorado at Boulder, publishes a doctoral thesis on the calculation of stresses in dam structures using finite elements [11]. It is the 2nd thesis ever published demonstrating what the method could achieve.

Throughout the 1970s, the main trends are, first, the development of computational software that implements the FE method and, second, the justification by applied mathematicians of its scientific rigor. Theoretical work leads to advances in the stability and convergence properties of finite elements. The equivalence is established between strong and weak solutions, and all the pieces are in place to promote the development of the method as the main analysis tool in solid mechanics and structural dynamics. Fast forwarding through five decades of development, one can evoke many theoretical breakthroughs and practical applications in disciplines such as a posteriori error indicators, mesh adaptation, fluid–structure interaction, particle and geo-physics transport methods, stability analysis, vibration, acoustics, and nonlinear dynamics.

6.2.2 The Equations-of-Motion Considered

The general-purpose Equation-Of-Motion (EOM) considered in this work is the equation of linear dynamics written as:

$$\left(M \frac{\partial^2 \bullet}{\partial t^2} + D \frac{\partial \bullet}{\partial t} + K \right) U(t) = F_{Ext}(t) \tag{6.1}$$

where M, D, K are the master (assembled) mass, viscous damping, and stiffness matrices of the FE representation, respectively; $F_{Ext}(t)$ is a time-varying vector of applied forces and moments; and U(t) is the resulting, time-varying vector of displacement and rotation Degrees-Of-Freedom (DOF). With the assumption of time-space decoupling, modal superposition can be applied to Eq. (6.1), leading to the well-known linear equation of non-damped, free vibration:

$$K \Psi = M \Psi \Omega^2 \tag{6.2}$$

Table 6.1 Comparison of attributes of the stiffness and flexibility FE methods

Criterion	Stiffness method	Flexibility method
Are element matrices easy to compute?	Easy	Difficult
Are master matrices easy to assemble?	Easy	Difficult
How easy is it to handle rigid body modes?	Difficult	Easy
Is the numerical solver expensive?	Expensive	Cheap
What is the master (linear) equation-of-motion?	$Z(s)\, U(s) = F_{Ext}(s)$	$U(s) = H(s)\, F_{Ext}(s)$
How is the master matrix stored?	Sparse	Full
What is the algorithm to solve the equations?	Matrix inversion	Matrix product

where Ψ is the matrix of mode shape deflections (one vector per column), and the diagonal matrix Ω stores the corresponding resonant frequencies. Unless otherwise noted, the present discussion is based on the equation of vibration Eq. (6.2), written compactly for a single mode as:

$$Z(\omega_k)\ \Psi_k = 0 \tag{6.3}$$

where $Z(s) = K - s^2 M$ is the dynamic stiffness matrix at frequency "s." [Note that Eq. (6.3) is written with $s = \omega_k$ for the kth resonant mode.] Even though it is not used here, the discussion can also be applied to the linear EOM in statics, where a vector U of generalized displacements results from applied forces and moments F_{Ext} according to:

$$K\, U = F_{Ext} \tag{6.4}$$

FE model updating in the context of nonlinear dynamics, where the EOM is described by the momentum equation where inertia forces and internal F_{Int} forces balance the externally-applied forces F_{Ext}, such as:

$$M \frac{\partial^2 U(t)}{\partial t^2} + F_{Int}(t) = F_{Ext}(t) \tag{6.5}$$

is not discussed for two main reasons. First and foremost, the early development of FE updating had an almost exclusive focus on the equation of linear dynamics [Eq. (6.2)]. Second, it is the authors opinion that generalizing FE updating concepts, such as those overviewed herein, to nonlinear dynamics has not yielded significant achievements, except in the case of limited-scope, "niche-like" applications. For a discussion of nonlinear model updating, see [12].

### 6.2.3 Basic Concepts of the Finite Element Method

The basic concept of the FE method, or most other computational methods as a matter of fact, is that the EOM can be solved analytically for elemental geometries with simple-enough boundary conditions. Here, "analytical" refers to a solution of the continuous EOM that can be derived in closed-form or with high accuracy using, for example, Gauss-point quadrature rules. The geometry of the original problem, therefore, is discretized into these elemental geometries. The *continuous* problem is then decomposed into a multitude of similar, yet, *discrete* problems formulated on elemental geometries that are the finite elements.

There are two formulations of the FE method that are dual of one another, and can be referred to in broad terms as the *stiffness* and *flexibility* methods. Table 6.1 summarizes the main attributes of these two approaches. In the stiffness method, the applied forces are known and the momentum equation, that is, $F_{Ext} = M\, d^2U/dt^2$, is converted to a displacement-based equation by assuming representations of, first, the kinetic condition and, second, the material behavior within each element. In statics (for simplicity), it gives Eq. (6.4). In comparison, the flexibility method calculates the displacements using a matrix–vector multiplication such as:

$$U = H\, F_{Ext} \tag{6.6}$$

Historically, both approaches were developed in parallel. Dr. Richard McNeal, who investigated the stiffness approach, moved on to fame and glory by creating the NASTRAN™ software. Who remembers the name of the other engineer tasked with developing the flexibility method? It is nevertheless interesting to note that, in dynamics, the flexibility method yields a representation, $U(\omega_k) = H(\omega_k)\, F(\omega_k)$ for the kth resonant mode, analogous to vibration measurements. Adopting a

Fig. 6.2 Illustrations of the two fundamental rules of the stiffness FE method. (**a**) Assembly of three truss elements. (**b**) Assembly of four shell elements
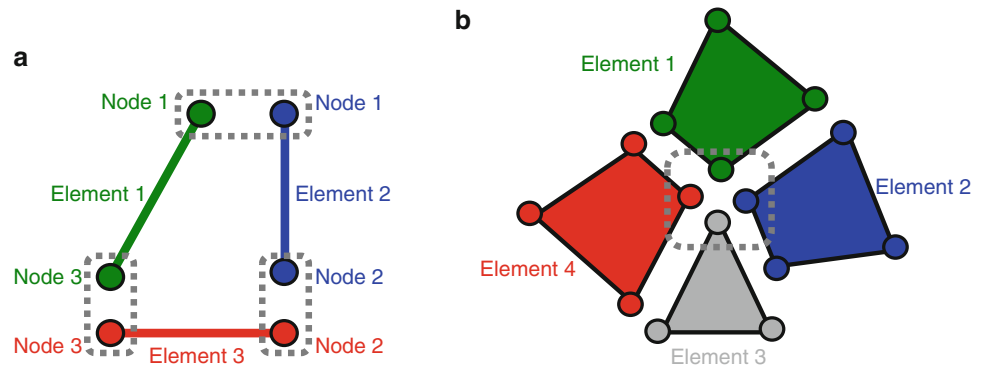
flexibility representation, as opposed to the conventional stiffness approach, would make it much easier to compare vibration measurements to FE predictions. Discussion presented in the remainder focuses on the stiffness method.

The stiffness method is articulated around two fundamental rules:

Rule 1: The summation of all forces contributed by finite elements that share a common node, or DOF, is equal to the externally applied force.

Rule 2: Displacements contributed by different finite elements at the same node, or DOF, are equal.

These rules are illustrated on the left side of Fig. 6.2 in the case of truss (or bar) elements. The right side of Fig. 6.2 suggests that similar rules apply to continuous elements such as shell (or membrane) finite elements.

The aforementioned rules are briefly illustrated for the three-truss example of Fig. 6.2a, which is useful to highlight properties of FE matrices that are discussed later in the context of model updating. The first rule provides the principle to equilibrate the forces at the kth node, or DOF, of the FE discretization. For the three-truss example, it can be written as:

$$\text{Rule 1} \quad \rightarrow \quad F^{(1)} + F^{(2)} + F^{(3)} = F_{Ext,k} \tag{6.7}$$

Representations of the kinetic condition and material behavior, discussed further in Eqs. (6.11)–(6.13) below, lead to a force-displacement equation expressed within each element as:

$$F^{(e)} = k^{(e)} \, U^{(e)} \tag{6.8}$$

The second rule converts the generalized displacement unknowns contributed by each element, denoted by $U^{(e)}$, into a single unknown per DOF:

$$\text{Rule 2} \quad \rightarrow \quad U^{(1)} = U_k, \; U^{(2)} = U_k, \; U^{(3)} = U_k \tag{6.9}$$

Inserting Eq. (6.8) in the summation [Eq. (6.7)] for each element, then, replacing element-specific displacements $U^{(e)}$ with the global DOF unknown U_k from Eq. (6.9), leads to the definition of the master stiffness matrix as:

$$\left(k^{(1)} \, U^{(1)}\right) + \left(k^{(2)} \, U^{(2)}\right) + \left(k^{(3)} \, U^{(3)}\right) = F_{Ext,k} \tag{6.10a}$$

$$\left(k^{(1)} + k^{(2)} + k^{(3)}\right) U_k = F_{Ext,k} \tag{6.10b}$$

$$\underbrace{\sum_{e=1\cdots N_E} k^{(e)}}_{K} U = F_{Ext} \tag{6.10c}$$

It is noted that, for simplicity, Eqs. (6.7)–(6.10) are derived symbolically in the local orientation frame of each element and the transformation to the global frame-of-reference is not included. For completeness, this omission is corrected in Eq. (6.14).

What remains to complete this description of the stiffness method, is a brief discussion of three so-far-overlooked aspects. The first two are assumptions made to describe, first, the kinetic relation that connects the element-level displacements to

strain deformations and, second, the constitutive law implemented to describe material behavior. Irrespective of how these conditions are defined, they lead to equations that can be written as:

$$\varepsilon^{(e)}_{Local} = B^{(e)} \, U^{(e)} \tag{6.11a}$$

$$\sigma^{(e)}_{Local} = C^{(e)} \, \varepsilon^{(e)}_{Local} \tag{6.11b}$$

Equation (6.11a) converts the element-level displacements and rotations in a strain vector, while Eq. (6.11b) expresses the constitutive behavior that transforms the element-level strains into stresses. Equation (6.11b) is written for linear, isotropic elasticity and additional terms would be added to express a nonlinear strength model with, for example, plastic deformation.

The internal energy is, by definition, equal to the contracted tensor product $\varepsilon{:}\sigma$ integrated over the volume of the finite element. Substituting Eq. (6.11), and using the vector notation $\varepsilon^T \sigma$ for simplicity, one can verify that the element-level stiffness matrix is obtained as:

$$\left(U^{(e)}\right)^T k^{(e)} \, U^{(e)} = \int_{\Omega^{(e)}} \left(\varepsilon^{(e)}_{Local}\right)^T \sigma^{(e)}_{Local} \, dV \tag{6.12}$$

where:

$$k^{(e)} = \int_{\Omega^{(e)}} \left(B^{(e)}\right)^T C^{(e)} \, B^{(e)} \, dV \tag{6.13}$$

Finally, the master (assembled) stiffness matrix can be written by summing the element-level stiffness contributions for all finite elements of the geometry discretization, as previously shown in the case of the three-truss example of Fig. 6.2a:

$$K = \sum_{e=1 \cdots N_E} \left(T^{(e)}\right)^T \left(\int_{\Omega^{(e)}} \left(B^{(e)}\right)^T C^{(e)} \, B^{(e)} \, dV \right) T^{(e)} \tag{6.14}$$

It is emphasized that the definition of master stiffness matrices in Eqs. (6.10c) and (6.14) are analogous. The main difference is that Eq. (6.14) introduces the transform matrix, $T^{(e)}$, used to convert the local coordinate system (x; y; z), defined in the frame-of-reference of the element, to the global (or laboratory frame) orientation (X; Y; Z).

One important aspect of Eqs. (6.11) and (6.13) is that only the constitutive law $C^{(e)}$ depends on material properties such as a modulus of elasticity, E, or Poisson's ratio, ν. The matrix $B^{(e)}$ that discretizes the kinetic relation might depend of geometric attributes, such as a length or shell thickness, but it does not depend on material properties. The local-to-global orientation matrix $T^{(e)}$ is a transform that, again, does not depend on the material behavior. These observations are important to consider when the calibration of material properties is sought.

6.2.4 Discussion of Implications for FE Model Updating

The previous discussion of FE modeling has implications for model updating. It is important to account for these considerations when implementing a semi-automatic correction method. This was not always the case, however, in the early developments of model updating. We briefly address four important implications.

1. *The sparsity of a FE stiffness matrix represents the structural load path.* It implies that a calibration procedure should not be allowed to make corrections to this load path, otherwise, the definition of the problem is fundamentally changed. One exception might be structural damage detection, where the presence of damage can severely alter the ability of a component to carry loads from one point to another. But under no circumstance should a non-existing load path be created by calibration; this would be a non-physical calibration of FE matrices.
2. *Rigid-body modes are essential properties of the FE representation.* Whether they are calibrated or not, FE matrices should preserve the rigid body dynamics and other fundamental characteristics, such as the center of mass and moments

of inertia of the "real" structure. These constraints, unfortunately, are usually not accounted for when formulating FE model updating.

3. *Constitutive properties are defined for elements of the discretization.* In the FE method, the principle of decomposing the geometry into simple elements is foundational. The element is the point-of-focus that implements descriptions of the kinetic condition, such as Eq. (6.11a), and material behavior, such as Eq. (6.11b). It implies that modeling an energy dissipation mechanism that would dissipate *across* element boundaries is nearly impossible within linear dynamics. A consequence is that model updating is fundamentally limited to adjust for modeling errors that would take their origin in these dissipation mechanisms.

4. *A FE model "flows" information from local elements to global responses.* Equation (6.14) indicates that the FE representation assembles element-level information into the master matrix. Hence, information "flows" from local elements to global responses, such as static deflections or mode shape eigenvectors. Model updating, on the other hand, is an *inference* that starts from global-level measurements and attempts to correct the element-level discretization. It raises the question of sensitivity versus error localization. Corrections brought to the model can be caused by the influence that specific elements exercise on predictions, instead of the modeling error.

6.3   A Classification of Finite Element Model Updating Methods

To discuss the history of FE model updating, a classification of methods is proposed. The classification is not exhaustive; it helps, however, to map the vast body of literature and discuss the rationale for its evolution in the last five decades. Early developments of FE model updating are discussed in Sect. 6.3.1. Section 6.3.2 introduces three categories: optimum matrix updating methods, small perturbation methods, and iterative sensitivity-based methods. Each category is then briefly discussed in the subsequent Sects. 6.3.3–6.3.5.

6.3.1   Early Developments of Finite Element Model Updating

The main driver for the development of semi-automated correction approaches, applicable to the FE method in the early 1960s, is the U.S. aerospace industry. Novel analysis techniques are sought to address challenging designs, such as the Delta wing concept, and to support the space launch industry. Model updating simply follows in the wake of these new techniques, with the desire to demonstrate that model predictions are capable to reproduce the measurements.

This early history is illustrated in Fig. 6.3 that depicts the Saturn-V launch vehicle (Fig. 6.3a) and adjustments brought to a 1D beam model of vibration dynamics (Fig. 6.3b). This example is extracted from [13]; it focuses on lateral vibrations of the Saturn-V. The FE model, back in 1974, consisted of 28 beam elements whose shear and bending stiffness coefficients were calibrated using experimental modal data acquired with 19 accelerometers. The updating was formulated as a Bayesian calibration method. The procedure reduced the prediction error of resonant frequencies from $\approx 5\%$ error, before calibration, to less than 0.05 %, after calibration. Collins et al. [13] was a milestone for its ability to apply updating to a "real-life" problem and, more importantly, for being the first technique, to the best of the author's knowledge, to account for experimental variability in the calibration of an aerospace FE model.

The other important driver of the 1960s early model updating technology, is the development of closed-loop controllers for guidance and navigation. For the most part, these applications also originate from the aerospace industry (missile guidance, satellite navigation, etc.). In a typical controller, the structure is described by low-frequency resonances and mode shape deflections; they constitute the target modes that the control algorithm attempts to stabilize. The need for a simple model, that reproduces these (measured) target modes with as-high-as-possible fidelity, had the consequence to orient model updating towards techniques that bring global adjustments to the mass and stiffness matrices.

A formulation can be, for example, to seek corrections ΔM and ΔK of the master matrices such that the equation of free vibration is verified when the measured dynamics $(\Psi_{\text{Test}}; \Omega_{\text{Test}})$ are substituted to the FE-based eigen-solutions:

$$(K + \Delta K)\ \Psi_{\text{Test}} -\ (M + \Delta M)\ \Psi_{\text{Test}}\ \Omega_{\text{Test}}^2 = 0 \qquad (6.15)$$

Formulations such as Eq. (6.15) lead to numerous model updating schemes, with little-to-no consideration for constraints such as preserving the load path representation of the original FE model, or even preserving the symmetry of FE matrices. The
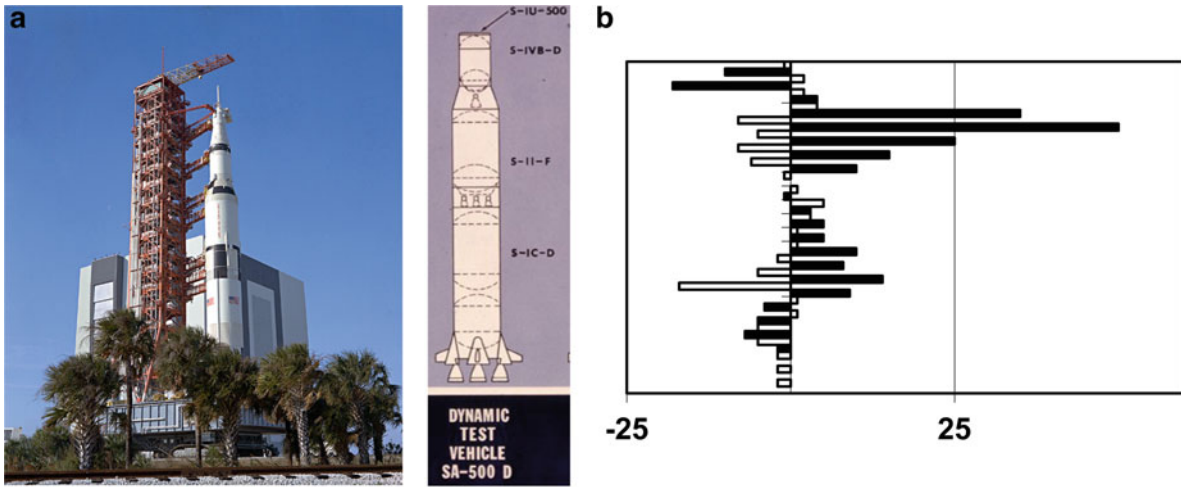
Fig. 6.3 FE model updating of a beam vibration model of the Saturn-V rocket, 1974. (**a**) Rocket (*left*), conceptual model (*right*). (**b**) Bending and shear stiffness updating [credit: NASA archive (**a**) and [13] (**b**)]

goal of these techniques, identified below as "optimal matrix updating," was simply to develop a model whose predictions match the measurements.

6.3.2 Three Broad Categories of Model Updating Techniques

At a high level, updating is nothing but the calibration of a model. If so, why not simply select a parameterization and formulate it as a "standard" calibration problem? Doing so would entail defining a cost function J(p) to minimize and, possibly, constraints C(p) to satisfy:

$$\min_{\{p\}} J(p) \text{ subject to constraints } C(p) \geq 0 \tag{6.16}$$

In Eq. (6.16), the cost function and constraints depend on parameters $p = \{p_1; p_2; \ldots p_N\}$ of the model. The cost function can be, for example, the error between measured and predicted frequencies or out-of-balance residuals defined from Eqs. (6.2) and (6.4). The constraints can be defined from the lower and upper bounds of model parameters. It would not be desirable, for example, to allow a negative-valued material density or shell thickness.

Early FE model updating techniques developed in the 1960s and 1970s did not formulate the problem in this way, first, because of a lack of adequate computing resource required to solve an optimization problem and, second, due to the fact that standard calibration tends to treat the model as a "black box." Instead, early developments strived to take advantage of fundamental FE properties, such as the local-to-global assembly procedure. Today's availability of efficient numerical optimization solvers, that rely on parallel processing, renders the aforementioned "plain vanilla" calibration of Eq. (6.16) much more attractive.

To organize the overview of early model updating, a classification into three broad categories is proposed. The first category is the optimum matrix updating (Sect. 6.3.3), where closed-form solutions are derived for global matrix corrections such as those shown in Eq. (6.15) of free vibrations. The second category is the small perturbation updating (Sect. 6.3.4) that consists in writing Taylor series-like expansions to linearize the optimization problem. The third category generalizes this last approach to iterative, sensitivity-based updating (Sect. 6.3.5). It is noted, once again, that this classification is not meant to be a review of existing literature. Imregun and Visser [14], Mottershead and Friswell [15] and Friswell and Mottershead [16] are examples of survey articles, recommended to complement our discussion.

6.3.3   The First Category: Optimum Matrix Updating (OMU)

The first category of updating methods is the Optimum Matrix Updating (OMU) that derives closed-form solutions of global matrix corrections, ΔM and ΔK. As alluded to previously, the emergence of this approach was due to the combination of limited computing power and desire to develop mass-stiffness representations that reproduce the measured data for applications such as launcher-payload coupled loads analysis, guidance and vibration control.

Amongst the early "founding fathers" of OMU, Dr. Alex Berman, Kaman Aerospace Corporation, and Professor Menahem Baruch, Technion (Israel), can be cited [17, 18]. In [18], the updating problem is defined as the estimation of global corrections ΔM and ΔK such that the adjusted FE model minimizes a user-defined error criterion, $J(\Delta M; \Delta K)$:

$$\min_{\{\Delta M; \Delta K\}} J(\Delta M; \Delta K) \text{ subject to constraints } C(\Delta M; \Delta K) \geq 0 \tag{6.17}$$

An updating method is an OMU if it achieves a direct solution, that is, no iteration is required, by analytically writing and solving the Kuhn–Tucker conditions of the optimization problem [Eq. (6.17)]. The set of equations to solve is shown next, assuming for simplicity that only a stiffness correction is sought (that is, $\Delta M = 0$), and using Lagrange multipliers, λ, to account for constraints, $C(\Delta K)$:

$$\frac{\partial}{\partial \Delta K}(J(\Delta K) + \lambda C(\Delta K)) = 0, \quad \frac{\partial}{\partial \lambda}(J(\Delta K) + \lambda C(\Delta K)) = 0 \tag{6.18}$$

In the OMU formulation [Eq. (6.17)], constraints are used to enforce fundamental properties, such as the symmetry, positive-definiteness, and sparsity pattern that represents the load path, of FE matrices. Examples of OMU schemes, that implement different combinations of constraints, are given in [19–22]. When simple-enough cost functions and constraints are defined, and further approximations are made (discussed below), the system of Eq. (6.18) can be solved in closed-form, hence, providing global correction matrices ΔM and ΔK whose evaluation requires no computationally expensive, iterative solver or optimization solver.

What about the cost function? Because the early OMU focus was on "matching measurements," cost functions were generally defined as error norms between the physical measurements and model predictions. For example, reproducing the resonant frequencies can be written as:

$$J(\Delta M; \Delta K) = \left\| \Omega_{\text{Test}}^2 - \Omega^2 \right\| \tag{6.19}$$

where, even though the notation is simplified, the FE-derived resonant frequencies stored in Ω^2 depend on matrix corrections $(\Delta M; \Delta K)$. Another commonly encountered approach is to define the cost function using the norm of residuals obtained from the EOM. Equation (6.2) of free vibrations is used for illustration. Because of the presence of modeling error, the equation is not verified when resonant frequencies and mode shape deflections predicted by the FE model are replaced by their measured counterparts:

$$K \Psi_{\text{Test}} \neq M \Psi_{\text{Test}} \Omega_{\text{Test}}^2 \tag{6.20}$$

This inequality can be taken advantage of to define out-of-balance residual forces, R:

$$R = K \Psi_{\text{Test}} - M \Psi_{\text{Test}} \Omega_{\text{Test}}^2 \tag{6.21}$$

The global matrix corrections $(\Delta M; \Delta K)$ are sought such that the vibration equation is verified, as proposed in Eq. (6.15). Collecting the unknown terms in the left-hand side, leads to:

$$\Delta K \Psi_{\text{Test}} - \Delta M \Psi_{\text{Test}} \Omega_{\text{Test}}^2 = -R \tag{6.22}$$

Equation (6.22) is the basis for many model updating schemes of the OMU and other categories.

Most OMU methods pay particular attention to preserving convexity of the optimization problem. This is because, with a convex problem, positivity of the Hessian does not need to be verified, and the Kuhn–Tucker conditions [Eq. (6.18)] are sufficient to calculate the minimum solution. Clearly, adopting the L^2 norm, that is, $\|y\|_2^2 = y^T y$ or $\|A\|_2^2 = \text{trace}(A^T A)$, is advantageous in this regard.
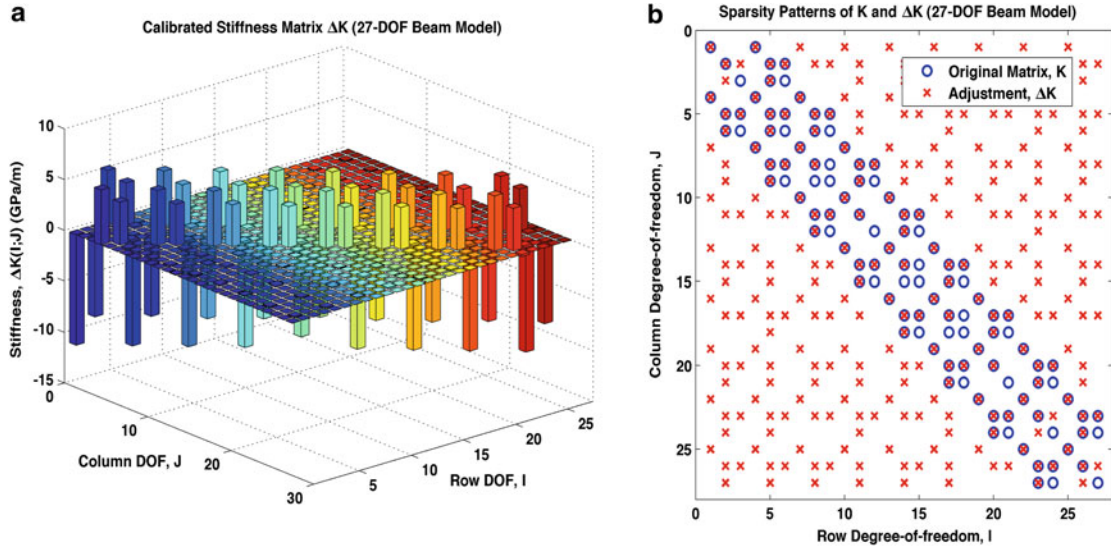
Fig. 6.4 Optimum matrix updating of a 27-DOF tapered wing beam model. (**a**) Global stiffness adjustment, ΔK. (**b**) Sparsity patterns of K and $(K + \Delta K)$

Another characteristic of OMU methods is the manner in which the Kuhn–Tucker conditions [Eq. (6.18)] are solved. The emphasis, again, is to derive a closed-form solution that avoids computationally expensive solvers. A technique commonly encountered is to rely on the spectral decomposition properties of linear dynamics. For example, the updated stiffness can be decomposed as:

$$(K + \Delta K) = (M \, \Psi) \, \Omega^2 \left(\Psi^T \, M \, \Psi \right)^{-1} (M \, \Psi)^T \tag{6.23a}$$

$$\Omega^2 = \left(\Psi^T \, M \, \Psi \right)^{-1} \Psi^T \, (K + \Delta K) \, \Psi \tag{6.23b}$$

With the spectral decomposition [Eq. (6.23b)], and assuming for simplicity that no mass correction is sought ($\Delta M = 0$), it can be verified that the measured frequencies can be reproduced using:

$$\Omega^2 = \Omega_{\text{Test}}^2 \tag{6.24a}$$

$$\left(\Psi^T \, M \, \Psi \right)^{-1} \Psi^T \, (K + \Delta K) \, \Psi = \Omega_{\text{Test}}^2 \tag{6.24b}$$

$$K + \Delta K = (M \, \Psi) \, \Omega_{\text{Test}}^2 \left(\Psi^T \, M \, \Psi \right)^{-1} (M \, \Psi)^T \tag{6.24c}$$

Equation (6.24c) defines the global stiffness correction ΔK without requiring an iterative solver. It corresponds to minimizing the cost function $J(\Delta K) = \|\Omega_{\text{Test}}^2 - \Omega^2\|_2$, defined with the L^2 norm.

An illustration is given in Fig. 6.4 in the case of a 27-DOF beam model of cantilever wing with tapered cross-section. The first five measured eigenvalues Ω_{Test}^2 are specified in the right-hand side [Eq. (6.24c)], and the corresponding stiffness correction ΔK is shown in Fig. 6.4a. It is verified that the updated matrix representation $(K + \Delta K; M)$ reproduces the target frequencies exactly. Figure 6.4b compares the sparsity of the original and adjusted matrices. Non-zero entries of K are identified as blue circles, while those of $(K + \Delta K)$ are shown with red crosses. The tendency of the OMU solution to introduce fill-in is evident; it means that the updated matrix $(K + \Delta K)$ does not preserve the structural load path of the original FE representation.

Before closing this section on OMU, an important caveat must be evoked. Derivations assume that the FE representation is defined over the same set of DOF as the measurement locations. None of Eqs. (6.20)–(6.24) make sense if FE matrices (K; M), their corresponding mode shape vectors Ψ, and measured eigenvectors Ψ_{Test}, are defined at differing locations. This is referred to as spatial "incompatibility" in the remainder. Because this constraint is generally not satisfied, a pre-processing step must be implemented to define a common set of finite element DOF and measurement locations. FE matrices, for

Fig. 6.5 Notional evolution of the FE model updating technology
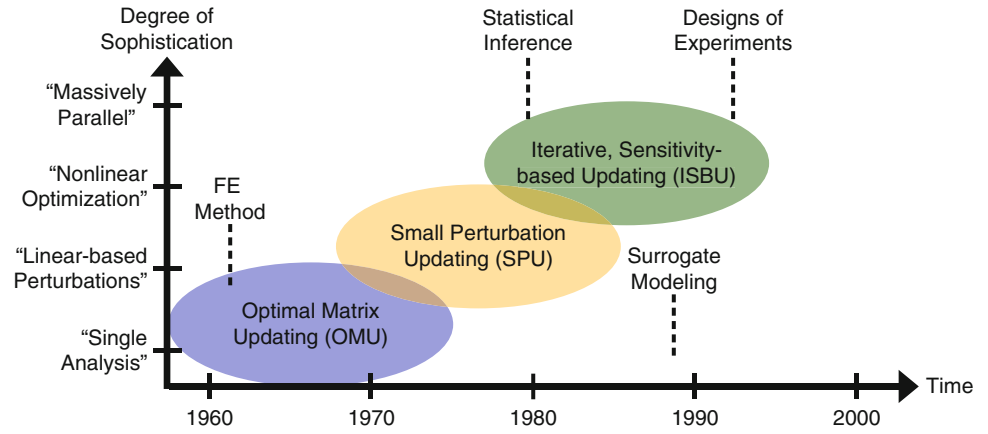
example, can be converted to measurement locations using techniques inspired from Component Mode Synthesis (CMS). Such matrix reductions are used in [23–25]; Balmès [26] develops a coherent organization of CMS methods.

Kammer [27] proposes a unified framework for stiffness matrix correction, where the matrix adjustment is decomposed into normal and residual contributions, $K + \Delta K = K_N + K_R$. Different OMU schemes result from differing choices of K_N and K_R, which are contributions to the stiffness matrix from measured normal modes and un-modeled residual dynamics, respectively. Another survey of OMU approaches can be found in [28].

6.3.4 The Second Category: Small Perturbation Updating (SPU)

The second category of updating methods is the Small Perturbation Updating (SPU). These methods are based on small perturbations of a quantity-of-interest or governing EOM. Hence, SPU borrows from the concept of re-design in engineering mechanics. Hoff et al. [29] and Chen and Lin [30] are two examples of application to linear dynamics.

The basic idea is to search for small perturbations of the mass and stiffness matrices, denoted by (δk; δm), that achieve small changes in predictions. These changes are sought such that the FE model predictions get closer to measurements. For example, adjusting a stiffness matrix, or some of its parameters, such that a resonant frequency is changed, can be written as:

$$\omega_{\text{Test}}^2 \approx \omega^2(k) + \delta\omega^2(k + \delta k) \tag{6.25}$$

A condition such as Eq. (6.25) can then be expressed as an inverse problem that estimates the perturbation δk such that the adjusted prediction $\omega^2 + \delta\omega^2$ matches the measurement ω_{Test}^2. SPU methods are mostly based on small perturbations of the vibration equation. Garba and Wada [31] is an example of first-order Taylor series expansion that arrives at a linear system of equations to adjust parameters of the FE model. This strategy is discussed further in the following.

In many regards, SPU can be viewed as "stop-gap" technology that contributed to evolve model updating away from closed-form corrections of global matrices, and closer to sensitivity-based methods. The latter were out-of-reach in the late 1960s and early 1970s for lack of computing power and efficient software. As soon as these restrictions were lifted, methods were developed to achieve large adjustments by relying on either nonlinear optimization or iterative, sensitivity-based perturbations. Figure 6.5 expresses this view by mapping the three broad categories of FE model updating in a two-dimensional space, as a function of time and degree-of-sophistication.

To relate them to the OMU category discussed in Sect. 6.3.3, SPU methods can be thought of as a Taylor series expansion of the cost function that expresses the "distance" between physical measurements and FE model predictions:

$$\underset{\text{1-by-1}}{J(k + \delta k)} = \underset{\text{1-by-1}}{J(k)} + \underset{\text{1-by-}N_P}{\delta k^T} \underset{N_P\text{-by-1}}{\nabla J(k)} + \underset{\text{1-by-}N_P}{\delta k^T} \underset{N_P\text{-by-}N_P}{\nabla^2 J(k)} \underset{N_P\text{-by-1}}{\delta k} + O(\delta k^2) \tag{6.26}$$

Equation (6.26) indicates dimensions (number of rows by number of columns) to emphasize that the equation is written for N_P calibration parameters, $k = (k_1; k_2; \ldots k_{NP})$. Limiting the expansion to first-order terms, and searching for an adjustment δk that minimizes the cost function, that is, $J(k + \delta k) = 0$, leads to a linearized system of equations:

$$\underset{\text{1-by-}N_P}{\nabla J(k)^T} \underset{N_P\text{-by-1}}{\delta k} = \underset{\text{1-by-1}}{-J(k)} \tag{6.27}$$

where the gradient vector of the dot-product collects partial derivatives of the cost function with respect to each parameter defined for calibration:

$$\underset{N_P\text{-by-1}}{\nabla J(k)} = \left[\begin{array}{cccc} \frac{\partial J(k)}{\partial k_1} & \frac{\partial J(k)}{\partial k_2} & \cdots & \frac{\partial J(k)}{\partial k_{Np}} \end{array} \right]^T \tag{6.28}$$

Equation (6.27) can be solved in a single step, in which case the adjustment brought to FE model parameters is $k^{(Updated)} = k^{(Original)} + \delta k$. An alternative is to implement an iterative solver where the solution, at the $(n + 1)^{th}$ iteration of the algorithm, is $k^{(n+1)} = k^{(n)} + \delta k^{(n+1)}$, with a least-squares solution obtained as:

$$\underset{N_P\text{-by-1}}{\delta k^{(n+1)}} = (1 - \lambda) \underset{N_P\text{-by-1}}{\delta k^{(n)}} - \lambda \left(\frac{J\left(k^{(n)}\right)}{\nabla J\left(k^{(n)}\right)^T \nabla J\left(k^{(n)}\right)} \right) \underset{N_P\text{-by-1}}{\nabla J\left(k^{(n)}\right)} \tag{6.29}$$

Equation (6.29) illustrates a predictor-corrector algorithm, where the scalar λ, $0 < \lambda \leq 1$, is a user-defined relaxation parameter that specifies the magnitude of the nth correction step. The full step is given by $\lambda = 1$ (no iteration); a value $\lambda \leq 1$ defines a linear combination between the previous-iteration solution $\delta k^{(n)}$ and the current correction. Implementing iterations, such as suggested in Eq. (6.29), is a way to limit the FE adjustment to small perturbations. This matters greatly to ensure that the first-order approximation [Eq. (6.27)] remains valid; it is important in situations where the cost function $J(k)$ is a nonlinear function of the correction parameters $(k_1; k_2; \ldots k_{NP})$.

The system of Eq. (6.27) is written for a single cost function; it can also be generalized to multiple cost functions. (Section 6.3.5 discusses this generalization.) Irrespective of this choice, the solution procedure involves linear matrix algebra. SPU methods, therefore, are somewhat more sophisticated than OMU that provides closed-form solutions for the calibration.

Many methods, based on the concept of small perturbation outlined in Eqs. (6.26)–(6.29), can be found in the literature. Chen and Garba [32] and Ojalvo [33] are two examples that use errors between measured and predicted resonant frequencies and mode shapes of a structure to define cost functions.

The analogy between SPU and design/shape optimization is noteworthy. Optimization methods attempt to optimize design parameters of a model to meet user-defined performance criteria that are often paired with design constraints. For example, the shape, mass and stiffness properties of an aircraft wing can be optimized to minimize weight, while avoiding a potential coupling of the bending and torsional modes to prevent aerodynamic flutter. Arora and Li [34] is an example of design optimization; Kikuchi et al. [35] is an application where the authors propose to optimize the topology of a FE mesh to achieve a performance requirement. It is interesting to note that the difference between SPU and design/shape optimization is that, in the latter, measurements are replaced by target requirements. The point made is that much about SPU can be learned by studying methods developed for design/shape optimization.

In the late 1980s and early 1990s, one witnesses an increasing integration of techniques developed for model updating (calibration), design and shape optimization, and the estimation of resonant frequency and mode shape derivatives. Similarly, CMS methods used to condense FE models and generate super-elements have demonstrated their maturity beyond the Guyan and Craig-Bampton reductions [25]. Such a "convergence" of the technology leads to the third category of sensitivity-based updating overviewed next.

6.3.5 The Third Category: Iterative Sensitivity-Based Updating (ISBU)

The third category of updating methods is the Iterative, Sensitivity-based Updating (ISBU). It represents the most versatile and powerful updating methods, which explains its popularity for a wide range of applications. ISBU methods seek to minimize a cost function that represents, as before, the error between measurements and model predictions. Spatial incompatibility between measurement locations and nodes of the FE discretization is treated with CMS-based reduction or expansion techniques [26], and numerical solvers are used to optimize the model parameters based on the error criterion defined.

Cost functions of ISBU do not need to be discussed in details, since they come from the same criteria of test-analysis correlation as those previously overviewed. The frequency differences of Eq. (6.19), as well as mode shape differences, are frequently encountered choices. Another common criterion is to minimize the norm of out-of-balance residual forces of Eq. (6.21):

$$J(p) = \left\| K \, \Psi_{\text{Test}} - M \, \Psi_{\text{Test}} \, \Omega_{\text{Test}}^2 \right\| \tag{6.30}$$

Once the test-analysis correlation criterion is defined, and additional constraints are potentially added, an iterative method is implemented to solve the corresponding optimization problem, as illustrated in Eqs. (6.26)–(6.29). The main difficulties become implementation issues, such as the accuracy of cost function gradients, reaching a global optimum solution, and time-to-solution.

The first significant difference with SPU methods is that the definition of parameters optimized steps away from global corrections, such as "$p = \Delta K$," or matrix entries, such as "$p = K_{I,J}$." Instead, the parameters are defined at the element level. They can be corrections brought to the element-level mass and stiffness matrices, descriptors of the geometry (mass, length, thickness, etc.), or coefficients of a constitutive material model (modulus of elasticity, Poisson's ratio, etc.).

The second significant difference is that, generally, the system of equations defined to calculate the parameter correction, δp, is solved iteratively with successive re-evaluations of the gradient matrix. Iterative solvers are better suited to the estimation of parameter corrections that exercise a nonlinear effect on FE model predictions.

For illustration, we give an example of ISBU method where the expansion [Eq. (6.26)] is limited to first-order terms. The cost function is defined as the prediction error of resonant frequencies. Instead of writing a global error norm, such as shown in cost function [Eq. (6.19)], the linearization [Eq. (6.27)] can be written for each resonant frequency (ω_1; ω_2; ... ω_m). Collecting these "m" equations yields:

$$\begin{bmatrix} \frac{\partial \omega_1(p^{(n)})}{\partial p_1} & \frac{\partial \omega_1(p^{(n)})}{\partial p_2} & \cdots & \frac{\partial \omega_1(p^{(n)})}{\partial p_{N_P}} \\ \frac{\partial \omega_2(p^{(n)})}{\partial p_1} & \frac{\partial \omega_2(p^{(n)})}{\partial p_2} & \cdots & \frac{\partial \omega_2(p^{(n)})}{\partial p_{N_P}} \\ \vdots & \vdots & \ddots & \vdots \\ \frac{\partial \omega_m(p^{(n)})}{\partial p_1} & \frac{\partial \omega_m(p^{(n)})}{\partial p_2} & \cdots & \frac{\partial \omega_m(p^{(n)})}{\partial p_{N_P}} \end{bmatrix} \begin{Bmatrix} \delta p_1^{(n+1)} \\ \delta p_2^{(n+1)} \\ \vdots \\ \delta p_{N_P}^{(n+1)} \end{Bmatrix} = \begin{Bmatrix} \omega_1^{\text{Test}} - \omega_1(p^{(n)}) \\ \omega_2^{\text{Test}} - \omega_2(p^{(n)}) \\ \vdots \\ \omega_m^{\text{Test}} - \omega_m(p^{(n)}) \end{Bmatrix} \tag{6.31}$$

The system [Eq. (6.31)] can be solved in a least-squares sense if enough equations are available, that is, $m \geq N_P$. One difficulty is to evaluate entries $\partial \omega_p / \partial p_q$ of the gradient matrix. It can be verified that the partial derivative of the pth frequency, with respect to the qth parameter, is obtained as:

$$\frac{\partial \omega_p^2}{\partial p_q} = \frac{\Psi_p^T \frac{\partial K}{\partial p_q} \Psi_p}{\Psi_p^T M \Psi_p} - \frac{\Psi_p^T \frac{\partial M}{\partial p_q} \Psi_p}{\left(\Psi_p^T M \Psi_p\right)^2} \tag{6.32}$$

Equation (6.32) suggests that the difficulty is shifted away from estimating the gradients $\partial \omega_p / \partial p_q$, towards the partial derivatives of master matrices. This degree of difficulty depends on how the parameters are defined. A judicious choice is to select parameters that represent geometrical or material properties of individual elements, or groups of elements, such that the derivatives can be evaluated in closed-form. Optimizing, for example, the elastic modulus of a linear constitutive law, $\sigma = E \cdot \varepsilon$, gives an element-level sensitivity matrix that is simply $\partial k^{(e)} / \partial E = 1/E \, k^{(e)}$. The global sensitivity matrix, $\partial K / \partial E$, can then be assembled from the element-level sensitivities.

Derivations are more subtle for static deflection derivatives, $\partial U / \partial p_q$, or mode shape derivatives, $\partial \Psi_p / \partial p_q$. The evaluation of these sensitivities involves the computationally expensive procedure of inverting a master matrix. Nelson [36] and Hou and Kenny [37] propose schemes that can be implemented to obtain derivatives, such as $\partial \Psi_p / \partial p_q$, while bypassing the potential matrix singularities involved.

ISBU formulations based on out-of-balance residuals [Eq. (6.30)] are discussed in [38–40]. Ladevèze and Reynier [41] defines a dual approach where residuals are defined as virtual displacements as opposed to out-of-balance forces. An extension of this technique to damping errors is proposed in [42]. Piranda et al. [43] applies the sensitivity approach [Eqs. (6.26)–(6.29)] to resonant frequency and mode shape vector errors. The efficiency of many of these techniques has been assessed in benchmarks, such as the study reported in [44]. Link [45] offers a discussion of ISBU methods, and the advantages and limitations that this calibration technology offers.
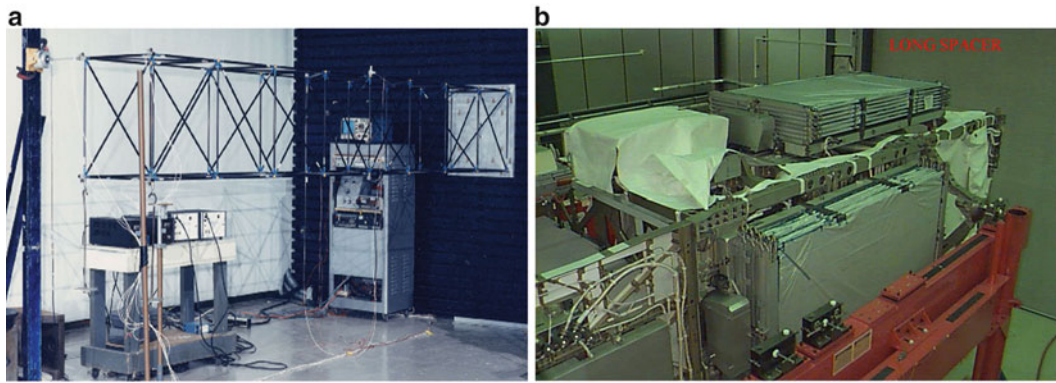
Fig. 6.6 Vibration testing of the ISS main truss. (**a**) NASA 8-bay truss testbed. (**b**) International Space Station main truss (courtesy: NASA [48])

Table 6.2 Correlation of the ISS main truss after calibration [48]

Mode number	Comparison of resonant frequencies			Mode shape correlation (MAC) (%)
	Measured (Hz)	Predicted (Hz)	Error (%)	
1	6.98	6.98	0.00	98.3
2	10.95	10.60	−3.19	97.5
3	12.42	12.40	−0.16	65.3
4	13.06	12.70	−2.76	89.8
5	13.87	13.67	−1.44	86.0

The versatility of ISBU has promoted application to many disciplines. One of them is Structural Health Monitoring (SHM), where model predictions augment physical measurements to locate, and assess the severity of, structural damage. Surveying the application of FE model calibration to SHM is beyond the scope of this discussion; a review can be found in [46]. One accomplishment, that we wish to highlight, is the work of Professor David Zimmerman, and his research team at the University of Houston, Texas. Their eigen-structure assignment technique [47, 48] was successful to calibrate models of the NASA International Space Station (ISS) main truss, illustrated in Fig. 6.6. Linear NASTRAN™ models with up to 66,000 DOFs were updated to achieve less than 3 % modal frequency error and at least 95 % mode shape correlation. These correlation requirements originate from recommended "best practices" [49]. Table 6.2 indicates a typical test-analysis agreement reached after FE model calibration for the ISS main truss.

6.4 A Brief Discussion of Challenges to Updating Methods

The overview of FE model calibration is concluded by briefly discussing several issues that present challenges. The first three are practical issues that, unfortunately, need to be dealt with: ill-conditioning, spatial incompatibility and error localization. Our view is that these issues do not offer fundamental challenges to FE model updating. The next four topics are more foundational: information-theoretic limitations of test-analysis correlation, experimental variability, truncation error and the application of FE model updating to nonlinear dynamics.

6.4.1 Numerical Ill-Conditioning of Inverse Problems

Inverse problems are, by definition, ill-posed. At best, it means that a parameter correction δp obtained by solving, for example, Eq. (6.27) or (6.31), is poor-quality due to contamination from numerical ill-conditioning. At worst, a calibration is ambiguous because an infinite number of solutions are available. Unless there are multiple solutions to choose from, ill-conditioning is not an issue that challenges FE model updating; it is an inconvenience to be dealt with.

Several approaches are available to mitigate the effects of ill-conditioning, such as discussed in [16]. Regularization can be applied. The well-known Tikhonov regularization adds a "minimum perturbation" term to the cost function, the effect of which is to orient the search towards solutions that do not deviate too much from the nominal values of model parameters. Calibration methods formulated with the Bayesian statistical framework introduce a "prior" term whose effect is analogous to regularization. Lastly, good practices of numerical analysis can be implemented, such as filtering out the null space of the gradient matrix inverted.

6.4.2 Mismatch Between Measurement Locations and FE Discretization

Spatial incompatibility between measurement locations and FE discretization nodes was evoked previously. (See, for example, the second-to-last paragraph of Sect. 6.3.3.) The fact is that a discretization is arbitrary; FE nodes have no reason to be co-located with measurement points. Spatial incompatibility, therefore, is another practical difficulty that must be dealt with.

There are two basic possibilities to handle spatial incompatibility. The first one is to expand the measurement locations to the FE spatial discretization. The second approach is to reduce the FE-based global matrices to measurement points. These two strategies are dual of each other. Methods, such as those presented in [26], can be applied to either expand the spatial measurements, reduce the FE matrices, or implement a hybrid approach that borrows from both strategies. The challenge is that both vector projection and matrix reduction rely on information derived from the FE model. Any modeling error "contaminates" the vector projection or matrix reduction step, hence, introducing an inextricable coupling between spatial incompatibility and the modeling error that one is attempting to correct through parameter calibration.

6.4.3 Localization of the Modeling Error

Calibration parameters are usually selected a priori. Sensitivity analysis can also be used to select them, keeping only those parameters that provide large derivatives of the cost function, $|\partial J/\partial p_k|$. A first issue is that the source and location of modeling error might be unknown, and the parameter selection might not allow to describe it accurately. Another issue is that modeling error does not necessarily coincide with high sensitivities, $|\partial J/\partial p_k|$. It implies that an adjustment is often brought to a FE parameter because this parameter exercises a large influence on the cost function, not necessarily because it is where the modeling error is located.

To address these uncertainties, it is often tempting to calibrate as many parameters as possible. Including large numbers of parameters, however, tends to increase ill-conditioning; it also tends to "spread" the corrections throughout the FE model instead of focusing them where they are really needed, that is, where modeling error is located. This dilemma goes back to a previously mentioned issue of FE modeling: there are limitations to inferring local model parameters from globally obtained, resonant frequency and mode shape information.

There are situations where error localization may not be such a serious issue. This is the case when the analyst knows the source of the modeling error, for example, at joints or connections between structural components. SHM is another application where damage scenarios might be known a priori. Deploying a posteriori error indicators, such as the residuals [Eq. (6.21)], can also offer a mapping of the modeling error on the computational mesh.

6.4.4 Information-Theoretic Limitations of Model Updating

Model updating can be viewed as a special case of the statistical inference of parameters given physical observations or measurements. In statistical sciences, the Cramér–Rao inequality provides a lower bound of the variance with which model parameters can be estimated [50]. The lower bound depends on the inverse of the Fisher information that represents the "curvature," or second derivative Hessian matrix, of the likelihood function defined for test-analysis correlation.

The information-theoretic limitation implies a lower bound on the accuracy of model parameters that can be estimated. This accuracy would depend on the formulation of the updating method, and amount and quality of physical measurements available for calibration. Even though it is not similar to the Cramér–Rao bound, one example of limit is derived in [51]:

$$\min_{1\leq k\leq m} \left|\omega^2_{\text{Test,k}} - \omega^2_k\right| \leq \frac{\|R\|_2}{\|\Psi_{\text{Test}}\|_2} \leq \max_{1\leq k\leq m} \left|\omega^2_{\text{Test,k}} - \omega^2_k\right| \tag{6.33}$$

where it is shown that the L^2 norm of out-of-balance residuals [Eq. (6.21)] cannot be made smaller than the minimum error in resonant frequency. The authors are not aware of investigations that would study lower bounds of parameter accuracy in the context of FE model updating. Nevertheless, it suggests that it makes no sense to calibrate model parameters beyond these theoretical limits. Doing so would be a manifestation of "over-fitting," which, unfortunately, is often encountered.
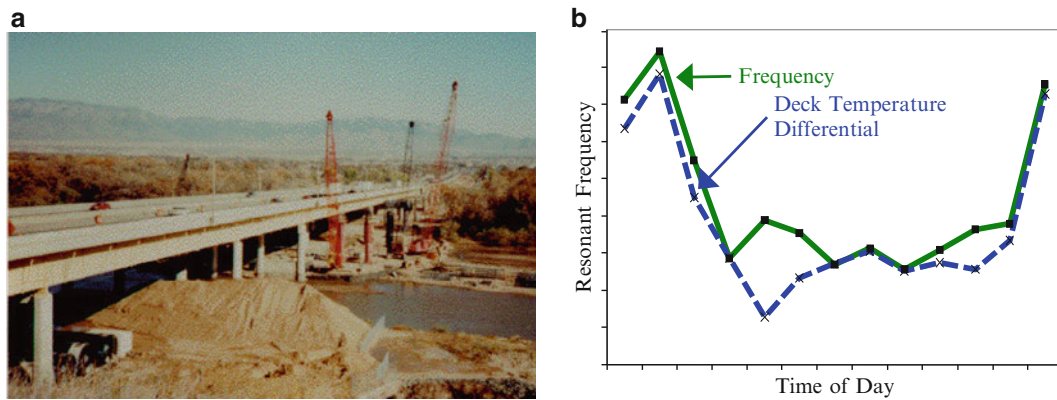
Fig. 6.7 Damage detection of the I-40 bridge in New Mexico. (**a**) I-40 bridge over the Rio Grande. (**b**) Variation of frequencies over time (credit: [53])

6.4.5 Accounting for Experimental Variability and Uncertainty

Another foundational challenge to FE model updating is experimental variability. As alluded to in Sect. 6.4.4, there is a theoretical limit to the accuracy of an inference. Likewise, the level of experimental variability, with which measurements are collected, should be taken into account as it sets a "threshold" beyond which calibrating the FE parameters becomes inefficient.

Farrar et al. [52, 53] were amongst the first ones to indicate the effect of experimental variability on the calibration of FE model parameters. Figure 6.7 illustrates this study that attempts to locate structural damage using a combination of vibration tests and FE predictions. Figure 6.7b plots the variation amplitude of the first resonant frequency over a 24-h period. It is observed that the variation is greater than the change induced by simulating structural damage with the model, leading to the conclusion that damage cannot be identified reliably in this application.

Many approaches inspired from Bayesian statistics have been developed in the mid-1990s to account for experimental variability in calibration. In Sect. 6.3.1, we have also evoked an early variant of Bayesian-like FE model updating [13], published in 1974. Rebba et al. [54, 55] offer a rigorous framework to account for experimental variability. With this and similar works, the focus of calibration shifts away from optimizing parameters, such that model predictions reproduce the measurements. Instead, one seeks to describe the parameter uncertainty with a probability law which, when sampled, yields a population of predictions that is consistent with the population of measurements. No single prediction matches any single measurement; test-analysis correlation is sought, instead, in the sense of ensemble statistics between predictions and measurements.

6.4.6 Accounting for Numerical Uncertainty Caused by Truncation

Similarly to experimental variability that can be thought of as defining bounds within which the "true-but-unknown" measurement is located relative to the data collected, truncation error defines bounds within which the "true-but-unknown" prediction is located relative to the values provided by simulations. Truncation error originates from discretizing the continuous EOM with a particular numerical method, and using a given level of mesh discretization. Using, for example, quadratic FE shape functions and low bulk viscosity does not produce the same error as a linear basis with high bulk viscosity. Truncation error is not known, except for a few code verification test problems, which means that it becomes an additional source of uncertainty in the problem.

Numerical uncertainty, that originates from truncation effects, should be accounted for during FE model updating, as it defines another contribution to the lower bound of prediction accuracy that can be achieved during calibration. Unfortunately, it is common in computational engineering to "run with a single mesh" and ignore truncation effects. Roache [56] and Hemez and Kamm [57] present techniques to quantify this truncation-based uncertainty, such that it can be accounted for. Applications can be found in the literature, for example, to the validation of wind turbine blade models [58, 59].
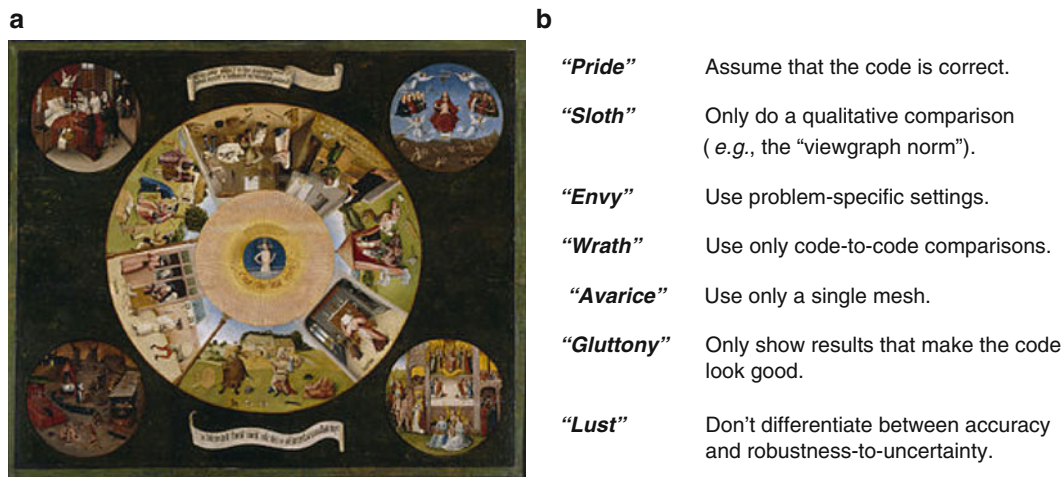
"Pride"	Assume that the code is correct.
"Sloth"	Only do a qualitative comparison (*e.g.,* the "viewgraph norm").
"Envy"	Use problem-specific settings.
"Wrath"	Use only code-to-code comparisons.
"Avarice"	Use only a single mesh.
"Gluttony"	Only show results that make the code look good.
"Lust"	Don't differentiate between accuracy and robustness-to-uncertainty.

Fig. 6.8 A metaphor of commonly encountered flaws in test-analysis correlation. (**a**) H. Bosch's "*Seven Deadly Sins*," 1485. (**b**) "Sins" of test-analysis correlation [credit: Prado Museum, Madrid, Spain (**a**) and [64] (**b**)]

6.4.7   Calibration of FE Representations for Nonlinear Dynamics

Model updating is typically applied to linear representations, using Fourier-based responses (resonant frequencies, mode shapes, etc.). When the response is significantly nonlinear and/or only very short time histories are available, assumptions underpinning the Fourier analysis can be violated. Sources of nonlinearity which can disrupt these assumptions are: nonlinear material response, contact, friction, other energy loss mechanisms and short-duration responses.

Nonlinearity, irrespective of its source, offers a foundational challenge to updating because the response can no longer be decoupled via modal analysis. Approaches have been proposed to expand the conventional space-time decoupling of the EOM to nonlinear systems [60, 61]. While these approaches have shown promise, applicability remains limited to "mild" nonlinearities that, for example, are isolated on the structure or do not perturb the (linear) response too severely. A non-exhaustive review of nonlinear model updating is proposed in [12].

Defining a general-purpose FE calibration technique, applicable to arbitrary nonlinear dynamics, seems an unattainable goal due to the vast diversity of sources and types of nonlinearities. One noticeable attempt is a formulation for nonlinear system identification, grounded in concepts of optimal control [62, 63]. These works highlight the significant computational burden of tracking a nonlinear time-domain response at multiple locations. To the best of the author's knowledge, this approach has not been applied to "real-life" problems. Fundamentally, a nonlinear response is described by three independent kinetic fields (displacement, velocity, acceleration) at every point of the structure. Experimentally, these three fields would have to be measured separately; computationally, they would have to be evolved independently. Neither experimental techniques nor computational methods are currently mature enough to meet these stringent requirements.

6.4.8   Closure

In closure, we re-iterate that technology for FE model updating has made great progress and achieved undeniable successes in three decades from the mid-1960s to the mid-1990s. This is especially the case for linear statics or linear dynamics. The technology, originally limited to closed-form corrections of master matrices, has evolved towards general-purpose sensitivity methods able to calibrate individual design parameters using diverse data (resonant frequency, mode shape, frequency response function, etc.). Current advances in modeling and analysis, pre- and post-processing software, and experimental methods for vibration testing, are likely to push forward the FE model updating technology even more.

Difficulties, some of which are discussed above, have also seriously hindered the transfer of FE model updating to industry. We prognosticate that some of these challenges will progressively disappear as simulation capabilities and experimental techniques keep improving. It should be the case for the quality of solutions (Sect. 6.4.1) and mismatch between measurement locations and FE discretization nodes (Sect. 6.4.2). Other difficulties, such as lower bounds on the value of information learned during calibration (Sect. 6.4.3) and nonlinear dynamics (Sect. 6.4.7), are foundational challenges to model updating. Another significant challenge is educational: "poor practices" of test-analysis comparison, illustrated in Fig. 6.8, are often encountered [64].

In the last 15 years, the computational physics and engineering communities have explored a change of paradigm towards Verification and Validation (V&V) [65]. We conclude by noting that V&V makes sense if the emphasis is on developing, and establishing the credibility of, a predictive capability. Verifying the quality of the analysis code, learning important sensitivities, and quantifying prediction uncertainty before starting to compare predictions to measurements, promotes "best practices" that mitigate short-comings, such as those illustrated in Fig. 6.8. The V&V technology offers another avenue of growth for FE model updating.

References

1. Oden T (1976) An introduction to the mathematical theory of finite elements. Wiley, New York
2. Zienkiewicz OC (1977) The finite element method in engineering sciences. McGraw-Hill, London
3. Dhatt G, Touzot G (1984) The finite element method displayed. Wiley, New York
4. Hughes T (1987) The finite element method: linear static and dynamic finite element analysis. Prentice Hall, Englewood Cliffs
5. Clough RW (1991) Original formulation of the finite element method. Finite Elem Anal Des 7:89–101
6. Wilson EL (1960) Matrix analysis of nonlinear structures. In: Proceedings of the 2nd ASCE conference on electronic computation, Pittsburg, September 1960
7. Clough RW, Wilson EL (1962) Stress analysis of a gravity dam by the finite element method. In: Symposium on the use of computers in civil engineering, Lisbon
8. Fraeijs de Veubeke BM (1951) Diffusion des Inconnues Hyperstatiques dans les Voilures à Longeron Couplés. Bulletin du Service Technique de l'Aéronautique, No. 24, Imprimerie Marcel Hayez, Bruxelles, p 56
9. Fraeijs de Veubeke BM (1974) Variational principles and the patch test. Int J Numer Meth Eng 8:783–801
10. Argyris J (1954) Energy theorems and structural analysis. Aircraft Engineering
11. Felippa CA (1966) Refined finite element of linear and nonlinear two-dimensional solids. UC Berkeley Report No. 66/22. University of California, Berkeley, October 1966
12. Hemez FM, Doebling SW (2001) Review and assessment of model updating for nonlinear, transient dynamics. Mech Syst Signal Process 15(1):45–74
13. Collins JD, Hart GC, Hasselman TK, Kennedy B (1974) Statistical identification of structures. AIAA J 12(2):185–190
14. Imregun M, Visser WJ (1991) A review of model updating techniques. Shock Vib Digest 23(1):19–20
15. Mottershead JE, Friswell MI (1993) Model updating in structural dynamics: a survey. J Sound Vib 162(2):347–375
16. Friswell MI, Mottershead JE (1995) Finite element model updating in structural dynamics. Kluwer Academic, Dordrecht
17. Berman A, Flannelly WG (1971) Theory of incomplete models of dynamic structures. AIAA J 9(8):1481–1487
18. Baruch M (1982) Optimal correction of mass and stiffness matrices using measured modes. AIAA J 20(11):1623–1626
19. Berman A, Nagy EJ (1983) Improvement of large analytical model using test data. AIAA J 21(8):1168–1173
20. Sidhu J, Ewins DJ (1984) Correlation of finite elements and modal test studies of a practical structure. In: 2nd SEM international modal analysis conference, Orlando, February 1984, pp 756–762
21. Kabe AM (1985) Stiffness matrix adjustment using mode data. AIAA J 23(9):1431–1436
22. Zhang Q, Lallement G (1987) Dominant error localization in a finite element model of a mechanical structure. Mech Syst Signal Process 1(2):141–149
23. Craig R, Bampton M (1968) Coupling of substructures for dynamic analyses. AIAA J 6(7):1313–1319
24. Hurty WC (19644) On the dynamic analysis of structural systems using component modes. In: 1st AIAA annual meeting, Washington, DC, June 1964 (Paper No. 64-487)
25. Masson G, Ait Brik B, Bouhaddi N, Cogan S (2006) Component mode synthesis (CMS) based on an enriched Ritz approach for efficient structural optimization. J Sound Vib 296:845–860
26. Balmès E (1996) Parametric families of reduced finite element models, theory and applications. Mech Syst Signal Process 10(4):381–394
27. Kammer DC (1988) Optimal approximation for residual stiffness in linear system identification. AIAA J 26(1):104–112
28. Smith SW, Beattie CA (1991) Secant-method adjustment of structural models. AIAA J 29(1):119–126
29. Hoff CJ, Bernitsas MM, Sandstrom RE, Anderson WJ (1984) Inverse perturbation method for structural redesign with frequency and mode shape constraints. AIAA J 22(9):1304–1309
30. Chen YM, Lin Y (1983) An iterative algorithm for solving inverse problems in structural dynamics. Comput Meth Appl Mech Eng 19:825–829
31. Garba JA, Wada BK (1977) Application of perturbation methods to improve analytical model correlation with test data. In: SAE aerospace technology conference and exposition, Los Angeles, November 1977 (Paper No. 77-0959)
32. Chen JC, Garba JA (1980) Analytical model improvement using modal test results. AIAA J 18(6):684–690
33. Ojalvo I (1992) A consistent first-order theory for structural model parameter improvement based upon dynamic test data. In: 33rd AIAA/ASME/ASCE/AHS/ASC structures, structural dynamics and materials conference, Dallas, April 1992
34. Arora JS, Li G (1993) Constrained conjugate direction methods for design optimization of large structures. AIAA J 91(2):388–395
35. Kikuchi N, Chung KY, Torigaki T, Taylor JE (1986) Adaptive finite element methods for shape optimization of linearly elastic structures. Comput Meth Appl Mech Eng 57:67–91
36. Nelson RB (1976) Simplified calculation of eigenvector derivative. AIAA J 14(9):1201–1205

37. Hou GJ-W, Kenny SP (1992) Eigenvalue and eigenvector approximate analysis for repeated eigenvalue problems. AIAA J 30(9):2317–2326
38. Berger H, Chaquin JP, Ohayon R (1984) Finite element model adjustment using experimental data. In: 2nd SEM international modal analysis conference, Orlando, February 1984
39. Ricles JM, Kosmatka JB (1992) Damage detection in elastic structures using vibratory residual forces and weighted sensitivity. AIAA J 30(9):2310–2316
40. Farhat C, Hemez FM (1993) Updating finite element dynamic models using an element by element sensitivity methodology. AIAA J 31(9):1702–1711
41. Ladevèze P, Reynier M (1989) A localization method of stiffness errors for adjustment of finite element models. ASME Vib Anal Tech Appl 18(4):350–355
42. Chouaki AT, Ladevèze P, Proslier L (1998) Updating structural dynamics models with emphasis on the damping properties. AIAA J 36(6):1094–1099
43. Piranda J, Lallement G, Cogan S (1991) Parametric correction of finite element models by minimization of an output residual improvement of the sensitivity method. In: 9th SEM international modal analysis conference, Firenze, February 1991, pp 363–369
44. Link M, Friswell M (2002) Generation of validated structural dynamic models; results of a benchmark study utilising the GARTEUR SM-AG19 testbed. In: International conference on noise and vibration engineering, University of Leuven, Leuven, September 2002
45. Link M (2001) Updating of analytical models: review of numerical procedures and application aspects. In: Ewins DJ, Inman DJ (eds) Structural dynamics @2000: current status and future directions. Research Studies Press, Baldock
46. Sohn H, Farrar CR, Hemez FM, Shunk DD, Stinemates DW, Nadler BR (2004) A review of structural health monitoring literature: 1996–2001. Technical Report LA-13976-MS. Los Alamos National Laboratory, Los Alamos
47. Zimmerman DC, Widengren M (1990) Correcting finite element models using a symmetric eigenstructure assignment technique. AIAA J 28(9):1670–1676
48. Zimmerman DC, Kaouk M (1992) Eigenstructure assignment approach for structural damage detection. AIAA J 30(7):1848–1855
49. Hasselman TK, Coppolino RN, Zimmerman DC (2000) Criteria for modeling accuracy: a state-of-the-practice survey. In: 18th SEM international modal analysis conference, San Antonio, February 2000
50. Rao CR (1945) Information and the accuracy attainable in the estimation of statistical parameters. Calcutta Math Soc Bull 37:81–89
51. Hemez FM (1998) Can model updating tell the truth? In: 16th SEM international modal analysis conference, Santa Barbara, February 1998, pp 1–7
52. Farrar CR, Cone KM (1995) Vibration testing of the I-40 bridge before and after the introduction of damage. In: 13th SEM international modal analysis conference, February 1995, pp 203–209
53. Farrar CR, Duffey TA, Goldman PA, Jauregui DV, Vigil JS (1996) Finite element analysis of the I-40 bridge over the Rio Grande. Technical Report LA-12979-MS. Los Alamos National Laboratory, Los Alamos
54. Rebba R, Mahadevan S (2006) Validation of models with multivariate output. J Reliab Eng Syst Saf 91(8):861–871
55. Rebba R, Mahadevan S, Huang S (2006) Validation and error estimation of computational models. J Reliab Eng Syst Saf 91(10–11):1390–1397
56. Roache PJ (1998) Verification and validation in computational science and engineering. Hermosa, Albuquerque
57. Hemez FM, Kamm JR (2008) A brief overview of the state-of-the-practice and current challenges of solution verification. In: Graziani F (ed) Computational methods in transport: verification and validation. Springer, Heidelberg, pp 229–250
58. Mollineaux MG, Van Buren KL, Hemez FM, Atamturktur S (2013) Simulating the dynamics of wind turbine blades: Part I. Model development and verification. Wind Energy 16:694–710
59. Van Buren KL, Mollineaux MG, Hemez FM, Atamturktur S (2013) Simulating the dynamics of wind turbine blades: Part II. Model validation and uncertainty quantification. Wind Energy 16:741–758
60. Lenaerts V, Kerschen G, Golinval J-C (2000) Parameter identification of nonlinear mechanical systems using proper orthogonal decomposition. In: 18th SEM international modal analysis conference, San Antonio, February 2000, pp 133–139
61. Hasselman TK, Anderson MC, Wenshui G, Principal components analysis for nonlinear model correlation, updating and uncertainty evaluation. In: 16th SEM international modal analysis conference, Santa Barbara, February 1998, pp 664–651
62. Mook DJ (1989) Estimation and identification of nonlinear dynamic systems. AIAA J 27(7):968–974
63. Dippery KD, Smith SW (1998) An optimal control approach to nonlinear system identification. In: 16th SEM international modal analysis conference, Santa Barbara, February 1998, pp 637–643
64. Kamm JR, Hemez FM, Brock JS (2007) Verification and validation: overview, opinions and applications. In: 2nd international conference on advanced computing and simulation, Centre for Mathematical Sciences, University of Cambridge, June 2007
65. Hemez FM (2005) Uncertainty quantification and the verification and validation of computational models. In: Farrar C (ed) Damage prognosis for aerospace, civil and mechanical systems. Wiley, London, pp 201–219

Chapter 7
Techniques for Synthesizing FRFs from Analytical Models

Hasan G. Pasha, Randall J. Allemang, and Allyn W. Phillips

Abstract Modal correlation of test and analytical data is an important step in system identification and model updating. The Frequency Response Assurance Criterion (FRAC) is one of the metrics that can be used to quantify the strength of correlation between the test and analytical degrees of freedom (DOF). To calculate FRAC for test and analytical data, frequency response functions (FRF) are required. Techniques to synthesize FRFs from finite element models are discussed in this paper. Methods to represent damping in analytical models are also presented. These techniques were applied to synthesize FRFs from a finite element model of a rectangular steel plate structure. Comparing the synthesized FRFs with the measured FRFs for the rectangular plate structure aided in calibrating the rectangular plate FE model. The techniques presented in this paper can be used to visually check if the test and analytical data are well correlated and for calculating FRAC metric to quantify the strength of correlation.

Keywords FRF synthesis • Damping in analytical models • Modal Correlation • FRAC • Model Calibration

Notation

Symbol	Description
$[\cdot]^*$	Complex conjugate $[\cdot]$
α	Mass matrix multiplier for damping
β	Stiffness matrix multiplier for damping
η	Loss factor
λ	System pole (rad/s)
ω	Frequency (rad/s)
ψ	Mode shape coefficient
ζ	Damping ratio
m	Maximum mode number
p	Output DOF
q	Input DOF
$\{x\}$	Displacement vector
$\{\dot{x}\}$	Velocity vector
$\{\ddot{x}\}$	Acceleration vector
A_{pq}	Residue
$[C]$	Damping matrix of reduced model
$[C_R]$	Stiffness matrix of reduced model
$\{f\}$	Applied force
$[H(\omega)]$	FRF Matrix ($[\frac{X}{F}]$)
$[K]$	Stiffness matrix of full model

H.G. Pasha (✉) • R.J. Allemang • A.W. Phillips
Structural Dynamics Research Lab (UC-SDRL), University of Cincinnati, Cincinnati, OH, USA
e-mail: pashahg@mail.uc.edu

$[K_j]$ Stiffness matrix for material j
$[K_R]$ Stiffness matrix of reduced model
$[M]$ Mass matrix of full model
$[M_i]$ Mass matrix for material i
$[M_R]$ Mass matrix of reduced model
$[N_f]$ Number of frequency lines
$[N_i]$ Number of input degrees of freedom
$[N_o]$ Number of output degrees of freedom
FRAC   Frequency response assurance criterion
FRF   Frequency response function

7.1   Introduction

The finite element (FE) technique is used to represent complex structural systems. However, there is uncertainty related to how well the FE model represents the true structure. Generally, modal testing is performed to correlate, validate and calibrate the FE model. Such a FE model could then be used for any future studies instead of performing resource intensive testing.

The order of the number of measurement DOFs is quite small compared that of a FE model. Model order reduction of the FE model to measurement DOFs or expansion of the measurement DOFs to DOFs of the FE model should be done before performing modal correlation. Modal correlation technique involves using various metrics to correlate the analytical results with the experimental results. Generally, modes are paired and the relative error of modal frequencies gives an estimate of the variation in modal frequencies. The Modal Assurance Criteria (MAC) and Pseudo Orthogonality Check (POC) are metrics that could be used to check the linear independence of the modal vectors.

These comparisons are based on the parameters derived from the FE model and parameters obtained by fitting a model to the measured FRF data. A mechanism that could compare the raw measured FRF data with the input-output relationships derived from a FE model would give a better idea of the level of correlation, provide additional insight to validate, and calibrate the FE model. The Frequency Response Assurance Criterion (FRAC) is a metric that compares any two frequency response functions representing the same input-output relationship. This metric can be used to check how well the analytical FRFs compare with the measured FRFs.

Techniques to synthesize a system FRF matrix from a FE model are discussed in the following section. Structural examples of a rectangular steel plate are also presented to demonstrate the techniques discussed. Often damping is ignored while developing a FE model. Many FE software packages now have a provision to prescribe damping using standard parameters that correspond to established damping models. Implementation details on defining damping, retrieving system matrices, and performing the system FRF computations are also discussed in this paper.

7.2   Synthesizing FRFs from Analytical Models

For a multi-degree of freedom dynamic system, the equations of motion are in the form shown in Eq. (7.1).

$$[M]\{\ddot{x}\} + [C]\{\dot{x}\} + [K]\{x\} = \{f\} \tag{7.1}$$

When the excitation is harmonic, the response of the system is expressed using the frequency response function (FRF) matrix $[H(\omega)]$. Typically, the FRF matrix is a $N_o \mathsf{x} N_i \mathsf{x} N_f$ matrix. It is computed using Eq. (7.2).

$$[H(\omega)] = \left([K] - \omega^2[M] + \mathrm{j}\omega[C]\right)^{-1} \tag{7.2}$$

The FRFs can be synthesized from an analytical model in one the following ways described below.

7.2.1 Full Space Method

Once a model of the structure is developed in a FE software package, the mass, stiffness and damping matrices of the full model can be retrieved. The FRF matrix for the system can be computed using the expression shown in Eq. (7.2). The disadvantages of this approach are that since the order of the FE model is huge, the system matrices are huge. Hence, computations take enormous amount of resources, both time and memory.

7.2.2 Synthesizing FRFs from Reduced Order Models

In order to address the issue of the model order, the full model could be reduced using condensation techniques. Both static and dynamic condensation techniques exist. Static condensation techniques, such as the Guyan reduction, are simple, but a lot details are lost. As a result, the reduced order model is not truly representative of the full model. Only the stiffness matrix of the system is considered in static reduction, while mass and damping information are neglected. Dynamic condensation techniques consider the mass and stiffness matrices in calculations, and therefore provide a better approximation of the full model.

Once the requirements of the analysis are determined, an appropriate condensation technique to perform model order reduction of the full model can be selected and transformation of the full model's mass, stiffness and damping matrices to reduced space is performed. It is important to realize that the DOFs in the FE model that correspond to the location of the measurement DOFs should be retained while performing the model order reduction. The FRF matrix for the reduced model can be computed using the expression shown in Eq. (7.3).

$$[H(\omega)] = \left([K_R] - \omega^2[M_R] + \mathrm{j}\omega[C_R]\right)^{-1} \tag{7.3}$$

7.2.3 Modal Superposition Method

Modal superposition method is a special form of model order reduction and a quite popular technique in structural dynamics. The modal parameters, namely the modal frequencies and modal coefficients, are used as generalized coordinates to perform the order reduction. The partial fraction model for FRF, shown in Eq. (7.4), can be used for computing the FRF at response location p when the system is excited at reference location q.

$$H(\omega)_{pq} = \sum_{r=1}^{m} \frac{A_{pq_r}}{\mathrm{j}\omega - \lambda_r} + \frac{A_{pq_r}^*}{\mathrm{j}\omega - \lambda_r^*} \tag{7.4}$$

The residue A_{pq_r} and its complex conjugate $A_{pq_r}^*$ can be computed using Eq. (7.5)

$$A_{pq_r} = Q_r \psi_{p_r} \psi_{q_r} \tag{7.5}$$

where Q_r is the scaling constant for mode r, and ψ_{p_r} and ψ_{q_r} are the modal coefficients. These parameters can be easily retrieved from a FE modal analysis project.

7.2.4 Implementation Details

Frequency response function at multiple response locations due to unit force applied at a particular reference location can be computed using FE software, such as ANSYS Workbench—Harmonic Analysis module. However, in order to compute the FRF matrix for the whole system, this process can be inefficient and slow. When the system FRF matrix is required, the system matrices could be retrieved from the FE model and the FRF computation can be performed separately. The sections below provide information pertaining to retrieving system matrices from ANSYS Workbench and computing the system FRF matrix using Matlab.

7.2.4.1   Retrieving System Matrices with ANSYS Workbench

The ANSYS Workbench has submodules to perform specific analyses. The Modal Analysis module, as the name suggests, can be used to perform modal analysis of a structure. In order to retrieve the system matrices of a structure, a Modal Analysis project needs to be setup. This requires defining the material model, building or importing the geometry, setting up and executing the analysis. If the geometry is simple, it can be built using ANSYS Workbench Design Modeler module. However, if the geometry is complex it can be built using any design software and imported into ANSYS Workbench. In order to retrieve the system matrices from the output database, the option to save the output database after the analysis is complete should be set. System matrices are generally sparse. They can be retrieved as dense or sparse matrices from ANSYS. A command object should be added to retrieve the system matrices at a specific memory location. Code snippets to retrieve the system matrices as sparse and dense matrices are shown below.

```
! Stiffness *DMAT,MatKD,D,IMPORT,FULL,file.full,STIFF *PRINT,MatKD,Kdense.matrix
! Mass *DMAT,MatMD,D,IMPORT,FULL,file.full,MASS *PRINT,MatMD,Mdense.matrix
! below commands create sparse matrix
*SMAT,MatKS,D,IMPORT,FULL,file.full,STIFF *PRINT,MatKS,Ksparse.matrix
For Mass *SMAT,MatMS,D,IMPORT,FULL,file.full,MASS *PRINT,MatMS,Msparse.matrix
```

7.2.4.2   Computing the FRF

Once the system matrices or modal parameters are retrieved, Matlab could be used to compute the FRF matrix using the relations shown in previous sections. Open source codes to read sparse matrices generated by ANSYS and converting them to Matlab format exist. The frequency resolution can be controlled using the Matlab program to provide reasonable results in stipulated execution time.

7.3   Damping

In an ideal vibratory system, the energy changes its form back and forth between potential energy and kinetic energy. However, since there are losses associated with the energy conversion in a practical system, the vibration eventually dies out in the absence of any external excitation to the system. The energy loss is quantified by damping. There are several mechanisms by which energy dissipation can take place, such as, friction, hysteresis, etc. It is difficult to model damping based on microscopic phenomena. Simple mathematical models exist that can be used to quantify damping, e.g. viscous damping model, structural damping model.

7.3.1   Modeling Damping with ANSYS Workbench

The system damping matrix in ANSYS Workbench R14.5 is computed using Eq. (7.6) [1]. ANSYS has provision to prescribe damping by specifying various parameters.

$$
[C] = \underbrace{\alpha[M] + \sum_{i=1}^{N_{ma}} \alpha_i^m [M_i]}_{\text{Mass Damping}} + \underbrace{\left(\beta + \frac{2}{\omega}\zeta\right)[K] + \sum_{j=1}^{N_{mb}} \left(\beta_j^m + \frac{2}{\omega}\zeta_j\right)[K_j]}_{\text{Structural Damping}}
$$
$$
+ \underbrace{\sum_{k=1}^{N_e}[C_k]}_{\text{Element Damping}} + \underbrace{\sum_{l=1}^{N_g}[G_l]}_{\text{Gyroscopic Damping}} + \underbrace{\sum_{m=1}^{N_v}\frac{1}{\omega}[C_m]}_{\text{Viscoelastic Damping}}
$$

(7.6)

The values for α, β and ζ can be set at the global or the material level. In a structure with multiple material layers, for example when a coating material is used, the damping properties of the coating material can be different from the base material. The terms highlighted in blue in Eq. (7.6) indicate that material specific damping can be specified. In addition, a

viscous damper can be modeled using the spring element connector and specifying the damping values, which is referred as element damping in Eq. (7.6).

7.4 Frequency Response Assurance Criteria (FRAC)

Any two frequency response functions representing the same input-output relationship can be compared using a metric known as the Frequency Response Assurance Criterion (FRAC). Once the FRFs are synthesized from FE model, they can be compared with the measured FRFs and the FRAC can be computed to understand the strength of correlation. For example, the FRAC for two FRFs, measured FRF $H_{pq}(\omega)$ and analytical FRF $\hat{H}_{pq}(\omega)$, representing the relation between output DOF p and input DOF q, can be computed using the expression shown in Eq. (7.7). The frequency resolution of the analytical FRF data and measured FRF data should match.

$$\mathsf{FRAC}_{pq} = \frac{\left|\sum_{\omega=\omega_1}^{\omega_2} H_{pq}(\omega)\hat{H}_{pq}^*(\omega)\right|^2}{\sum_{\omega=\omega_1}^{\omega_2} H_{pq}(\omega)H_{pq}^*(\omega)\ \sum_{\omega=\omega_1}^{\omega_2} \hat{H}_{pq}(\omega)\hat{H}_{pq}^*(\omega)} \tag{7.7}$$

7.5 Experimental Example

A FE model of a rectangular steel plate structure of dimensions $0.86 \times 0.57 \times 0.0063$ m ($34'' \times 22.5'' \times .25''$) was developed using ANSYS Workbench R14.5. A cold rolled steel rectangular plate structure was fabricated ($\mathsf{E} = 2.05 \times 10^{11}$ Pa (2.9734×10^7 psi), $\nu = 0.29$ and $\rho = 7850$ kg/m^3 (0.2836 lb/in^3)), with 160 points marked on a 0.05×0.05 m ($2'' \times 2''$) grid. Each of these 160 points were impacted and FRFs were measured at 21 reference locations using uniaxial accelerometers.

The system mass, damping and stiffness matrices were obtained from the FE model. A *named selection* of points corresponding to the impact locations (which also included the sensor locations) was created. The displacement for the named selection represents the modal coefficients. The analytical FRFs were generated using the full space method from the analytical model.

7.5.1 FRF Comparison

The FE model was calibrated to the match measured modal frequencies and modal vectors. The FE model was validated by comparing analytical FRFs from the model with the measured FRFs. In addition, the results obtained for two perturbed mass configurations with unconstrained boundaries were compared with the predictions from the updated model to check its robustness. Figure 7.1 shows a comparison of the driving-point and cross-point FRFs for the rectangular plate.

7.5.2 Effect of Structural Damping

The structural damping does not affect the modal frequency. Its effect is only to limit the response at resonance. The effect of structural damping on the plate was studied. The FRF for various values of loss coefficient values are plotted in Fig. 7.2. It is evident that the modal frequencies do not change with increasing η values, but the amplitude of the response at resonance is reduced.

7.6 Conclusions

- Modal correlation, updating, validation and calibration are important tasks in order to reduce uncertainty in predictions from a FE model. Various metrics to perform modal correlation are available. The Frequency Response Assurance Criterion (FRAC) aims to quantify the strength of correlation between measured and synthesize FRFs. It is particularly advantageous to correlate FRFs as it works directly on raw input-output relations.

Fig. 7.1 Comparison of FRFs.
(**a**) Driving-point FRFs.
(**b**) Cross-point FRFs
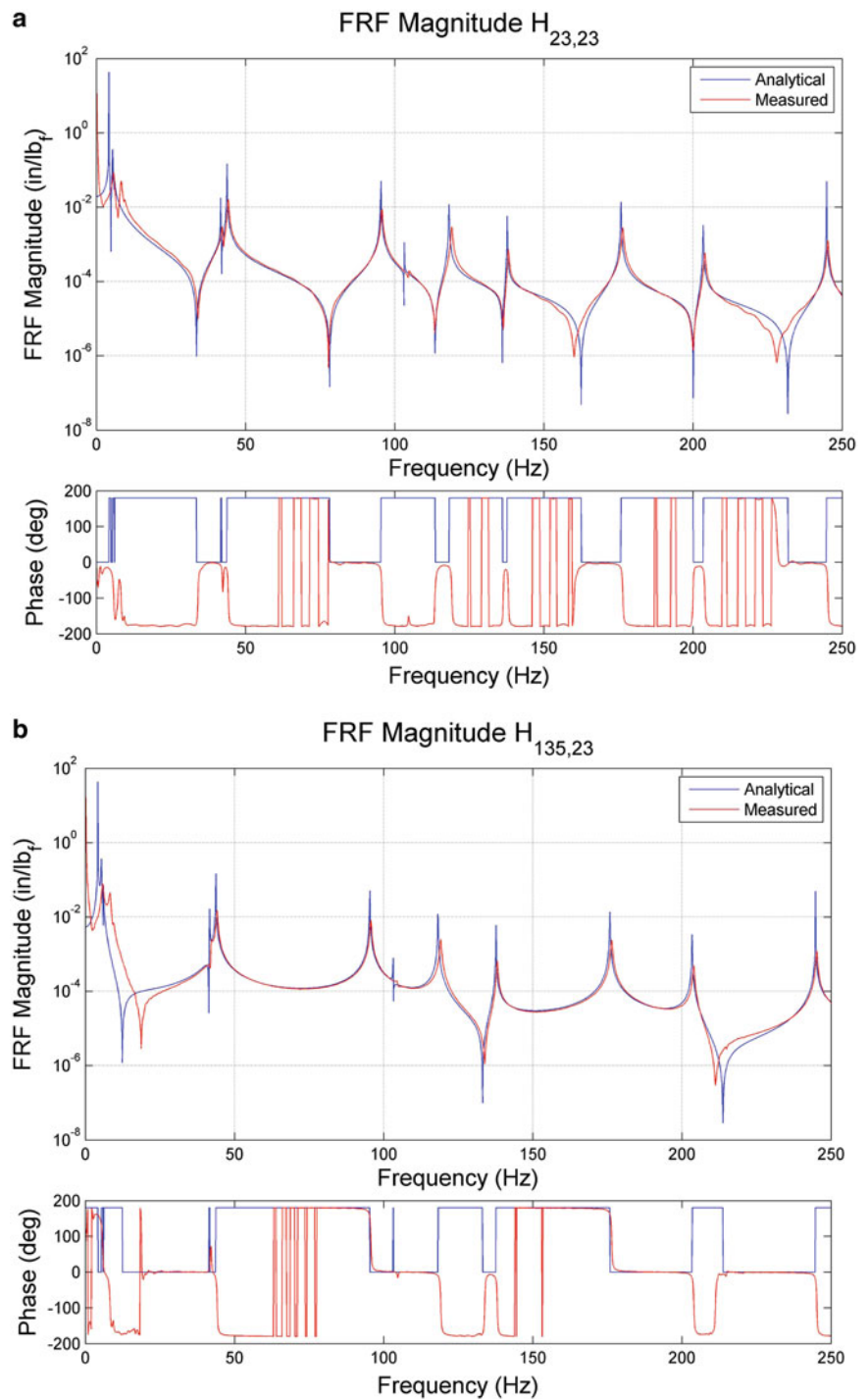
- Techniques to synthesize frequency response functions from analytical models were discussed. FRFs can be synthesized by full order model, reduced order model or by modal superposition. Full order method can be resource intensive. The reduced order method or the modal superposition method provide reasonable results while being less resource intensive.
- FE packages, such as ANSYS, have provisions to output system or element mass, stiffness and damping matrices. ANSYS also has the capability to prescribe damping for a model by specifying parameters for standard damping models. Implementation details to retrieve the system matrices and to compute the system FRF matrix were discussed.
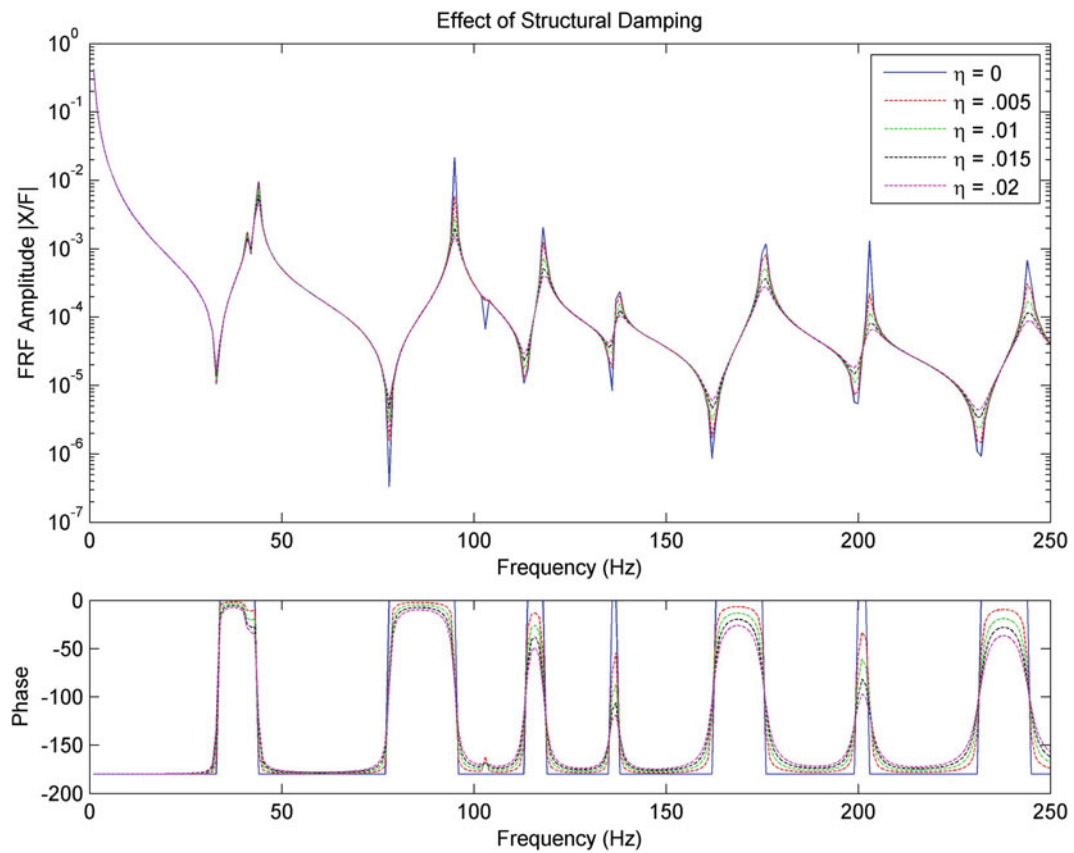
Fig. 7.2 Rectangular plate—effect of structural damping

- A rectangular plate structure was used to demonstrate how the analytical FRFs could be compared with measured FRFs. The effect of structural damping on the FRF of the steel plate structure was also presented.

Reference

1. ANSYS, Inc. (2013) ANSYS mechanical linear and nonlinear dynamics, Lecture 3: Damping, ANSYS release 14.5

Chapter 8
An Analytical Method and Its Extension for Linear Modal Analysis of Beam-Type Systems Carrying Various Substructures

Zhenguo Zhang, Xiuchang Huang, Zhiyi Zhang, and Hongxing Hua

Abstract This study is concerned with an analytical solution and its extension on determining natural frequencies and mode shapes of beam-type systems carrying various substructures such as intermediate discontinuities and flexible foundations, etc. First, the method of separation of variables is utilized to devise the governing equation of the Timoshenko beams. Second, compatibility conditions attributed to various discontinuities as well as the complicated boundary conditions are expressed by coefficient matrices with the transfer matrix approach. Furthermore, flexible attachments and flexible foundations considered are described by frequency response functions (FRFs). Finally, the natural frequencies are determined by non-trivial solutions of the resulting matrix equation and the associated mode shapes are derived with Heaviside function. An important objective of this study is to demonstrate the applicability of the proposed methodology. This is achieved by selected numerical examples including a simple double-beam structure with elastic coupling. A new range of results is presented for beam-type structures which can be used as a benchmark to approximate solutions.

Keywords Modal analysis • Beam-type system • Substructure • Analytical solution • Discontinuity

8.1 Introduction

The problem of flexural beams coupled with complexities such as flexible foundations, multiple discontinuities (including intermediate support, elastic spring-mass system, concentrated mass, internal connectors, etc.) has been considered by many authors [1–13]. A variety of different styles of analysis have been dedicated to theoretical investigations for the vibrations of beams with those additional complexities, e.g. Green's functions [1], the Jacquot's method [2], the Dunkerley-based approximate formula [3], the Lagrange multiplier formalism [4], the numerical assembly method [5, 6], the transfer matrix solution [7], the Laplace Transform et al. [8]. Although these approaches are available for several particular forms of complexities in some actual systems, there is no general solution to account for arbitrary complexities.

Combined systems modeled with the Euler–Bernoulli beam and the Timoshenko beam theories have been considered. The literature regarding the free vibration analysis of Bernoulli–Euler beams carrying multiple additional complexities are plenty, but fewer researchers have studied the free vibrations of beams with different discontinuities according to the Timoshenko beam theory. Abramovich and Hamburger [9] investigated cantilever Timoshenko beams with a tip mass and intermediate rotational and translational springs. Rossi et al. [10] solved analytically the problem of free vibration of Timoshenko beams carrying elastically mounted concentrated masses. Lee and Lin [11] derived an exact solution for the free vibrations of a symmetric non-uniform Timoshenko beam with a tip mass at one end and elastically restrained at the other. Posiadala [4] handled the problem of free vibrations of Timoshenko beams with several attachments by means of the Lagrange multiplier formalism. Lin and Chang [7] studied the free vibration of a multi-span Timoshenko beam with an arbitrary number of intermediate flexible constraints by combining the separation of variables with the transfer matrix solution. The similar method was also extended by Zhang et al. [12] to present analytical solutions of beams with arbitrary discontinuities and flexible attachments. Wu and Chen [5] obtained the exact solution of a uniform Timoshenko beam carrying any number of spring-mass systems by using the numerical assembly method.

Z. Zhang (✉) • X. Huang • Z. Zhang • H. Hua
B219, Institute of Vibration, Shock & Noise, Shanghai Jiao Tong University, 800 Dongchuan Road, Shanghai 200240 P. R. China
e-mail: zzgjtx@sjtu.edu.cn; hhx@sjtu.edu.cn

It should also be pointed out that some special subsystems in the beam-type systems, such as the flexible foundation (float valve systems and rotor-bearing-foundation systems etc.) and the flexible attachments (bladed-disk assemblies in turbomachinery or propeller-shaft assemblies in propulsion systems etc.) are generally unfit to be simply approximated to rigid or elastic concentrated masses. The structure flexibility should be carefully considered and estimated in order to obtain all frequency components of systems [13, 14]. However, according to our best knowledge, no analytical solution has been carried out to overcome this difficulty [12]. In this study, the technique combining the separation of variables with the transfer matrix solution, which leads to a non-trivial solution with only a four-order determinant, is used to obtain the exact natural frequencies and exact normal modes for the vibrating Timoshenko beams [7, 12]. However, in the present work, the approach considered has been greatly extended to investigate the free vibrations of more complicated beam-type systems. Moreover, owing to the substructure synthesis method [15], flexible attachments and the elastic foundation can be described as appropriate frequency response functions and integrated into the final overall coefficient matrix, which results in the general formulation of eigenvalue problem.

8.2   The Mathematical Model and Formulation

Figure 8.1 shows the sketch of a typical beam-type system of length L with various substructures, including the flexible foundation, flexible attachments (A and B) and multiple discontinuities (1, 2 ... k +1). Various intermediate attachments, such as rotational and translational springs, concentrated mass with rotary inertia and undamped spring-mass oscillator, used in most practical cases are accounted for. The whole beam is subdivided into k +1 segments with length L_i ($i = 1, 2 \ldots k$ +1) by the discontinuity points located at x_i ($i = 1, 2 \ldots k$). Based on the Timoshenko beam theory [16] and the method of separation of variables, the equation of motion for the i-th beam segment can be readily stated as

$$Y_i''''(x) + (\sigma_i + \tau_i) Y_i''(x) - (\alpha_i - \sigma_i \tau_i) Y_i(x) = 0 \tag{8.1}$$

$$\Phi_i''''(x) + (\sigma_i + \tau_i) \Phi_i''(x) - (\alpha_i - \sigma_i \tau_i) \Phi_i(x) = 0 \tag{8.2}$$

where the prime denotes the differentiation of x, and $\sigma_i = \rho_i \omega^2 / E_i$, $\tau_i = \rho_i \omega^2 / (\kappa_i G_i)$, $\alpha_i = \rho_i A_i \omega^2 / (E_i I_i)$. $Y_i(x)$ and $\Phi_i(x)$ are the mode shape functions with respect to the transverse displacement and the bending slope of the i-th segment at position x ($x_{i-1} < x < x_i$). E_i, G_i, I_i, κ_i, ρ_i and A_i are, respectively, the Young's modulus, shear modulus, the moment inertia of the cross section about the neutral axis, the shape factor, the density and cross-sectional area of the i-th beam segment.

The general solution of Eqs. (8.1) and (8.2) can then be derived in the following form [16]

$$Y_i(x) = C_{1i} \cosh \lambda_i (x - x_{i-1}) + C_{2i} \sinh \lambda_i (x - x_{i-1}) + C_{3i} \cos \bar{\lambda}_i (x - x_{i-1}) + C_{4i} \sin \bar{\lambda}_i (x - x_{i-1}) \tag{8.3}$$

$$\Phi_i(x) = C_{1i} q_i \sinh \lambda_i (x - x_{i-1}) + C_{2i} q_i \cosh \lambda_i (x - x_{i-1}) + C_{3i} \bar{q}_i \sin \bar{\lambda}_i (x - x_{i-1}) - C_{4i} \bar{q}_i \cos \bar{\lambda}_i (x - x_{i-1}) \tag{8.4}$$
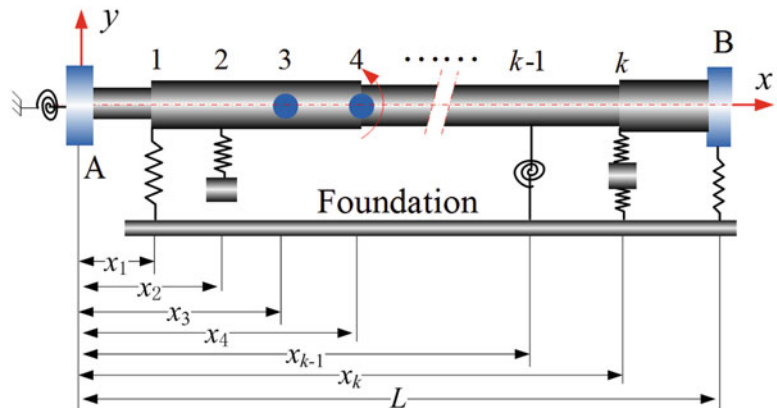

Fig. 8.1 A beam-type system with various substructures

where C_{pi} ($p = 1, 2, 3, 4$ and $i = 1, 2 \dots k + 1$) is the integration constant associated with the i-th segment, and

$$\lambda_i = \sqrt{\sqrt{\left(\frac{\sigma_i - \tau_i}{2}\right)^2 + \alpha_i} - \frac{\sigma_i + \tau_i}{2}}, \tag{8.5a}$$

$$\overline{\lambda}_i = \sqrt{\sqrt{\left(\frac{\sigma_i - \tau_i}{2}\right)^2 + \alpha_i} + \frac{\sigma_i + \tau_i}{2}} \tag{8.5b}$$

$$q_i = \frac{\omega^2 \rho_i}{\kappa_i G_i \lambda_i} + \lambda_i, \tag{8.6a}$$

$$\overline{q}_i = \frac{\omega^2 \rho_i}{\kappa_i G_i \overline{\lambda}_i} - \overline{\lambda}_i. \tag{8.6b}$$

8.2.1 Evaluation of the Intermediate Discontinuities

The intermediate discontinuities induced by different attachments can be characterized with different compatibility conditions across the discontinuity point. However, for all cases as shown in Fig. 8.1, the bending moment and the shear force are the discontinuous at the location of discontinuities; while other parameters, such as deflection and the slope are continuous. In fact, effects of attachments considered in this study can all be reasonably replaced by translational or rotational springs with the equivalent translational or rotational stiffness [12]. Consequently, the compatibility conditions associated with the i-th intermediate attachment can be expressed in matrix form as [7, 12]

$$\mathbf{T}^{(i+1)}\mathbf{C}^{(i+1)} = \mathbf{T}^{(i)}\mathbf{C}^{(i)} \tag{8.7}$$

where $\mathbf{T}^{(i+1)}$ and $\mathbf{T}^{(i)}$ are 4×4 coefficient matrices with regard to the $(i+1)$-th and the i-th segments. $\mathbf{C}^{(i+1)} = [C_{1(i+1)}\ C_{2(i+1)}\ C_{3(i+1)}\ C_{4(i+1)}]^T$ and $\mathbf{C}^{(i)} = [C_{1i}\ C_{2i}\ C_{3i}\ C_{4i}]^T$. With the matrix transformation, their transitive relationship can be easily constructed as

$$\mathbf{C}^{(i+1)} = \left(\mathbf{T}^{(i+1)}\right)^{-1}\mathbf{T}^{(i)}\mathbf{C}^{(i)} = \mathbf{T}_{\text{tf}}^{(i)}\mathbf{C}^{(i)} \tag{8.8}$$

By repeated application of Eq. (8.8), therefore, the multiplication of the transfer matrices of all segments from the left to the right end successively yields

$$\mathbf{C}^{(k+1)} = \mathbf{T}_{\text{tf}}^{(k)}\mathbf{T}_{\text{tf}}^{(k-1)} \cdots \mathbf{T}_{\text{tf}}^{(1)}\mathbf{C}^{(L)} = \mathbf{U}_{4 \times 4}\mathbf{C}^{(1)} \tag{8.9}$$

which has reduced the number of independent constants to four and $\mathbf{U}_{4 \times 4}$ is the overall transfer matrix.

8.2.2 General Formulations of Boundary Conditions

The boundaries can be regarded as special discontinuity points at the ends of the beam. Of course, the boundary conditions can also be represented in a systematic manner with coefficient matrices [12]

$$\mathbf{R}^{(R)}\mathbf{C}^{(k+1)} = \mathbf{0}, \tag{8.10a}$$

$$\mathbf{R}^{(L)}\mathbf{C}^{(1)} = \mathbf{0} \tag{8.10b}$$

where $\mathbf{R}^{(R)}$ **and** $\mathbf{R}^{(L)}$ are 2×4 coefficient matrices with regard to the right and the left boundaries.

Fig. 8.2 A coupled beam with
two flexible substructures
at the ends
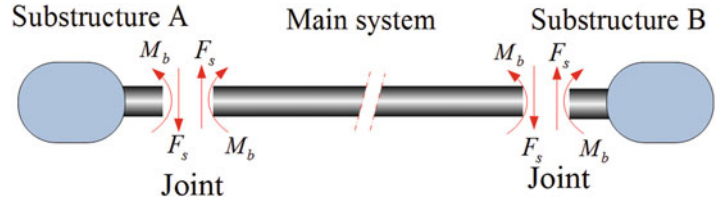
8.2.3 Consideration of Flexible Attachments

Considering a coupled system as shown in Fig. 8.2, the subsystems A and B represent the flexible attachments and the main system represents the beam. By resorting to the essential idea in substructure synthesis method [15], the relationship between the displacement and the force at coupling interfaces of subsystem A and the main system can be built up via frequency response functions (FRF) as

$$
\begin{bmatrix} \phi_j\left(x_{end}, t\right) \\ y_j\left(x_{end}, t\right) \end{bmatrix} = \begin{bmatrix} H_{MR}\left(\omega\right) & -H_{FR}\left(\omega\right) \\ H_{MT}\left(\omega\right) & -H_{FT}\left(\omega\right) \end{bmatrix} \begin{bmatrix} M_b \\ F_s \end{bmatrix} \tag{8.11}
$$

where $H_{FR}(\omega)$, $H_{MR}(\omega)$, $H_{FT}(\omega)$ and $H_{MT}(\omega)$ are driving-point receptances of the subsystem A and denote the FRFs between force/moment and the displacement/angle, respectively. Expressing M_b and F_s in Y_1 and Φ_1, for the left end of Part III, Eq. (8.11) can be rewritten as [12]

$$
E_1 I_1 \frac{\partial \Phi_1(0)}{\partial x} H_{MR}\left(\omega\right) - \kappa_1 G_1 A_1 \left[\Phi_1(0) - \frac{\partial Y_1(0)}{\partial x} \right] H_{FR}\left(\omega\right) = \Phi_1(0) \tag{8.12a}
$$

$$
-\kappa_1 G_1 A_1 \left[\Phi_1(0) - \frac{\partial Y_1(0)}{\partial x} \right] H_{FT}\left(\omega\right) + E_1 I_1 \frac{\partial \Phi_1(0)}{\partial x} H_{MT}\left(\omega\right) = Y_1(0) \tag{8.12b}
$$

Similar expressions can also be obtained for the right end of subsystem B [12]. Substituting Eqs. (8.3) and (8.4) into Eq. (8.12), one can easily obtain the boundary conditions in matrix form analogous to Eq. (8.10), where $\mathbf{R}^{(R)}$ and $\mathbf{R}^{(L)}$ have been replaced to involve the receptance relation between substructures.

8.2.4 Condensation of the Eigenvalue Problem

Combing Eq. (8.10a) with Eq. (8.9) results in two equations of the integration constants relating to the first segment of the beam

$$
\mathbf{R}^{(R)}\mathbf{C}^{(k+1)} = \mathbf{R}^{(R)}\mathbf{U}_{4\times4}\mathbf{C}^{(1)} = \mathbf{B}_{2\times4}\mathbf{C}^{(1)} = \mathbf{0} \tag{8.13}
$$

Then, only four unknowns remain (C_{11}, C_{21}, C_{31} and C_{41}) in the four equations given by Eqs. (8.13) and (8.10b), and the existence of non-trivial solutions requires the following determinant is equal to zero

$$
\begin{vmatrix} \mathbf{B}_{2\times4} \\ \mathbf{R}^{(L)} \end{vmatrix} = 0 \tag{8.14}
$$

which provides a characteristic equation for the solution of the angular frequency ω. Once the frequency parameters have been determined, the values of the constants (C_{1i}, C_{2i}, C_{3i} and C_{4i}) can then be easily obtained by the use of the transfer matrix method. And the corresponding mode shape function of the whole beam can be readily expressed as

$$
Y(x) = \sum_{i=1}^{k+1} Y_i(x) H\left(x - x_{i-1}\right) - \sum_{i=1}^{k+1} Y_i(x) H\left(x - x_i\right) \tag{8.15}
$$

where $H(x-x_i)$ is Heaviside function which jumps from zero to unit at location x_i.

Fig. 8.3 A complex beam-type system with two flexible substructures at the ends and flexible foundation
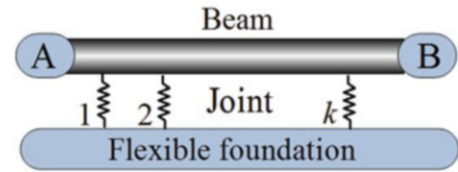

Table 8.1 Comparison of the lowest five nature frequencies (rad/s) for the Timoshenko beam with various discontinuities

| Case | Methods | Frequency (rad/s) | | | | |
		ω_1	ω_2	ω_3	ω_4	ω_5
Case 1	Present study	343.51439	791.23957	2,476.90184	4,777.24695	6,465.08113
	[6]	343.51430	791.23950	2,476.90180	4,777.24700	6,465.08130
	FEM [6]	343.51440	791.23970	2,476.90590	4,777.26330	6,465.12200
Case 2	Present study	686.76884	1,563.82513	4,647.74203	8,663.06436	11,614.25418
	[6]	686.76880	1,563.82510	4,647.74200	8,663.06450	11,614.25540
	FEM [6]	686.76880	1,563.82670	4,647.77910	8,663.21950	11,614.54460

8.3   Extension to More Complex Systems

Beam-type systems are often encountered in technological applications. The foundations are generally assumed as the rigid substructures. However, in some special cases as shown in Fig. 8.3, such as propeller-shaft system in large ships, rotor-bearing-foundation systems and complicated shafts in aerospace engineering, the foundation flexibility should be considered with discretion in order to provide accurate estimates of the natural frequencies of the combined structure as well as the associated modes of vibration. Combining with the FRF-based substructures coupling method [15], it is expected that the proposed method can be reasonably extended to deal with some of these problems. First, the beam is treated as the main system and expressed in the analytical way as stated in Sect. 8.2. Second, all their relevant mechanical characteristics of substructures (consisting of foundations and the flexible attachments) can be described via appropriate frequency response functions (FRF). Next, coupling interfaces between the beam and substructures are considered as discontinuities of the beam; and then corresponding compatibility conditions or boundary conditions can be derived. Finally, the natural frequencies are determined by non-trivial solutions of the determinant of the final coefficient matrix. For the complicated substructures such as propellers in propulsion systems, the present method has the advantage of using the measured or the numerical FRFs directly. This point will be presented with a simple example of a double-beam structure in the following sections.

8.4   Numerical Examples

8.4.1   Example 1: Validation of the Present Method

A uniform Timoshenko beam with several discontinuities as illustrated in [6] was taken as a validation example. The pinned–pinned beam carrying three point masses, two rotary inertias, two linear springs, one rotational spring and one mass-spring system was considered. Results are available for two cases with different cross-section of the beams. For the purpose of simplification, physical parameters are not given here, but one can reference [6] for details. The corresponding numerical results are tabulated in Table 8.1. It can be seen an excellent agreement between the present and the reference results [6] is observed.

8.4.2   Example 2: Flexural Vibration of a Double-Beam Structure

A double-beam structure is shown in Fig. 8.4. The upper fixed-free beam with the length $L_1 = 5$ m is regarded as the main system while the lower pinned–pinned one with the length $L_2 = 10$ m is considered as the flexible foundation. The whole system is subdivided into four segments (1, 2, 3, 4) by a translational spring with stiffness $K = 1 \times 10^7$ or $K = 5 \times 10^7$ N/m.

Fig. 8.4 Scheme of a
double-beam system
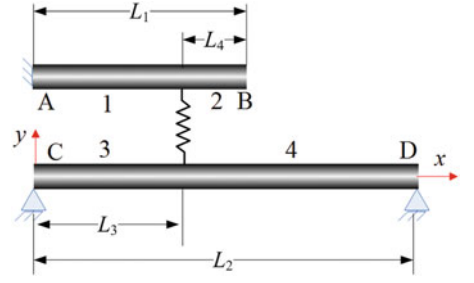
And the four ends are numbered with A, B, C, D, respectively. System properties of the beam are set as follows: $L_3 = 4$ m, $L_4 = 1$ m, the Young's modulus $E = 2.1 \times 10^{11}$ Pa, the shear modulus $G = 7.9577 \times 10^{10}$ Pa, the Poisson ratio $\nu = 0.3$, the mass density $\rho = 7,850$ kg/m^3 and the shear factors $\kappa = 0.511$. The cross-section of the beam is the hollow circle with the inner radius $R_1 = 0.0875$ m and the outer radius $R_2 = 0.12$ m. On the basis of Sects. 8.2 and 8.3, two different approaches can be extended to obtain the modal characteristics of the coupled system.

8.4.2.1 Approach 1: The Analytical Solution

If two Timoshenko beams are separately considered and modeled, according to the methodology in Sect. 8.2.2, four integration constant vectors ($\mathbf{C}^{(1)}$, $\mathbf{C}^{(2)}$, $\mathbf{C}^{(3)}$ and $\mathbf{C}^{(4)}$) should be remained in order to obtain the analytical solution. Considering the elastic coupling interface between the beams, the transitive relationship between the four constant vectors can be easily built up as

$$\begin{cases} \mathbf{C}^{(2)} = \left(\mathbf{T}^{(2)}\right)^{-1}\mathbf{T}^{(1)}\mathbf{C}^{(1)} + \left(\mathbf{T}^{(2)}\right)^{-1}\mathbf{T}_{23}\mathbf{C}^{(3)} \\ \mathbf{C}^{(4)} = \left(\mathbf{T}^{(4)}\right)^{-1}\mathbf{T}^{(3)}\mathbf{C}^{(3)} + \left(\mathbf{T}^{(4)}\right)^{-1}\mathbf{T}_{32}\mathbf{C}^{(1)} \end{cases} \tag{8.16}$$

where $\mathbf{T}_{23}$ and $\mathbf{T}_{32}$ are the coefficient matrices related to the translational spring. Satisfying the boundary conditions, the characteristic equations can then be derived in matrix form as:

$$\begin{bmatrix} \mathbf{R}^{(A)} & \mathbf{0}_{2\times4} \\ \mathbf{0}_{2\times4} & \mathbf{R}^{(C)} \\ \mathbf{R}^{(B)}\left(\mathbf{T}^{(2)}\right)^{-1}\mathbf{T}^{(1)} & \mathbf{R}^{(B)}\left(\mathbf{T}^{(2)}\right)^{-1}\mathbf{T}_{13} \\ \mathbf{R}^{(D)}\left(\mathbf{T}^{(4)}\right)^{-1}\mathbf{T}_{31} & \mathbf{R}^{(D)}\left(\mathbf{T}^{(4)}\right)^{-1}\mathbf{T}^{(3)} \end{bmatrix} \begin{bmatrix} \mathbf{C}^{(1)} \\ \mathbf{C}^{(3)} \end{bmatrix} = \mathbf{U}_{8\times8} \begin{bmatrix} \mathbf{C}^{(1)} \\ \mathbf{C}^{(3)} \end{bmatrix} = \mathbf{0}_{8\times1} \tag{8.17}$$

where $\mathbf{U}_{8\times8}$ is the final coefficient matrix and can be used to obtain the exact natural frequencies of the system. For each frequency ω_i, the corresponding mode shape functions can be analytically determined.

8.4.2.2 Approach 2: The Hybrid Analytical/FRF Solution

Once the mechanical characteristics of the lower beam are described via numerical FRF, the other approach as stated in Sect. 8.3 can also be extended. Replacing the equivalent translational stiffness in Eq. (8.7) by $K_T = K/(-KH(\omega) + 1)$, where $H(\omega)$ denotes the driving-point receptance of the lower beam and represents the FRF between force and the displacement as shown in Fig. 8.5, and then the standard process in Sect. 8.2 can be used to obtain the modal characteristics of the system. However, only the shape functions of the main system (the upper beam in this study) can be obtained with the hybrid solution.

The corresponding numerical results of natural frequencies are given in Table 8.2. Excellent agreement between the present and the FEM results can be observed, which shows that both the analytical and the hybrid approaches can provide accurate estimates of the natural frequencies of the double-beam system. Thus, efficiency and application of the proposed methodology are well demonstrated. The lowest three mode shapes for the case 1 are shown in Fig. 8.6. It should also be noticed that one of the major benefits of the proposed method is that one can obtain the exact functions of mode shapes

Fig. 8.5 FRF at the coupling interface of lower beam
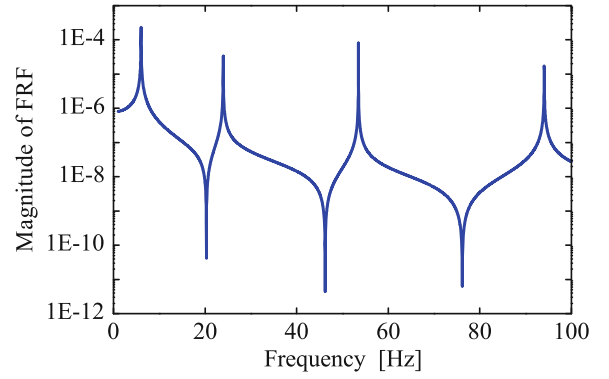
Table 8.2 Comparison of the lowest five nature frequencies (Hz) for the double-beam system

Case	Methods	Frequency (Hz)				
		ω_1	ω_2	ω_3	ω_4	ω_5
Case 1	Analytical	6.8591	21.8763	32.6142	52.7710	54.8886
$K = 1 \times 10^7$ N·m	Hybrid	6.8573	21.8662	32.6140	52.7707	54.8723
	FEM	6.8592	21.8766	32.6149	52.7887	54.9047
Case 2	Analytical	6.8770	22.6641	47.8784	52.7889	67.2485
$K = 5 \times 10^7$ N·m	Hybrid	6.8753	22.6522	47.8654	52.7878	67.2463
	FEM	6.8777	22.6649	47.8735	52.8075	67.2498

Fig. 8.6 The lowest three mode shapes for the case 1 with $K = 1 \times 10^7$ N/m
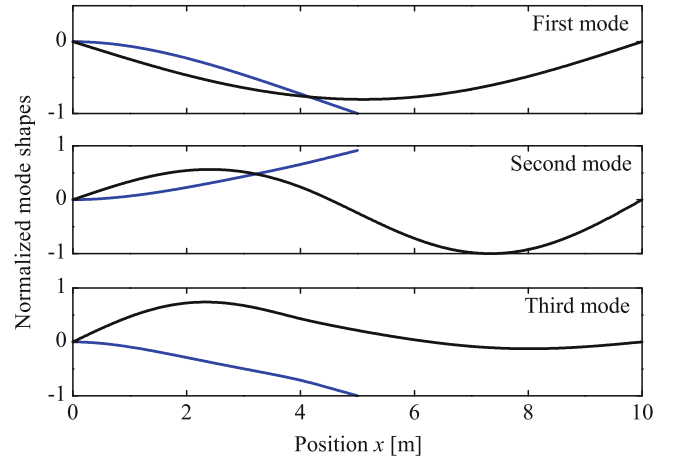
which may be required for the further calculations, such as transient responses. For instance, according to Eq. (8.15), the mode shape function of the fundamental frequency for the case 1, where $\lambda_1 = 0.3347$ and $\overline{\lambda}_1 = 0.3353$, can be given in the style of segmented functions as

$$
\begin{cases}
Y_1 = 0.88 \cosh \lambda_1 x - 0.698 \sinh \lambda_1 x - 0.88 \cos \overline{\lambda}_1 x + 0.698 \sin \overline{\lambda}_1 x \\
Y_2 = 0.554 \cosh \lambda_1 (x - 4) + 0.37 \sinh \lambda_1 (x - 4) + 0.483 \cos \overline{\lambda}_1 (x - 4) + 0.785 \sin \overline{\lambda}_1 (x - 4) \\
Y_3 = 0.0595 \sinh \lambda_1 x + \sin \overline{\lambda}_1 x \\
Y_4 = 0.106 \cosh \lambda_1 (x - 4) - 0.11 \sinh \lambda_1 (x - 4) + 0.974 \cos \overline{\lambda}_1 (x - 4) + 0.46 \sin \overline{\lambda}_1 (x - 4)
\end{cases}
\tag{8.18}
$$

8.5   Conclusions

The analytical study on the linear modal analysis of beam-type systems with various substructures such as intermediate discontinuities and flexible foundations is carried out. Various discontinuities can be induced into the modal displacement of the beam at the locations of additional elements. Combining with the FRF-based substructures coupling method, the analytical approach can be extended to account for flexible attachments and foundations by describing them with FRFs.

Natural frequencies and the mode shape functions can be derived analytically. To validate the present analysis, several practical examples are carried out and the obtained results are compared with those calculating with other solution procedures. Good agreement is observed and it shows the present method can provide an efficient tool to modal analysis of the beam-type systems in technological applications.

References

1. Kukla S, Posiadala B (1994) Free vibrations of beams with elastically mounted masses. J Sound Vib 175(4):557–564
2. Ercoli L, Laura PA (1987) Analytical and experimental investigation on continuous beams carrying elastically mounted masses. J Sound Vib 114(3):519–533
3. Gürgöze M (1996) On the eigenfrequencies of cantilevered beams carrying a tip mass and spring-mass in-span. Int J Mech Sci 38(12): 1295–1306
4. Posiadala B (1997) Free vibrations of uniform Timoshenko beams with attachments. J Sound Vib 204(2):359–369
5. Wu JS, Chen DW (2001) Free vibration analysis of a Timoshenko beam carrying multiple spring-mass systems by using the numerical assembly technique. Int J Numerical Methods Eng 50(5):1039–1058
6. Lin HY (2009) On the natural frequencies and mode shapes of a multispan Timoshenko beam carrying a number of various concentrated elements. J Sound Vib 319((1–2)):593–605
7. Lin HP, Chang SC (2005) Free vibrations analysis of multi-span beams with intermediate flexible constraints. J Sound Vib 281(1–2):155–169
8. Liu WH, Wu JR, Huang CC (1998) Free vibration of beams with elastically restrained edges and intermediate concentrated masses. J Sound Vib 122(2):193–207
9. Abramovich H, Hamburger O (1992) Vibration of a uniform cantilever Timoshenko beam with translational and rotational springs and with a tip mass. J Sound Vib 154(1):67–80
10. Rossi RE et al (1993) Free vibrations of Timoshenko beams carrying elastically mounted, concentrated masses. J Sound Vib 165(2):209–223
11. Lee SY, Lin SM (1992) Exact vibration solutions for non-uniform Timoshenko beams with attachments. AIAA J 30:2930–2934
12. Zhang ZG, Chen F et al (2013) Vibration analysis of non-uniform Timoshenko beams coupled with flexible attachments and multiple discontinuities. Int J Mech Sci 80:131–143
13. Loewy RG, Khader N (1984) Structural dynamics of rotating bladed-disk assemblies coupled with flexible shaft motions. AIAA J 22(9): 1319–1327
14. Chen JH, Shih YS (2007) Basic design of a series propeller with vibration consideration by genetic algorithm. J Mar Sci Technol 12:119–129
15. Liu W, Ewins DJ (2002) Substructure synthesis via elastic media. J Sound Vib 257(2):361–379
16. Timoshenko SP (1974) Vibration problems in engineering. Wiley, New York

Chapter 9
Computationally Efficient Nonlinear Dynamic Analysis for Stress/Strain Applications

Julie Harvie and Peter Avitabile

Abstract Dynamic response of analytical models is commonly studied to determine strain induced on systems for normal design loadings. Due to the complexity of the analytical models combined with the possibility of nonlinear effects encountered, traditional methods for computing the time response can be extremely computationally intensive.

In this work, several recently developed techniques are combined to get a more computationally efficient calculation of full field stress and strain on a finite element model (FEM). The full space FEM is reduced to an intermediate space using a combination of reduction techniques. The time response is calculated using an efficient nonlinear response approach – Modal Modification Response Technique (MMRT) or Equivalent Reduced Model Technique (ERMT). The displacement results for the nonlinear system are expanded back to the full space FEM to determine time-dependent full field stress and strain. Results are presented for the nonlinear response of a system involving multiple contact elements to show the accuracy and computational efficiency of the process.

Keywords Nonlinear • Model reduction/expansion • Dynamic strain

Nomenclature

Symbols

$\{X_n\}$	Full set displacement vector
$\{X_a\}$	Reduced set displacement vector
$\{X_d\}$	Deleted set displacement vector
$[M_a]$	Reduced mass matrix
$[M_n]$	Expanded mass matrix
$[K_a]$	Reduced stiffness matrix
$[K_n]$	Expanded stiffness matrix
$[U_a]$	Reduced set shape matrix
$[U_a^G]$	Guyan reduced set shape matrix
$[U_n]$	Full set shape matrix
$[U_a{}^g]$	Generalized inverse
$[T]$	Transformation matrix
$\{p\}$	Modal displacement vector
$[M]$	Physical mass matrix
$[C]$	Physical damping matrix
$[K]$	Physical stiffness matrix
$\{F\}$	Physical force vector

J. Harvie (✉) • P. Avitabile

Structural Dynamics and Acoustic Systems Laboratory, University of Massachusetts Lowell, One University Avenue, Lowell, MA 01854, USA
e-mail: harvie.julie@gmail.com

$\{\ddot{x}\}$ Physical acceleration vector
$\{\dot{x}\}$ Physical velocity vector
$\{x\}$ Physical displacement vector
α Parameter for newmark integration
β Parameter for newmark integration
Δt Time step
$[U_{12}]$ Mode contribution matrix

9.1   Introduction

Detailed finite element models are often generated for the simulation of dynamic response on structural systems. With the current technology available, models are becoming increasingly larger and prominently more detailed to accurately capture the precise dynamics experienced throughout the structure. Such sizeable models require significant computational resources to solve the time response using conventional methods; the computations become further lengthened when nonlinearities are introduced to the system and a nonlinear solution scheme must be employed.

A nonlinear solution scheme is required to accurately capture the dynamics of a system where discrete nonlinear connection elements (bilinear springs, gaps, slip–stick, or contact elements) are added to a linear model, although the response of the original linear model will dominate the response of the system. When the response of these types of nonlinear systems is studied, the nonlinear response can be broken into a piecewise linear solution where different configurations occur within the time block. This work focuses on a system with gap-spring contact elements, as shown in Fig. 9.1, to demonstrate the principles at hand on a system with a severe kind of nonlinear connection; the principles also apply to systems with other types of nonlinear connection elements. The system consists of two components with two possible spring contacts as an example of this type of a nonlinear system. An analysis of the dynamic response of the system in Fig. 9.1 will generally be dominated by the linear response of the individual components, and the response will only become nonlinear when the springs come into contact between the beams. The traditional response calculation requires a nonlinear solution scheme that can be extremely computationally expensive but must be employed to capture the nonlinear response even though the nonlinearities occur at discrete time points and at discrete locations.

The proposed approach for efficiently calculating full field strain is shown in Fig. 9.2 and further detailed by Harvie [1]. The approach involves reducing the full space model to a more manageable size and then calculating the response using an efficient response calculation, Modal Modification Response Technique (MMRT) or Equivalent Reduced Modeling Technique (ERMT). The highly reduced order models are used to accurately approximate the full field dynamic characteristics while significantly reducing the computation time; the traditional approach, outlined on the left of Fig. 9.2, requires an extremely lengthy computation time due to the nonlinear solution scheme.

As seen in Fig. 9.2, there are several possible paths that can be used to accurately calculate the full field strain at a fraction of the computational cost. This work focuses on the results obtained using a SEREP reduction in conjunction with ERMT; however the other techniques will produce similar results and are explored further by Harvie [1] but are not presented in this paper due to space restrictions.

Several pieces of the proposed approach have already been investigated in depth. Recent work has been performed by Marinone et al. [2–4] on MMRT and Thibault et al. [5–7] on ERMT to confirm the accuracy and efficiency of the nonlinear time response calculations for displacement results. Pingle [8–14] and Carr [15–18] have explored the application for full field strain on linear systems using expansion of limited sets of data. Nonis [19, 20] and others [21, 22] have proven that a reduced order system assembly can be expanded to full space using information from the uncoupled component modes. The focus of this work is to combine the theory behind these separate sets of work to determine full field strain from the expansion of the highly reduced order models used to determine the response of systems with nonlinear component interactions.
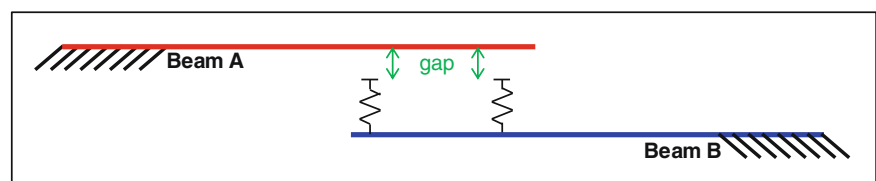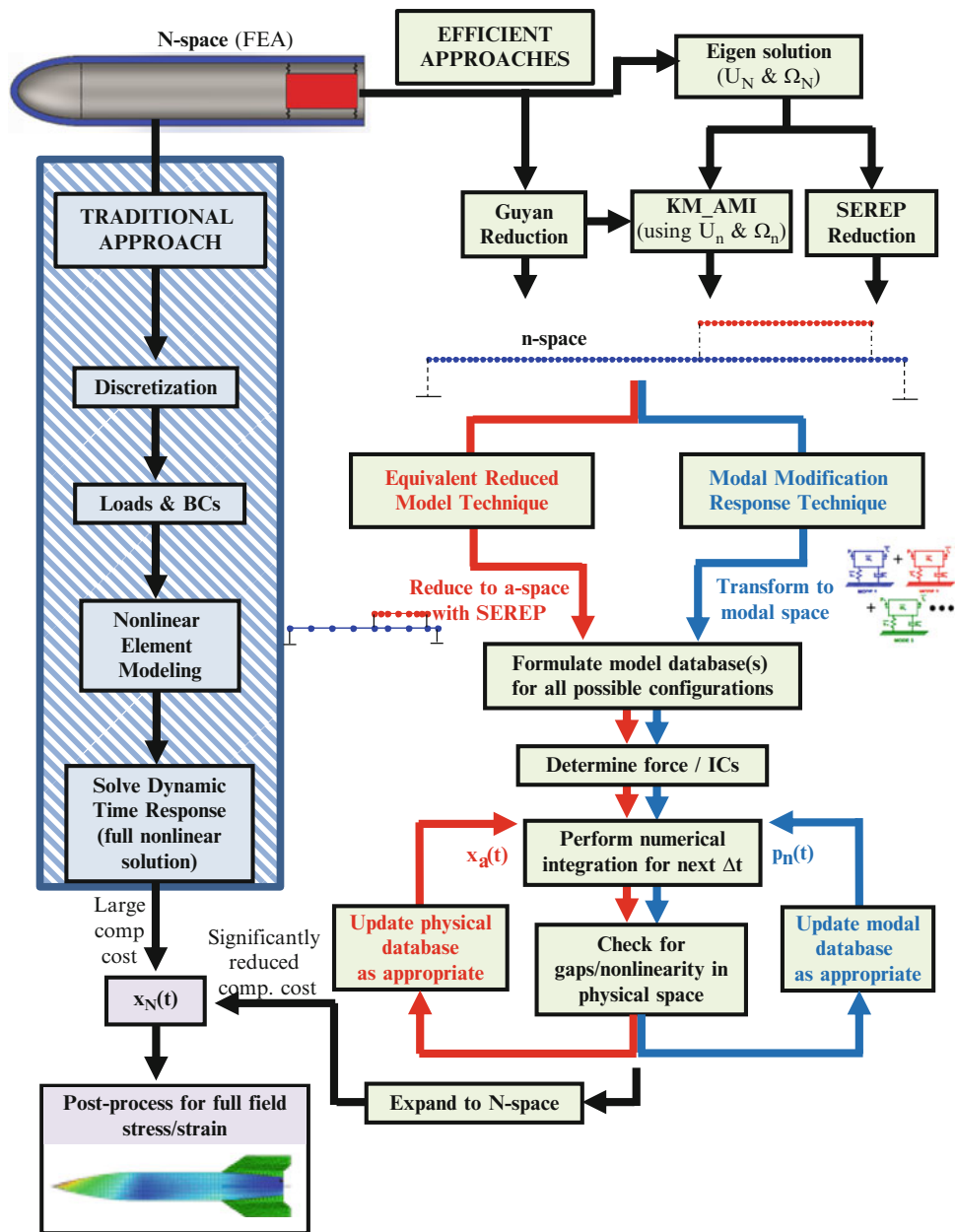

Fig. 9.1 System containing two components and springs contacts

Fig. 9.2 Traditional vs. efficient approaches to calculate stress and strain

9.2 Theory

9.2.1 Basic Equations of Motion

For a multiple degree of freedom system subjected to an external force $\{F\}$, the equation of motion can be written as

$$[M]\{\ddot{x}\} + [C]\{\dot{x}\} + [K]\{x\} = \{F\} \qquad (9.1)$$

The $[M]$, $[C]$, and $[K]$ matrices are the square symmetric mass, damping, and stiffness matrices, respectively. These matrices are generally coupled and can contain hundreds of thousands to millions of degrees of freedom, depending on the size of the finite element model. To uncouple the matrices, an eigensolution can be performed on the mass and stiffness matrices using

$$[[K] - \lambda[M]]\{x\} = \{0\} \qquad (9.2)$$

The eigensolution of Eq. (9.2) provides the eigenvalues (natural frequencies) of the system, along with an eigenvector (mode shape) for each frequency. The eigenvalues and eigenvectors are generally arranged as

$$
\begin{bmatrix} \ddots & & \\ & \Omega^2 & \\ & & \ddots \end{bmatrix} = \begin{bmatrix} \omega_1{}^2 & & \\ & \omega_2{}^2 & \\ & & \ddots \end{bmatrix} \text{ and } [U] = [\{u_1\}\{u_2\}\dots]
\tag{9.3}
$$

If a limited set of eigenvectors are used to describe the system, as is typical, then the resulting [U] matrix will be rectangular with 'n' DOF and 'm' modes. The relationship between the coupled, physical set of equations and uncoupled, modal set of equations is defined as

$$
\{x\} = [U]\{p\} = [\{u_1\}\{u_2\}\dots] \begin{Bmatrix} p_1 \\ p_2 \\ \vdots \end{Bmatrix}
\tag{9.4}
$$

This transformation to modal space allows for the equation of motion to be written in normal form as

$$
[U]^T [M] [U] \{\ddot{p}\} + [U]^T [C] [U] \{\dot{p}\} + [U]^T [K] [U] \{p\} = [U]^T \{F\}
\tag{9.5}
$$

This equation transforms the highly coupled system into a set of simple, uncoupled systems due to the orthogonality condition. The mode shapes are linearly independent and orthogonal with respect to the mass and stiffness matrices, yet the damping matrix may or may not be proportional. The damping matrix is typically not linearly independent and orthogonal with respect to the mode shapes, but a proportional damping matrix is often approximated to satisfy the orthogonality condition. The proportional damping matrix can be generated using several techniques, and the Wilson–Penzien damping formulation is utilized in this work. Thus the diagonal mass, damping, and stiffness matrices can be written in modal space as

$$
\begin{bmatrix} \ddots & & \\ & \overline{M} & \\ & & \ddots \end{bmatrix} = [U]^T [M] [U]
$$

$$
\begin{bmatrix} \ddots & & \\ & \overline{C} & \\ & & \ddots \end{bmatrix} = [U]^T [C] [U]
\tag{9.6}
$$

$$
\begin{bmatrix} \ddots & & \\ & \overline{K} & \\ & & \ddots \end{bmatrix} = [U]^T [K] [U]
$$

With a modal matrix [U] of size $n \times m$ ("n" DOF and "m" modes), the modal properties calculated in (9.6) will be square and symmetric of size $m \times m$. If "m" is less than "n", then the physical mass, damping, and stiffness matrices of size $n \times n$ will be reduced to the modal mass, damping, and stiffness matrices of size $m \times m$.

9.2.2 Model Reduction and Expansion

Solving dynamic response using the equation of motion in (9.1) can become computationally intensive when a full space finite element model contains millions of DOF. The computation can be simplified by reducing the FEM with model reduction/expansion techniques. Using model reduction, the size of a model can be reduced to a limited 'a' DOF and 'm' modes while retaining the full space dynamic characteristics. Using model expansion, a full field solution can be obtained from a subset of points; expansion is commonly used to expand test data to locations that were not included in the reduced set of DOF. Several techniques are available for reduction and expansion, each with their own benefits and drawbacks. Guyan

Condensation is one of the more commonly used techniques and is available in most commercially available software, but the Guyan transformation matrix is stiffness based and therefore does not preserve inertial characteristics exactly. Additional processing of the Guyan reduced matrices using the KM_AMI model reduction process [23–28] allows for exact reduced dynamic characteristics if target vectors from the full space model are used. SEREP [29] also preserves the exactness of eigenvalues and eigenvectors in the reduction/expansion process because the full space eigensolution is used in the transformation matrix calculation. While a multitude of reduction/expansion techniques could be used to transform the matrices, the results shown in the case studies were obtained using the accurate SEREP reduction and therefore only SEREP is detailed here. For further details on the various reduction techniques, see [1].

The main concept behind model reduction and expansion involves the mapping between a large model containing 'n' DOF and a reduced model containing a limited 'a' set of DOF. The general transformation between the full model and reduced DOF is given as

$$\{x_n\} = \begin{Bmatrix} x_a \\ x_d \end{Bmatrix} = [T]\{x_a\} \tag{9.7}$$

where the full 'n' space model is made up of 'a' master DOF and 'd' deleted DOF. The transformation matrix, [T], contains the appropriate mapping information to relate the full and reduced models. By employing energy conservation principles, the mass and stiffness of the reduced 'a' DOF can be calculated using the transformation matrix with

$$[M_a] = [T]^T[M_n][T] \tag{9.8}$$

$$[K_a] = [T]^T[K_n][T] \tag{9.9}$$

Once the mass and stiffness matrices are determined at the reduced DOF, the equations of motion are written in the same form as (9.1) and an eigensolution is performed using (9.2). The eigenvalues and eigenvectors of the reduced matrices are ideally preserved as accurately as possible when compared to the full space solution, but the accuracy is dependent on the specific technique employed. The reduction/expansion technique utilized in this work is discussed next.

The SEREP transformation matrix can be used to exactly replicate eigenvalues and eigenvectors between a full and reduced model [29]. SEREP involves partitioning the modal equations representing a physical system using

$$\{x_n\} = \begin{Bmatrix} x_a \\ x_d \end{Bmatrix} = \begin{bmatrix} U_a \\ U_d \end{bmatrix} \{p\} = [U_n]\{p\} \tag{9.10}$$

where the active 'a' set can be described using

$$\{x_a\} = [U_a]\{p\} \tag{9.11}$$

In Eq. (9.11), the $[U_a]$ matrix contains mode shapes for 'a' DOF and 'm' modes. For a case where the number of modes retained in the reduced model is less than or equaled to the number of reduced DOF ($m \leq a$), a least squares solution provides

$$\{p\} = \left([U_a]^T[U_a]\right)^{-1}[U_a]^T\{x_a\} = [U_a]^g\{x_a\} \tag{9.12}$$

Substituting (9.12) into (9.10) gives

$$\{x_n\} = [U_n][U_a]^g\{x_a\} \tag{9.13}$$

Hence the SEREP transformation matrix is written as

$$[T_U] = [U_n][U_a]^g \tag{9.14}$$

The development of this transformation matrix leads to vast computational advantages. Using unit modal mass scaling, Eqs. (9.8) and (9.14) can be combined to efficiently compute the mass matrix as

$$[M_a] = [T_U]^T[M_n][T_U] = [U_a{}^g]^T[U_a{}^g] \tag{9.15}$$

Fig. 9.3 Sample components arranged into common matrix space
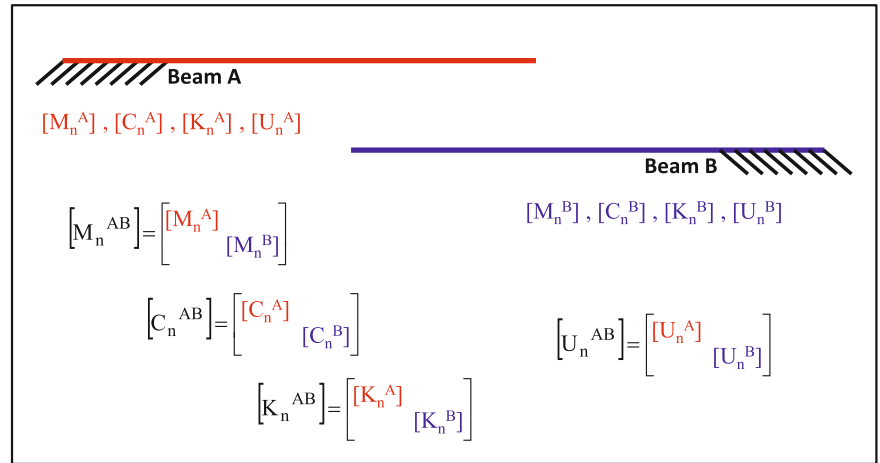
Similarly, Eqs. (9.9) and (9.14) can be used to efficiently compute the stiffness matrix as

$$[K_a] = [T_U]^T [K_n] [T_U] = [U_a^g]^T [\Omega^2] [U_a^g] \tag{9.16}$$

Again assuming unit modal mass scaling is used. Therefore the mass and stiffness matrices can be computed using only the mode shapes and frequencies of a system due to the properties of SEREP.

The reduced mass and stiffness matrices calculated in (9.15) and (9.16) are of size 'a', but rank 'm'. Therefore when the number of retained modes is less than the number of retained DOF (m < a), the reduced matrices will be rank deficient. Care must be taken when dealing with the rank deficient matrices. For the cases studied here, the rank deficiency is avoided by retaining the same number of modes and DOF (a = m) in the reduced model and is sometimes referred to as SEREPa. Such cases contain matrices that are fully ranked and well-conditioned.

9.2.3 System Modeling and Mode Contribution

Various techniques are available for the coupling of several component models into a single system model. These system modeling techniques are used to define the various states that the system will undergo when the different contact connections are considered in the nonlinear response of the system. The system modeling can be performed in physical space, modal space, or a combination of both physical and modal space. Consider two beams that are completely independent of one another, as illustrated in Fig. 9.3.

The two beams shown in Fig. 9.3 are completely uncoupled and will respond independent of one another when excited. A system model of the uncoupled components is generated by simply writing the variables in common matrix space, as shown in the diagram. To generate a coupled system model, specific coupling terms must be introduced at the desired locations. To include the spring(s) in the system modeling, either a modal or physical approach can be employed. The modal approach involves using Structural Dynamic Modification (SDM) and Component Mode Synthesis (CMS). The physical approach involves using a physical tie matrix to couple the beams. Both approaches involve the use of a mode contribution matrix to determine the appropriate number of component modes that contribute to the system modes. For the results presented here, physical system modeling techniques were used to generate databases for the various configurations.

The equation of motion of a system with a physical change in mass or stiffness can be written at full space as

$$\begin{bmatrix} \begin{bmatrix} [M_n^A] & \\ & [M_n^B] \end{bmatrix} + [\Delta M_{12}] \end{bmatrix} \begin{Bmatrix} \ddot{x}_n^A \\ \ddot{x}_n^B \end{Bmatrix} \\ + \begin{bmatrix} \begin{bmatrix} [K_n^A] & \\ & [K_n^B] \end{bmatrix} + [\Delta K_{12}] \end{bmatrix} \begin{Bmatrix} x_n^A \\ x_n^B \end{Bmatrix} = \begin{Bmatrix} f_n^A \\ f_n^B \end{Bmatrix} \tag{9.17}$$

Once the physical system matrices are generated at full space, the system is reduced to a set of 'a' DOF and 'm' modes in this work. Truncation can be avoided in the reduction by including enough modes to span the space of the problem. To determine the appropriate modes of the original components that contribute to the final system modes, a mode contribution
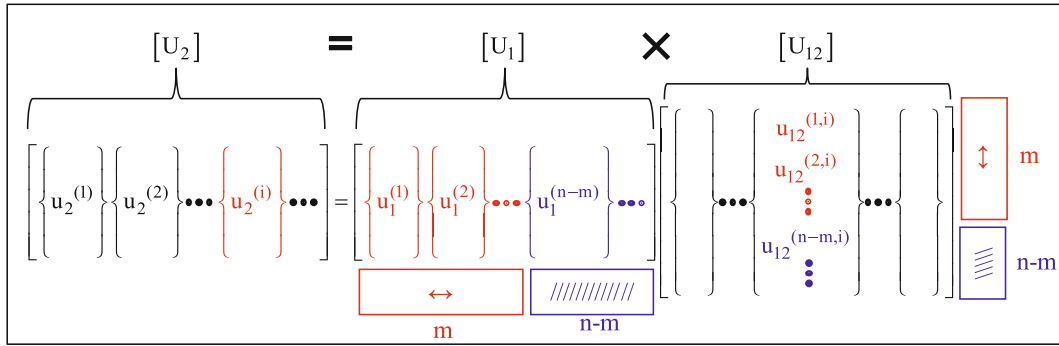
Fig. 9.4 Use of $[U_{12}]$ matrix to determine final system mode shapes

matrix is used. The mode contribution matrix calculated using this technique is equivalent to the $[U_{12}]$ matrix calculated in SDM/CMS [30–32]. As presented by Thibault [6], the mode contribution matrix in physical system modeling is calculated using vectors from the original system state, 1, and final system state, 2, using

$$[U_{12}] = [U_1]^T [M_2] [U_2] \tag{9.18}$$

The mode contribution matrix is important because it identifies which modes of the unmodified system are necessary to construct the modified system modes. This transformation matrix contains scaling coefficients that specify which of the original state $[U_1]$ vectors are necessary to construct the final state $[U_2]$ vectors. A physical representation of the multiplication in (9.18) is shown in Fig. 9.4.

The mode contribution matrix is used to determine which original mode shapes are necessary for the accurate reconstruction of each of the desired final mode shapes. If a dynamic response involves multiple system states, then the $[U_{12}]$ matrix must be computed for each configuration to determine the number of original system modes to appropriately span the space of the solution and avoid truncation. If a component mode has a high value in the contribution matrix for a certain desired system mode and that component is not included in the reduction or modes retained, then the system mode will be in error and is said to be truncated. Conversely, components modes with low contribution values for desired system modes do not participate significantly in the system modes and therefore are not necessary to include in the solution. The mode contribution matrix is important because it can identify the minimal set of component modes that are necessary to include in a system model; retaining fewer modes in a reduced model can result in higher computational savings.

9.2.4 Uncoupled Expansion of Coupled Systems

A breakthrough in the expansion of coupled reduced order components using uncoupled component information has recently been established. The main idea behind the work is that if a coupled reduced order system is comprised of uncoupled components, the full space coupled system modes can be generated using the uncoupled component transformation information. SDM principles show how the mode shapes of a coupled system can often be constructed using appropriate combinations of the uncoupled system mode shapes. The $[U_{12}]$ matrix is used to determine the necessary number of modes of an uncoupled system that must be included in system modeling activities to accurately represent the coupled system mode shapes. Recent analyses by Nonis [19, 20] and others [21, 22] have shown how these SDM principles can be extended to model reduction and expansion, and the transformation matrix of an uncoupled system can be used to expand a coupled system if enough modes of the uncoupled system are included.

Figure 9.5 shows a simple example where model expansion is used on a cantilever beam. In Case A, no modifications have been made to the beam and a straightforward expansion is performed using the SEREP transformation matrix calculated using Eq. (9.14). For Case B, the reduced model contains a spring modification near the tip. Traditionally, a new transformation matrix would need to be computed to relate the reduced and expanded mode shapes with the spring modification in place. However, SDM principles show that the mode shapes for the modified beam in Case B are made up of combinations of the mode shapes for the original beam in Case A. Therefore given that enough modes are included in the expansion, the same transformation matrix that is used to expand the mode shapes in Case A on the original, unmodified beam can be used to expand the modified system in Case B.

Fig. 9.5 Simple beam with and without spring modification
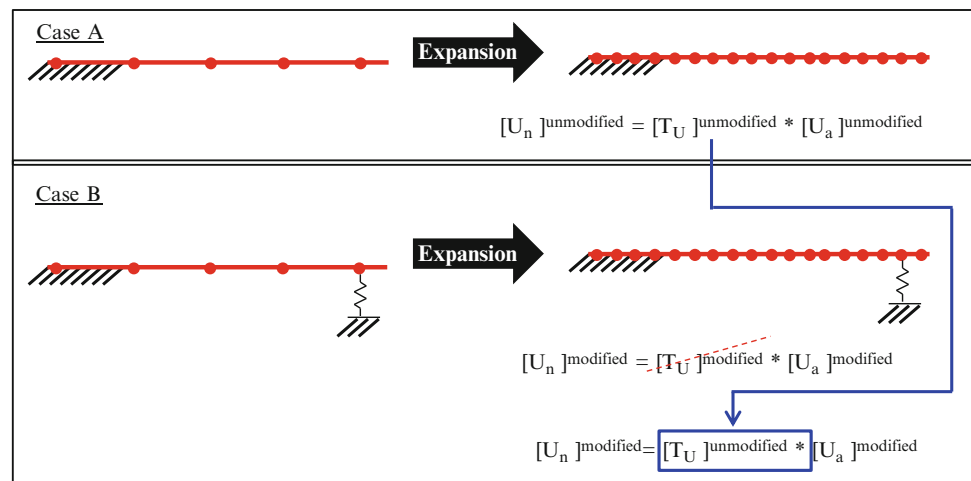
The results obtained using the technique outlined in Fig. 9.5 will yield exactly the same results as a full space SDM model containing the same number of modes as the reduced model [20]. Therefore in a case where not enough modes are included in the solution, the SDM and uncoupled expansion techniques will contain the same level of truncation. The only possible source of error inherent to the expansion could be truncation if not enough modes are included to span the space of the problem. However if enough modes are included in the reduced model to accurately represent the coupled system modes, the uncoupled transformation matrix will be able to accurately expand the coupled system mode shapes.

The expansion methodology is not limited to a single component such as the one in Fig. 9.5. For a coupled system comprised of multiple components, only the uncoupled transformation matrices of the individual components are needed to expand mode shapes of a system where the components are joined. The coupled system can be expanded to full space using the uncoupled transformation matrices as long as the modes required to accurately produce the coupled system modes are included from the uncoupled system. Furthermore the components are expanded independent from one another, and therefore both components do not need to be expanded to full space if full space information is not desired on all components. The necessary modes to include in the reduced model and transformation matrix can be determined using the mode contribution matrix $[U_{12}]$.

Chipman [33–36] and others [8–18] have shown that a transformation matrix can be used to expand not only mode shapes, but dynamic time response data. Therefore the same principles presented above can be extended to the expansion of coupled response using uncoupled component information. The response of the coupled system at reduced space can be expanded to full space using the transformation matrices of the individual, unconnected beams because the dynamic characteristics of the system are directly related to the dynamic characteristics of the uncoupled components. If the $[U_{12}]$ matrix is evaluated to include enough modal information in the reduced model to accurately represent the system with the coupling elements present, then the time response of the coupled system is accurately expanded to full space using information from the uncoupled components.

For this work, nonlinear systems are analyzed where several possible configurations can exist during response. If all possible configurations are made up of linear combinations of the component mode shapes, then the expansion of nonlinear response of a reduced model can be expanded using the original transformation matrix regardless of the configurations encountered. As long as enough modal information is included in the reduced order models to accurately represent all possible configurations, the expansion of nonlinear coupled response can be performed using information from the uncoupled components. Figure 9.6 shows the process for determining full space dynamic response of a nonlinear system using the original transformation matrices. Although several configurations exist within the time block shown, all modified states can be generated based on the mode shapes of the original system. Therefore only the transformation matrices of the original, uncoupled components are necessary to expand the nonlinear dynamic response of the system regardless of the configurations encountered.

Although the system in Fig. 9.6 experiences multiple changes of state, all configurations are made up of the mode shapes from the original, uncoupled system. Therefore the nonlinear response of the system at reduced space is accurately expanded to full space using only the mode shapes from the original system, as long as enough mode shapes of the unmodified system are included in the solution.
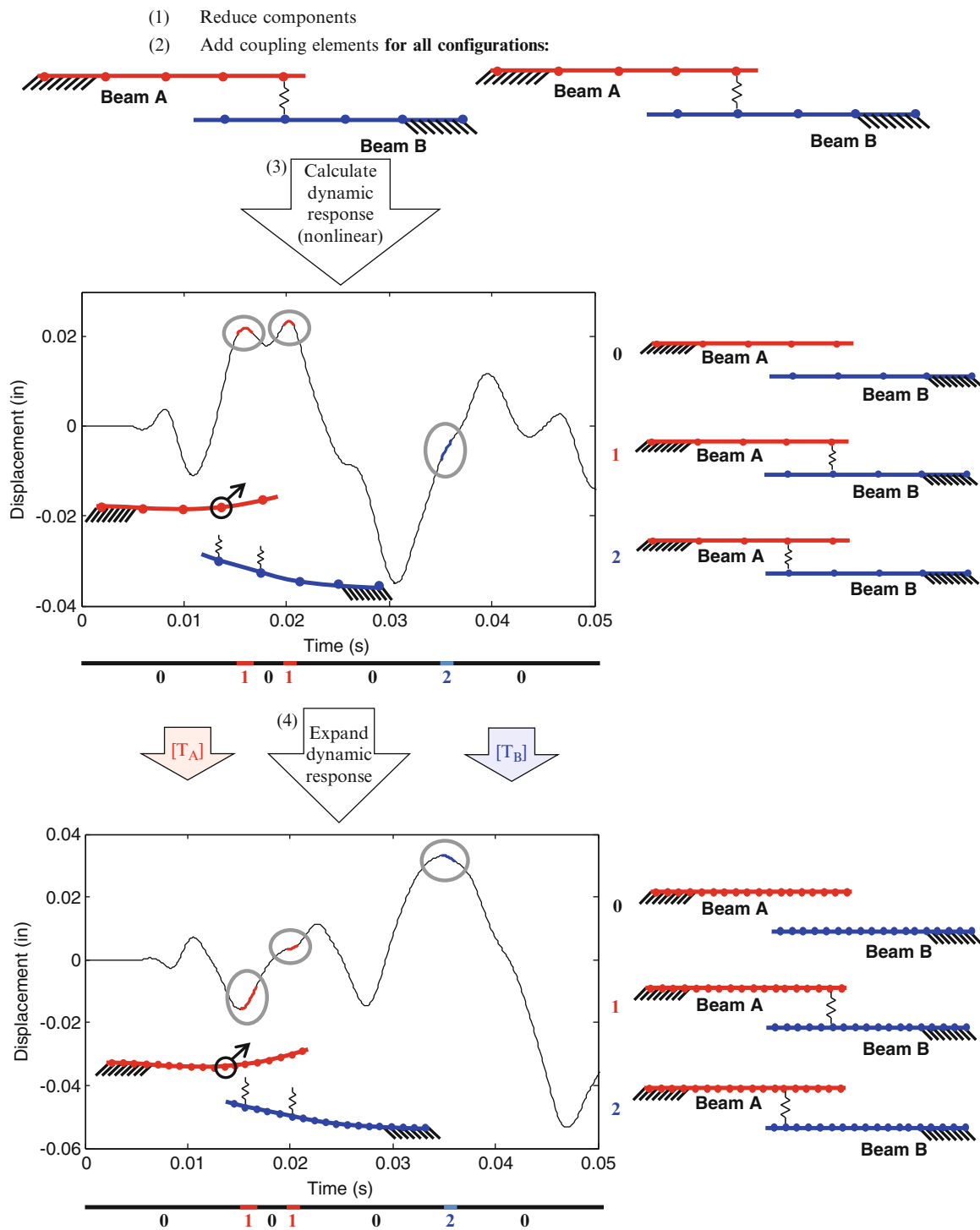
(1) Reduce components
(2) Add coupling elements **for all configurations:**

Fig. 9.6 Expansion of nonlinear response using component mode shapes

9.2.5 *Efficient Time Response Calculation*

Several techniques are available to calculate the time response of a linear or nonlinear system more efficiently than solving the full space solution. Two techniques, the Modal Modification Response Technique (MMRT) and the Equivalent Reduced Model Technique (ERMT), were presented by Avitabile and O'Callahan [37] and analyzed in detail by Marinone [2–4] and Thibault [5–7], respectively. MMRT involves integrating the equations of motion in modal space using a subset of modes to

reduce computation time. ERMT involves integrating the equations of motion in physical space using reduced order models to increase efficiency. Both techniques are able to further reduce computational costs in nonlinear response by avoiding a lengthy nonlinear solution scheme; both techniques treat the nonlinear response as piecewise linear response. ERMT provides a slightly more efficient calculation because MMRT requires a projection to physical space at each time step to determine if contacts are engaged, while the ERMT calculation is performed without projection to a different domain. However, in terms of each technique, the ERMT works well with physical models are reduced from a full finite element model where as the MMRT works well with modal data which can come from either a finite element model or from an experimental test. The ERMT process is described next and was used in the following case studies due to the slightly more efficient calculation.

The Equivalent Reduced Model Technique can be used to compute forced response for both linear and nonlinear systems. An outline of the ERMT process is shown in Fig. 9.2. First, databases are generated at reduced space for all possible configurations of the system using system modeling techniques as necessary. The forcing function and initial conditions are identified and input to the system. The equations of motion are numerically integrated for the next time step. At this point, the displacements at locations where interaction is possible are monitored to determine whether contact has occurred. At each time step the appropriate system matrices are utilized for the given configuration. The integration is performed for each time step through the desired time period. Therefore the total forced response of a system, regardless of linearity, can be computed with traditional integration using this technique. Once the time response is computed at the reduced DOF, the results are expanded to the full model. As presented in [21, 22], only the transformation matrix for the original system is needed to expand the time response back to n-space, regardless of the types of configurations that are encountered.

9.2.6 Correlation Tools

Several correlation tools are available for the comparison of a system's time response. The main tools used in this work are the Modal Assurance Criterion (MAC) and Time Response Assurance Criterion (TRAC).

MAC is used to compare two shapes at a single instance in time and is calculated using

$$\text{MAC} = \frac{\left[\{x_{n1}\}^T \{x_{n2}\}\right]^2}{\left[\{x_{n1}\}^T \{x_{n1}\}\right]\left[\{x_{n2}\}^T \{x_{n2}\}\right]} \tag{9.19}$$

where MAC values approaching 1 indicate high level of correlation.

TRAC is used to compare two time response plots at a single degree of freedom and is calculated similarly using

$$\text{TRAC} = \frac{\left[\{x_{n2}\}^T \{x_{n1}\}\right]^2}{\left[\{x_{n2}\}^T \{x_{n2}\}\right]\left[\{x_{n1}\}^T \{x_{n1}\}\right]} \tag{9.20}$$

where once again values approaching 1 indicate good correlation.

In this work, the MAC is calculated between the shapes of the full space reference solution and estimated solution obtained from the reduced order model at each time step. Similarly the TRAC is used to compare the time response from the reduced order model to the time response from the full space finite element solution at each degree of freedom. A diagram detailing the two comparison techniques is shown in Fig. 9.7.

9.3 Cases Studied

For this study, a simple two-beam system was used to demonstrate the proposed approach for calculating full field strain at a fraction of the full space computational cost. Two cases were studied to show the influence of higher order modes when hard nonlinear contact springs are present in a system. Additional cases and further details on all analyses performed can be found in [1]. The cases presented here are summarized as:

Case 1: Nonlinear Solution with Smaller Reduced Model
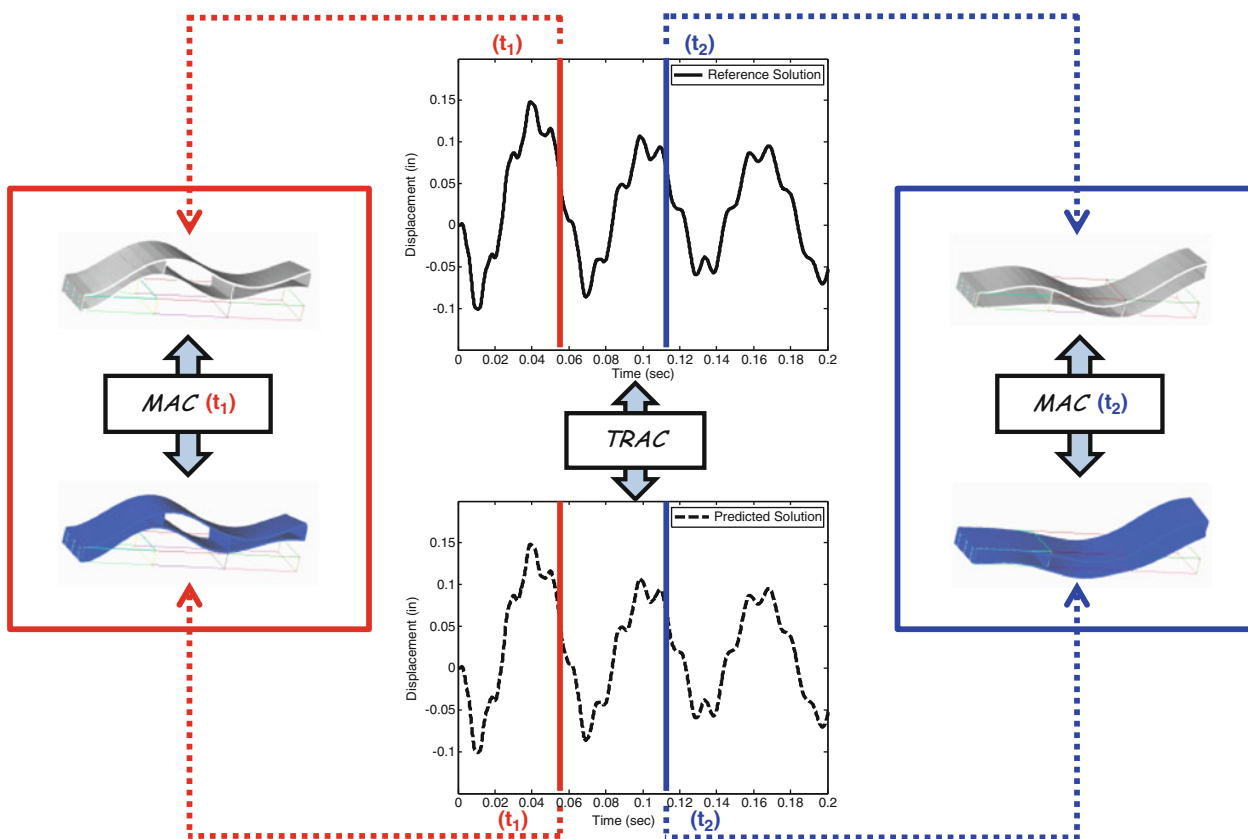Case 2: Nonlinear Solution with Reduced Model Including Additional Modes

Fig. 9.7 Physical interpretation of MAC and TRAC

9.3.1 Structure Description and General Modeling/Testing Performed

A finite element model was generated using Abaqus/CAE [38]. The two-beam system, as illustrated in Fig. 9.8, was generated to imitate a large, complicated model to accurately demonstrate the principles at hand while maintaining a feasible model size on which reference calculations are performed; note that the diagram shown in Fig. 9.8 is not to scale. The main beam, Beam B, is 140 inches in length and joined to the smaller Beam A, 50 inches in length, using 10,000,000 lb/in. translation springs; the main beam is grounded using 10,000 lb/in. translation springs.

The full space model contains nodes with 0.2 in. spacing on each beam; therefore there are 251 nodes on Beam A and 701 nodes on Beam B. Each node contains a shear DOF and a rotational DOF to capture planar beam bending only. Details on the properties of the structure can be found in Table 9.1; note that the modeling properties are only applicable for the large N-space model.

To introduce discrete nonlinearities to the system, a gap-spring interface was used to simulate a contact; the stiffness of the spring contact is either set to a predefined stiffness value when the specified gap distance is closed, or set to zero when the specified gap distance is open. The nonlinear cases have two contact locations between the beams, as shown in Fig. 9.9; these contact locations were chosen so that both contact springs could engage during the response. The initial gap distance was set to 0.003 in. for the nonlinear cases; once again this value was chosen merely so that both contact springs would engage during the response. The three possible configurations that the beams can encounter with the springs engaged are also shown in Fig. 9.9. An eigensolution was performed on the model to determine natural frequencies and mode shapes for the original system and with the possible spring attachments. The frequencies up to 1,000 Hz for all configurations are listed in Table 9.2.

For all cases, a frequency band-limited analytical force pulse was utilized to excite a frequency range of roughly 400 Hz; the frequency range excited by the force pulse includes roughly 13 modes in all configurations, as listed in Table 9.2. The use of such a force pulse allows for minimal excitation of higher modes and controls the number of modes that substantially participate in the system response due to the impulse. The force was applied at the left-most node of Beam B, and the force was applied perpendicular to the beam to excite modes along the weak axis; this approximation was made to demonstrate the principles at hand and could be extended to different forcing functions and locations.
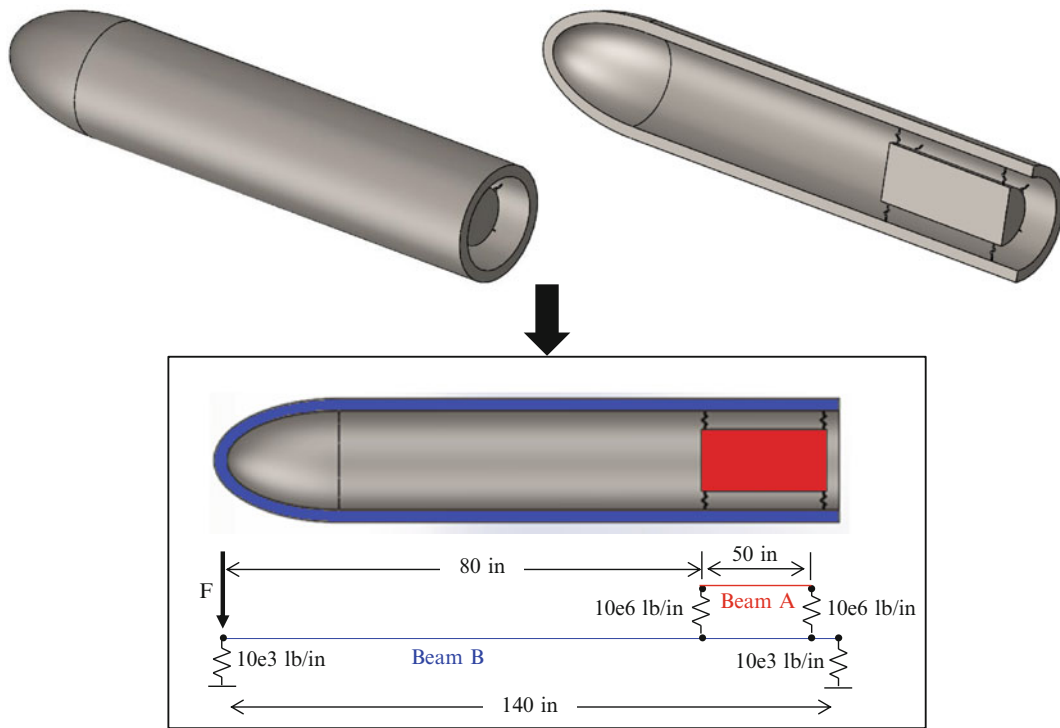
Fig. 9.8 Physical representation of two-beam system

Table 9.1 Geometric, modeling, and material properties of two-beam system

Property		Beam A	Beam B
Geometric	Beam width (in.)	2	2
	Beam height (in.)	1	1
	Length (in.)	50	140
Modeling	# of elements	250	700
	# of nodes	251	701
	# of DOF	502	1,402
	Node spacing (in.)	0.2	0.2
Material	Material	Aluminum	Aluminum
	Density (lb/in^3)	2.538e−4	2.538e−4
	Young's Modulus (psi)	10e6	10e6
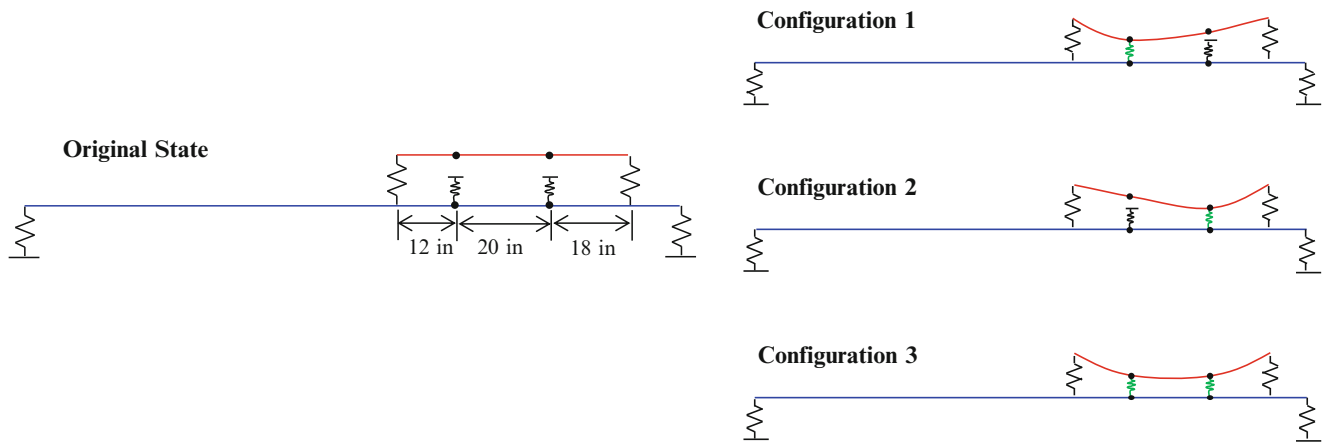
Fig. 9.9 Contact locations and configurations for nonlinear cases

Table 9.2 Natural frequencies through 1,000 Hz of full-space system with and without hard contacts

	Frequency (Hz)			
Mode	Original	Config 1	Config 2	Config 3
1	3.88	4.14	4.07	4.14
2	14.61	15.01	15.05	15.08
3	26.91	27.18	26.97	27.34
4	38.37	43.42	43.11	43.49
5	44.03	67.08	66.73	67.10
6	67.10	76.99	92.65	98.80
7	96.85	99.19	113.84	144.79
8	141.42	145.76	144.79	187.79
9	153.93	190.90	189.58	208.79
10	190.93	227.85	229.99	234.73
11	255.93	262.04	264.22	269.05
12	322.30	325.28	328.99	329.20
13	335.25	383.76	338.36	391.88
14	404.54	404.55	406.64	407.48
15	496.67	499.47	497.10	499.56
16	584.91	585.47	590.07	591.58
17	590.09	591.95	615.35	615.52
18	707.96	707.97	708.67	708.68
19	814.95	815.99	816.16	816.98
20	901.54	907.93	909.59	915.61
21	949.60	950.01	950.13	950.71
22	1,078.50	1,078.53	1,078.71	1,078.73

Fig. 9.10 Description of model sizes from initial reduction

N-space
- 952 nodes (shear & rotary with 0.2" spacing)
- 1904 DOF
- 1904 modes

n-space
- 97 nodes (shear & rotary with 2" spacing)
- 194 DOF
- 194 modes
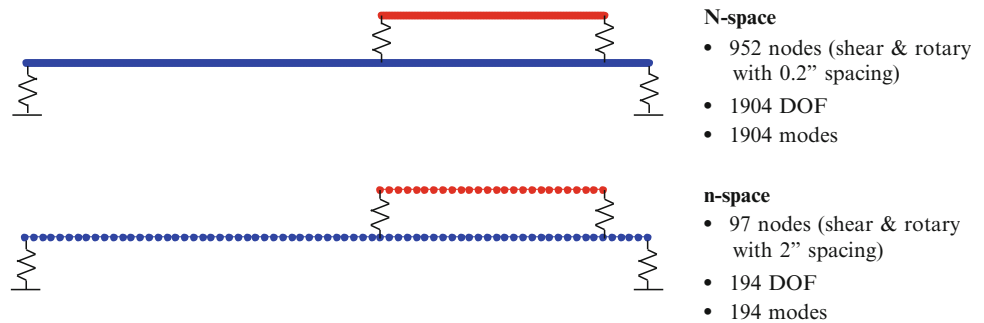
Fig. 9.11 Description of model sizes for smaller, reduced order models

a-space
- 24 nodes (shear, variable spacing, max 10")
- 24 DOF
- 24 modes

aa-space
- 13 nodes (shear, variable spacing, max 20")
- 13 DOF
- 13 modes
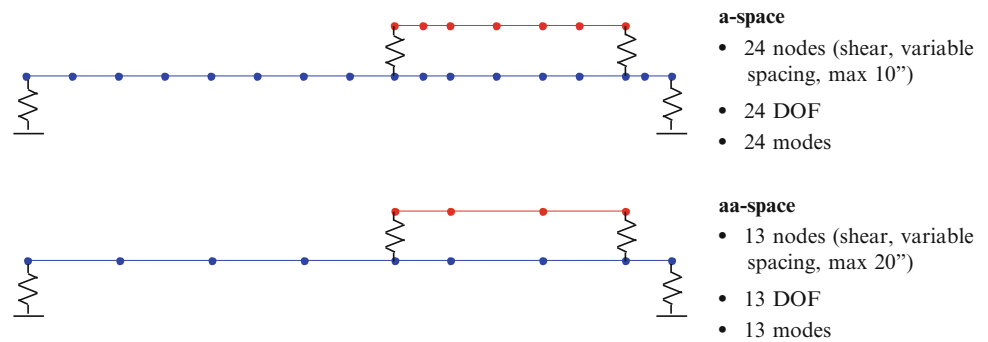
The large N-space model was reduced from 1,904 modes and DOF to an n-space model with 194 modes and DOF by retaining every tenth node from the full space model. A comparison of model sizes for this reduction is shown in Fig. 9.10. All nodes in both models contain both shear and rotary DOF. This reduction was performed to produce a more reasonable sized model.

The n-space model was reduced further for use with ERMT. Two model sizes, a-space and aa-space, were generated for the various analyses. The a-space model contains 24 modes and DOF while the aa-space model contains only 13 modes and DOF, as outlined in Fig. 9.11. Details on the levels of modeling are shown in Table 9.3, including the specific DOF and modes

Table 9.3 Specific modes and DOF active in each size model

Model	# of DOF	Modes	Active DOF
N-space	952	1–1,904	1–1,904
n-space	194	1–194	1–2, 21–22, 41–42, ….1,903–1,904
a-space	24	1–24	1, 101, 201, 301, 401, 501, 601, 701, 801, 861, 921, 1,021, 1,121, 1,301, 1,341, 1,401, 1,403, 1,463, 1,523, 1,623, 1,723, 1,803, 1,903
aa-space	13	1–13	1, 201, 401, 601, 801, 921, 1,121, 1,301, 1,401, 1,403, 1,523, 1,723, 1,903

that remain active in each model. The a-space model includes modes of the original system up to approximately 1,300 Hz while the aa-space model includes modes up to only 400 Hz. Without any additional information, the aa-space model with 13 modes and DOF would seem appropriate to represent the system in all configurations due to the applied force pulse.

The mode contribution matrices were calculated at full space for the modified system in all configurations, and the matrices are shown in Fig. 9.12. As identified previously, the force pulse excites roughly 13 modes of the system in all configurations, and those modes are highlighted in the matrices. The modes of the original system retained in the smallest aa-space model are outlined in red, while the additional modes of the original system retained in the a-space model are outlined in blue. The aa-space model, which includes 13 modes and DOF, includes many of the original system modes that make up the first 13 system modes in the various configurations. However, there are also some minor contributions from higher order modes for the system modes with the contacts engaged. The a-space model with 24 modes contains enough modal information to span the space of the problem for all configurations encountered.

Direct integration of the equations of motion was performed using Newmark time integration [39] to compute the time response for all cases; details regarding the integration technique are shown in [1]. Newmark integration was utilized for similarity to the solver used in Abaqus [38], where the Hilber–Hughes–Taylor (HHT) variation of the Newmark method is used. The damping of the system was approximated using a Wilson–Penzien formulation, as detailed in [1], with 1 % of critical damping for all modes. Proportional damping was assumed to keep a straightforward solution procedure, but a state space solution could be used to solve systems with nonproportional damping.

9.3.2 Case 1: Nonlinear Solution with Smaller Reduced Model

This case utilizes a reduction to the smallest aa-space model with 13 modes and DOF. A reference full space displacement calculation was computed and compared to the solution obtained using the proposed efficient techniques; the comparison is shown in Table 9.4. The MAC and TRAC values show that acceptable results are achieved using the technique, but there are some differences between the full and approximate solutions. The reduced solution took less than a second to compute, while the full space solution took over 12 min to compute. This shows a reduction in computation time of over 3,000 times, while the reduced model was only two orders of magnitude smaller than the full space model. As the model size is increased to the much larger FEM used in industrial applications, the reduction in computation time is expected to be further improved.

The dynamic displacement at an arbitrary location on Beam A is plotted in Fig. 9.13; both the time response and corresponding Fast Fourier Transform (FFT) are shown. The initial transient compares very accurately between the full and approximate solutions because no springs have come into contact during that period of time. Following the linear region, some differences in amplitude are observed throughout the remainder of the time trace. Similarly, the FFTs of the response compare rather well at low frequencies, but notable differences are observed at higher frequencies. This trend is unsurprising when the $[U_{12}]$ matrices in Fig. 9.12 are taken into account because not enough modes of the system were retained in the reduced order model to accurately capture the excited system modes of the various configurations.

The same dynamic displacement is shown alongside the dynamic strain in Fig. 9.14. The solution produced using the efficient technique follows the same trends as the full solution, but higher frequency content is missing from the efficient solution. The differences associated with mode truncation are apparent in the displacement solution, but are more noticeable in the amplitudes of the dynamic strain. The predicted solution provides a reasonable approximation, but rapid changes in displacement and strain are not captured using the efficient calculation with the aa-space model.

The approximation in this case may be appropriate for certain applications. If only the general contour of the response curves is desired, then this solution will be appropriate. However many peak values were not calculated very accurately due to the lack of necessary modes included in the reduced solution. One important point to make is that while the applied force appears to only require the 13 modes used in this solution, the differences occur mainly because the nonlinear contact occurs with a hard gap stiffness which tends to excite higher modes. Had the contact spring been a lower contact stiffness, then
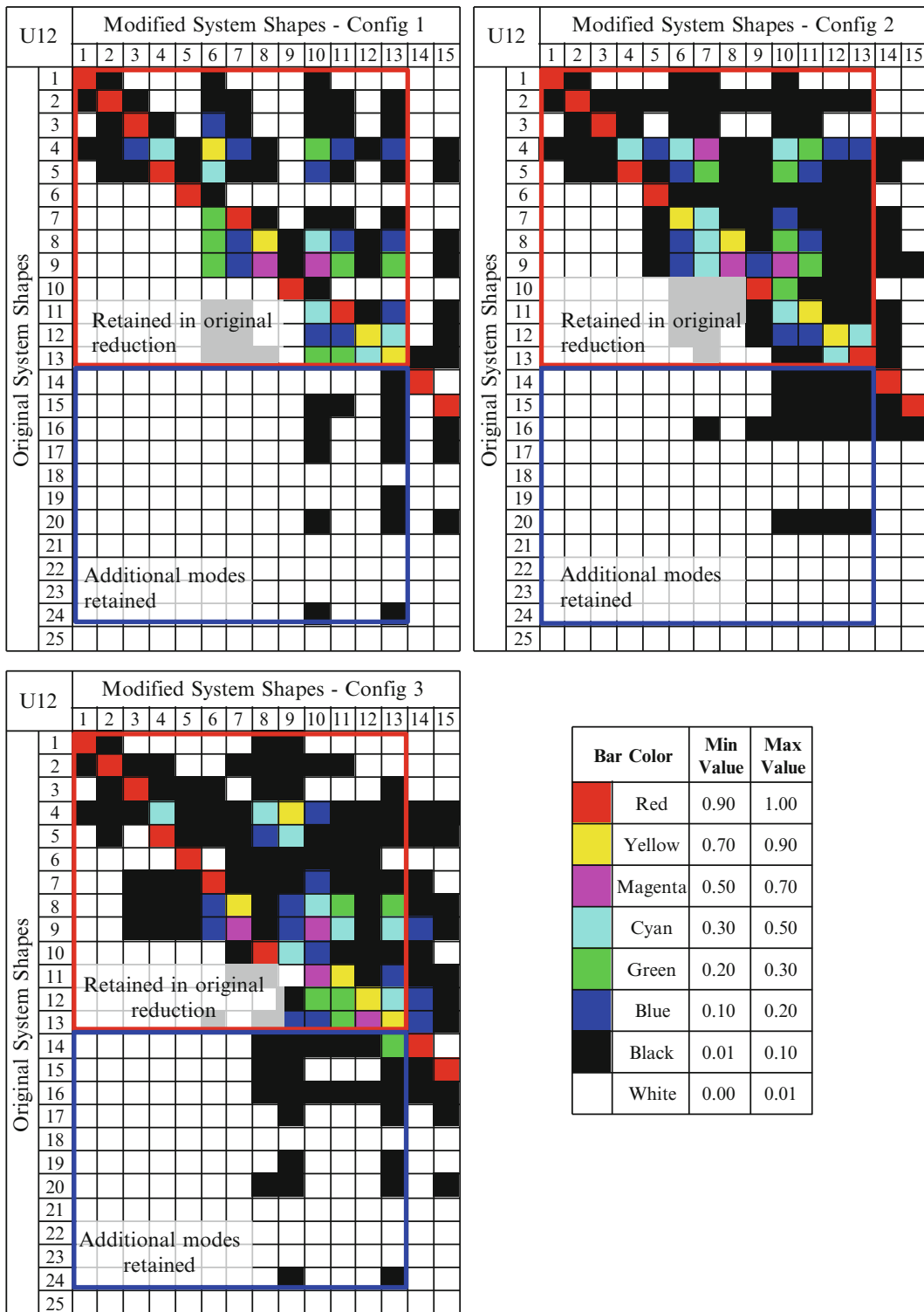
Fig. 9.12 Mode contribution matrix for beams in all configurations (color figure online)

the results would have matched much better (as shown by Harvie [1]). Due to the hardness of the contact, more modes are needed to properly span the space of the actual response of the system. To overcome these issues presented here, the next case contains a reduced order model with more modes.

Table 9.4 Comparison of reduced and full solution for case with hard contacts

Model	# of DOF	Solution time (s)	Average MAC	Average TRAC
Full space	1,904	740.18	0.9892	0.9918
Reduced	13	0.23		
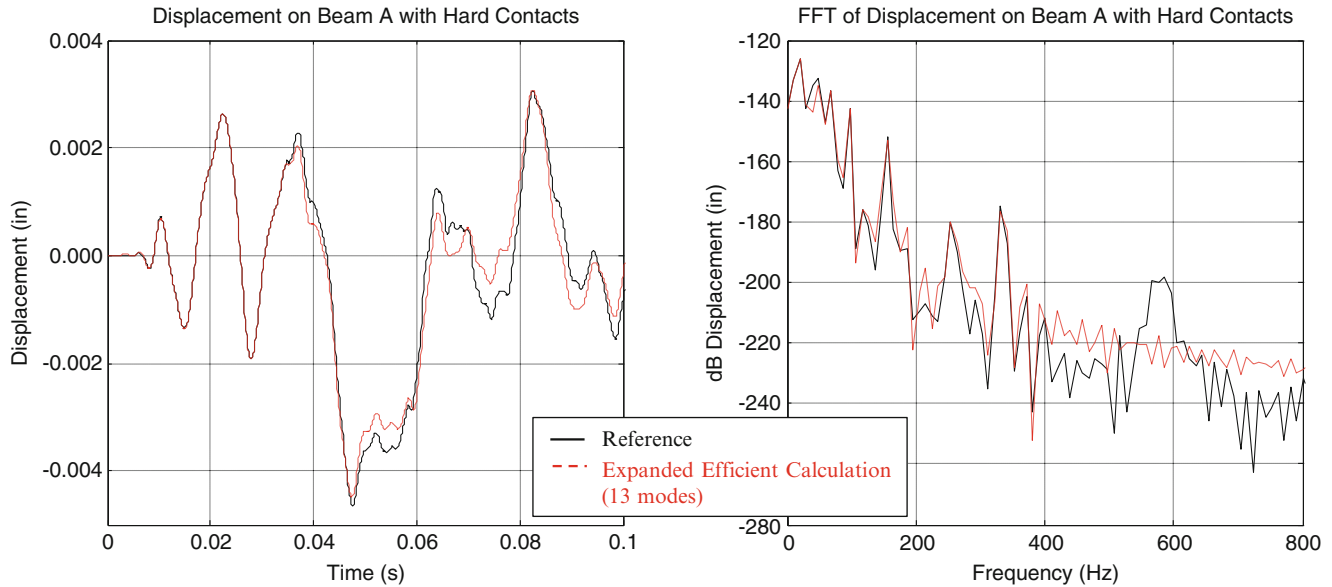
Fig. 9.13 Time response corresponding FFT on Beam A for hard contact case

9.3.3 Case 2: Nonlinear Solution with Reduced Model Including Additional Modes

Upon examination of the $[U_{12}]$ matrices in Fig. 9.12, there are several modes of the original system higher than mode 13 that have a substantial contribution to the modified system modes within the excited frequency range. Therefore this case was generated where the reduced a-space model contains 24 modes and DOF. As seen in the matrices, all three configurations require at least 20 modes to accurately represent the first 13 final system modes, and certain configurations have notable contribution from up to 24 modes.

The full space displacements were determined using both a full space solution and the proposed efficient technique. Comparisons of the computation time and accuracy for this case are shown in Table 9.5. Yet again the solution time was reduced significantly by utilizing such a smaller model to solve for the response. The accuracy of this model is higher than that of the previous case because including more modes in the reduced order model allows for the observation of higher frequency content excited by the hard contact springs. For this case, very high accuracy was obtained using an extremely reduced model.

The displacement results for the full and predicted displacement are shown in the time and frequency domains in Fig. 9.15. For this case, the comparison of displacement overlays nearly perfectly in both domains between the two response calculations. The frequency range of the original system modes included in the reduction extends over 1,300 Hz, so the energy distribution of the response is accurately captured in the frequency domain.

The displacement is also shown in Fig. 9.16 with the corresponding dynamic strain at the location of interest. Both the displacement and strain are predicted more accurately using the reduced order model implemented in this case. The model used in the efficient technique is able to better predict the higher order curvature in the dynamic displacement and strain response because more modes were included in the reduction. While the efficient calculation of the dynamic displacement matches nearly perfectly to the reference solution, some high frequency content is present in the reference strain solution that is not captured using the efficient calculation. The slight differences in the strain calculations can be further reduced by including even more modes in the reduced order model. The strain and displacement results calculated efficiently compare very accurately to the full space model for this case, yet the solution time for the reduced order model is substantially lower than the time required for a full space calculation.

The results obtained from this case compared more accurately to the full space solution because more modes were retained in the reduced solution to accurately represent the system dynamics for all possible configurations. The full solution took over 12 min to compute, but accurate strain and displacement data could be obtained in less than a second without compromising
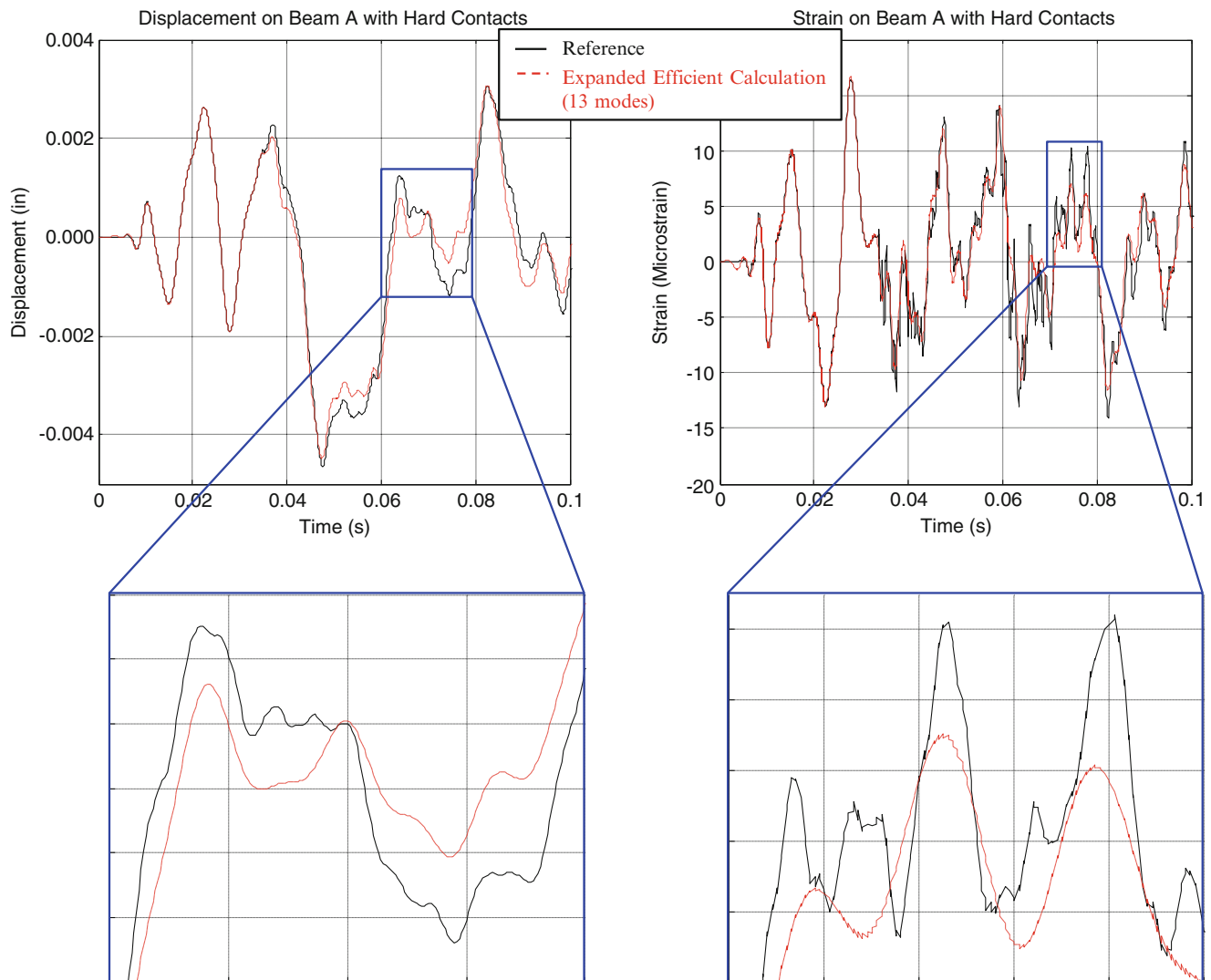
Fig. 9.14 Displacement and corresponding strain on Beam A for hard contact case

Table 9.5 Comparison of reduced and full solution for hard contact case with more modes

Model	# of DOF	Solution time (s)	Average MAC	Average TRAC
Full space	1, 904	740.18	0.9998	0.9999
Reduced	24	0.28		

accuracy. Although the addition of hard contact springs in the system causes the necessity for additional modes to be retained in a reduced order model, the full space model can still be substantially reduced to retain only the dynamic characteristics that are necessary to the response.

9.4 Conclusions

This paper demonstrates the usefulness of a proposed approach for calculating full field strain on nonlinear systems at a fraction of the computational cost. The proposed approach involves using highly reduced order models to solve the piecewise linear response of systems with discrete nonlinear elements rather than utilizing a nonlinear solution scheme on a large finite element model. The accurate prediction of dynamic displacement requires including enough modes of the original system in the reduced model to accurately capture the dynamics of the system in all possible configurations. If not enough modes are included in the reduced model, as dictated by the mode contribution matrix, then truncation will be present in the predicted
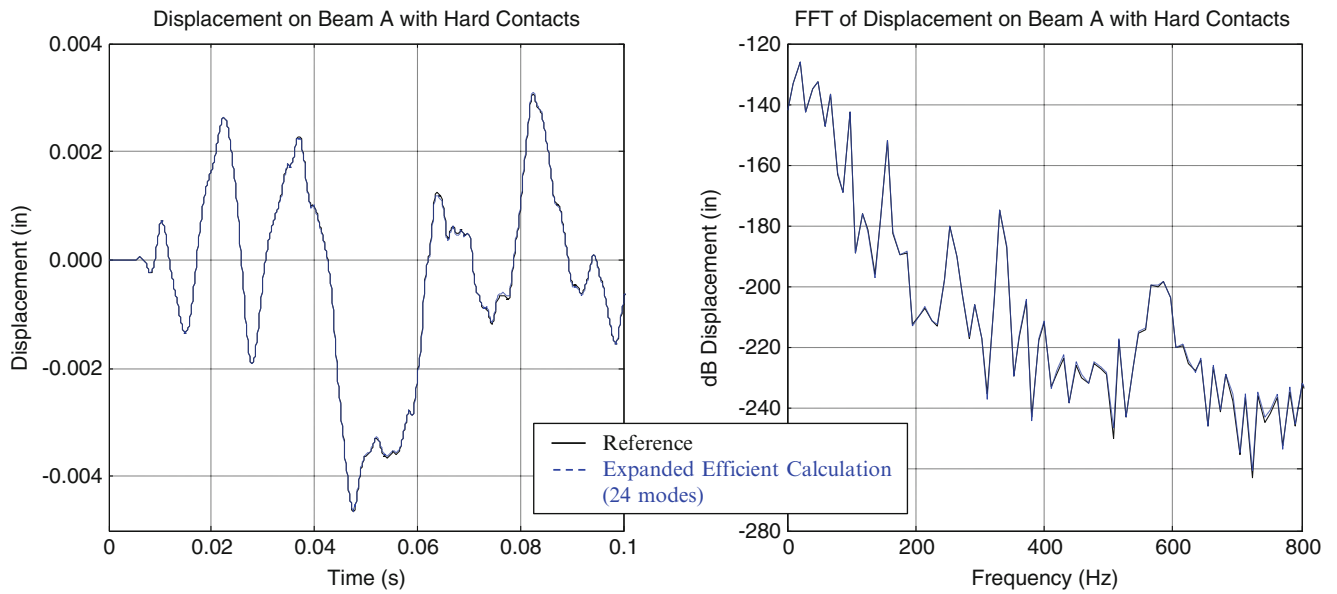
Fig. 9.15 Time response and corresponding FFT on Beam A for hard contact case with more modes
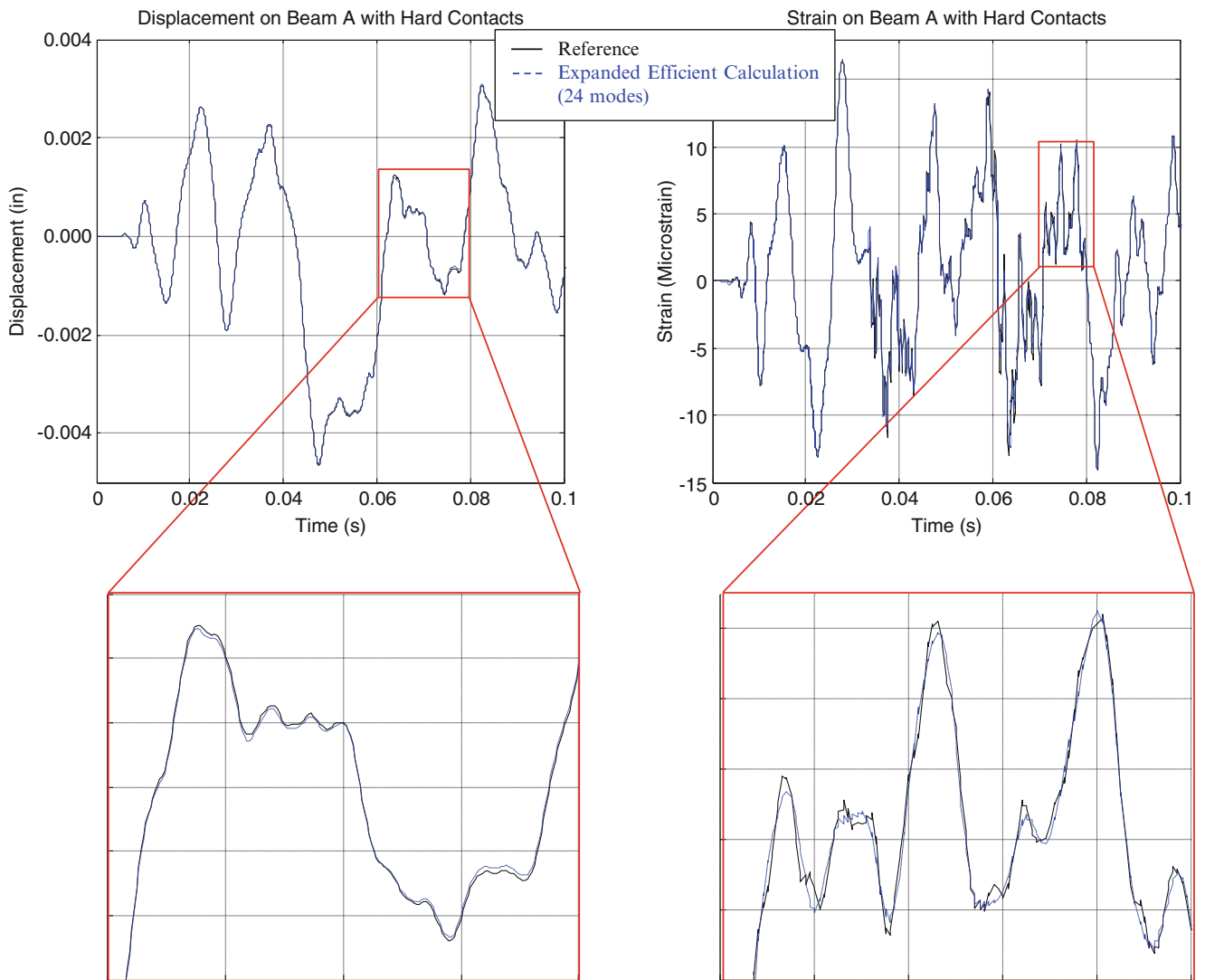
Fig. 9.16 Displacement and corresponding strain on Beam A for hard contact case with more modes

nonlinear response. To accurately predict dynamic strain in a system, more modes are generally required in the reduced model than for just the prediction of dynamic displacement. Overall, the full space dynamic strain and displacement were computed accurately and efficiently on a system involving nonlinear contact elements using highly reduced order models.

References

1. Harvie J (2013) Computationally efficient reduced order models for full field nonlinear dynamic strain predictions. Master's thesis, University of Massachusetts Lowell, Lowell
2. Marinone T, Avitabile P, Foley J, Wolfson J (2012) Efficient computational nonlinear dynamic analysis using modal modification response technique. Mech Syst Signal Process 31:67–93. doi:10.1016/j.ymssp.2012.02.011, ISSN: 0888-3270
3. Marinone T (2012) Efficient computational nonlinear dynamic analysis using modal modification response technique. Master's thesis, University of Massachusetts Lowell, Lowell
4. Marinone T, Avitabile P, Foley J, Wolfson J (2012) Efficient computational nonlinear dynamic analysis using modal modification response technique. In: Proceedings of the thirtieth international modal analysis conference, Jacksonville, February 2012
5. Thibault L, Avitabile P, Foley J, Wolfson J (2013) Equivalent reduced model technique for nonlinear dynamic response. Mech Syst Signal Process 36:422–455. doi:10.1016/j.ymssp.2012.07.013
6. Thibault L (2012) Development of equivalent reduced model technique for linear modal components interconnected with nonlinear connection elements. Master's thesis, University of Massachusetts Lowell, Lowell
7. Thibault L, Avitabile P, Foley J, Wolfson J (2012) Equivalent reduced model technique for nonlinear dynamic response. In: Proceedings of the thirtieth international modal analysis conference, Jacksonville, February 2012
8. Avitabile P, Pingle P (2012) Prediction of full field dynamic strain from limited sets of measured data. Shock Vib 19:765–785. doi:10.3233/SAV-2012-0686
9. Pingle P, Avitabile P (2010) Prediction of full field dynamic stress/strain from limited sets of measured data. In: Proceedings of the twenty-eighth international modal analysis conference, Jacksonville, February 2010
10. Pingle P, Avitabile P (2011) Limited experimental displacement data used for obtaining full-field dynamic stress/strain. In: Proceedings of the twenty-ninth international modal analysis conference, Jacksonville, February 2011
11. Pingle P, Avitabile P (2011) Full field dynamic stress/strain estimation from limited sets of measured data. In: Proceedings of the twenty-ninth international modal analysis conference, Jacksonville, February 2011
12. Pingle P, Niezrecki C, Avitabile P (2011) Full field numerical stress–strain from dynamic experimental measured data. In: Eighth international conference on structural dynamics EURODYN, Leuven, July 2011
13. Avitabile P (2011) Alternate techniques/new approaches for identification of full field dynamic stress strain from limited sets of measured data. In: International conference on experimental dynamics, ICEDyn conference Keynote speech/paper, Tavira, June 2011
14. Pingle P (2010) Prediction of full-field dynamic stress/strain from limited sets of measured data. PhD dissertation, University of Massachusetts Lowell, Lowell
15. Carr J, Baqersad J, Niezrecki C, Avitabile P (2013) Predicting dynamic strain on wind turbine blade using digital image correlation techniques in conjunction with analytical expansion methodologies. In: Proceedings of the thirty-first international modal analysis conference, Garden Grove, February 2013
16. Carr J, Baqersad J, Niezrecki C, Avitabile P (2012) Dynamic stress–strain on turbine blade using digital image correlation techniques, part 1 – static calibration. In: Proceedings of the thirtieth international modal analysis conference, Jacksonville, February 2012
17. Carr J, Baqersad J, Niezrecki C, Avitabile P (2012) Dynamic stress–strain on turbine blade using digital image correlation techniques, part 2 – dynamic measurements. In: Proceedings of the thirtieth international modal analysis Conference, Jacksonville, February 2012
18. Carr J (2013) Application of dynamic expansion from limited measurements for full-field stress/strain on wind turbine blades. Master's thesis, University of Massachusetts Lowell, Lowell
19. Nonis C, Avitabile P (2013) System model modes developed from expansion of uncoupled component dynamic data. Recent advances in structural dynamics, Pisa, July 2013
20. Nonis C, Thibault L, Marinone T, Avitabile P (2013) Development of full space system model modes from expansion of reduced order component modal information. In: Proceedings of the thirty-first international modal analysis conference, Los Angeles, February 2013
21. Harvie J, Obando S, Avitabile P (2013) Reduced order system model nonlinear response and expansion for full field results. Recent advances in structural dynamics, Pisa, July 2013
22. Marinone T, Thibault L, Avitabile P (2013) Expansion of nonlinear system response using linear transformation matrices from reduced component model representations. In: Proceedings of the thirty-first international modal analysis conference, Los Angeles, February 2013
23. O'Callahan JC, Avitabile P, Leung R (1984) Development of mass and stiffness matrices for an analytical model using experimental modal data. In: Proceedings of the second international modal analysis conference, Orlando, February 1984
24. O'Callahan JC, Leung R (1985) Optimization of mass and stiffness matrices using A generalized inverse technique on the measured modes. In: Proceedings of the third international modal analysis conference, Orlando, January 1985
25. Avitabile P, O'Callahan JC, Tsuji H, DeClerck JP (2004) Reallocation of system mass and stiffness for achieving target specifications. Int J Vehicle Noise Vib 1(1/2):97–121

26. Avitabile P, O'Callahan JC, Tsuji H, DeClerck JP (2005) Reallocation of system mass and stiffness for achieving target specifications using a superelement/substructure methodology. Int J Vehicle Noise Vib 1(3/4):307–327
27. Avitabile P, O'Callahan JC, Tsuji H, DeClerck JP (2003) Reallocation of system mass and stiffness for achieving target specifications. In: Proceedings of the twenty-first international modal analysis conference, Orlando, February 2003
28. Avitabile P, O'Callahan JC, Tsuji H, DeClerck JP (2004) Reallocation of system mass and stiffness for achieving target specifications using a superelement/substructuring methodology. In: Proceedings of the twenty-second international modal analysis conference, Dearborn, January 2004
29. O'Callahan JC, Avitabile P, Riemer R (1989) System equivalent reduction expansion process. In: Proceedings of the seventh international modal analysis conference, Las Vegas, February 1989
30. Avitabile P (2003) Twenty years of structural dynamic modification – a review. Sound Vib 37(1):14–27
31. Avitabile P, O'Callahan J (1991) Understanding structural dynamic modification and the effects of truncation. Int J Anal Exp Modal Anal 6(4):215–235
32. Avitabile P, O'Callahan J, Pechinsky F (1990) Understanding structural dynamic modification truncation. In: Proceedings of the eighth international modal analysis conference, Orlando, January 1990
33. Chipman C, Avitabile P (2012) Expansion of transient operating data. Mech Syst Signal Process. Accepted April 2012. doi:10.1016/j.ymssp.2012.04.013
34. Chipman C, Avitabile P (2009) Expansion of transient operating data. In: Proceedings of the twenty-seventh international modal analysis conference, Orlando, February 2009
35. Chipman C, Avitabile P (2008) Expansion of real time operating data for improved visualization. In: Proceedings of the twenty-sixth international modal analysis conference, Orlando, February 2008
36. Chipman C (2009) Expansion of real time operating data. Master's thesis, University of Massachusetts Lowell, Lowell
37. Avitabile P, O'Callahan JC (2009) Efficient techniques for forced response involving linear modal components interconnected by discrete nonlinear connection elements. Mech Syst Signal Process 23(1):45–67 (Special issue: non-linear structural dynamics)
38. Abaqus 6.10 Analysis user's manual, volume II: analysis. Dassault Systèmes Simulia Corp., Providence, 2011
39. Newmark NM (1959) A method of computation for structural dynamics. ASCE J Eng Mech Div 85:67–94

Chapter 10
An Improved Expansion Process for Guyan Reduced Models: Technique for Improved Guyan Expansion Reconstruction (TIGER)

Julie Harvie and Peter Avitabile

Abstract While many model reduction techniques exist, often times Guyan reduction is still performed mainly due to the fact that this is generally the only model reduction scheme available in all of the commercial finite element codes. As long as a sufficient number of active DOF are utilized, the Guyan reduction can produce reasonable results. However, there are errors due to the reduction and subsequent expansion of the reduced model back to the full space of the finite element model.

In order to compensate for these, an alternate expansion methodology is proposed that makes two adjustments to the set of vectors obtained from the Guyan reduced model. First, the modal vectors are adjusted in reduced space and second, the Guyan transformation matrix is adjusted to properly account for the true modes of the system from the full space model. These adjustments essentially morph the Guyan reduced model and Guyan reduced transformation to a more appropriate transformation to achieve a better representation of the modal vectors associated with the full space finite element model.

Several models are presented to illustrate the usefulness of the proposed methodology and technique. Advantages are discussed and limitations are presented for the cases studied.

Keywords Model reduction/expansion

Nomenclature

$\{X_n\}$	Full set displacement vector
$\{X_a\}$	Reduced set displacement vector
$\{X_d\}$	Deleted set displacement vector
$[T]$	Transformation matrix
$[M_a]$	Reduced mass matrix
$[M_n]$	Expanded mass matrix
$[K_a]$	Reduced stiffness matrix
$[K_n]$	Expanded stiffness matrix
$[U_a]$	Reduced set shape matrix
$[U_a^G]$	Guyan reduced set shape matrix
$[U_n]$	Full set shape matrix
$[U_n^G]$	Guyan expanded full set shape matrix
$[U_a^g]$	Generalized inverse of reduced shape matrix
$\{p\}$	Modal displacement vector
$\{F\}$	Physical force vector
$[U_1]$	Original state shape matrix
$[U_12]$	Mode contribution matrix
$[U_2]$	Modified state shape matrix

J. Harvie (✉) • P. Avitabile
Structural Dynamics and Acoustic Systems Laboratory, University of Massachusetts Lowell, One University Avenue, Lowell, MA, 01854 USA
e-mail: harvie.julie@gmail.com; peteravitabile@uml.edu

[T$_G$]   Guyan transformation matrix
[T$_U$]   SEREP transformation matrix
[U^{morph}] Shape matrix to "Morph" Guyan toward SEREP

10.1   Introduction

Model reduction techniques are well known in the area of structural dynamic modeling and correlation of analysis with measured test data. Many different techniques [1–5] have been developed for this purpose. However, still today many finite element modeling software packages only implement Guyan reduction as the preferred (and sometimes only) method for model reduction. Much has been written in regards to the difficulty for the Guyan reduction process to adequately retain the mass of the reduced system when the transformation only provides reduction in regards to the stiffness of the system.

Thus the expansion process of the reduced model results will have errors due to the reduction process only retaining the stiffness of the system accurately. The expanded results will always contain errors and the results will always be affected due to that.

An extension of the expansion process is considered in this work to make adjustments to the expansion matrix to attempt to improve the overall expanded results. Essentially, the Guyan transformation matrix is morphed into a more suitable transformation to attempt to better represent the final expanded vectors using the full space finite element mode shapes in the adjustment process. The paper presents the transformation/morphing process and presents test cases to show the improvement in the expansion process.

10.2   Theory

The general theory of model reduction and expansion are presented first, followed by extensions to improve the Guyan expansion process.

10.2.1   General Reduction Techniques

Model reduction is typically performed to reduce the size of a large analytical model to develop a more efficient model for further analytical studies. Most reduction or condensation techniques affect the dynamic characteristics of the resulting reduced model. Model reduction is performed for a number of reasons, but the technique is used primarily as a mapping technique for expansion. In general, a relationship between the full set of finite element DOFs and the reduced set of DOFs needs to be formed as

$$\{X_n\} = \left\{ \begin{array}{c} X_a \\ X_d \end{array} \right\} = [T]\{X_a\} \tag{10.1}$$

The 'n' subscript denotes the full set of finite element DOFs, the 'a' subscript denotes the active set of DOFs (sometimes referred to as master DOFs), and the subscript 'd' denotes the deleted DOFs (sometimes referred to as omitted DOFs); the [T] transformation matrix relates the mapping between these two sets of DOFs.

The reduced mass and stiffness matrices are related to the full-space mass and stiffness matrices using

$$[M_a] = [T]^T [M_n] [T] \quad \text{and} \quad [K_a] = [T]^T [K_n] [T] \tag{10.2}$$

What is most important in model reduction is that the eigenvalues and eigenvectors of the original system are preserved as accurately as possible in the reduction process. If this is not maintained then the matrices are of questionable value. The eigensolution is then given by

$$[[K_a] - \lambda [M_a]] \{X_a\} = \{0\} \tag{10.3}$$

The Guyan Condensation [2] and Improved Reduced System Technique [3] are based primarily on the stiffness of the system, the eigenvalues and eigenvectors will not be exactly reproduced in the reduced model. However, the System Equivalent Reduction Expansion Process (SEREP) [1] exactly preserves the eigenvalues and eigenvectors in the reduced model.

10.2.2 Guyan Reduction Process

The Guyan reduction process relies on the static condensation of the stiffness matrix and this same matrix is used to condense the mass matrix. For a static system, the equation of motion can be written in partitioned form as

$$\begin{bmatrix} [K_{aa}] & [K_{ad}] \\ [K_{da}] & [K_{dd}] \end{bmatrix} \begin{Bmatrix} X_a \\ X_d \end{Bmatrix} = \begin{Bmatrix} F_a \\ F_d \end{Bmatrix} \tag{10.4}$$

The 'a' subscript denotes the master or active set of DOF and the 'd' subscript denotes the embedded or deleted DOF. Assuming that the forces on the deleted DOF are zero, the second equation of the partitioned set of equation (10.4) can be expanded as

$$[K_{da}] \{X_a\} + [K_{dd}] \{X_d\} = \{0\} \tag{10.5}$$

which can be solved for the displacement at the deleted DOF as

$$\{X_d\} = -[K_{dd}]^{-1} [K_{da}] \{X_a\} \tag{10.6}$$

The first equation of the partitioned set of equation (10.4) can be expanded as

$$[K_{aa}] \{X_a\} + [K_{ad}] \{X_d\} = \{F_a\} \tag{10.7}$$

Upon substitution of the displacement at the deleted DOF in (10.6), equation (10.7) becomes

$$[K_{aa}] \{X_a\} + [K_{ad}] [K_{dd}]^{-1} [K_{da}] \{X_a\} = \{F_a\} \tag{10.8}$$

Therefore, a relationship is available relating the active DOF to the full set of DOF as

$$\{X_n\} = \begin{bmatrix} [I] \\ -[K_{dd}]^{-1} [K_{da}] \end{bmatrix} \{X_a\} = [T_G] \{X_a\} \tag{10.9}$$

10.2.3 System Equivalent Reduction Expansion Process (SEREP)

The SEREP modal transformation relies on the partitioning of the modal equations representing the system DOFs relative to the modal DOFs using

$$\{X_n\} = \begin{Bmatrix} X_a \\ X_d \end{Bmatrix} = \begin{bmatrix} U_a \\ U_d \end{bmatrix} \{p\} \tag{10.10}$$

Using a generalized inverse, this can be manipulated to give

$$\{p\} = \left([U_a]^T [U_a]\right)^{-1} [U_a]^T \{X_a\} = [U_a]^g \{X_a\} \tag{10.11}$$

which is then used to relate the 'n' DOFs to the 'a' DOFs as

$$\{X_n\} = [U_n] [U_a]^g \{X_a\} = [T_U] \{X_a\} \tag{10.12}$$

with

$$[T_U] = [U_n] [U_a]^g \tag{10.13}$$

Equation (10.13) represents the SEREP transformation matrix that is used in the reduction of the finite element mass and stiffness matrices as described in Eq. (10.2).

10.2.4 Development of Matrices to Improve Guyan Results

The expansion of mode shapes using the Guyan expansion process can be written as

$$\left[U_n^G\right] = [T_G] \left[U_a^G\right] \tag{10.14}$$

But the Guyan transformation matrix is known to not provide perfect results due to the fact that the reduction is only based on stiffness and does not include mass (which implies that the dynamics may not be perfectly preserved). The SEREP process on the other hand does preserve the dynamics of the system. So the $[T_G]$ needs to be adjusted to get $[T_U]$.

The easiest way to show how to achieve this is to use the concept from structural dynamic modification process [6–8] where the final modes $[U_2]$ are developed from the starting modes $[U_1]$ and a matrix of mixing ingredients $[U_{12}]$ which is written as

$$[U_2] = [U_1] [U_{12}] \tag{10.15}$$

This can be written in terms of the Guyan reduced shapes as

$$[U_n] = \left[U_n^G\right] [U_{12}] \tag{10.16}$$

In order to accomplish this, the Guyan T_G must be "morphed" into the SEREP T_U

$$[T_U] = [T_G] \left[U^{morph}\right] \tag{10.17}$$

Rearranging gives

$$[T_G] = [T_U] \left[U^{morph}\right]^{-1} \tag{10.18}$$

or

$$\left[U^{morph}\right] = [T_G]^{-1} [T_U] \tag{10.19}$$

Now substituting (10.18) into (10.14) gives

$$[U_n] = [T_U] \left[U_a^{morph}\right]^{-1} \left[U_a^G\right] \tag{10.20}$$

And including (10.19) gives

$$[U_n] = [T_U] \left[[T_G]^{-1} [T_U]\right]^{-1} \left[U_a^G\right] = [T_U] [T_U]^{-1} [T_G] \left[U_a^G\right] \tag{10.21}$$

Therefore the improved transformation matrix is written as

$$[T_I] = [T_U] [T_U]^{-1} [T_G] \tag{10.22}$$

Equation (10.22) is the computation to make adjustments to the Guyan expansion matrix. Note that less adjustment is necessary when $[T_G]$ is closer to $[T_U]$. In fact when $[T_G]$ actually becomes $[T_U]$ then (10.22) represents one of the Moore Penrose conditions for the generalized inverse.

10.3 Model Description and Cases Studied

A simple aluminum beam was used as the test subject in this work to study the possibility for an improved expansion technique. The first two cases were generated to study the TIGER expansion technique on the beam after being reduced using Guyan Condensation; the first case utilizes a pinned–pinned boundary condition while the second case has the beam in a cantilever configuration. The third case utilizes the TIGER principles to perform both a reduction and expansion on the cantilever beam. The cases can be summarized as:

Case 1: Pinned–pinned beam with TIGER for expansion
Case 2: Cantilever beam with TIGER for expansion
Case 3: Cantilever beam with TIGER for reduction and expansion

10.3.1 Structure Description and General Modeling Performed

A planar element beam model was generated using MAT_SAP [9], which is a finite element modeling (FEM) program developed for MATLAB [10], and was used for all of the cases studied. The physical properties outlined in Table 10.1 were used to generate a simple aluminum beam with a solid cross-section. Note that two degrees of freedom, shear and rotary, are present at each node for a total of 38 degrees of freedom (DOF).

A pinned–pinned boundary condition was simulated using 10^3 lb/in. translational springs on the first and last nodes. A cantilever boundary condition was simulated using a 10^7 lb/in. translational spring and 10^7 rotational spring at the first node. The approximation of both boundary conditions is illustrated in Fig. 10.1. An eigensolution was performed on each model to determine the natural frequencies and mode shapes. In Fig. 10.2, the first ten natural frequencies are displayed alongside the first four modes in each configuration.

For both models, the reduced space model contains shear DOF from every other node of the full space model. The DOF contained in each model size are outlined in Fig. 10.3.

Table 10.1 Physical properties used to model aluminum beam

Property	Value
Young's Modulus (psi)	10^7
Mass Density (lb/in.^{3})	2.54×10^{-4}
Beam Length (in.)	40
Beam Width (in.)	0.5
Beam Height (in.)	0.25
Nodes	19
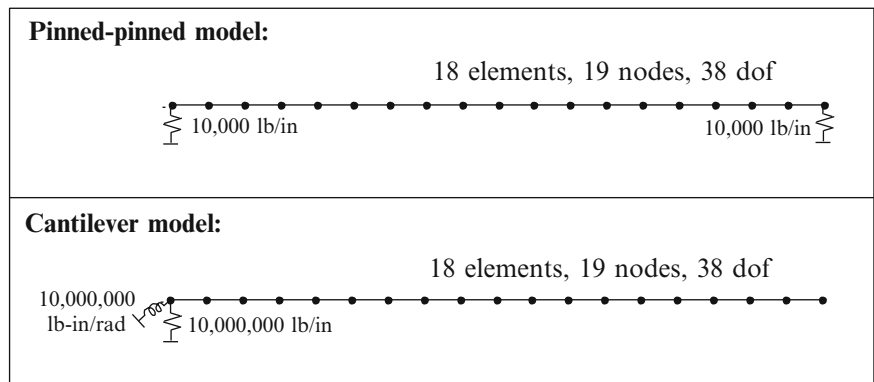
Fig. 10.1 Details on beam model for each case studied

Mode #	Frequency (Hz)	
	Pinned-pinned	Cantilever
1	14.06	5.01
2	56.21	31.40
3	126.35	87.91
4	224.32	172.28
5	349.93	284.84
6	502.94	425.63
7	683.06	594.79
8	889.97	792.52
9	1123.29	1019.15
10	1382.52	1275.13
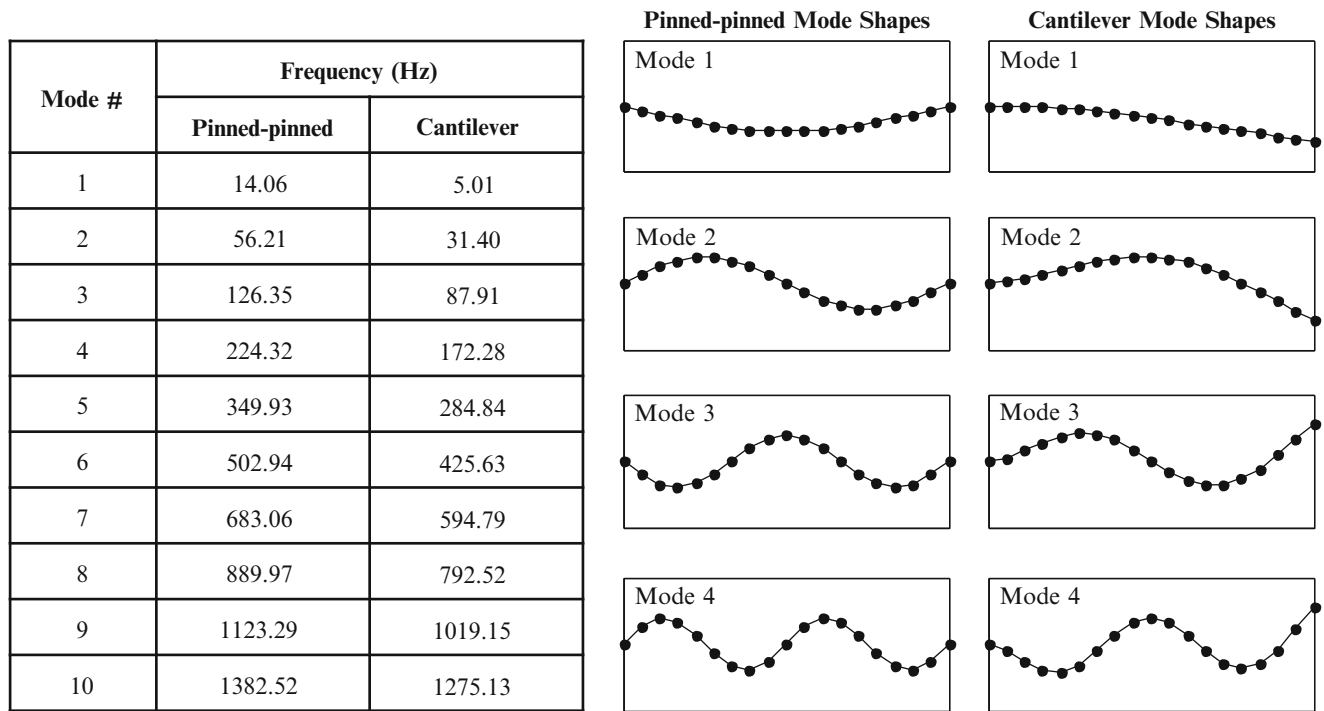
Fig. 10.2 Frequencies and mode shapes for cantilever and pinned–pinned beams

Fig. 10.3 Model sizes for full and reduced space
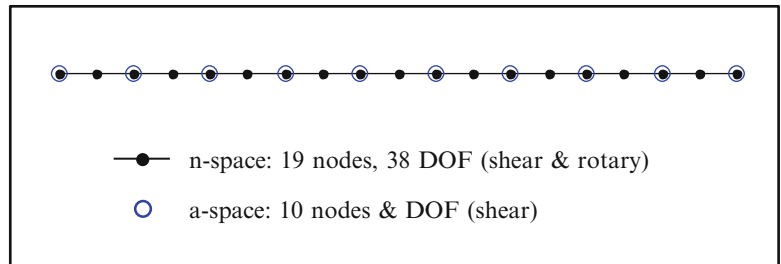
10.3.2 Case 1: Pinned–Pinned Beam with TIGER for Expansion

The pinned–pinned beam was first reduced to a-space using Guyan reduction. The Guyan reduced model is compared to the full space model in Fig. 10.4. The plots of the first few mode shapes show good correlation. The correlation is confirmed by the relatively low frequency difference and high MAC values. The modes with high shape correlation (as evidenced by high MAC value) as well as low frequency difference (less than 10 %) to the reference model are highlighted in the table of Fig. 10.4; for this case modes one through seven of the reduced model compare accurately to the reference full space model. The quality of the reduction degrades for the higher modes, and a very low shape correlation is seen for the tenth mode.

The Guyan reduced model was then expanded to n-space using both Guyan expansion and TIGER. The expanded solutions are compared to the full space model in Fig. 10.5 using mode shape plots as well as MAC comparisons. The expansion does not affect the frequencies of the reduced model, so the natural frequencies are not shown for the expanded model but are equal to the frequencies of the reduced model.

More accurate results were obtained using the TIGER expansion than the Guyan expansion for this case. While the overall shape of the first few modes compare rather well using both expansion techniques, the zoomed portion of mode 6 shows that the nodes of the TIGER expanded model are closer to the reference solution than the nodes of the Guyan expanded model. Furthermore, the MAC values between the TIGER expanded model and the reference solution are higher than the MAC values for the Guyan expanded model for all modes. The TIGER expanded model produces very accurate shapes up to mode seven, which is the same number of modes accurately reduced by the Guyan reduced model. Therefore the TIGER expansion seems to be limited by the quality of the initial reduction for this case. Overall, improved results were seen throughout this case using the TIGER expansion as compared to the Guyan expansion.

Mode	Frequency (Hz)		% Difference in Frequency	MAC
	Reference	Guyan Reduced		
1	14.06	14.06	0.00	1.000
2	56.21	56.22	-0.02	1.000
3	126.35	126.47	-0.10	1.000
4	224.32	225.19	-0.39	1.000
5	349.93	354.08	-1.19	1.000
6	502.93	518.57	-3.11	1.000
7	683.06	730.39	-6.93	1.000
8	889.97	988.57	-11.08	0.997
9	1123.29	2749.10	-144.74	0.940
10	1382.52	2763.07	-99.86	0.146
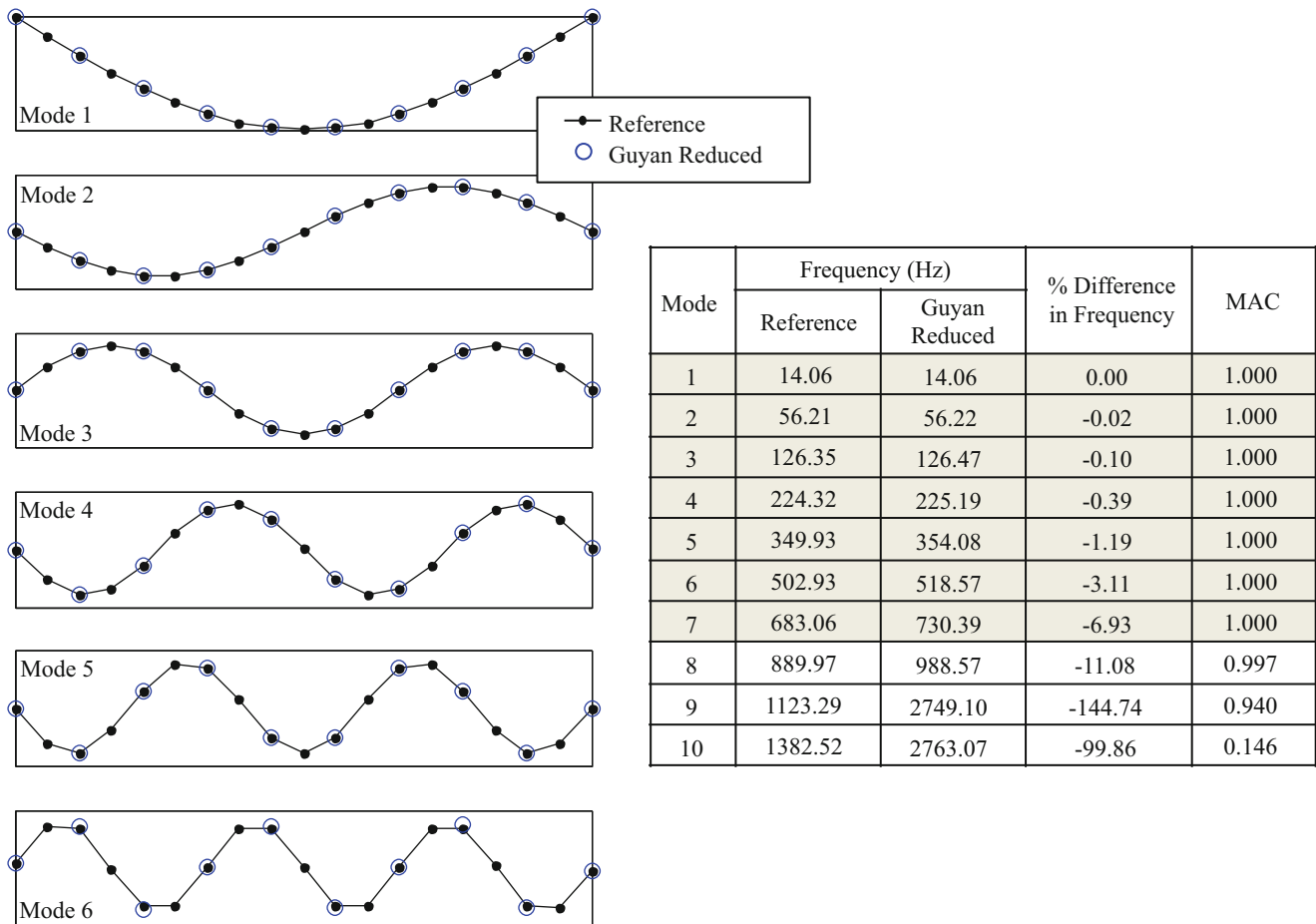
Fig. 10.4 Comparison between full space and Guyan reduced mode shapes for pinned–pinned beam

10.3.3 Case 2: Cantilever Beam with TIGER for Expansion

The cantilever beam model was also reduced to a-space using Guyan Condensation. The Guyan reduced model is compared to the reference full space model in Fig. 10.6. The plots of the first few mode shapes compare accurately, and the high MAC values and low frequency differences confirm the accuracy of the majority of corresponding modes. All modes except the tenth mode have MAC values above 0.95 and frequency differences within 10% to the reference model.

The Guyan reduced model of the cantilever beam was then expanded back to n-space using both Guyan Condensation and TIGER. The full space mode shapes obtained using a Guyan expansion and a TIGER expansion are compared to the reference mode shapes in Fig. 10.7; mode shape plots for the first few modes are shown along with a MAC comparison to the full space model for each expansion technique. Once again, the natural frequencies of the expanded models are the same as the frequencies of the reduced model because the expansions only affect the mode shapes.

While the first few mode shapes appear to compare accurately using both expansion techniques, a zoomed-in portion of mode 6 shows how the nodes in the TIGER expanded model are slightly closer to the reference model than the nodes in the Guyan expanded model. The TIGER expanded model produces more accurate results than the Guyan expanded model for all modes retained in the reduction, as evidenced by the higher MAC values. The final tenth mode has a MAC value that is less than ideal using both techniques, but the TIGER expanded mode shape is still more accurate than the Guyan expanded mode shape; the initial Guyan reduction did not produce an accurate tenth mode at reduced space and the proposed expansion is not able to completely overcome the differences. The results obtained using a TIGER expansion were better than the results obtained using a Guyan expansion for all modes in this case.

	MAC to Original Full Space Model	
Mode	Guyan Reduced, Guyan Expanded	Guyan Reduced, TIGER Expanded
1	1.000	1.000
2	1.000	1.000
3	1.000	1.000
4	1.000	1.000
5	0.999	1.000
6	0.994	1.000
7	0.964	1.000
8	0.823	0.826
9	0.055	0.695
10	0.110	0.824
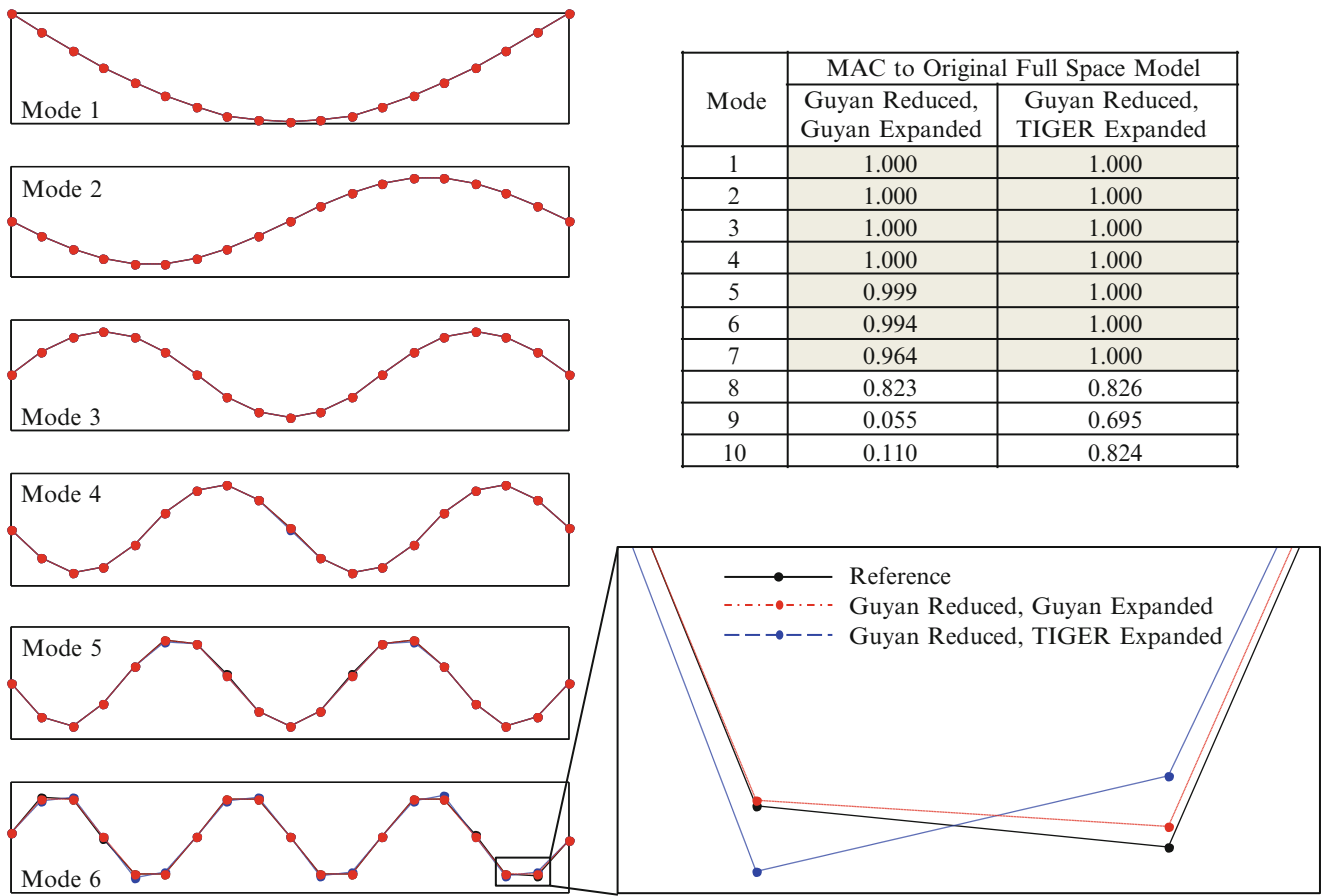
Fig. 10.5 Comparison of Guyan expansion and TIGER expansion on Guyan reduced pinned–pinned beam

10.3.4 Case 3: Cantilever Beam with TIGER for Reduction and Expansion

For the third case, the initial reduction was performed using the proposed transformation matrix calculated in (10.22). The TIGER transformation matrix was used to reduce the mass and stiffness matrices, as presented in (10.2). An eigensolution was performed on the reduced mass and stiffness matrices, and a comparison of the natural frequencies and mode shapes of the TIGER reduced model are compared to the reference model in Fig. 10.8. The frequencies of this reduced model compare perfectly with the original model; however many of the reduced mode shapes do not compare as well for this case as the Guyan reduced modes.

The TIGER reduced mode shapes were also expanded to n-space using the TIGER expansion; the results from the expansion are compared to the reference model in Fig. 10.9. The results from the model using both a TIGER reduction and TIGER expansion produce mode shapes identical to that of the full space model. With the reduced model frequencies being unchanged by the expansion, the full space results obtained using the TIGER technique were completely accurate in both frequency and shape for all modes.

While the TIGER approach produced exact full space results when used for both reduction and expansion, the reduced model was not calculated with perfect accuracy. The SEREP transformation matrix, which is part of the improved TIGER transformation matrix, was used for both reduction and expansion and therefore a SEREP transformation could have been performed using the resources utilized in this case. However the results are presented for this case to show the interesting features of the technique that were observed.

Mode	Frequency (Hz)		% Difference in Frequency	MAC
	Reference	Guyan Reduced		
1	5.01	5.01	0.00	1.000
2	31.40	31.40	0.00	1.000
3	87.91	87.97	-0.07	1.000
4	172.28	172.72	-0.26	1.000
5	284.84	287.02	-0.77	1.000
6	425.63	433.75	-1.91	1.000
7	594.79	618.24	-3.94	1.000
8	792.52	839.67	-5.95	0.998
9	1019.15	1053.40	-3.36	0.968
10	1275.13	65764.48	-5057.47	0.005
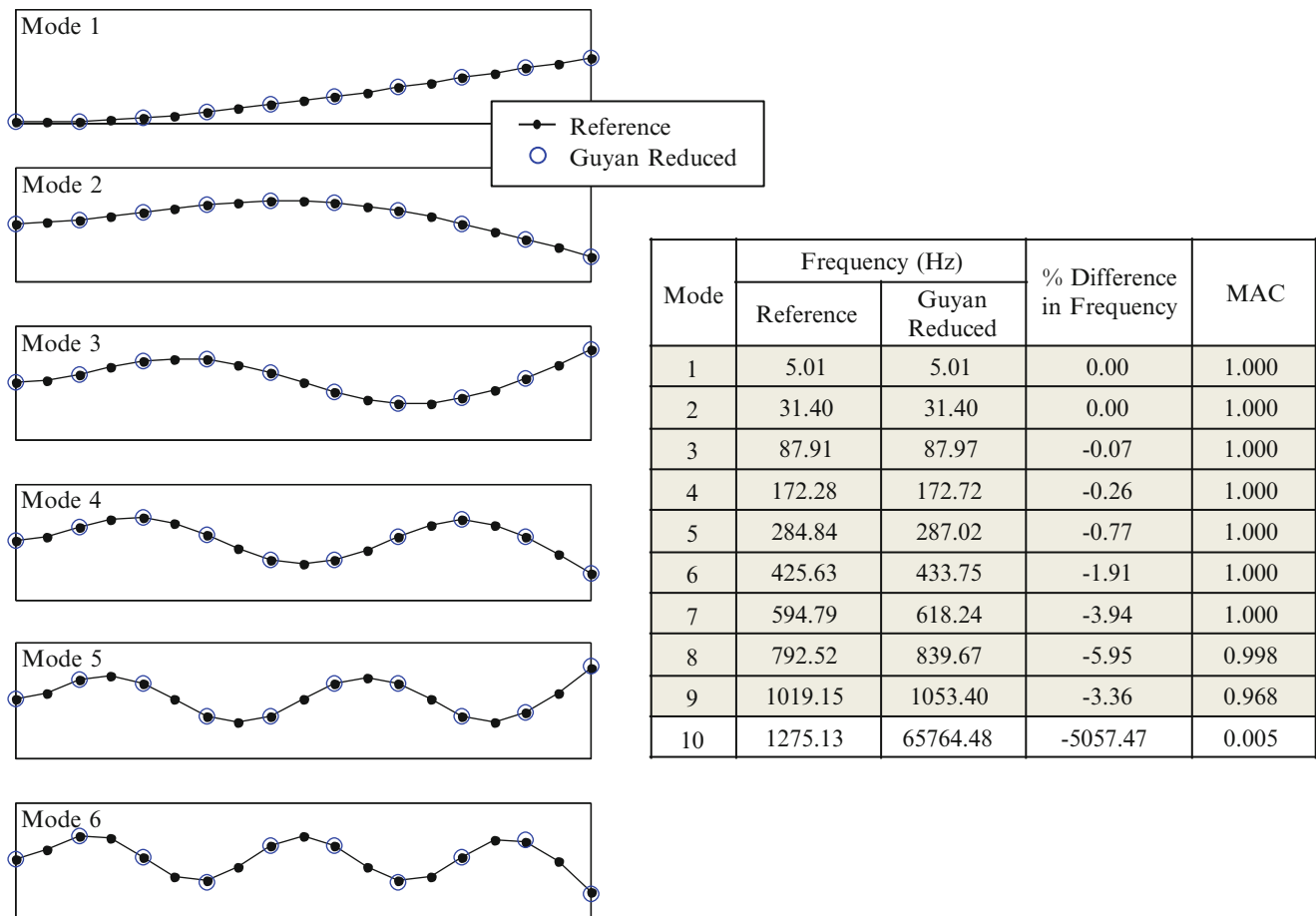
Fig. 10.6 Comparison between full space and Guyan reduced mode shapes for cantilever beam

10.4 Conclusion

An adjustment to the expansion transformation to improve the Guyan expansion process was presented. The technique developed shows that the Guyan transformation process can be adjusted to provide improvements in the expanded mode shapes to provide a better representation of the expanded shapes. The mode shapes are adjusted in reduced space followed by an adjustment to account for the true modal vectors from the full space model.

Obviously, the closer the original reduced mode shapes are to the actual shapes of the modal vectors, the less adjustment that is needed to improve the expanded shapes. However, if the original shapes from the Guyan reduction are significantly different from the actual reduced shapes then the more difficult it is for the improvement process to actually improve the vectors; drastically different vectors cannot effectively be improved when large difference exist.

While the initial studies are promising, there is much work to be done to study the expansion improvement process for a wide variety of cases and models to understand the degree of improvement that can be expected from this new process.

| Mode | MAC to Original Full Space Model | |
	Guyan Reduced, Guyan Expanded	Guyan Reduced, TIGER Expanded
1	1.000	1.000
2	1.000	1.000
3	1.000	1.000
4	1.000	1.000
5	0.999	1.000
6	0.997	0.999
7	0.985	0.995
8	0.949	0.962
9	0.943	0.992
10	0.017	0.588
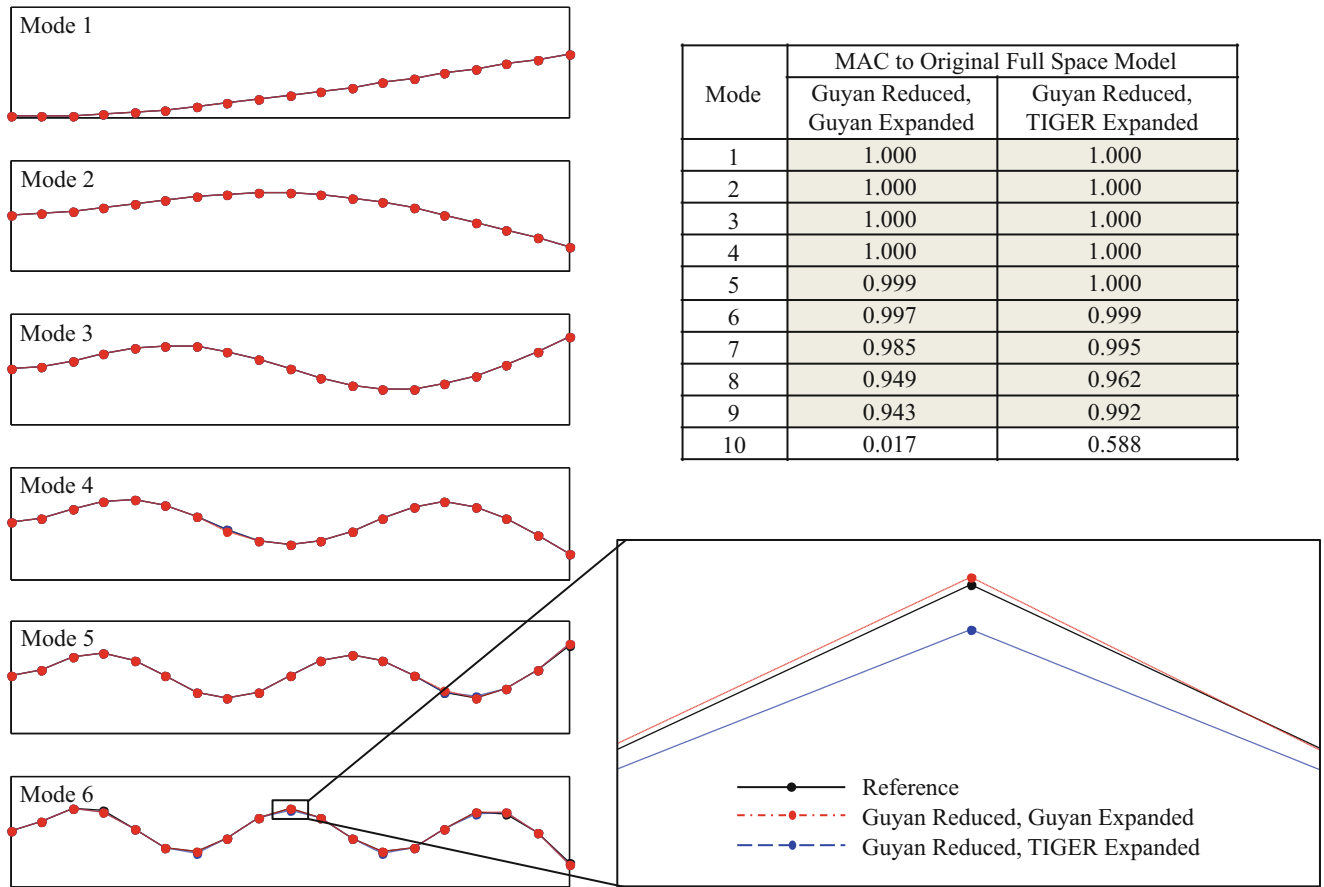
Fig. 10.7 Comparison of Guyan expansion and TIGER expansion on Guyan reduced cantilever beam

Mode	Frequency (Hz)		% Difference in Frequency	MAC
	Reference	TIGER Reduced		
1	5.01	5.01	0.00	1.000
2	31.40	31.40	0.00	1.000
3	87.91	87.91	0.00	1.000
4	172.28	172.28	0.00	1.000
5	284.84	284.84	0.00	0.999
6	425.63	425.63	0.00	0.976
7	594.79	594.79	0.00	0.985
8	792.52	792.52	0.00	0.368
9	1019.15	1019.15	0.00	0.988
10	1275.13	1275.13	0.00	0.000
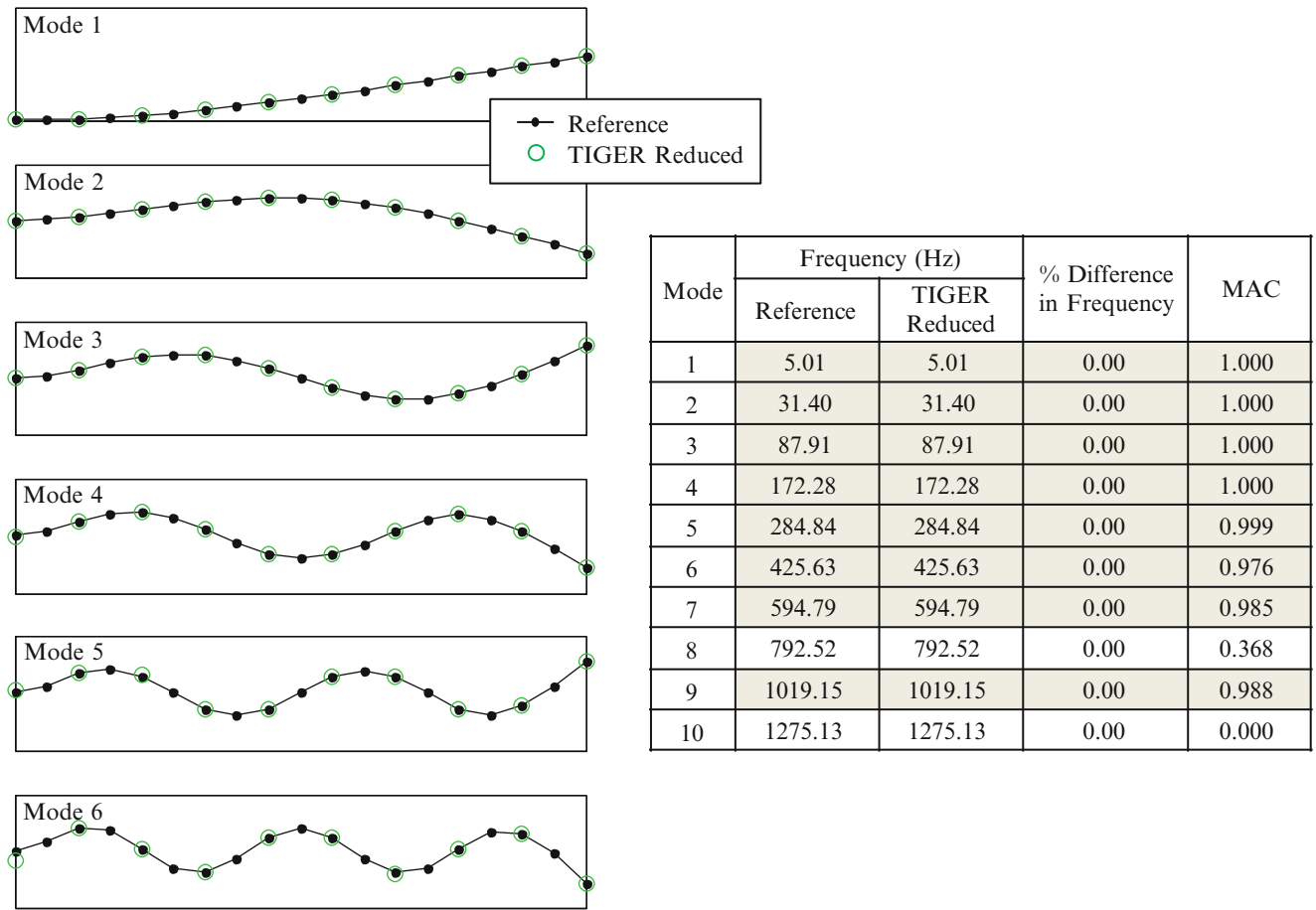
Fig. 10.8 Comparison between full space and TIGER reduced mode shapes for cantilever beam

Mode	MAC to Original Full Space Model	
	Guyan Reduced, Guyan Expanded	TIGER Reduced, TIGER Expanded
1	1.000	1.000
2	1.000	1.000
3	1.000	1.000
4	1.000	1.000
5	0.999	1.000
6	0.997	1.000
7	0.985	1.000
8	0.949	1.000
9	0.943	1.000
10	0.017	1.000
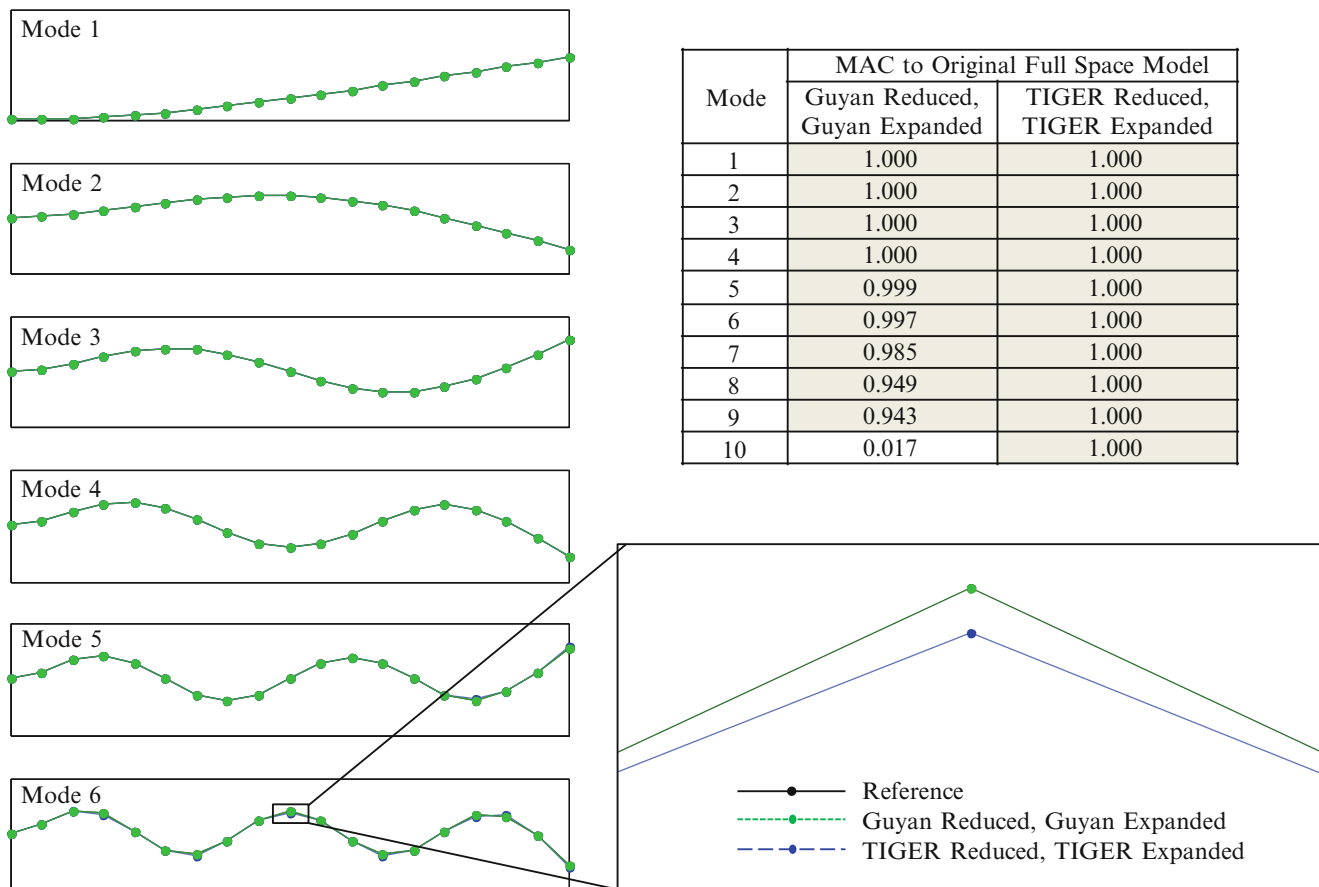
Fig. 10.9 Comparison of Guyan reduction & expansion and TIGER reduction & expansion on cantilever beam

References

1. O'Callahan JC, Avitabile P, Riemer R (1989) System equivalent reduction expansion process. In: Proceedings of the seventh international modal analysis conference, Las Vegas
2. Guyan RJ (1965) Reduction of stiffness and mass matrices. AIAA J 3(2):380
3. O'Callahan JC (1989) A procedure for an improved reduced system (IRS) model. In: Proceedings of the seventh international modal analysis conference, Las Vegas
4. Kammer DC (1991) A Hybrid approach to test-analysis-model development for large space structures, Journal of Vibration and Acoustics 113:325–332
5. Avitabile P, O'Callahan JC, Pan EDR (1989) Effects of various model reduction techniques on computed system response. In: Proceedings of the seventh international modal analysis conference, Las Vegas
6. Avitabile P (2003) Twenty years of structural dynamic modification – a review. Sound Vib Mag 37:14–27
7. Avitabile P, O'Callahan J (1991) Understanding structural dynamic modification and the effects of truncation. Int J Anal Exp Modal Anal 6(4):215–235
8. Avitabile P, O'Callahan J, Pechinsky F (1990) Understanding structural dynamic modification truncation. In: Proceedings of the eighth international modal analysis conference, Orlando
9. MAT_SAP/MATRIX (1986) A general linear algebra operation program for matrix analysis. Dr. John O'Callahan, University of Massachusetts Lowell
10. MATLAB R2007a, The MathWorks Inc., Natick, MA

Chapter 11
Towards a Technique for Nonlinear Modal Reduction

T.L. Hill, A. Cammarano, S.A. Neild, and D.J. Wagg

Abstract In this paper we discuss an analytical method to enable modal reduction of weakly nonlinear systems with multiple degrees-of-freedom. This is achieved through the analysis of backbone curves—the response of the Hamiltonian equivalent of a system—which can help identify internal resonance within systems. An example system, with two interacting modes, is introduced and the method of second-order normal forms is used to describe its backbone curves with simple, analytical expressions. These expressions allow us to highlight which particular interactions are significant, as well as specify the conditions under which they are important. The descriptions of the backbone curves are validated against the results of continuation analysis, and a comparison is also made with the response of the system under various levels of forcing and damping. Finally, we discuss how this technique may be expanded to systems with a greater number of modes.

Keywords Backbone curves • Second-order normal forms • Modal analysis • Modal interaction • Modal reduction

11.1 Introduction

Engineering systems often require the modelling of a large number of degrees-of-freedom (DOF). As the demands on such systems broaden, nonlinear effects becoming increasingly important, and their models become increasingly complex. The interactions resulting from nonlinearities within large systems often involve multiple linear modes, requiring computationally expensive models. Furthermore, variations in the forcing and damping conditions can result in a wide spectrum of dynamic responses leading to uncertainty in the models and limited operating envelopes.

In linear systems, the tools of modal analysis and superposition may be employed to reduce these large models to smaller, independent ones [1]. As these tools are not applicable to nonlinear systems, an alternative approach must be taken. One such approach proposed by Shaw et al. [2] and further developed in [3] employs the use of nonlinear normal modes. A comprehensive review of nonlinear normal modes and their applications has been given in [4, 5]. Although effective in certain circumstances, this approach requires a computationally expensive formulation of the model and must be implemented numerically.

In this paper we propose the use of backbone curves to identify resonant interactions within nonlinear systems. A backbone curve describes the response of the Hamiltonian equivalent of a system—i.e. the response of the system with damping and forcing removed. These curves represent the underlying behaviours of the system and, by simplifying the response, can be used to interpret the fundamental dynamics of the system. This not only helps identify resonant interactions, but does so for a more generalised case, independent of forcing and damping. This allows all potential resonances to be identified, some of which could be overlooked if specific forcing and damping combinations are considered.

The second-order normal form technique is used to develop expressions describing the backbone curves. The analytical nature of these expressions allow for simple adaptation of the model and for testing the effects of parameter changes. This technique may be automated for efficient implementation, and the resulting equations may be handled computationally for efficient analysis. These properties mean that the technique lends itself for application to larger systems.

T.L. Hill (✉) • A. Cammarano • S.A. Neild • D.J. Wagg
Department of Mechanical Engineering, University of Bristol, Queens Building, University Walk, Bristol, BS8 1TR, UK
e-mail: tom.hill@bristol.ac.uk

11.2 Second-Order Normal Form Technique

The second-order normal form technique has been adopted due to its ability to analytically describe the response of weakly nonlinear systems. This has advantages over numerically-based approaches such as numerical continuation [6] and nonlinear normal modes [4, 5]. Furthermore, its second-order formulation lends itself to such problems more naturally than the, more traditional, first-order formulation—see, for example, [7]. The limitations of the technique lie in the assumption that the nonlinear and damping terms are small in comparison to the undamped, linear terms. The further this assumption is broken, the less accurate the result.

A number of works describe the technique, see for example [8, 9]. However, for completeness, a brief outline follows, describing how the method can be used to describe backbone curves.

Taking a forced and damped N-DOF system in the form:

$$\mathbf{M\ddot{x}} + \mathbf{C\dot{x}} + \mathbf{Kx} + \boldsymbol{\Gamma}_x(\mathbf{x}, \dot{\mathbf{x}}) = \mathbf{P}_x \cos(\Omega t), \tag{11.1}$$

where $\mathbf{x}$ is an $N \times 1$ vector of displacements, $\boldsymbol{\Gamma}_x$ is an $N \times 1$ vector of nonlinear terms, $\mathbf{P}_x$ is an $N \times 1$ vector of linear forcing amplitudes and $\mathbf{M}$, $\mathbf{C}$ and $\mathbf{K}$ are $N \times N$ mass, damping and stiffness matrices respectively. As we are concerned only with the underlying Hamiltonian system, this can simply be reduced to

$$\mathbf{M\ddot{x}} + \mathbf{Kx} + \boldsymbol{\Gamma}_x(\mathbf{x}, \dot{\mathbf{x}}) = 0. \tag{11.2}$$

11.2.1 The Linear Modal Transform: $(\mathbf{x} \rightarrow \mathbf{q})$

Taking Eq. (11.2), the undamped linear terms are decoupled using a linear modal transform $\mathbf{x} = \boldsymbol{\Phi}\mathbf{q}$, where $\boldsymbol{\Phi}$ is an $N \times N$ matrix where the nth column describes the modeshape of the nth linear mode. This leads to the modal dynamic equation

$$\mathbf{\ddot{q}} + \boldsymbol{\Lambda}\mathbf{q} + \mathbf{N}_q(\mathbf{q}, \dot{\mathbf{q}}) = 0, \tag{11.3}$$

where $\boldsymbol{\Lambda}$ is an $N \times N$ diagonal matrix where the nth diagonal element is the square of the nth linear natural frequency ω_{nn}^2. $\boldsymbol{\Lambda}$ and $\boldsymbol{\Phi}$ may be calculated by considering the eigenvalues and eigenvectors of $\mathbf{M}^{-1}\mathbf{K}$, respectively.

In the standard formulation of the second-order normal form technique the next step is a forcing transform. However, as backbone curve analysis considers the unforced system, this step is omitted.

11.2.2 The Nonlinear Near-Identity Transform: $(\mathbf{q} \rightarrow \mathbf{u})$

Here, the transform $\mathbf{q} = \mathbf{u} + \mathbf{h}(\mathbf{u}, \dot{\mathbf{u}})$ is applied to Eq. (11.3), where $\mathbf{u}$ describes the fundamental response and $\mathbf{h}$ contains all harmonic components of $\mathbf{q}$. This must be near-identity such that $\mathbf{h}$ is small and is written $\mathbf{h} \approx \mathbf{h}_1$, from the expansion $\mathbf{h} = \varepsilon \hat{\mathbf{h}}_1 + \varepsilon^2 \hat{\mathbf{h}}_2 + \varepsilon^3 \hat{\mathbf{h}}_3 + \ldots$ where ε is a parameter denoting *smallness*. We also require our nonlinear terms to be small, such that we can write $\mathbf{N}_q \approx \mathbf{n}_{q1}$ and $\mathbf{N}_u \approx \mathbf{n}_{u1}$ using similar expansions. For further details see [8, 9].

The aim of this step is to describe the fundamental response of each linear mode in terms of displacement $\mathbf{u}$, which may be expressed in the equation

$$\mathbf{\ddot{u}} + \boldsymbol{\Lambda}\mathbf{u} + \mathbf{N}_u(\mathbf{u}, \dot{\mathbf{u}}) = 0, \tag{11.4}$$

in which all terms are resonant. To calculate the fundamental response, we assume a trial solution for the nth element of $\mathbf{u}$ as

$$u_n = u_{np} + u_{nm} = \frac{U_n}{2}e^{+j(\omega_{rn}t - \phi_n)} + \frac{U_n}{2}e^{-j(\omega_{rn}t - \phi_n)}, \tag{11.5}$$

where ω_{rn} and ϕ_n are the frequency and phase of the fundamental response of the nth linear mode respectively. Using these, we can define the vector $\mathbf{u}^*$, an $L \times 1$ column vector containing each unique combination of the variables u_{np} and u_{nm}. This can be used to describe $\mathbf{n}_{u1}$, $\mathbf{n}_{q1}$ and $\mathbf{h}_1$ using the matrix of coefficients $[n_u]$ such that

$$\mathbf{n}_{u1}(\mathbf{u}, \dot{\mathbf{u}}) = [n_u]\mathbf{u}^*(\mathbf{u}_p, \mathbf{u}_m), \tag{11.6a}$$

$$\mathbf{n}_{q1}(\mathbf{u}, \dot{\mathbf{u}}) = [n_q]\mathbf{u}^*(\mathbf{u}_p, \mathbf{u}_m), \tag{11.6b}$$

$$\mathbf{h}_1(\mathbf{u}, \dot{\mathbf{u}}) = [h]\mathbf{u}^*(\mathbf{u}_p, \mathbf{u}_m). \tag{11.6c}$$

We now determine which terms in $\mathbf{u}^*$ are resonant which, when combined with Eq. (11.6), gives us a vector of resonant nonlinear terms $\mathbf{n}_{u1}$. This can be done by firstly describing the ℓth term of $\mathbf{u}^*$ as

$$u_\ell^* = \prod_{n=1}^{N} \{u_{np}^{s_{n\ell p}} u_{nm}^{s_{n\ell m}}\} \tag{11.7}$$

along with the $L \times N$ matrix $\boldsymbol{\beta}$, which can be used to relate $[n_q]$ to $[n_u]$ and $[h]$, with the expression for element (n, ℓ)

$$n_{q,n\ell} = n_{u,n\ell} + \beta_{n\ell}h_{n\ell}. \tag{11.8}$$

As terms are either resonant (and thus have coefficients stored in $[n_u]$, with the corresponding term in $[h]$ being zero) or non-resonant (and thus stored in $[h]$, with the corresponding term in $[n_u]$ being zero) then for each element (n, ℓ) we have one of two options

$$n_{u,n\ell} = n_{q,n\ell} \qquad \& \quad h_{n\ell} = 0, \tag{11.9a}$$

$$h_{n\ell} = n_{q,n\ell}/\beta_{n\ell} \& \; n_{u,n\ell} = 0. \tag{11.9b}$$

Hence, if $\beta_{n\ell}$ is small, then Eq. (11.9b) breaks the assumption of $h_{n\ell}$ being small and so Eq. (11.9a) must be used. Conversely, a large $\beta_{n\ell}$ indicates that the term is non-resonant and must be stored in $[h]$ (i.e. Eq. (11.9b) must be used).

It is found that $\beta_{n\ell}$ (element n, ℓ of a matrix $\boldsymbol{\beta}$) can be described by

$$\beta_{n\ell} = \left[\sum_{k=1}^{N}(s_{\ell kp} - s_{\ell km})\omega_{rk} \right]^2 - \omega_{rn}^2, \tag{11.10}$$

where $s_{\ell kp}$ and $s_{\ell km}$ are taken from Eq. (11.7).

Combining the coefficients in $[n_u]$ with the variables in $\mathbf{u}^*$ (see Eq. (11.6a)) allows us to form the equations of motion for the fundamental response of each of the linear modes. It is found that each of these equations can be expressed in the form

$$\chi_n e^{+j\omega_{rn}t} + \tilde{\chi}_n e^{-j\omega_{rn}t} = 0, \tag{11.11}$$

where χ_n and $\tilde{\chi}_n$ are complex conjugates. Equating to zero the contents of the equations corresponding to either χ_n or $\tilde{\chi}_n$ allows us to solve for $\mathbf{u}$. Substituting this solution back into the non-resonant terms stored in $\mathbf{h}$ (see Eq. (11.9b)), we obtain the harmonic components of the response. Combining these with the fundamental response, $\mathbf{u}$, gives the total modal response $\mathbf{q}$. Finally, the total response in terms of the physical coordinates, $\mathbf{x}$, may be calculated using $\mathbf{x} = \boldsymbol{\Phi}\mathbf{q}$.

11.3   Example: A 3 Degree-of-Freedom Oscillator

We now demonstrate for a 3DOF system how, by describing its backbone curves, the model used to describe its response can be simplified. The application of the second-order normal form technique has been automated using a program written in MATLAB. As such, rather than describing each step of the application of the technique, the key steps and observations will be summarised whilst omitting the, somewhat laborious, details regarding the individual processes.

The system considered is represented in Fig. 11.1. It is formed of three masses with displacements x_1, x_2 and x_3. It has a symmetric structure such that the first and third masses are both m_1 whilst the second mass is m_2. The first and third masses are connected to ground by linear dampers, with constant c_1, and nonlinear springs, with force-deflection relationships $F_{k1} = k_1(\Delta x) + \kappa_1(\Delta x)^3$. Linear dampers and nonlinear springs, with constants c_2 and force-deflection relationships $F_{k2} = k_2(\Delta x) + \kappa_2(\Delta x)^3$ respectively, also connect the first and third masses to the second mass. A sinusoidal forcing of amplitude P and frequency Ω acts on the first mass.

Fig. 11.1 A schematic diagram of a 3-mass oscillator with a symmetric structure
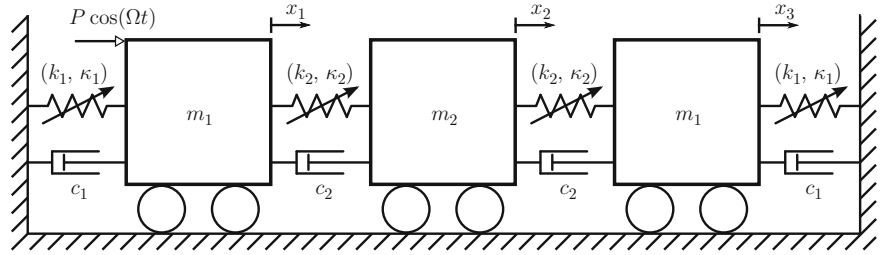
In this example, the parameter values $m_1 = m_2 = 1$, $c_1 = c_2 = 0.03$, $k_1 = 1$, $k_2 = 1.75$ and $\kappa_1 = \kappa_2 = 0.1$ are used. Also, the forcing acts only on the first mass and in the frequency range $0.7 \rightarrow 1$ rad/s at an amplitude of 0.1. This may be described in the form of Eq. (11.1), however as we are interested in the backbone curves of the system, this can be reduced to the form of Eq. (11.2).

Before applying the linear modal transform, we must calculate $\boldsymbol{\Lambda}$ and $\boldsymbol{\Phi}$ from which we compute the linear natural frequencies (to four significant figures) to be

$$\omega_{n1} \approx 0.7886 \text{ rad/s}, \qquad \omega_{n2} \approx 1.6583 \text{ rad/s}, \qquad \omega_{n3} \approx 2.3724 \text{ rad/s}, \tag{11.12}$$

and that the corresponding modeshapes (to four significant figures) are

$$\begin{pmatrix} x_1 \\ x_2 \\ x_3 \end{pmatrix} = \begin{bmatrix} -0.5361 & -0.7071 & +0.4610 \\ -0.6520 & 0 & -0.7582 \\ -0.5361 & +0.7071 & +0.4610 \end{bmatrix} \begin{pmatrix} q_1 \\ q_2 \\ q_3 \end{pmatrix}. \tag{11.13}$$

It can be seen from Eq. (11.12) that the forcing is acting in the vicinity of the first linear mode; hence we shall only consider backbone curve responses in this vicinity. Furthermore, Eq. (11.13) shows that x_1 has a component in each of the linear modes. Therefore, as forcing is applied to the first mass in the complete system, each of the linear modes are subjected to a forcing.

Applying the linear modal transform we now get an equation in the form of Eq. (11.3) where the nonlinear terms are in the form

$$\mathbf{N}_q = \begin{pmatrix} N_{11} \cdot q_3^3 + N_{12} \cdot q_2^2 q_3 + N_{13} \cdot q_1 q_3^2 + N_{14} \cdot q_1 q_2^2 + N_{15} \cdot q_1^2 q_3 + N_{16} \cdot q_1^3 \\ N_{21} \cdot q_2 q_3^2 + N_{22} \cdot q_2^3 + N_{23} \cdot q_1 q_2 q_3 + N_{24} \cdot q_1^2 q_2 \\ N_{31} \cdot q_3^3 + N_{32} \cdot q_2^2 q_3 + N_{33} \cdot q_1 q_3^2 + N_{34} \cdot q_1 q_2^2 + N_{35} \cdot q_1^2 q_3 + N_{36} \cdot q_1^3 \end{pmatrix}. \tag{11.14}$$

We may now apply the nonlinear near-identity transform by substituting $\mathbf{q} = \mathbf{u} + \mathbf{h}$. Next, all available combinations of the variables in $\mathbf{u}^*$ (see Eq. (11.6)), along with the associated parameters in $[n_v]$ must be determined. From this, and defining each element in $\mathbf{u}^*$ using Eq. (11.7), we can calculate $\boldsymbol{\beta}$ using Eq. (11.10). As we know that the forcing frequency is near the first linear natural frequency, and that $\omega_{n2}/\omega_{n1} \approx 2.1029$ and $\omega_{n3}/\omega_{n1} \approx 3.0084$ then we shall assume that u_2 and u_3 respond at 2 and 3 times the frequency of u_1 respectively (i.e. $\omega_{r2} = 2\omega_{r1}$ and $\omega_{r3} = 3\omega_{r1}$). In this case there exists 56 possible combinations of the variables, however as each term has a complex conjugate we may reduce this by considering only one set of conjugate terms (see Eq. (11.11))

$$
\tilde{\mathbf{u}}^* = \begin{pmatrix}
u_{3m}^3 \\
u_{3p}u_{3m}^2 \\
u_{2m}^2 u_{3m} \\
u_{2p}u_{2m}u_{3m} \\
u_{2m}^2 u_{3p} \\
u_{1m}u_{3m}^2 \\
u_{1m}u_{3p}u_{3m} \\
u_{1m}u_{2m}^2 \\
u_{1m}u_{2p}u_{2m} \\
u_{1m}^2 u_{3m} \\
u_{1m}^3 \\
u_{1p}u_{3m}^2 \\
u_{1p}u_{2m}^2 \\
u_{1p}u_{1m}u_{3m} \\
u_{1p}u_{1m}^2 \\
u_{1p}^2 u_{3m} \\
u_{2m}u_{3m}^2 \\
u_{2m}u_{3p}u_{3m} \\
u_{2m}^3 \\
u_{2p}u_{3m}^2 \\
u_{2p}u_{2m}^2 \\
u_{1m}u_{2m}u_{3m} \\
u_{1m}u_{2p}u_{3m} \\
u_{1m}^2 u_{2m} \\
u_{1p}u_{2m}u_{3m} \\
u_{1m}u_{2m}u_{3p} \\
u_{1p}u_{1m}u_{2m} \\
u_{1p}^2 u_{2m}
\end{pmatrix}, \quad
[\tilde{n}_v]^T = \begin{bmatrix}
N_{11} & 0 & N_{31} \\
3N_{11} & 0 & 3N_{31} \\
N_{12} & 0 & N_{32} \\
2N_{12} & 0 & 2N_{32} \\
N_{12} & 0 & N_{32} \\
N_{13} & 0 & N_{33} \\
2N_{13} & 0 & 2N_{33} \\
N_{14} & 0 & N_{34} \\
2N_{14} & 0 & 2N_{34} \\
N_{15} & 0 & N_{35} \\
N_{16} & 0 & N_{36} \\
N_{13} & 0 & N_{33} \\
N_{14} & 0 & N_{34} \\
2N_{15} & 0 & 2N_{35} \\
3N_{16} & 0 & 3N_{36} \\
N_{15} & 0 & N_{35} \\
0 & N_{21} & 0 \\
0 & 2N_{21} & 0 \\
0 & N_{22} & 0 \\
0 & N_{21} & 0 \\
0 & 3N_{22} & 0 \\
0 & N_{23} & 0 \\
0 & N_{23} & 0 \\
0 & N_{24} & 0 \\
0 & N_{23} & 0 \\
0 & N_{23} & 0 \\
0 & 2N_{24} & 0 \\
0 & N_{24} & 0
\end{bmatrix}, \quad
\tilde{\boldsymbol{\beta}}^T = \omega_{r1}^2 \begin{bmatrix}
80 & - & 72 \\
8 & - & 0 \\
48 & - & 40 \\
8 & - & 0 \\
0 & - & -8 \\
48 & - & 40 \\
0 & - & -8 \\
24 & - & 16 \\
0 & - & -8 \\
24 & - & 16 \\
8 & - & 0 \\
24 & - & 16 \\
8 & - & 0 \\
8 & - & 0 \\
0 & - & -8 \\
0 & - & -8 \\
- & 60 & - \\
- & 0 & - \\
- & 32 & - \\
- & 12 & - \\
- & 0 & - \\
- & 32 & - \\
- & 0 & - \\
- & 12 & - \\
- & 12 & - \\
- & -4 & - \\
- & 0 & - \\
- & -4 & -
\end{bmatrix},
\tag{11.15}
$$

where $\tilde{\mathbf{u}}^*$, $[\tilde{n}_v]$, and $\tilde{\boldsymbol{\beta}}$ denote one set of complex conjugates of $\mathbf{u}^*$, $[n_v]$, and $\boldsymbol{\beta}$ respectively. Note that in $\tilde{\boldsymbol{\beta}}$, elements corresponding to a zero value in $[\tilde{n}_v]$ are of no importance and are marked with a dash. From these, we can determine which terms in $[\tilde{n}_v]$ are resonant (i.e. those terms in $[\tilde{n}_v]$ corresponding to a 0 value in $\tilde{\boldsymbol{\beta}}$) and hence will contribute to $[\tilde{n}_u]$ (see Eq. (11.9a)). The terms that are non-resonant are stored in $\tilde{\mathbf{h}}$ (see Eq. (11.9b)). Using $[\tilde{n}_v]$ and $\tilde{\mathbf{u}}^*$ we can then calculate $\tilde{\mathbf{n}}_{u1}$ as

$$
\tilde{\mathbf{n}}_{u1} = \begin{bmatrix}
2N_{13}u_{1m}u_{3p}u_{3m} + 2N_{14}u_{1m}u_{2p}u_{2m} + 3N_{16}u_{1p}u_{1m}^2 + N_{15}u_{1p}^2 u_{3m} + N_{12}u_{2m}^2 u_{3p} \\
2N_{21}u_{2m}u_{3p}u_{3m} + 3N_{22}u_{2p}u_{2m}^2 + 2N_{24}u_{1p}u_{1m}u_{2m} + N_{23}u_{1m}u_{2p}u_{3m} \\
3N_{31}u_{3p}u_{3m}^2 + 2N_{32}u_{2p}u_{2m}u_{3m} + N_{36}u_{1m}^3 + 2N_{35}u_{1p}u_{1m}u_{3m} + N_{34}u_{1p}u_{2m}^2
\end{bmatrix},
\tag{11.16}
$$

where all terms in element n are resonant with $e^{-j\omega_{rn}t}$. Substituting this into Eq. (11.4) for the conjugate terms also resonant with $e^{-j\omega_{rn}t}$ we obtain an equation of motion for $\mathbf{u}$

$$
\left\{ 4(\omega_{n1}^2 - \omega_{r1}^2) + \left[2N_{13}U_3^2 + 2N_{14}U_2^2 + 3N_{16}U_1^2 + N_{15}U_1 U_3 e^{-j(3\phi_1 - \phi_3)} \right] \right\} U_1 e^{+j\phi_1} + N_{12}U_2^2 U_3 e^{+j(2\phi_2 - \phi_3)} = 0, \tag{11.17a}
$$

$$
\left\{ 4(\omega_{n2}^2 - 4\omega_{r1}^2) + \left[2N_{21}U_3^2 + 3N_{22}U_2^2 + 2N_{24}U_1^2 + N_{23}U_1 U_3 e^{+j(\phi_1 - 2\phi_2 + \phi_3)} \right] \right\} U_2 = 0, \tag{11.17b}
$$

$$
\left\{ 4(\omega_{n3}^2 - 9\omega_{r1}^2) + \left[3N_{31}U_3^2 + 2N_{32}U_2^2 + 2N_{35}U_1^2 \right] \right\} U_3 e^{+j\phi_3} + N_{36}U_1^3 e^{+j3\phi_1} + N_{34}U_1 U_2^2 e^{+j(2\phi_2 - \phi_1)} = 0, \tag{11.17c}
$$

where the definitions for u_{nm} and u_{np}, given in Eq. (11.5), have been used.

As we are using these backbone curves to describe a system forced at a frequency close to ω_{n1}, we can assume that u_1 is always active (i.e. $U_1 \neq 0$). Also, it can be seen that Eq. (11.17b) is satisfied by setting $U_2 = 0$. In this case (where u_1 is active and u_2 is inactive), Eq. (11.17c) requires that $U_3 \neq 0$. Hence, a backbone curve containing only u_1 is not possible, but one containing u_1 and u_3 is possible. Another combination is the case where $U_1 \neq 0$, $U_2 \neq 0$ and $U_3 = 0$. In this case, the final two terms in Eq. (11.17c) must balance whilst Eqs. (11.17a) and (11.17b) must also be satisfied. This does not lead to a valid solution (i.e. one in which both U_1 and U_2 are real and positive), and hence a backbone curve where only u_1 and u_2 are active is not possible. Finally, a solution in which u_1, u_2 and u_3 are all active leads to a case where all three equations must be satisfied, which is possible.

Considering the first case, in which $U_1 \neq 0$, $U_2 = 0$ and $U_3 \neq 0$, Eqs. (11.17a) and (11.17c) may be written

$$4(\omega_{n1}^2 - \omega_{r1}^2) + 2N_{13}U_3^2 + 3N_{16}U_1^2 + N_{15}U_1U_3 e^{-j(3\phi_1 - \phi_3)} = 0, \tag{11.18a}$$

$$4(\omega_{n3}^2 - 9\omega_{r1}^2) + 3N_{31}U_3^2 + 2N_{35}U_1^2 + N_{36}U_1^3 U_3^{-1} e^{+j(3\phi_1 - \phi_3)} = 0. \tag{11.18b}$$

Taking the imaginary parts of these lead to the expression $\sin(3\phi_1 - \phi_3) = 0$ and hence we may define $p_1 = e^{j|3\phi_1 - \phi_3|} = \pm 1$, where $p_1 = +1$ corresponds to $3\phi_1 - \phi_3 = 0$ and $p_1 = -1$ corresponds to $3\phi_1 - \phi_3 = \pi$. This allows us to rewrite Eq. (11.18) as

$$4(\omega_{n1}^2 - \omega_{r1}^2) + 2N_{13}U_3^2 + 3N_{16}U_1^2 + p_1 N_{15}U_1U_3 = 0, \tag{11.19a}$$

$$4(\omega_{n3}^2 - 9\omega_{r1}^2) + 3N_{31}U_3^2 + 2N_{35}U_1^2 + p_1 N_{36}U_1^3 U_3^{-1} = 0, \tag{11.19b}$$

which may be solved to produce the backbone curves $S1^+$ and $S1^-$ corresponding to the cases $p_1 = +1$ and $p_1 = -1$ respectively.

Now considering the case in which u_1, u_2 and u_3 are all active, we may rewrite Eq. (11.17) as

$$4(\omega_{n1}^2 - \omega_{r1}^2) + 2N_{13}U_3^2 + 2N_{14}U_2^2 + 3N_{16}U_1^2 + N_{15}U_1U_3 e^{-j(3\phi_1 - \phi_3)} + N_{12}U_1^{-1}U_2^2 U_3 e^{-j(\phi_1 - 2\phi_2 + \phi_3)} = 0, \tag{11.20a}$$

$$4(\omega_{n2}^2 - 4\omega_{r1}^2) + 2N_{21}U_3^2 + 3N_{22}U_2^2 + 2N_{24}U_1^2 + N_{23}U_1U_3 e^{+j(\phi_1 - 2\phi_2 + \phi_3)} = 0, \tag{11.20b}$$

$$4(\omega_{n3}^2 - 9\omega_{r1}^2) + 3N_{31}U_3^2 + 2N_{32}U_2^2 + 2N_{35}U_1^2 + N_{36}U_1^3 U_3^{-1} e^{+j(3\phi_1 - \phi_3)} + N_{34}U_1U_2^2 U_3^{-1} e^{-j(\phi_1 - 2\phi_2 + \phi_3)} = 0. \tag{11.20c}$$

In a similar fashion to the treatment of Eq. (11.18), taking the imaginary part of Eq. (11.20b) leads to the definition $p_2 = e^{j|\phi_1 - 2\phi_2 + \phi_3|} = \pm 1$ where $p_2 = +1$ corresponds to $\phi_1 - 2\phi_2 + \phi_3 = 0$ and $p_2 = -1$ corresponds to $\phi_1 - 2\phi_2 + \phi_3 = \pi$. Using this and taking the imaginary part of Eqs. (11.20a) or (11.20c) leads, again, to $p_1 = e^{j|3\phi_1 - \phi_3|} = \pm 1$ where ϕ_1 and ϕ_3 can be defined from this as before.

Using these definitions we can rewrite Eq. (11.20) as

$$4(\omega_{n1}^2 - \omega_{r1}^2) + 2N_{13}U_3^2 + 2N_{14}U_2^2 + 3N_{16}U_1^2 + p_1 N_{15}U_1U_3 + p_2 N_{12}U_1^{-1}U_2^2 U_3 = 0, \tag{11.21a}$$

$$4(\omega_{n2}^2 - 4\omega_{r1}^2) + 2N_{21}U_3^2 + 3N_{22}U_2^2 + 2N_{24}U_1^2 + p_2 N_{23}U_1U_3 = 0, \tag{11.21b}$$

$$4(\omega_{n3}^2 - 9\omega_{r1}^2) + 3N_{31}U_3^2 + 2N_{32}U_2^2 + 2N_{35}U_1^2 + p_1 N_{36}U_1^3 U_3^{-1} + p_2 N_{34}U_1U_2^2 U_3^{-1} = 0. \tag{11.21c}$$

which now results in four backbone curves $S2^{++}$, $S2^{+-}$, $S2^{-+}$ and $S2^{--}$ corresponding to $[p_1, \ p_2] = [+1, \ +1]$, $[+1, \ -1]$, $[-1, \ +1]$ and $[-1, \ -1]$ respectively.

For these two cases the displacement in terms of $\mathbf{q}$ is found by substituting the calculated values of $\mathbf{u}$ into $\mathbf{h}$ using equation $\mathbf{q} = \mathbf{u} + \mathbf{h}$. Finally, the physical displacement coordinate, $\mathbf{x}$, can be calculated using $\mathbf{x} = \mathbf{\Phi q}$.

Panels (a) and (b) in Fig. 11.2 show the forcing frequency (Ω) against the maximum displacements of x_1 and x_2 respectively. The response in x_3 is not shown as, due to the symmetry of the system, it is similar to that of x_1. The solid black lines show the stable response of the forced, damped system, as calculated by continuation analysis using AUTO-07p [6], whilst the red dashed lines show the unstable section of this response. The solid blue lines represent the $S1^\pm$ backbone curves (in which the first and third linear modes are active) and the solid green lines represent the $S2^{\pm\pm}$ backbone curves (in which all three linear modes are active). As it is assumed that $\omega_{r1} = \Omega$, these backbone curves have been plotted with respect to the forcing frequency.
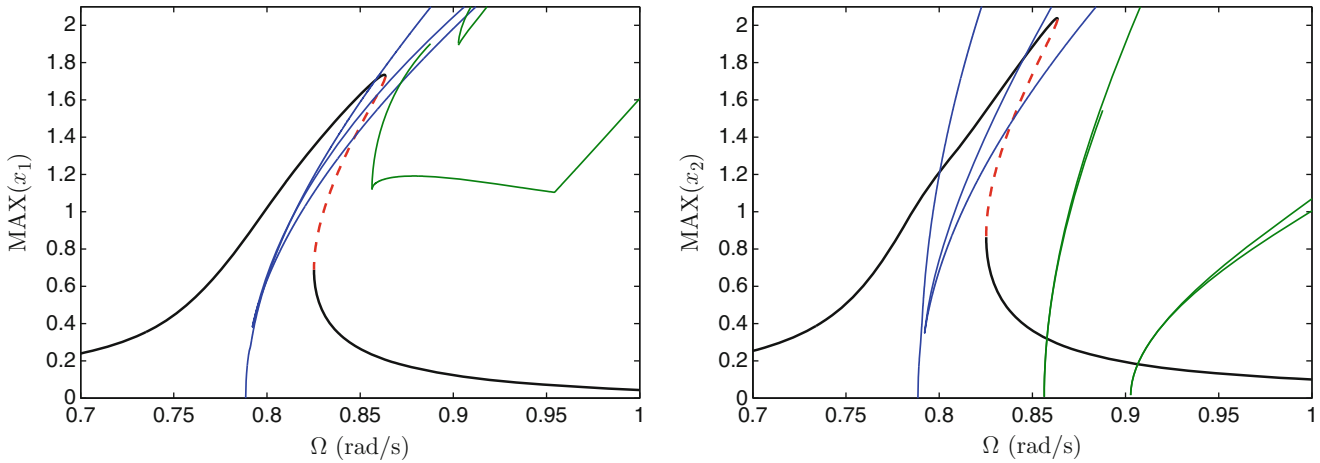
Fig. 11.2 The response of the system in terms of forcing frequency (Ω) against the maximum displacement of (**a**) x_1 and (**b**) x_2, calculated by continuation analysis using AUTO-07p. The *solid black lines and dashed red lines* show, respectively, the stable and unstable response of the forced and damped system. The *solid blue lines* represent the $S1^{\pm}$ backbone curves, containing the first and third linear modes. The *solid green lines* represent the $S2^{\pm\pm}$ backbone curves, containing all three linear modes
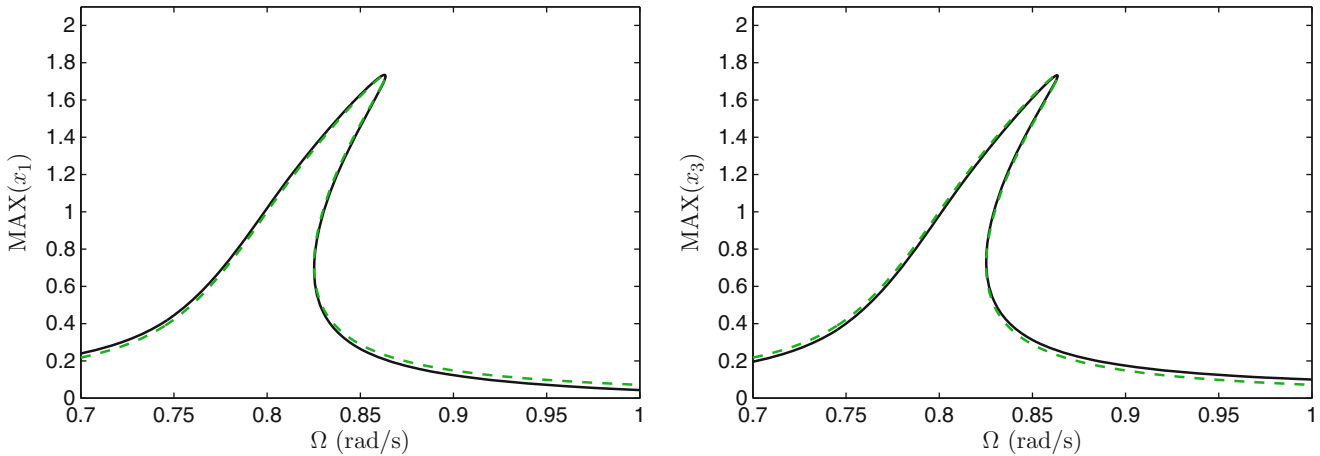
Fig. 11.3 The response of the system in terms of forcing frequency (Ω) against the maximum displacement of (**a**) x_1 and (**b**) x_3, calculated by continuation analysis using AUTO-07p. The *solid black lines* show the response of the complete forced and damped system (when all three linear modes are considered). The *dashed green lines* show the response of the reduced system containing only the responses of the first and third linear modes

A number of interesting observations may be drawn from these plots; however the main point of interest in this work is that the forced response is clearly tending to envelop the $S1^{\pm}$ backbone curves. Although it could be argued that the response in x_1 may show the system tending towards the $S2^{\pm\pm}$ backbone curves, inspection of the response in x_2 shows that this is not the case. It can also be seen that by following the $S1^{\pm}$ backbone curves, the $S2^{\pm\pm}$ curves will not be reached. It can therefore be stated that the response of this system, for this range of forcing frequencies, may be described using a model reduced to the response of just the first and third linear modes. Many of these features may by described by the backbone curves whose solutions are given by Eq. (11.19).

To confirm this, Fig. 11.3 also shows the response of the forced, damped system in terms of the forcing frequency against a maximum physical displacement. Panel (a) shows the maximum displacement of x_1 and panel (b) shows the maximum displacement of x_3 (in this case x_2 is irrelevant as it is independent of q_2—see Eq. (11.13)). The solid black line shows the response of the complete system and the dashed green line shows the response when only the first and third linear modes are considered. It can be seen that the agreement between the two cases is very good, thus demonstrating that modal reduction can be applied on this system.

11.4 Discussion

For this particular system, the same result may have been achieved by projecting the forced response in the physical coordinates onto the linear modal coordinates and inspecting these responses. From this it would be seen that the second linear mode does not respond. However some resonances are only reached under certain forcing amplitudes or configurations which may be overlooked by considering only a limited number of cases. As backbone curves are independent of forcing and damping, the resonances that may not be observed in individual forcing cases can be predicted. Furthermore, techniques are in development that allow backbone curves to be related to the response of the forced system in terms of the forcing and damping conditions. This will enable constraints to be set on the forcing and damping in which particular interactions will be observed. Another feature that may be overlooked by simply observing particular forcing cases is that, in larger systems, interactions may occur in sets but without interaction between sets. As a response will be observed in all linear modes within these sets, it will be assumed that they are all interacting; however the backbone curve analysis will reveal that the system can be further reduced.

11.5 Conclusion

In this paper we have demonstrated how, by using backbone curves to deduce the underlying behaviour of the response of a forced system, we can simplify the model used to describe it. This approach has been applied to a 3DOF system, for a given forcing frequency range and amplitude, and used to produce an accurate model describing just two of the three linear modes. The second-order normal form technique is able to describe these backbone curves analytically allowing conclusions to be drawn regarding the nature of the interactions. Furthermore, the approach taken here is a generalised one that may be expanded to larger systems.

This approach may be further developed to include techniques for predicting the forcing and damping necessary to achieve (or avoid) particular responses observed in the backbone curves. Additionally, a method of analysing the accuracy of the backbone curves is necessary to give confidence in their predictions.

References

1. Ewins DJ (2000) Modal testing: theory, practice, and application. Research Studies Press, Philadelphia, PA
2. Shaw SW, Pierre C, Pesheck E (1999) Modal analysis-based reduced-order models for nonlinear structures: an invariant manifold approach. Shock Vib Digest 31:3–16
3. Pesheck E, Boivin N, Pierre C, Shaw SW (2001) Nonlinear modal analysis of structural systems using multi-mode invariant manifolds. Nonlinear Dynam 25:183–205
4. Kerschen G, Peete rs M, Golinval JC, Vakakis AF (2009) Nonlinear normal modes, Part I: A useful framework for the structural dynamicist. Mech Syst Signal Process 23:170–194
5. Peeters M, Viguié R, Sérandour G, Kerschen G, Golinval JC (2009) Nonlinear normal modes, Part II: Toward a practical computation using numerical continuation techniques. Mech Syst Signal Process 23:195–216
6. Doedel EJ, with major contributions from Champneys AR, Fairgrieve TF, Kuznetsov YuA, Dercole F, Oldeman BE, Paffenroth RC, Sandstede B, Wang XJ, Zhang C (2008) AUTO-07P: Continuation and bifurcation software for ordinary differential equations. Concordia University, Montreal. http://cmvl.cs.concordia.ca
7. Murdock J (2002) Normal forms and unfoldings for local dynamical systems. Springer, New York
8. Neild SA, Wagg DJ (2010) Applying the method of normal forms to second-order nonlinear vibration problems. Proc Roy Soc A Math Phys Eng Sci 467:1141–1163
9. Neild SA (2012) Approximate methods for analysing nonlinear structures. Springer, Vienna

Chapter 12
Identification of Independent Inputs and Their Spatial Positions

D. Bernal and A. Ussia

Abstract This paper examines the problem of determining the number and the spatial distribution of the inputs that act on a linear system from observation of the outputs. It is shown that the number of independent inputs can be obtained from the effective rank of a matrix that can be formulated from the Fourier transform of the response signals and that the input location information is encoded in the image of the same matrix. A scheme to identify the time histories once the input positions are established is outlined.

Keywords Number • Spatial distribution • Image • Deconvolution • Time history

12.1 Introduction

There are situations where the loading environment on a system is complex but a replacement that can provide a reasonable approximation may suffice for certain objectives. A flexible bridge for which one wants to design a vibration mitigation system offers an example. In this instance a model for the wind excitation can help and there are two ways to go about it. One is to formulate the loading model analytically and the other, which is the approach we examine in this paper, is to use measurements of the response to estimate it. Under the assumption that a direct measurement of the input is not feasible the questions are: (1) how many independent loads are needed to capture the situation, (2) where should these loads be placed and what are their lines of action and (3) what are reasonable time histories. In this paper, we consider the idealized situation where the true loading condition is defined by a limited set of point loads and we want to identify their number, position and time histories. A study focusing on location and number of inputs using the concept of transmissibility is presented in [1]. The method adopts a trial and error procedure that essentially checks all possible combinations and is thus impracticable in large problems. The approach in this paper circumvents these difficulties by determining the number of inputs in a data-driven fashion and obtaining the locations without the need for a combinatorial search. The literature on input identification is large and we do not attempt to review it here. Part of the work presented here was first reported in [2].

12.2 On the Number of Inputs

Let's assume that the situation is such that one is able to collected j sets of output data, all of which satisfy the condition that the m observed outputs decay (in each set) to negligible amplitude. For these conditions one can write

$$Y_j(\omega) = G(\omega) U_j(\omega) \tag{12.1}$$

D. Bernal (✉)
Civil and Environmental Engineering Department, Center for Digital Signal Processing, Northeastern University, Boston, MA 02115, USA
e-mail: bernal@coe.neu.edu

A. Ussia
University of Trento, Trento, Italy
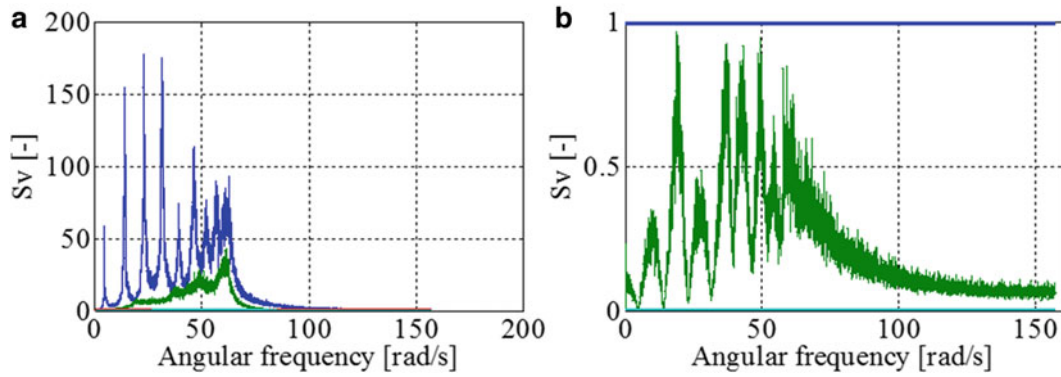
Fig. 12.1 Plot of the singular values for the ideal case of j experiments, (**a**) not normalized and (**b**) normalized respect to the maximum SV

where $G(\omega)$ is the transfer matrix for the input-output coordinates, $Y_j(\omega)$ is the Fourier transform of the output signals for the jth experiment and $U_j(\omega)$ is the transform of the input. Let $B_{FFT}(\omega)$ be a matrix containing the transform of the output from each experiment at frequency ω; since the columns of $B_{FFT}(\omega)$ are given by the product in Eq. 12.1, the rank of B_{FFT} cannot exceed the number of independently inputs and it is thus possible to infer the number of inputs by inspecting the rank of the above-mentioned matrix.

12.2.1   Illustration

The model selected for the numerical illustration is a 10-dof uniform chain fixed at one end (the end close to dof#1) with 2 % modal damping. There are inputs at dof # 2 and #5 and the measurement are accelerations at dof {1, 3, 7 and 10}. The fundamental and highest frequencies are 0.75 and 9.95 Hz respectively. The inputs are non-zero for 250 s and the output is recorded for 500 s. Figure 12.1a shows the plot of the singular values B_{FFT} as a function of frequency and part (b) shows the same result with the plot normalized respect to the maximum singular value. As can be seen, there are two non-zero singular values, indicating that there are two independent inputs acting on the structure.

12.2.2   The Practical Case

In most instances the input acts continuously and is not possible to collect N sets of data where the output decays to negligible values. It is generally possible, however, to collect a long data set which can then be divided into segments and treat (each segment that is) as resulting from a periodic excitation. The underlying theoretical framework in this case shifts from the continuous Fourier transform of Eq. 12.1 to that of a periodic analysis in terms of Fourier series. The approximation that is incurred in this instance derives from the fact that the coefficients of the Fourier series expansion of the output contain error due to initial conditions that prevail in each window (due to the periodic assumption). Nevertheless, as the window size grows the relative importance of this error source decreases and for sufficiently long widows (the necessary length depending on the damping) sufficiently accurate results can be obtained. From an implementation perspective the approach appears essentially the same as in the situation of Eq. 12.1, except for the fact that in this case the output is transformed to frequency using the FFT (periodic premise).

12.2.3   Illustration

Figure 12.2 shows results for the same conditions considered previously except that in this case only one long output is assumed available. One notes, as expected, that the clarity in the fact that the rank of the matrix is two increases as the dimension of the window increases. Needless to say, the solution presented for the number of inputs requires that the number of outputs be greater than the number of inputs.
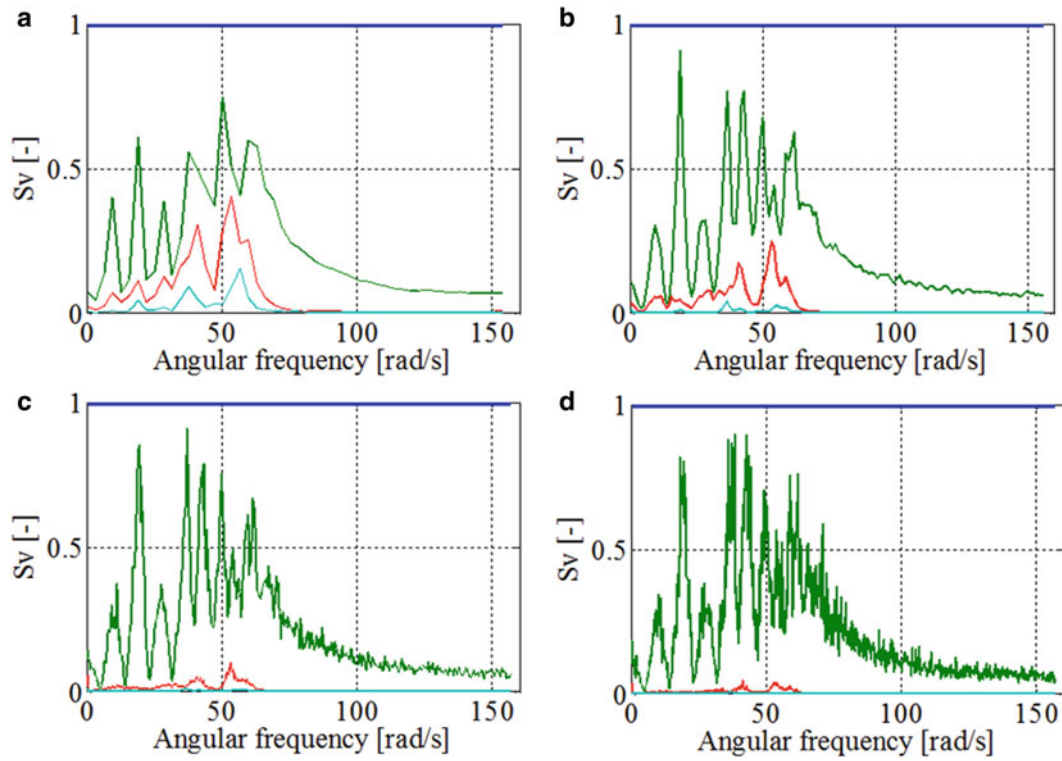
Fig. 12.2 Rank definition as a function of the window size
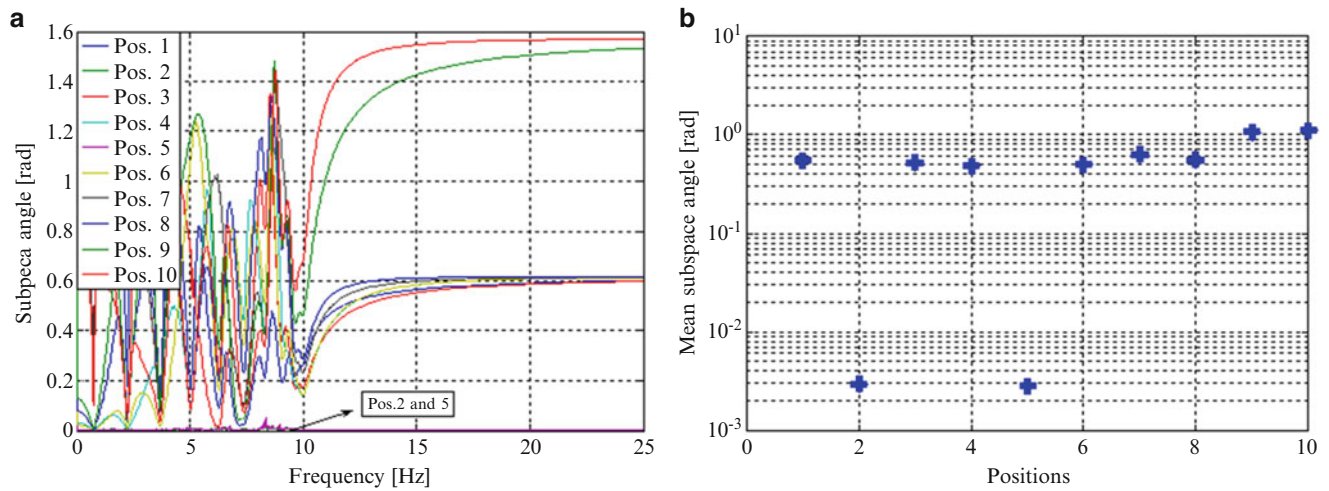
Fig. 12.3 (**a**) Subspace angle vs. frequency and (**b**) mean subspace angle vs. position

12.3 On the Location

Having identified the number of independent inputs the next question on their characterization is to determine their distribution in space. The localization can be ascertained by noting that the span of the matrices $B_{FFT}(\omega)$ is the same as that of the columns of the transfer matrix for the columns associated with the position of the inputs. While is evident that one can locate the position of the inputs by finding the combination of the columns of the transfer matrix of a model that has the same span of $B_{FFT}(\omega)$ this approach is combinatorial and is thus not scalable for models with a large number of dof when there are several inputs. Fortunately, however, it is not necessary to check all the possible combinations as it suffices to test each position individually. Figure 12.3a illustrates the subspace angle that the columns of the transfer matrix of the model

make with $B_{FFT}(\omega)$. As can be seen, the positions #2 and #5 are readily identified. Figure 12.3b shows the mean subspace angle respect to each position and confirms that the correct positions are #2 and #5.

12.4 Time Histories

The well-known input to state and state to output relations are

$$
\begin{aligned}
x_{k+1} &= A_d x_k + B_d u_k \\
y_k &= C_d x_k + D_d u_k
\end{aligned}
\tag{12.2}
$$

With $x_{k+1} \in \mathbb{R}^{2n}$ the state vector, $u_{k+1} \in \mathbb{R}^r$ is the input vector and $y_k \in \mathbb{R}^m$ is the measurement vector. A_d, B_d, C_d and D_d are real matrices of appropriate dimensions. If the system and the inputs are finite dimensional, following the recurrence, one finds that:

$$
y_k = C A_d^k x_0 + \sum_{j=0}^{k} Y_j u_{k-j}
\tag{12.3}
$$

where

$$
Y_0 = D_d
\tag{12.4a}
$$

$$
Y_j = C_d A_d^{j-1} B_d
\tag{12.4b}
$$

Stacking the inputs and outputs in columns gives

$$
y_{[0,\ell]} - Ob_\ell \cdot x_0 = H u_{[0,\ell]}
\tag{12.5}
$$

where $H \in R^{(\ell_1 m) x (\ell_1 r)}$, Ob_ℓ is the observability matrix of order ℓ, where ℓ is total number of time steps and $\ell_1 = \ell + 1$ is the total number of time stations. The general solution of Eq. 12.5 is

$$
u_{[0,\ell]} = H^{-*} y_{[0,\ell]} - H^{-*} Ob_\ell \cdot x_0 + Z \cdot h
\tag{12.6}
$$

where $-*$ stands for pseudo-inversion, $Z = N(H)$ is the null space of H and h is an arbitrary vector of appropriate dimension. If data are collected from collocated acceleration the null space of H is empty and consequently there is only a set of $u_{[0,\ell]}$ for $y_{[0,\ell]}$. Otherwise, the null space is a not empty and the inputs are identifiable within the range [0,p]. In this case the reconstructed input over [0,p] is,

$$
\bar{u}_p = Q_p H^{-*} \left(y_{[0,\ell]} - Ob_\ell \cdot x_0 \right)
\tag{12.7}
$$

where p is value determined by the delay between inputs and outputs (details appear in [2]). The input at coordinate #2 reconstructed using Eq. 12.7 is compared with the actual values in Fig. 12.4. The reconstruction in not exact because 0.5 % NSR was added to the measurements.

12.5 Conclusions

It is shown that the number of inputs can be identified in a data-driven fashion provided this number is less than the measurements and that the available output is sufficiently long. The position of the inputs can subsequently be established with the aid of a model. Sensitivity of the position to inevitable model error is not studied here. Once the input spatial positions are determined the time histories can be de-convolved, with proper consideration given to the delay resulting from wave propagation in the non-collocated scenario.

Fig. 12.4 Detail of the comparison predicted and the actual input in position #2
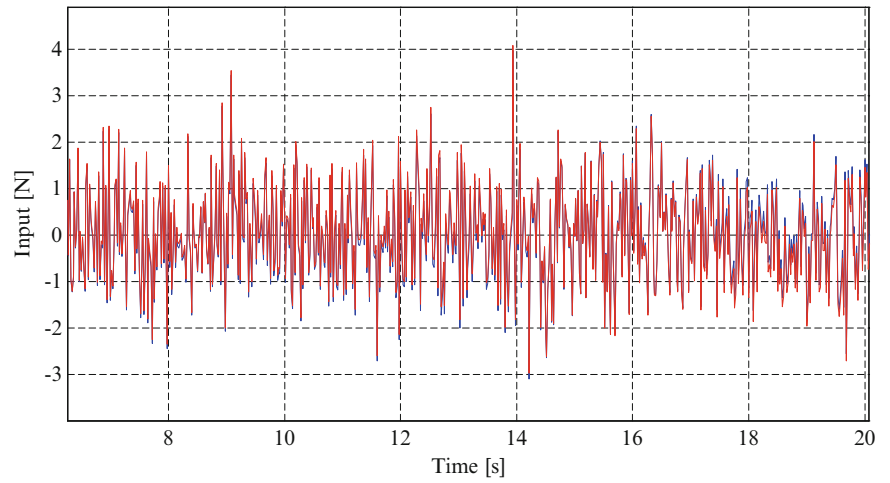
References

1. Maia NMM, Lage YW, Neves MM (2012) Recent advances on force identification in structural dynamics, Chapter 6. http://dx.doi.org/10.5772/51650.
2. Bernal D, Ussia A. Sequential deconvolution input reconstruction. Mech Syst Signal Process (in review)

Chapter 13
Shock Response Fixture Developed from Analytical and Experimental Data and Customized Using Structural Dynamics Modification Techniques

Kai Aizawa and Peter Avitabile

Abstract In order to characterize the acceleration response of a structure due to shock environments, the Shock Response Spectrum method is widely used in the qualification process for the spacecraft industry. Generally, this test is performed with a shock testing machine but alternate test fixture designs, including a shock plate, have recently been considered. In order to develop an appropriate design methodology to design such a fixture, a simple beam type structure is utilized to deploy the approach; the beam is chosen so as to introduce the SRS method into an educationally motivated treatment of the material for use in a graduate level course.

In this paper, the development of a Shock Response Spectrum for a beam-type structure from both analytical and experimental approaches is presented. From these models, frequencies, damping and mode shapes can be extracted to identify the response at various locations on the structure that are needed to develop the Shock Response Spectrum. In order to customize the shock spectrum, various mass perturbations applied to the structure can be considered by using Mass Sensitivity Analysis. The effects of the changes to the mass of the basic shock test fixture can be easily developed by using the Structural Dynamic Modification technique.

A comparison of the Shock Response Spectrum computed from the Analytical Model and from the Experimental Model is provided for various scenarios of different configurations studied.

Keywords Shock response spectrum (SRS) • Experimental and analytical SRS

Nomenclature

[M]	Mass matrix in physical space
[K]	Stiffness matrix in physical space
[C]	Damping matrix in physical space
$[\overline{M}]$	Mass matrix in modal space
$[\overline{K}]$	Stiffness matrix in modal space
$[\overline{C}]$	Damping matrix in modal space
[U]	Mode shapes
[λ]	Eigenvalues
X	Physical displacement in time domain
$\ddot{X}$	Physical Acceleration in time domain
F	Time vector of applied force
P	Modal displacement in time domain
$\ddot{p}$	Modal acceleration in time domain
$X(s)\vert_{s=j\omega}$	Physical displacement in frequency domain

K. Aizawa
Acoustic Systems Laboratory (CAMAL), Chuo University, 1-13-27 Kasuga, Bunkyo-ku, Tokyo 112-8551, Japan

P. Avitabile (✉)
Structural Dynamics and Acoustic Systems Laboratory, University of Massachusetts Lowell, One University Avenue, Lowell, MA 01854, USA
e-mail: peteravitabile@uml.edu

$\ddot{X}(s)\big|_{s=j\omega}$ Physical acceleration in frequency domain
$H(s)|_{s=j\omega}$ Frequency response Function (FRF)
$[\Delta M]$ Mass modification matrix in physical space
$[\Delta K]$ Stiffness modification matrix in physical space

13.1   Introduction

13.1.1   Background

The Shock Response Spectrum has been widely used in the aerospace industry for many years to address many shock conditions including pyroshock which is a very high amplitude and short duration pulse. For more than 50 years, NASA has used the SRS for the majority of qualification of equipment used in a shock environment. While analyses can be performed, at some point the structure must be subjected to these shock loads in a laboratory environment. A variety of different shock machines have been developed to support this qualification effort.

NASA has created a standard to estimate the maximum shock value [1]. This standard facilitates the shock test and allows engineers to develop an input pulse that will cause the desired or specified shock spectrum. By using this standard, engineers can identify a possible maximum response on the structure with an arbitrary natural frequency and determine whether the structure can withstand the shock or not. The spectrum obtained by this standard is called the Shock Response Spectrum (SRS) and is used to determine suitability of equipment for different applications. The SRS was first developed in the U.S. Department of Defense and now defined in ISO 18431-4 [2] and an example of SRS is shown in Fig. 13.1. A SRS consists of a series of maximum acceleration response which is caused by an input force applied to a discrete number of single degree of freedom (SDOF) systems.

Typically the SRS is developed with a vibration shaker or a specifically designed shock machine. These machines are very specific and typically the cost to conduct these tests is very high. Recently [5], alternate methods have been considered to conduct this shock test that is less expensive to run. Specifically a SRS plate has been considered [5] and some preliminary studies have shown that this is a viable and economical approach to conducting SRS tests. That work showed some of the basic approaches to use the finite element (FE) model to identify the basic shock performance of the shock plate. But in order to customize the SRS, attachment masses need to be moved around the structure to obtain the desired SRS; extensive work was not performed in that earlier work nor was any optimal configuration studied or identified. But the customization of the specific spectrum does require some effort.
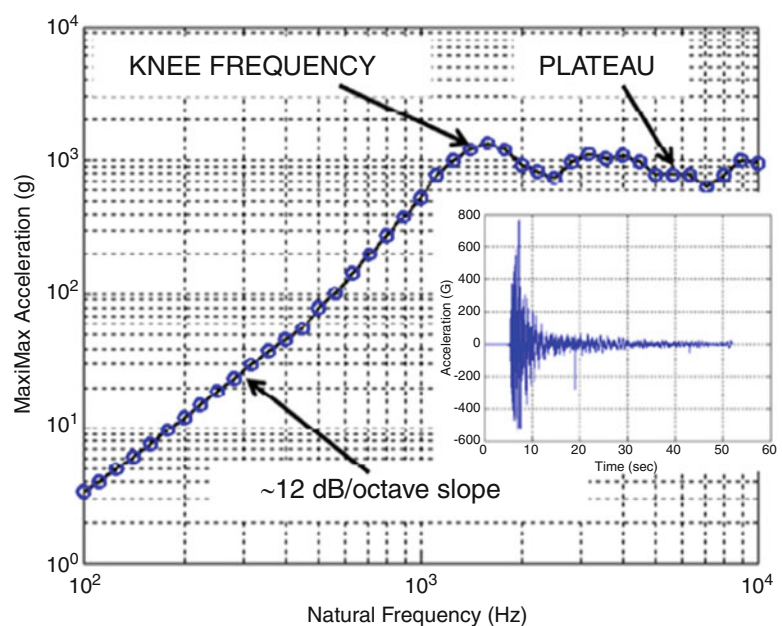
Fig. 13.1 Input pulse and calculated SRS for pyroshock (from [1])

In order to develop a methodology which can be useful for customizing SRS characteristics, in this paper, a simple beam will be used for the development of both experiment and analytical models. The beam is selected mainly as a "proof of concept" for the methodology presented and is not intended to be the final shock test configuration; ultimately the plate configuration studied in [5] is the more practical configuration. The main reason for selecting the beam is to use this shock test machine design as an educational tool for the study of vibration, shock and related topics necessary to perform these shock type calculations. In addition to the beam model, a more basic 5-degree of freedoms (DOF) analytical model will be used to determine proper configurations and to test some methodologies in this work and to illustrate some key points.

The design of the shock test machine involves the identification of the frequencies and mode shapes of the structure. This basic information is used for the prediction of the response of the set of SDOF systems that describe the structure and their response due to the shock excitation. The peak response of each of these SDOF systems are used to define the envelope of the SRS curve; mode contribution effects help to clearly see how individual modes affect the overall SRS curve desired. However, the SRS for the structure may not achieve the desired SRS and modifications may need to be considered. One very effective way to accomplish this is to use the Device Under Test (DUT) mounting block as a variable and movable mass which can be modified and attached at different locations to achieve different overall SRS at different points on the structure and/or introduce additional masses to attach to the structure.

To perform this mass modification, the Structural Dynamics Modification (SDM) will be conducted along with the Mass Sensitivity Analysis (MSA). In order to verify the relationship between each mode and each peak of the SRS, contribution analysis will also be used in this procedure. These will be performed for the FE model as well as an experimental configuration to show the benefits of using both analytical and experimental approaches to address the development of the SRS. The FE model is very useful in the design stage of the shock test fixture whereas the experimental approach helps to accurately predict the actual performance characteristics of the actual hardware configuration.

13.1.2   Motivation

In the previous paper [5], some numerical configurations for a proper FE model development were discussed. In that work, the effects of different damping values and the effects of the number of modes used for the SRS computation were studied. This was very useful but the earlier work did not adequately consider the experimental data as part of the development of the SRS; this was mainly due to the lack of correlation to the measured data and was not further studied or used for the SRS computation. However, there were some useful experimental mass modifications explored that clearly show the significant effect on the envelope of the SRS but only a few different configurations were explored in a somewhat random manner and optimization of the SRS spectrum was not considered in that work. Clearly more work can be performed to better understand the SRS spectrum and how it is developed from contribution of the different modes of the shock fixture and how to modify the structure to achieve certain performance goals. Due to this, a basic methodology to simulate a configuration of the SRS fixture will be discussed in this paper. Furthermore, a useful methodology to customize the SRS using optimized mass modification will be presented. Understanding these methodologies will be able to help design a proper SRS fixture and modify the SRS so that an acceptable configuration to satisfy the SRS envelop will be achieved.

13.2   Methodology

There are two main goals for this project: developing an appropriate methodology which is useful to simulate a shock response fixture and SRS customization to get the desired SRS. To perform this work, tools such as modal analysis, structure dynamics modification, time response computation and SRS computation are needed; the complete flow of analysis is summarized in Fig. 13.2. Modal parameters will be obtained from the Finite Element Analysis (FEA) or Experimental Modal Analysis (EMA). These parameters will be compared to each other and experimental modal damping values will be used in the FE model to simulate a proper experimental configuration. Using these verified modal parameters, the SDM, including the MSA to identify optimal location for mass modification, will be performed in case of the customization procedure. With these original or modified modal parameters, a direct time integration method using modal solution or an Inverse Fourier Transform (IFT) method will be performed to obtain the physical response. In addition, an acceleration signal is also measured with an actual experiment to compare the analytical model and measured structure data. These original or modified response signals from the FEA, EMA and an experiment will be treated as an input acceleration signal to compute the SRS. Then, a set of SRS envelopes obtained will be compared and the methodology proposed in this paper for the SRS computation and the SRS modification will be verified along with these results.

Fig. 13.2 Flow chart for this research
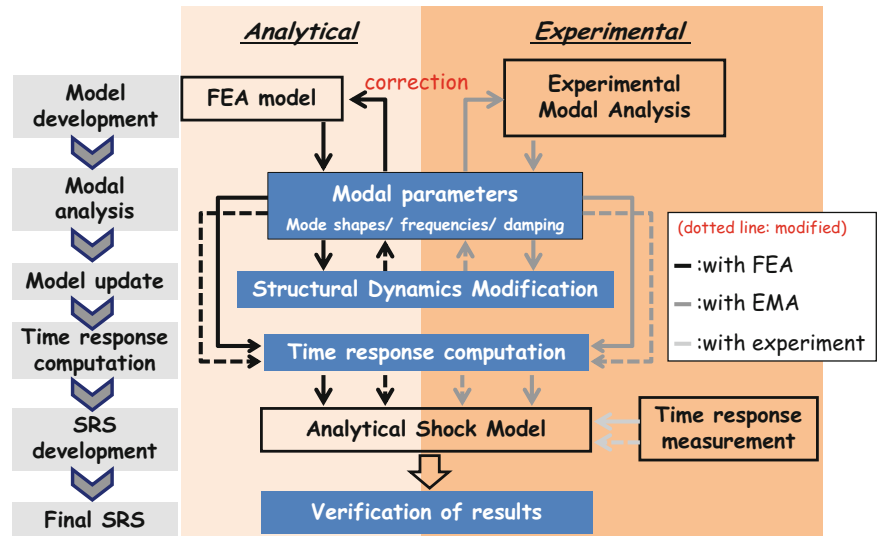
13.3 Theoretical Background

The background theories related to all the analyses are briefly described in this section. Because a time response will be required to develop a SRS, two methods will be examined to obtain the time response: the time domain and the frequency domain solution. The various related analyses to accomplish this work are described in separate sections identified as:

1. Equation of Motion and Modal Space Representation
2. Time Response Computation with Modal Superposition Technique in Time Domain
3. Time Response Computation with Frequency Response Function (FRF) in Frequency Domain
4. Shock Response Spectrum (SRS)
5. Contribution Analysis and Mass Sensitivity Analysis (MSA)
6. Structure Dynamics Modification (SDM)

The background theory and description of each of these follow.

13.3.1 Equation of Motion and Modal Space Representation

The equation of motion in physical space is used for the development of the FE model but the solutions are cast in modal space for easy computation as well as identifying a clear effect of the contribution that each mode makes to the overall response. The benefit of using the modal space solution is that the computation may be performed faster than the physical solution because the number of modes used for the computation is much smaller than the total number of DOFs (nDOF) in the FE model. The equation of motion in physical space for a multiple degree of freedoms (MDOF) system can be written as

$$[M]\{\ddot{X}\} + [C]\{\dot{X}\} + [K]\{X\} = \{F\} \tag{13.1}$$

The eigensolution of this system is written as

$$[[K] - \lambda_i [M]]\{X\} = \{0\} \tag{13.2}$$

From Eq. 13.2, eigenvalues λ and eigenvectors U will be obtained. Using these eigenvectors, the physical MDOF system set of equations can be uncoupled. The transformation from physical coordinates into modal coordinates is written as

$$\{X\} = [U]\{p\} \tag{13.3}$$

Substituting Eq. 13.3 into Eq. 13.1 and pre-multiplying $[U]^T$ in Eq. 13.1 results in

$$\left[\overline{M}\right]\{\ddot{p}\} + \left[\overline{C}\right]\{\dot{p}\} + \left[\overline{K}\right]\{p\} = [U]^T\{F\} \tag{13.4}$$

This represents the equation of motion in modal space and will be used for direct time integration to compute the physical acceleration. If the mode shape is scaled to the unit modal mass, due to the orthogonality and linear independence, the transformation from physical space to modal space will provide the modal mass and stiffness matrices written as follows

$$
[U^T][M][U] = \begin{bmatrix} \ddots & & \\ & \overline{M} & \\ & & \ddots \end{bmatrix} \rightarrow \begin{bmatrix} \ddots & & \\ & I & \\ & & \ddots \end{bmatrix} \tag{13.5}
$$

$$
[U^T][K][U] = \begin{bmatrix} \ddots & & \\ & \overline{K} & \\ & & \ddots \end{bmatrix} \rightarrow \begin{bmatrix} \ddots & & \\ & \omega^2 & \\ & & \ddots \end{bmatrix} \tag{13.6}
$$

The modal damping matrix can also be identified providing that proportional damping is assumed and written as

$$
[U^T][C][U] = \begin{bmatrix} \ddots & & \\ & \overline{C} & \\ & & \ddots \end{bmatrix} \rightarrow \begin{bmatrix} \ddots & & \\ & 2\zeta\sqrt{\overline{M}\overline{K}} & \\ & & \ddots \end{bmatrix} \tag{13.7}
$$

Here, ζ should not be a constant factor but be measured in an experiment to develop a proper SRS [5]. Due to this reason, a series of ζ for every one of the modes of interest will be selected from the EMA.

13.3.2   Time Response Computation with Modal Superposition Technique in Time Domain

The Newmark Direct Integration Method [7] is used to obtain a time response signal. This method uses a direct integration of the equation of motion in modal space shown in Eq. 13.1 with subscript of "$t = i$" as

$$
[\overline{M}]\{\ddot{p}_{t=i}\} + [\overline{C}]\{\dot{p}_{t=i}\} + [\overline{K}]\{p_{t=i}\} = \{\overline{F}_{t=0}\}, \text{where } \{\overline{F}\} = [U]^T\{F\} \tag{13.8}
$$

In order to achieve an acceleration response, the Newmark method will require the initial acceleration $\ddot{p}_{t=0}$ for the first step of computation and its form is written as

$$
\{\ddot{p}_{t=0}\} = [\overline{M}]^{-1}\left[\{\overline{F}_{t=0}\} - [\overline{C}]\{\dot{p}_{t=0}\} - [\overline{K}]\{p_{t=0}\}\right] \tag{13.9}
$$

Using these initial values for the displacement, velocity and acceleration, the displacement for the next time step is written using the constant factor α and β and time increment Δt as

$$
\{p_{t=i+1}\} = \left[\frac{1}{\alpha(\Delta t)^2}[\overline{m}] + \frac{\beta}{\alpha\Delta t}[\overline{c}] + [\overline{k}]\right]^{-1}\left[\begin{array}{l}\{\overline{f}_{t=i+1}\} + [\overline{m}]\left(\frac{1}{\alpha(\Delta t)^2}\{p_{t=i}\} + \frac{1}{\alpha\Delta t}\{\dot{p}_{t=i}\} + \left(\frac{1}{2\alpha}-1\right)\{\ddot{p}_{t=i}\}\right) \\ + [\overline{C}]\left(\frac{\beta}{\alpha\Delta t}\{p_{t=i}\} + \left(\frac{\beta}{\alpha}-1\right)\{\dot{p}_{t=i}\} + \left(\frac{\beta}{\alpha}-2\right)\frac{\Delta t}{2}\{\ddot{p}_{t=i}\}\right)\end{array}\right],
$$
$$
where \; i = 0, 1, 2 \ldots, maximum \; time \; length
$$
$$
\tag{13.10}
$$

Then, the acceleration for the same time step is calculated using the displacement obtained for the next time step and the initial conditions for the displacement, velocity and acceleration using

$$
\ddot{p}_{t=i+1} = \frac{1}{\alpha(\Delta t)^2}\left(\{p_{t=i+1}\} - \{p_{t=i}\}\right) - \frac{1}{\alpha\Delta t}\{\dot{p}_{t=i}\} - \left(\frac{1}{2\alpha}-1\right)\{\ddot{p}_{t=i}\} \tag{13.11}
$$

Fig. 13.3 Computation flow of
IFT method
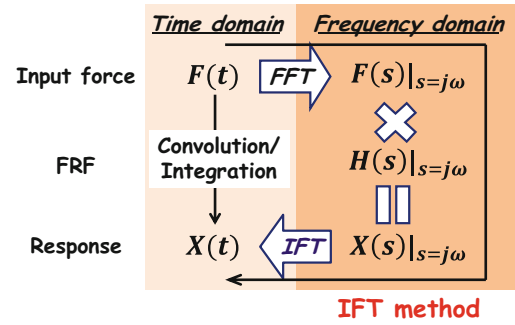
The velocity for the same time will also be calculated with the acceleration obtained and the initial condition for velocity as

$$\dot{p}_{t=i+1} = \{\dot{p}_{t=i}\} + (1 - \beta)\,\Delta t\,\{\ddot{p}_{t=i}\} + \beta \Delta t\,\{\ddot{p}_{t=i+1}\} \tag{13.12}$$

Solving Eqs. 13.10, 13.11 and 13.12 repeatedly with the values obtained from these equations, the displacement, velocity and acceleration response will be obtained and the acceleration will be used for the SRS computation. The result of the Newmark solution depends on the constant factors such as the α, β and Δt. In this work, the α and β are set to 1/4 and 1/2 because the acceleration response for the system may be assumed to be constant for t = i and t = i + 1 [7]. The Δt is set to at least ten times smaller than the period of the highest frequency of interest to avoid numerical damping [5].

The modal acceleration responses obtained from the Newmark method will be transformed back to physical space using Eq. 13.3 and the number of modes used can be limited to the first set of M modes of the N possible modes for faster computation. The size of the mode shapes is also limited to M modes and then, the physical response with the limited number of modes will be obtained.

13.3.3 Time Response Computation with Frequency Response Function (FRF) in Frequency Domain

The time response computation in the frequency domain will also be calculated to compare the result with the Newmark method. Because the computation will be performed in the frequency domain, an input force needs to be transformed into the frequency domain using the Fast Fourier Transform (FFT) method and then a FRF will be multiplied by that spectrum. The result will be a response spectrum and a response time signal will be obtained from the IFT of this spectrum. The computation flow is summarized in Fig. 13.3 and the relationship between the input and output spectra is written as

$$X(s)\big|_{s=j\omega} = H(s)\big|_{s=j\omega} \times F(s)\big|_{s=j\omega} \tag{13.13}$$

Here, the FRF $H(s)|_{s=j\omega}$ is obtained with the partial fraction form as

$$H(s)\bigg|_{s=j\omega} = \sum_{r=1}^{ndof} \left(\frac{q_r u_{jr} u_{kr}}{s - p_r} + \frac{q_r{}^* u_{jr}{}^* u_{kr}{}^*}{s - p_r{}^*} \right)\bigg|_{s=j\omega}, \tag{13.14}$$

where $q_r = \frac{1}{2j\omega_r}$, $p_r = -\zeta_r \omega_r \pm i\omega_r \sqrt{1 - \zeta^2}$ and u is mode shape value of rth mode at j or k

The input and output location are defined with the subscript j and k and the FRF will be calculated up to the Nyquist frequency, which is equal to Fs/2 Hz.

In order to obtain an acceleration spectrum from the result of Eq. 13.13, the displacement spectrum is scaled using

$$\ddot{X}(s)\big|_{s=j\omega} = -\omega^2 X(s)\big|_{s=j\omega} \tag{13.15}$$

For the acceleration spectrum obtained, the IFT will be applied and a response acceleration time signal will be achieved.

Fig. 13.4 SDOF model used in
SRS calculation
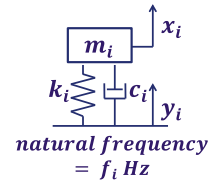
The accuracy of this computation and the computation speed may depend on the frequency resolution of the spectrum or FRF. Each spectrum used in the frequency domain should have the same resolution to perform the multiplication of Eq. 13.13 and the frequency resolution can be written as

$$\Delta f = \frac{F_s}{nfft}, \; \textit{where } F_s \textit{ is sampling frequency and nfft is number of FFT points} \tag{13.16}$$

In order to make an easy comparison between the Newmark method and IFT method, the same sampling frequency as the Newmark method should be used for the IFT method because both of the results should have the same Δt, which is the time increment. If the time increment is set very small in the Newmark method, the sampling frequency of the IFT method will be large and the computation frequency range may be much wider than the frequency of interest. On the other hand, because the time response from this IFT method will have length of the number of FFT points (nfft), the nfft should be selected to the closest 2^n ($n = 1, 2, 3 \ldots$) considering the calculation steps of the Newmark method for faster computation.

13.3.4   Shock Response Spectrum (SRS)

The SRS can be obtained with a set of time responses excited by the shock input. An input shock may be measured data or a result of the FEA. Then, this shock will be treated as a base excitation and the upper SDOF structure will be anticipated to have a natural frequency of f_i Hz, which is shown in Fig. 13.4. The m_i, k_i and c_i represent mass value, stiffness value and damping value for the additional SDOF system in physical space. The m_i, k_i may vary based on the assumed natural frequency but the system is usually assumed to have a critical damping of 5 % (or some other prescribed constant value such as 1 or 2 %); this is generally due to the fact that the actual damping is not known before the structure is built. The input signal to the SDOF system is represented as y_i and the corresponding response is described as x_i. Basically, if an additional structure is attached to an arbitrary point of the base structure, the corresponding mass and stiffness of the base structure will be affected by the structural parameters of the additional structure. However, those are assumed to have negligible effect at the base structure in the SRS computation.

The SRS is always calculated only for a set of center frequencies of 1/6 or 1/12 octave band because any values in a particular band are assumed to have almost the same value. In this work, 1/12 octave band starting from approximately 1 Hz will be used for the SRS computation, which means the SRS will be calculated for a set of natural frequencies written as

$$\text{Center frequency } f_c = 1,000 \times 2^{\frac{1}{12}n} \text{ Hz, where n} = -120, \ldots, -1, 0, 1, 2, \ldots \tag{13.17}$$

The upper frequencies and lower frequencies for each octave band will also be described as

$$\text{Upper frequency } f_u = f_c \times 2^{\frac{1}{24}} \text{ Hz} \tag{13.18}$$

$$\text{Lower frequency } f_l = f_c / 2^{\frac{1}{24}} \text{ Hz} \tag{13.19}$$

This frequency band is determined based on the reference frequency of 1,000 Hz. The highest frequency of the octave band will be determined to one-eighth times of the sampling frequency to minimalize the potential computation error [6].

In order to obtain time responses for each SDOF system, the equation of motion for the SDOF model is written as

$$m\ddot{x}_i = -c\,(\dot{x}_i - \dot{y}_i) - k\,(x_i - y_i) \tag{13.20}$$

Fig. 13.5 Example of SRS computation
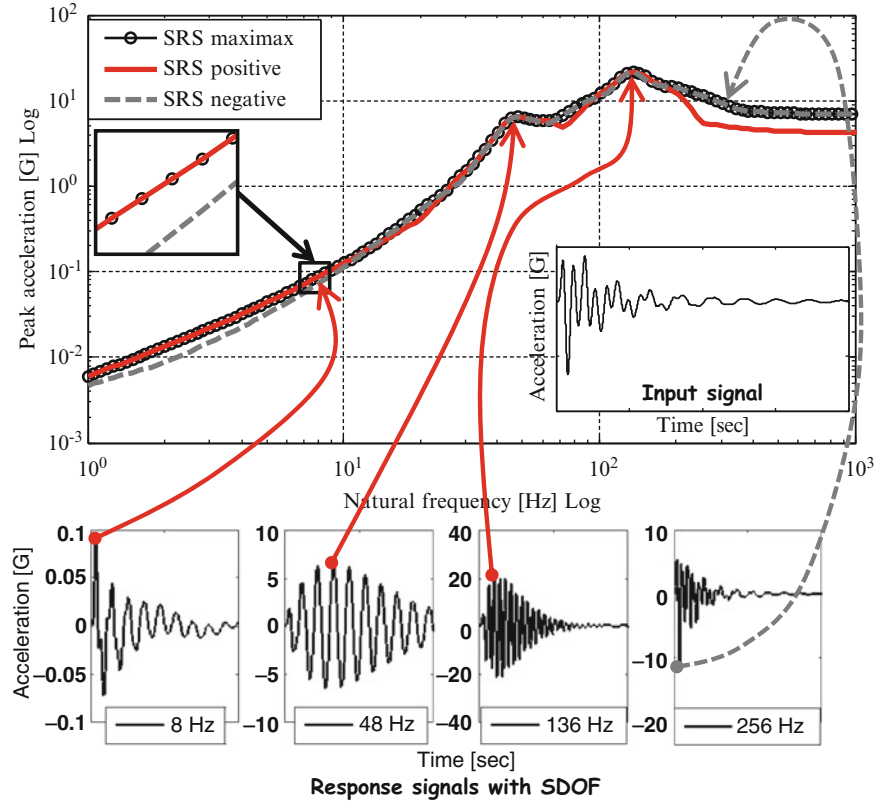
Then, $(x_i - y_i)$ can be re-written as z_i which represents the relative displacement. Using the z_i, Eq. 13.20 can be re-written to represent the relative response and its form is written as

$$\ddot{z} + 2\zeta\omega_n\dot{z} + \omega_n^2 z = -\ddot{y}(t), \ where \ \omega_n = \sqrt{\frac{k}{m}}, \ \zeta = 5\% \tag{13.21}$$

The convolution integration approach will be used in Eq. 13.21 and the final form for the acceleration response is written as [6]

$$\ddot{x}_i = 2\exp\left(-\zeta\omega_n\Delta t\right)\cos\left(\omega_d\Delta t\right)\ddot{x}_{i-1} - \exp\left(-2\zeta\omega_n\Delta t\right)\ddot{x}_{i-1}$$

$$+2\zeta\omega_n\Delta t\,\ddot{y}_i + \omega_n\Delta t\,exp\left(-\zeta\omega_n\Delta t\right)\left\{\frac{\omega_n}{\omega_d}\left(1 - 2\zeta^2\right)\sin\left(\omega_d\Delta t\right) - 2\zeta\cos\left(\omega_d\Delta t\right)\right\}\ddot{y}_{i-1}, \tag{13.22}$$

$$where \ \omega_d = \omega_n\sqrt{1 - \zeta^2}, \ \Delta t = \frac{1}{F_s} = time \ increment$$

This equation will be applied to every natural frequency of interest which is defined in Eq. 13.17 and will be treated as a FIR filter applied to an input signal [6]. Then, a set of time responses will be obtained and in those signals, the maximum response value will be identified and plotted into the SRS. The procedure is shown schematically in Fig. 13.5. The lower four plots show examples for time responses caused by a shock input which is shown in the middle of Fig. 13.5. In those response signals, the maximum value will be picked up but the response acceleration may have its maximum value in positive or negative direction. In order to distinguish the effect of direction, there are two ways the SRS calculations are performed referred to as "Maximax SRS" and "Positive/ Negative SRS". The difference of these two methods is seen in Fig. 13.5. The Maximax SRS, which will be used in this work, is used to consider the absolute value of the response acceleration because the Maximax SRS will collect the maximum absolute value. On the other hand, the Positive or Negative SRS will pick up only for the positive maximum value or negative maximum value. They are used when an additional structure might have different endurance acceleration value for positive or negative direction.

13.3.5 Contribution Analysis and Mass Sensitivity Analysis (MSA)

In order to determine the effective location for mass modification, the MSA for the eigenvalues and FRF is widely used in field of modal analysis [8, 9]. Using these MSA, the most effective location to modify the natural frequency or amplitude of response vibration can be determined to meet the design. If the relationship between the modes and peaks of the SRS can be revealed by using the contribution analysis, these MSA will be useful to customize the envelope of the SRS.

Here, two ways computing the contribution analyses will be proposed. The first method is superimposing the FRF on SRS envelope. The FRF will be computed using Eq. 13.14 but the summation will not be performed in this case because the FRF for each mode needs to be plotted separately to make the contribution clearer. By comparing the peak of the FRF and the peak of the SRS, the contribution can be better understood. For example, if the FRF has a peak at a particular frequency and if the SRS has a peak at the same frequency, a mode existing at that frequency can be considered to have a significant contribution on the SRS, which means, in order to customize the SRS, the frequency and amplitude of that mode needs be customized. In the other case, if two or three modes exist in one octave band, all of these modes may need to be customized because these modes contribute to one peak of the SRS. The second method is the SRS computation with each modal response. If a set of SRSs are computed with each modal acceleration response scaled by mode shapes, each of these SRSs will show the contribution of each modal response on the envelope of the SRS. Superimposing these SRSs with modal response on the SRS with the original physical response, the contribution will be confirmed the same as the first method.

From the contribution analyses discussed above, an evaluation is needed to define which mode needs to be modified to obtain the desired SRS. And for the mode which is identified, two approaches for mass sensitivity analyses will be used to modify the contributions of the mode; the MSA for the eigenvalues and for FRF.

The MSA for the eigenvalues represents the sensitivity for eigenvalue modification [8]. The typical form of the equation of the eigensolution for each nDOF is written as

$$\left[[K] - \omega_n{}^2 [M] \right] \{X\} = \{0\}, \ where \ n \ is \ nDOF \tag{13.23}$$

If a partial differential is applied to Eq. 13.23, the sensitivity for the eigenvalues will be obtained and its form can be written as

$$\frac{\partial \omega_n}{\partial \gamma_i} = \frac{1}{2\omega_n} \frac{\partial \omega_n{}^2}{\partial \gamma_i} = \frac{1}{2\omega_n}[U]^T \left[\frac{\partial [K]}{\partial \gamma_i} - \omega_n{}^2 \frac{\partial [M]}{\partial \gamma_i} \right] [U], \ where \ n \ is \ nDOF \ and \ fl_i \ is \ design \ variable \tag{13.24}$$

where design variable γ_i are composed only with mass number because only the mass modification will be conducted.

For example, if the mass sensitivity for the DOF 1 is required, the equation will be written as

$$\frac{\partial \omega_n}{\partial m_1} = \frac{1}{2\omega_n}[U]^T \begin{bmatrix} -\omega_n{}^2 & & & & \\ & 0 & & & \\ & & 0 & & \\ & & & 0 & \\ & & & & 0 \end{bmatrix} [U], \ where \ n \ is \ nDOF \tag{13.25}$$

This process will be done for every nDOF and each sensitivity value will be divided by the corresponding natural frequency in rad/s to regularize the values because sensitivity values of higher modes will always have higher values than the lower frequencies. Then, a sensitivity matrix with only negative values will be obtained because mass addition will lead to a decrease in the natural frequencies. The modification effect will be proportional to the modification value and, in order to increase the natural frequency, the mass value needs to be decreased.

Although the MSA for the eigenvalues can identify the effective mass location for eigenvalue modification, the sensitivity cannot estimate the behavior of the amplitude of the FRF, which means the FRF after the modification may have higher amplitude than the original one. To avoid this situation, the sensitivity analysis for the amplitude of FRF should also be considered in the customization process. The equation of motion shown in Eq. 13.1 is re-written as following in Laplace domain

$$\left[[M] s^2 + [C] s + [K] \right] \{X(s)\} = \{F(s)\} \tag{13.26}$$

Then, this equation can be transformed as

$$\{X(s)\} = \left[[M]s^2 + [C]s + [K]\right]^{-1}\{F(s)\} \tag{13.27}$$

When a unit input is applied to the DOF of the input location in the F(s), Eq. 13.27 will represent a Transfer Function for the system. Then, Eq. 13.27 will be transformed into the frequency domain and the sensitivity will be obtained by a partial differential of Eq. 13.27 as

$$\left.\frac{\partial \text{H}(s)}{\partial \gamma_i}\right|_{s=j\omega} = \left\langle -\left[[M]s^2 + [C]s + [K]\right]^{-1}\left[\frac{\partial [M]}{\partial \gamma_i}s^2 + \frac{\partial [C]}{\partial \gamma_i}s + \frac{\partial [K]}{\partial \gamma_i}\right]\{H(s)\}\right\rangle\Big|_{s=j\omega}, \tag{13.28}$$

where design variable fl_i includes only mass for every nDOF

Because this sensitivity will be obtained as a series of complex numbers, these numbers need to be transformed into different levels for easier understanding of the sensitivity [9]. In addition, these sensitivity values in a particular octave bandwidth will be summed up to describe how each mass contribute to the SRS envelope; this is based on the estimation that, in order to reduce the amplitude of the SRS, all of the values of the FRF needs to have smaller amplitude in that octave band. In order to make a comparison of wide frequency easier, each summed value will be regularized with the maximum value of each mode because the sensitivity value in higher frequency will count values for wider frequency bandwidth than the lower frequency in the octave band. Due to this, the MSA for the amplitude of the FRF will have the maximum value of 1 or −1.

Comparing these two results of the sensitivity analyses, the effective mass location to obtain the desired SRS will be identified. If the contribution of the mode on the SRS is checked with the contribution analyses proposed, these sensitivities should have direct relationship with sensitivity for the SRS and should be useful for the SRS customization.

13.3.6 Structural Dynamics Modification (SDM)

The SDM [10] will be used to compute a response time signal for the modified system. The SDM can efficiently evaluate the modified response using the modal space representation for the system (either the original set of modes or the modified set of modes).

Using the SDM, the equation of motion for undamped system after the modification is written as[1,2]

$$\left[\begin{bmatrix} \ddots & & \\ & \overline{M_1} & \\ & & \ddots \end{bmatrix} + \left[\overline{M_{12}}\right]\right]\{\ddot{p}_1\} + \left[\begin{bmatrix} \ddots & & \\ & \overline{K_1} & \\ & & \ddots \end{bmatrix} + \left[\overline{K_{12}}\right]\right]\{p_1\} = 0, \tag{13.29}$$

$$\text{where } \left[\overline{M_{12}}\right] = [U_1]^T[\Delta M][U_1] \; and \; \left[\overline{K_{12}}\right] = [U_1]^T[\Delta K][U_1]$$

Here, $\left[\overline{M_{12}}\right]$ and $\left[\overline{K_{12}}\right]$ represent the modification effect in modal space. If the eigensolution is applied to Eq. 13.29, a set of new eigenvalues and eigenvector will be obtained. The eigenvalues from this solution represents a set of new natural frequencies for the modified system. The eigenvectors from Eq. 13.29 will provide

$$\{p_1\} = [U_{12}]\{p_2\} \tag{13.30}$$

With Eqs. 13.29 and 13.30, the equation of motion for the modified undamped system in modal space will be written as

---

[1]For the SDM, subscript 1 means parameter for the original model and subscript 2 means parameters for the modified model. In general, original structural and modal matrices will be presented without any subscripts.

[2]A term written in capital alphabet means matrix. A term with small alphabet means a component of matrix. For example, $\overline{M}$ means a modal mass matrix and $\overline{m}_i$ means a modal mass value for "i"th mode.

$$\begin{bmatrix} \ddots & & \\ & \overline{M_2} & \\ & & \ddots \end{bmatrix} \{\ddot{p}_2\} + \begin{bmatrix} \ddots & & \\ & \overline{K_2} & \\ & & \ddots \end{bmatrix} \{p_2\} = \{0\},$$

(13.31)

$$\text{where} \begin{bmatrix} \ddots & & \\ & \overline{M_2} & \\ & & \ddots \end{bmatrix} \rightarrow \begin{bmatrix} \ddots & & \\ & I & \\ & & \ddots \end{bmatrix} \text{ and } \begin{bmatrix} \ddots & & \\ & \overline{K_2} & \\ & & \ddots \end{bmatrix} \rightarrow \begin{bmatrix} \ddots & & \\ & \omega_2{}^2 & \\ & & \ddots \end{bmatrix}$$

The modified modal damping matrix $\overline{C_2}$ can also be obtained using Eq. 13.7 with the modified modal mass and stiffness matrices. Using these modal parameters, the Newmark method or the IFT method will be performed to obtain a time response for the modified system. If the time response computation is conducted in modal space with the Newmark solution, the response signal will be transformed back into physical space using mode shapes for the modified system which is written as

$$\{X_2\} = [U_2]\{p_2\} = [U_1][U_{12}]\{p_2\}$$

(13.32)

This summarizes the major tools that are necessary for the analysis of the response for the SRS computations. The next sections cover the two example systems: a simple analytical 5-DOF system and a beam structure (both a finite element model and experimental configuration).

13.4 Analytical Example for 5-DOF System

13.4.1 Trial of the Methodology for Customizing SRS

In this section, the methodology proposed in this paper will be presented with a simple example of a 5-DOF system. The model used here and its structural parameters are shown in Fig. 13.6 with system data shown in Table 13.1. For this model, the modal solution will be applied and the acceleration response will be computed both in the time domain and the frequency domain using Eq. 13.11 or 13.13. These two responses from the Newmark method and IFT method will be treated as input signals for the SRS computation for the original system. Then, an arbitrary peak will be chosen to demonstrate the methodology for SRS customization. In order to modify the peak of the SRS, the mode contribution will be performed and the MSA will be applied to identify the most effective mass location for the modification. For this location, the SDM will be conducted and the modified acceleration response will be computed using Eq. 13.31 and Eq. 13.32. Finally, the SRS for the modified system will be computed and the effect of the modification will be judged comparing the difference in the SRS.

For the 5-DOF model, the physical mass and stiffness matrices are developed and the eigensolution will be performed using Eq. 13.2 with the results shown in Table 13.1. Using Eqs. 13.5, 13.6 and 13.7, the modal mass, stiffness and damping matrix will also be obtained assuming that the critical damping is 5 % for every mode.

In order to obtain the acceleration time response, an input force needs to be applied. For this study, a simple half sine pulse shown in Fig. 13.7 is used. Then, the Newmark solution is performed with the modal parameters obtained to compute the modal responses and all of the modal responses will be used to calculate the physical response shown in Fig. 13.8. The Newmark solution performs the time integration in every 2.441e−5 s for 0.2 s time duration. The time duration is determined

Fig. 13.6 5-DOF model used

$$m_1 = m_2 = m_3 = m_4 = m_5 = 1\ [lbf]$$
$$k_1 = k_2 = k_3 = k_4 = k_5 = 1e6\ [lbf/in]$$
$$\text{Critical damping } \zeta = 5\ [\%]\ \text{for every mode}$$
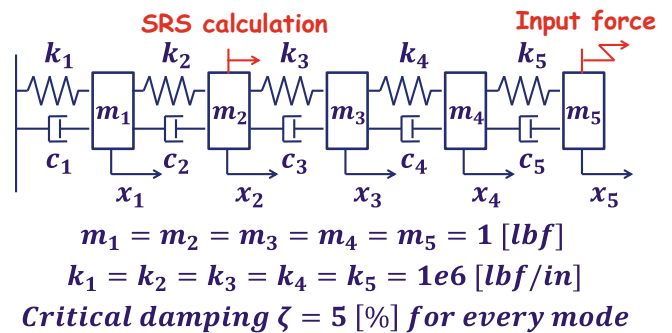
Table 13.1 Parameters for each mode

Mode number	Natural frequency (Hz)	Mode shapes	Critical damping (%)
1st	45.30		5
2nd	132.23		5
3rd	208.45		5
4th	267.78		5
5th	305.42		5

Fig. 13.7 Applied input force
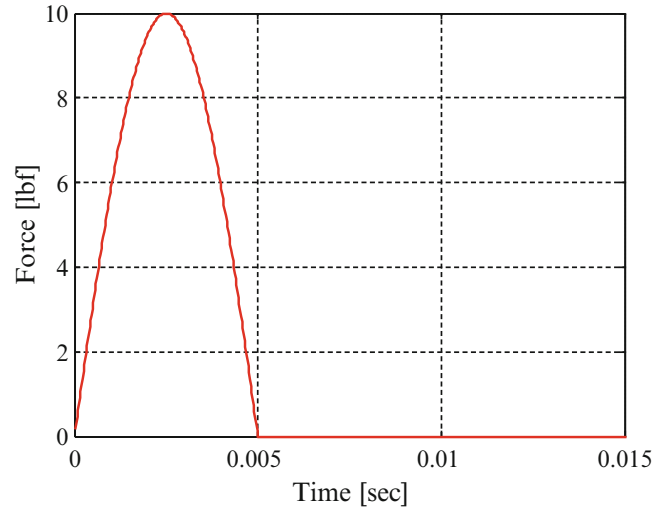
Fig. 13.8 Acceleration response with Newmark method
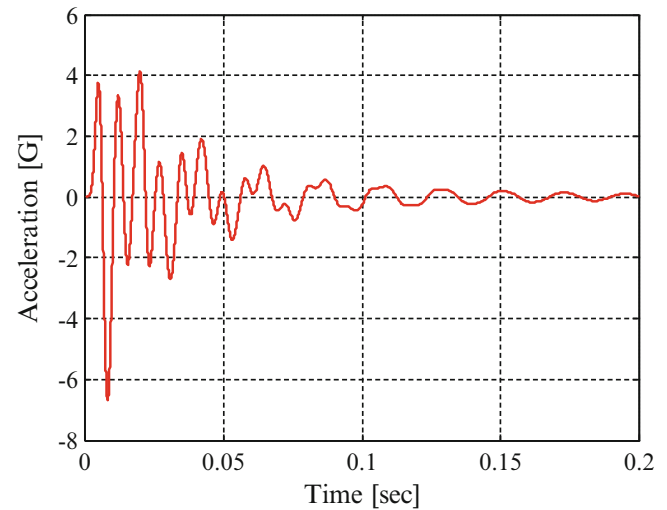
based on the damped response because the signal should be damped well in the time block to avoid the leakage error in the FFT or IFT. The valid upper frequency for this computation is considered as 4,096 Hz because the sampling frequency used is 40,960 Hz. Although this is much higher than the highest natural frequency of the system, the sampling frequency needs to be very high to allow small time increment to obtain the peak value in the resulting time signal correctly.

Because the time response will also be computed in the frequency domain, the input force will be transformed into the frequency domain using the FFT and the result is shown in Fig. 13.9. The nfft used is 131,072 and, with this value and the sampling frequency of 40,960 Hz, the frequency resolution for the spectrum will be 0.3125 Hz. Applying the modal parameters which are obtained from the eigensolution into Eq. 13.14, the FRF for the 5-DOF system can be obtained and is shown in Fig. 13.10 in terms of accelerance. With this FRF and the input spectrum obtained, the response spectrum will be calculated using Eq. 13.13. For the response spectrum obtained, IFT will be applied to obtain the time signal and the

Fig. 13.9 Input force spectrum
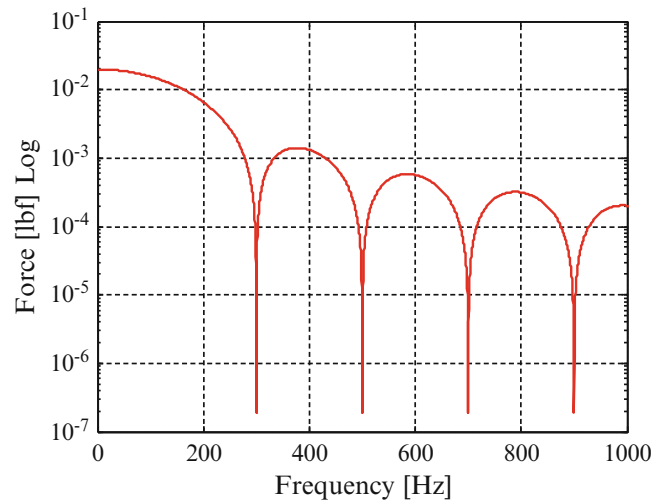
Fig. 13.10 FRF with modal solution
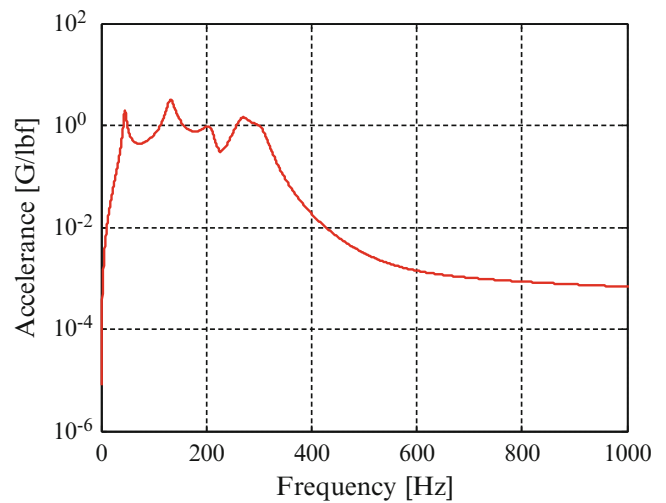
Fig. 13.11 Comparison of time response
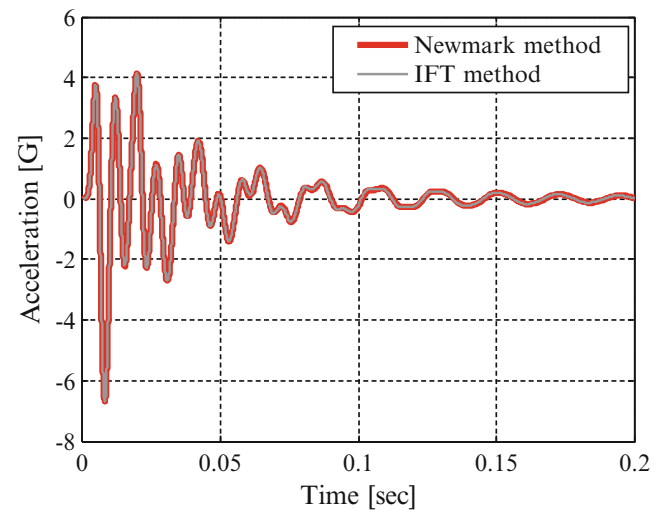
response signal will originally have length of 131,072 but only the first $Fs \times 0.2$ set of data will be used. The result is shown in Fig. 13.11 and the time response with the Newmark method is overlaid. Both of the signals compare well with less than 0.2 % difference on the peak point.

Using the acceleration signals computed from the Newmark method or IFT method shown in Fig. 13.11, the SRS will be developed using 1/12 octave band shown in Eq. 13.17. For each additional SDOF system whose natural frequency is the

Fig. 13.12 Comparison of SRS
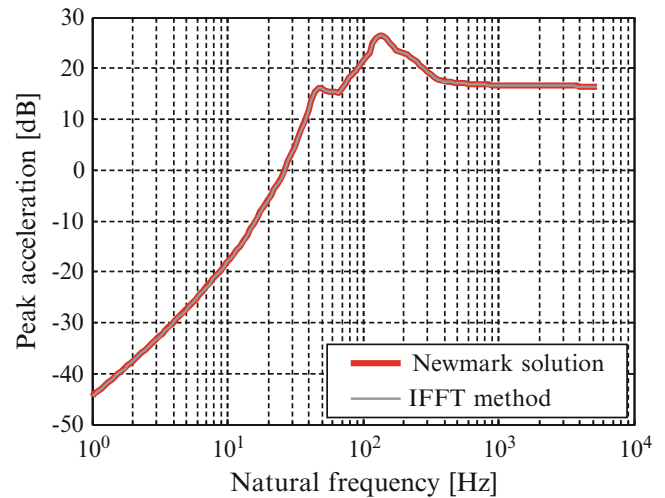
Fig. 13.13 FRF versus SRS
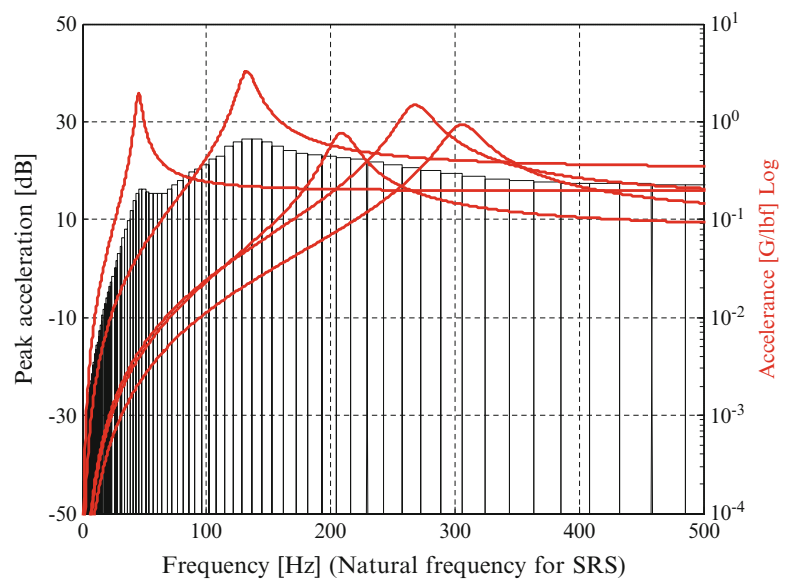
center frequency of the octave band, the maximum acceleration response value will be obtained with Eq. 13.22. The percent of critical damping of the SDOF system is assumed to be 5 %. Figure 13.12 shows the SRS developed with the time domain response and frequency domain response solution and the SRS is calculated up to one-eighth of the sampling frequency of the input signal, which is approximately 5,000 Hz. In this work, the SRS is plotted in decibel scaling with the reference value of 1 G; note that this value is different from the reference value defined in ISO 1683 [11]. Because both of SRSs shown in Fig. 13.12 provide almost the same result with less than 0.3 % difference in the maximum peak, both solutions in the time domain and frequency domain are considered to be useful for the SRS computation. However, the IFT method provides only the physical response and this is not convenient for entire flow of this work because the modal responses will be required to perform the contribution analysis. Due to this, the IFT method will be performed only for the comparison of the original SRS computation with the Newmark solution and will not be used for the SRS customization procedure.

The maximum peak on the SRS is found as a peak around 132 Hz. For the SRS customization procedure, this peak will be used for the demonstration of the methodology. In order to evaluate the relationship between the modes and peaks of the SRS, the contribution analysis will be performed in two ways: superimposing the FRF on the SRS or the SRS computation with modal response.

In Fig. 13.13, the FRF is superimposed on the SRS and the left Y-axis shows values of the SRS and the right Y-axis shows values of the FRF. The SRS is plotted in the form of bar graph because the relationship between a particular peak of the FRF and the value of a particular octave band will be obvious. From this result, each of the first and second modes is considered to have high contribution to each of the first and second peak of the SRS because the FRF has peaks close to the peak frequency

Fig. 13.14 SRS with modal
response
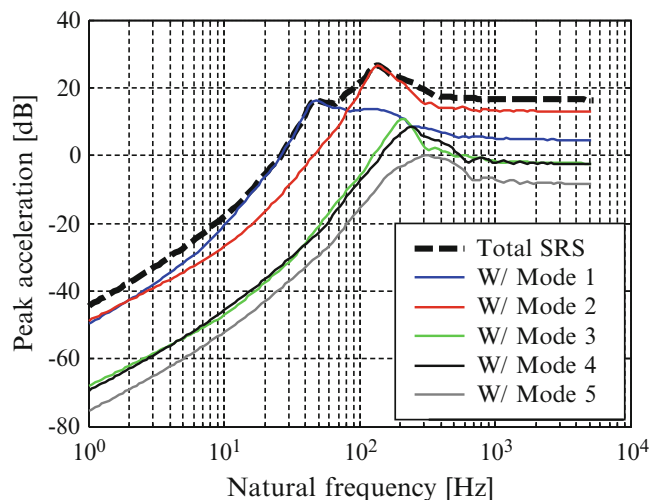
Fig. 13.15 MSA for the
eigenvalues
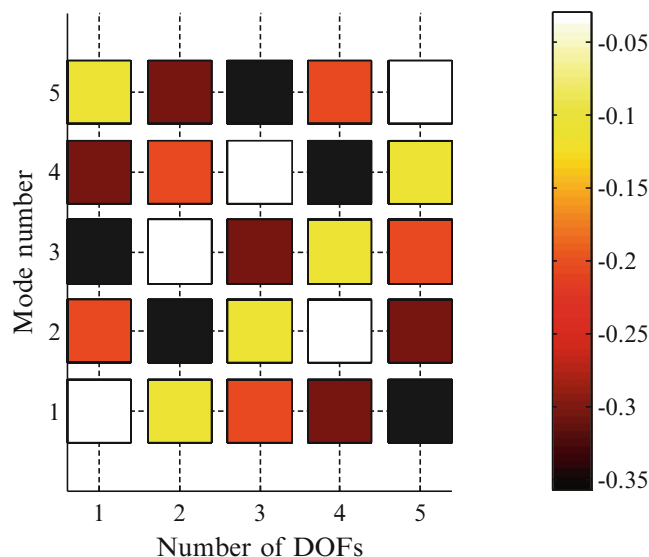
of the SRS. However, the third, fourth and fifth modes are considered to have small contribution because there are no obvious peaks of the SRS near to the peaks of the FRF.

In Fig. 13.14, each modal response which is computed with the Newmark method is used for the SRS computation. These modal responses used are scaled by the mode shapes separately and each SRS obtained is influenced only by each mode. Here, the SRSs with the first and second modal response have approximately the same peak values as the original SRS at the first and second peak. However, the SRSs with the third, fourth and fifth modal response have smaller values than the original SRS. Due to this, the first and second modes are considered to have strong contribution to the SRS but the others do not.

As a result, the maximum peak of this SRS is considered as being influenced largely by the second mode of the system. Because these contribution analyses showed the second mode of the system contributes to the second peak of the SRS strongly, in order to identify the most effective location for the modification, the MSA will be applied to the 5-DOF system.

Using Eq. 13.24, the MSA for the eigenvalues will be obtained as shown in Fig. 13.15 and the X-axis represents the DOF of the system and the Y-axis represents the number of modes. From this result, the DOF 2 or 5 are considered to be useful to lower the natural frequency of the second mode. On the other hand, the DOF 4 is thought to have small effect for eigenvalue modification because the DOF 4 is a node of the mode.

In addition, in order to identify the most effective location to decrease the amplitude of the FRF, the MSA for FRF will also be performed using Eq. 13.28. In this case, the MSA for FRF is summed up with bandwidths of seven octave bands each of which have the peak octave band at the middle, which means the result will show the sensitivity of amplitude reduction in those octave band entirely and which describes the effectiveness of the locations to modify each peak of the SRS. The

Fig. 13.16 MSA for FRF
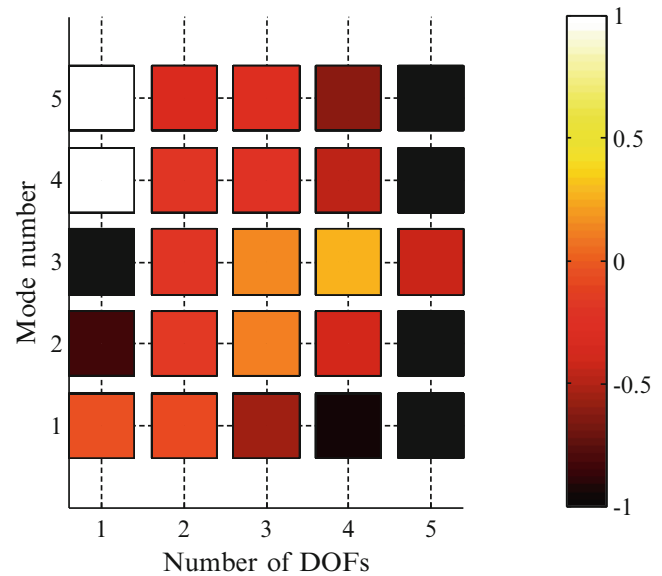
Table 13.2 Comparison of natural frequencies

| Mode number | Natural frequency (Hz) | | Diff. (%) |
	Original	Modified	
1st	45.30	41.55	−9.02
2nd	132.23	124.23	−6.44
3rd	208.45	200.99	−3.71
4th	267.78	263.49	−1.63
5th	305.42	304.20	−0.40

result is shown in Fig. 13.16 and the DOF 5 is considered to be effective for lowering the amplitude of the second mode because of the maximum sensitivity. If the MSA for FRF outputs positive values such as that for mode number 4 or 5 for the modification of DOF 1, the FRF modified will have higher amplitude in those defined frequency bandwidth.

If the goal of the modification is lowering the natural frequency and reducing amplitude of the FRF, then DOF 5 can be considered to be proper for the modification because this location has high sensitivity values for both sensitivity analyses.

In order to customize the second peak of the SRS, the SDM will be performed by increasing the mass value of the DOF 5 by + 50 % from the original model to check the effect. From Eq. 13.31, the natural frequency for the modified system will be achieved and, in Table 13.2, these values are shown with comparison of the original values. From this result, the natural frequency of the second mode is confirmed to be decreased from the original value.

In order to verify the change in the FRF, the original and modified FRF are superimposed in Fig. 13.17. Here, the modified FRF is computed using Eq. 13.14 with the modified modal parameters obtained from the SDM and a reference solution which is performing a modal solution directly on the modified system. These two modified FRFs are the same and have smaller amplitude at the second mode than the original FRF. Using the same set of modal parameters used for the FRF computation, the modified time response can be calculated with the Newmark method in modal space. The modified physical response from the SDM and the reference solution is shown in Fig. 13.18 and compared to the original response and two of the modified responses compare well. These accelerations are used for the SRS computation and the result is shown in Fig. 13.19. The modified SRS has smaller amplitude for the second peak and the peak frequency is shifted lower. The maximum peak frequency is shifted by 7 Hz and its amplitude is decreased by 3 dB. The modified SRSs with the SDM and the reference solution are the same because the signals used for the calculation are also the same. Due to this, the effect of the SRS modification can be measured with the modified response using the SDM procedure.

Although these figures showed good results and the modified SRS achieved the goal defined, the mass location of the modification may not be the best because the modification was attempted only for one location. In order to confirm the methodology, the same SDM procedure will be applied to every DOF and the modification value is consistently set to +50 %. Figure 13.20 shows the result and the DOF 5 is confirmed to have the smallest amplitude for the second peak of the FRF with the biggest frequency shift in these five patterns. Due to this, the methodology for customizing the SRS to meet the design is considered to be appropriate. In addition, the modification effect will be checked using various modification

Fig. 13.17 Comparison of FRF
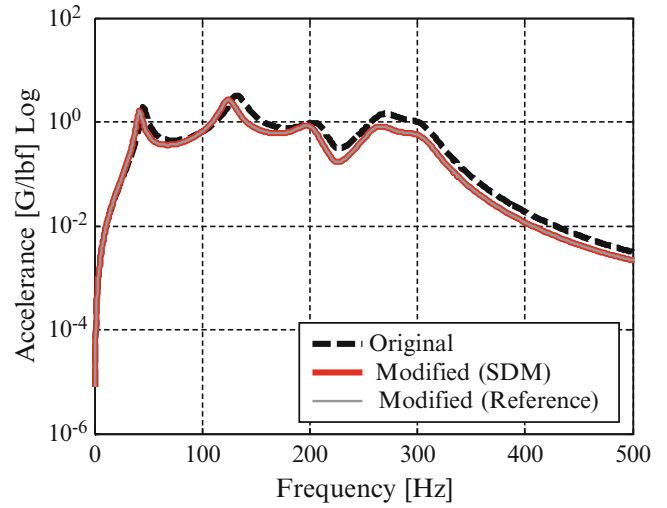
Fig. 13.18 Comparison of time signal
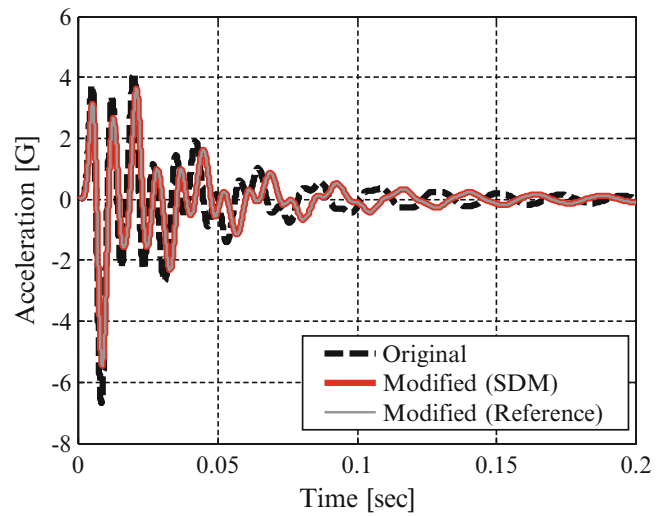
Fig. 13.19 Comparison of SRS
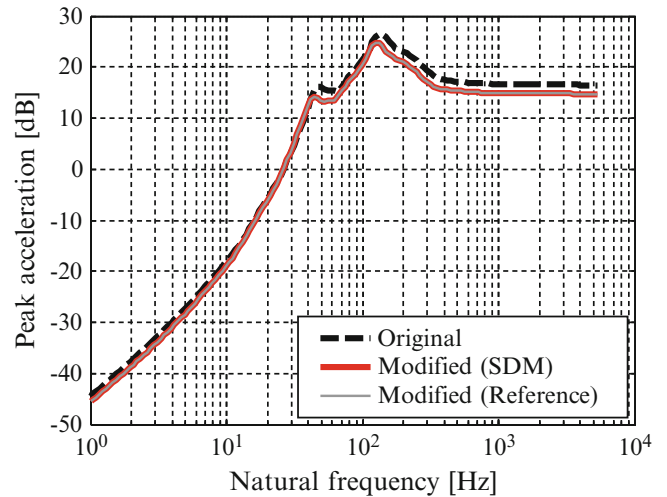
values for the best modification location of the DOF 5. Figure 13.21 shows the result for four different modification values: +10, +30, +50 and +100 %. From this result, the modification effect on the SRS is confirmed to be proportional to the modification value. If the value is modified significantly, the SRS will also be modified significantly but the modification value should be determined in a feasible range because +100 % modification may not be realistic for an actual design.

Fig. 13.20 Effect of
modification location
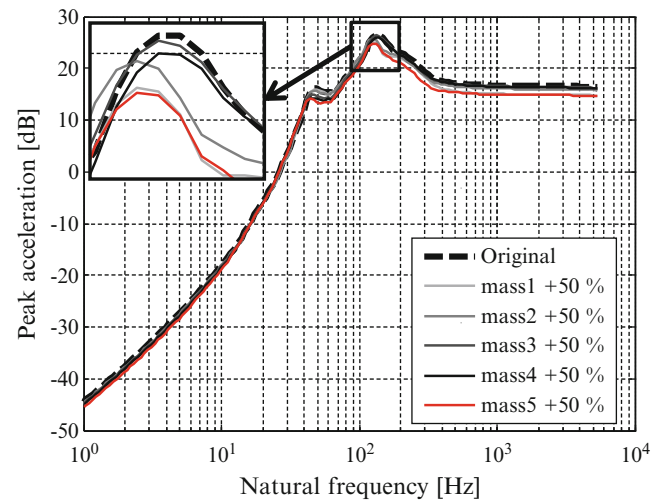
Fig. 13.21 Effect of
modification value
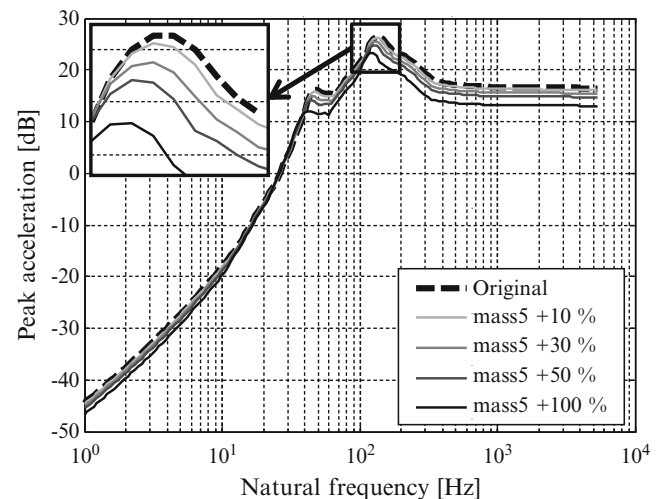
13.4.2 Proper Configurations for SRS Computation

Here, the following three configurations will be discussed for the proper SRS computation: the time duration of the input signal used for the SRS computation, the sampling frequency for that time signal, the number of modes used for the time signal computation.

The SRS developed in the previous section uses the acceleration signal with 0.2 s duration for its development. Because the specification of some frequency components may not clearly appear in a shorter time window, five different time lengths will be used for the discussion: 0.01, 0.05, 0.1, 0.2 and 0.5 s. The sampling frequency is set to 40,960 Hz and all of the modes are used for the time response computation with the Newmark method. Figure 13.22a shows the difference of the time signals and within approximately 0.2 s, the signal is considered to be damped well. Figure 13.22b shows a comparison of the SRSs computed with these five signals. From this result, if the signal for the SRS computation is too short like 0.01 s, which is just twice the input pulse duration, the SRS obtained will have different envelope from others because the each modal response has not achieved their maximum response. On the other hand, if a signal used for the SRS is long enough such as 0.1, 0.2 or 0.5 s, the response signal is considered to be adequate to collect the maximum response value to compose the envelope of the SRS because the peak specifications of the SRS are the same for these time signals. Due to this, the signal used for the computation needs to be long enough to collect the maximum response values but does not necessarily need to be damped well in the time span to estimate the peak values from the development of the SRS.

The sampling frequency will affect not only the upper frequency limit of the SRS computation but the peak values of the SRS because the acceleration time signal may have different peak values based on the time increment of the Newmark method if the sampling frequency is low. Here, some sampling frequencies will be used to discuss the effect; 2,560, 5,120, 10,240, 20,480 and 40,960 Hz. Time length of input signal is set to 0.2 s because 0.2 s signal was considered to be long
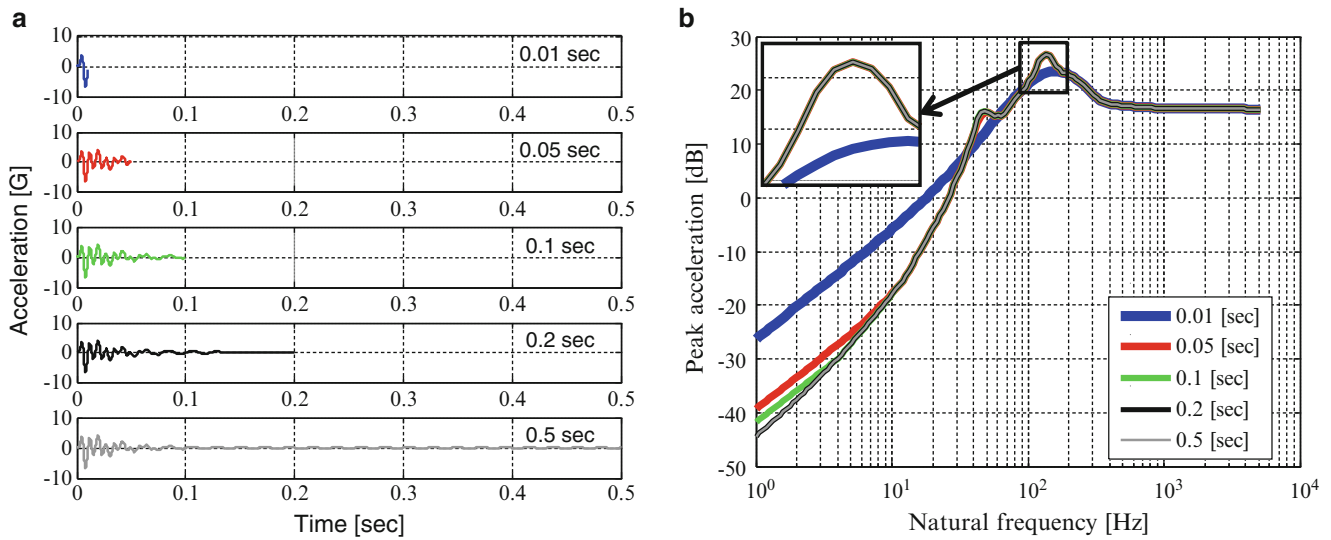
Fig. 13.22 Effect of input time length (**a**) acceleration signal, (**b**) SRS comparison
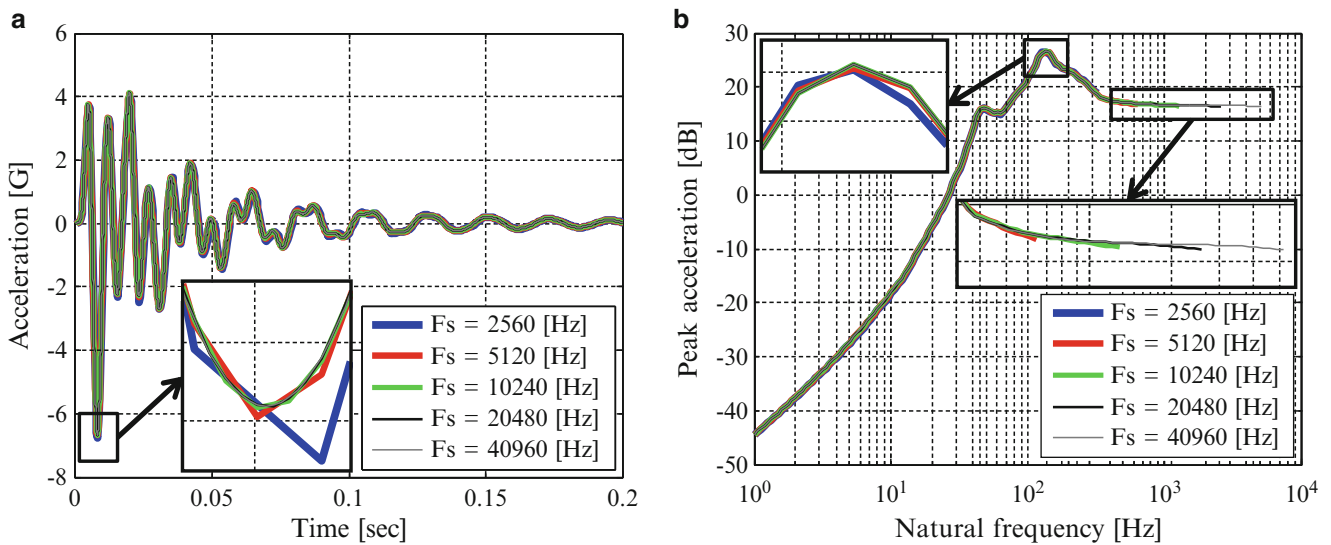
Fig. 13.23 Effect of sampling frequency (**a**) acceleration signal, (**b**) SRS comparison

enough for this study from the previous section and all modes are used for physical response computation. Figure 13.23a shows the effect of different sampling frequencies and there are some differences seen at some peaks as discussed above. This is because a signal with high sampling frequency has smaller time increment and high number of data points so the peak values are identified well. However, for the SRS shown in Fig. 13.23b, all of the signals have almost the same value. Because the SRS computation is done in every octave band, slight difference in amplitude or frequency of the input signal may not be so important for the SRS computation. As a result, although the sampling frequency does not affect the peak values of the SRS that much, the value should be high enough to reproduce a peak value in the time domain well and should be determined based on the upper limit of the frequency of interest.

This work uses the physical acceleration with the modal superposition techniques for the SRS computation if the computation is performed in the time domain. Here, the number of modes can be limited for faster computation. Although the computation will be faster if small number of modes is used, specification of the SRS may degrade. In order to check this effect, the number of modes used for the computation will be changed; only the first mode, first two modes, first three modes, first four modes and all modes. The time length and sampling frequency are set to 0.2 s and 40,960 Hz based on the previous considerations. Figure 13.24a shows a comparison of acceleration signals and these signals are used for the SRS computation. Figure 13.24b shows a comparison of the SRS. Of course, if a large number of modes is used for the
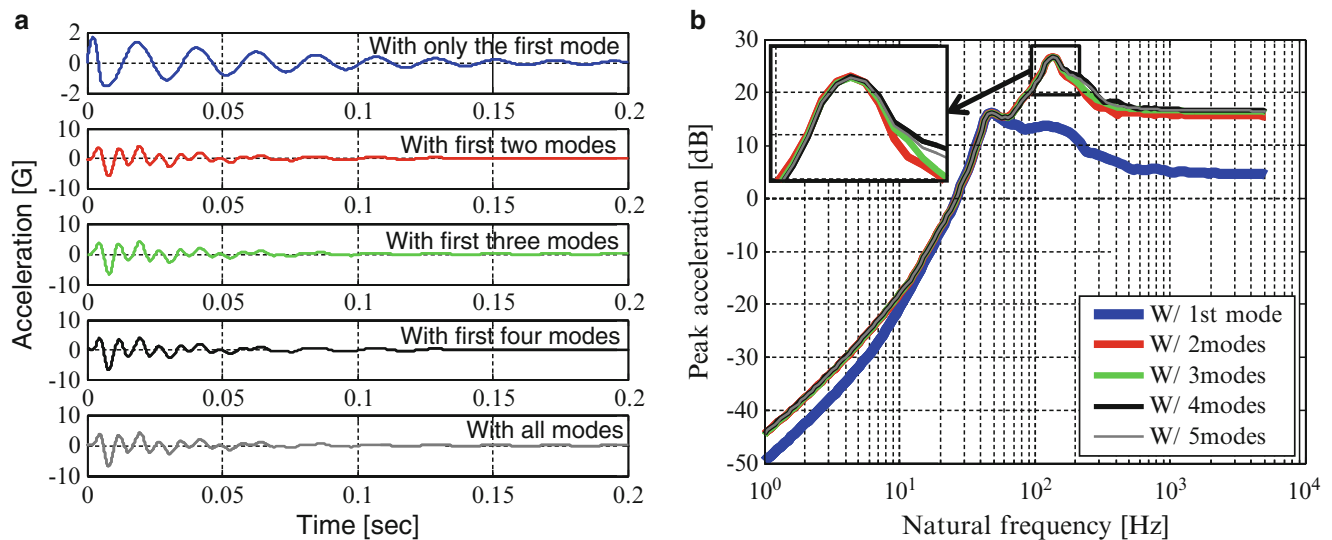
Fig. 13.24 Effect of number of modes (**a**) acceleration signal, (**b**) SRS comparison

computation, a more correct SRS will be obtained but the maximum peak value of the SRS can be estimated with the limited number of modes if the modal response which may cause the maximum response is included. For example, if the second peak of the SRS is dominant and if the second mode contributes to the peak well, the SRS calculated with the first two modes is enough to evaluate the maximum peak value.

13.5 Analytical/Experimental Example for Beam Structure

13.5.1 Experimental SRS Measurement/EMA for Acquiring Modal Parameter

For the studies performed here, a beam shown in Fig. 13.25 will be used to evaluate the methodology. The beam which has cross section of 2 in. by 1 in. with 6 ft length is suspended on the upper end of the beam to simulate free-free configuration. Free-free configuration is chosen because of its simplicity in the boundary condition. This beam is made of aluminum and the surface is covered with duct tape to provide some damping. An input force is applied to the lower end of the beam #19 and the SRS will be developed at the location of #8 which is 28 in. away from the upper end. For constant input, a pendulum shown in Fig. 13.25 is utilized and a load cell is introduced to the weight of the pendulum to measure the input signal and a soft tip is attached on the load cell. In order to measure the acceleration signal, an accelerometer is located to the location of #8.

For a proper experimental SRS measurement, some configurations including the measurement time duration, the sampling frequency and the number of modes used for signal computation need to be determined. Although the sampling frequency may affect the peak value of SRS and will limit the upper frequency, the sampling frequency is set to 40,960 Hz because this value will provide a small enough time increment and the computation time may be long if higher sampling frequency is used. Here, the acceleration signals with four different time lengths will be measured: 1.6, 4.0, 8.0 and 16 s time duration. Figure 13.26 shows the difference in the input time signals used for these four measurements and the pendulum is confirmed to produce essentially the same input consistently with less than 2 % difference in the peak value. These input signals cause the acceleration response at the output location and Fig. 13.27 shows the measured acceleration responses. Because the input signals have similar envelope and amplitude, the output signals also have high similarity. Using these acceleration signals, the experimental SRSs are developed using Eq. 13.22 and Fig. 13.28 shows the result. From this result, the SRS with the 1.6 s time duration signal is different from others in low frequency but all of them except for 1.6 s have high similarity for every peak of their SRS in high frequency. Due to this, the acceleration signal with 4.0 s length is considered to be long enough for the SRS computation for this case. Although the signal with 4.0 s duration is not damped well in its time duration, the SRS with 4.0 s signal has high similarity as SRSs with longer time duration because the maximum response values caused by the input signal are obtained in that duration. Furthermore, because the peak values of these four SRSs are almost the same, the input forces with less than 2 % difference are considered to be sufficient for measuring the effect of the modification. For the

Fig. 13.25 Measurement setup
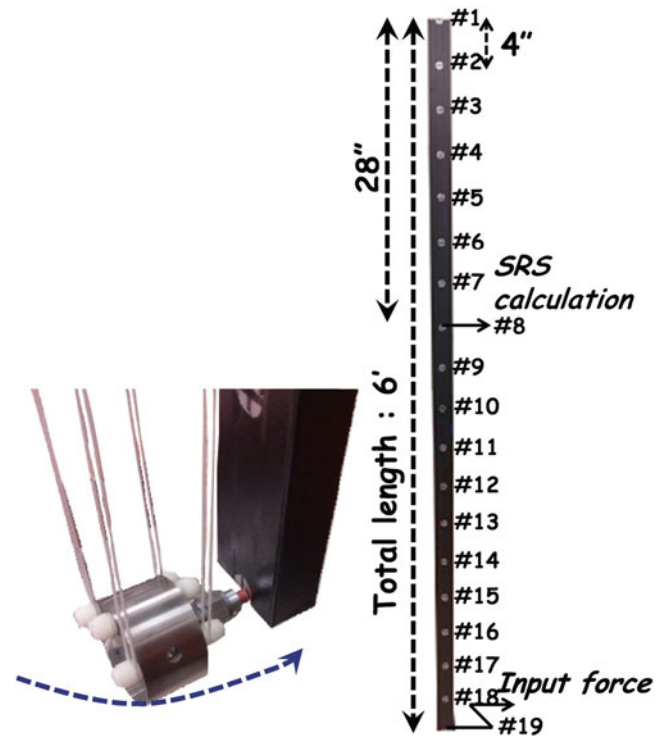
Fig. 13.26 Input signal
comparison
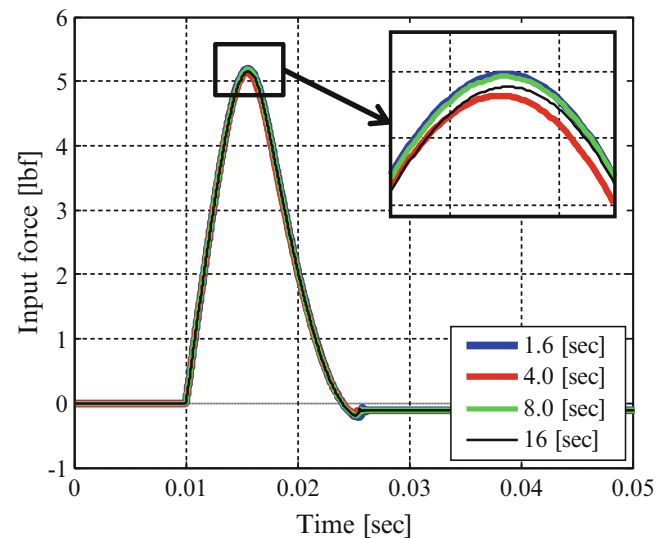
customization procedure, the biggest peak near 40 Hz will be used. The frequency of interest can be set as up to 2 kHz based on the envelope of the SRS and the physical response will be calculated with modes existing lower than 2 kHz.

Based on the frequency range of interest determined, the EMA will be conducted to develop a proper experimental or analytical model. Using three kinds of modal impact hammers, a set of FRFs will be measured to estimate the mode shapes, natural frequencies and dampings. The following three different configurations will be used for the EMA.

Configuration (i): Fs = 512 Hz, nfft: 32,768, $\triangle$f = 0.016 Hz, T = 64.0 s
Configuration (ii): Fs = 1,280 Hz, nfft = 32,768, $\triangle$f = 0.039 Hz, T = 25.6 s
Configuration (iii): Fs = 5,120 Hz, nfft = 32,768, $\triangle$f = 0.156 Hz, T = 6.4 s
(Fs: sampling frequency, $\triangle$f: frequency resolution, T: acquisition time)

These configurations are determined based on the estimation that lower modes might have low damping. Because a proper damping value is required for better SRS computation and applying any windows is not proper for better damping value estimation, the signal needs to be decayed well within the acquisition time to avoid the leakage error. The examples of the input forces and modal hammers used are shown in Fig. 13.29. With these hammers, the input forces will be added

Fig. 13.27 Output signal comparison
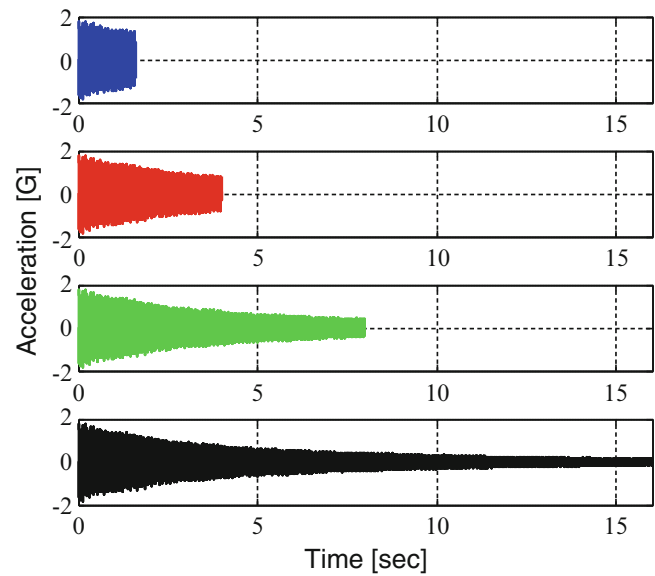
Fig. 13.28 SRS with various time spans
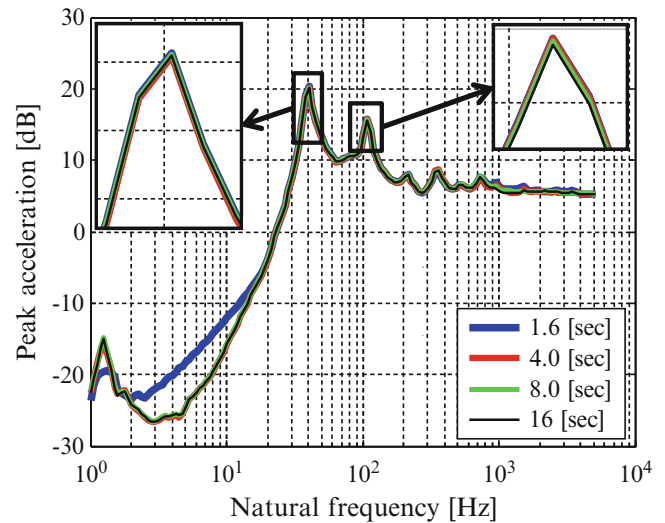
to all of the locations starting from #1 to #19. An accelerometer is consistently placed at the location #8 to measure the response acceleration and then, 19 sets of FRFs will be obtained with the three different configurations. Figure 13.30 shows the example of the FRFs measured with these three configurations between the input location #19 and the output location #8. Due to the leakage error depending on the short acquisition time, modal parameters of the first few modes are hard to estimate from the FRF shown in Fig. 13.30c which is measured with the configuration (iii). On the other hand, using a proper configuration, which is configuration (i), these modal parameters for the first few modes can be measured from the FRF shown in Fig. 13.30a. The first two rigid-body modes and two bending modes will be extracted from the FRF with the configuration (i) and the next three bending modes will be extracted with the configuration (ii) and for the other modes exist lower than 2 kHz, the configuration (iii) will be used. Table 13.3 shows the results of the EMA and the frequencies, damping and some examples of mode shapes are shown. Applying these parameters into Eqs. 13.5, 13.6 and 13.7, the modal mass, stiffness and damping matrices will be developed and the equation of motion will be developed experimentally. Figure 13.31 shows the FRF computed with these data using Eq. 13.14 compared to the measured FRF with the configuration (iii). This FRF will be called the synthesized FRF and this FRF will be used for the discussion of the contribution analysis and the SDM. The measured FRF has torsional modes at some frequencies but the synthesized does not because the modal parameters are extracted only for bending modes.

Fig. 13.29 Example of input forces
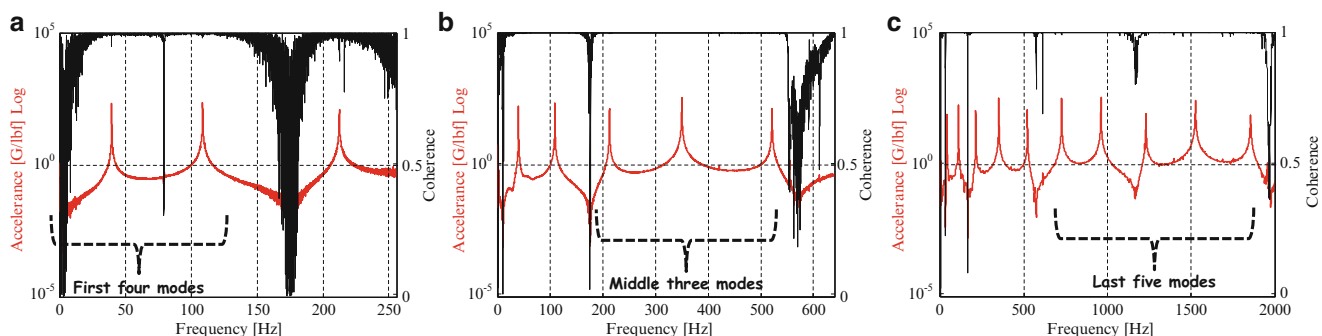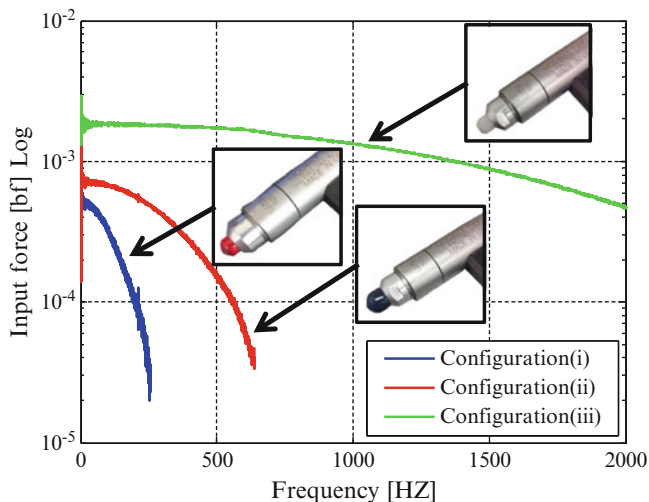
Fig. 13.30 Comparison of measured FRFs (**a**) FRF with configuration (i), (**b**) FRF with configuration (ii), (**c**) FRF with configuration (iii)

Table 13.3 Results of EMA

Mode #	Mode name	Natural frequency [Hz]	Mode shapes	Damping [%]
1	1st rigid-body	1.251		0.2309
2	2nd rigid-body	1.713		1.0244
3	1st bending	39.437		0.0272
4	2nd bending	108.478		0.0259
5	3rd bending	212.418		0.0283
6	4th bending	349.881		0.0260
7	5th bending	521.407		0.0209
8	6th bending	725.244		0.0193
9	7th bending	961.455		0.0232
10	8th bending	1230.080		0.0319
11	9th bending	1525.900		0.0346
12	10th bending	1855.130		0.0523

13.5.2 FE Model Development Using Measured Modal Parameters

In order to calculate a SRS from the FEA and compare the SRS with the one from the experiment or the EMA, an FE model will be developed to simulate the experimental model as shown in Fig. 13.32. The mass and stiffness matrices were developed using planar beam theory. The beam is made of aluminum, the mass density is 2.588e−4, the Young's modulus E is 10e6 psi and the moment of inertia I = $\frac{ab^3}{12}$ is 6.510e−4 in ^3 considering the rectangular cross section. The beam model is

Fig. 13.31 Synthesized FRF by EMA
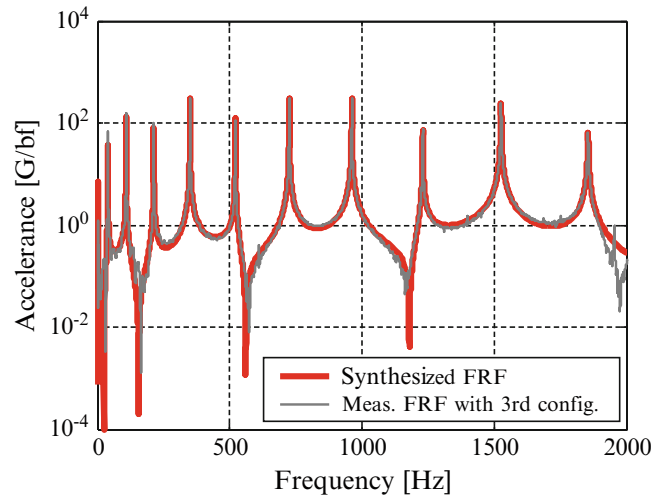
Fig. 13.32 FEA model
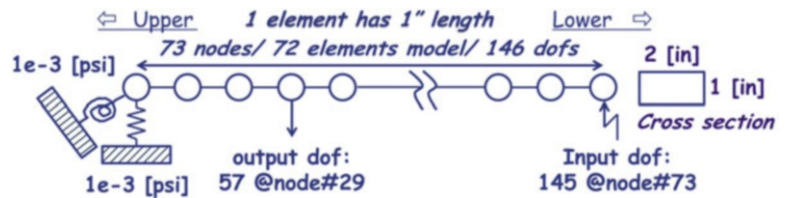
Table 13.4 Comparison of eigenvalues

Mode #	Mode name	Natural frequency (Hz)		Diff. (%)
		EMA	FEA	
1	1st rigid-body	1.251	0.0033	−3.78E+4
2	2nd rigid-body	1.713	0.0522	−3.18E+3
3	1st bending	39.437	38.98	−1.17
4	2nd bending	108.478	107.44	−0.97
5	3rd bending	212.418	210.63	−0.85
6	4th bending	349.881	348.18	−0.49
7	5th bending	521.407	520.13	−0.25
8	6th bending	725.244	726.46	0.17
9	7th bending	961.455	967.18	0.59
10	8th bending	1,230.080	1,242.30	0.98
11	9th bending	1,525.900	1,551.81	1.64
12	10th bending	1,855.130	1,895.72	2.14

evaluated in a free-free condition with very soft end springs. For the mass and stiffness matrices developed, an eigensolution is performed and these eigenvalues obtained are shown in Table 13.4 with comparison of the EMA data and the flexible mode natural frequencies are in very good agreement. The mode shapes from the FEA are shown in Fig. 13.33. The mode shapes from the EMA and FEA are compared using the Modal Assurance Criteria (MAC) given as

$$MAC_{ij} = \frac{\left(\{U_i\}^T\{U_j\}\right)^2}{\left(\{U_i\}^T\{U_i\}\right)\left(\{U_j\}^T\{U_j\}\right)}, \; \textit{where } U_i \textit{ and } U_j \textit{ represent mode shapes at j or k} \qquad (13.33)$$

All the vectors are very well correlated as seen in Fig. 13.34 except for the rigid body modes which are not of importance for the studies here. Using Eqs. 13.5 and 13.6, the modal mass and stiffness matrices will be computed from the FEA and, for modal damping matrix, the modal damping values measured in the EMA, which is shown in Table 13.3, will be used with Eq. 13.7. With these matrices, the equation of motion in modal space will be developed and the FRF will also be calculated. Figure 13.35 shows the comparison of the FRFs obtained from the EMA and FEA. These results are similar because the natural frequency and mode shapes of both models are very similar and the measured damping values are used for both computations. These FRFs will be used to compute a time response with the IFT method and used to compare the effect of the modification.

Fig. 13.33 Mode shapes (FEA)
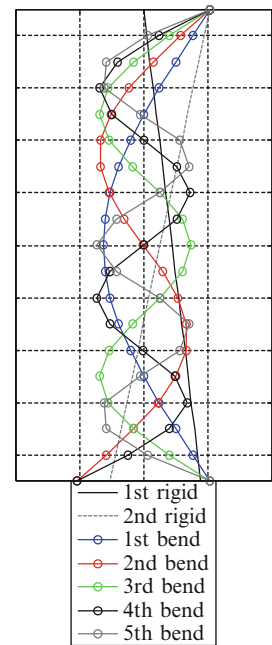
Fig. 13.34 MAC (FEA versus EMA)
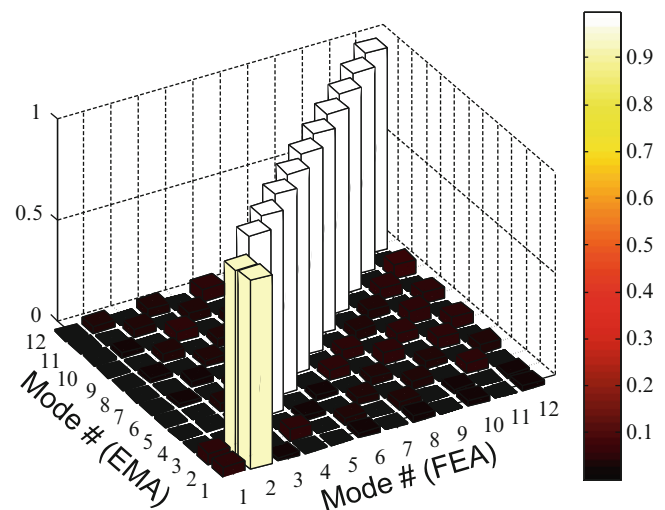
13.5.3   SRS Computation with Time Response from Measured Data/EMA/FEA

With the modal parameters obtained from the EMA or FEA, an acceleration time response can be computed. The input force used for the computation is determined from the measured input force signal. This signal is measured with the sampling frequency of 40960 Hz and the envelope is shown in Fig. 13.36. This signal is the same as the one shown in Fig. 13.26, which is for the configuration of 4.0 s measurement. Then, the Newmark method or IFT method can be applied to the equation of motion in modal space which is obtained from the EMA and FEA.

Using the Newmark method, the modal responses will be computed first and then transformed into physical space using mode shapes obtained from the EMA and FEA. Here, the acceleration signals for the first 12 modes will be used for the computation because these modes are considered to be sufficient for estimating the peak values of the SRS and the modal parameters for the first 12 modes are extracted from the EMA. The sampling frequency for the Newmark method is set as 40,960 Hz; the upper frequency of interest is 2 kHz but the small time increment is needed to assure that accurate time response is obtained.

On the other hand, for the IFT method, the FRF will be constructed with 40,960 Hz sampling frequency and the nfft of 262,144. The frequency resolution for the spectrum will be 0.15625 Hz and the response signal will have the time length of the nfft but the signal for the first $Fs \times 4.0$ set of data will be used. The FRF which will be used for this computation was shown in Fig. 13.35 and the response time signal will be affected by the first 12 modes.

Fig. 13.35 FRF comparison
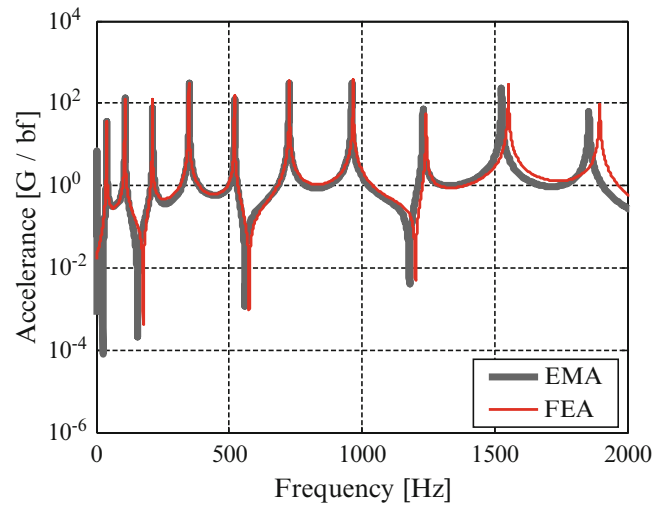
Fig. 13.36 Input force signal
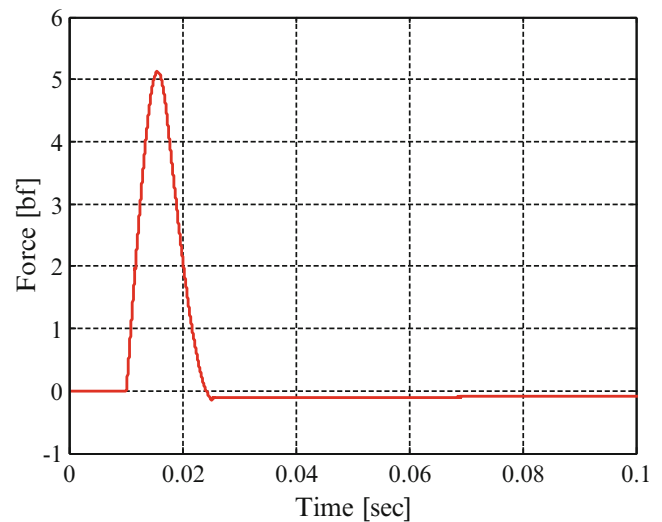
Figure 13.37 shows the comparison of the measured acceleration signal, results of the Newmark method and results of the IFT method. For the Newmark method and IFT method, time responses from the EMA and FEA are compared and all of the computed signals have almost the same response as the measured signal. Because the natural frequency and mode shapes of both solutions compare well and the measured damping values are used, the true signal is reproduced well as expected. However, the IFT method has slightly smaller amplitude than the Newmark solution and several reasons may explain why. First, the sampling frequency may not be small enough to accurately capture the peak time response. Second, the signal may suffer from slight leakage errors due to the overall sample period.

Finally, these signals will be used for the SRS computation and Fig. 13.38 shows the result. Compared to the SRS with the measured data, the SRSs with the Newmark method are very similar. Although the SRS with the IFT method is not different, the SRS with IFT method has slightly smaller value than the measured SRS or the SRS with the Newmark method because of the difference in amplitude of the time response signal. In addition, the SRS with the EMA data has smaller amplitude than the SRS with the FEA because of the same reason. Because the SRSs from the FEA are similar to the measured SRS, the SRS with the FEA data is considered to simulate the actual system well. Due to this, if the data from the EMA and FEA compare well and if the measured damping is used, the envelope of the SRS can be the same as the actual SRS and the first goal of this paper is achieved: the development of a correct solution for the SRS simulation.

Fig. 13.37 Comparison of
measured/calculated acceleration
signals
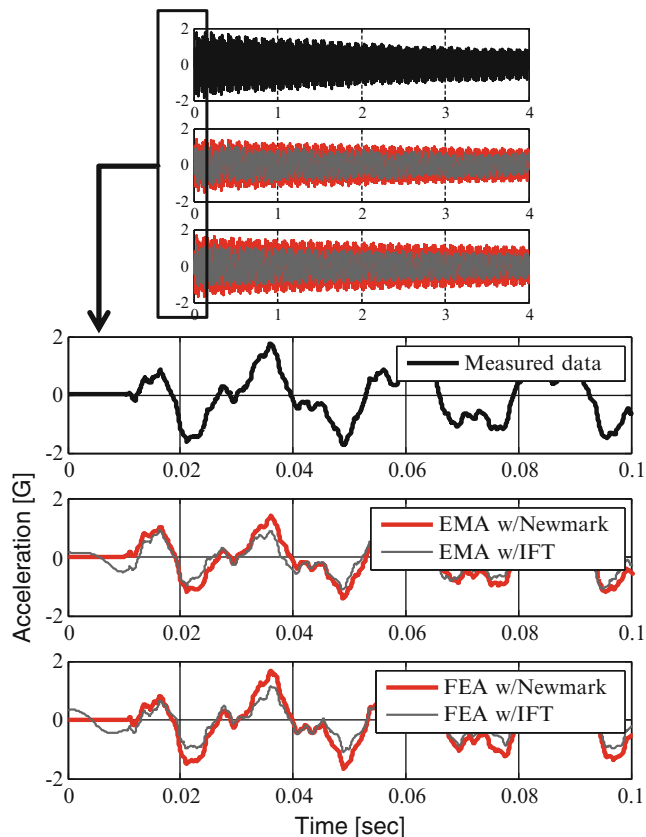
Fig. 13.38 Comparison of SRS
from experiment/EMA/FEA
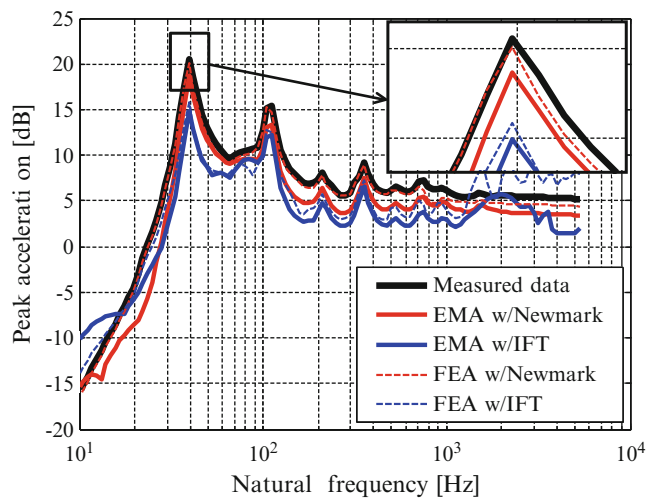
13.5.4 Trial of the Methodology for Customizing SRS

Here, the methodology proposed in this paper will be applied to the developed model. Using the SRS and modal parameters obtained from the EMA or FEA, the contribution of modes, MSA and SDM will be performed.

In order to clarify the relationship between the modes and peaks of the SRS, the contribution analysis will be performed. Here, a pair of SRSs which are developed from both the EMA and FEA will be used for the discussion. In Fig. 13.39, the FRFs computed from the EMA and FEA are superimposed on the corresponding SRSs. These SRSs are developed with the acceleration signals calculated with the modal parameters identified using the Newmark method. Here, the first four modal parameters of flexible modes are used to synthesize the FRF and the contribution is analyzed. From this result, the first and second modes of the beam are considered to have high contribution on the peaks of the SRS because the obvious peaks exist

Fig. 13.39 SRS versus FRF
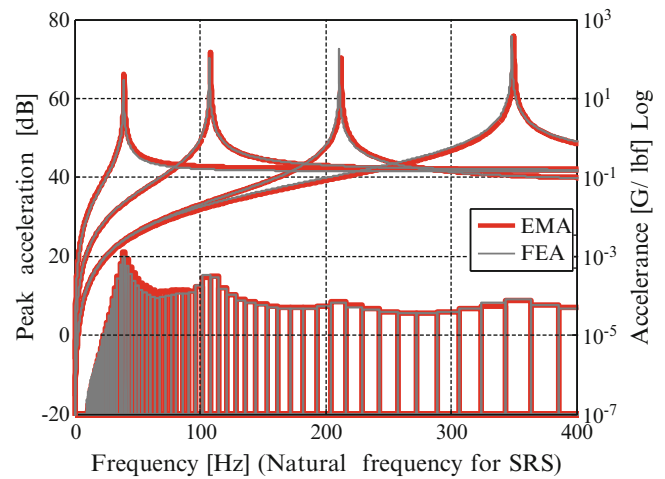
Fig. 13.40 SRS with modal response
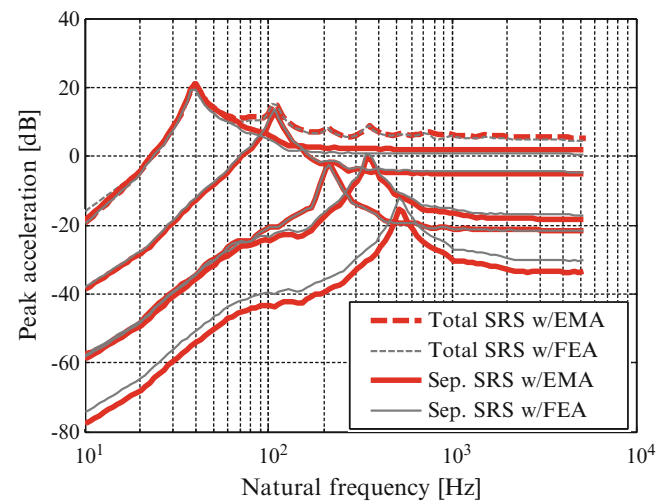
at the same frequency. For the peak of the SRS to be modified, which is a peak around 40 Hz, the first bending mode of the beam is considered to have large contribution to the peak of the SRS based on this analysis. The contribution can also be estimated from the separate SRSs developed with each modal acceleration response. Figure 13.40 shows the result and, for the modal acceleration computation, the first five modes are used to analyze the contribution. From this result, the same as the result discussed previously, the first and second modes are considered to have high contribution and the first bending mode can be judged as the most dominant for the biggest peak of the SRS.

Due to this, the first mode of the beam will be customized to obtain the desired SRS. In addition, because there is only really small difference between two solutions from the EMA and FEA, this contribution analysis can be performed with just the FEA because both data sets are similar.

In order to customize the maximum peak of the SRS, for the first bending mode of the beam, the MSA will be applied to identify the most effective location for the mass modification. The goal of this modification is defined as lowering the peak frequency and decreasing the amplitude at the peak. Using Eq. 13.24, the MSA for the eigenvalues can be obtained and the result is shown in Fig. 13.41. Although the modal parameters extracted from the EMA can also be used but for this computation, only the modal parameters obtained from the FEA are used and the number of nodes is limited to have the same nodes as the experiment. The computation is done only for the bending mode because the modal parameters of the FEA are very similar to the EMA data only for the first ten bending modes. From this result, both of the ends of the beam are considered to have high sensitivity for the eigenvalue modification for the first bending mode. In addition, the MSA for FRF can be obtained using Eq. 13.28 and the result for the first ten bending modes is shown in Fig. 13.42. The sensitivity values are summed up with bandwidths of seven octave bands each having the peak octave band in the middle. From this result, both ends of the beam are considered to have high sensitivity for amplitude reduction of the FRF the same as the MSA for the eigenvalues.

Fig. 13.41 MSA for the eigenvalues
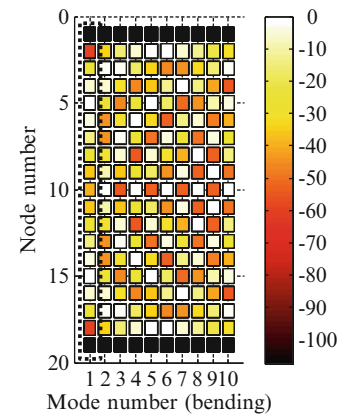
Fig. 13.42 MSA for the amplitude of the FRF
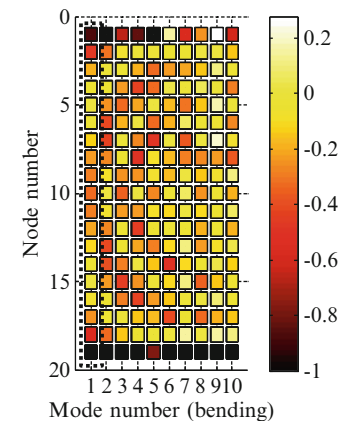
   As a result, both ends of the beam are considered to be useful to lower the natural frequency of the first bending mode and to decrease the amplitude of that mode. On the other hand, node #5 or #15 is considered to have small effect on the customization for the first bending mode because these locations have these sensitivities with a value of almost zero which is expected to results as these are close to the node of the mode.

   In order to estimate the effect of the modification for the biggest peak, the mass value of the DOFs which were identified to be effective/ineffective for the customization will be modified in the FE model developed. Although the SDM procedure can be applied to the EMA model, because the data from the EMA and FEA have high correlation in the frequency range of interest, only the FEA data will be used here. A 0.5 lb mass is added to for the mass location of experimental node #15 or #19 as a lumped mass, because these locations are considered to be the most effective/ineffective location for the customization of the first mode based on the result of the MSA. The SDM procedure will be used to simulate these two patterns of mass change and the FRFs obtained are shown in Fig. 13.43. In this work, the damping value for the modified system is set to the same as the values measured from the EMA of the original system. In Fig. 13.43, a set of FRFs simulating the mass modification for every experimental node is shown together. From this result, the FRF with the optimal mass change is confirmed to have the greatest effect on the frequency shift and amplitude reduction for the first mode. However, for every mode on the optimal FRF, the amplitude is decreased and the frequency is shifted lower the same as the first mode. This is because the edge of the beam has high sensitivities for every bending mode. On the other hand, the mass modification for the node location, which is #15, changes neither the frequency nor the amplitude of the first mode but, for the other modes, the effect on the frequency shift or amplitude reduction is seen because the sensitivities for the other modes are not small. The detailed modal parameters will be compared between the original and modified model with the experimental results in the next section. Figure 13.44 shows the comparison of the acceleration signals obtained from the original and modified modal parameters using the Newmark method. For both solutions, the same input force shown in Fig. 13.36 is used and the modified signal with the optimal mass modification has lower amplitude than the original signal because the amplitude of the FRF is decreased. Using these modified acceleration signals, the modified SRS can be developed and the result is shown in Fig. 13.45. In this figure, the mass modification for all nodes is also performed the same as Fig. 13.43 so the modified SRSs can be compared to the original SRS and a set of SRSs computed with the acceleration signals with randomized modifications. From this result, the modified SRS computed with the optimal mass modification based on the MSA has the smallest amplitude and

Fig. 13.43 FRF comparison
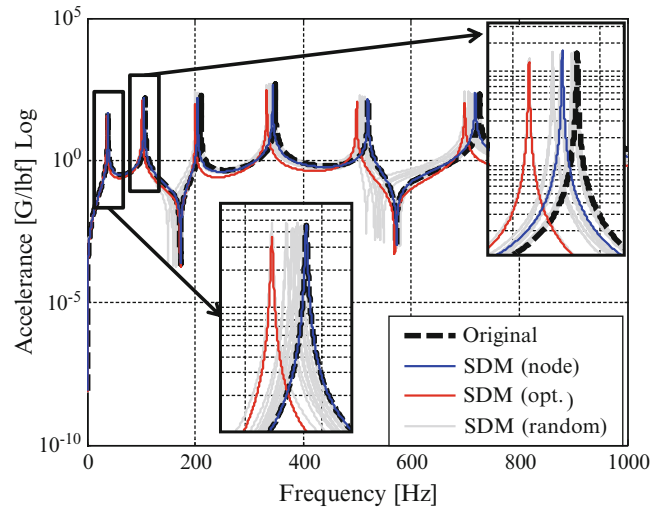
Fig. 13.44 Acceleration signals
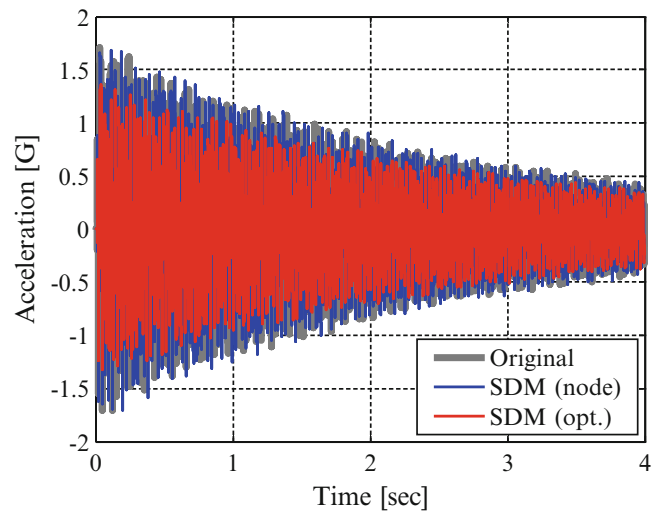
Fig. 13.45 SRS comparison
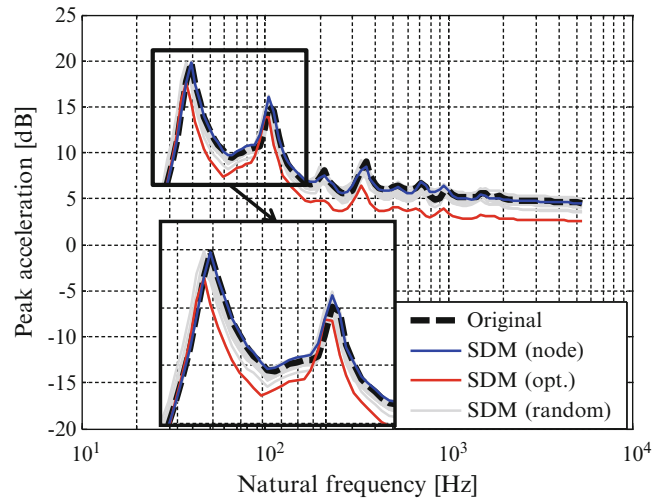
its frequency shift is the biggest. The amplitude reduction is about 3 dB and the peak frequency is shifted by 4 Hz. But for the SRS with mass modification for the location with small sensitivities, the modified SRS has almost the same peak value as the original SRS at the biggest peak. Due to the result described here, the SRS customization procedure proposed in this work is considered to be valid and useful because the mass modification with high sensitivity values is proved to be useful for the SRS customization and the mass modification with small sensitivity is shown to be not effective.

Fig. 13.46 Setup for mass modification
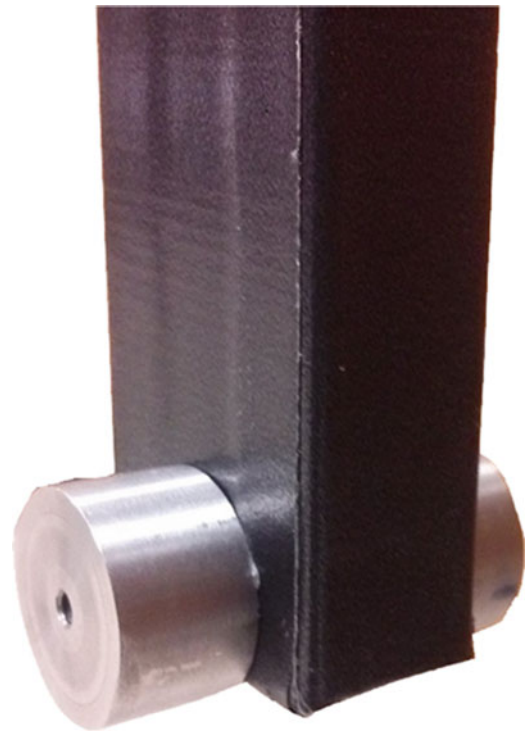
Fig. 13.47 [t] Experimental FRF comparison
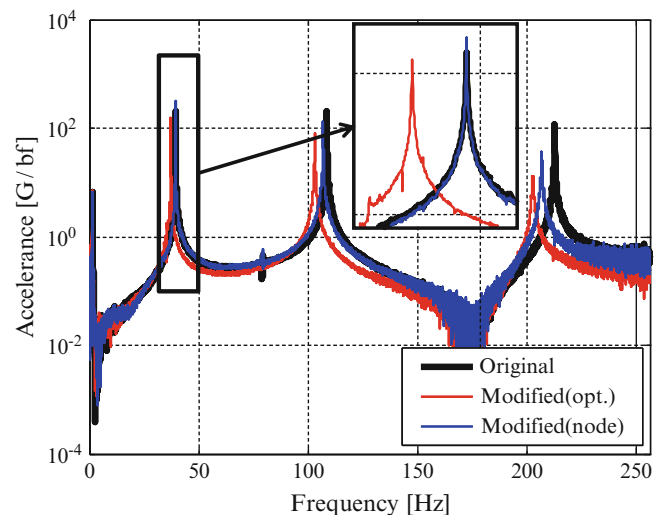
In order to check the accuracy of the analytical estimation for the SRS customization, an additional mass will be added to the actual beam system to simulate a SRS customization experimentally. Figure 13.46 shows the experimental setup for conducting the SDM. Two masses each of which has 0.25 lb and that are made of stainless steel is attached to the node #19 and #15 which are considered to have the highest and smallest sensitivities for the first mode. For both of modified systems, a pair of the FRFs will be measured using configuration (i) and the result is shown in Fig. 13.47 compared to the original FRF. From this result, the modified FRF with the optimal mass modification of #19 has lower frequency and smaller amplitude but the modified FRF with the poor location has the same peak specification as the original FRF. Although the added mass is different from the perfect lumped mass condition, this is considered to be reasonable to check the methodology because the FRF modified has the same tendency as the one from the FEA shown in Fig. 13.43, which uses the lumped mass configuration.

In addition, the EMA for the modified system will be performed to obtain the modified modal parameters using the same three configurations used for the measurement for the original model; this is done to obtain the modified modal parameters and compare them with the original one. In this case, only the optimally modified modal parameter is extracted. Table 13.5 shows the result of the EMA and a set of the modified natural frequencies and damping values are shown in the table.

Table 13.5 Modified modal parameters with optimal mass modification

Mode #	Mode name	Natural frequency				Critical damping	
		Modified value (Hz)		Modification effect (%)		Modified value (%)	Modification effect (%)
		EMA	FEA	EMA	FEA	EMA	EMA
3	1st bending	37.265	36.750	−5.83	−6.07	0.3240	16.06
4	2nd bending	102.996	101.856	−5.32	−5.48	0.0713	64.74
5	3rd bending	202.524	200.592	−4.89	−5.01	0.1801	85.29
6	4th bending	334.837	332.899	−4.49	−4.59	0.5246	95.04
7	5th bending	502.690	498.994	−3.72	−4.24	0.6561	96.82
8	6th bending	701.696	699.014	−3.36	−3.93	0.4648	95.85
9	7th bending	929.209	933.065	−3.47	−3.66	0.7685	96.99
10	8th bending	1,203.610	1,201.223	−2.20	−3.42	1.0351	96.91
11	9th bending	1,495.180	1,503.546	−2.05	−3.18	0.8065	95.71
12	10th bending	1,819.810	1,840.082	−1.94	−3.02	0.6595	92.07

Fig. 13.48 Synthesized FRF for modified system and comparison with FRF from the FEA
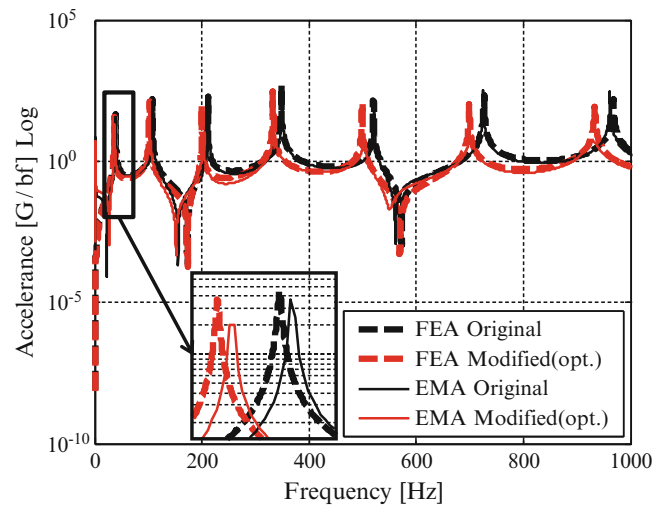
Furthermore, the modified natural frequency from the FEA is also shown and the modification effect is calculated based on the change from the original values shown in Tables 13.3 and 13.4. From this result, the change of the experimental natural frequency is similar to the one of the FEA. However, the modified analytical model was assumed to have the same damping as the original system in the process of the analytical modification but the measured damping values after this modification are different from the original values because the mass is added discretely to the structure. Because the actual damping values are hard to estimate before the actual system is built, the original damping values may be able to be used for the estimation of the modified response computation or the modified SRS computation. Using these modal parameters extracted from the EMA, the FRF for the modified system is synthesized using Eq. 13.14 and the result is shown in Fig. 13.48. Because both of the modified FRF from the analytical and experimental solution compare well and both of the modified FRFs have valid modification effect, the modification and the extraction of modal parameter for before/ after the modification are considered to be correct.

In order to develop the SRS for the modified system experimentally, the pendulum shown in Fig. 13.25 will be used to measure the modified acceleration signal and Fig. 13.49 shows the comparison of the input signals used for the original and modified acceleration signal measurement. The measurement will be done for the modified system with the optimal mass modification and the system with the location with small sensitivities. Because these three signals are similar, the modification effect can be judged sufficiently from the measured response signals. Figure 13.50 shows the comparison of the measured response signals before/ after the modification. This result is similar to the analytical result shown in Fig. 13.44.

Finally, the modified SRS will be computed with the measured acceleration signal for the modified model. Figure 13.51 shows the result and the original experimental SRS, the original and modified SRS from the FEA are also shown. The modified SRS with the ineffective location has the same peak value as the original SRS for the biggest peak but, for the modified SRS with the optimal mass location, the peak value is decreased by 2 dB and its frequency is shifted by 2 Hz. The change from the original SRS to the optimally modified SRS in the experiment is similar to the change in the FEA.

Fig. 13.49 Input force comparison
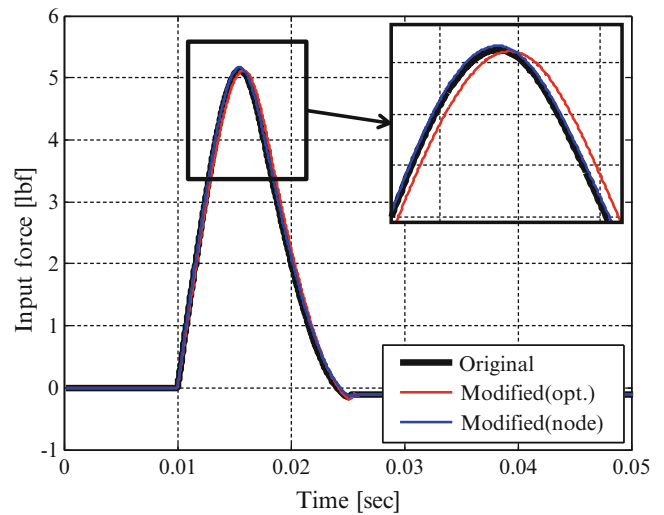
Fig. 13.50 Response signal comparison
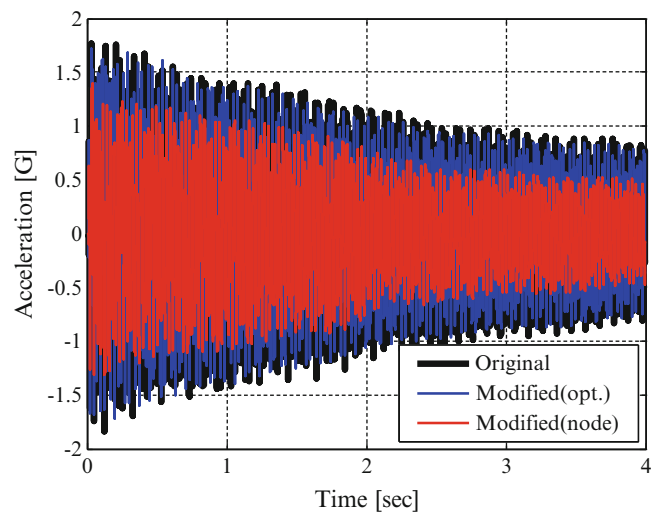
Fig. 13.51 Analytical and experimental SRS for original and modified system
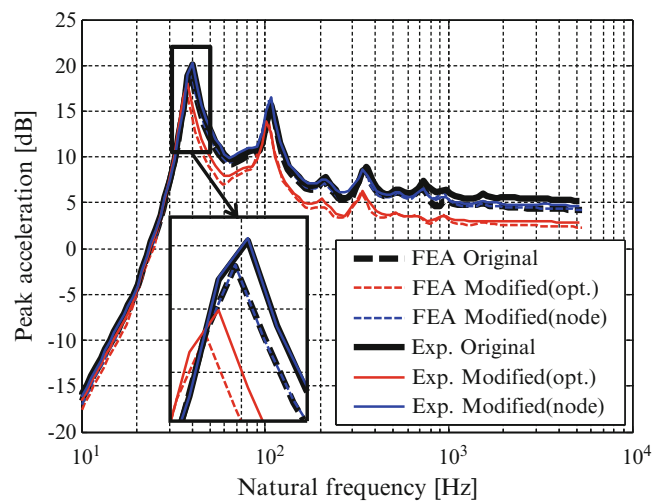
Due to this, the methodology proposed is confirmed with the analytical and experimental solution using the beam model. From both solutions, the modal parameters are compared and the measured modal damping is used for the FE model development for better model description. This method provides the analytical SRS which is very similar to the measured SRS and the modification effect is simulated properly using the FE model developed.

13.6 Conclusion

This paper presents the design methodology for the development of a shock response spectrum test structure that is developed from both analytical and experimental approaches using modal space as a basis for the description of the structure along with the traditional shock response base excitation approach. In addition, the design is further analyzed using both time domain and frequency domain response approaches that are further optimized using structural dynamic modification and mass sensitivity approaches to obtain the desired SRS envelop.

Cases are first presented for a simple 5-DOF analytical model to illustrate all of the techniques described. This is followed by the evaluation of a beam structure using both finite element and experimental modal approaches. Many different cases were evaluated to show all aspects of every approach that is presented in the paper to highlight the effectiveness of each approach. The approaches presented all support the design of a shock response spectrum structure.

References

1. NASA-STD-7003A (2011) NASA technical standard-pyroshock test criteria, National Aeronautics and Space Administration, Dec 2011
2. ISO 18431-4 Mechanical vibration and shock-signal processing—part 4: shock response spectrum analysis
3. Tuma J, Koci P (2009) Calculation of shock response spectrum. Colloquium dynamics of machines 2009, Feb 2009
4. Edward Alexander J (2009) Shock response spectrum—a primer. Sound Vib
5. Richard Hsieh et al (2013) Analysis and dynamic characterization of a resonant plate for shock testing. Proceedings of the 31st international modal analysis conference
6. Irvine T An introduction to the shock response spectrum
7. Rao S (2010) Mechanical vibrations, 5th edn. Prentice Hall, New Jersey, pp 968–971
8. Okubo N, Toi T (2000) Sensitivity analysis and its application for dynamic improvement. Sadhana 25(3):291–303
9. Kohei Furuya et al (2005) FRF-sensitivity analysis using eigenvalue analysis of stiffness matrix for a car body structure. Proc. Jpn Soc Automot Eng. No 37-05-188
10. Avitabile P (2001) Twenty years of structural dynamics modification—a review. Proceedings of the 20th international modal analysis conference, Feb 2001
11. ISO 1683-2008 Acoustics—preferred reference values for acoustical and vibratory levels

Chapter 14
Parameter Identification for Nonlinear Dynamic Systems via Multilinear Least Square Estimation

Sushil Doranga and Christine Q. Wu

Abstract The Nonlinear Resonant Decay Method is an approach for the nonlinear system identification of continuous, multi-mode and lightly damped systems. In this method the identified nonlinear model is expressed in a linear modal space with additional terms representing the nonlinear behaviour. These additional nonlinear terms are obtained by performing least square regression in a modal space. Implementing this methodology in a structure, a large number of these nonlinear terms may exist but not all of them are significant. The problem of deciding which and how many terms are required for an accurate identification is still challenging. The challenges are (1) a term which is deemed insignificant at an early stage of regression may actually prove to be significant in later steps when the model size is smaller. (2) A term which has been removed cannot be reinstated and the identified model will be sub-optimal. This paper attempts to address these challenges by using a least square regression algorithm in a statistical sense. A "Coefficient of Determination" criterion is used to select the essential nonlinear terms. Only those terms which have the largest correlation with the nonlinear restoring force are entered into the model. The proposed methodology is demonstrated through simulations numerical in a five degree-of freedom system and in a cantilever beam. Simulation results shows that this methodology is robust for estimating the local nonlinearity of the system.

Keywords Nonlinear parameter identification • Multilinear least square estimation • Coefficient of determination

14.1 Introduction

Nonlinear resonant decay method is one of the methods for representing a nonlinear system in a modal space. It aims to simplify the unknown nonlinear model structure, with too many parameters by using a multi-exciter force pattern to excite one mode at a time. This approach is in essence based upon the idea of force appropriation which permits the determination of a monophase force vectors from the measured frequency response functions (FRFs) matrix. These force vectors will induce single mode behaviour when applied to a linear system at the relevant undamped natural frequency. A single mode may thus be tuned and measured. Scaling these force vectors at a level great enough to excite the nonlinearity present in the structure yield two possible results: (1) the excited mode dominate the response in the steady-state phase. In this case the mode is nonlinearly uncoupled. (2) Other modes also exhibit a significant response. This is due to the nonlinear cross coupling between the modes.

A suitable curve fit may then be used to identify the linear and nonlinear modal parameters based on restoring force-state mapping. For uncoupled nonlinear modes, the curve fitting involves the modal response associated with that mode. For coupled linear or nonlinear modes, the curve fitting includes all modes coupled to the mode of interest. It should be noted that appropriate basis functions need to be choose in curve fittings. The problem associate with the curve fitting is to determine which of the candidate basis functions are actually required for an accurate representation of the nonlinear system. Some terms may simply not be present in the system, some may not be significant at the level of the measured responses, some may be masked by noise or other measurement errors and some may not have been adequately excited by the forces applied to the structure. It is important that these terms need to be removed to ensure that the final model is parsimonious and truly

S. Doranga • C.Q. Wu (✉)
Department of Mechanical Engineering, University of Manitoba, Winnipeg, MB, Canada R3T 5V6
e-mail: cwu@cc.umanitoba.ca

represent the dynamics of the nonlinearity. To address these issues Platten et al. [2–4] proposed three algorithm which are Forward Selection (FS) algorithm, Backward Elimination (BE) algorithm and Genetic Algorithm optimization. However, the problem associated with implementing these algorithms are that (1) a term which is deemed insignificant at an early stage of regression may actually prove to be significant in later steps when the model size is smaller, (2) a term which has been removed cannot be reinstated and the identified model will be sub-optimal, (3) there are no exact guidelines for selecting a suitable term and (4) there is no basis to deal with the noisy signal. So, there is a necessity of improving the algorithm such that the above mentioned problems can be addressed. In this paper a statistical based multilinear least square algorithm is proposed and is applied to a simulated five degree of freedom system and in a cantilever beam. A statistical based least square curve fitting has been widely used in the field of electrical engineering for time series modeling [3, 5]. Similarly a multilinear regression model along with artificial neural network (ANN) has been used successfully for nonlinear modeling of time series data [1, 6]. It has been shown in [7] that maximum likelihood estimation is efficient in estimating the parameter of a nonlinear system with polynomial nonlinearities.

The paper is organised as follows. The NLRDM approach is outlined first. A statistical based least square estimation algorithm is proposed for nonlinear parameter estimation. Following the least square estimation algorithm, two nonlinear parameter selection techniques are presented which are solely based on the correlation coefficient. The proposed parameter selection algorithm is demonstrated through a simulated five degree-of freedom lumped parameter nonlinear system and in a cantilever beam.

14.2 Nonlinear Resonant Decay Method (NLRDM)

The NLRDM technique is used to identify the nonlinear system with Multi-Degree-Of-Freedom. It has been successfully applied for a number of simulated and experimental structures [2–4]. The NLRDM technique consists of: (1) linear system identification, (2) Force vector approximation (linear), (3) excitation with approximated scaled force vectors to excite nonlinearities of the structure (4) data processing (integration and transforming into modal space) and (5) least square estimation to obtain the nonlinear parameters. During the linear system identification (first stage), the linear parameters of the structure such as mode shapes, modal mass, modal damping ratios and modal stiffness are identified using the conventional experimental modal analysis technique (EMA). The second stage of this methodology consists of approximating the appropriate force vectors required to excite the mode of interest. This can be achieved by using a multivariate mode indicator function (MMIF) [8–11]. The third stage is the excitation with the appropriate force vector obtained from the second stage. In this stage a scaled force vector is used to excite the particular mode of interest. The excitation force vector is scaled such that it is high enough to induce nonlinear behaviours. The fourth stage is the data processing stage in which the measured response data along with the applied force vector are transformed to the modal space. The final stage of the NLRDM is the suitable curve fitting on an excited mode to obtain the nonlinear parameters.

14.2.1 Least Square Estimation

In this section, the least square regression technique originally proposed in [2–4] is discussed first. The potential issues and drawbacks associated with the technique proposed in [2–4] are summarized. To overcome these drawbacks a statistical least square estimation algorithm is proposed. This estimation technique shows the potential nonlinear variable which has a first priority to enter into the model and the variable which has a least priority to enter into the model. This section also shows the new criteria for the measurement of the Goodness-Of-Fit of the identified coefficients. The proposed statistical least square estimation methodology is based on the assumption that a stochastic relationship exist between the nonlinear restoring force and the nonlinear variables [6, 7].

After the successful implementation of the fourth stage of NLRDM, the final stage consists of the curve fittings of the excited nonlinear mode to the measured modal force and response data in a least squares sense. Previous authors [2–4] have shown the least square curve fitting algorithm in the form of the changes in the mean square error. Here the same concept is addressed first and the new concept of coefficient of determination in terms of statistical least square estimation is introduced in the later section. The nonlinear modal equation for the excited mode in a modal space can be written as,

$$m_i \ddot{q}_{in} + c_i \dot{q}_{in} + k_i q_{in} + g_i \{q_n, \dot{q}_n\} = f_{in} \tag{14.1}$$

where m_i, c_i and k_i are the modal mass, damping and stiffness for the ith mode. f_i is the modal force for the ith mode. g_i is the nonlinear modal restoring force. $n = 1, \ldots, N$, where q_n is the value of q (modal response) at the nth time instance q_{in} denotes the nth value of the ith modal displacement and f_{in} denotes the nth value of the ith modal force. A candidate set of basis function is selected such that,

$$g_i \{q, \dot{q}\} = \alpha_{1f} \, t_1 \{q_n, \dot{q}_n\} + \alpha_{2f} \, t_2 \{q_n, \dot{q}_n\} + \alpha_{3f} \, t_3 \{q_n, \dot{q}_n\} + \alpha_{4f} \, t_4 \{q_n, \dot{q}_n\} + \ldots \cdots = \boldsymbol{\alpha}_i{}^T \{t\} \tag{14.2}$$

where $\{t\}$ is the column vector containing the basis functions. $\boldsymbol{\alpha}_i$ is the column vector containing the coefficients of the basis functions for the ith mode. The superscript T denotes the transpose. Combining the force and the response data from all time points and moving the linear terms to the right hand side, we have,

$$
\begin{bmatrix}
t_1 \{p_1, \dot{p}_1\} & t_2 \{p_1, \dot{p}_1\} & t_3 \{p_1, \dot{p}_1\} & \cdots \\
t_1 \{p_1, \dot{p}_1\} & t_2 \{p_1, \dot{p}_1\} & t_3 \{p_1, \dot{p}_1\} & \cdots \\
\vdots & \vdots & \vdots & \cdots \\
t_1 \{p_1, \dot{p}_1\} & t_2 \{p_1, \dot{p}_1\} & t_3 \{p_1, \dot{p}_1\} & \cdots
\end{bmatrix}
\begin{Bmatrix}
\alpha_{1f} \\ \alpha_{2f} \\ \alpha_{3f} \\ \vdots \\ \cdot
\end{Bmatrix}
=
\begin{Bmatrix}
f_{i1} \\ f_{i2} \\ \vdots \\ \cdot \\ f_{iN}
\end{Bmatrix}
- m_i
\begin{Bmatrix}
\ddot{q}_{i1} \\ \ddot{q}_{i2} \\ \vdots \\ \ddot{q}_{iN}
\end{Bmatrix}
- c_i
\begin{Bmatrix}
\ddot{q}_{i1} \\ \ddot{q}_{i2} \\ \vdots \\ \ddot{q}_{iN}
\end{Bmatrix}
- k_i
\begin{Bmatrix}
q_{i1} \\ q_{i2} \\ \vdots \\ q_{iN}
\end{Bmatrix}
\tag{14.3}
$$

Equation (14.3) can be reformed as,

$$[D] \{a_i\} = \{q_i\}$$

where $[D]$ is named as the design matrix and $\{q_i\}$ is the right hand side vector for the ith mode. The right hand side of the equation is known from the linear identification stage and nonlinear excitation stage, Eq. (14.3) can be solved in the least squares sense to estimates the coefficients, $\{a_i\}$. There are various algorithms to estimate the coefficients in the least squares sense. The commonly used one in the literature is the mean square error criteria, and the second algorithm introduced over here is the statistical least square algorithm which defines the best model in terms of the coefficient of determination. At first the existing methodology described in [2–4] is used.

The mean square error (MSE) between the reconstituted restoring force and the measured modal restoring force is defined as a measure of the Goodness-of-Fit of the identified coefficients [8–11]. The error vector can be defined by the following equation.

$$
\begin{Bmatrix}
\varepsilon_{i1} \\ \varepsilon_{i2} \\ \vdots \\ \vdots \\ \varepsilon_{iN}
\end{Bmatrix}
=
\begin{Bmatrix}
f_{i1} \\ f_{i2} \\ \vdots \\ \vdots \\ f_{iN}
\end{Bmatrix}
- m_i
\begin{Bmatrix}
\ddot{q}_{i1} \\ \ddot{q}_{i2} \\ \vdots \\ \ddot{q}_{iN}
\end{Bmatrix}
- c_i
\begin{Bmatrix}
\dot{q}_{i1} \\ \dot{q}_{i2} \\ \vdots \\ \dot{q}_{iN}
\end{Bmatrix}
- k_i
\begin{Bmatrix}
q_{i1} \\ q_{i2} \\ \vdots \\ q_{iN}
\end{Bmatrix}
-
\begin{bmatrix}
t_1 \{p_1, \dot{p}_1\} & t_2 \{p_1, \dot{p}_1\} & t_3 \{p_1, \dot{p}_1\} & \cdots \\
t_1 \{p_1, \dot{p}_1\} & t_2 \{p_1, \dot{p}_1\} & t_3 \{p_1, \dot{p}_1\} & \cdots \\
\vdots & \vdots & \vdots & \cdots \\
t_1 \{p_1, \dot{p}_1\} & t_2 \{p_1, \dot{p}_1\} & t_3 \{p_1, \dot{p}_1\} & \cdots
\end{bmatrix}
\begin{Bmatrix}
\alpha_{1i} \\ \alpha_{2i} \\ \alpha_{3i} \\ \vdots \\ \cdot
\end{Bmatrix}
$$

$$\tag{14.4}$$

and the MSE error is defined as

$$MSE_i = \frac{\varepsilon_i{}^T \varepsilon_i}{N} \tag{14.5}$$

The optimum combination of basis function is sought by using three techniques, which are Backward elimination, Forward selection and Genetic algorithm optimization. The ultimate goal of those techniques is to find out which of the candidate basis functions should be used in the construction of design matrix and to eliminate those terms which are irrelevant or insignificant. The major drawback of the three techniques described in [2–4] is that there are no any specific rules for selecting the basis function. One can come up with an infinite number of irrelevant nonlinear terms in the model which satisfy the minimum mean square criteria. The major unanswered question to the methodology proposed in [2–4] is which candidate function is the best and get the first priority to enter into the model. To address this problem, there need to be definite criteria in which the nonlinear variables can entered into the model. This criteria is addressed in Sect. 14.2.2.

14.2.2 Coefficient of Determination Criteria

This section describes the criteria in which the nonlinear variables are entered into the model. Three model selection criteria are also mentioned in this section. The coefficient of determination measures the percentage of variation in the nonlinear restoring force that is explained by the input variables. The input variables are the product of basis functions and its coefficients. In other words the coefficient of determination provides a measure of how well future outcomes are likely to be predicted by the model. The value of the coefficient of determination lies between 0 and 1. A value of 1 indicates that a regression line fits the data well. The coefficient of determination is found through the multiple regression criteria. The mathematical concept behind the coefficient of determination criteria is discussed below.

Consider the following stochastic relationship between the output variables (nonlinear restoring force) f_{nl} for an ith individual mode and the individual's k input variables $q_1, q_2, \ldots \ldots, q_k$. In the present study $q_1, q_2, \ldots \ldots, q_k$ are the participating modes to form the nonlinear modal restoring force of f_{nl} for an ith individual mode.

$$f_{nl} = \beta_1 \, q_{in} + \beta_2 \, q_{in} \, q_{jn} + \beta_3 \, q_{in}^2 + \cdots + \beta_{kn} \, q_{kn} \, q_{jn} + \varepsilon_n, \quad n = 1, 2, \ldots N \tag{14.6}$$

where $\beta_1, \beta_2, \beta_3, \ldots.. \beta_k$ are the unknown regression coefficients (the coefficients of the nonlinear function in the present study) of the model and it is assumed that the stochastic errors ε_n are independent and identically distributed with zero mean and constant variance. In this setting it is optimal to estimate these parameters by the method of least squares which minimizes the following sum of the square error function.

$$S = \sum_{n=1}^{N} \left(f_{nl} - \beta_1 \, q_{in} - \beta_2 \, q_{in} \, q_{jn} - \beta_3 \, q_{in}^2 - \cdots - \beta_{kn} \, q_{kn} \, q_{jn} \right)^2 \tag{14.7}$$

It is undoubtly true that one can use the constant coefficient β_0 in Eq. (14.6). In this case the regression line makes an intercept of β_0 instead of passing through the origin. Differentiating Eq. (14.7) with respect to $\beta_1, \beta_2, \beta_3, \ldots.. \beta_k$, the solution of Eq. (14.7) is in the form of the following normal equations.

$$\sum_{n=1}^{N} 2 \left(f_{nl} - \beta_1 \, q_{in} - \beta_2 \, q_{in} \, q_{jn} - \beta_3 \, q_{in}^2 - \cdots - \beta_{kn} \, q_{kn} \, q_{jn} \right) (-1) = 0 \tag{14.8}$$

$$\sum_{n=1}^{N} 2 \left(f_{nl} - \beta_1 \, q_{in} - \beta_2 \, q_{in} \, q_{jn} - \beta_3 \, q_{in}^2 - \cdots - \beta_{kn} \, q_{kn} \, q_{jn} \right) (-q_{in}) = 0 \tag{14.9}$$

$$\ldots \ldots \ldots \ldots \ldots \ldots \ldots \ldots \ldots \ldots \ldots \ldots \ldots \ldots$$

$$\sum_{n=1}^{N} 2 \left(f_{nl} - \beta_1 \, q_{in} - \beta_2 \, q_{in} \, q_{jn} - \beta_3 \, q_{in}^2 - \cdots - \beta_{kn} \, q_{kn} \, q_{jn} \right) (-q_{kn} \, q_{in}) = 0 \tag{14.10}$$

The "normal" equations represent a system of K non-homogeneous, linear equations with K unknowns β_1, $\beta_2, \beta_3, \ldots \ldots, \beta_k$. These equations can easily be solved by matrix algebra assuming that none of the input variables can be written as a linear combination of the other input variables. Let us denotes these solutions, called the ordinary least square estimates $\widehat{\beta}_1, \widehat{\beta}_2, \widehat{\beta}_3, \ldots \widehat{\beta}_k$. The fit of Eq. (14.6) is represented by the sum of squared errors (SSE)

$$SSE = \sum_{n=1}^{N} \widehat{\varepsilon n}^2 = \sum_{n=1}^{N} \left(f_{nl} - \widehat{f}_{nl} \right)^2 = \left(f_{nl} - \widehat{\beta}_1 \, q_{in} - \widehat{\beta}_2 \, q_{in} \, q_{jn} - \widehat{\beta}_3 \, q_{in}^2 - \cdots - \widehat{\beta}_k \, q_{kn} \, q_{jn} \right)^2 \tag{14.11}$$

where $\widehat{\varepsilon}_n$ denotes the residual of the regression fit of the observation on the output variable for the i-th individual and the fitted value of the observation of the output of the ith individual is represented by,

$$\widehat{f}_{nl} = \widehat{\beta}_1 \, q_{in} + \widehat{\beta}_2 \, q_{in} \, q_{jn} + \widehat{\beta}_3 \, q_{in}^2 + \cdots + \widehat{\beta}_k \, q_{kn} \, q_{jn} \tag{14.12}$$

In this setting, the ordinary least squares estimates are optimal with respect to being the best of all unbiased, linear estimators of the parameters $\beta_1, \beta_2, \ldots \ldots, \beta_k$.

A measure of the Goodness-Of-Fit of Eq. (14.6) is represented by the so called R-square (R^2) or coefficient of determination:

$$R^2 = 1 - \frac{SSE}{SST} \tag{14.13}$$

where SST is known as the total sum of square errors. In other words it is the total sum of squares of the observations from their mean and is represented by,

$$SST = \sum_{i=1}^{N} \left(f_{nl} - \widehat{f}_{nl} \right)^2 \tag{14.14}$$

R^2 is defined in such a way as to satisfy the inequality $0 \leq R^2 \leq 1$. In other words R^2 is the percentage of the variation in f_{nl} (dependent variable) that is explained by the input variables $q_i, q_i\, q_j, \ldots.., q_k$.

As a measure of goodness-of-fit, some authors [4, 5] mentioned that R^2 is inappropriate for making a choice between competing regression models with different numbers of input variables because R^2 can be arbitrarily grown to be as close to 1 (a perfect fit) as one would like by simply adding more and more input variables to the regression Eq. (14.6). An alternative measure of Goodness-of-fit that contains a "penalty" for growing regression models unnecessarily large is introduced which is called as adjusted R^2 criterion by statisticians [6]:

$$\overline{R^2} = 1 - \frac{N-1}{(N-K-1)} \left(1 - R^2 \right) \tag{14.15}$$

The optimum combination of input variables is sought mainly by two techniques. The forward selection technique and the backward elimination technique. In a forward selection technique variable are sequentially entered into the model. The first variable considered for entry into the model is the one with the largest correlation with the dependent variables [Eq. (14.16)]. In the second case, the independent variable which is not in the model and has the largest correlation is entered. The procedure stops when there are no variables that meet the entry criterion. Backward elimination is just opposite of forward selection. All variables are entered into the model and then sequentially removed. The variable with the smallest partial correlation with the dependent variable is considered first for removal. After the first variable is removed, the variable remained in the model with the smallest partial correlation is considered next. The procedure stops when there are no variables in the model that satisfy the removal criteria. The measure of correlation coefficients between the nonlinear restoring force and potential nonlinear variables is given by,

$$r = \frac{N \sum f_{nl}z - \left(\sum z \right) \left(\sum f_{nl} \right)}{\sqrt{N \left(\sum z^2 \right) - \left(\sum z \right)^2} \sqrt{n \left(\sum f_{nl}^2 \right) - \left(\sum f_{nl} \right)^2}} \tag{14.16}$$

where r is the correlation coefficient and z is the potential nonlinear terms which is in the form of $q_{in}\, q_{jn}, q_{in}^2, q_{kn}\, q_{jn} \ldots$ …. The exact terms and their structure are initially unknown.

14.3 Problem Formulation

In order to demonstrate the proposed methodology of statistical least square regression, two case studies are chosen for demonstration. (a) A five-degree-of freedom lumped parameter system with cubic stiffness nonlinearity and (b) a cantilever beam with a grounded cubic stiffness nonlinearity. For the case study of (a) the system is designed to be symmetric in its linear components so as to yield very simple mode shapes (Fig. 14.1). Hardening cubic stiffness nonlinearity is inserted between masses 2 and 4. If the displacements of masses are denoted by w_1, w_2, w_3, w_4 and w_5, the free vibration equations of motion for the system shown in Fig. 14.1 can be written as,

Fig. 14.1 Five degree-of freedom system
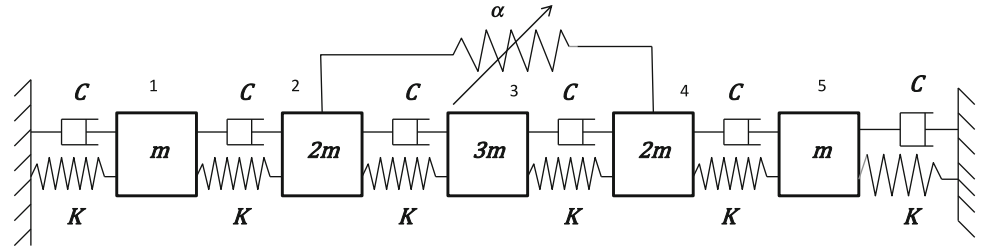
Table 14.1 Natural frequencies and mode shapes of five degree-of freedom system

Modal frequencies (Hz)	Mode shapes				
	1	2	3	4	5
3.51	1	−1	1	1	1
8.01	1.88	−1.37	0.87	−0.37	−0.41
10.72	2.3	0	−1.23	0	0.16
15.48	1.88	1.37	0.87	0.37	−0.41
15.63	1	1	1	−1	1

$$
\begin{bmatrix} m & 0 & 0 & 0 & 0 \\ 0 & 2m & 0 & 0 & 0 \\ 0 & 0 & 3m & 0 & 0 \\ 0 & 0 & 0 & 2m & 0 \\ 0 & 0 & 0 & 0 & m \end{bmatrix} \{\ddot{w}\} + \begin{bmatrix} 2c & -c & 0 & 0 & 0 \\ -c & 2c & -c & 0 & 0 \\ 0 & -c & 2c & -c & 0 \\ 0 & 0 & -c & 2c & -c \\ 0 & 0 & 0 & -c & 2c \end{bmatrix}
$$

$$
\{\dot{w}\} + \begin{bmatrix} 2k & -k & 0 & 0 & 0 \\ -k & 2k & -k & 0 & 0 \\ 0 & -k & 2k & -k & 0 \\ 0 & 0 & -k & 2k & -k \\ 0 & 0 & 0 & -k & 2k \end{bmatrix} \{w\} + \begin{pmatrix} 0 \\ -\alpha(w_4 - w_2)^3 \\ 0 \\ \alpha(w_4 - w_2)^3 \\ 0 \end{pmatrix} = 0
$$

(14.17)

where $\{w\} = \begin{bmatrix} w_1 & w_2 & w_3 & w_4 & w_5 \end{bmatrix}^T$. c, k, and α are the damping, linear stiffness and nonlinear stiffness respectively. The parameter used for the simulation are $m = 1$ kg, $c = 4.8$ N s/m, $k = 4 \times 10^3$ N/m and $\alpha = 5 \times 10^9$ N/m^3. The resulting natural frequencies and mode shapes of the undamped system are shown in Table 14.1.

Let $[\varnothing]$ denotes the mode shape matrix, and then the mode shapes matrix can be written as,

$$
[\varnothing] = \begin{bmatrix} 1 & -1 & 1 & 1 & 1 \\ 1.88 & -1.37 & 0.87 & -0.37 & -0.41 \\ 2.3 & 0 & -1.23 & 0 & 0.16 \\ 1.88 & 1.37 & 0.87 & 0.37 & -0.41 \\ 1 & 1 & 1 & -1 & -1 \end{bmatrix}
$$

Equation (14.17) can be represented in the form,

$$
[M]\{\ddot{w}\} + [C]\{\dot{w}\} + [K]\{w\} + \{g\} = 0
$$

(14.18)

Introducing the term $w = [\varnothing]\{q\}$ and multiplying both sides by $[\varnothing]^T$, Eq. (14.18) becomes,

$$
[\varnothing]^T [M][\varnothing]\{\ddot{q}\} + [\varnothing]^T [C][\varnothing]\{\dot{q}\} + [\varnothing]^T [K][\varnothing]\{q\} + [\varnothing]^T \{g\} = 0
$$

(14.19)
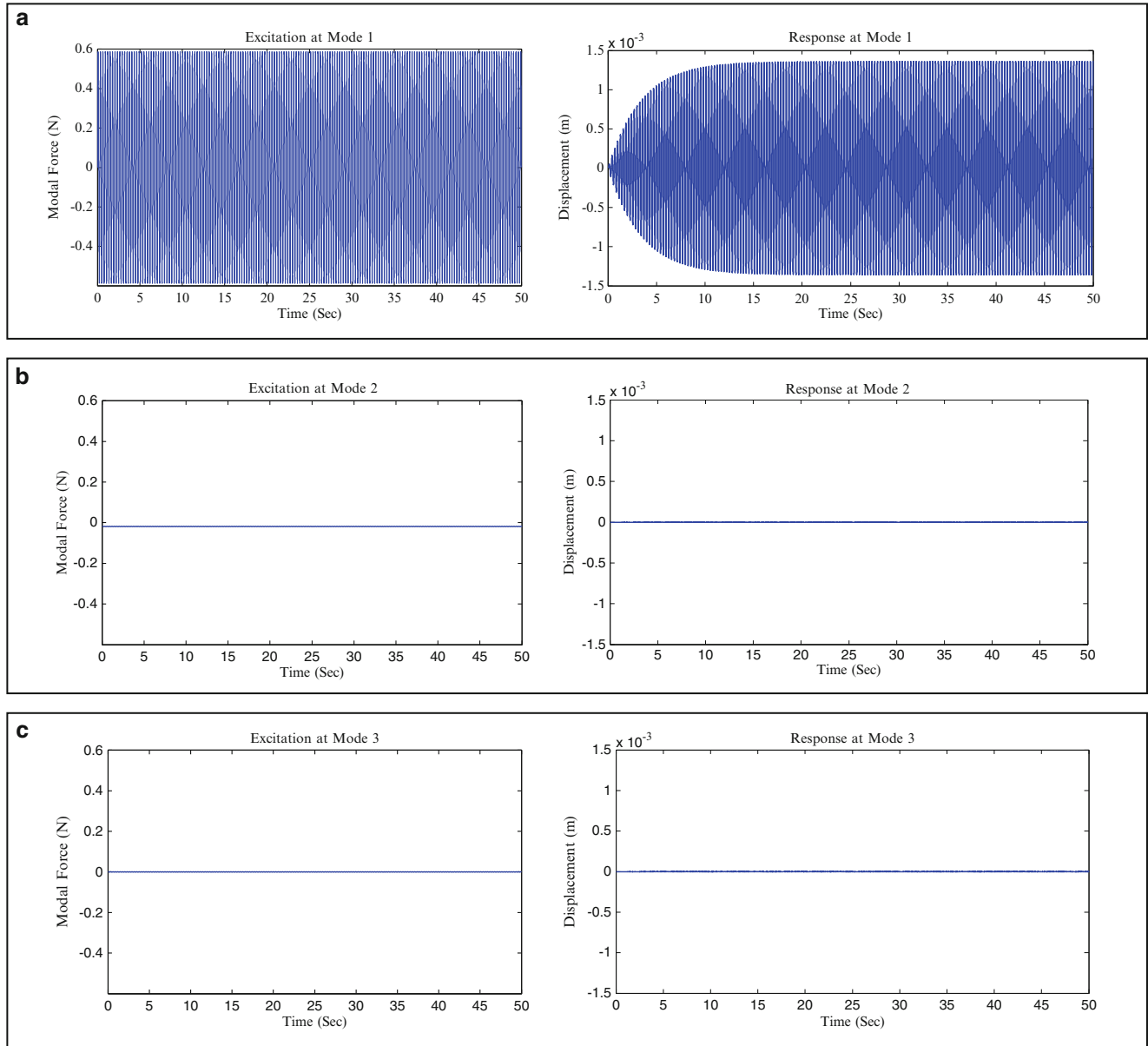
Fig. 14.2 Modal forces and responses due to perfect excitation at Mode 1 [(**a**) Mode 1, (**b**) Mode 2, (**c**) Mode 3, (**d**) Mode 4, (**e**) Mode 5]

Equation (14.19) represents the linear equation of system in the modal space with the nonlinearities in the physical coordinates. Utilizing Eq. (14.19) one can write the system of equations as,

$$32\,\ddot{q}_1 + 18.77\,\dot{q}_1 + 1.56 \times 10^4 q_1 = 0 \tag{14.20}$$

$$9.5\,\ddot{q}_2 + 28.93\,\dot{q}_2 + 2.41 \times 10^4 q_2 + 1.37 \times 10^{10}(w_4 - w_2)^3 = 0 \tag{14.21}$$

$$9.56\,\ddot{q}_3 + 52.1\,\dot{q}_3 + 4.34 \times 10^4 q_3 = 0 \tag{14.22}$$

$$2.54\,\ddot{q}_4 + 28.93\,\dot{q}_1 + 2.4 \times 10^4 q_4 + 3.7 \times 10^{09}(w_4 - w_2)^3 = 0 \tag{14.23}$$

$$2.75\,\ddot{q}_5 + 31.8\,\dot{q}_4 + 2.65 \times 10^4 q_5 = 0 \tag{14.24}$$
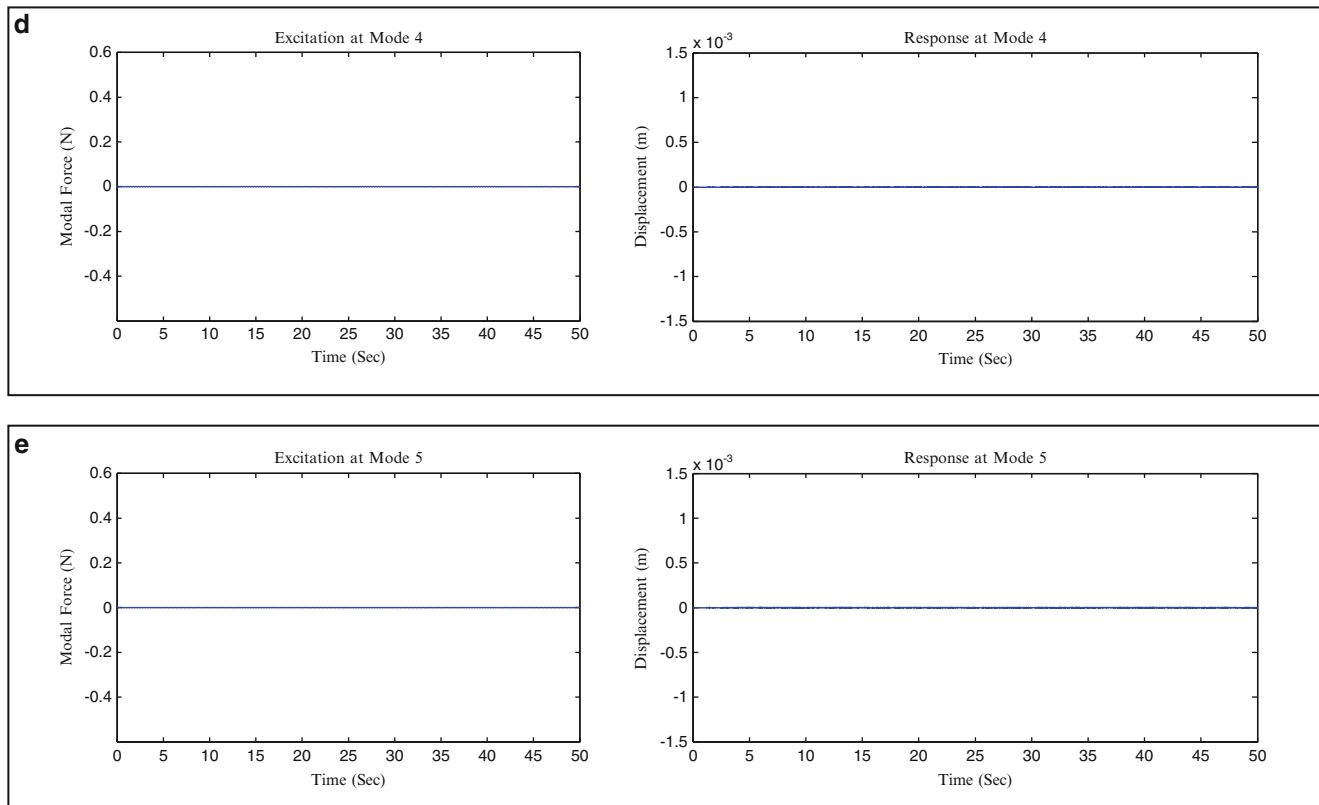
Fig. 14.2 (continued)

Equations (14.20)–(14.24) show that some of the modes are completely uncoupled. Only the second and fourth modes are coupled to each other. If the nonlinear terms in Eqs. (14.21) and (14.23) are transformed to the modal coordinate system, the equations of motion for Mode 2 and 4 become,

$$9.5\,\ddot{q}_2 + 28.93\,\dot{q}_2 + 2.41 \times 10^4 q_2 + 2.74 \times 10^{10}(1.37q_2 + 0.37q_4)^3 = 0 \tag{14.25}$$

$$2.54\,\ddot{q}_4 + 28.93\,\dot{q}_4 + 2.4 \times 10^4 q_4 + 7.4 \times 10^{09}(1.37q_2 + 0.37q_4)^3 = 0 \tag{14.26}$$

An optimum force pattern for each mode is obtained through the normal mode tuning procedure [8–11]. To excite the nonlinearity in an equal amount, a scaling factor is applied to the obtained force vector. The representation of the linear dynamics of a system in a modal space is shown in Fig. 14.2. In the physical coordinate system the force is applied to all the mass (Fig. 14.1), however due to the optimum force vector, Mode 1 is only excited at the modal space (Fig. 14.2). The nonlinear response of Mode 4 is shown in Fig. 14.3. In Fig. 14.3, it is seen that, there is some response in Mode 2 without any excitation force in Mode 2. The response in Mode 2 is due to the cross-coupling nonlinearity between Mode 2 and Mode 4. The cross-coupling nonlinearity is shown in Eqs. (14.25) and (14.26) respectively.

14.3.1 Curve Fitting of Numerical Problem

A numerical problem of lumped mass system mentioned in Fig. 14.1 is demonstrated through the curve fitting procedure. The response of the system is simulated in MATLAB/SIMULINK using adaptive 4th order Runge–Kutta algorithm. For the brevity, in non-linear system analysis only Mode 4 is taken. The force required to excite only Mode 4 for a linear system is obtained through force appropriation technique as described earlier. This force is scaled such that, when it is applied to a structure will induce nonlinearity, if present in the structure. As shown in Fig. 14.3. The response is due to the excitation of the fourth mode. As Mode 4 is connected nonlinearly with Mode 2, there is some response in Mode 2 also. As the input to the
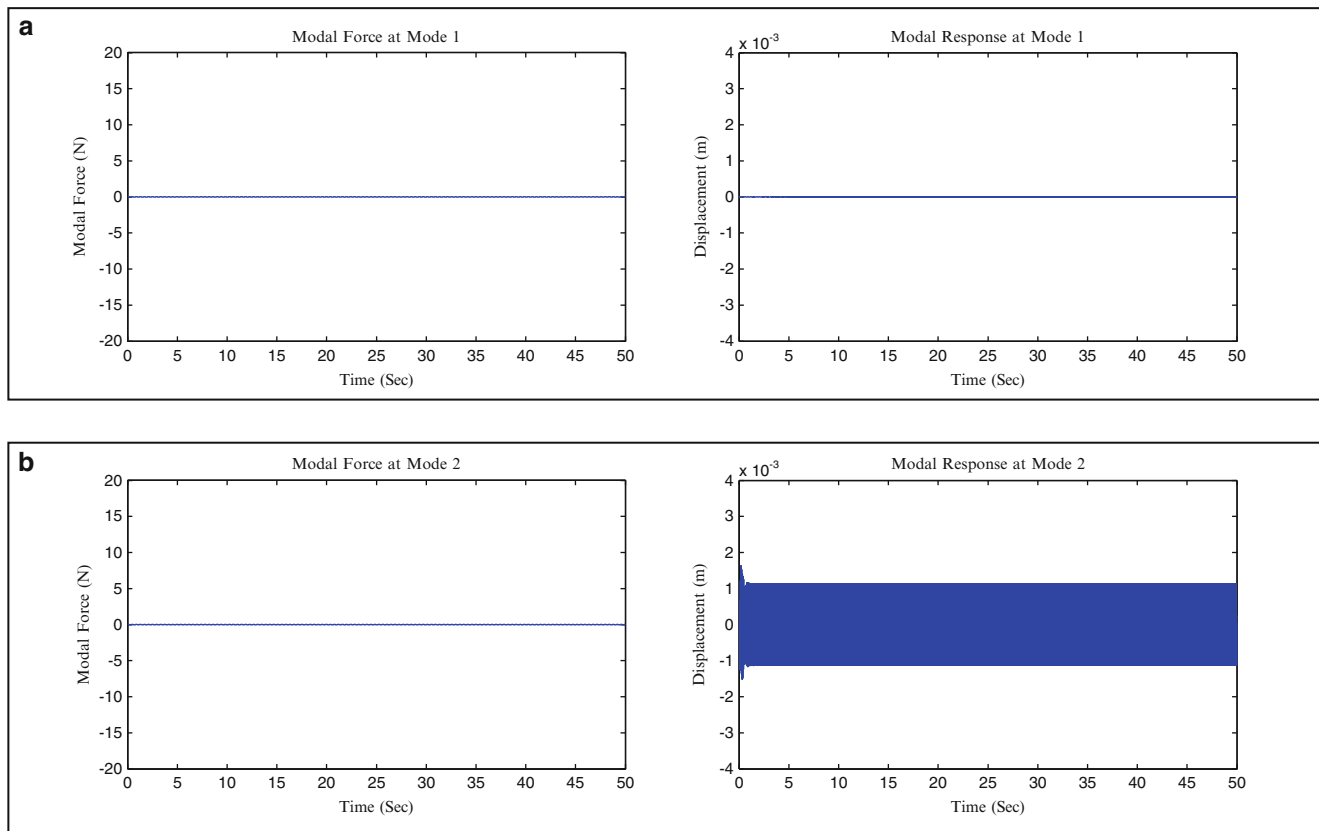
Fig. 14.3 Nonlinear responses due to high level force excitation at Mode 4 [(**a**) Mode 1, (**b**) Mode 2, (**c**) Mode 3, (**d**) Mode 4, (**e**) Mode 5]

system and the linear parameters are known, the nonlinear parameters are extracted in this problem through the curve fitting techniques. To estimate the parameter forward selection technique is applied. An adjusted $\overline{R^2}$ criteria is used to measure the Goodness-Of-Fit between the identified and true nonlinear coefficients. if a_{r1}, a_{r2}, a_{r3} and a_{r4} are the nonlinear coefficients corresponding to Mode 4, the true coefficients corresponding to Mode 4 can be obtained from Eq. (14.26). The identified coefficients are obtained from forward selection technique. The result is presented in Table 14.2.

14.3.2 Cantilever Beam

A cantilever beam made of Aluminium T6061 (Fig. 14.4) is chosen for the second case study. The beam used for the case study has the following dimensions: length: 1 m; width: 0.0254 m; and, thickness: 0.00125 m. A spring of cubic stiffness nonlinearity $K = 5 \times 10^8$ N/m^3 is inserted at the node 2 of the beam. The modal damping ratio for each mode is assumed to be 0.001. The detail of the beam is shown in Fig. 14.4, where three degrees of freedom are taken for measurement as indicated by red ovals. Three modes are taken for the analysis, the mode shapes and natural frequencies of the beam are obtained by solving the governing partial differential equation of the beam. The natural frequencies of the beam for first three modes are obtained as, 2.55, 17.1 and 47.3 Hz respectively. Optimum combinations of three force vector are used to excite the particular mode of interest. The Runge–Kutta integration method is used to find out the nonlinear response data of the beam. The detail implementation of Runge–Kutta method is described below.

The basic idea of the Runge–Kutta integration method is to find a solution for the equilibrium equation at a discrete time point. In the case of a dynamic engineering structure, the equilibrium equation can be described by a set of second-order differential equations given by,

$$[M]\{\ddot{x}\} + [K]\{x\} + [C]\{\dot{x}\} + \{g\} = \{F\} \tag{14.27}$$
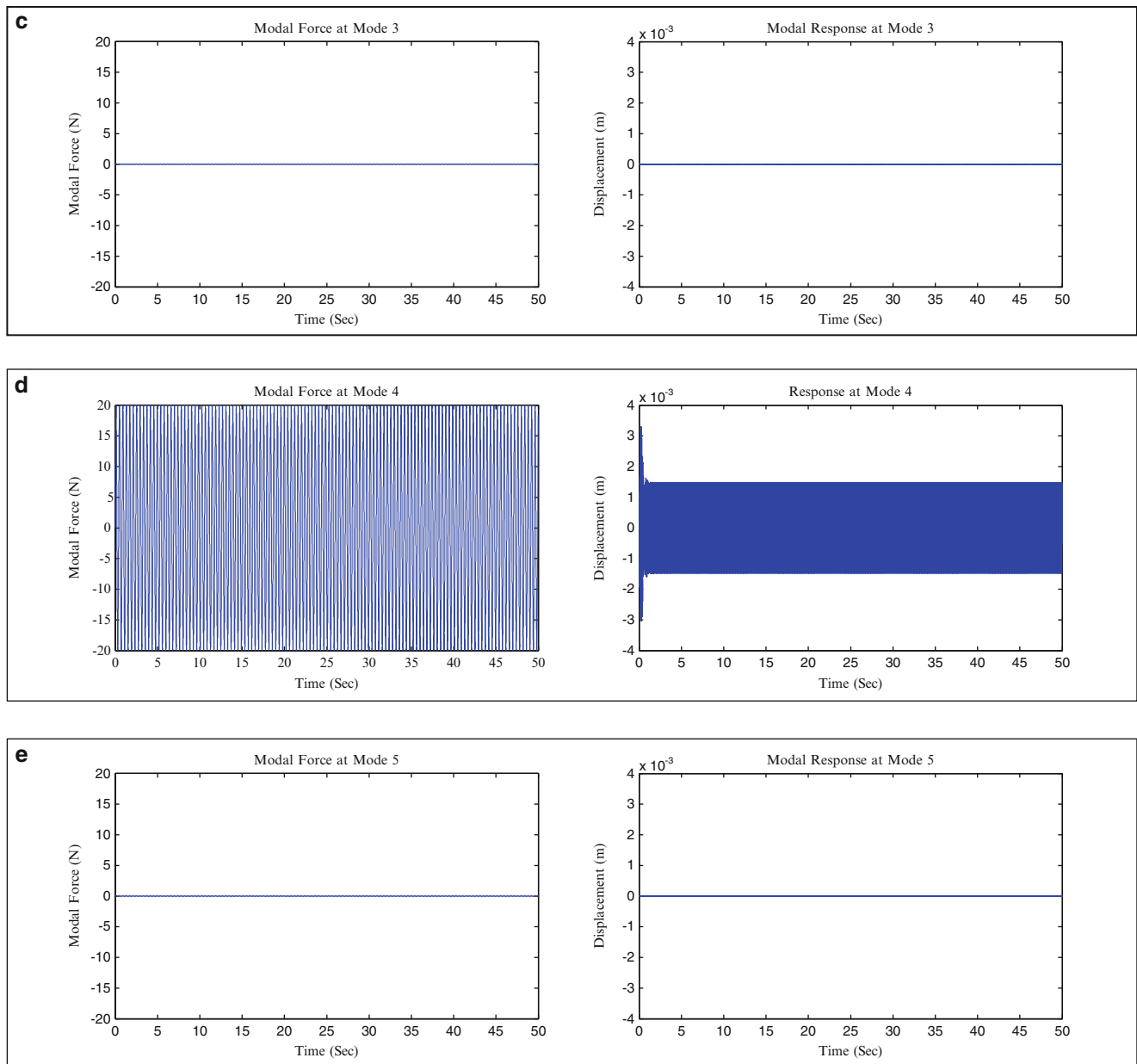
Fig. 14.3 (continued)

Table 14.2 Identified and true nonlinear coefficients of mode 4 of five degree-of freedoms simulated system

| Parameter | Non linear cubic stiffness coefficients (N/m^3) | | | | $\overline{R^2}$ |
	a_{r1}	a_{r2}	a_{r3}	a_{r4}	
True	3.74×10^{08}	4.1637×10^{09}	1.54×10^{10}	1.9028×10^{10}	1
Identified	3.74832×10^{08}	4.1636×10^{09}	1.541×10^{10}	1.9018×10^{10}	

where $[M]$, $[K]$ and $[C]$ is the mass, stiffness and damping matrix of the structure. $\{F\}$ is the input force vector and $\{g\}$ is the nonlinear restoring force vector.

Multiplying both sides of Eq. (14.27) by mode shapes matrix $[\Phi]^T$ and introducing the term $[\Phi][\Phi]^{-1} = I$, Eq. (14.27) becomes,

$$[\Phi]^T [M] [\Phi] [\Phi]^{-1} \{\ddot{x}\} + [\Phi]^T [K] [\Phi] [\Phi]^{-1} \{x\} + [\Phi]^T [C] [\Phi] [\Phi]^{-1} \{\dot{x}\} = [\Phi]^T \{F - g\} \qquad (14.28)$$

Fig. 14.4 Cantilever beam with
a nonlinear element at node 2
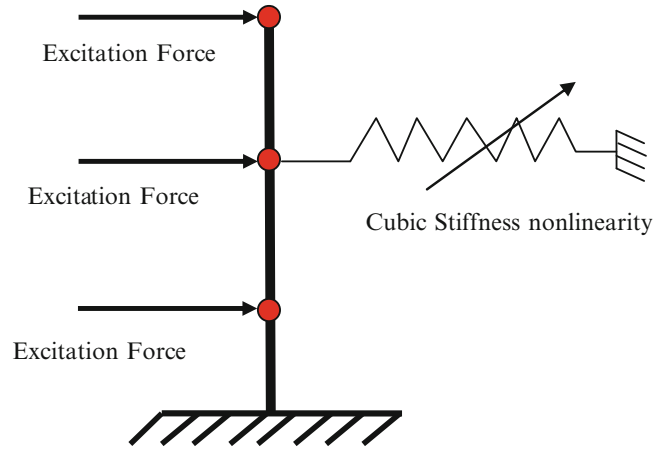
For mass normalized mode shapes and proportional damping assumptions, the orthogonal properties of the linear mode shape matrix $[\Phi]$, can be written as,

$$[\Phi]^T [M][\Phi] = I \tag{14.29}$$

$$[\Phi]^T [K][\Phi] = \left\{ \left[w_r^2 \right]_{diag} \right\} \tag{14.30}$$

$$[\Phi]^T [C][\Phi] = [2\zeta_r w_r]_{diag} \tag{14.31}$$

Using Eqs. (14.29)–(14.31) in Eq. (14.28) we get,

$$[\Phi]^{-1} \{\ddot{x}\} + \left[w_r^2 \right]_{diag} [\Phi]^{-1} \{x\} + [2\zeta_r w_r]_{diag} [\Phi]^{-1} \{\dot{x}\} = [\Phi]^T \{F - g\} \tag{14.32}$$

Integration of Eq. (14.32) by the Runge–Kutta method involves first reducing the second order differential equation into a first order differential equation by rewriting as two first order equations.

$$\dot{x} = u \tag{14.33}$$

$$[\Phi]^{-1} \{\dot{u}\} + \left[w_r^2 \right]_{diag} [\Phi]^{-1} \{x\} + [2\zeta_r w_r]_{diag} [\Phi]^{-1} \{u\} = [\Phi]^T \{F - g\} \tag{14.34}$$

Equations (14.33) and (14.34) can be written in matrix form as,

$$\begin{bmatrix} [\Phi]^{-1} & 0 \\ 0 & I \end{bmatrix} \begin{Bmatrix} \dot{u} \\ \dot{x} \end{Bmatrix} + \begin{bmatrix} [2\zeta_r w_r]_{diag} [\Phi]^{-1} & \left[w_r^2 \right]_{diag} [\Phi]^{-1} \\ -I & 0 \end{bmatrix} \begin{Bmatrix} u \\ x \end{Bmatrix} = [\Phi]^T \begin{Bmatrix} F - g \\ 0 \end{Bmatrix} \tag{14.35}$$

The ordinary differential Eq. (14.27) is reduced to a coupled first order differential Eq. (14.35) which has the explicit form shown by Eq. (14.36),

$$\{\dot{z}\} = \{f(t, z)\} \tag{14.36}$$

where $\{f(t,z)\}$ is known and given by Eq. (14.37),

$$\{f(t, z)\} = \begin{bmatrix} [\Phi]^{-1} & 0 \\ 0 & I \end{bmatrix}^{-1} \left([\Phi]^T \begin{Bmatrix} F - g \\ 0 \end{Bmatrix} - \begin{bmatrix} [2\zeta_r w_r]_{diag} [\Phi]^{-1} & \left[w_r^2 \right]_{diag} [\Phi]^{-1} \\ -I & 0 \end{bmatrix} \{z\} \right) \tag{14.37}$$

The displacement $\{z\}$ is given by Eq. (14.38),

Fig. 14.5 Mode shapes of the cantilever beam
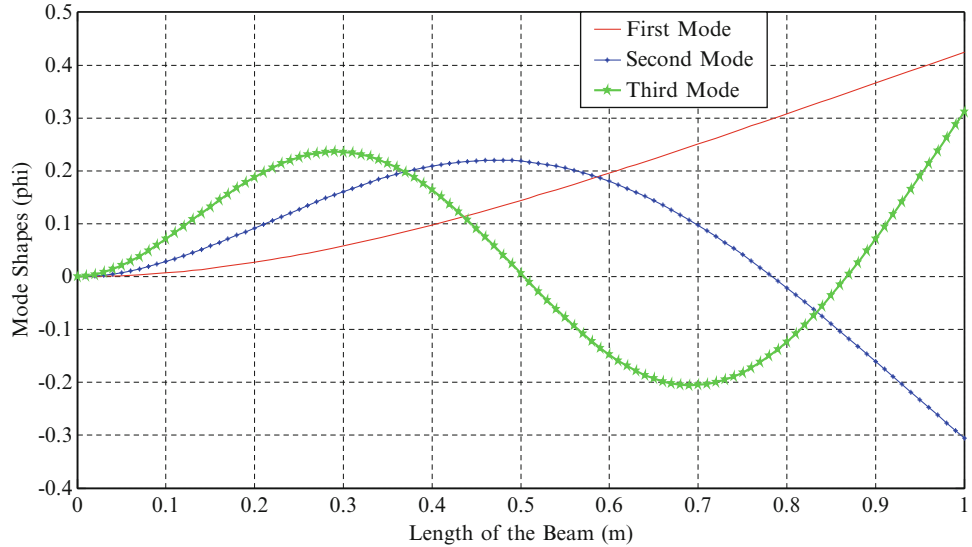
$$\{z\} = \begin{Bmatrix} \dot{x} \\ x \end{Bmatrix} = \begin{Bmatrix} u \\ x \end{Bmatrix} \tag{14.38}$$

Implementation of Eq. (14.37) required the mode shapes matrix. The mode shapes matrix is obtained by solving the partial differential equation of motion. Once the mode shapes matrix is obtained, the solution for the Eq. (14.37) is obtained by implementing the MATLAB solver ode45. Figure 14.5 Shows the mode shapes of the beam, where the first three modes are shown.

14.3.3 Modal Space Equation

The modal space of the beam is approximated by using the standard Eq. (14.28). Using $\{x\} = [\Phi]\{q\}$ in Eq. (14.28), all the response vectors in the physical coordinates are transformed to the modal space. Where $\{q\}$ is the modal displacement. Using Eq. (14.28), we can write,

$$\{\ddot{q}\} + [2\zeta_r w_r]_{diag}\{\dot{q}\} + [w_r{}^2]_{diag}\{q\} = [\Phi]^T\{F - g\} \tag{14.39}$$

In Eq. (14.39) $[\Phi]^T\{F\}$ is the modal force and $[\Phi]^T\{g\}$ is the nonlinear restoring force. The mode shapes matrix $[\Phi]$ is obtained from Fig. 14.5, 2.234×10^6 is the input excitation vector which is obtained from MMIF. 2.5×10^6 is the nonlinear restoring force vector with cubic stiffness nonlinearity at Node 2. Using the numerical values in Eq. (14.39), we can write the modal equation for Mode 1 as,

$$\ddot{q}_1 + 0.0320\,\dot{q}_1 + 256.7096q_1 + 1.0595 \times 10^8(0.2119q_1 + 0.1598q_2 + 0.1783q_3)^3 = 2.2453 \times Sin\,(16.0226 * t) \tag{14.40}$$

14.3.4 Implementation of Curve Fitting Algorithm

The optimum excitation force vector required to excite the first mode of the beam is obtained by using MMIF. These optimum excitation force vector are found to be 3.7090, 3.6223 and 0.5780 N at the Node 1, 2 and 3 respectively. The response data of the beam is obtained by solving Eq. (14.32) in MATLAB using ode45. Figures 14.6, 14.7, and 14.8 shows the response data of the beam by using the above mentioned excitation vector. The response data of the beam are than transformed to modal space by using mode shapes matrix. A least square regression in a modal space for Mode 1 is carried out using the forward selection technique. The results of the estimated and the exact nonlinear parameters are shown in Table 14.3. The exact

Fig. 14.6 Response of the beam
at the first node
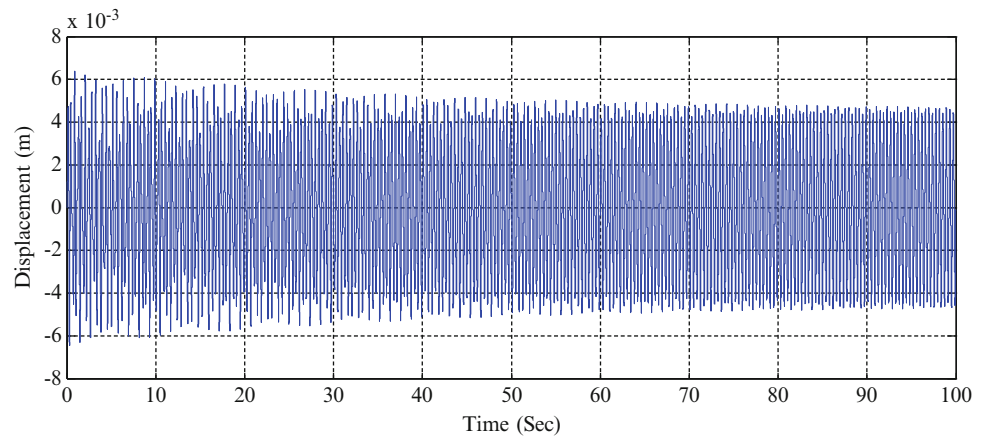
Fig. 14.7 Response of the beam
at the second node
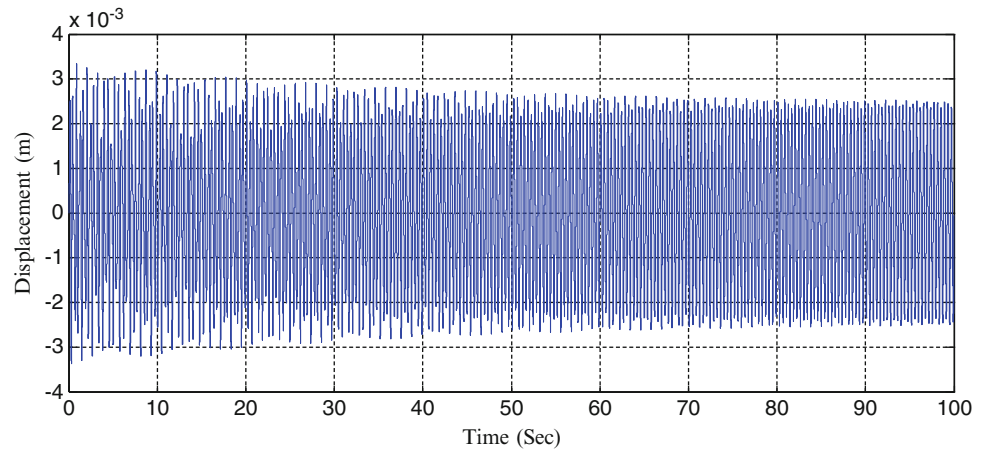
Fig. 14.8 Response of the beam
at the third node
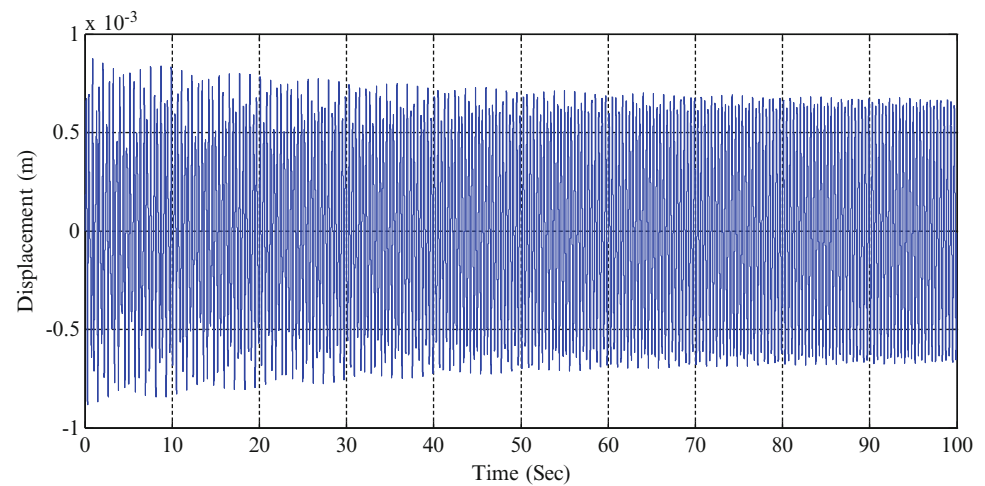
nonlinear parameters are given by Eq. (14.40) whereas the true parameters are estimated through regression. As shown in Table 14.3, the deviation between the estimated and the true coefficient of $q_1 \, q_2 \, q_3$ and q_3^3 are quite high. There are several reasons for this deviation. The main reasons are: (1) only three nodes are taken during simulation and (2) only three modes are taken for analysis.

Table 14.3 Estimated and true nonlinear coefficients

Modal couplings	True coefficient (N/m^3)	Estimated coefficient (N/m^3)	R^2
q_1^3	1.006×10^6	0.8×10^6	0.91
$q_1^2 q_2$	2.234×10^6	2.5×10^6	
$q_1 q_2^2$	1.66×10^6	1.31×10^6	
q_2^3	4.415×10^6	3.432×10^6	
$q_1^2 q_3$	-2.541×10^6	-0.8×10^6	
$q_1 q_2 q_3$	-3.83×10^6	-1×10^7	
$q_2^2 q_3$	-1.37×10^6	-1.5×10^6	
$q_1 q_3^2$	2.13×10^6	3.16×10^6	
$q_2 q_3^2$	1.52×10^6	2.57×10^6	
q_3^3	-5.7×10^6	-2×10^7	

14.4 Concluding Remarks

This paper presents the improved algorithm for nonlinear parameter estimation of nonlinear dynamic system. A statistical based multilinear least square estimation technique has been proposed to estimate the nonlinear parameters in a modal space. The nonlinear resonant decay method is applied to quantify the modes which are behaving linearly and nonlinearly. For modes which are behaving nonlinearly, the accurate estimation of the nonlinear function is essential. A large number of nonlinear variables may exist but all of them may not represent the dynamics of the system. A term which is deemed to be insignificant may actually proven to be significant while performing multilinear regression. To overcome this scenario a correlation criteria is set to enter the essential nonlinear terms into the model. A coefficient of determination criteria is used to measure the Goodness-Of-Fit of the identified model. The proposed methodology is demonstrated through simulation in a five degree-of freedom lumped parameter system and a cantilever beam with cubic stiffness nonlinearity. The nonlinear parameter estimation is found to be sufficiently accurate with error less than 0.1 % for the lumped parameter system, whereas for a continuous system there are some discrepancies. These discrepancies are due to (1) fewer number of modes and (2) only three nodes are taken during simulations.

References

1. Platten MF, Wright JR, Dimitriadis G, Cooper JE (2009) Identification of multi-degree of freedom non-linear systems using an extended modal space model. Mech Syst Signal Process 23:8–29
2. Naylor S (1998) Identification of non-proportionally damped systems using a force appropriation technique. PhD thesis, University of Manchester
3. Sarmast M (2005) Identification of nonlinear dynamic systems using the nonlinear resonant decay method. PhD thesis, University of Manchester
4. Platten FM, Wright JR, Worden K, Dimitrladis G, Cooper JE (2007) Nonlinear identification in modal space using a genetic algorithm approach for model selection. Int J Appl Math Mech 3(1):72–89
5. Ezekiel M, Fox KA (1959) Methods of correlation and regression analysis: linear and curvilinear. Wiley, Oxford, p 548
6. Sharma S, Isik S, Srivastava P, Kalin L (2013) Deriving spatially distributed precipitation data using the artificial neural network and multilinear regression models. J Hydrol Eng 18(2):194–205
7. Voss HU, Timmer J, Kurths J (2004) Nonlinear dynamic system identification from uncertain and indirect measurements. Int J Bifurcat Chaos 14(6):1905–1933
8. Nash M (1998) Use of the multivariate mode indicator function for normal mode identification. In: IMAC, pp 740–744
9. Balmès E, Chapelier C, Lubrina P (1995) An evaluation of modal testing results based on the force appropriation method. In: IMAC-XIII, pp 47–53
10. Van der Auweraer H, Otte D, Debille J, Leuridan J (1992) Optimum force vector conditioning in incremental sine testing. In: IMAC, pp 299–306
11. Balmès E, Chapelier C, Lubrina P (1995) An evaluation of modal testing results based on the force appropriation method. In: IMAC-XIII, pp 47–53

Chapter 15
Support Systems for Developing System Models

Hasan G. Pasha, Karan Kohli, Randall J. Allemang, David L. Brown, and Allyn W. Phillips

Abstract From a system modeling perspective, it is important to develop an accurate mathematical model of a structure. Such a model can be built with measured frequency response functions obtained from a modal test. The test structure can be subjected to free, constrained or operating boundary conditions. Setting up a structure with either constrained or operating boundary conditions is impractical/prohibitive. It is easier to approach free boundary condition in the lab using soft supports, such as foam, shock cords, air suspension, etc. A good support system should have the least intrusion. It should not introduce nonlinearity or damping. The effectiveness of a good support system is quantified by the extent of separation of the rigid body modes from the elastic modes and a high degree of uncoupling of the dynamics of support system and the structural modes. The influence of various boundary conditions and soft support systems chosen for modeling a lightweight structures, such as Formula SAE racecar space frame, a rectangular steel plate structure and a circular aluminum plate are discussed.

Keywords Support systems • Modal testing

15.1 Introduction

In a lab environment it is tough to simulate unconstrained or completely constrained boundary conditions. However, it is relatively easier to approach unconstrained boundary conditions by supporting the test structure on a soft support system such as foam, shock cords or air rides. The primary goal of a support system is to insure that it does not add any stiffness or damping to the test structure, which could affect the dynamic characteristics of the test structure. For a pseudo unconstrained structure (nearly free–free), the rigid body modes should be observed close to $0\,\mathrm{Hz}$ and well separated from the elastic modes.

From a system modeling perspective, it is important to develop an accurate mathematical model of a structure. Such a model can be built from measured frequency response functions in a modal test. However, in the process of setting up and exciting the test structure, acquiring and processing the data, several errors can creep in. As mentioned earlier, it would be ideal to test a completely unconstrained structure. However, since the structure has to be supported in some manner to be able to conduct the testing, it is extremely important to analyze the effectiveness and suitability of support systems for conducting modal testing on a particular structure.

The primary requirement is that the support system should be non-intrusive, in that it should not introduce any additional mass or stiffness to the test structure. It should also not introduce nonlinearity or damping. In addition, the dynamics of the support system should be isolated from the dynamics of the test structure. It is also desirable to be able to build an inexpensive support system without the need for sophisticated gadgets where possible.

The following sections focus on reviewing the basic guidelines for selecting support systems for conducting modal tests in a lab environment. The various supports available for modal testing are briefly discussed. The results obtained with different support systems while testing structures such as, a Formula SAE racecar space frame, a rectangular steel plate and a circular aluminum plate, are presented. During the setup and testing, relatively inexpensive supports were used that yielded good quality data.

H.G. Pasha (✉) • K. Kohli • R.J. Allemang • D.L. Brown • A.W. Phillips
Structural Dynamics Research Lab (UC-SDRL), University of Cincinnati, Cincinnati, OH, USA
e-mail: pashahg@mail.uc.edu

15.2 Guidelines for Selecting Support Systems

There are some general guidelines in selecting support systems.

15.2.1 Separation of Elastic Modes from Rigid Body Modes

The rigid body modes must be well separated from the elastic modes. A *frequency separation ratio* (ratio of the lowest elastic mode frequency to that of the highest rigid body mode) of 10 is highly preferable, but it is hard to achieve. While conducting a modal test, a frequency separation ratio of at least 3–5 is recommended and used by test engineers [1]. The first few modes that are close to the rigid body modes are affected the most due to a stiff support system.

15.2.2 Location of Supports

The location of the supports in relation to the mode shapes of the structure can impact the results significantly. Ideally, if the structure is supported on its nodal points, the supports have negligible support–structure interaction. Due to the modal distribution, this is not possible in general. A compromise on the location of supports should be reached. If the modes of interest are identified, the supports can be located at their nodal points.

15.2.3 Isolation of Test Structure from the Support System and External Noise Sources

The dynamics of the support system can interact with the test structure. For instance, the support system can act as a vibration absorber if its frequency is in the vicinity of any of the elastic modes of the structure for that particular mode. In addition, vibration from external noise sources can be transmitted to the test structure through the support system. During the test setup, the response of the support system should be examined to ascertain that the support motion is negligible.

15.3 Types of Support Systems

Various supports are available to support structures while performing modal testing. The decision to select the support system is driven by the weight of the structure, ease of mounting the test structure and to a certain extent the cost and availability of the components. A direct relationship is evident between the support stiffness and the modal frequencies. Generally, modal frequencies increase when supported by stiffer components like springs as compared to softer support systems made of foam. Commonly used support system components are shown in Fig. 15.1.

15.3.1 Shock Cords

The shock cords are flexible and simple, which makes them suitable to suspend a light weight test structure. Shock cords are available in various sizes and stiffness. The test structure is generally suspended using shock cords of negligible mass and stiffness as compared to the test structure. Shock cords practically contribute negligible stiffness in the transverse direction. Thus the test structure is very weakly constrained in the transverse direction, which is ideal for measuring the elastic modes of interest. The position of shock cords generally has negligible influence on modal frequencies but can affect the damping estimates.

Fig. 15.1 Support systems used in modal testing

15.3.2 Soft Foam

Soft foam is relatively inexpensive and can be used to support test structures in a modal test. It is helpful in isolating the test structure the influence of external noise sources. In comparison to shock cords, which are generally considered weightless, foam could add more damping to structure. It is difficult to predict the damping effects. Foam supports can also have more mass loading effect as compared to shock cords. However, in the case of shaker tests, foam supports are considered advantageous to isolate the shaker excitation of a common shaker-structure base such as the floor.

15.3.3 Coil Springs

Coil springs can be used to support test structures. Springs are available in various sizes and stiffness. They are relatively stiffer than other typically used supports. They can also cause clicking noise or rattle, which could be transmitted to the test structure.

15.3.4 Air Springs

Air springs are typically used in modal testing of heavy structures, such as auto-bodies. They offer flexibility in terms of adjusting the support stiffness and typically result in very low rigid body frequencies, in the order of 3 Hz. They offer relatively higher degree of isolation compared to other types of supports. They are compact and light weight. Racquet balls and tennis balls could be used as air springs for supporting lightweight structures.

15.4 Experimental Examples

Relatively light weight structures, such as Formula SAE racecar space frame, a rectangular steel plate and a circular aluminum plate were tested with various support systems and configurations. The results obtained are discussed in the following sections. Soft support systems including foam, bubble wrap, springs, shock cords and air springs were used

Fig. 15.2 Formula SAE racecar space frame supports. (**a**) Car frame suspended using springs. (**b**) Car frame supported on soft foam blocks
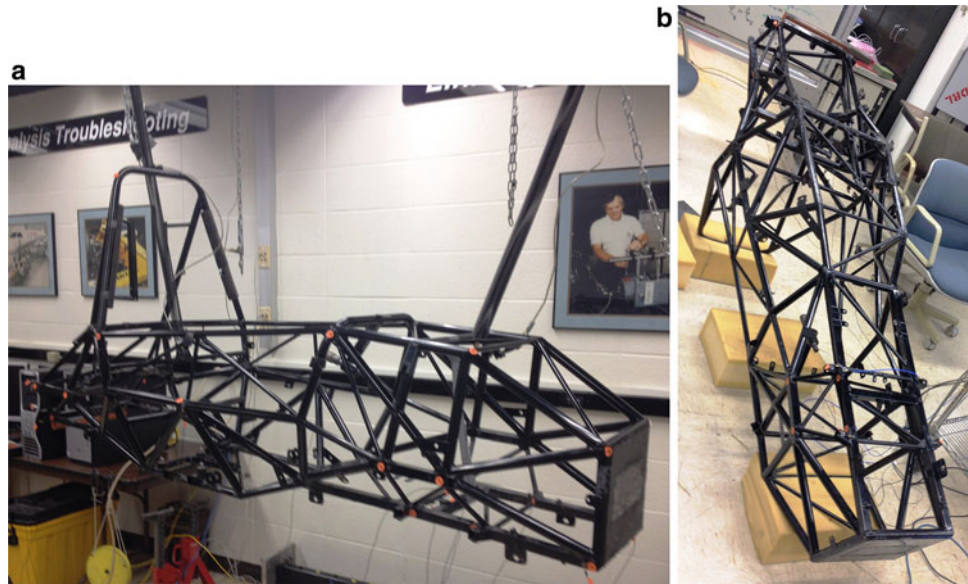
to simulate unconstrained boundary condition. The constrained boundary condition was also simulated for a structure. The effectiveness of the support systems is evaluated using the mode indicator functions, mode shape animations and consistency diagrams.

15.4.1 Formula SAE Racecar Space Frame

The car space frame is a welded steel structure containing various cross members, weighing about 55 lb. The objective of the modal test was to estimate the static torsional stiffness of the frame using driving-point and cross-point FRF measurements at the four shock absorber connection points. This method to estimate the static torsional stiffness is highly sensitive to the quality of the FRF measurements. Any localized stiffness could yield incorrect estimates for the static torsional stiffness value.

The frame was supported in two different configurations to simulate the unconstrained boundary condition. In the first configuration it was suspended using two garage door extension springs and in the other configuration it was rested on soft foam blocks as shown in Fig. 15.2a and b respectively.

In the spring suspension configuration, there were two modes observed in the 65–70 Hz frequency range. However, in the foam support configuration there was only one mode observed in the frequency range, as evident from the CMIF comparison plot shown in Fig. 15.3. This suggests that there is a dynamic coupling of the spring support system with the frame in the suspended configuration. The supports act as a vibration absorber at the first mode and the peak splits in the case of spring supports. In addition, small peaks are noticeable in the spring support system (blue curves in Fig. 15.3). It was also determined that the roof was excited due to an unbalanced ventilation fan. The external noise was transmitted to the car frame through the spring supports. However, the foam blocks damped out the noise and isolated the frame. The data acquired with soft foam supports was chosen to estimate the static torsional stiffness for the frame as it offered better isolation of the frame from the supports and external noise source.

15.4.2 Rectangular Steel Plate

A rectangular steel plate structure of dimensions $34'' \times 22.5'' \times 0.25''$ and weight of about 52.5 lb was tested. The goal of the modal test was to obtain a modal model of the plate to calibrate the FE model of the rectangular plate. The rectangular plate was tested in various configurations with different support systems.

Fig. 15.3 Comparison of CMIF
plots for car frame supports
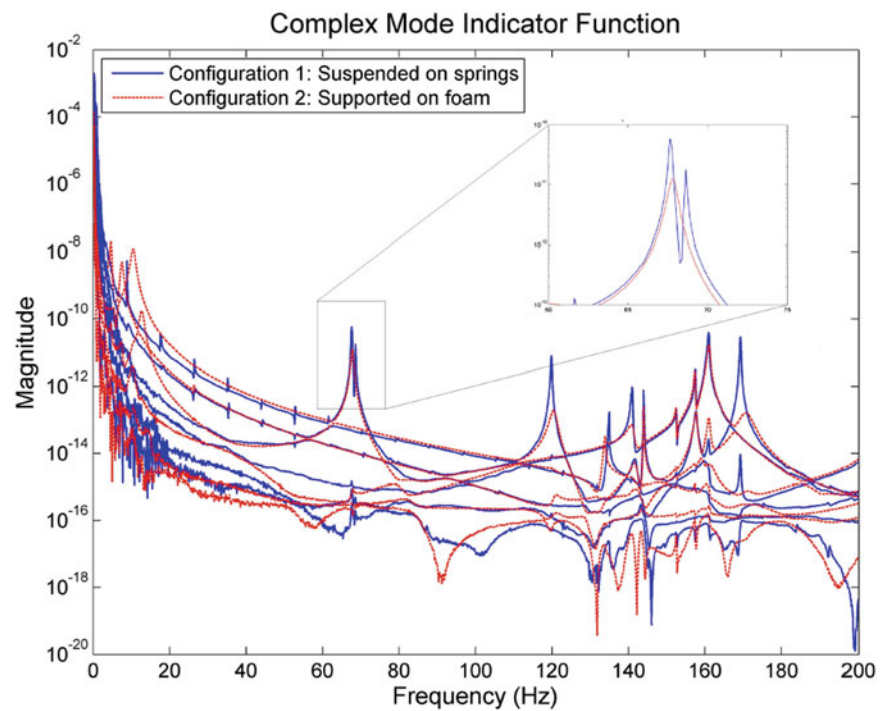
15.4.2.1   Unconstrained Boundary Condition Testing

To simulate the unconstrained boundary condition, the plate was supported on soft foam, bubble wrap, shock cords and air springs.

A limited impact test was performed to evaluate the quality of data obtained with different supports. The soft foam and bubble wrap supports did not yield good quality data. The relative error of the first elastic mode in these cases was too high. As a result, these configurations were not considered for further testing. The shock cords offered a high frequency separation ratio of 16.05 between the elastic modes and the rigid body modes, which is highly preferable. The stiffness of the cords was about 0.59 lb$_f$/in. However, the supports act as a vibration absorber for the third mode (II torsion mode at around 92 Hz) as evident from the consistency diagram shown in Fig. 15.7.

Air springs have been traditionally used for supporting airplanes and auto bodies while conducting modal tests. Smaller sized basketballs had been successfully used for supporting sail planes in previous tests conducted by UC-SDRL. The test structures typically tested in the lab as part of projects are relatively very light weight compared to airplanes or auto bodies. The goal is to come up with an inexpensive support system that could support light weight structures in a lab environment. In order to support lighter structures, such as the rectangular plate, stress balls, tennis balls and racquet balls were considered. Tennis balls are typically filled with compressed air (1 psi) and were relatively stiffer compared to stress balls and racquet balls. The stress balls tend to deform a lot and created a large contact patch (3–4″ diameter) on the plate, which could introduce localized damping into the plate. Racquet balls seemed to be optimum supports for the plate. With a relatively smaller contact patch (less than an 1″ diameter), there were no concerns of additional damping from the balls that could affect the quality of data obtained. It was also reasonably easier to control the location of the balls without gluing them down to the plate (Figs. 15.5 and 15.6; Tables 15.1 and 15.2).

In comparison to the shock cords, the racquet ball supports provided a lower frequency separation ratio. However, the plate structure was well isolated from the supports. This configuration provided the best quality data. The plate was supported with the racquet balls supported close to the nodal lines of the first four elastic modes (shown in Fig. 15.4).

15.4.2.2   Constrained Boundary Condition Testing

The plate was also tested in a constrained boundary configuration. The plate was clamped to ground at two locations near one of the edges using steel spacers, which in turn were grounded to a huge isolated mass as shown in Fig. 15.8.
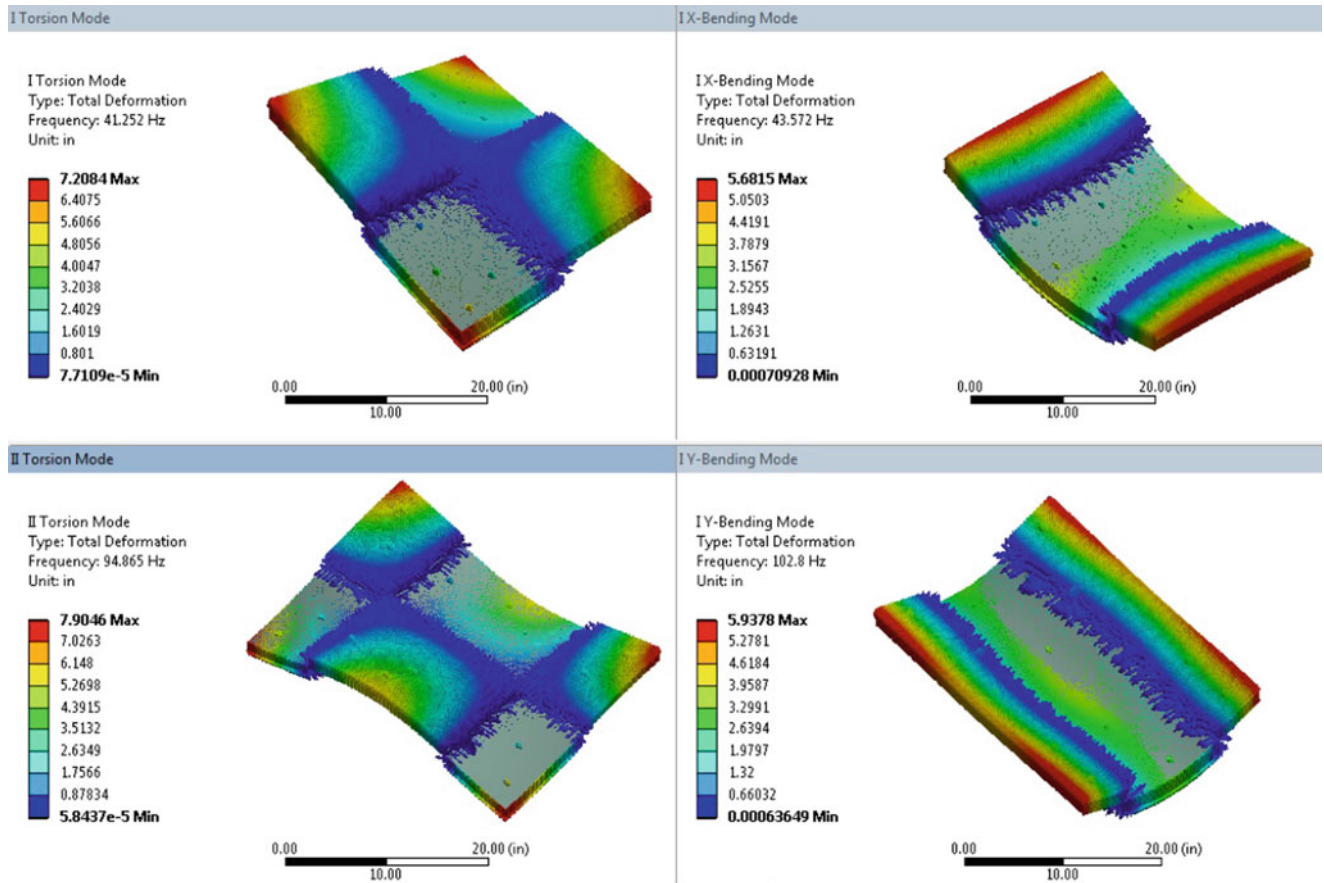
Fig. 15.4 Rectangular plate suspended using shock cords—consistency diagram

Fig. 15.5 Rectangular plate supports. (**a**) Rectangular plate suspended by shock cords. (**b**) Rectangular plate supported on racquet balls
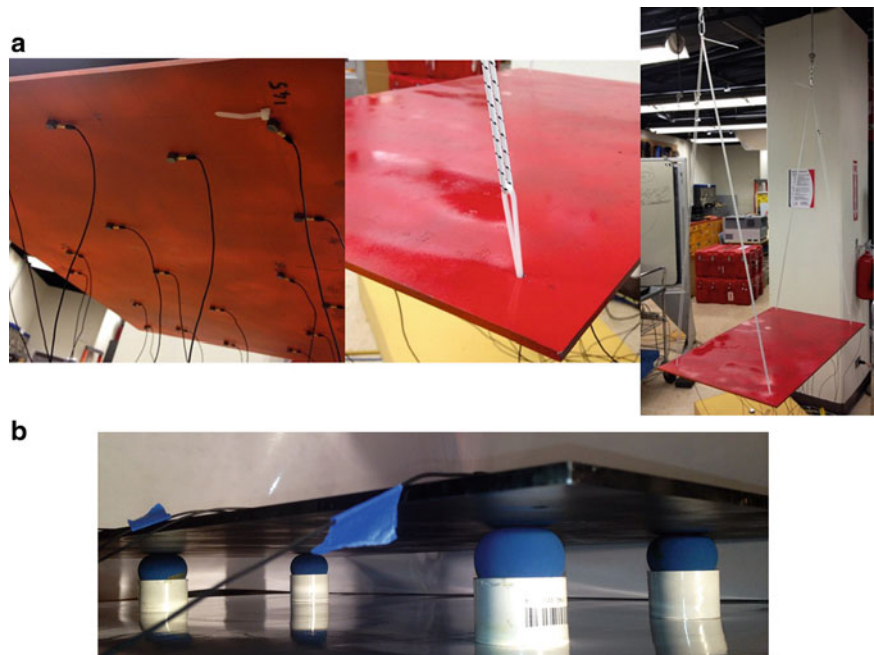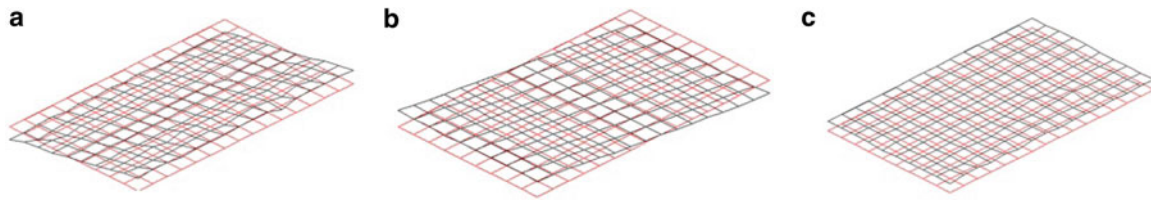
Fig. 15.6 Rigid body modes of the rectangular plate. (**a**) Roll mode (X-axis rotation); (**b**) pitch mode (Y-axis rotation); (**c**) bounce mode (Z-axis translation)

Table 15.1 Rigid body modes of the rectangular plate

Excitation	Support	Description	Freq (Hz)	Frequency separation ratio
Impact	Shock cords	Bounce	1.4	16.05
		Pitch	1.54	
		Roll	2.46	
Impact	Racquet balls	Roll	5.5	4.499
		Bounce	8.16	
		Pitch	9.37	
Shaker	Racquet balls	Roll	5.38	4.639
		Bounce	8.05	
		Pitch	9.06	

Table 15.2 Comparison of modal frequencies (relative error %) for various support systems used for testing rectangular plate

FE model (Hz)	Bubble wrap (Hz)	Foam (Hz)	Shock cord (Hz)	Stress balls (Hz)	Tennis balls (Hz)	Racquet balls (Hz)
41.33	39.96 (3.33)	40.19 (2.76)	39.53 (4.35)	42.03 (1.69)	43.75 (5.86)	42.16 (2.01)
43.71	43.09 (1.42)	42.96 (1.72)	42.66 (2.41)	44.06 (0.80)	44.49 (1.78)	44.16 (1.03)
95.04	92.75 (2.41)	92.80 (2.36)	92.34 (2.84)	95.63 (0.62)	95.72 (0.72)	95.58 (0.57)
103.10	104.50 (1.36)	103.87 (0.75)	103.75 (0.63)	104.69 (1.54)	104.80 (1.65)	104.60 (1.45)
118.19	115.52 (2.26)	115.85 (1.98)	115.47 (2.30)	119.22 (0.87)	119.00 (0.69)	119.05 (0.73)
137.38	139.19 (1.32)	138.48 (0.80)	138.13 (0.54)	137.97 (0.43)	138.40 (0.74)	137.98 (0.44)
175.52	172.80 (1.55)	172.98 (1.45)	172.66 (1.63)	176.56 (0.59)	176.40 (0.50)	176.38 (0.49)
202.86	200.62 (1.10)	200.57 (1.13)	200.47 (1.18)	204.06 (0.59)	203.80 (0.46)	203.72 (0.42)

In order to evaluate the effectiveness of the constrained boundary conditions employed in the "Measured Constrained" structure, the CMIF of the measured data was compared with that of the modeled data. The data from an unconstrained boundary modal test with driving-point FRF measurements at locations corresponding to the clamping locations was obtained. Impedance modeling technique was applied to ground the clamping locations using very stiff springs to obtain a "Modeled Constrained" system. Clamping constrains rotation of the plate in addition to constraining the vertical motion. This is evident from Fig. 15.9, the *Measured Constrained* system is considerably stiffer than the *Modeled Constrained* system.

15.4.3   Circular Aluminum Plate

A circular aluminum plate structure, shown in Fig. 15.10a, of diameter 30″, thickness 0.25″ and weight of about 17.5 lb was tested. The goal of the modal test was to perform a modal correlation of the impact test based modal model with the FE modal model. Thirty uniaxial accelerometers were mounted on the plate and thirty driving-point locations were impacted. The circular plate was supported on 3 coil springs placed about 10.5″ away from the center and 120° apart as shown in Fig. 15.10b. In order to prevent rattle, the springs were glued to the plate.

The glue material is viscoelastic. As a result, there is some localized damping introduced to the structure at the support points. At the 565 Hz and 770 Hz modes, there is considerable motion at the support points as shown in Fig. 15.11a,b respectively. Due to local damping at the support points, these modes are slightly complex. This was evident by observing

Fig. 15.7 Node lines for first
four elastic modes of the
rectangular plate
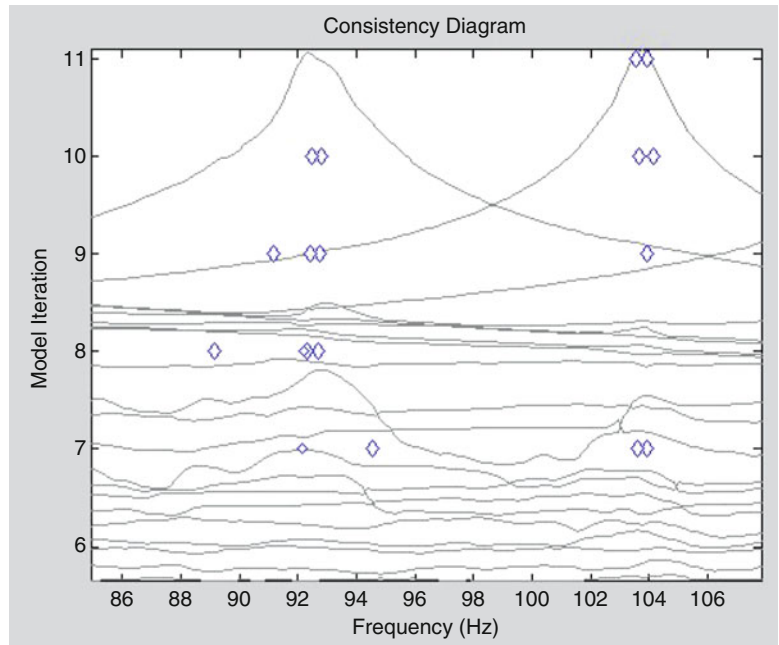
Fig. 15.8 Constrained plate.
(**a**) Constrained plate setup;
(**b**) clamping supports and
location
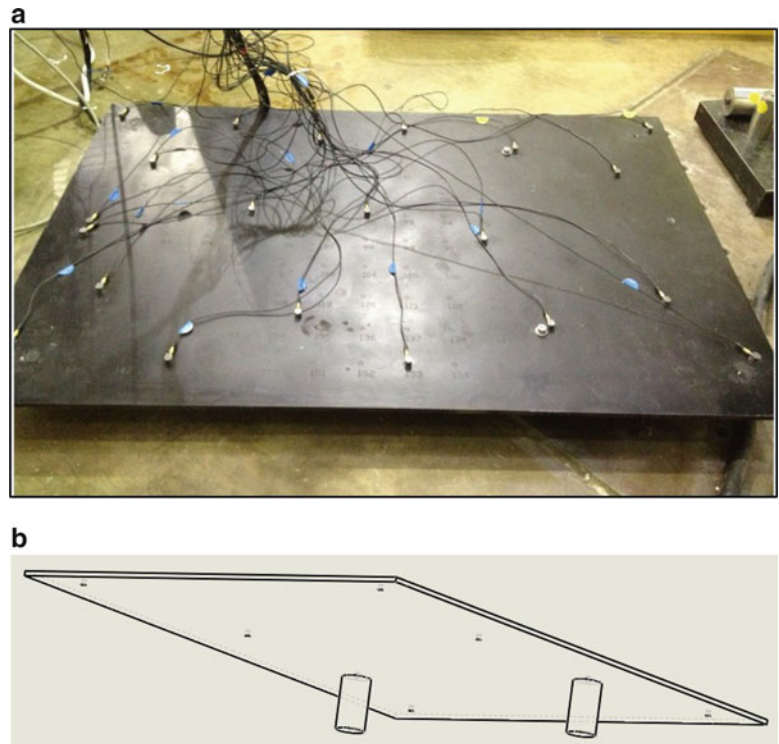
the mode shape animations and by examining the Modal Phase Collinearity (MPC) criterion displayed in the Consistency Diagram (Fig. 15.12). The MPC criterion for real modes is close to 1; however, for the 565 Hz and 770 Hz modes the values were 0.643 and 0.538 respectively.

Fig. 15.9 Comparison of CMIF plots: constraints modeled using impedance modeling vs measured
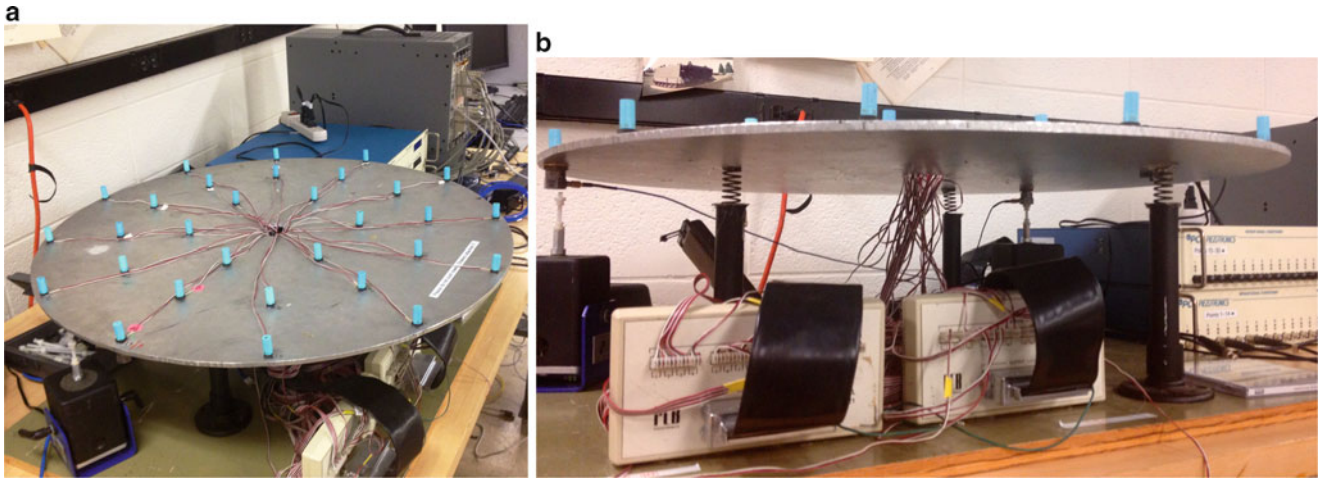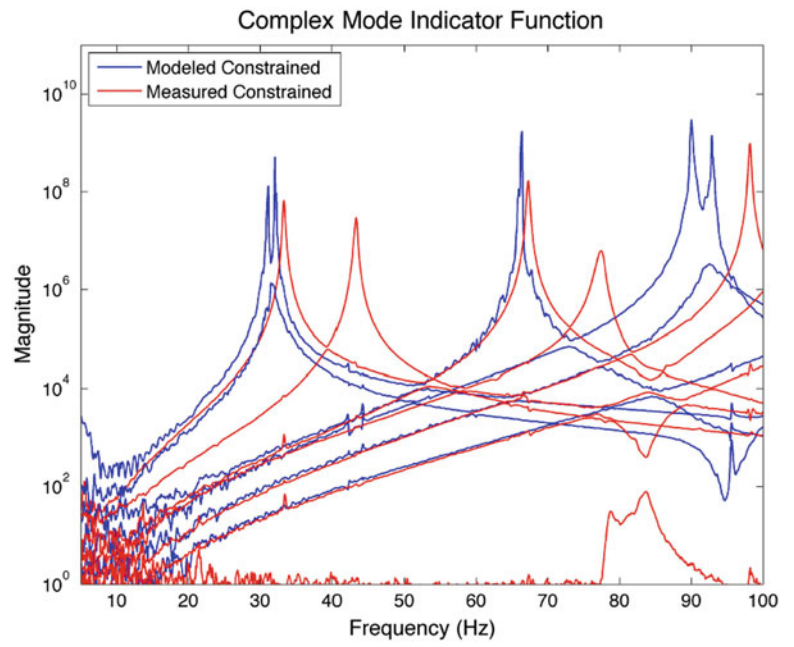
Fig. 15.10 Circular plate. (**a**) Circular plate with accelerometers; (**b**) support system
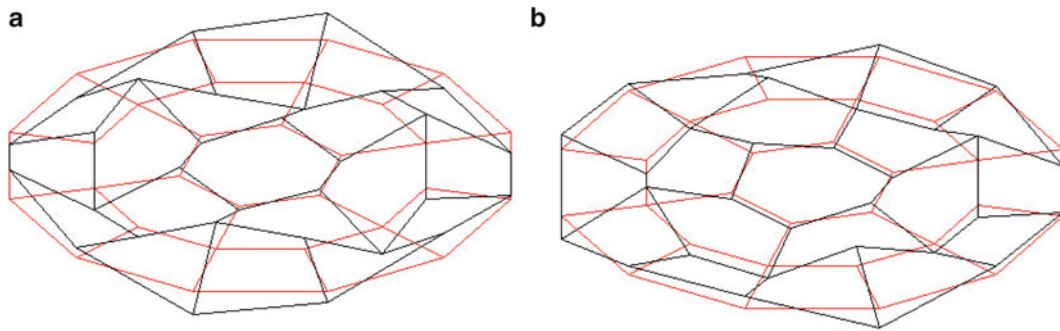
Fig. 15.11 Circular plate—complex modes. (**a**) Mode at 565 Hz; (**b**) mode at 770 Hz
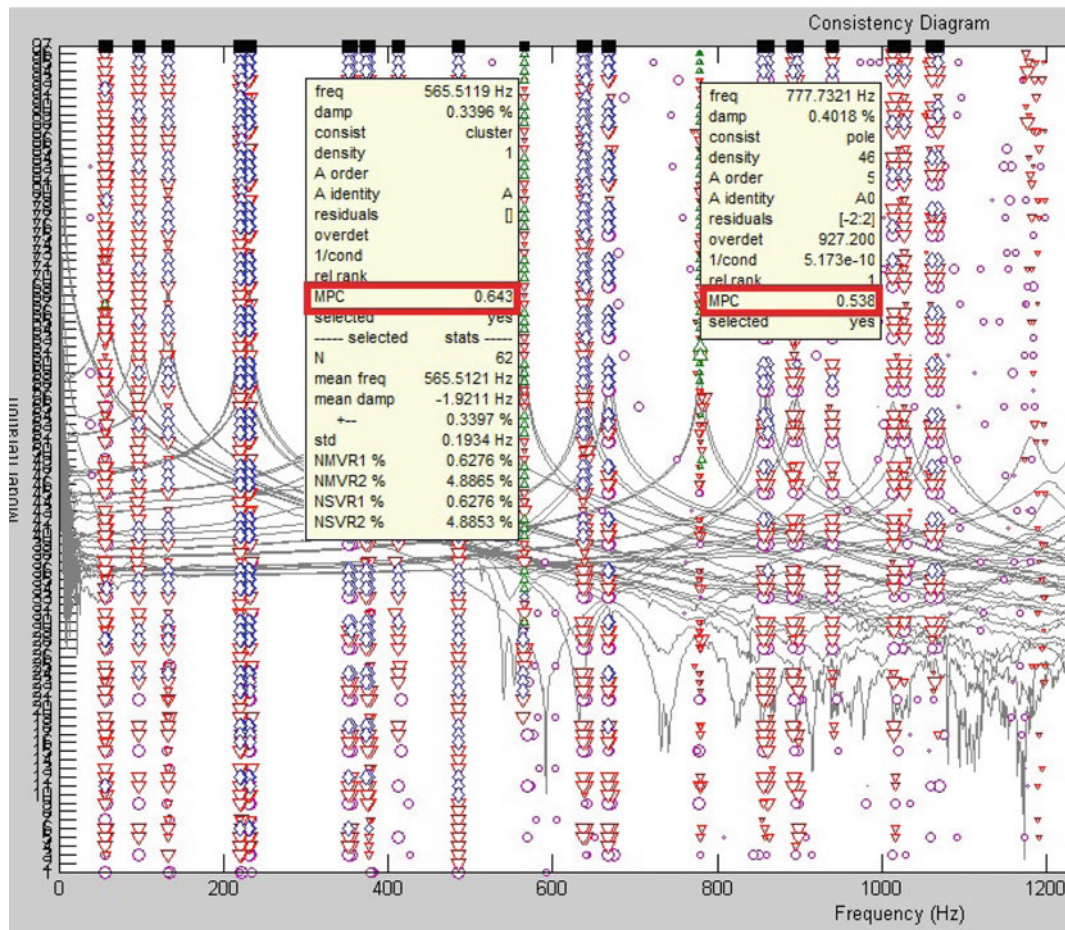
Fig. 15.12 Circular plate—consistency diagram

15.5 Conclusions

- It is easier to simulate unconstrained boundary condition in the lab when compared to clamped or operating boundary conditions.
- Certain guidelines should be followed while selecting support systems for modal testing:

  1. The frequency separation ratio of 10 is highly preferred for a support system. However, it should be at least in the range of 3–5.
  2. Based on the purpose of the modal test, the supports should be positioned at or near the node line of the modes of interest if possible.
  3. While support system that offers higher frequency separation ratio is more desirable, special care should be taken to insure that the structure is isolated from the support system and external noise sources.

- The first few elastic modes are affected the most due to a stiff support system.
- Typically soft foam, shock cords and springs are used to support lightweight structures in the lab. Air springs are typically used to support heavier structures, such as auto-bodies and airplanes. Racquet balls could be used as air springs for supporting light weight structures.
- The mode indicator functions, mode shape animations and consistency diagrams aid in determining the effectiveness of a support system.
- In the case of rectangular plate structure it was evident that though shock cords provided the desirable frequency separation ratio greater than 10, they were dynamically coupled with the test structure.

- Racquet balls could be used as inexpensive and effective support systems for supporting lightweight structures. For the rectangular steel plate structure, they offered a frequency separation ratio of about 4.5 and a high degree of dynamic isolation.

References

1. Wolf JA Jr (1984) The influence of mounting stiffness on frequencies measured in a vibration test, SAE Paper 840480. Society of Automotive Engineers, Inc.
2. Carne TG, Griffith DT, Casias ME (2007) Support conditions for experimental modal analysis. Sound Vib 10–15
3. Badshah S (2013) On modal testing and analysis of aluminum foam: experimental setup and approach. Int J Emerg Technol Adv Eng 3(4)
4. The Fundamentals of Modal Testing, Application Note 243-3, Hewlett-Packard Company, US 1997
5. Blevins RD, Formulas for Natural Frequency and Mode Shape, Krieger Publishing Company, 1979
6. Schwarz BJ, Richardson MH (1999) Experimental modal analysis. In: CSI Reliability Week, Orlando, FL, October 1999

Chapter 16
Nonlinear Modeling for Adaptive Suppression of Axial Drilling Vibration

Benjamin Winter, Garrison Stevens, Rex Lu, Eric Flynn, and Eric Schmierer

Abstract Vibrations developed during drilling present challenges in an array of industries including mechanical, medical, structural, and oil extraction. Velocity weakening, intracranial vibrations, large amplitude standing pressure waves in material cavities, and failure of drill strings are prominent issues among these fields. Stick-slip (torsional) and bit-bounce (axial) vibrations have been found to be particularly problematic in precision drilling jobs such as machining to tight tolerances, dismantling vibration-sensitive devices, and surgical work. Current technologies to detect and suppress systematic vibrations have several shortcomings including malfunctioning, complete failure, complexity, and high power consumption. This paper proposes a method to suppress vibrations of drilling material surfaces using adaptive positive position feedback (APPF) control for efficient tunable damping. An experiment-based parametric study has been conducted to determine the relationship of force, rotational velocity, and acceleration on both drill vibrations and drilling material surface vibrations. Results of a parametric study and Rational Polynomial Fraction method are used to estimate fundamental behaviors of the drilling system to create a refined numerical model for simulating the drilling process. An APPF controller together with the model provided a method to evaluate new actuator designs for vibration suppression and has shown a 69.8 % reduction of displacement vibrations.

Keywords Drilling dynamics • Adaptive positive position feedback • Vibration suppression • Rational polynomial fraction

16.1 Introduction

Issues that exist with drilling reach across several industries involving low and high precision processes. Vibratory issues that affect these industries exist in the torsional and axial directions commonly known as stick-slip and bit-bounce, respectively. Problems associated with drill bit vibration impact mechanical and structural systems along with the medical field and the oil drilling industry. Zho et al. have shown that vibratory propagation through materials is a prominent issue in the medical

---

B. Winter
Department of Civil Eng, Michigan Technological University, Houghton, MI, 49931 USA
e-mail: bdwinter@mtu.edu

G. Stevens
Glenn Department of Civil Eng, Clemson University, Clemson, SC, 29632 USA
e-mail: gnsteve@g.clemson.edu

R. Lu
Department of Mechanical Eng, University of California Riverside, Riverside, CA, 92507 USA
e-mail: rlu003@ucr.edu

E. Flynn (✉)
Engineering Institute, Los Alamos National Laboratory, Los Alamos, NM, 87545 USA
e-mail: eflynn@lanl.gov

E. Schmierer
ITP Energy Systems, Los Alamos National Laboratory, Los Alamos, NM, 87545 USA
e-mail: schmierer@lanl.gov

industry that can lead to perceivable and uncomfortable audio within the ear canal [1]. Intracranial vibrations have been simulated in rodents to model the behavior of hair cells within the cochlea. These studies have shown that hearing loss (temporary and permanent) is possible under easily achievable ranges of vibrations either propagating from the source of drilling or amplified within cranial cavities [1]. Noise associated with large drilling operations, such as in coal mines, causes deafness, one of the most common illnesses within the high noise exposure related occupations [2].

Another problem observed in drilling applications particular to mechanical and structural systems is often observed. When assembling/dismantling vibration-sensitive devices or repairing bridges amplified vibrations occur in material cavities. These large amplitude standing pressure waves can cause undesired behavior of mechanical parts and fracture aggregate or concrete in columns [3]. Drilling into the ground may cause standing pressure waves, but the issues observed in this industry are damage to or failure of drill strings [4]. Drill strings fail when oscillating in the axial and lateral (bending) directions. The aforementioned problems can be effectively eliminated if the drill system could control vibrations in a manner adaptive to change in vibrations and non-homogeneity.

Current approaches for dissipating vibrations within the drilling system focus on damping the material directly. Creasy et al. have shown that attempts to suppress the vibrations of drilling material using passive damping have been successful [3]. However, with these attempts came apparent shortcomings that are common in most passive systems. Passive dampers are non-tunable to unforeseen scenarios; hence fail to provide any damping when vibrations exceed 10 % beyond specification of each damping system. An increase in vibrations often leads to passive dampers becoming destroyed [3, 5]. Work to overcome the failure within passive damping strategies brought about active damping devices, such as piezoelectric actuators. Active dampers will damp vibrations of the drilling material directly and can damp to known peak frequencies and frequency fluctuations. The downfall associated with fully-active damping devices are increased power consumption. The required power directly relates to accommodating for previously collected vibration/frequency records. Though active dampers can be used in similar applications related to the original purpose they lack the ability to behave properly to new drilling conditions. Additionally, active devices can potentially weaken a structure when not used as intended. Active dampers can apply loading to the structure that excite resonances rather than mitigating them [6]. To overcome these shortcomings this paper proposes the use of an adaptive positive position feedback (APPF). The adaptability of the actuator-controller system utilizes lower amounts of power unlike traditional active dampers and allows for actuators to be used in many applications. Adaptive feedback for actuators is more robust because both the damping coefficient and applied force are tuned to changing dominant frequencies obtained through Fourier analysis of the model. This robustness ensures the actuator will not be subject to manufactured limits of frequency range seen in passive damping.

The purpose of this analysis is to create a model that best captures the modal behavior of the interactions between the drill and part material as shown in Fig. 16.1. With test data, the model can be refined to demonstrate modal properties observed during actual drilling. The model also utilizes vibrational frequencies found in the drill bit as a result of the nonlinear interaction of the bit to part interface. To refine the model the nonlinear behavior of the system is attributed to the main cantilever mode of the different mechanical apparatuses. With the proposed model, an APPF controller is exploited to suppress high amplitude frequencies detected in the model. Prior to drilling, parameter estimation is used to get initial stiffness and damping ratio parameters characterizing the fundamental behavior of the system. During the drilling process a Fourier analysis of sampled acceleration data provides the dominant frequency as a response to the axial motion of the drill bit and the controller. The APPF controller uses the governing frequencies that change over time to adaptively eliminate chatter by diminishing different modes using multiple actuators. The coupled model will be used to determine sensor information and relationships between parameters that will be critical for the future implication of an APPF system in the field.

16.2 Model Development

The goal of this research is to develop a model coupled with an Adaptive Positive Position Feedback controller that can be used to simulate many different drilling tools and materials. For this reason, the model needs to be simple and flexible enough to be adjusted to different situations. Reducing the system to a mass-spring-damper (MSD) system allows the model to be flexible to variation in tool and material dynamics while maintaining fidelity in simulations. Since the main interest of this paper is to implement a model for adaptive vibration suppression, the axial vibrations induced in the material being drilled are our main concern, as this result in the largest vibrations. Thus, the developed model to be used with the adaptive controller is a nonlinear, single axis, 2nd order ODE system. The MSD model of the system is displayed in Fig. 16.2 with $\mathbf{M_1}$ as the mass of the material, $\mathbf{M_2}$ as the tool, $\mathbf{F}$ as an applied constant load, $\mathbf{K}$ as the spring constant, and $\mathbf{C}$ as the damping constant, and $\mathbf{u(\omega)}$ as an applied displacement related to the operating drill speed. The mathematical equation from the MSD model is shown in Eq. (16.1) as state-space form. As previously described in Sect. 16.2, frequency and damping for the

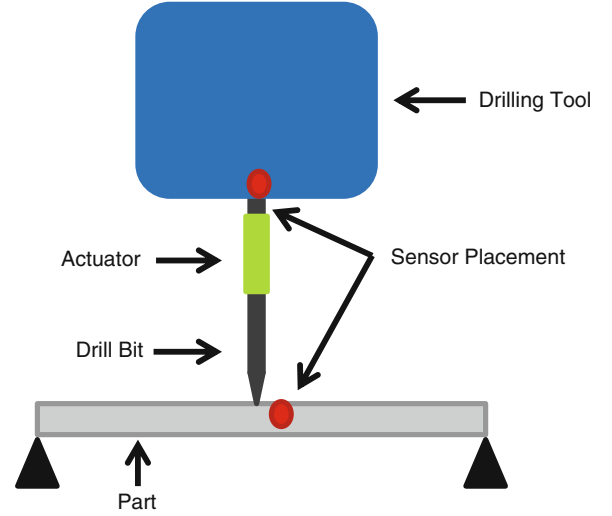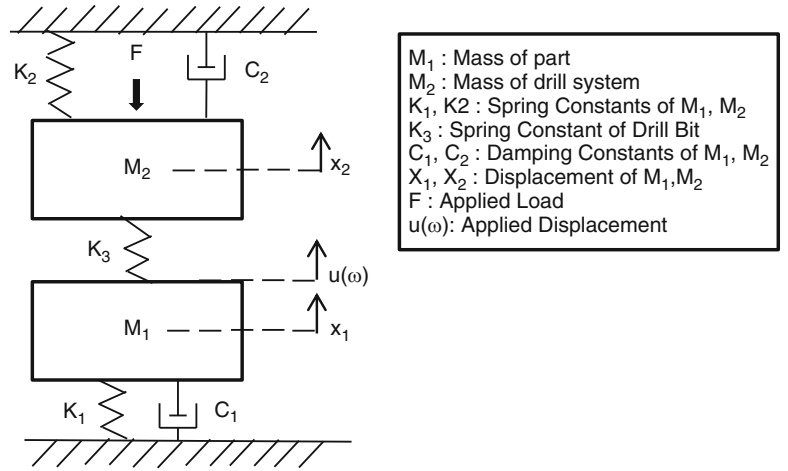**Fig. 16.1** Proposed drill/part vibration suppression system

Fig. 16.2 Two degree of freedom drill system model

M_1 : Mass of part
M_2 : Mass of drill system
K_1, K2 : Spring Constants of M_1, M_2
K_3 : Spring Constant of Drill Bit
C_1, C_2 : Damping Constants of M_1, M_2
X_1, X_2 : Displacement of M_1,M_2
F : Applied Load
u(ω): Applied Displacement

drill system and the material must be determined experimentally. The mass of each component is measured, if possible, or assumed. The spring and damping constants for the drill system and part (K_1, K_2, C_1 and C_2) are determined experimentally as later described in Sect. 16.3.1. The spring constant for the drill bit (K_3) is determined experimentally as described in Sect. 16.3.2.

$$\begin{bmatrix} 0 & 1 & 0 & 0 \\ -\frac{k_1+k_3}{m_1} & -\frac{c_1}{m_1} & \frac{k_3}{m_1} & 0 \\ 0 & 0 & 0 & 1 \\ \frac{k_3}{m_2} & 0 & -\frac{k_2+k_3}{m_2} & -\frac{c_2}{m_2} \end{bmatrix} \cdot \begin{Bmatrix} x_1 \\ \dot{x}_1 \\ x_2 \\ \dot{x}_2 \end{Bmatrix} + \begin{Bmatrix} 0 \\ -\frac{k_3 u}{m_1} \\ 0 \\ \frac{F+k_3}{m_2} \end{Bmatrix} = \begin{Bmatrix} \dot{x}_1 \\ \ddot{x}_1 \\ \dot{x}_2 \\ \ddot{x}_2 \end{Bmatrix} \tag{16.1}$$

A constant force, **F**, and a varying displacement, **u(ω)**, are the inputs driving the model. The applied displacement functions as a simulation of the frequencies being input to the system relative to the rotational speed of the drill i.e.

$$\mathrm{Sin}\left(\frac{570 \text{ rpm}}{60 \text{ rpm/Hz}} *2\pi *t\right) + \mathrm{Sin}\left(\frac{1720 \text{ rpm}}{60 \text{ rpm/Hz}} *2\pi *t\right), \tag{16.2}$$

where the spindle speed is set using belts in this example to be 570 rpm and the motor speed is a constant 1,720 rpm). Inputting these frequencies as a displacement essentially creates an acting force on both masses in equal and opposite directions, forcing them apart. To simulate the non-linearity introduced due to the drill bit and material coming in and out of contact the spring representing the drill bit is a bi-linear spring. When the K_3 and M_1 are in contact, the spring has a stiffness equivalent to the stiffness of the drill bit, however, when they are not in contact the stiffness of K_3 becomes zero, as shown

Fig. 16.3 Bi-linear spring stiffness, **K₃**, as a function of distance between **M₁** and **M₂**
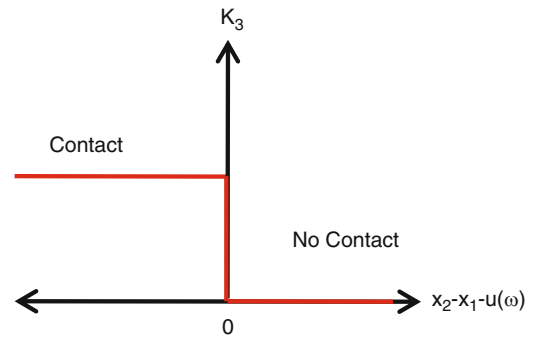
in Fig. 16.9. Therefore, by the spring stiffness going to zero in the out of contact condition, the force being applied to the system will not be transferred to the bottom mass, inducing nonlinear behavior. Nonlinearity in the model can be seen in Fig. 16.3, where the red areas display the harmonic response frequencies. Resonant frequencies are also seen around 150 Hz and 220 Hz, corresponding to the first mode of the plate alone and the first mode of the plate and drill in contact, respectively.

16.3 Experimental Study of Model Parameters

The experimental approach discussed in this paper is used to obtain necessary parameters for the developed model. First, each component was studied separately through modal testing to gain an understanding of their dynamic characteristics. Parameter estimation was used to interpret the data and determine the spring and damping parameters needed for the model. During the drilling process, bit-bounce causes the drill bit and plate to come out of contact at some points in time, resulting in nonlinear behavior. To understand the changes introduced by the change in contact condition, the components were also tested while in contact to determine the dynamics of the entire system. By progressing in this manner, the interacting dynamics between different components when in contact and out of contact can be observed.

16.3.1 Experimental Study of Independent Model Parameters

For this study, a Jet JDP-15MF drill press was the drilling tool analyzed. Modal analysis of the drill press was completed to determine the dynamics that the tool will contribute to the vibrations of the material being drilled. Impact testing using a PCB Piezotronics impact hammer was conducted with 27 PCB Piezotronic accelerometers attached to nine locations of the drill press for tri-axial data acquisition, using a National Instruments LabVIEW system. The experimental test setup is shown in Fig. 16.4.

Results of the modal analysis showed the plate of the drill press to support the drilling material had the most motion. For this reason, the decision was made to use a separate table to support the drilling material to isolate the dynamics of the drilling components of the system and remove the dynamics of the supporting plate, which is a better representation of real-world drilling scenarios.

For initial model development, aluminum plates ($30.0 \times 30.0 \times 0.6$ cm) were used as the drilling material. Plates were clamped at the corners to the supporting table. Nine accelerometers were placed on the plate, evenly spaced on a 7.5×7.5 cm grid to measure acceleration in the vertical direction. The plate was impacted with an impact hammer at the node in the center of the plate. The experimental setup is shown in Fig. 16.5.

16.3.2 Parameter Estimation

Modal parameter estimation is the process of determining frequency, damping ratios, and mode shapes from experimental data. Input force data measured by the impact hammer and acceleration data measured by accelerometers were used to create the frequency response function (FRF) for the two components individually. This FRF was then used with parameter estimation techniques to determine the modal parameters, such as frequency and damping ratio, for each component. This

Fig. 16.4 Drill press modal analysis experimental setup

One Tri-axial Accelerometer

0.254 m   0.254 m   0.279 m

Speed Selection Belts

Drill Press

0.076 m

Motor

Drill Chuck/Spindle

0.483 m

Drill Bit

Column

0.279 m

0.381 m

Table

Table Clamp

0.686 m

0.305 m

0.025 m
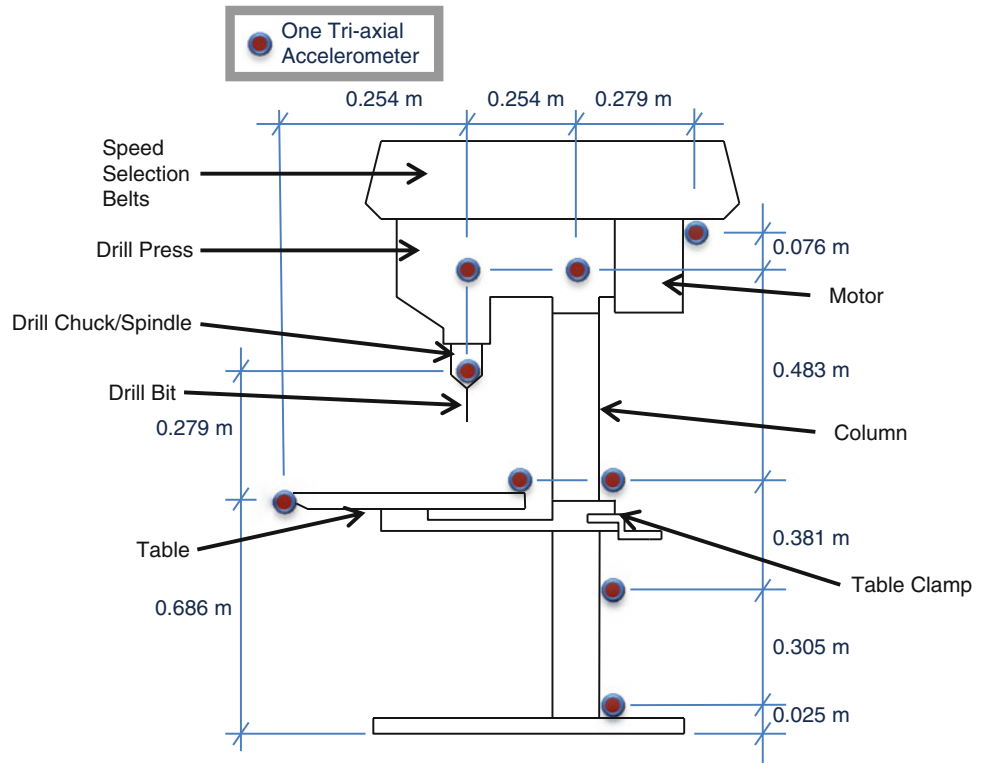
Fig. 16.5 Aluminum plate modal analysis experimental setup
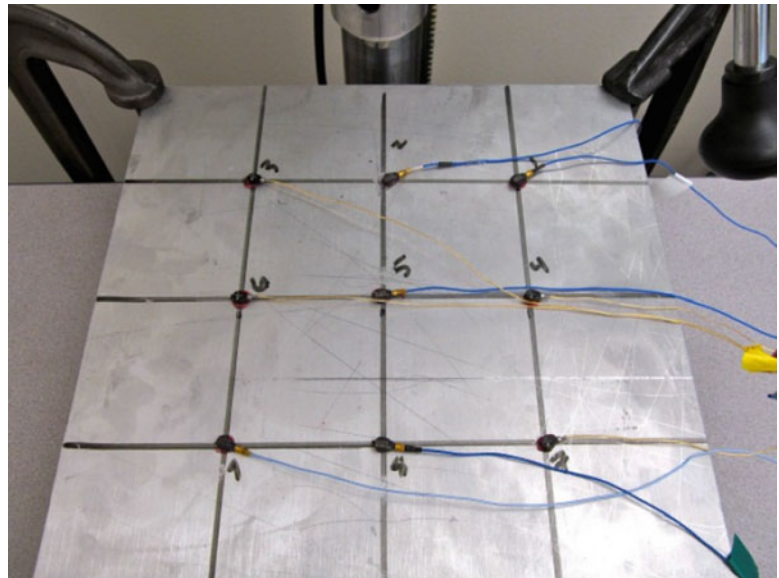
process, which is a form of curve fitting, has been implemented in the past 40 years to characterize the linear dynamic properties of structures [7–9]. The Rational Fraction Polynomial (RFP) method, developed by Richardson and Formenti, is a technique to estimate parameters directly from the FRF. The RFP method solves a set of linear equations for the unknown numerator and denominator polynomial coefficients of a given frequency data set. The curve fitting models can be described as either Eq. (16.3) or Eq. (16.4) also known as Rational Fraction Form or Partial Fraction Form, respectively (where r_k and p_k are the kth residue and pole $(-\sigma_k + j\omega_k)$ respectively, σ_k is the kth rate of decay, ω_k is the kth oscillation frequency, and $j = \sqrt{-1}$) (Richardson and Formenti 1982).
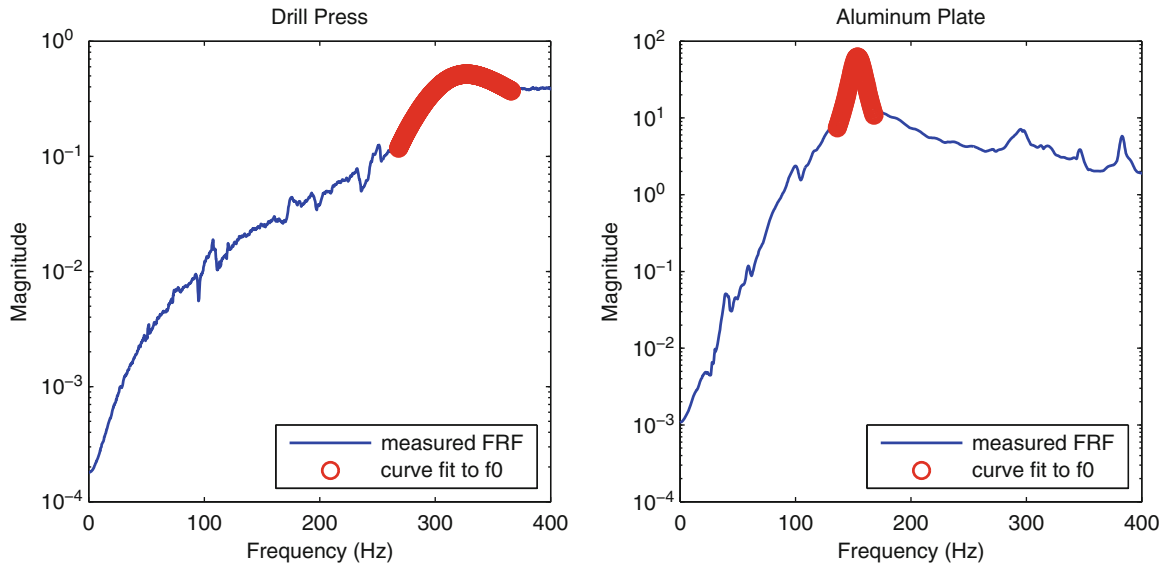
Fig. 16.6 FRF of drill press (*left*) and aluminum plate (*right*) obtained experimentally and curve fit FRF for desired frequency range

Table 16.1 Estimated modal parameters

	Drill press	Aluminum plate
Frequency (Hz)	308.0	153.0
Damping (%)	6.50	1.45

$$H(\omega) = \frac{\sum_{k=0}^{m} a_k s^k}{\sum_{k=0}^{m} b_k s^k}\bigg|_{s-j\omega} \tag{16.3}$$

$$H(\omega) = \sum_{k=1}^{n/2} \left[\frac{r_k}{s - p_k} + \frac{r_k^*}{(s - p_k)^*} \right]\bigg|_{s-j\omega} \tag{16.4}$$

The RFP uses the rational fraction polynomials to solve for the poles and residues. The number of unknown coefficients of both the numerator and denominator polynomials, (a_k, k = 0, k = 1, ..., m) and (b_k, k = 0, k = 1, ..., n), are proportional to the number of determined modes. By applying RFP across a small, desired frequency range, the parameters of the experimental FRF data obtained from the drill press can be estimated. For the purpose of this model, it was necessary to characterize the modal parameters of the fundamental mode of each component. The curve fit and parameter estimation of the modal drill test and the modal plate test are shown in Fig. 16.6 and Table 16.1.

16.3.3 Experimental Study of Drill Bit Model Parameters

Separate analyses of the drilling tool and material were necessary to determine modal parameters of the components for modeling. However, it was also necessary to complete an analysis of the components when in contact in order to characterize properties of the drill bit, which serves as the connection between the two systems. To study the characteristics of the drill bit, particularly how the additional contact condition affects the fundamental frequency of the plate, an impact test was completed with the drill bit and plate in contact. Five accelerometers placed on the plate collected acceleration data from an impact at the center of the plate. The experimental setup is shown in Fig. 16.7.

The test was completed three times, each with an increased load applied to the plate. The load being applied to the down feed handle was measured using a force gauge. The FRF for the plate at each different preload was compared to the FRF of the plate with no load applied to analyze the shift resulting in the fundamental frequency, as shown in Fig. 16.8. Following this test, a finite element model was developed using ABAQUS to determine the effective spring stiffness of the drill which would cause the frequency shift observed experimentally. Results of the spring analysis are shown in Fig. 16.9 and Table 16.2.

Fig. 16.7 Plate being preloaded with a measured force for testing of drill and plate in contact
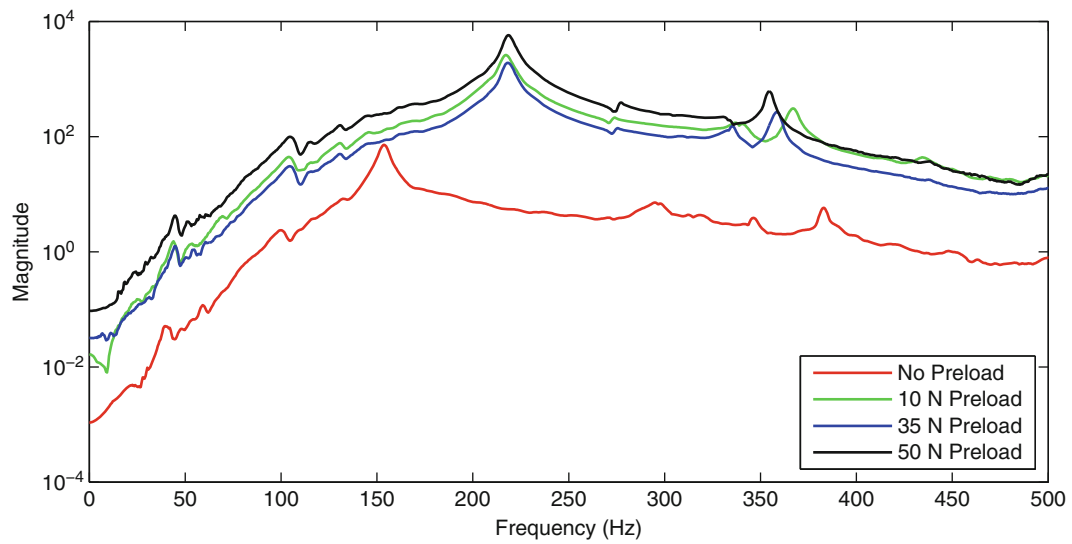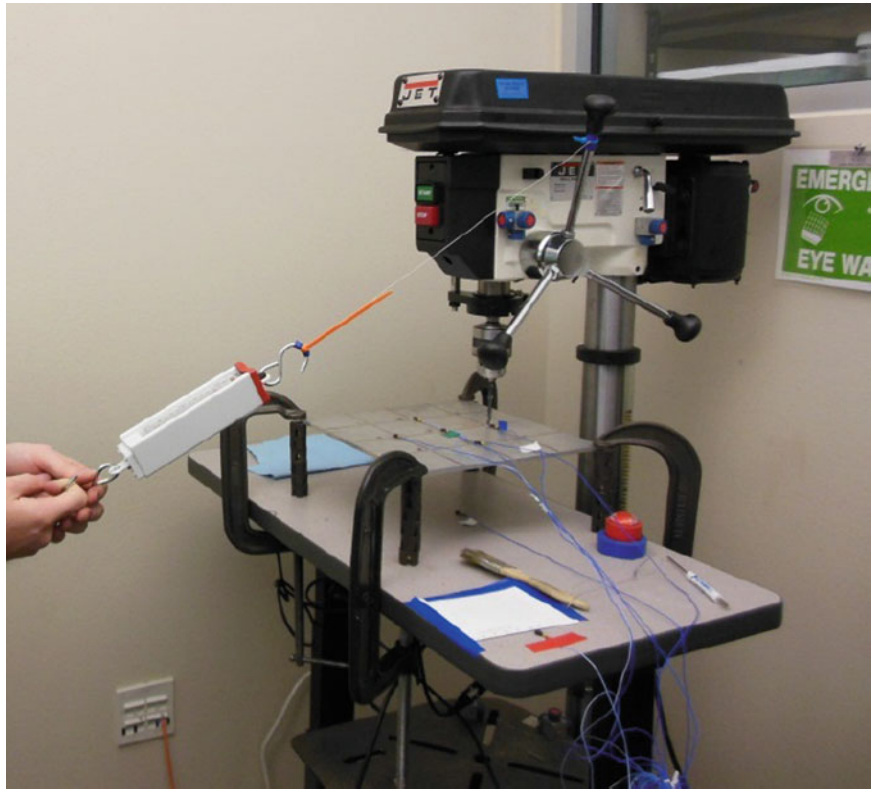
Fig. 16.8 FRF of plate with increasing preloads

The finite element analysis determined a spring stiffness of approximately 3 MN/m was necessary to achieve a frequency equivalent to the shifted frequency of 220 Hz observed experimentally.
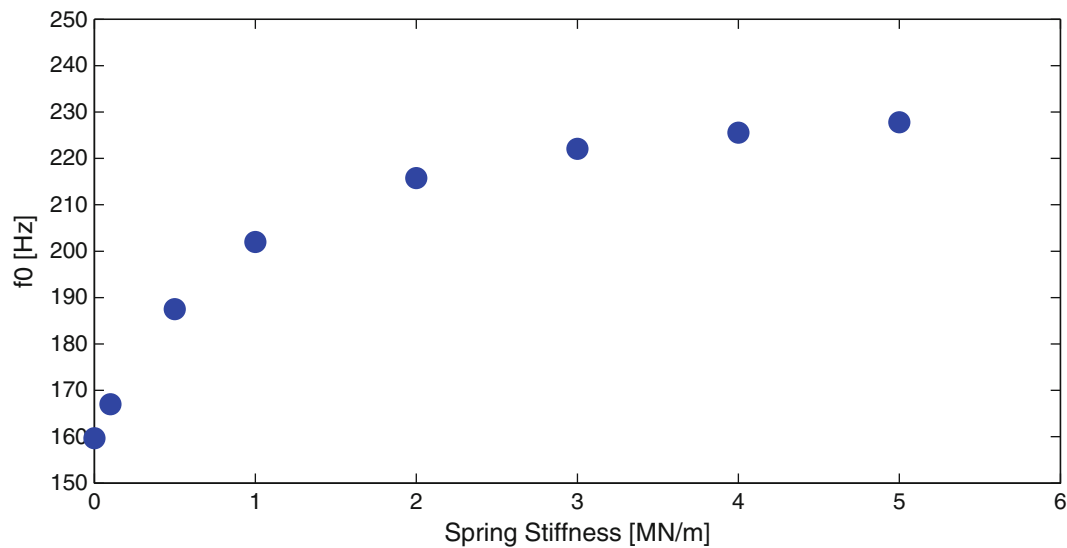
Fig. 16.9 Frequency shift as spring stiffness in increased

Table 16.2 Stiffness and frequencies

Stiffness (MN/m)	f_0 (Hz)
0	159.67
0.1	166.97
0.5	187.52
1	201.98
2	215.75
3	222.04
4	225.57
5	227.81

16.4 Test Analysis Correlation to Experiments

The ability of the numerical model to predict frequencies and accelerations similar to the true system was evaluated through test analysis correlation to experiments. First, the model was tested with a linear case where the drill press and plate are always in contact. Next, the model was expanded to a nonlinear case to test the ability of simulations to produce harmonics

16.4.1 Linear Modal Analysis

Testing the model in a linear case was performed first to ensure the model in a simple case functions correctly. Linear simulations were completed by setting the spring constant of the drill bit to be constant rather than bi-linear. An impulse excitation was applied to the system by applying an initial velocity and no disturbance input. The FRF of the simulations was used to determine the two frequencies corresponding to the modes of the system. The simulation results were then compared to an experimentally obtained FRF of the system always in contact with an impulse excitation created by an impact on the plate. Comparison of the simulation and experimental FRFs is shown in Fig. 16.10. Both the simulation and experiments were found to have a first dominant mode around 215 Hz and a second dominant mode around 370 Hz.

16.4.2 Nonlinear Acceleration Response to Drilling

After confirming the model's ability to predict frequencies in the linear case, the spring constant of the drill bit was made bi-linear and a disturbance, $\mathbf{u}(\omega)$, was applied. Figure 16.11 shows the frequency magnitude of accelerations of $\mathbf{M_2}$ produced by a range of input frequencies. Harmonic frequencies are produced by the simulations in the non-linear case as well as the
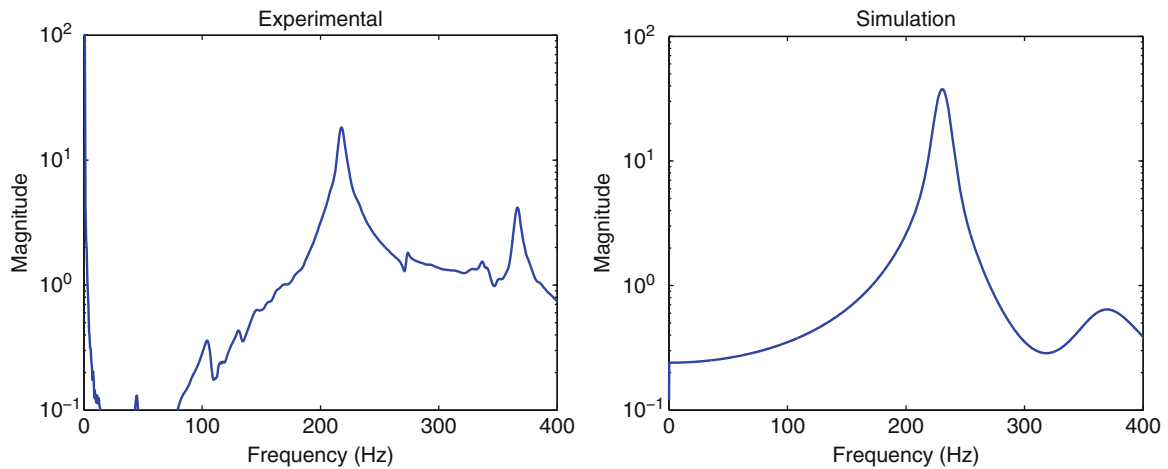
Fig. 16.10 FRF of simulation (*left*) and experiments (*right*) in linear case with impulse excitation
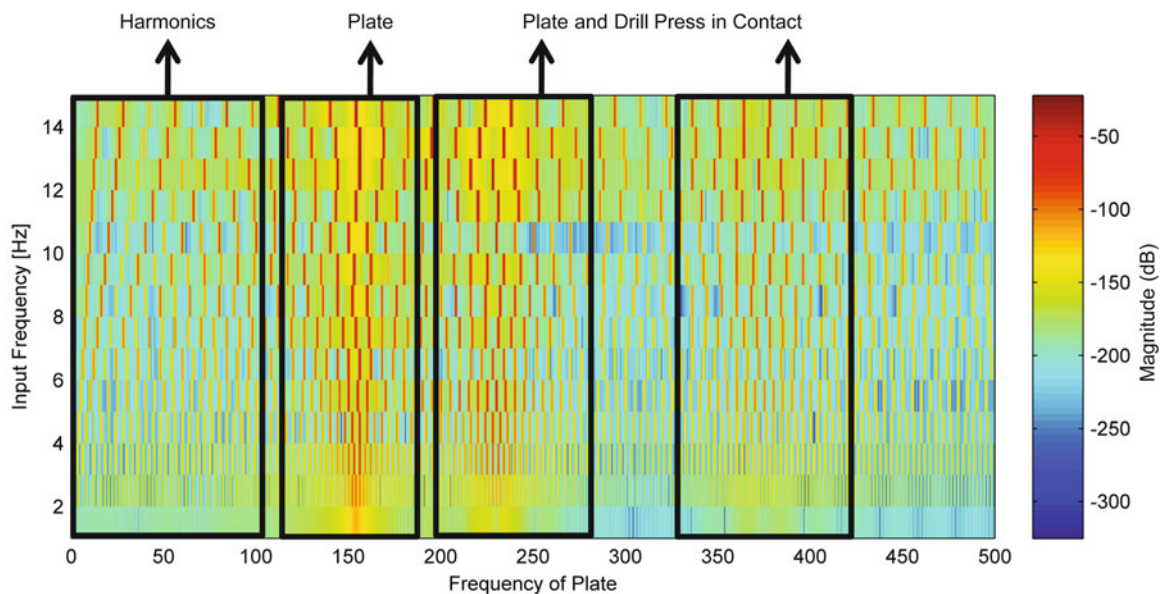
Fig. 16.11 Magnitude of plate frequency with for varying input frequencies

resonant frequencies of the plate when the drill press is not in contact and the two resonant frequencies when the plate and drill press are in contact. These responses confirm that the model is acting as a non-linear system.

The non-linear model was then compared to experimental acceleration data collected on the plate while drilling was completed. The material used in this experiment was an aluminum ($30.0 \times 30.0 \times 0.6$ cm) plate with five accelerometers measuring vertical acceleration. The plate was clamped to a separate structure, rather than the drill table, as to not induce additional dynamics from the supporting table of the drill press. The drilling was completed at a speed of 540 rpm (9 Hz) while the motor of the drill press was operating at 30 Hz. For the simulations, a disturbance, $\mathbf{u}(\omega)$, of sinusoids related to the drilling speed and motor speeds of the experiments was the input to the system. Figure 16.12 shows a comparison of the frequencies excited in simulations and experiments. Comparison showed that the harmonics and general shape of the simulations correspond with the experiments well; however, several flaws in the simulation results remain. Further studies of the model inputs as well as damping are necessary for improved correlation of simulations and experiments.
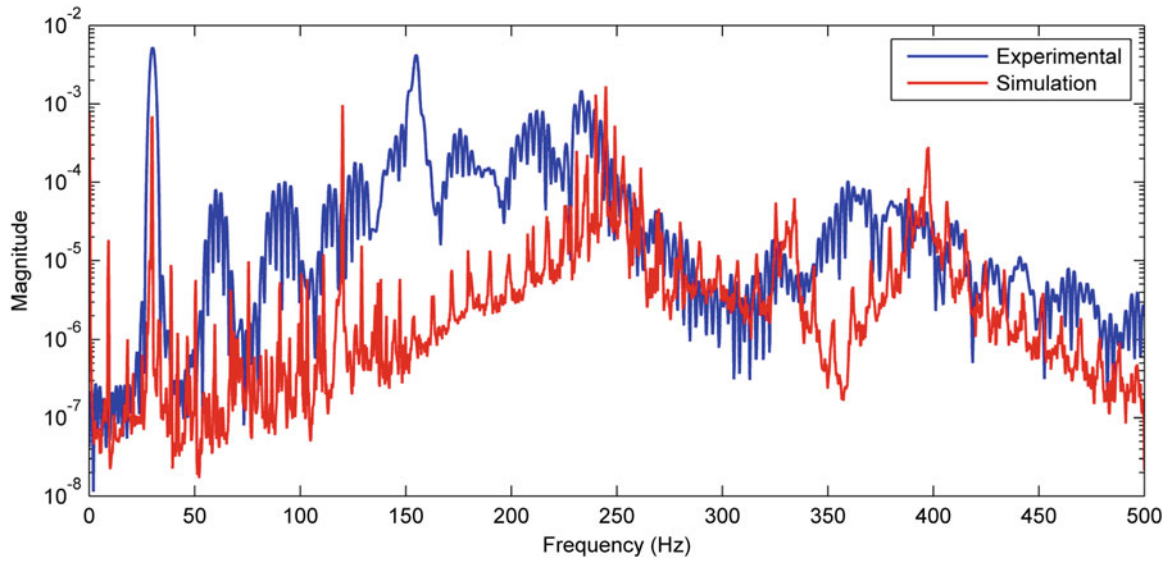
Fig. 16.12 Numerical simulations (*top*) and experimental data (*bottom*) of acceleration measurements on the plate during drilling

16.5 Adaptive Positive Position Feedback Controller

An adaptive positive position feedback (APPF) controller was applied to the model to dampen out unwanted vibrations of the material and tool. For a device to dynamically control the stability of a structure, Goh and Caughey introduced a method known as positive position feedback (PPF) control [10]. The control method was not sensitive to signal contamination via excitation of uncontrolled parameters; this signal contamination phenomenon is known as spillover. Resistance to spillover, along with providing stability related to the structure's stiffness properties, allows for more robustness of the controller. The controller is described as a second order compensator, and conditions to ensure the stability depend only on the natural frequency of the structure. Thus, the advantage of PPF control is that the frequency response of the controller rolls off quickly, making the closed loop system robust to spillover [5]. The general PPF control was developed for a single-input-single-output (SISO) system with a single-degree-of-freedom model as described in Eq. (16.5), where ξ is the structure coordinate, η is the controller coordinate, ω_f and ω are the frequency of the structure and controller, respectively, and ζ_f and ζ are the structural and controller damping ratios, respectively [11].

$$
\begin{aligned}
\text{Structure}: \quad & \ddot{\xi} + 2\zeta_f\omega_f\dot{\xi} + \omega_f^2\xi = G\omega_f^2\eta \\
\text{Controller}: \quad & \ddot{\eta} + 2\zeta\omega\dot{\eta} + \omega^2\eta = \omega^2\xi
\end{aligned}
\tag{16.5}
$$

By using an APPF controller as opposed to a non-adaptive PPF, the desired frequencies to be suppressed can be updated in real-time. This allows the controller to better suppress vibrations due to changing dominant frequencies in nonlinear systems. Recent research teams, such as [3] and [12], have implemented a self-tuning regulator (STR) in their APPF controller for vibration suppression. The adaptive portion implemented in the APPF controller of this research was designed to update the frequency value of the control algorithm in real-time given an initial value of zero. The adaptive algorithm selects the largest magnitude frequency within a selected frequency range of the structural model. Additionally, the frequency range was obtained by taking the FFT of the buffered data from a discretization of our simulated signal. Next, the controller's frequency is then set to the determined dominant frequency of the model. The feedback control diagram for adaptive drill vibration suppression is suggested in Fig. 16.13.

The described APPF controller coupled with the proposed nonlinear MSD model of the drill tool/part was simulated in MATLAB/Simulink to demonstrate the effectiveness of the controller for vibration suppression. The controller can be viewed as an attached actuator which applies forces in phase with the induced vibrations to subdue the excited displacement of the part and tool. The previously developed model of the drill/part with the implemented controller is illustrated in Fig. 16.14. In addition, the controller implemented has been designed to mimic the effects of the bilinear spring. Our model assumes that the controller cannot apply any force onto the part when not in contact during bit-bounce, but resumes its action when in contact. To consider that the drilling tool and part are not in contact, the constraint chosen was that the displacement between the tool/part and disturbance excitation has to be greater than the applied controller displacement.

In the proposed control loop for this simulation, the disturbance input is generated as a sum of sinusoids which, with the constraints, is fed into our MSD model. The output of the model is the relative displacement between the tool and part. This relative displacement output is fed into the adaptive algorithm to update the controller's frequency component. This updated frequency value along with the relative displacement output is fed into the PPF controller. With the controller tuned, a force output is generated back into the MSD model. This cycle repeats to generate a force signal proportional to the disturbance input in order to suppress the induced vibrations.

16.6 Results

In this research, we have simulated the adaptive and non-adaptive PPF controller on the developed nonlinear model. By coupling the adaptive controller with the model, a 69.8 % reduction in the overall plate displacement vibration was obtained by comparing the Root-Mean-Square (RMS) value of the controlled output and non-controlled. This was achieved by using a force gain **G** of 750 and controller damping ratio ζ of 28 % in Eq. (16.5). The buffer of data used was 1,024 points collected at a sampling rate of 2,048 Hz with an overlap of 512 points to allow the controller to update every 0.25 s incrementally throughout the total simulation time of 5 s. To assess the controller's ability to adaptively tune its frequency component to the dominant frequency exciting the structure, an initial value of 0 Hz was chosen as the controller's frequency component. The adaptive algorithm then chooses the frequency with the largest magnitude exciting the structure, which in our case is 30 Hz (the motor speed of 1,720 RPM), and sets the controller's frequency component to that value and damps out the structure at the selected frequency.

As shown in Fig. 16.15, after one buffer period the controller maintained damping of the plate vibrations induced by the motor of the drill press throughout the entire simulation. As a result of dampening the motor speed (30 Hz) with the aforementioned parameters, Fig. 16.16 shows the reduction in absolute displacement from a time section of plate vibration position. Additionally, Fig. 16.17 highlights that by suppressing the dominant or driving frequency, additional frequencies, including harmonics, are also suppressed. To assess the energy content of the vibrations in the part, the instantaneous kinetic vibrational power of the plate was analyzed, as described in Eq. (16.6), where **P(t)** is the power output with respect to time, **m** is the mass of the part, and **x** is the axial coordinate.

$$P(t) = -m\ddot{x}(t)\dot{x}(t) \tag{16.6}$$

Using Eq. (16.6), it was determined that the vibrational power of the plate was reduced by 30.14 % when comparing the RMS of the adaptively controlled and non-controlled energy output of the plate as shown in Fig. 16.18.
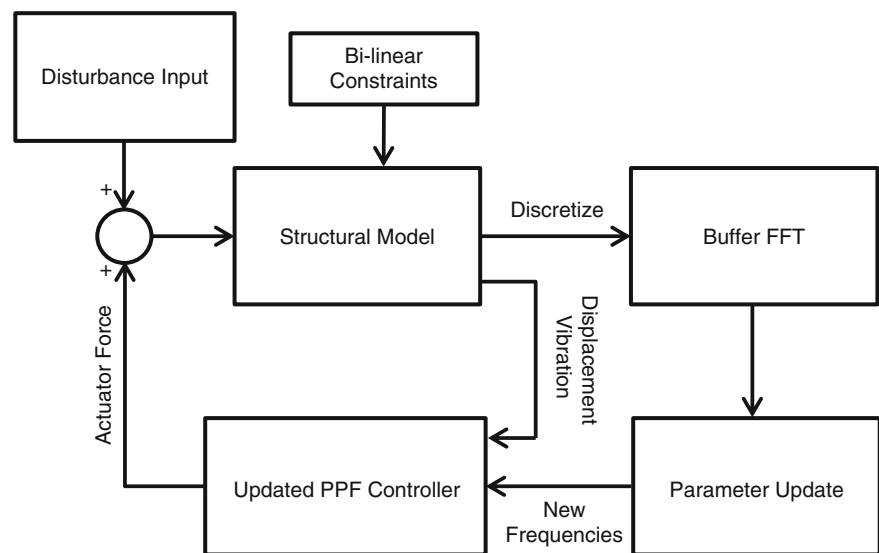
Fig. 16.13 Adaptive Positive Position Feedback loop for controlling vibrations

Fig. 16.14 Model with APPF
Control integrated
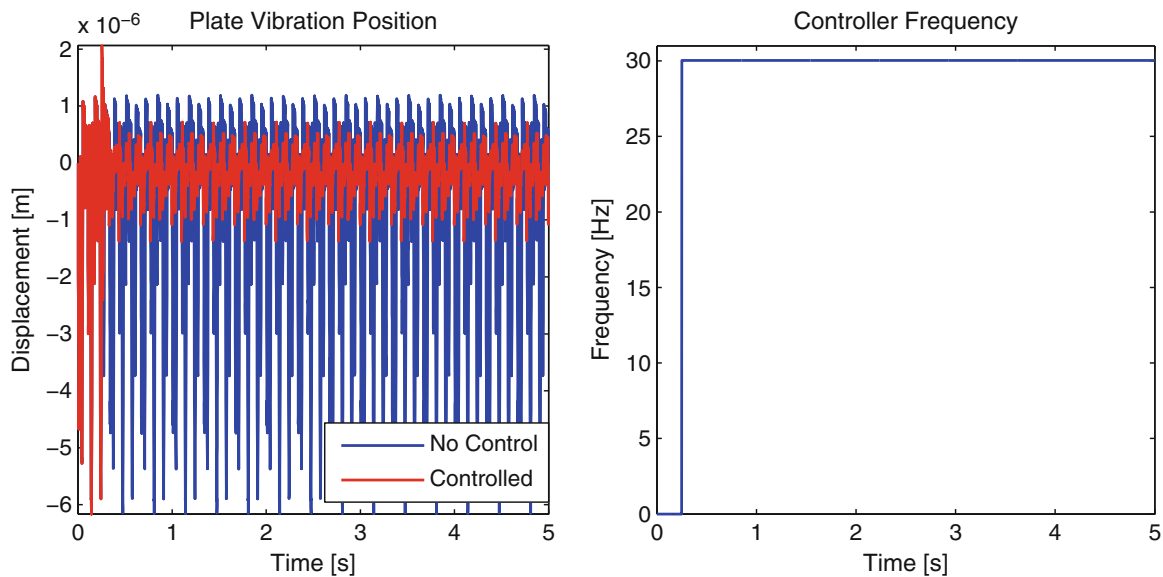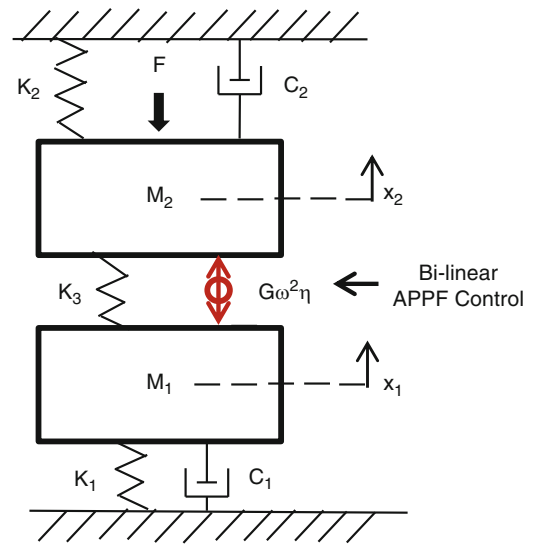
Fig. 16.15 Vibration suppression of plate displacement using APPF control

16.6.1 Results of Non-adaptive Controller Suppression

The previous presented results demonstrate the feasibility of using APPF control to suppress axial vibrations induced by the drill tool onto the part. The position displacement, the frequency content, and the vibrational power were reduced using the adaptive controller. However, one major drawback for the current adaptive algorithm is in the transient phase of the controller. The current method used by the controller to update its frequency component results in a step transition. This sudden step transition intensifies the acceleration content of the controller, thus resulting in a large force onto the part and tool. In order to observe the effects of the controller suppression without the sudden transient phase, a non-adaptive version of the controller was executed. The initial frequency content of the controller was set to the disturbance motor frequency (30 Hz). Table 16.3 describes the comparison between the controller suppression with the transient and without the transient on the part and tool. The results indicate that the PPF controller can considerably suppress vibrations once the controller's frequency component is in static conditions.

However, the results presented below in Table 16.3 on the Non-adaptive case are significantly notable because the disturbance excitation frequency was already known beforehand. By setting the controller's frequency to the disturbance input signal, the induced vibrations are highly damped out without transient conditions. Although if the vibrational excitation is not known beforehand, the adaptive portion of the controller will have to be exercised. One method to improve the
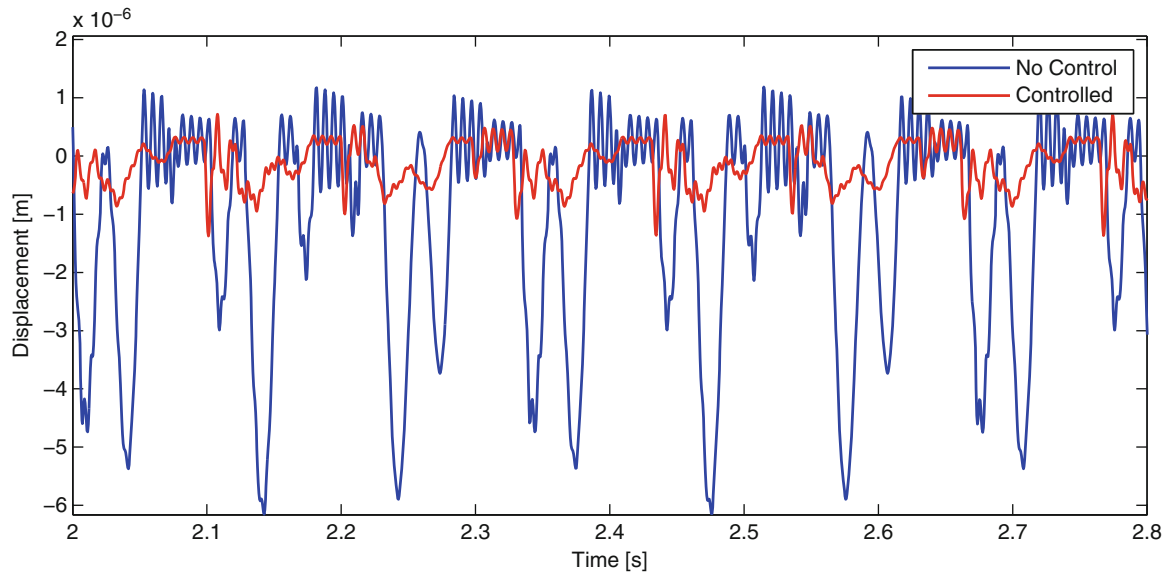
Fig. 16.16 Displacement reduction using APPF control
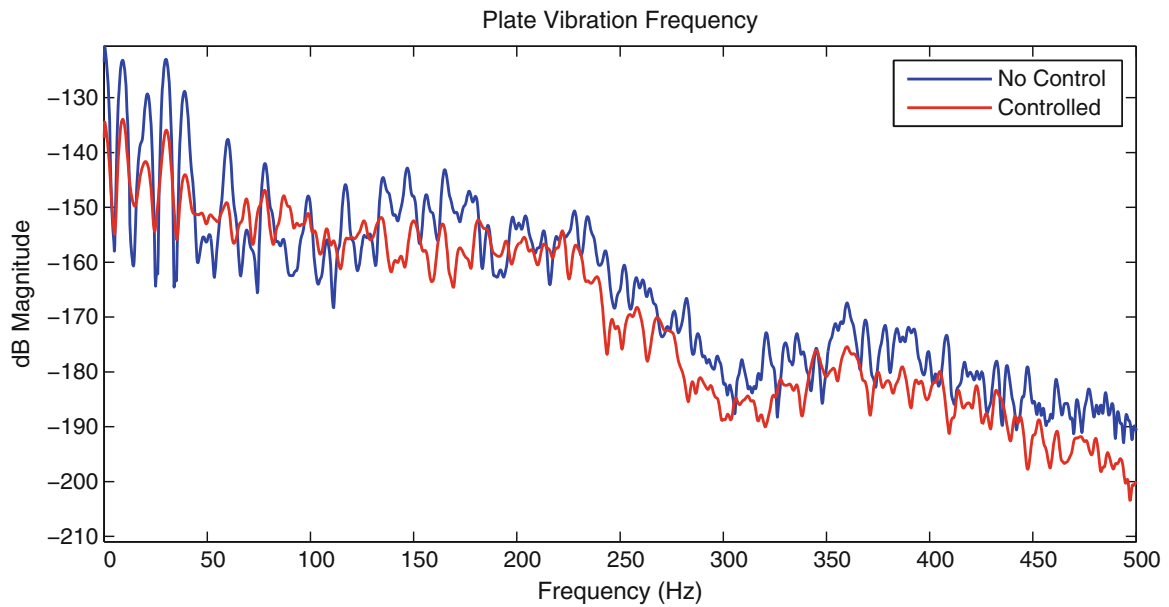
Fig. 16.17 Frequency dB reduction in absolute displacement of the plate

	With transient (adaptive) (%)	Without transient (non-adaptive) (%)
Plate Displacement	69.8	81.6
Drill Displacement	69.5	81.3
Plate Vibration Power	30.1	73.4
Drill Vibration Power	40	81

Table 16.3 Comparison of vibration suppression with and without transient

adaptive PPF controller is to smooth out the transition during updating the frequency content of the controller. A sinusoidal or quadratic function may be used instead of a step transition.
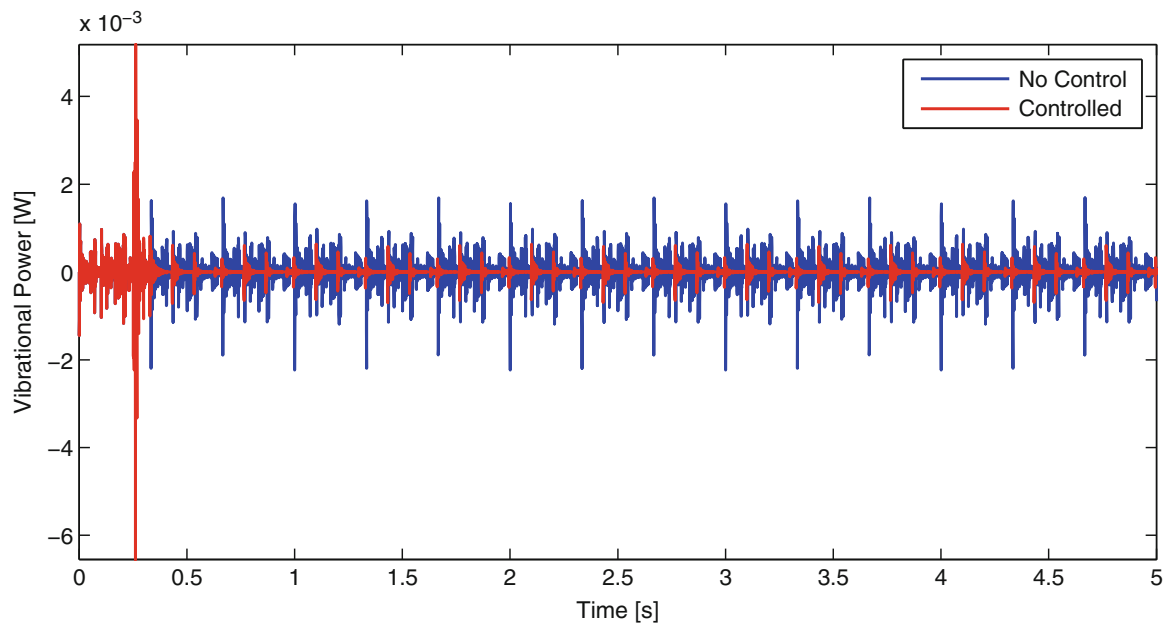
Fig. 16.18 Instantaneous kinetic vibrational power of plate

16.6.2 *Future Sensor Placement and Actuator Type*

From the results, accelerometers were determined to be the sensor that would easily provide the necessary information needed by the controller and they are also commercially available. Since the PPF controller reads in displacement or position of the structure as the input, using accelerometers might be not provide the most optimized results for displacement calculations. Thus, a modified PPF controller which feeds in acceleration instead of displacement might be more reliable. However, assuming the accelerometer readings are filtered and has relatively low noise, they can be used to obtain the changes in displacement through finite integration methods if the initial positions are known. These accelerometers should be attached relatively close to the desired drilling area of the part. Modal analysis of the part is recommended before drilling, if possible, to obtain the best parameters necessary by the controller.

From the previously simulated vibration suppression using the APPF controller, the desired force signal is shown in Fig. 16.19. The range of the signal from the model was determined to be ±25 Newton and the displacement is proportional to the bi-linear spring stiffness of the model. This type of axial force can be easily achievable by piezo-stack actuators, which can output linear displacement forces in the kilo-Newton range, and displacement output to be in the micro-meter range. The piezo-stack actuators are also small enough to be inserted inside the drill bit. An electrical signal produced by the controller can be applied to the piezo-stack actuators to obtain the desired forces necessary to suppress axial vibrations. The advantages of using piezo-actuators are the bi-functional effects of piezoelectric materials. They can be simultaneously used as sensors, for displacement measurement, and actuators, for force generation.

Another type of smart material to be used in vibration dampening are Magneto-rheological elastomers (MREs). The mechanical properties of the Magneto-rheological material changes when subjected to a magnetic field usually using an electromagnet. Hoang et al. has used MREs to suppress vibrations of powertrain systems in vehicles [13]. A MRE drill bit can be develop for use in the drill tool allowing for the control of vibration dampening of the system by changing the mechanical properties.

16.7 Conclusion

This paper explored the dominant vibrations present within one type of drilling setup involving the use of a drill press and aluminum plates. Through modal analysis on each of the drilling apparatus and its components, a two-degree-of-freedom model was developed to best capture the modal characteristics observed. Initially, a linear model was built to capture the resonances determined from the experimental results. This model was later expanded to a nonlinear model by presenting
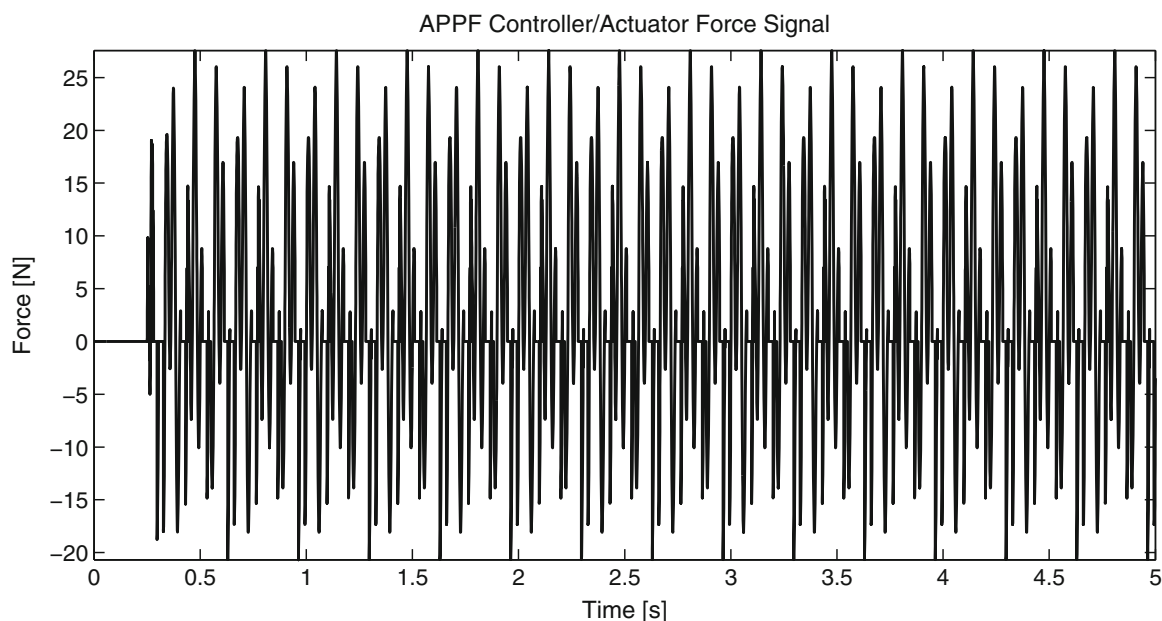
Fig. 16.19 Force signal required by actuator

changes in boundary conditions at the point of drilling. This condition simulated the phenomenon of axial bit-bounce or chatter. In order to refine the model, data was collected during drilling to provide insight on the excitation disturbance which was found to cause vibrational behaviors on the plate. Vibrations examined in the frequency domain displayed apparent dominant frequencies consistent with the motor speed of the drill press and spindle speed and their corresponding harmonics, suggesting the existence of nonlinearity in the true system. With this developed model capturing features of the true system, a model for an APPF controller was incorporated to test the capabilities for suppression. The controller coupled model gave the expected force signal and demonstrated a ~69 % reduction of axial vibrations by using forces achievable in most piezo-stack actuators. The forces were applied to damp the dominant frequencies, thus as a result, the harmonics were also effectively damped due to nonlinearities. The non-adaptive controller resulted in a greater suppression of vibrations due to the static conditions given. However, the transient condition induces an increased force due to the instantaneous change in acceleration of the controller output. We have recommended a smoothing algorithm instead of using a step transition in the adaptive portion of the controller to reduce the additional acceleration excited by the controller.

For future works, the effectiveness achieved by the linear APPF control will be compared to other controllers such as PID controllers as well as Multi-PPF controllers or multiple applied PPF controllers. Although the linear controller is able to provide adequate damping of the nonlinear system, we will also be looking into the use of a nonlinear PPF controller, as recently used in [14]. For performance and validation of the controller/two-degree-of-freedom model, experimental tests should be performed with actuator(s) integrated within the true drill system. Further investigation is needed to refine the model to account for all aspects of the forcing vibration in the system, including potential coupling of lateral, torsional, and axial forces.

References

1. Zou J, Pyykkö I, Sutinen P, Toppila E (2005) Vibration induced hearing loss in guinea pig cochlea: expression of TNF-α and VEGF. Hearing Res 202(1):13–20
2. Michael R, Yantek D, Johnson D, Ferro E, Swope C (2011) Development of elastomeric isolators to reduce roof bolting machine drilling noise. Noise Control Eng J 59(6):591–612
3. Creasy MA, Leo DJ, Farinholt KM (2008) Adaptive positive position feedback for actively absorbing energy in acoustic cavities. J Sound Vib 311(1):461–472
4. Sarker M, Mejbahul D, Rideout DG, Butt SD. Dynamic Model of an Oilwell Drillstring with Stick-Slip and Bit-Bounce Interaction. International Conference on Bond Graph Modeling, 2012
5. Friswell MI, Inman DJ (1999) The relationship between positive position feedback and output feedback controllers. Smart Mater Struct 8(3):285–291

6. Cheng FY, Jiang H, Lou K (2008) Smart structures: innovative systems for seismic response control. CRC, Boca Raton

7. Schwarz B, Richardson M. Modal Parameter Estimation from Operating Data. Sound and Vibration Magazine, 2003

8. Richardson MH, Formenti DL (1982) Parameter Estimation from Frequency Response Measurements Using Rational Fraction Polynomials, 1st IMAC Conference, Orlando, FL. November, 1982

9. Formenti DL, Richardson MH (2002) parameter estimation from frequency response measurements using rational fraction polynomials (20 years of progress), 20th IMAC Conference, Los Angeles, CA. January 2002

10. Goh CJ, Caughey TK (1985) On the stability problem caused by finite actuator dynamics in the control of large space structures. Int J Control 41(3):787–802

11. Fanson JL, Caughey TK (1990) Positive position feedback control for large space structure. AIAA J 28:717–724

12. Radecki PP, Farinholt KM, Park G, Bement MT (2010) Vibration suppression in cutting tools using a collocated piezoelectric sensor/actuator with an adaptive control algorithm. ASME J Vib Acoust 132(5):051002

13. Hoang N, Zhang N, Du H (2009) A dynamic absorber with a soft magnetorheological elastomer for powertrain vibration suppression. Smart Mater Struct 18(7):074009

14. El-Ganaini WA, Saeed NA, Eissa M (2013) Positive position feedback (PPF) controller for suppression of nonlinear system vibration. Nonlinear Dyn 72(3):517–537

Chapter 17
A Regenerative Approach to Energy Efficient Hydraulic Vibration Control

Jonathan L. du Bois

Abstract Active vibration control technologies are reaching maturity in many applications, in both periodic and transient operating regimes. Historically these systems have been designed without regard for the power they consume, which is not only inefficient and costly, but limits their adoption in applications where it is impractical to provide large power supplies. Strategies for reducing power consumption include semi-active and regenerative methods. The former limits the device action to dissipative forces, through adjustable spring and/or damping rates. The latter uses the dissipative portion of the cycle to store energy in a reservoir, which can then be used in the remainder of the cycle. This paper looks at the benefits of using hydraulic devices in this context instead of the prevalent electromechanical devices. A case study of regenerative hydraulic vibration control is presented using digital hydraulics concepts, analogous to the switching power supplies and amplifiers that have revolutionised the efficiency of modern electronic equipment. The limitations and trade-offs are examined and projections are made as to the performance that could be achieved as the limitations of contemporary hydraulic components are improved upon.

Keywords Active vibration control • Regenerative damper • Digital hydraulics • Seismic • Earthquake

17.1 Introduction

Active vibration control is a well established field, and books and papers on the topic abound [1, 2]. Where energy supply is scarce, typically semiactive control is employed [3]. More recently, regenerative concepts have started to appear, where instead of dissipating vibration energy, a vibration mitigation device absorbs the energy from the structure and stores it for use in fully-active portions of the control strategy. Typically such devices are advocated for automotive use and store the energy in electrical form, using electro-mechanical means to convert stored energy to and from motion [4–6].

Hydraulic devices have advantages over other technologies: principally in the range of their power density. Large forces can be generated with high velocity, making them suitable for heavy duty applications, for example the focus of this study which is the motion control of large buildings. The drawback of hydraulic devices in this context is their efficiency. The more-or-less ubiquitous approach to pressure modulation in hydraulic systems is to use a proportional valve, throttling the flow and dissipating large amounts of energy in turbulence and ultimately viscous heat losses. If energy is to be conserved in the device, flow throttling is clearly an untenable approach. The prospect of using regenerative hydraulic systems helps to address one of the major concerns in implementing active vibration control for the mitigation of seismic response in buildings: that of continued operation in the event of power failure.

Digital hydraulic methods employ discrete elements in an effort to mitigate effects such as these. In particular, fast valve switching can be employed to create a device which modulates the output pressure in proportion to the duty cycle of the valve: in essence a pulse-width modulated (PWM) control [7]. The approach is used in a crude form in the hydraulic ram pump [8]. An analogy can be drawn between the emerging digital hydraulic methods and the evolution of efficient Class D amplifiers and switched-mode power supplies in the electrical world. In the case of the latter, fast switching transistors

J.L. du Bois (✉)

Department of Mechanical Engineering, University of Bath, Claverton Down, Bath, BA2 7AY, UK

e-mail: j.l.du.bois@bath.ac.uk

offered a revolution which made the technology possible, whereas for hydraulic systems continued efforts to improve on valve switching speeds are pushing the envelope to the point where the technology presented in this paper is feasible.

The work in this paper sets out the case for the use of digital hydraulic control in regenerative active vibration control. The principle is to improve the efficiency of energy harvesting in hydraulic devices through the use of fast-switching valves and analogue filtering elements to approach active vibration control performance without the need for an external hydraulic power supply.

17.2 Active Control

The work of Lazar et al. [9] shows that while semi-active vibration control approaches can come close to the performance of fully-active systems, the performance is significantly enhanced if the passivity constraint is relaxed. A semi-active device cannot input power to the system so the passivity constraint is

$$p(t) = u_{MR}v_{MR} \leq 0 \tag{17.1}$$

where u_{MR} is the control force applied by the device and v_{MR} is the relative velocity between the attachment points. Lazar et al. demonstrate that significant improvements can be achieved by imbuing the device with limited fully-active capabilities:

$$p(t) = u_{MR}v_{MR} \leq \gamma p_A \tag{17.2}$$

where p_A is the maximum power dissipation of the device and γ is a value between 0 and 1 governed by the efficiency of the energy harvesting, or regeneration processes. (NB the definition here is subtly different from that of Lazar et al. but follows on naturally from their demonstration.) Their findings indicate that a value of $\gamma = 0.75$ produces results that would be indistinguishable from a fully active system for practical purposes. Hence, the objective in this work is to demonstrate in principle a methodology for regenerative vibration control that can achieve this level of performance in a hydraulic device.

Following the methods of reference [9], a two degree-of-freedom (DOF) model of a small two-storey building is simulated. The same model parameters are used here, so that the mass of each floor slab is 500 kg and the frame beams create a stiffness of 3,500 kN/m between each storey. Damping is included to produce a modal damping ratio of 5%. Linear quadratic regulator theory [10] is applied to determine gains for a full-state-feedback controller, to give

$$u(t) = -\begin{bmatrix} 21.4065 & -18.0327 & 0.3436 & 0.1322 \end{bmatrix} \begin{Bmatrix} x_1 \\ x_2 \\ \dot{x}_1 \\ \dot{x}_2 \end{Bmatrix} \tag{17.3}$$

Figure 17.1 shows the response of the uncontrolled system and the actively controlled system to a chirp signal ranging from 1 to 20 Hz. The frequency increases linearly with time over the 100 s so the peak at ∼40 s corresponds to the natural frequency at 8.23 Hz. Figure 17.2 shows the power input to the structure from the active control system. While the overall effect of the active control is to dissipate power, there is a non-negligible amount of power input to the system for segments of its operation. This supports the idea of storing energy during the dissipative part of the cycle and returning some of that energy to the structure at the appropriate points in the cycle. The fact that the active control device dissipates energy on aggregate means that there is scope for efficiency losses in the energy conversion and storage processes, making the proposition herein a realistic one.

17.3 Hydraulic Buck Converter

Figure 17.3 shows a schematic for the hydraulic equivalent of what would be called a Buck Converter in an electrical context. It steps down from a high pressure reservoir to low pressure with minimal loss of total pressure, thus conserving energy. The system is closed-circuit, so the energy storage takes the form of a symmetric, dual-chamber piston with a spring on the piston rod acting as the energy storage element. A servovalve is used to provide a pulse width modulated pressure according to the
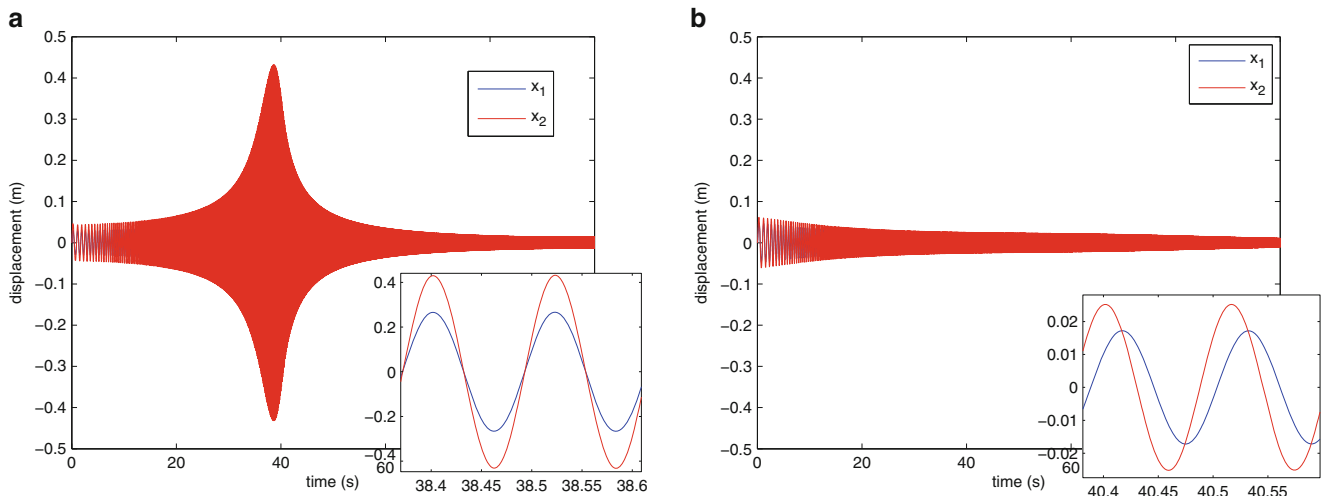
Fig. 17.1 Response of structure to chirp acceleration input from 1 to 20 Hz, with the passive structure alone compared to the active control scheme. (**a**) Uncontrolled; (**b**) active control
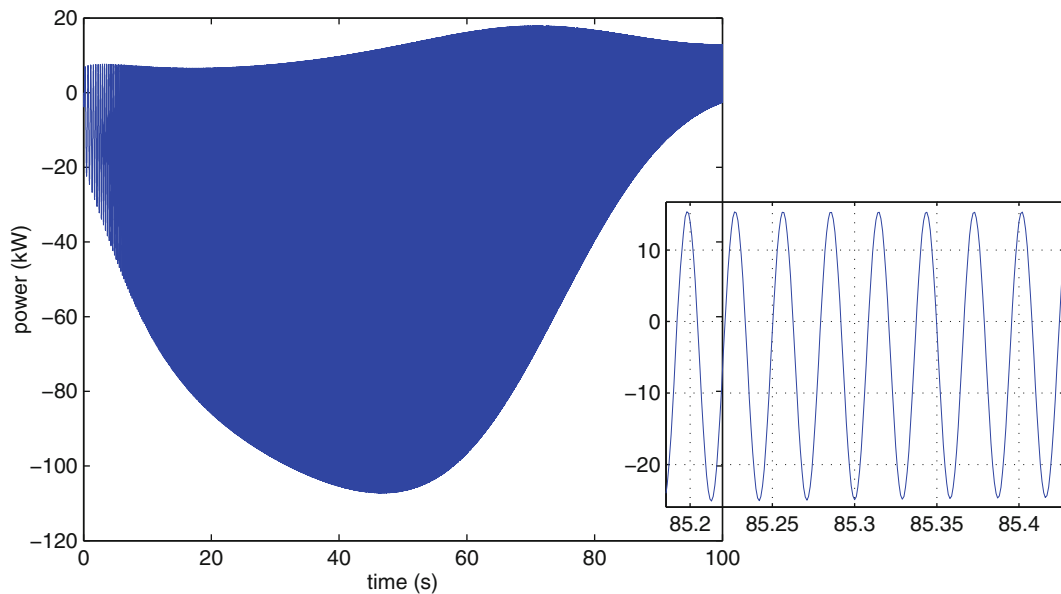
Fig. 17.2 Power input to system from active control

required output pressure, and this pressure is filtered by means of an inertance tube and a pair of accumulators to give a smoothed pressure output. This then drives a piston for the purpose of the vibration control, represented in the diagram as a dissipative load.

The biggest limiting factor in the performance fast-switching hydraulic circuits is the valve response. Recent advancements have seen high flow rates combined with switching times of $\sim$1 ms [11, 12]. Correspondingly, in this study the valve dynamics are modelled with a second order transfer function, with undamped natural frequency of $\omega_0 = 500$ Hz and a damping ratio of $\zeta = 0.75$. The output of the transfer function is set to saturate at 0 and 1 for the lower and upper limits, respectively. The resulting step response can be seen in Fig. 17.4.

Pressure losses across the valve orifice are modelled by means of a turbulent orifice flow, with the relationship

$$\Delta p \propto Q|Q| \tag{17.4}$$

Fig. 17.3 Schematic for a
hydraulic buck converter
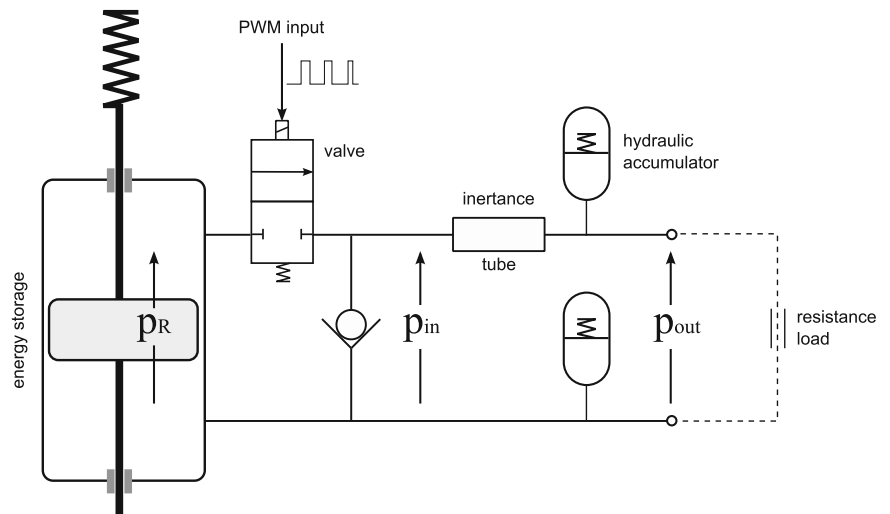
Fig. 17.4 Step response for the
hydraulic valve
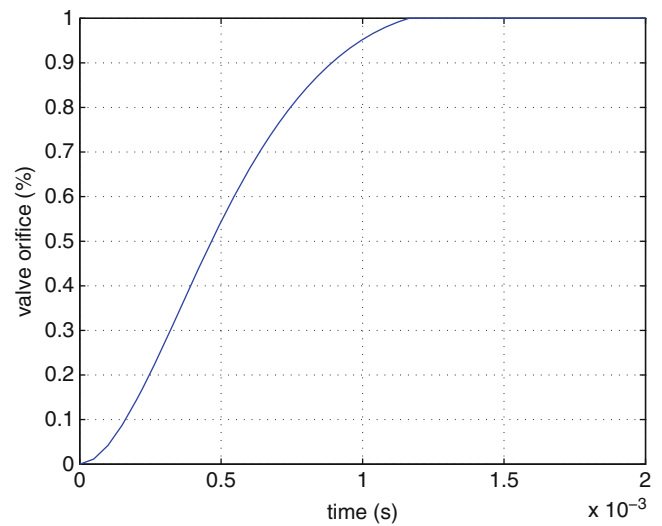
where Δp is the pressure loss and Q is the volumetric flow rate through the valve (incompressible assumptions are made for the hydraulic fluid throughout this analysis). When fully open, from [12], a loss coefficient of 20×10^8 can be achieved, and from [13] the loss coefficient is found to be inversely proportional to the square of the orifice area.

The inertance tube's dynamics are described as a single state system by

$$A\Delta p = m\ddot{x} \tag{17.5}$$

where A is the tube area, Δp is the pressure difference across the tube, m is the mass of fluid in the tube, and $\ddot{x}$ is the acceleration of the fluid in the tube. From this,

$$Q_I = \frac{A}{\rho L} \int \Delta p \, \mathrm{dt} \tag{17.6}$$

where Q_I is the flow through the tube, ρ is the density of the fluid, and L is the length of the tube.

The accumulators act as one in this model due to the incompressibility assumption and the closed-circuit configuration (with no other compressible elements included in the circuit). They can be described in terms of their combined pressure-charge characteristic,

$$p_A = k_A \int Q \, \mathrm{dt} \tag{17.7}$$

where k_A is a linear coefficient for the accumulators and $\int Q\,\mathrm{d}t$ is the volumetric charge of the accumulators. The pressure p_A is the pressure differential between the two accumulators and the charge represents the volume displaced from the lower to the upper accumulator.

These two components comprise the filter for smoothing out the PWM pressures from the valve. The relationship between the input pressure p_{in} and the output pressure p_{out} is described by

$$p_{out} = p_A = k_A \int (Q_I - Q_L)\mathrm{d}t \tag{17.8}$$

or

$$p_{out} = k_A \int \left(\frac{A}{\rho L} \int \Delta p\,\mathrm{d}t - Q_L \right) \mathrm{d}t \tag{17.9}$$

where Q_L is the flow through the load attached to the output of the buck converter. The pressure across the inertance tube, Δp is given by

$$\Delta p = p_{in} - p_{out} \tag{17.10}$$

and the output load is assumed to have a linear pressure-flow relationship so that

$$p_{out} = k_A \int \left(\frac{A}{\rho L} \int (p_{in} - p_{out})\mathrm{d}t - \frac{p_{out}}{c_L} \right) \mathrm{d}t \tag{17.11}$$

where c_L is the laminar loss coefficient associated with the dissipative load. This can be rearranged to

$$\frac{\rho L}{A k_A} \ddot{p}_{out} + \frac{\rho L}{A c_L} \dot{p}_{out} + p_{out} = p_{in} \tag{17.12}$$

Or in the frequency domain,

$$P_{out}(s) = \frac{1}{\frac{\rho L}{A k_A} s^2 + \frac{\rho L}{A c_L} s + 1} P_{in}(s) \tag{17.13}$$

This is a second order system where

$$\omega_0{}^2 = \frac{A k_A}{\rho L} \qquad \text{and} \qquad \frac{2\zeta}{\omega_0} = \frac{\rho L}{A c_L} \tag{17.14}$$

To prevent undesirable oscillation, a critical damping ratio is used so $\zeta = 1$ and

$$\omega_0 = \frac{2 A c_L}{\rho L} = \sqrt{\frac{A k_A}{\rho L}} \tag{17.15}$$

Now stipulating a cutoff frequency for the filter, $\omega_0 = 2\pi f_c$,

$$k_A = 4 \frac{A}{\rho L} c_L{}^2 \qquad \text{and} \qquad \pi f_c = \frac{A c_L}{\rho L} \tag{17.16}$$

and finally, combining these gives

$$k_A = 4\pi f_c c_L \qquad \text{and} \qquad \frac{A}{\rho L} = \frac{\pi f_c}{c_L} \tag{17.17}$$

This determines the constants for the accumulators and for the inertance tube dependent upon the filter cutoff frequency (i.e. the maximum operating frequency of the vibration control device) and the expected load characteristics of the structure whose vibrations are being controlled. In practice this will vary dramatically throughout operation, but this analysis gives a starting point for assigning some values. The peak load characteristic should be used as increasing the load for a given set of component parameters will cause the system to be underdamped (from Eq. (17.14)).

The drawback of assuming too high a value for the cutoff frequency is that the unwanted harmonics of the PWM carrier frequency, known as pressure ripple, will become more pronounced in the output pressure (and resultant piston force), while the drawback of a low cutoff frequency is that it will impinge on the bandwidth of the device in operation. The obvious solution is to increase the PWM carrier frequency, but this is limited by the response time of the hydraulic valve. Setting the carrier frequency too high for the valve results in a controller that fails to track the reference signal and suffers from reduced efficiency on account of the greater proportion of the cycle spent with the valve between states.

17.4 Hydraulic Component Sizing

From Fig. 17.2 the peak power input to the structure is just under 18 kW. Using the linear pressure-flow relationship

$$p = c_L Q \tag{17.18}$$

combined with the expression for hydraulic power

$$\Omega = pQ \tag{17.19}$$

where Ω is the power leaving the device and entering the structure, the equivalent loss coefficient c_L can be found from

$$c_L = \frac{\Omega}{Q^2} = \frac{p^2}{\Omega} \tag{17.20}$$

The equivalent loss coefficient is thus determined by the output piston sizing for the device: it is the piston size that relates the velocity of the structural DOF at peak power to the flow rate in the device. This is seemingly a free choice, but in practice will need careful optimisation. Larger piston areas will result in smaller pressures and larger flow rates, thus giving a small c_L for a given power and velocity. This is beneficial because a small c_L permits shorter inertance tubes and lower stresses on accumulators. Larger flow rates, however, will produce greater losses across valves and other restrictions. Conversely, small piston areas will lead to lower flow rates and higher pressures. The turbulent losses across flow restrictors will be reduced, but the inertance tube will need to be longer and thinner, resulting in greater laminar losses coupled with the spurious elastic and compressible behaviour associated with high pressures. For the purposes of this paper a piston area of

The velocity of the structural DOF coinciding with the peak power is $0.5\,\text{ms}^{-1}$. Moog's current Hydrostatic Bearing Test Actuator range uses a piston area of $86.6\,\text{cm}^2$ for the 160 kN model, which would be needed for the $\sim$125 kN forces seen in this example. A piston area of $86.6 \times 10^{-4}\,\text{m}^2$ at $0.5\,\text{ms}^{-1}$ gives a flow rate of $43.3 \times 10^{-4}\,\text{m}^3\,\text{s}^{-1}$. Using this in Eq. (17.20) with a power of 18 kW gives

$$c_L = \frac{\Omega}{Q^2} = \frac{18 \times 10^3}{(43.3 \times 10^{-4})^2} = 9.6 \times 10^8 \text{ Nsm}^{-5} \tag{17.21}$$

A PWM carrier frequency of 100 Hz is chosen, so that the valve spends $\sim$80% of its time in a fully-open or fully-closed position. A filter cutoff frequency of $f_c = 10$ Hz is used to mitigate the 100 Hz ripple and harmonics thereof. These values are borderline values; ideally greater margins would be desirable but the valve switching speed is the key limitation here. The inertance tube and accumulator sizing is then taken from Eq. (17.17) to give

$$k_A = 1.21 \times 10^{11} \text{ Nm}^{-5} \quad \text{and} \quad \frac{A}{\rho L} = 3.27 \times 10^{-8} \text{ m}^4\,\text{kg}^{-1} \tag{17.22}$$

This study makes the simplifying assumption of a constant reservoir pressure, justified by the understanding that more energy needs to be dissipated from the structure than returned to it. Two alternative flow paths are included to permit return flow into the reservoir, with the servovalve and check valve in Fig. 17.3 exchanged for the case of flow returning to the energy storage chamber. Finally, when the active force control demand changes direction, a four-port servovalve is used to swap the connectivity of the output pressure and invert the sign of the pressure difference. A reservoir pressure of 150 bar is used to provide a margin over the 125 kN forces required of the $86.6 \times 10^{-4}\,\text{m}^2$ piston.

The PWM control uses a triangular-wave signal compared to the reference pressure signal to determine the on/off state of the pulse. As well as the feedforward pressure demand, there is a proportional feedback controller using the measured pressure output. A gain of 10 is used for the proportional gain.

17.5 Results

The force demand from the results of Sect. 17.2 are used, scaled by the output piston area, as the reference signal for the hydraulic transformer. The demand and actual output pressures are shown in Fig. 17.5. Below 3 Hz the device tracks the reference pressure moderately well. There are some artefacts from the abrupt swapping of the output ports at the zero crossing, and the physicality of the behaviour here should be questioned because of the ideal representation of the servovalve used to swap these ports in the model, but overall the tracking is reasonable. Beyond 3 Hz, the performance drops off rapidly. The phase begins to lag, and the switching behaviour at the zero-crossing becomes increasingly problematic. This configuration turns out to be particularly unsuitable as the tracking performance drops off: the momentum in the inertance tube imposes the wrong sign on the time-derivative of the pressure immediately after the zero-crossing of the reference, exacerbating both the spurious transient dynamics and the intrinsic tracking problems. By the time the first resonant frequency is reached at ~8 Hz, or 40 s, the amplitude has dropped off significantly and the pressure no longer resembles that of the reference signal.

The pressure is low-pass filtered with a cutoff of 500 Hz, then sampled at 1,000 Hz and the resulting spectral decomposition is shown in Fig. 17.6. Some aliasing artefacts remain. But I'm not processing this again now; you get the idea. The reference signal is comprised mainly of a single harmonic frequency, whereas the output pressure is clearly seen to suffer from higher harmonic components with a strong onset at around 3 Hz (15 s) and steady worsening towards the higher frequency bands.

Two observations stand out from these results. The first is that the topology of the device, with a four-port valve used to switch the pressure direction at zero-crossings in the reference, produces unnecessary difficulties in tracking. A potential solution would be to use two such devices in a push–pull arrangement. The second observation is that the switching speeds for the hydraulic valves impose consequential restrictions on the operational bandwidth of the device. With current valve technology the vibration control approach proposed here remains infeasible for frequencies above 1 or 2 Hz.
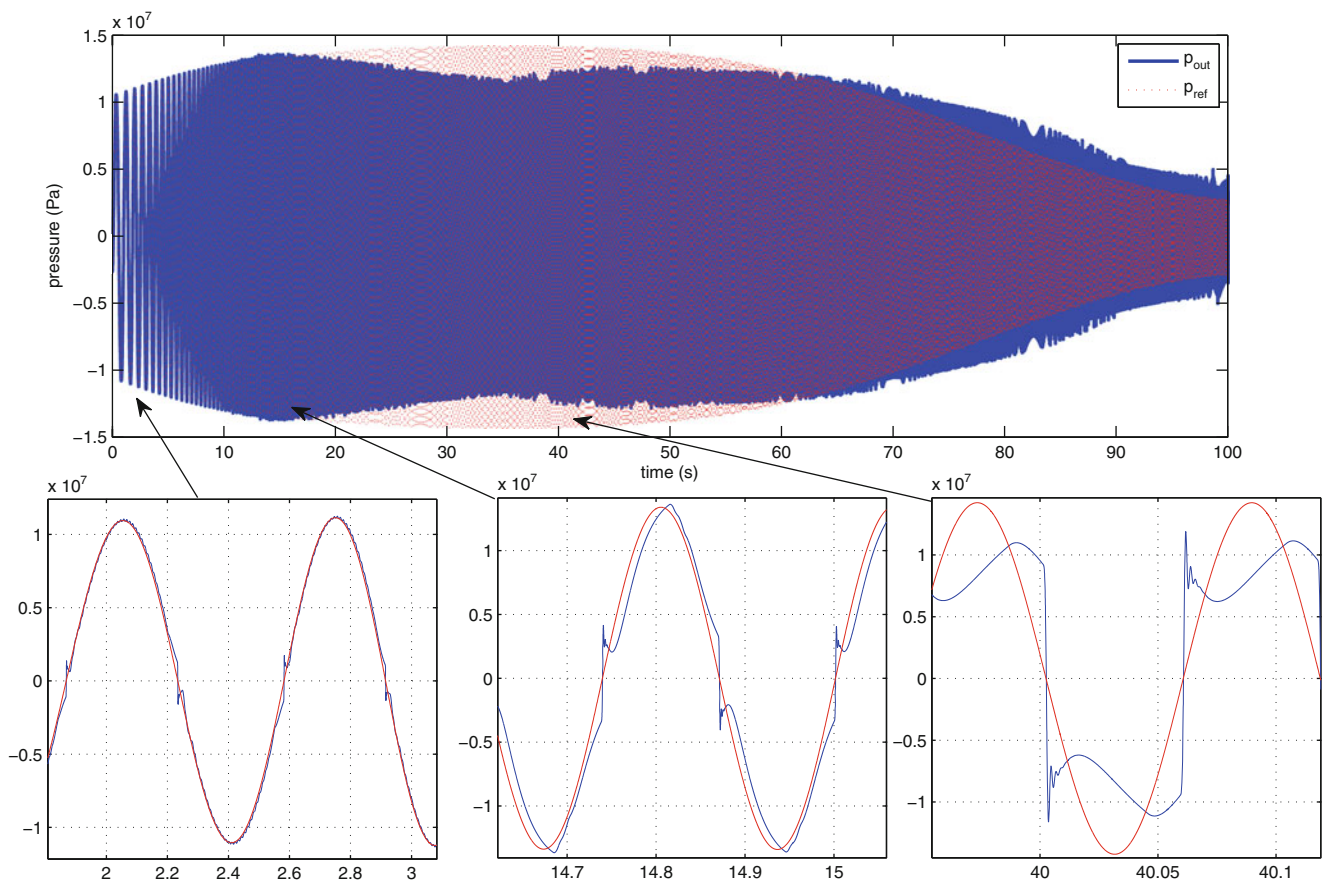
Fig. 17.5 Reference and output pressure signals
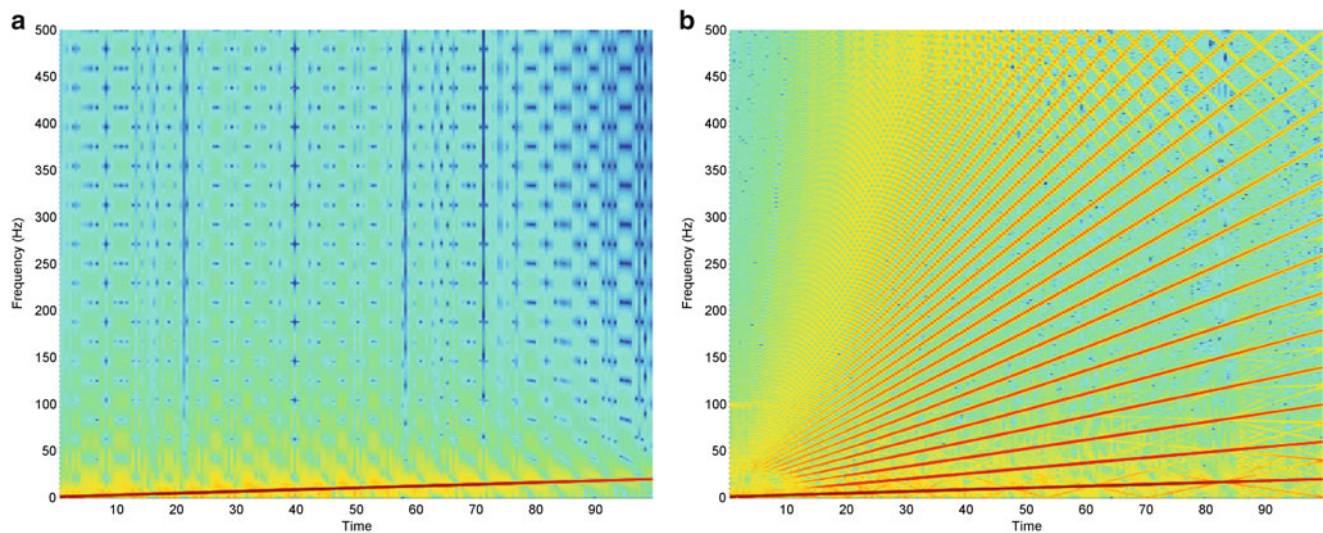
Fig. 17.6 Spectral decomposition with a STFFT for the reference and output pressures of the hydraulic device. (**a**) Reference pressure; (**b**) output pressure

One final set of results is presented here, exploring the effect of higher valve switching bandwidth. The undamped natural frequency of the valve is changed to 5,000 Hz, exploring the effect of a tenfold increase in the switching speed. The PWM carrier frequency is increased to 1 kHz and the analogue filtering cutoff frequency is raised to 50 Hz. The result, unsurprisingly, is a marked improvement in the pressure tracking. Figure 17.7 shows the time history, while Fig. 17.8 shows the spectral content. It is postulated that this performance would be of a satisfactory level for vibration control in the context of low-frequency seismic response suppression. An immediate target for hydraulic valve performance for this application is thus a switching time of 0.1 ms.

17.6 Conclusions

This paper has set out to explore the feasibility of using digital hydraulic concepts to create regenerative vibration control device, capable of harvesting energy to sustain fully-active vibration control without the need for an external hydraulic power supply. Modelling with realistic constraints has been used to evaluate the readiness of the technology in the context of low-frequency ($\sim$0–20 Hz) seismic vibrations in a two-storey building. The following conclusions have been reached.

Firstly, the supporting component technologies are on the verge of maturing to the point where the suggested approach could be implemented. The simulations suggest that for very low frequencies, up to 1 or 2 Hz, the approach *may* already prove feasible. For higher bandwidths, faster valve switching technologies need to evolve to meet the requirements of a system. This study suggests that a tenfold improvement on the existing technology to produce a valve switching time of 0.1 ms would offer the possibility of using these approaches to control vibrations up to 20 Hz or more.

The second conclusion is that the single-switch configuration used here is inadequate for controlling both positive and negative pressure differentials across the output piston; at the zero-crossing the switching of the hydraulic ports produces undesirable transient dynamics. A push–pull configuration is recommended, employing two such devices with one connected to each chamber of the output piston. This type of configuration is common in the analogous class-D amplifiers.

Finally, future work will seek to implement the above change while improving upon the fidelity of the component models. A full simulation will be performed, integrating the hydraulic device fully into the structural model. Experimental work will seek to verify the results of the simulation.
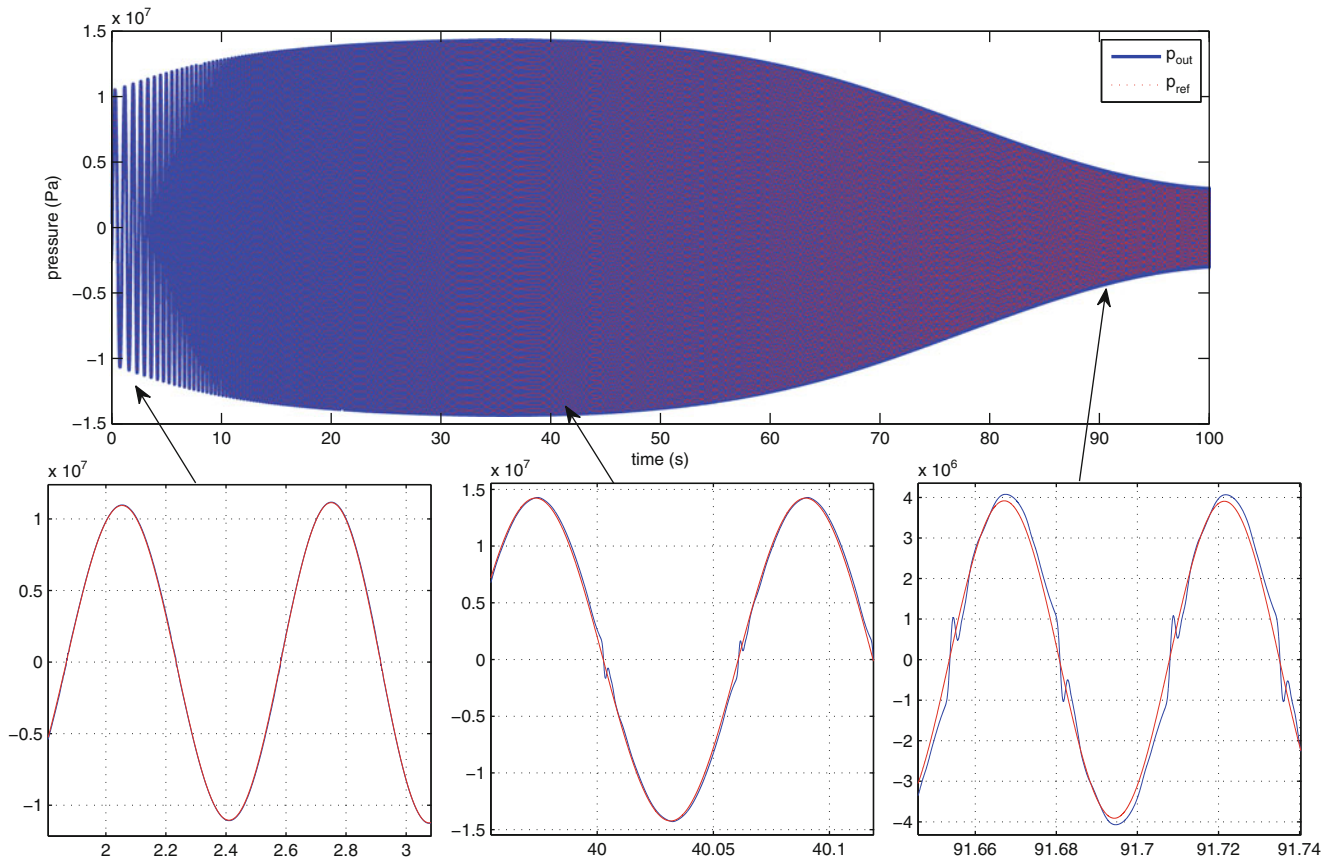
Fig. 17.7 Reference and output pressure signals with tenfold increase in valve switching speed
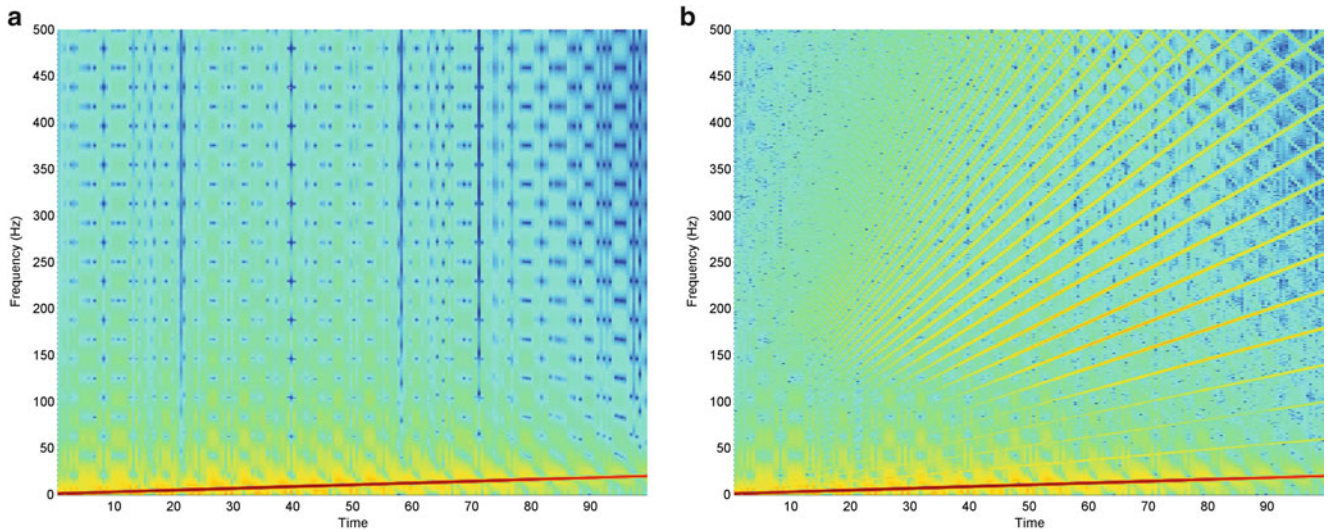
Fig. 17.8 Spectral decomposition with a STFFT for the reference and output pressures of the hydraulic device with tenfold increase in valve switching speed. (**a**) Reference pressure; (**b**) output pressure

References

1. Wagg D, Neild S (2010) Nonlinear vibration with control: for flexible and adaptive structures, vol 170. Springer, Berlin
2. Fuller CC, Elliott S, Nelson PA (1996) Active control of vibration. Access Online via Elsevier
3. Karnopp D (1995) Active and semi-active vibration isolation. J Mech Des 117:177

4. Okada Y, Harada H (1996) Regenerative control of active vibration damper and suspension systems. In: Proceedings of the 35th IEEE conference on decision and control, vol 4, pp 4715–4720

5. Suda Y, Nakadai S, Nakano K (1998) Hybrid suspension system with skyhook control and energy regeneration (development of self-powered active suspension). Veh Syst Dyn 29(S1):619–634

6. Nakano K (2004) Combined type self-powered active vibration control of truck cabins. Veh Syst Dyn 41(6):449–473

7. Pan M, Johnston N, Plummer A, Kudzma S, Hillis A (2013) Theoretical and experimental studies of a switched inertance hydraulic system. Proc Inst Mech Eng Part I J Syst Control Eng 228(1):12–25

8. Jeffery TD, Thomas TH, Smith AV, Glover PB, Fountain PD et al (1992) Hydraulic ram pumps: a guide to ram pump water supply systems. Intermediate Technology Publications, London, UK, ISBN 9781853391729

9. Lazar I, Wagg D, Neild S (2012) Reducing the clipping effect of semi-active clipped optimal control of a two storey building. In: ISMA2012 international conference on noise and vibration engineering, Leuven, Belgium, September 2012

10. Brogan WL (1991) Modern control theory, 3rd edn. Prentice-Hall, Englewood Cliffs

11. Sangiah DK, Plummer AR, Bowen CR, Guerrier P (2013) A novel piezohydraulic aerospace servovalve. Part 1: design and modelling. Proc Inst Mech Eng Part I J Syst Control Eng 227(4):371–389

12. Branson DT, Wang FC, Johnston DN, Tilley DG, Bowen CR, Keogh PS (2011) Piezoelectrically actuated hydraulic valve design for high bandwidth and flow performance. Proc Inst Mech Eng Part I J Syst Control Eng 225(3):345–359

13. Titurus B, du Bois J, Lieven N, Hansford R (2010) A method for the identification of hydraulic damper characteristics from steady velocity inputs. Mech Syst Signal Process 24(8):2868–2887

Chapter 18
Virtual Sensing of Acoustic Potential Energy Through a Kalman Filter for Active Control of Interior Sound

A. Kumar and S.V. Modak

Abstract An important problem in systems such as aerospace interiors, automobile passenger compartments and other cavities is the control of low frequency interior noise. The present paper addresses an issue related to the feedback control of interior sound through active structural acoustic control approach. Feedback control strategy will be useful when the primary disturbance is broadband or when reference signals cannot be derived in an application. This paper presents development of a strategy for virtual sensing of acoustic potential energy through a Kalman filter, for LQG based active structural acoustic control (ASAC) of sound inside a cavity. The Kalman filter is designed to estimate the states of the cavity-structure subjected to disturbances based on a piezoelectric patch mounted on the structure at a suitable location. The Kalman filter is coupled to a radiation filter to predict the acoustic potential energy inside the cavity that can serve as a cost function in the optimal control. Paper also presents the selection of location of a collocated piezoelectric sensor and actuator pair so that the acoustic potential energy could be sensed effectively. A numerical example of rectangular box cavity backed by flexible plate is considered. The performance of the Kalman filter is evaluated for the various levels of process and measurement noise.

Keywords Interior noise • Virtual sensing • Active structural acoustic control • Kalman filter • Radiation filter • Acoustic potential energy

Nomenclature

$\mathbf{M}_T$	Structure and piezoelectric combined mass matrix
$\mathbf{K}_T$	Structure and piezoelectric combined stiffness matrix
$\mathbf{C}_T$	Structural damping matrix
$\mathbf{K}_{w\phi}^a$, $\mathbf{K}_{w\phi}^s$	Electro-mechanical coupling matrix for actuator and sensor
$\mathbf{K}_{\phi\phi}^a$, $\mathbf{K}_{\phi\phi}^s$	Electric capacitance matrix for actuator and sensor
$\mathbf{w}$	Vector of mechanical displacement in z direction
ϕ_a, ϕ_s	Electric potential difference for actuator and sensor
q_a, q_s	Electric charge at the actuator and sensor electrodes
$\mathbf{f}_d$	Vector of externally applied loads on structure
$\mathbf{S}$	Structural-acoustic coupling matrix
$\mathbf{M}_A$	Acoustic mass matrix
$\mathbf{K}_A$	Acoustic stiffness matrix
$\mathbf{D}_A$	Acoustic damping matrix
$\mathbf{p}$	Vector of nodal acoustic pressure
$\boldsymbol{\psi}_S$	Structural mass normalized mode shape matrix
S_{ca}	Sensitivity of charge amplifier
$\boldsymbol{\lambda}^2$	Matrix of eigen values
ξ	Viscous modal damping factor

A. Kumar (✉) • S.V. Modak
Indian Institute of Technology, Delhi, Hauz Khaz, New Delhi 110016, India
e-mail: ashokgem10.nit@gmail.com

ω	Excitation frequency
$\boldsymbol{\eta}_P$	Vector of modal displacements of plant
$\mathbf{B}_{wP}$	Process noise coefficient matrix of plant
$\mathbf{g}_P$	Process noise vector of plant
$\mathbf{v}_P$	Measurement noise vector of plant
ϕ_{ca}	Plant sensor output without noise
y_{sP}	Plant sensor output with measurement noise
$\mathbf{A}_P, \mathbf{B}_{cP}, \mathbf{B}_{dP}, \mathbf{C}_P$	State space matrices of Plant
$\mathbf{A}_K, \mathbf{B}_{cK}, \mathbf{C}_K$	State space matrices of Kalman filter
$\widehat{\boldsymbol{\eta}}_K$	Estimated vector of modal displacements by Kalman filter
$\mathbf{L}$	Steady state Kalman gain matrix
$\widehat{\phi}_{sK}$	Estimate of sensor output voltage by Kalman filter
$\widehat{\mathbf{P}}$	Estimated vector of acoustic pressure
$\mathbf{Z}_a$	Structure to acoustic radiation transfer function matrix
$E, \widehat{E}$	True and estimated virtual acoustic potential energy
$\overline{\mathbf{C}}_{As}$	Modal structural-acoustic coupling matrix
$\mathbf{A}_{Rad}, \mathbf{B}_{Rad}, \mathbf{C}_{Rad}$	State space matrices of radiation filter
$\mathbf{r}$	Vector of radiation filter states
na	Number of acoustic modes

18.1 Introduction

An important problem in systems such as automobile passenger compartments, aerospace interiors, helicopters, marine vehicles, launch vehicles and other cavities is the control of low frequency interior noise generated by the vibration of the elastic structures. Passive noise and vibration control techniques such as: sound absorption and damping materials, structural modifications through re-design, vibration isolation, and vibration absorber, added mass, damping through visco-elastic material and treatment, porous layer, use of stiffened and heavy materials with high damping ratio, use of double-glazing or thicker glass are not so effective for the control of low frequency noise. This is because the wavelength of sound at low frequencies is quite large requiring very thick layers of sound absorbing materials. Due to this reason the passive control strategies have a limitation for attenuation of low frequency noise because it generally leads to addition of a lot of mass to the light flexible structures. With the advances in digital computers and development of modern control theories active methods have emerged as practical alternatives to passive methods for suppressing unwanted noise in the low frequency range. The passive methods are generally used for disturbances above 1,000 Hz, while the active methods are used below 1,000 Hz [1]. The idea of active noise control was conceived by Leug in his patent on noise control in a duct [2]. A major advantage of active strategy over a passive strategy is its ability to adapt to different operating conditions [3]. Active noise control technology has been gaining development in recent years and can be divided into three categories: first category involves the active noise cancellation (ANC), which uses the interior acoustic sources such as loudspeakers to cancel the noise with the error signal from acoustic sensors (microphones); second category employs vibration sources such as shakers or surface mounted piezoelectric actuators and acoustic sources for error signal in the radiated acoustic field; and the third method, which is known as active structural acoustic control (ASAC), employs both structural actuators and structural error sensors [4].

The ASAC strategy can be used for attenuating the radiated acoustic power or acoustic potential energy in the interior of a cavity. In active structural acoustic control (ASAC), structural actuators such as shape memory alloys (SMA), piezoelectric materials (PZT), magnetostrictive materials and Magneto-rheological (MR) fluids and structural sensors such as PZT, PVDF, and fiber optics can be integrated into the walls in such a way as to modify or reconstruct the vibration of the flexible panels and reduce the sound radiation or transmission [5]. Active structural acoustic control with active/adaptive structures is presented in [6]. The PZT patches can be glued on the structure to sense response and provide the necessary inputs for control of structural response as well as acoustic radiation [7].

The three important elements in the design of any active control system are: Control strategy, type of Disturbance and Control objective [8]. The interior noise in cavities, encountered in automotive and aerospace vehicles, occurs due to both deterministic and random disturbances. Feedforward and feedback control are the two main control strategies that have been used for interior noise control. The feedforward technique has been used mainly to control interior noise due to harmonic and periodic disturbances arising from operation of IC engine in case of automotive vehicles and from the jet engine in

case of aerospace vehicles. However, feedforward control requires measurement of the disturbance in some form which may not always be possible and also requires error sensors to be mounted at the control points. It is also difficult to achieve global control using this technique. Random and broadband disturbances may also act on cavities like: disturbances due to a rough road, disturbances due to aerodynamic effects/turbulent boundary layer, acoustic load disturbance on a satellite during launching, broadband disturbances in a helicopter being some of the examples. These disturbances are difficult to be dealt effectively using feedforward technique due to problems of causality and acoustic feedback. Feedback control is expected to be an effective strategy in cases where disturbances are random or broadband as well as in cases where it is difficult to measure reference signals corresponding to disturbances. Feedback control can also be implemented to achieve global control of acoustic response with lesser level of control system complexity [5]. In view of this, the present paper addresses an issue related to the feedback control of interior noise through ASAC approach.

In the control of flexible structures, feedback control strategy is used as: active damping and optimal full state feedback control [5]. Active damping can generally be achieved with direct velocity feedback.

Optimal feedback control involves applying a control input that minimizes a certain cost function taken as a combination of quantity to be controlled and the control effort. Such an optimal control strategy is referred as Linear Quadratic Regulator (LQR) control and that with a Kalman filter used as an optimal observer as Linear Quadratic Gaussian (LQG) control. For noise control, the cost function provides a method of weighting heavily the modes of the structure that are known to be efficient acoustic radiators and similarly allows diminished weighting of the inefficiently radiating modes.

Reference [9] considers feedback control of interior noise using structural sensing. An LQG based feedback control with Kalman-Bucy filter as the state estimator is used. Reference [10] demonstrated the use of an extended Kalman filter (KF) as a virtual sensor for non-measurable vehicle states and unknown vehicle parameters. Reference [11] used Kalman filter approach to develop a virtual sensing algorithm that computes optimal estimates of the error signals at the virtual locations and implemented that algorithm on an acoustic duct arrangement. Reference [12] reviewed a number of virtual sensing algorithms developed for active noise control and investigated the effectiveness of using virtual sensors in a pure tone diffuse sound field [13]. Authors also developed stochastically optimal virtual microphones and virtual energy density sensors for use in diffuse sound fields. In [14] a virtual sensor design to estimate broadband acoustic interior sound pressure using structural sensors has been proposed, with robustness against certain dynamic uncertainties occurring in an acoustic–structurally coupled enclosure. Reference [15] proposed an optimization approach for structural sensor placement to improve the performance of vibro-acoustic virtual sensor for active noise control applications. The vibroacoustic virtual sensor was designed to estimate the interior sound pressure of an acoustic structural coupled enclosure using structural sensors.

In the case of Linear Quadratic Regulator (LQR), it is assumed that the system is deterministic and all the states of the system or plant are known to us and available for feedback, which however is difficult to implement in practice for flexible structures. Moreover, the actual system/plant may also have model uncertainties and measurement of output can have noise. Therefore, an optimal observer is required, in the framework of LQG control, which can estimate all the unmeasured states of the structure in presence of noise. In addition, the observer should be able to predict the acoustic variable to be finally control. This paper presents development of a strategy for virtual sensing of acoustic potential energy through a Kalman filter, for LQG based feedback control of sound inside a cavity. The Kalman filter is designed to estimate the states of the cavity-structure subjected to disturbances. The Kalman filter is coupled to a radiation filter to predict the acoustic potential energy inside the cavity which can serve as a cost function in the optimal control. Paper also presents the selection of location of a collocated piezoelectric sensor and actuator pair so that the acoustic potential energy could be sensed effectively.

18.2   Development of a Numerical Model of the Piezo-Structural-Acoustic System

18.2.1   Finite Element Model

A numerical model of the open loop system is developed using finite element method. The flexible-plate is modeled by four-nodded Kirchoffs thin plate bending elements that have three degrees of freedom, out of plane displacement and two rotations, at each of their nodes [16]. The acoustic domain, with air as medium, is modeled with eight-nodded solid acoustic elements with acoustic pressure as the degree of freedom at each of its nodes [5]. The piezoelectric patches that are supposed to be glued on the flexible plate are modeled with classical lamination theory using piezo-electric constitution relations [17]. For each patch, two electrical degrees of freedom in terms of the voltages at its two electrodes are considered. One of the electrodes for each patch is grounded.

The finite element equation coupling the piezoelectric, structural and the acoustic domain in its final form can be written as given in Eq. 18.1. The details of FE formulation leading to the FE equation for the individual domains can be seen in the references mentioned above.

$$
\begin{bmatrix} \mathbf{M}_T & 0 & 0 & 0 \\ 0 & 0 & 0 & 0 \\ 0 & 0 & 0 & 0 \\ -\mathbf{S}^T & 0 & 0 & \mathbf{M}_A \end{bmatrix} \begin{Bmatrix} \ddot{\mathbf{w}} \\ \ddot{\phi}_a \\ \ddot{\phi}_s \\ \ddot{\mathbf{p}} \end{Bmatrix} + \begin{bmatrix} \mathbf{C}_T & 0 & 0 & 0 \\ 0 & 0 & 0 & 0 \\ 0 & 0 & 0 & 0 \\ 0 & 0 & 0 & \mathbf{D}_A \end{bmatrix} \begin{Bmatrix} \dot{\mathbf{w}} \\ \dot{\phi}_a \\ \dot{\phi}_s \\ \dot{\mathbf{p}} \end{Bmatrix} + \begin{bmatrix} \mathbf{K}_T & \mathbf{K}_{w\phi}^a & \mathbf{K}_{w\phi}^s & 0 \\ \mathbf{K}_{w\phi}^{a\,T} & \mathbf{K}_{\phi\phi}^a & 0 & 0 \\ \mathbf{K}_{w\phi}^{s\,T} & 0 & \mathbf{K}_{\phi\phi}^s & 0 \\ 0 & 0 & 0 & \mathbf{K}_A \end{bmatrix} \begin{Bmatrix} \mathbf{w} \\ \phi_a \\ \phi_s \\ \mathbf{p} \end{Bmatrix} = \begin{Bmatrix} \mathbf{f}_d \\ -q_a \\ -q_s \\ 0 \end{Bmatrix}
$$

$$(18.1)$$

It is noted that in the FE equation presented above, the piezo and the structural domains are coupled through two-way coupling. On the other hand, the structural and the acoustic domains are assumed to have only one-way coupling from structure to acoustic. The coupling from acoustic domain to structure is neglected as it is generally small in most of the cavities encountered in aerospace and automotive applications.

18.2.2 State Space Model of the Plant

This section describes development of a finite element based state space model of the plant representing structure and piezoelectric sensor and actuator. Following equations can be written from Eq. 18.1

$$
\mathbf{M}_T\ddot{\mathbf{w}} + \mathbf{C}_T\dot{\mathbf{w}} + \mathbf{K}_T\mathbf{w} + \mathbf{K}_{w\phi}^a\phi_a + \mathbf{K}_{w\phi}^s\phi_s = \mathbf{f}_d \tag{18.2}
$$

$$
\mathbf{K}_{w\phi}^{a\,T}\mathbf{w} + \mathbf{K}_{\phi\phi}^a\phi_a = -q_a \tag{18.3}
$$

$$
\mathbf{K}_{w\phi}^{s\,T}\mathbf{w} + \mathbf{K}_{\phi\phi}^s\phi_s = -q_s \tag{18.4}
$$

Assuming short circuit electric boundary condition for sensor, we get,

$$
\mathbf{M}_T\ddot{\mathbf{w}} + \mathbf{C}_T\dot{\mathbf{w}} + \mathbf{K}_T\mathbf{w} + \mathbf{K}_{w\phi}^a\phi_a = \mathbf{f}_d \tag{18.5}
$$

$$
q_s = -\mathbf{K}_{w\phi}^{s\,T}\mathbf{w} \tag{18.6}
$$

Transformation to modal coordinates can be done using the eigenvectors of the structure-piezo system as,

$$
\mathbf{w} = \boldsymbol{\psi}_S\boldsymbol{\eta} \tag{18.7}
$$

Substituting Eq. 18.7 in Eq. 18.5, and pre-multiplying by $\boldsymbol{\psi}_S^T$

$$
\boldsymbol{\psi}_S^T\mathbf{M}_T\boldsymbol{\psi}_S\ddot{\boldsymbol{\eta}} + \boldsymbol{\psi}_S^T\mathbf{C}_T\boldsymbol{\psi}_S\dot{\boldsymbol{\eta}} + \boldsymbol{\psi}_S^T\mathbf{K}_T\boldsymbol{\psi}_S\boldsymbol{\eta} = \boldsymbol{\psi}_S^T\left(\mathbf{f}_d - \mathbf{K}_{w\phi}^a\phi_a\right) \tag{18.8}
$$

After using the orthogonality properties, we obtain

$$
\mathbf{I}\ddot{\boldsymbol{\eta}} + \boldsymbol{\Lambda}\dot{\boldsymbol{\eta}} + \boldsymbol{\lambda}^2\boldsymbol{\eta} = \boldsymbol{\psi}_S^T\left(\mathbf{f}_d - \mathbf{K}_{w\phi}^a\phi_a\right) \tag{18.9}
$$

Choosing the structural modal displacement and velocity as state variables and differentiating we get,

$$
\boldsymbol{\eta}_1(t) = \boldsymbol{\eta}(t); \quad \boldsymbol{\eta}_2(t) = \dot{\boldsymbol{\eta}}(t) \tag{18.10}
$$

$$
\dot{\boldsymbol{\eta}}_1(t) = \dot{\boldsymbol{\eta}}(t) = \boldsymbol{\eta}_2(t) \tag{18.11}
$$

$$
\dot{\boldsymbol{\eta}}_2(t) = \ddot{\boldsymbol{\eta}}(t) \tag{18.12}
$$

In view of above Eq. 18.9 can be written as,

$$\ddot{\eta} = \psi_S^T \left(\mathbf{f}_d - \mathbf{K}_{w\phi}^a \phi_a \right) - \Lambda \dot{\eta} - \lambda^2 \eta \tag{18.13}$$

$$\dot{\eta}_2 = \ddot{\eta} = \psi_S^T \mathbf{f}_d - \psi_S^T \mathbf{K}_{w\phi}^a \phi_a - \Lambda \eta_2 - \lambda^2 \eta_1 \tag{18.14}$$

Using Eqs. 18.11 and 18.14, state space equation model of the plant can be written as,

$$\begin{Bmatrix} \dot{\eta}_1 \\ \dot{\eta}_2 \end{Bmatrix} = \begin{bmatrix} \mathbf{0} & \mathbf{I} \\ -\lambda^2 & -\Lambda \end{bmatrix} \begin{Bmatrix} \eta_1 \\ \eta_2 \end{Bmatrix} + \begin{bmatrix} \mathbf{0} & \mathbf{0} \\ \psi_S^T & -\psi_S^T \mathbf{K}_{w\phi}^a \end{bmatrix} \begin{Bmatrix} \mathbf{f}_d \\ \phi_a \end{Bmatrix} \tag{18.15}$$

The charge output of the piezoelectric sensor is feed to a charge amplifier having sensitivity S_{ca} giving voltage output as,

$$\phi_{ca} = \begin{bmatrix} S_{ca} \mathbf{K}_{w\phi}^{s}{}^T \psi_S & \mathbf{0} \end{bmatrix} \begin{Bmatrix} \eta_1 \\ \eta_2 \end{Bmatrix} \tag{18.16}$$

λ^2 is the matrix of eigen values of the plant and $\Lambda = 2\xi_i \omega_i$.

18.3 Virtual Sensing of Acoustic Potential Energy

In this paper the aim of the virtual sensing is to compute an accurate estimate of the acoustic potential energy inside the cavity using a structural sensor. The problem of virtual sensing for active control of sound is formulated as a linear estimation problem using Kalman filter. The basic strategy used here is depicted in Fig. 18.1. The Figure shows that the piezoelectric sensor output is used to estimate modal states of plant using Kalman filter and then estimated modal states are used to compute the total acoustic potential energy inside the cavity through a radiation filter.

18.3.1 Development of a Steady State Kalman Filter

The Kalman filter is an optimal state observer for a system contaminated with process and measurement noise.

From Fig. 18.1, one can observe that, the plant input is influenced with unknown input/process noise (**g**) and plant output is also corrupted with measurement noise (**v**). The state and output equation for a system/plant with external noises can be written from Eqs. 18.15 and 18.16 as:
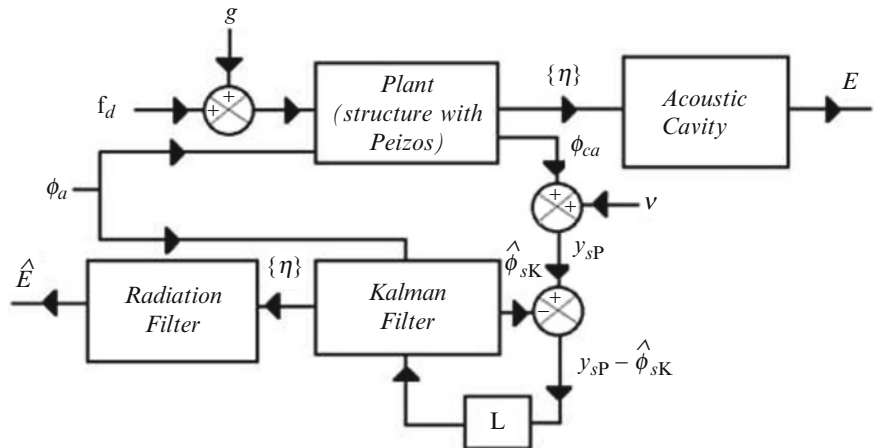
Fig. 18.1 Block diagram of virtual sensing strategy

$$\begin{Bmatrix} \dot{\eta}_1 \\ \dot{\eta}_2 \end{Bmatrix} = \begin{bmatrix} \mathbf{0} & \mathbf{I} \\ -\lambda^2 & -\mathbf{\Lambda} \end{bmatrix} \begin{Bmatrix} \eta_1 \\ \eta_2 \end{Bmatrix} + \begin{bmatrix} \mathbf{0} \\ -\boldsymbol{\psi}_S^T \mathbf{K}_{w\phi}^a \end{bmatrix} \phi_a + \begin{bmatrix} \mathbf{0} \\ \boldsymbol{\psi}_S^T \end{bmatrix} \mathbf{f}_d + \mathbf{B}_w \mathbf{g} \tag{18.17}$$

$$y_s = \begin{bmatrix} S_{ca} \mathbf{K}_{w\phi}^{s\,T} \boldsymbol{\psi}_S & \mathbf{0} \end{bmatrix} \begin{Bmatrix} \eta_1 \\ \eta_2 \end{Bmatrix} + I\mathbf{v} \tag{18.18}$$

Equations 18.17 and 18.18 can be represented compactly as,

$$\dot{\boldsymbol{\eta}}_P = \mathbf{A}_P \boldsymbol{\eta}_P + \mathbf{B}_{cP} \phi_a + \mathbf{B}_{dP} \mathbf{f}_{dP} + \mathbf{B}_{wP} \mathbf{g}_P \tag{18.19}$$

$$y_{sP} = \mathbf{C}_P \boldsymbol{\eta}_P + I \mathbf{v}_P \tag{18.20}$$

$\mathbf{B}_{wP}$ is the process noise coefficient matrix for plant and is assumed to be same as $\mathbf{B}_{dP}$. $\mathbf{g}_P$ and $\mathbf{v}_P$ are the process and measurement noise vectors for plant, respectively.

Measured voltage y_{sP} is fed to the Kalman filter. The difference (called as error) between the estimate of the y_{sP} computed by the Kalman filter and y_{sP} itself is used to adapt the states of the Kalman filter through a Kalman gain matrix $\mathbf{L}$. In this way the error is progressively reduced and in the process the states of the Kalman filter converge to the states of the plant. Representing the copy of the plant model used in the Kalman filter by a subscript K, the state space model of the Kalman filter in compact form but including the effect of Kalman gain matrix can be written as,

$$\dot{\widehat{\boldsymbol{\eta}}}_K = \mathbf{A}_K \widehat{\boldsymbol{\eta}}_K + \mathbf{B}_{cK} \phi_a + \mathbf{L} \left(y_{sP} - \mathbf{C}_K \widehat{\boldsymbol{\eta}}_K \right) \tag{18.21}$$

Simplification gives,

$$\dot{\widehat{\boldsymbol{\eta}}}_K = \left(\mathbf{A}_K - \mathbf{L}\mathbf{C}_K \right) \widehat{\boldsymbol{\eta}}_K + \mathbf{B}_{cK} \phi_a + \mathbf{L} y_{sP} \tag{18.22}$$

The sensor output voltage predicted by the Kalman filter is

$$\widehat{\phi}_{sK} = \mathbf{C}_K \widehat{\boldsymbol{\eta}}_K \tag{18.23}$$

In the above equations, $\widehat{\boldsymbol{\eta}}_K$ is vector of modal displacement of plant estimated by Kalman filter and $\mathbf{L}$ is the steady state Kalman filter gain matrix. The objective in the design of the Kalman filter is to minimize the expected value of the error between true and estimated states given by

$$J = E \left\{ \left(\boldsymbol{\eta}_P(t) - \widehat{\boldsymbol{\eta}}_K(t) \right)^T \left(\boldsymbol{\eta}_P(t) - \widehat{\boldsymbol{\eta}}_K(t) \right) \right\} \tag{18.24}$$

The minimization of above error function leads to the solution of the algebraic Riccati equation,

$$\mathbf{A}_K \mathbf{P}_e + \mathbf{P}_e \mathbf{A}_K^T - \mathbf{P}_e \mathbf{C}_K^T s_v^{-1} \mathbf{C}_K \mathbf{P}_e + \mathbf{B}_{wK} s_g \mathbf{B}_{wK}^T = 0 \tag{18.25}$$

that yields error covariance $\mathbf{P}_e$. The filter gain matrix $\mathbf{L}$ is then calculated as

$$\mathbf{L} = -\mathbf{P}_e \mathbf{C}_K^T s_v^{-T} \tag{18.26}$$

where $\mathbf{B}_{wK}$ is the process noise coefficient matrix for Kalman filter model, and s_g and s_v are process and measurement noise covariances respectively. The convergent solution to the Riccati equation yields the steady state gain for the Kalman filter. The final convergent gain is the optimal gain for steady state Kalman filter, but for unsteady Kalman filter the gain continuously changes with time.

18.3.2   Development of Radiation Filter

As shown in Fig. 18.1, the Kalman filter is coupled to a radiation filter to predict the acoustic potential energy inside the cavity. The radiation filter is nothing but a model of the structural-acoustic coupling in the cavity. The acoustic modal pressure amplitudes $\widehat{\mathbf{P}}$, within the cavity, arising from the vibration of the structure are given by the product of the estimated structural modal velocity vector $\dot{\widehat{\boldsymbol{\eta}}}_K$, and the modal structural-acoustic radiation transfer function matrix $\mathbf{Z}_a$,

$$\widehat{\mathbf{P}} = \mathbf{Z}_a \dot{\widehat{\boldsymbol{\eta}}}_K \tag{18.27}$$

The matrix $\mathbf{Z}_a$ is the structural to acoustics modal transfer function matrix at frequency ω whose terms are given by:

$$\mathbf{Z}_a = j\omega\overline{\boldsymbol{\alpha}}_A \overline{\mathbf{C}}_{As} \tag{18.28}$$

where $\overline{\mathbf{C}}_{As}$ and $\overline{\boldsymbol{\alpha}}_A$ is the modal structural acoustic coupling matrix and modal acoustic transfer function matrix respectively. Substituting Eq. 18.28 into Eq. 18.27, the modal pressure amplitudes, $\widehat{\mathbf{P}}$ within the cavity are given by:

$$\widehat{\mathbf{P}} = j\omega\overline{\boldsymbol{\alpha}}_A \overline{\mathbf{C}}_{As} \dot{\widehat{\boldsymbol{\eta}}}_K \tag{18.29}$$

The modal expansion for the estimated acoustic potential energy evaluated over number of acoustic modes is given by [18]:

$$\widehat{E} = \widehat{\mathbf{P}}^H \widehat{\mathbf{P}} \tag{18.30}$$

By putting Eq. 18.27 into Eq. 18.30, it is possible to get the modal expansion for the estimated acoustic potential energy as:

$$\widehat{E} = \dot{\widehat{\boldsymbol{\eta}}}_K^H \mathbf{Z}_a{}^H \mathbf{Z}_a \dot{\widehat{\boldsymbol{\eta}}}_K \tag{18.31}$$

Referring to Eq. 18.28, the matrix $\mathbf{Z}_a$ can be factored as

$$\mathbf{Z}_a = \mathbf{F}\overline{\mathbf{C}}_{As} \tag{18.32}$$

where $\mathbf{F}$ is an $na \times na$ diagonal matrix whose elements are given by

$$\mathbf{F}_{r,r} = \frac{s}{s^2 + 2\xi_r \omega_r s + \lambda_r^2}, \tag{18.33}$$

where ξ_r, ω_r, λ_r^2, are the viscous damping loss factor, natural frequency, and eigen value of the rth acoustic mode respectively and s has been substituted for $j\omega$. The frequency dependent part of the radiation transfer function matrix has been moved entirely to $\mathbf{F}$. Frequency dependent matrix $\mathbf{F}$ is now converting into state space form:

$$\dot{\mathbf{r}} = \mathbf{A}_{Rad}\mathbf{r} + \mathbf{B}^*{}_{Rad}\dot{\widehat{\boldsymbol{\eta}}}_K \tag{18.34}$$

$$\widehat{\mathbf{P}} = \mathbf{C}_{Rad}\mathbf{r} \tag{18.35}$$

To represent the complete state space model for the radiation transfer function matrix $\mathbf{Z}_a$, $\mathbf{B}^*{}_{Rad}$ must be post-multiplied with $\overline{\mathbf{C}}_{As}$ giving radiation state space model as,

$$\dot{\mathbf{r}} = \mathbf{A}_{Rad}\mathbf{r} + \mathbf{B}_{Rad}\dot{\widehat{\boldsymbol{\eta}}}_K \tag{18.36}$$

$$\widehat{\mathbf{P}} = \mathbf{C}_{Rad}\mathbf{r} \tag{18.37}$$

The acoustic nodal pressure inside the cavity can be calculated by pre-multiplying $\widehat{\mathbf{P}}$ with mass normalized mode shape matrix $\boldsymbol{\psi}_A$ of acoustic cavity. The instantaneous acoustic potential energy can be computed, i.e., virtually sensed, from Eq. 18.30 using the knowledge of modal acoustic pressure amplitudes.

18.4 Numerical Example

A numerical study is presented here to demonstrate the effectiveness of virtual sensing of acoustic potential energy using the approach described in previous section. Table 18.1 gives details of the geometric and material properties and other relevant details of the piezoelectric, structural and the acoustic domains of the cavity including details of their finite element models. A proportional viscous damping is simulated in the structural and the acoustic domains of the cavity.

Figures 18.2 and 18.3 show the finite element mesh of the structural and acoustic system used to model the 3D rectangular box cavity.

18.4.1 Selection of Optimal Locations of Sensor and Actuator

Selecting location and optimal placement of the piezoelectric patches is also an important issue. Ref [19] proposed an optimization method for selecting optimal location of actuators and sensors. Reference [20] reviewed the various methods for optimal placement of piezoelectric sensors and actuators on a smart structure. In this paper, the optimal placement is being done using the observability/controlability gramian matrix that is calculated as,

$$\mathbf{W}_o = \int_0^\infty e^{\mathbf{A_P}^T t} \mathbf{C_P}^T \mathbf{C_P} e^{\mathbf{A_P} t} dt \tag{18.38}$$

The matrix $\mathbf{W}_o$ is calculated for different locations of piezo-sensor. The diagonal elements of the matrix $\mathbf{W}_o$ in this case correspond to different structural mode as the state space matrices used in Eq. 18.38 are in the modal domain. Since, the finite element mesh is symmetric, the possible locations are considered to be restricted to only one quadrant of the plate. Table 18.2 shows a comparison of the diagonal values of the Observability gramian matrix $\mathbf{W}_o$ for different positions of sensor in a quadrant.

Table 18.1 Properties of structure, piezo transducers and rigid walled acoustic cavity

Property	Structure	Piezo	Acoustic cavity
Material	Steel	P-876 A12 Dura Act piezoelectric patch transducers	Thick acrylic sheetsandMedium: air
$L_x \times L_y \times L_z$ (m^3)	$0.261 \times 0.300 \times 0.001$	$0.0522 \times 0.050 \times 5 \times 10^{-4}$	$0.261 \times 0.300 \times 0.686$
Young's Modulus (GPa)	200	23.3	–
Density (kg/m^3)	7,800	7,800	1.21
Modal damping factor, ξ	0.005 for all modes	–	0.05 for all modes
Poisson's ratio	0.3	0.34	–
Speed of sound (m/s)	–	–	340
Piezoelectric strain coefficient e_{31}, e_{32} (C/m^2)	–	-8.9678	–
Dielectric constant ε_{33} (F/m)	–	6.6075×10^{-9}	–
Boundary conditions	Clamped at all edges	Sensor: short circuitActuator: voltage is applied by it	5 sides: rigidly fixed1 side: flexible steel plate
Element type	4 nodded rectangular bending element with 12 dofs	4 nodded rectangular bending element with 12 dofs and 2 electric dof (voltage)	8-nodded Hexahedral element with 8 acoustic pressure dofs
Mesh size	10×12	2×2	$10 \times 12 \times 14$

Fig. 18.2 Finite element mesh of the structural domain of the cavity
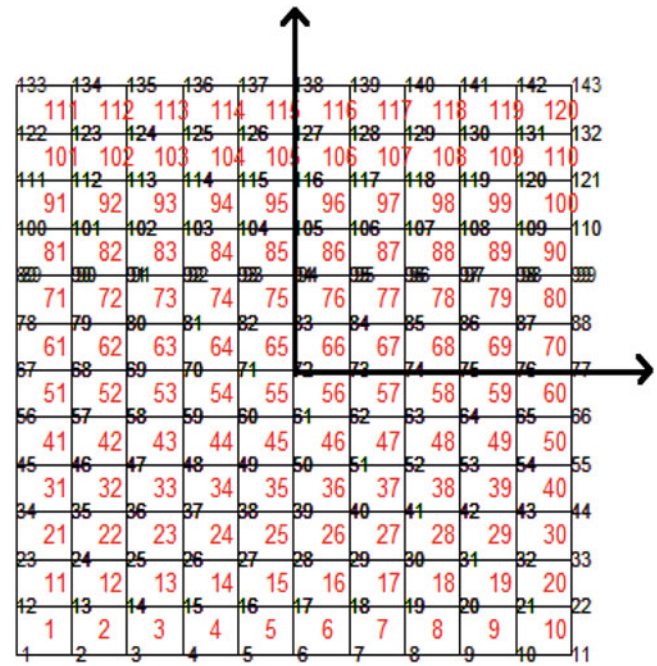
Fig. 18.3 Finite element mesh of the acoustic domain of the cavity
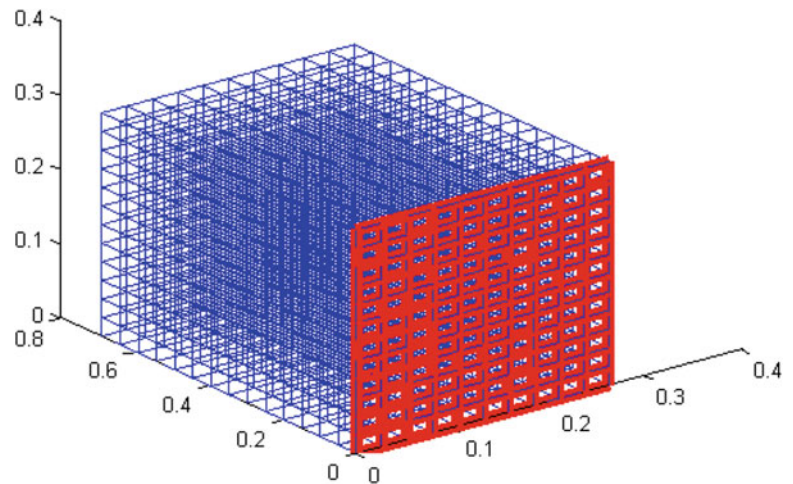
Table 18.2 Observability gramian eigen values for first few modes of structure

	Finite element numbers on structure where piezoelectric is located				
	L1	L2	L3	L4	L5
	55 56 65 66	76 77 86 87	96 97 107 106	98 99 108 109	78 79 88 89
Mode no. (structure and piezos)	(1× 1e08)	(1× 1e08)	(1× 1e08)	(1× 1e08)	(1× 1e08)
1	5.11	2.44	0.03	0.05	0.05
2	0.00	7.49	2.21	0.15	1.49
3	0.00	3.46	0.40	0.40	3.15
4	0.00	5.33	3.99	3.42	6.72
5	16.75	0.65	8.29	2.21	0.30
6	19.19	2.36	0.70	2.68	11.10
7	0.00	1.09	6.41	9.58	0.25
8	0.00	2.68	2.49	9.66	17.38

Fig. 18.4 Finite element mesh of the piezo-structural domain of the cavity
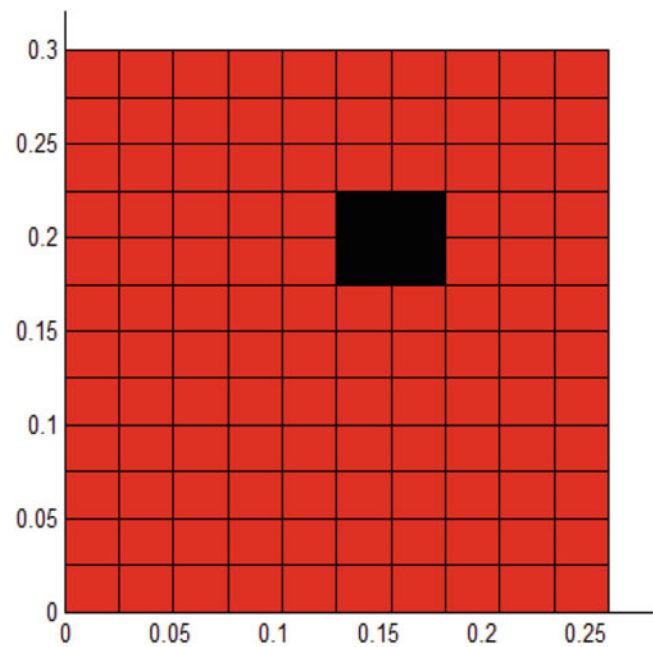
Table 18.3 Natural frequencies structure, piezo-structural (at optimal location), and the acoustic domain

S.No.	Natural frequencies of structural part of the cavity (Hz)	Natural frequencies of the piezo-structural part of the cavity (Hz)	Natural frequencies of the Acoustic cavity (Hz)
1	112.62	111.50	0
2	208.65	210.29	250.52
3	248.04	251.56	504.21
4	331.60	335.31	573.30
5	363.18	364.89	625.65
6	457.34	462.01	659.79
7	472.77	490.46	705.76
8	531.74	538.31	763.48

Table 18.2 shows that if the sensor is placed at location **L2 (76 77 86 87)**, then all the desired modes are well observed. The optimal position of a collocated pair is shown in Fig. 18.4.

18.4.2   Eigen Value Analysis

An Eigen value analysis of the piezo-structural and the acoustic domain is carried out. Table 18.3 shows the natural frequencies of the first few modes.

18.4.3   Results and Discussion

Following three cases are discussed to show the effectiveness of Kalman filter performance and subsequently virtual sensing of the acoustic potential energy in an acoustic cavity surrounded by a flexible structure at different loadings.

18.4.3.1   Case 1. Virtual Sensing for Impulsive Disturbances

It is assumed that plant/actual system is perfectly modeled in state space form. The plant dynamics is used to calculate the Kalman gain matrix. For the purpose of simulation, and considering the low frequency range, first 20 modes of the plant are used. The disturbance of 10 N of impulse force applied at a certain node on the plate with unknown random input noise of covariance 1e-7 N^2 and measurement noise of covariance 1e-11 V^2.

Fig. 18.5 Overlay of true and estimated sensor output voltage
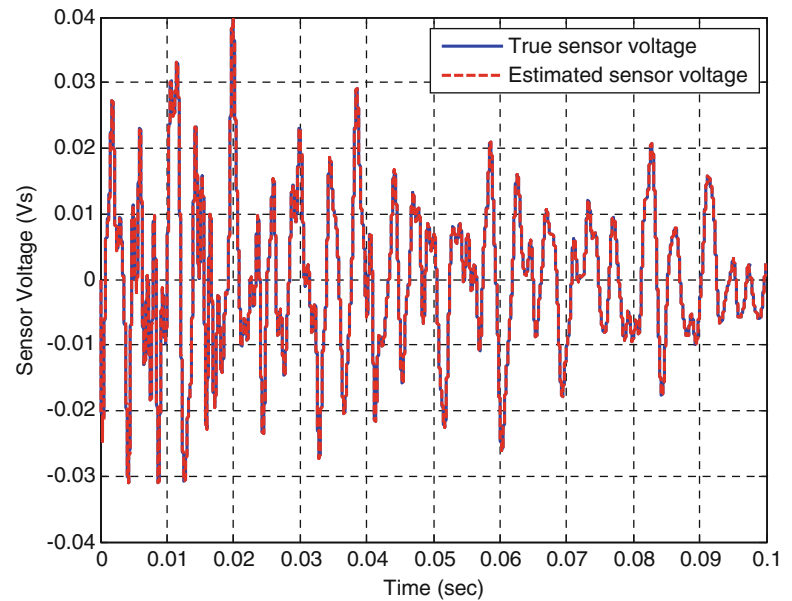
Figure 18.5 shows the comparison of sensor output voltage predicted from true and estimated states. The magnitude of estimated sensor voltage show good comparison with true sensor voltage. Figures 18.6a–c, 18.7a–c, and 18.8a–c show the comparison of true and estimated modal behavior i.e., modal displacement, velocity, and acceleration of the structure. First few structural modes are plotted to show the performance of Kalman filter. From plots, it is observed that Kalman filter is tracking the modal response very well and, it also takes less time to accurately track the true response. From Fig. 18.6b it is observed that tracking time to observe fifth mode is more as compared to other ones, because, as seen in Table 18.2 at optimal location **L2**, the Observability gramian eigen value for fifth mode is small as compared to others.

Figures 18.9, 18.10, and 18.11 show the comparison of true and estimated physical response of the structure. From above figures it is seen that Kalman filter is tracking well the physical displacement, velocity, and acceleration of the structure from the available sensor output of the plant.

Figure 18.12 shows the comparison of true and estimated acoustic potential energy inside the acoustic cavity. It is observed from Fig. 18.12 that initially potential energy is not exactly tracked by the Kalman filter but as the time reaches to 0.01 s the tracking is improved and acoustic potential energy is recovered by Kalman filter. Figure 18.13 shows the overlay of acoustic modal pressure inside the cavity. In Figs. 18.14 and 18.15, acoustic nodal pressure is predicted at node number 1094 inside the cavity. Results show that acoustic nodal pressure and SPL (dB) can be well calculated with Kalman filter and radiation filter states.

18.4.3.2   Case 2. Virtual Sensing for Random Disturbances

The unknown random input force of covariance 1e-3 N^2 is applied to the structure at a certain node. The sensor output of the plant is corrupted with measurement noise of covariance 1e-11 V^2.

Figure 18.16 shows the comparison of sensor output voltage predicted from true and estimated states. The magnitude of estimated sensor voltage show good comparison with true sensor voltage. Figure 18.17 shows the overlay of modal velocity of the structure at first mode. Figure shows that even if structure is excited by random disturbance, the velocity is perfectly tracked by the Kalman filter.

Figure 18.18 shows the comparison of true and estimated acoustic potential energy inside the cavity. It is observed that acoustic potential energy computed from Kalman filter and radiation filter states is well comparable with true values.

18.4.3.3   Case 3. Influence of Unmodeled Plant Dynamics on Virtual Sensing

In practice the plant represents an actual system and is continuous in nature while the model of the plant used in Kalman filter has a finite order. This means that the model of the plant essentially is a truncated model of the actual plant. To simulate this situation, in this section, a study is conducted to evaluate the influence of un-modeled plant dynamics on the performance of virtual sensing strategy. In view of above discussion, in this case, plant is simulated by considering the first 60 modes of
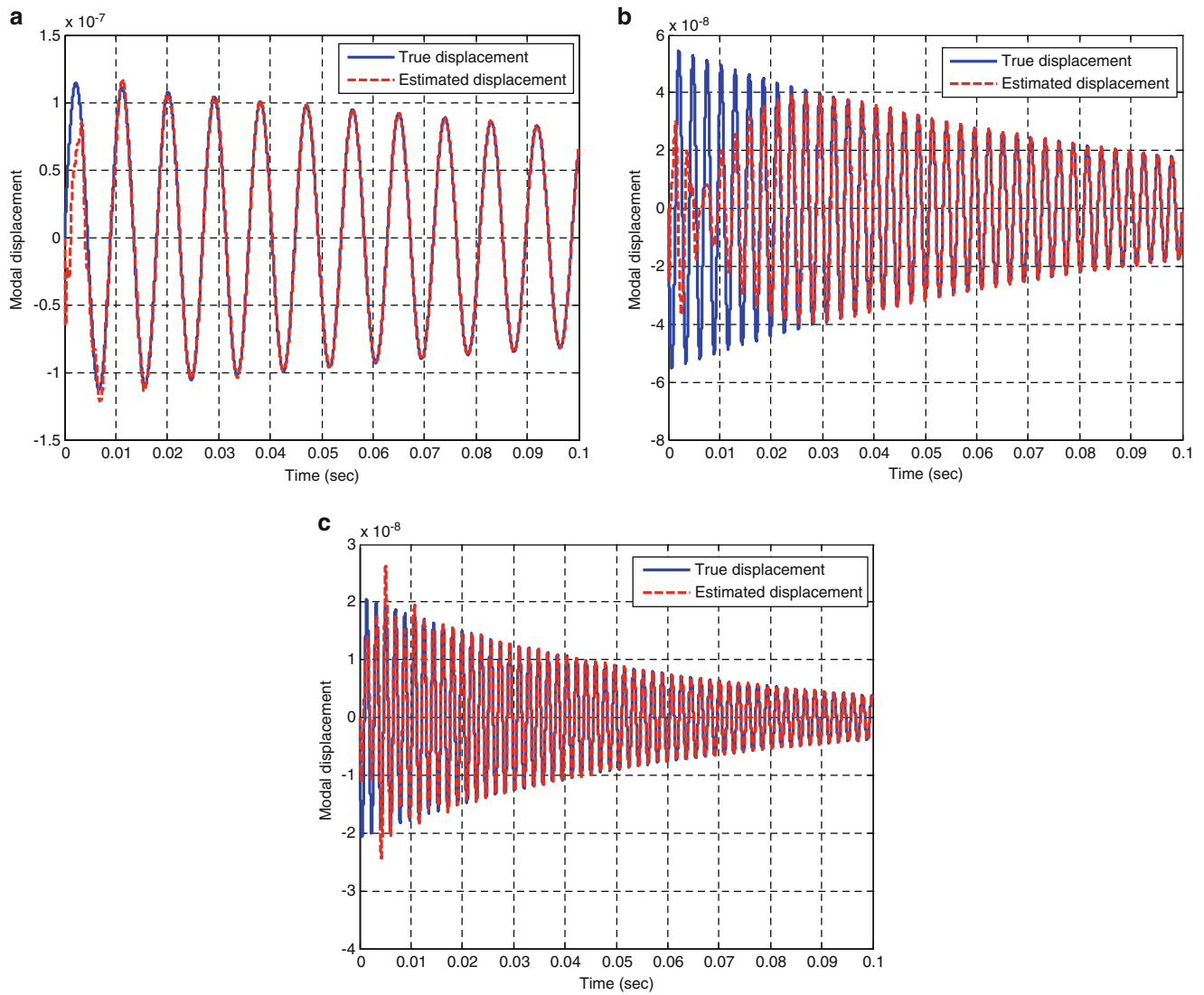
Fig. 18.6 (**a**) Overlay of first mode of the structure (111.50 Hz), (**b**) Overlay of fifth mode of the structure (364.89 Hz), (**c**) Overlay of eight mode of the structure (538.31 Hz)

structure and a replica of the plant model used for design of Kalman filter is simulated by taking first 20 structural modes only. So, there is a modal mismatch between the actual plant model and replica model which is used to design the Kalman filter. The disturbance of 10 N of impulse force applied at a certain node on the plate with unknown random input noise of covariance 1e-7 N^2 and measurement noise of covariance 1e-11 V^2.

Figure 18.19 shows the comparison of true and estimated modal behavior of the structure for the first mode. As shown in the figure, during tracking the response is initially high. This is because the Kalman filter is not able to track the contribution of high frequency modes since it is designed using only first 20 modes.

From Figs. 18.20 and 18.21, it is observed that the maximum magnitude of true acoustic potential energy is not exactly matching with the estimated output, but near or after 0.01 s estimated behavior show good agreement with the true response. It is however observed from Fig. 18.21 that acoustic nodal pressure is well estimated by Kalman and radiation filter.
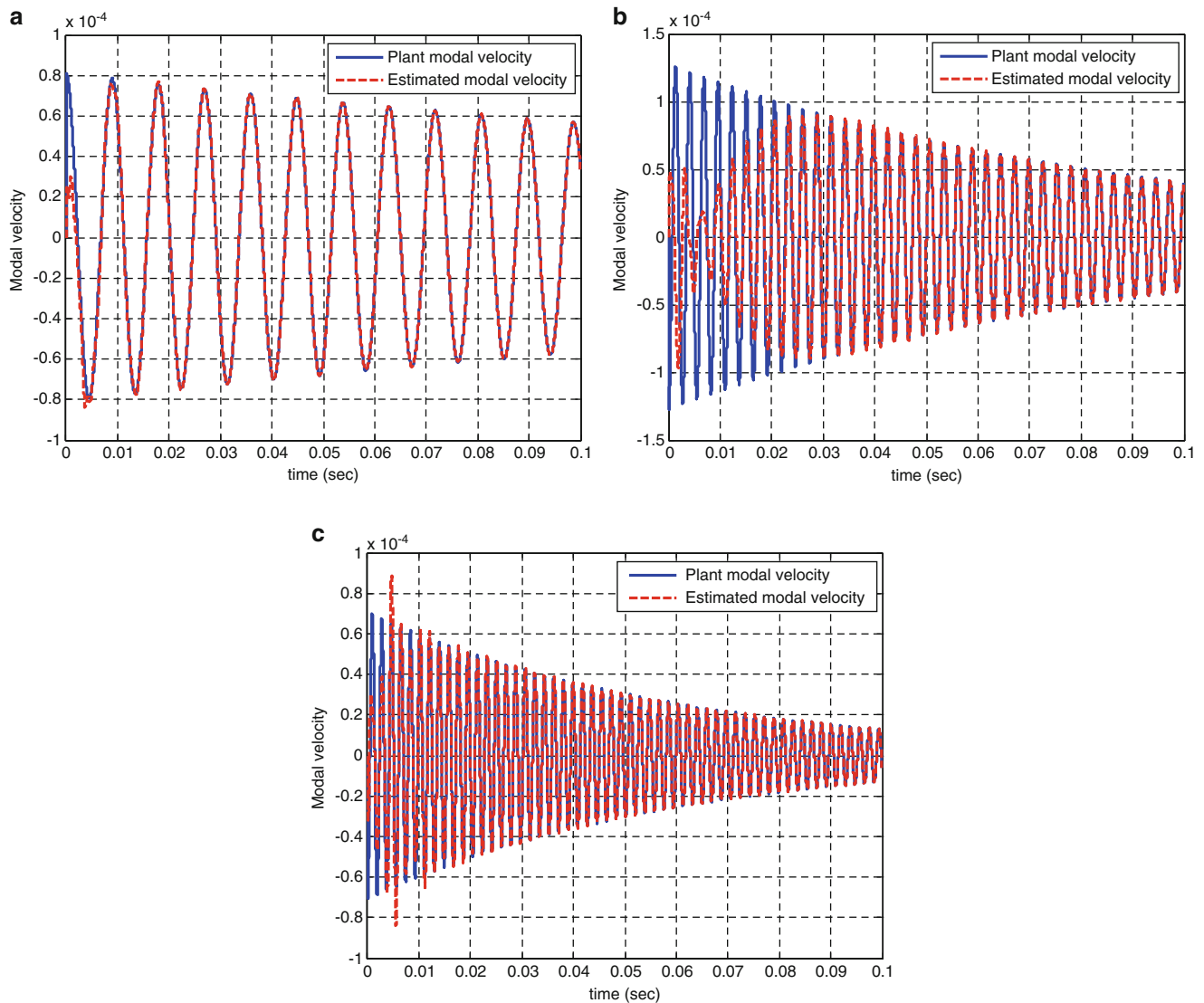
Fig. 18.7 (**a**) Overlay of first mode of the structure (111.50 Hz), (**b**) Overlay of fifth mode of the structure (364.89 Hz), (**c**) Overlay of eight mode of the structure (538.31 Hz)

18.5 Conclusions

This paper presented a strategy for virtual sensing of acoustic potential energy for active control of interior sound. It essentially combines Kalman filter used as an observer of the modal velocities of the structure and then using a radiation filter to compute acoustic potential energy. A structural sensor in the form of a piezoelectric patch is used to sense the vibration of the structure. The paper presents optimal placement of the sensor based on observability gramians to sense the structure modes in the frequency range of interest. A numerical study of a rectangular box cavity with a flexible plate is presented to test the effectiveness of the proposed strategy. Acoustic potential energy is virtually sensed for impulse and random disturbances on the structure and is compared with the actual acoustic potential energy. A study is also performed to evaluate the influence of un-modeled plant dynamics on the performance of virtual sensing strategy. The proposed strategy can accurately sense the acoustic potential energy virtually if an accurate model of the plant is available.
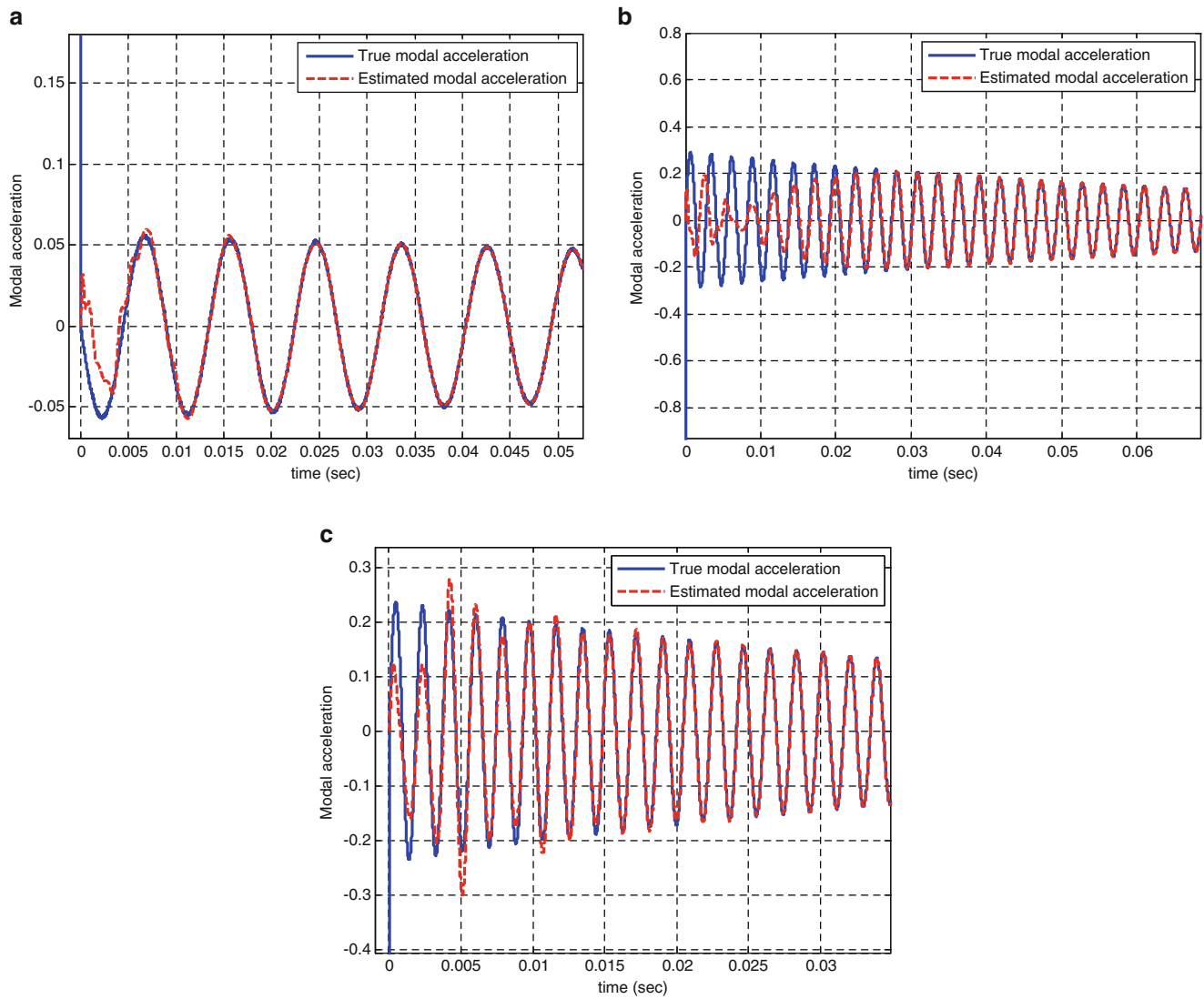
Fig. 18.8 (**a**) Overlay of first mode of the structure (111.50 Hz), (**b**) Overlay of fifth mode of the structure (364.89 Hz), (**c**) Overlay of eight mode of the structure (538.31 Hz)

Fig. 18.9 Overlay of true and estimated physical displacement of structure
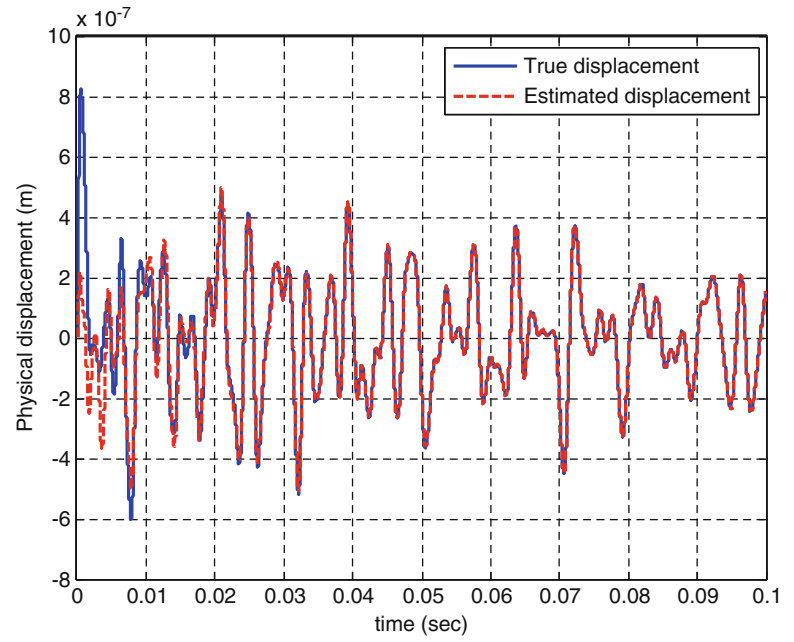
Fig. 18.10 Overlay of true and estimated physical velocity of structure
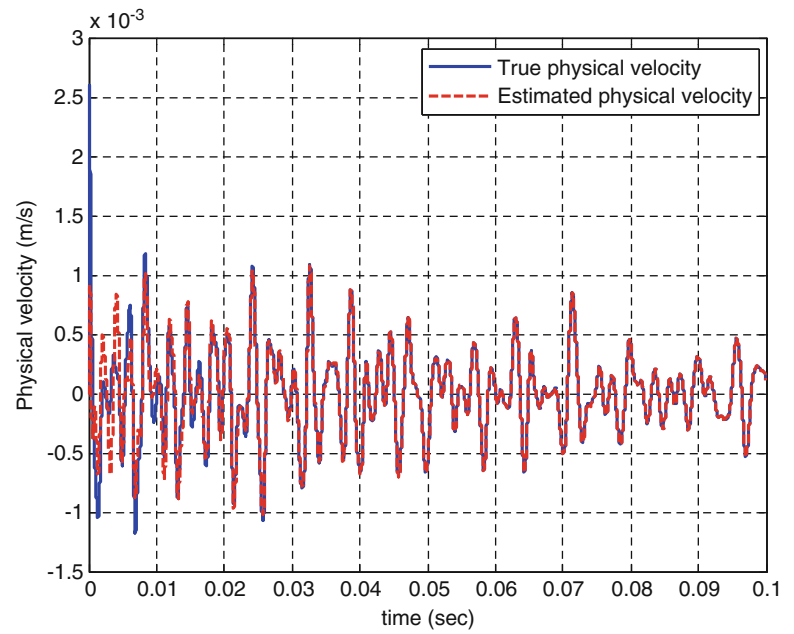
Fig. 18.11 Overlay of true and estimated physical acceleration of structure
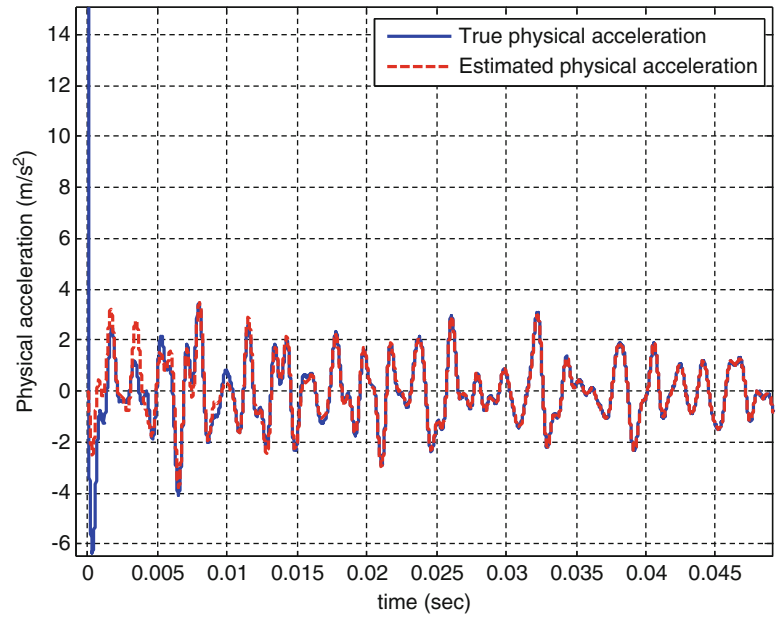
Fig. 18.12 Overlay of true and estimated total acoustic potential energy
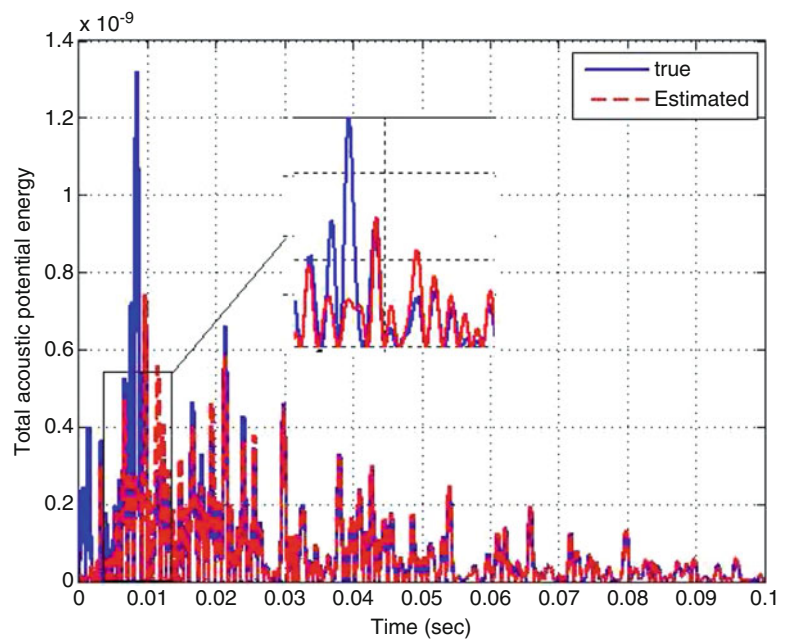
Fig. 18.13 Overlay of true and estimated first mode of acoustic modal pressure
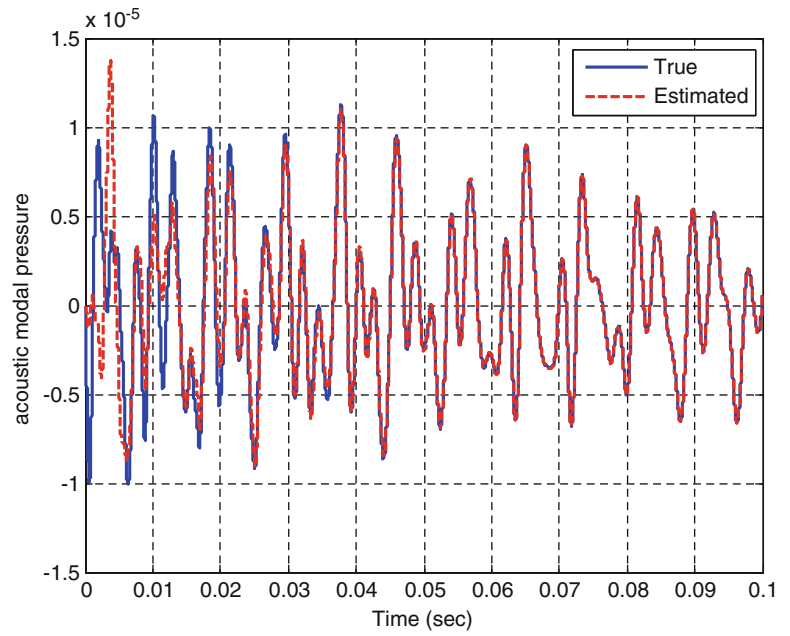
Fig. 18.14 Overlay of true and estimated acoustic nodal pressure inside the cavity
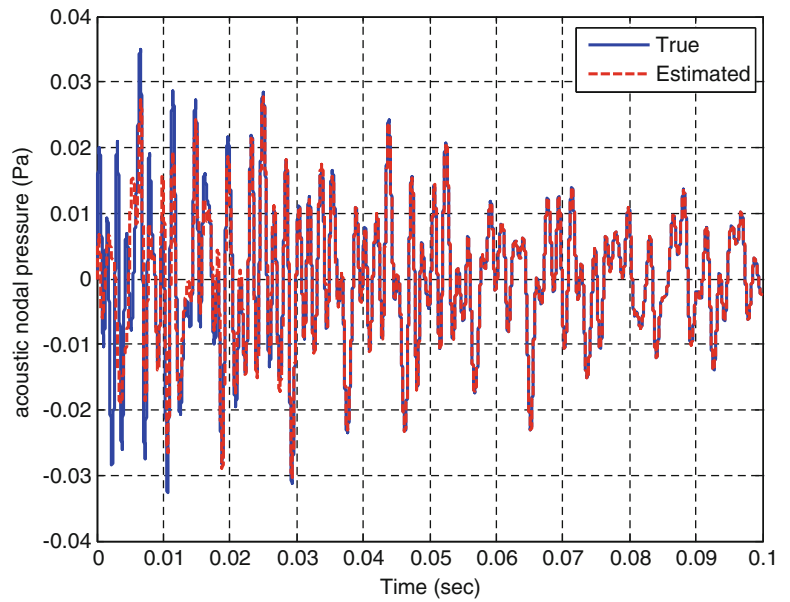
Fig. 18.15 Overlay of true and
estimated sound pressure level
(dB), $P_{ref} = 20\,\mu Pa$
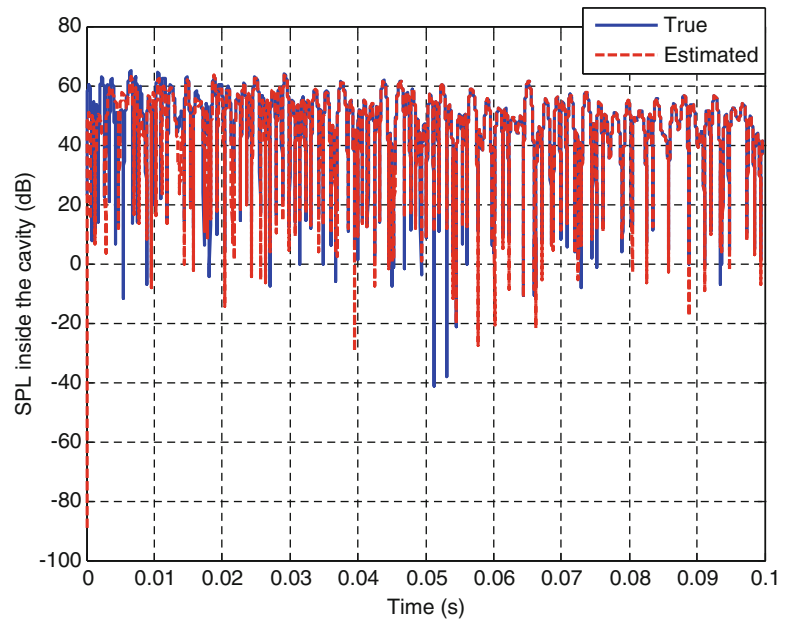
Fig. 18.16 Overlay of true and
estimated sensor output at
random input
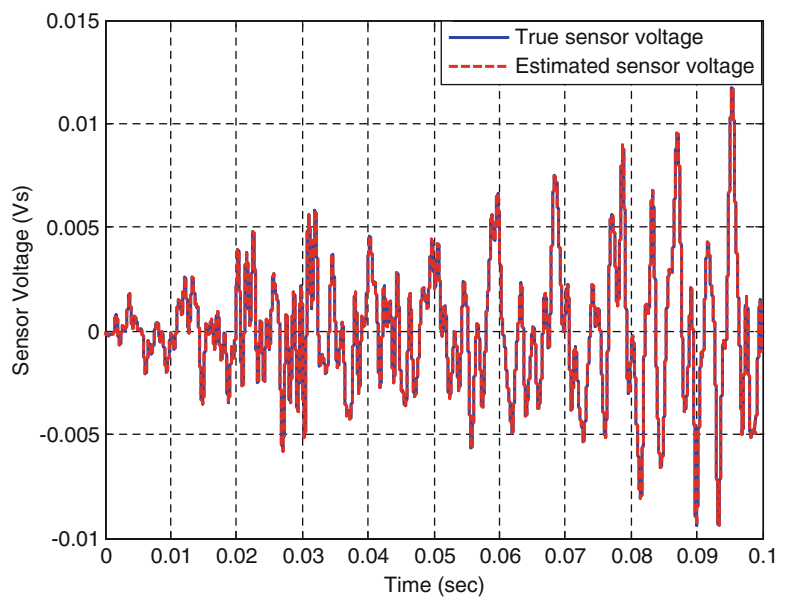
Fig. 18.17 Overlay of true and
estimated modal velocity
response at random input
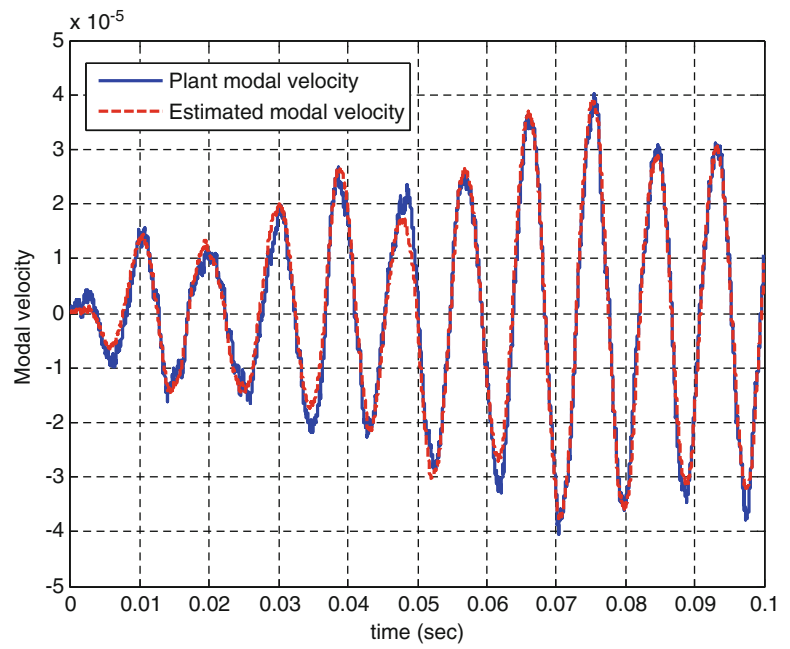
Fig. 18.18 Overlay of true and
estimated total acoustic potential
energy
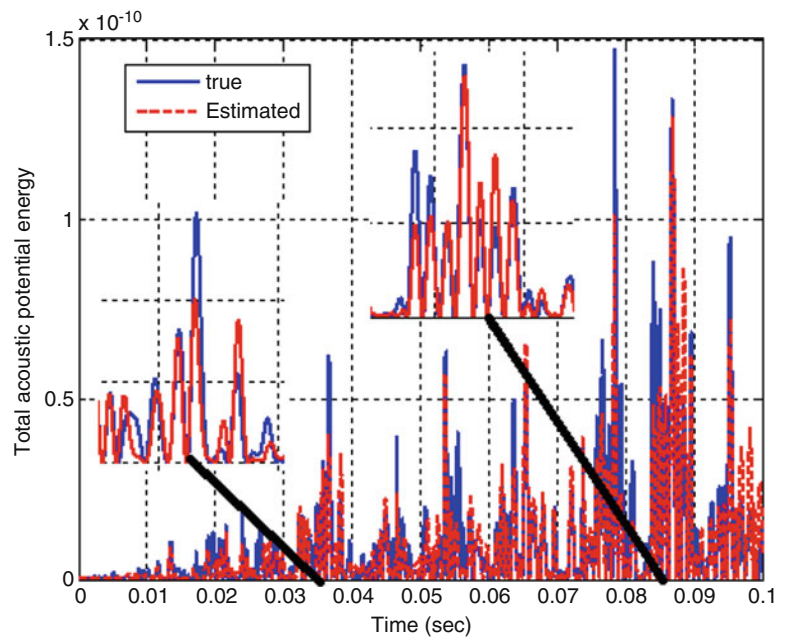
Fig. 18.19 Overlay of true and estimated first modal velocity of structure
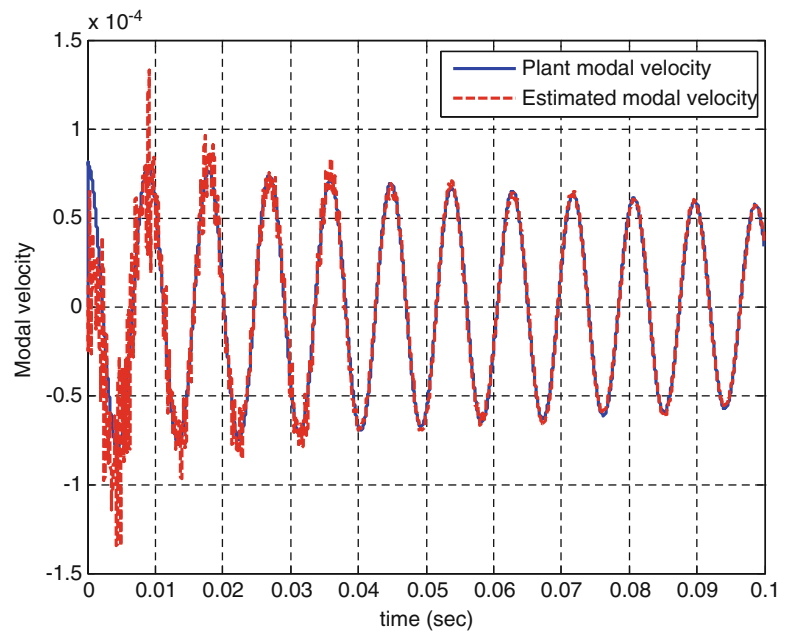
Fig. 18.20 Overlay of true and estimated total acoustic potential energy
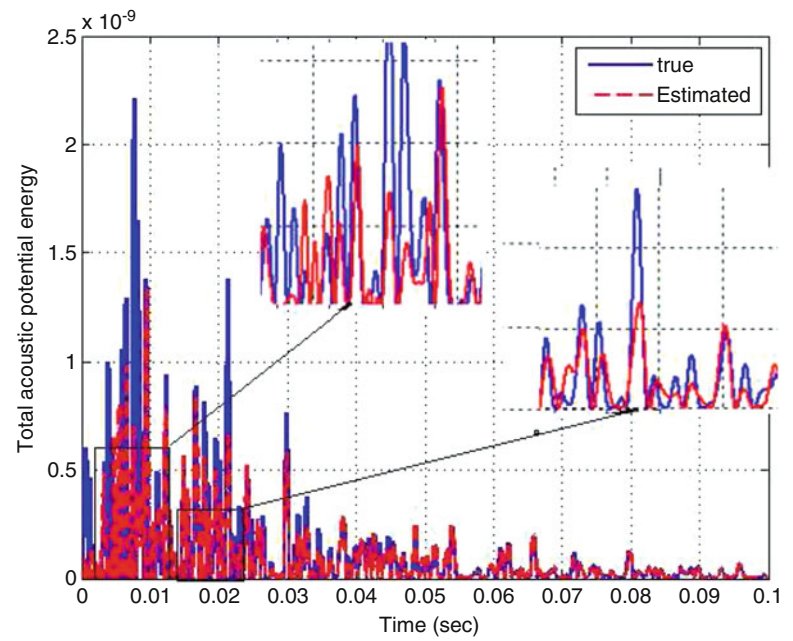
Fig. 18.21 Overlay of true and estimated acoustic nodal pressure at a node inside the cavity
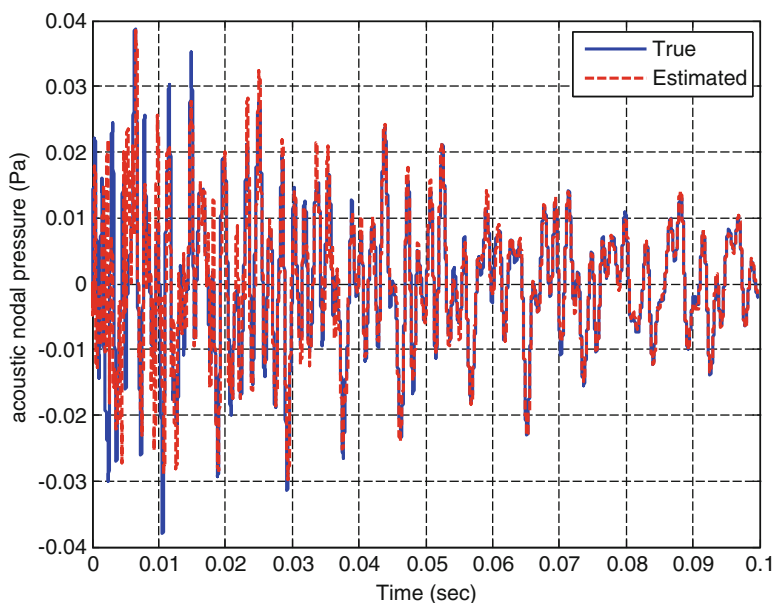
References

1. Fuller CR, VonFlotow AH (1995) Active control of sound and vibration. Control Syst IEEE 15:9–19
2. Leug P (1936) Process of silencing sound oscillations. US Patent 2043416
3. Tan CC, Hird CI (1997) Active control of the sound field of a constrained panel by an electromagnetic actuator—an experimental study. Appl Acoust 52(1):31–51
4. Li DS, Cheng L (2010) The design of synthesized structural acoustic sensors for active control of interior noise with experimental validation. J Sound Vib 329:123–139
5. Fahy F, Gardonio P (1987) Sound and structural vibration: radiation, transmission and response. Academic, London
6. Fuller CR, Rogers CA, Robertshaw HH (1992) Control of sound radiation with active/adaptive structures. J Sound Vib 157(1):19–39
7. Clark RL, Fuller CR (1992) Modal sensing of efficient acoustic radiators with polyvinylidene fluoride sensors in active structural acoustic control approaches. J Acoust Soc Am 91(6):3321–3329
8. Elliott SJ (1994) Active control of structure-borne noise. J Sound Vib 177(5):651–673
9. Griffin S, Hansen C, Cazzolato B (1999) Feedback control of structurally radiated sound into enclosed spaces using structural sensing. J Acoust Soc Am 106(5):2621–2628
10. Wenzel TA, Burnham KJ, Blundell MV, Williams RA (2007) Kalman filter as a virtual sensor: applied to automotive stability system. Trans Inst Meas Control 29(2):95–115
11. Petersen CD, Fraanje R, Cazzolato BS, Zander AC, Hansen CH (2008) A Kalman filter approach to virtual sensing for active noise control. Mech Syst Signal Process 22:490–508
12. Moreau D, Cazzolato BS, Zander AC, Petersen CD (2008) A review of virtual sensing algorithm for active noise control. Algorithms 1:69–99
13. Moreau DJ, Ghan J, Cazzolato BS, Zander AC (2009) Active noise control in a pure tone diffuse sound field using virtual sensing. J Acoust Soc Am 125(6):3742–3755
14. Halim D, Cheng L, Su Z (2011) Virtual sensors for active noise control in acoustic–structural coupled enclosures using structural sensing: robust virtual sensor design. J Acoust Soc Am 129(3):1390–1399
15. Halim D, Cheng L, Su Z (2011) Virtual sensors for active noise control in acoustic-structural coupled enclosures using structural sensing: Part II—Optimization of structural sensor placement. J Acoust Soc Am 129(4):1991–2004
16. Petyt M (1990) Introduction to finite element vibration analysis. Cambridge University Press, Cambridge
17. Preumont A (1997) Vibration control of active structures. Kluwer, Dordrecht, The Netherlands
18. Cazzolato BS, Hansen CH (1998) Active control of sound transmission using structural error sensing. J Acoust Soc Am 104(5):2878–2889
19. Bruant I, Proslier L (2005) Optimal location of actuators and sensors in active vibration control. J Intell Mater Syst Struct 16:197–205
20. Gupta V, Sharma M, Thakur N (2010) Optimization criteria for optimal placement of piezoelectric sensors and actuators on a smart structure: a technical review. J Intell Mater Syst Struct 21:1227–1243

Chapter 19
Wavenumber Decomposition Applied to a Negative Impedance Shunts for Vibration Suppression on a Plate

F. Tateo, K.A. Cunefare, M. Collet, and M. Ouisse

Abstract In the last few decades, researchers have given a lot of attention to new engineered materials with the purpose of developing new technologies and devices such as mechanical filters, low frequency sound and vibration isolators and acoustic waveguides. So-called metamaterials are an example of such, where apparent material properties are engineered into structures by exploiting periodicity as well as active and passive elements to achieve desired ends.

This paper explores the active vibration control performance of such a metamaterial, considered as a metacomposite comprising an active interface between two regions of an extended aluminum plate; one region has a disturbance input while the other region is meant to be protected by the active interface.

The active interface is a 75-element array of piezoelectric patches individually connected to synthetic negative capacitance control circuits. The performance is analyzed through a wavenumber decomposition of the velocity field in the wavenumber domain. The wavenumber decomposition is applied to each region individually, as well as to the entire plate. The wavenumber decomposition also provides insight into the potential control of radiated noise from the structure.

Keywords Negative capacitance • Semi-active vibration control • Smart materials • Wavenumber domain filtering • Metacomposites

19.1 Introduction

The design of innovative structures incorporating multiple physical functionalities represents a big challenge for both industrial and academic communities. This paper is a contribution to the challenges of designing and implementing a new class of integrated smart metacomposites capable of improved engineering performances in terms of mechanical and vibroacoustic behavior as compared to strictly passive structures.

The definition of a metacomposite combines two different aspects of vibration control:

- The first aspect is connected to periodic structure theories, which are usually associated with metamaterial developments.
- The second concept includes the definition of composite conceived in a broader sense, in which shunted piezoelectric materials, electronic components, controllers and the structure are intimately connected to each other.

The concept of metacomposite is therefore associated to the notion of programmable matter coined by Toffoli [6] to refer to an ensemble of computing elements arranged in space is now extended to smart materials based on distributed piezoelectric actuators able to modify the inherent vibroacoustic properties based on an input signal.

F. Tateo (✉) • M. Collet • M. Ouisse
Department of Applied Mechanics, Femto-st, Besançon, France
e-mail: flaviano.tateo@femto-st.fr

K.A. Cunefare
School of Mechanical Engineering, Georgia Institute of Technology, Atlanta, GA, USA

M. Collet
LTDS, Ecole Centrale de Lyon, Ecully, France

Over the years different solutions including such a new material have been proposed. To cite a few, in the field of light propagation, research has explored how to design and construct photonic crystals exhibiting photonic band gaps that prevent light from propagating in certain directions with specified frequencies. Other efforts have explored creation of photonic crystals able to propagate light in anomalous and useful ways [3]. In the acoustic domain, similar studies were carried out with the aim of preventing the propagation of elastic waves within a medium. For both light and acoustic waves, the band gap is obtained by periodically modulating some electromagnetic or mechanical properties [7].

This technique presents two main problems:

- the spatial modulation must be of the same order as the wavelength in the gap,
- the position of the band gap cannot be easily changed since it strongly depends on the materials employed (Bragg's band gap).

A possible solution for these problems is found using composites with locally resonant units. The periodicity of the crystal creates a stop band that can be shifted by modifying the properties of the resonators [4]. The same idea was extended in the vibroacoustic domain for the control of elastic waves propagating into a waveguide. The resonant units in this case were obtained using RL circuits shunted to piezoelectric ceramics embedded on the structure's surface. An elegant formulation of passive shunting was first proposed by Hagood and Von Flotow [2] and is still commonly used. The study showed how a piezoelectric material shunted through a series RL circuit, i.e., a resonant shunt, which would exhibit a behavior analogous to the well-known mechanical tuned mass damper. Periodically induced impedance-mismatch zones generate broader stop bands. The tunable characteristics of shunted piezo-patches allow the equivalent mechanical impedance of the structure to be tuned so that stop bands are generated over desired frequency ranges. The resistance allows the energy dissipation mechanism of shunted piezos to be exploited.

Eventually a broader control effect can be achieved by using negative capacitance shunts. In this configuration, a piezoelectric patch is shunted through a passive circuit to a synthetic negative impedance converter. In this way, the internal capacitance of the piezoelectric ceramic is artificially canceled and the impedance of the shunt circuit reduces to that of the passive circuit. Although the negative capacitance shunting strategy has been experimentally validated, it must be used with caution since it requires active elements that can destabilize the structure if improperly tuned. This technique requires in fact to tune the circuit very close to the stability limit.

In this paper, the metacomposite structure of interest consists of an array of piezoelectric patches periodically arranged over a limited region of the surface of a two-dimensional waveguide. This array of patches is intended to serve as an active interface between regions of the waveguide, formed from a plate. This active interface allows modification of the scattering properties of the waveguide in terms of reflected and absorbed energy. This controlling capability is obtained by correctly tuning the parameters of the external circuit by which almost arbitrary effective structural impedance may be obtained [1]. The novelty of the paper at hand is to use an array of periodic shunted patches to create a controllable impedance boundary between an upstream and downstream section of the two-dimensional plate waveguide.

The core of this work is to propose an experimental technique able to qualify the smart interface from the dynamic point of view. To do so a Scanning Laser Doppler Vibrometer (SLDV) is used to measure the velocity of the inspected surface in points belonging to a predefined grid. Scanning the grid and post-processing the data allows the detection and the visualization of the full wave-field as it propagates in the structure. The resulting images describe the main features of the propagating wave and show its interactions with discontinuities that may be encountered along the wave path.

Thanks to this approach the smart metacomposite is analized and the performances of the control system are estimated.

19.2 Metacomposite Design

This section introduces the design of the smart metacomposite including the plate structure, the design criteria leading to selection of the piezoelectric patches used in the active interface and the design and impedance characteristics of the shunting circuit.

The basic structure of the metacomposite comprises an aluminum plate and an array of piezoelectric ceramics arranged in a periodic fashion. Each subcomponent have the following dimensions: $2,100 \times 1,050 \times 3$ mm for the plate and $50 \times 50 \times 0.5$ mm for the piezoelectric patch respectively. Regard to the mechanical properties the plate has a mass density of $2,700 \, \text{kg/m}^3$, a Young's modulus of $70 \, \text{GPa}$ and a Poisson's ratio of 0.33. Each piezoelectric ceramic has a mass density of $7,650 \, \text{kg/m}^3$, a Poisson's ratio of 0.31, dielectric loss smaller than 0.05 % and a coupling factor of 0.31. The plate is suspended from a rigid frame by metallic wires in order to approximate free–free boundary conditions. The plate is equipped with 75 piezoelectric patches (Ferroperm Industries P Z26 series) arranged in a regular 15×5 array as seen in Fig. 19.1. The patches and the

Fig. 19.1 Photograph of plate with 75 element piezoelectric patch array comprising an active interface, connected to bank of 75 individual negative impedance shunt control circuits
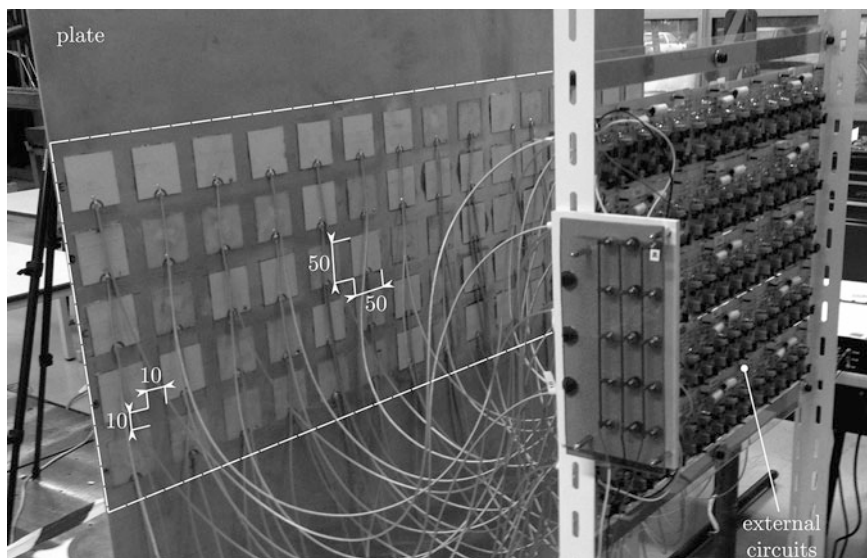
depth of the patch array were selected based on consideration of their size relative to the shortest structural wavelength of interest. The array was intended to be effective up to a frequency of 5,000 Hz. The plate's dispersion relation for the A_0 flexural mode at 5,000 Hz has a wavelength of about 30 cm. With patches having dimensions of 50×50 mm, there will be no charge cancellation on an individual patch as would occur if the patch dimensions were comparable to a wavelength. Further, the depth of the patch array is 350 mm such that it spans more than a wavelength at 5,000 Hz. Since the array elements are uncoupled electronically, each element within the array would still function at the highest frequency of interest, even though the entire array depth would be comparable to a wavelength. The thickness of the patch was selected considering the constraints of the electric circuit and the nature of the control technique. Different authors have shown that the best controlling effect is obtained when the negative impedance shut circuit is tuned close to the inherent patch capacitance. This property strongly depends on the material properties and the geometry of the patch. Once the material properties and the two dimensions of the piezoelectric patch are chosen, the only parameter which remains for selection is the thickness. Thin patches exhibit larger values of intrinsic capacitance which would yield increased control, however, this parameter cannot be reduced indefinitely due to the weakening of the piezoelectric patch itself. For these reasons, a thickness of 0.5 mm was selected.

The controlling capability is obtained by properly tuning the external circuit an optimization procedure [1] has been used with the objective of identifying the real and the imaginary parts of an imposed synthetic impedance. Two possible behaviors depending on the criterion used in the optimization have been identified: minimizing the velocity of the energy propagation in the region of the active array it is therefore possible to limit the propagation of the wave beyond the active interface; choosing a criterion based on exploiting the effect of electrical damping it is possible to modify the dynamic properties of the plate by increasing the energy absorption properties of the active interface.

However, the required electrical impedances for these two circuit optimization approaches cannot be readily reproduced experimentally because it is not possible to exactly recreate the optimal resistance and capacitance over the whole frequency range of interest. For the work presented here, the layout of the actual circuit implemented for control of the patches is presented in Fig. 19.2. This circuit contains a number of passive components, including the resistances R, R_2, R_3, R_4 and the capacitance C_2 as well as an active component, specifically, an operational amplifier that is essential for the circuit to reproduce the desired behavior. This specific circuit layout was chosen as opposed to others because of its simplicity and its effectiveness in the frequency range of interest. The impedance of the circuit in Fig. 19.2 is determined by the formula

$$Z_{eq}(\omega) = R - \frac{R_3 R_2}{R_4(1 + i\omega R_2 C_2)} \tag{19.1}$$

Figure 19.2 depicts the frequency-dependent behavior of the actual impedance produced by the circuit; in the top of the figure is the equivalent resistance and at the bottom the equivalent capacitance. Both terms vary as a function of the frequency; in particular the resistance at low frequency presents a negative value that can introduce some instability which can degrade the overall performance of the control system. From the practical point of view, the circuit presented in Fig. 19.2 is further modified. The resistances R_3 and R_4 were implemented through a single potentiometer R_{pot} with the aim of simplifying the

Fig. 19.2 Comparison between the desired performance of the ideal circuit and that of the physically implemented circuit. On the *left*, basic architecture of circuit; on the *right* the circuit's impedance depicted in terms of equivalent resistance (*top*) and equivalent capacitance (*bottom*)
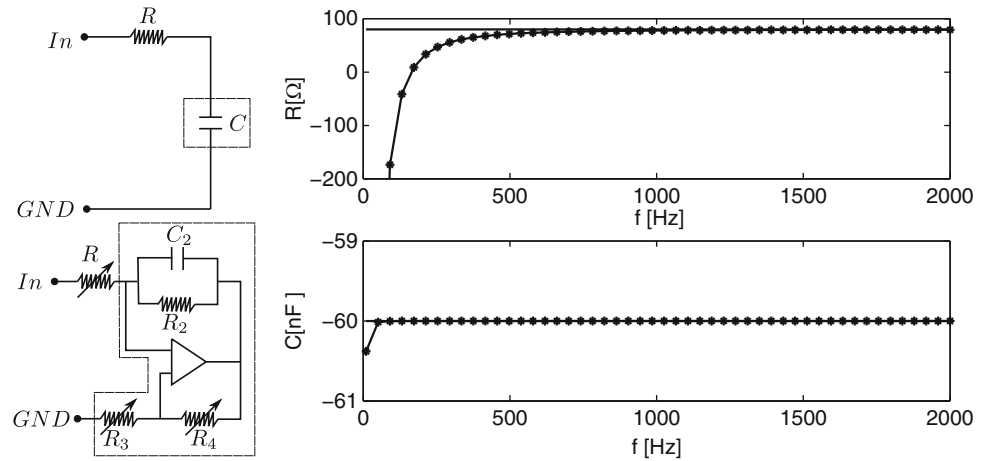
circuit layout. The negative impedance control technique requires tuning of the synthetic capacitance around the capacitance value of the piezoelectric ceramic at free stress condition; this value is intrinsic to the electromechanical coupling and depends upon the material properties, the geometry of the patches and the plate stiffness. The intrinsic capacitance of the piezoelectric patch can be estimated by measurement using a capacitance meter when the specimen is free of external forces (in the case at hand 52 nF). The actual circuit was tuned by varying the position of the potentiometer R_{pot} in small increments from high negative values of the synthetic capacitance to a value very close to the intrinsic capacitance value.

19.3 Experimental Setup

The structure of interest, described in the previous section, consists of an aluminum plate equipped with 75 piezoelectric actuators connected to external circuits and arranged so as to form a periodic array of 5×15 units. Standard epoxy glue was used to bond the piezoelectric ceramics to the top surface of the plate.

Elastic waves are excited by a shaker as depicted in Fig. 19.3. The input transducer, located in the lower part of the plate 840 mm away from the active interface (point E), is driven by a sinusoidal burst generated by a signal generator and amplified by an LDS power amplifier. The resulting elastic waves are recorded at the measurement grid points. The operation of the scanning laser vibrometer (Polytec PSV-400) requires the generation of a pulse at each grid point in order to record the corresponding response. Phase information is retained by triggering the excitation signal through a low frequency signal, which also defines the scanning rate. Upon completion of measurements at all grid points, the recorded responses are then post-processed to obtain full images of the propagating wave-field within the region of inspection. A schematic of the set-up considered for wave-field measurement is shown in Fig. 19.3. Measurements were conducted over a grid of 37×81 scan points with a spatial resolution of 20 mm in the horizontal and vertical directions. At each grid point, the laser measures the time history of the out-of-plane velocity

$$w_{3D} = w_{3D}(x, y, t). \tag{19.2}$$

Figure 19.4 presents the full-field velocity measurement obtained scanning the plate's surface with the laser beam. For each time step is possible to visualize the system response, after few *ms* some reflections due to the boundaries are observed the wave-field is clearly modified. This phenomenon can potentially create problems in the subsequent analysis since the interaction between the main wave-front and the reflections can generate undesired effects; the assumption of cylindrical waves freely propagating within the plate no longer applies.

19.4 Analysis of 2D Waveguide

In many applications guided waves are used in order to interrogate the integrity of a structure. In SHM application analysts need to isolate specific wave-modes associated to the reflections due to an obstacle (i.e. damage) from the global response. In these cases the nature of the propagating waves (direction, shape and amplitude) is modified. By simply analysing the raw data (time history) it is very hard to distinguish the different components associated to the propagating wave. In order
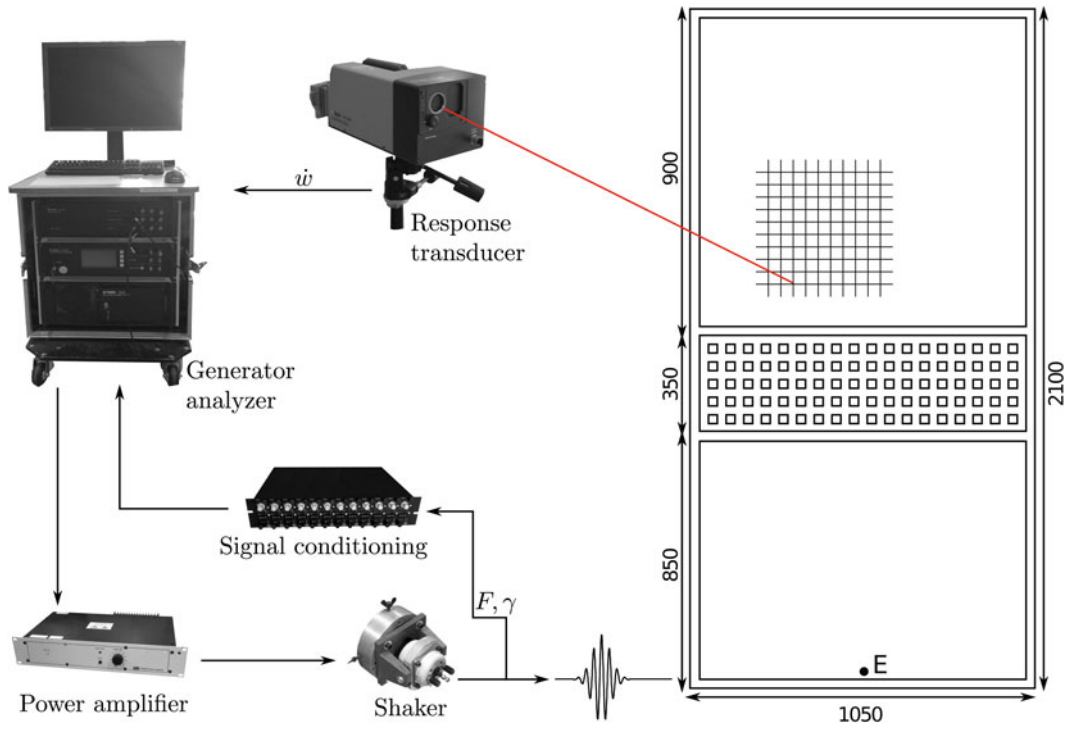
Fig. 19.3 Schematic of the experimental set-up for wave-field measurement

to overcome this specific difficulty a filtering technique in the wave number domain is used with the purpose of separating the different wave-modes composing the measured response [5]. The approach described so far is extended to the smart metacomposite by just assuming that the active interface is able to modify the scattering properties of the simple waveguide (plate). The raw signal w_{3D} is first modified by just considering the spatial response of the system along the y direction

$$w_{2D} = w_{2D}(y,t) = w_{3D}(\bar{x}, y, t) \tag{19.3}$$

as depicted in Fig. 19.4 (white line).

The signal w_{2D} is then Fourier transformed

$$W_{2D} = W_{2D}(k_y, f) = \mathcal{F}_{2D}(w_{2D}(y,t)) \tag{19.4}$$

obtaining a frequency/wavenumber representation that can be used to effectively isolate the targeted wave-mode from the overall response which is a combination of the primary wave generated by the exciter and the waves associated to the reflection (i.e. boundaries).

The 2D Fourier transform effectively separates the different wave components; by using a simple window functions is possible to filter out almost all the undesired components. The filtering procedure is based on the selection of the wave-modes having a dispersion relation (contour plot) similar to the theoretical dispersion relation associated to the bare plate (black line), as depicted in the top of Fig. 19.5.

Upon filtering, the residual signal can be transformed back through an inverse Fourier transform to the space/time domain for visualization and further processing. From this perspective, 2D Fourier transform based filtering represents an attractive approach to separate a given wave. Mathematically, the windowing process can be simply expressed as a function product between the wave's 2D Fourier transform and a 2D window function:

$$W_{2D}^* = H(k - k_0, \omega - \omega_0) W_{2D}(k, \omega) \tag{19.5}$$

where $H(k - k_0, \omega - \omega_0)$ denotes the window centered at k_0, f_0. The process is depicted graphically in Fig. 19.5, which respectively show a Hanning window overlapped to the signal's 2D spectrum and the residual signal upon filtering. The space/time domain approximation of the filtered response w_{2D}^* is expressed as

Fig. 19.4 Experimental full-field velocity measurement at different time steps. The lower images clearly indicates the presence of reflection occurred in correspondence of the boundaries
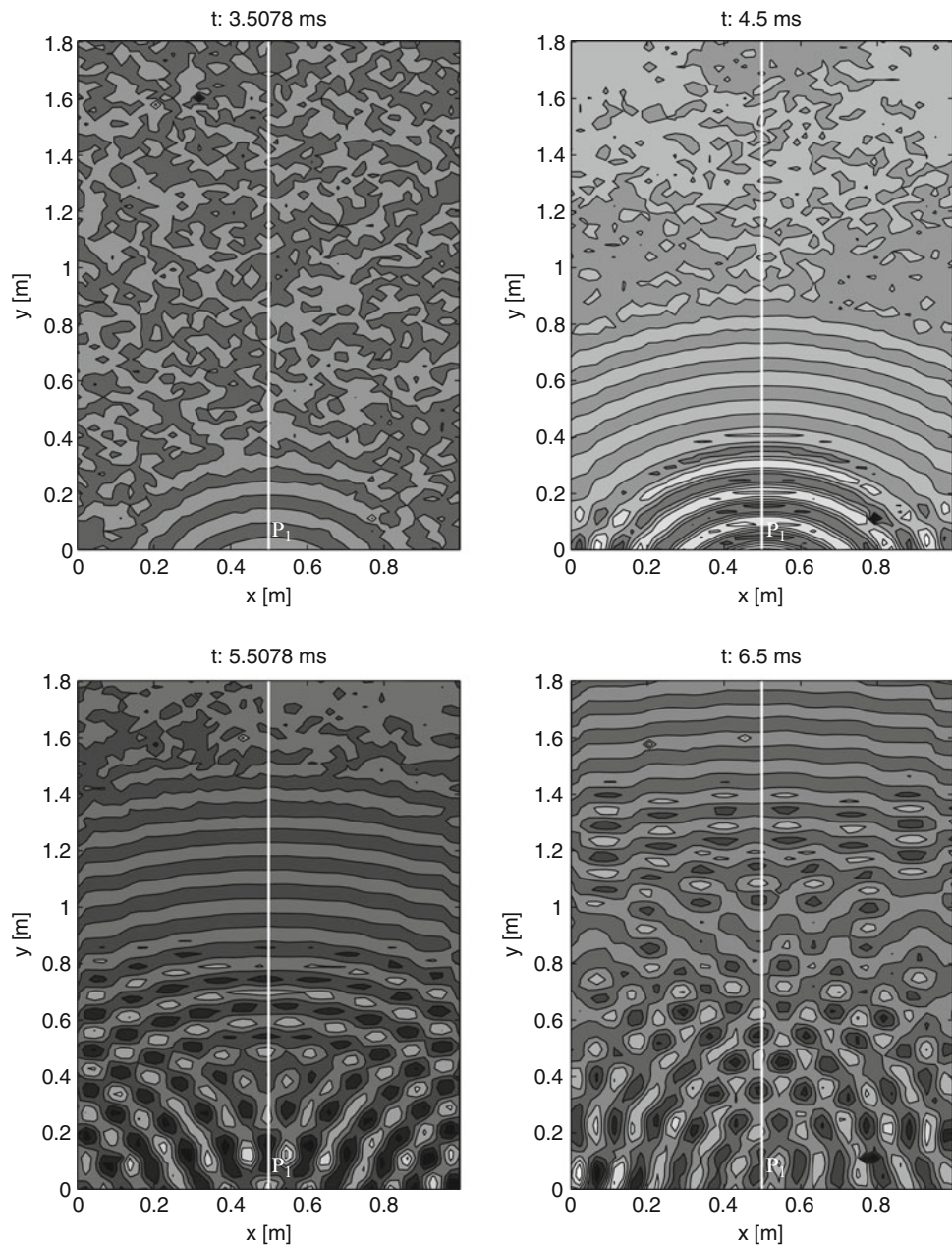
$$w_{2D}^* (x, t) = \mathcal{F}_{2D}^{-1} \left(W_{2D}^* (k, \omega) \right) \tag{19.6}$$

where $\mathcal{F}_{2D}^{-1}$ denotes the inverse 2D Fourier transform.

The filtered signal w_{2D}^* is then Hilbert transformed in order to obtain the envelope of the response for each measurement's point belonging to the white line depicted in Fig. 19.4.

Comparing the response of the system presented in Fig. 19.6 for two different conditions: uncontrolled (left) and controlled (right) a modification in the response is observed. Figure 19.7 represents the spatial attenuation of the waves propagating within the metacomposite it associates the maxima of the filtered response to the spatial position along the y direction. The blue line represents the uncontrolled system whereas the green line represents the controlled system. By comparison it is clear that the external circuits is able to modify the dynamic behavior of the waveguide by adding an extra amount of damping.

Fig. 19.5 Experimental vs. theoretical dispersion relations for the raw (*top*) and the filtered (*bottom*) signals. The image at the center represent the filter used in the wave number domain
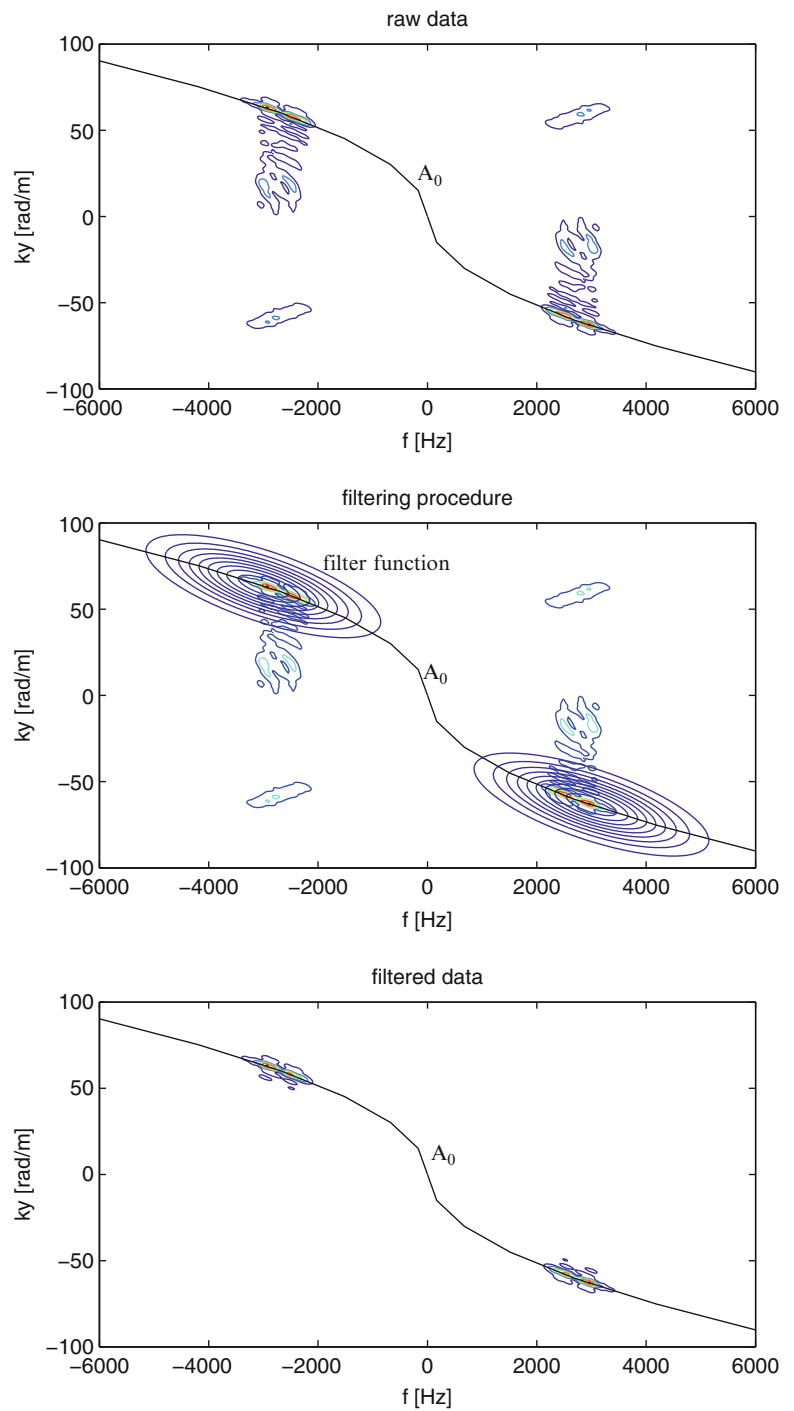
19.5 Conclusions

This paper presents a signal processing technique aimed at improving the visualization capabilities of full wave-field measurements. The technique operates in the frequency/wavenumber domain, where the presence of defect can be observed from the main signal generated for inspection. Upon filtering, the residual signal obtained just considering the A_0 mode highlights the modification of the dynamic properties of the waveguide due to the presence of the active interface.

Fig. 19.6 Experimental contour plot obtained by performing an inverse Fourier transform of the filtered signal for each spatial position for the uncontrolled (*left*) and controlled (*right*) system. The *white lines* represent the maximum of the response
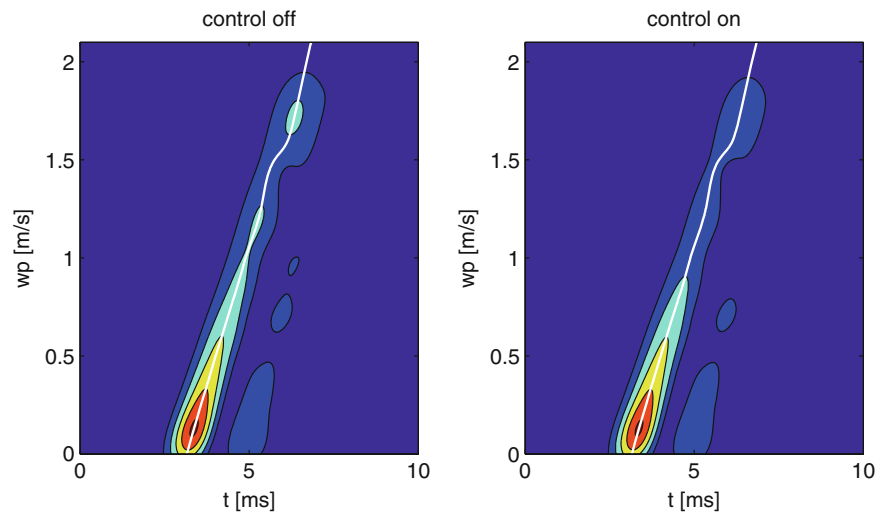
Fig. 19.7 Spatial attenuation of the smart metacomposite: uncontrolled system (*blue line*); controlled system (*green line*) (Color figure online)
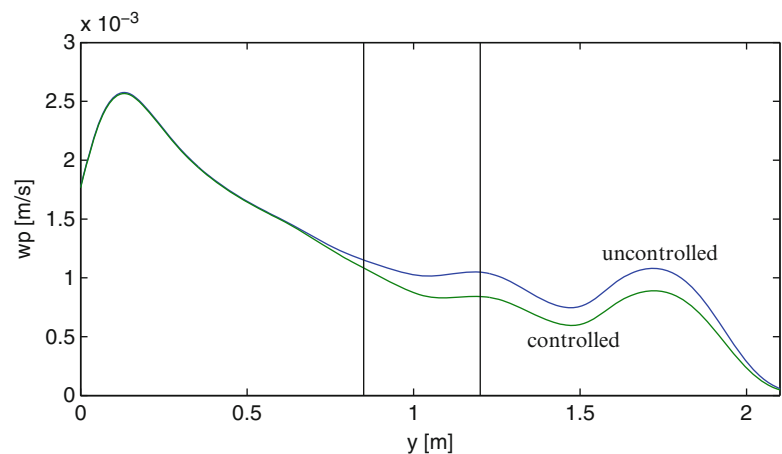
The presented results demonstrate the potential of the method and highlight future research needs. In particular, this method needs to be supported by a suitable technique able to suppress the effect related to the parasitic components associated to the boundaries reflections. This point is currently under investigation, by using a source images approach better results are expected.

References

1. Collet M, Ouisse M, Ichchou MN (2012) Structural energy flow optimization through adaptive shunted piezoelectric metacomposites. J Intell Mater Syst Struct 23(15):1661–1677
2. Hagood NW, von Flotow A (1991) Damping of structural vibrations with piezoelectric materials and passive electrical networks. J Sound Vib 146(2):243–268
3. Joannopoulos JD, Johnson SG, Winn JN, Meade RD (2008) Photonic crystals: molding the flow of light. Princeton University Press, Princeton
4. Liu Z, Zhang X, Mao Y, Zhu YY, Yang Z, Chan CT, Sheng P (2000) Locally resonant sonic materials. Science 289(5485):1734–1736
5. Michaels TE, Michaels JE, Ruzzene M (2011) Frequency-wavenumber domain analysis of guided wavefields. Ultrasonics 51(4):452–466
6. Toffoli T, Margolus N (1991) Programmable matter: Concepts and realization. Phys D Nonlinear Phenom 47(1–2):263–272
7. Yang S, Page JH, Liu Z, Cowan ML, Chan CT, Sheng P (2002) Ultrasound tunneling through 3D phononic crystals. Phys Rev Lett 88(10):104301

Chapter 20
Modal Parameter Estimation of a Two-Disk- Shaft System by the Unified Matrix Polynomial Approach

Naim Khader

Abstract Modal parameters, i.e., modal frequencies, damping ratios, and mode shapes of a two disk-shaft system are estimated in Multiple Input/Multiple Output (MIMO) scheme. The response at the output degrees of freedom (dof) of the considered structure due to the excitation at the input dofs is estimated from theoretical analysis. The generated theoretical data is used to estimate the Frequency Response Function (FRF) matrix, which relates the output (vibration) at response points with the input at the excitation points in the frequency domain. The corresponding Impulse Response Function (IRF) matrix, which relates response and excitation in the time domain, is obtained by Inverse Fast Fourier Transform (IFFT) of the FRF matrix. The unified Matrix Polynomial Approach (UMPA) is employed in the frequency and time domains with the estimated FRF and IRF matrices, respectively, to estimate the desired modal parameters. The obtained results are compared with results from Theoretical Modal Analysis (TMA).

20.1 Introduction

The multi disk-shaft system is found in numerous mechanical and aerospace applications, such as compressors, turbines, and hard disk drives. Stringent requirements on such systems resulted in highly flexible structure with strong coupling between modes of constituent components, i.e., modes of the shaft and individual disks. It is therefore of great importance to accurately predict their modal parameters to come up with a reliable design, free from resonance vibration during operation. This subject was examined by several researchers who employed different theoretical, numerical and experimental approaches to address this problem. Shahab and Thomas [1] developed a thick sector element to investigate the coupling effects between disks and shaft modes on the dynamic characteristics of the multiple-disk shaft system. Wu and Flowers [2] developed a transfer matrix procedure to account for disk flexibility and to investigate how it might influence the natural frequencies and critical speeds of practical rotors. Lee et al. [3] also used the substructure synthesis and the assumed modes method to calculate the natural frequencies of the coupled vibration of flexible shaft-multiple flexible disk systems, typically found in computer hard disk drives. They introduced some tuning parameters to accurately model the considered system, which resulted in close agreement between theoretical and experimental results of the examined hard disk drive spindle system. Chong-Won Lee and Sang-Bok Chun [4] studied the effect of multiple flexible disks on the vibration modes of a flexible shaft using the assumed modes method, which was applied to computer hard disk drive spindle system and to a simple flexible rotor system with two flexible disks. Jia [5] used the substructure synthesis technique to examine the coupled bending vibration of a multi span shaft, modeled as a Timoshenko beam, carrying several flexible circular disks and supported by multiple isotropic journal bearings. Jang et al. [6] used the finite element method and substructure synthesis technique to examine the free vibration of a spinning flexible disk-spindle system supported by ball bearing and flexible shaft and performed modal testing to verify theoretical results. Shen et al. [7] studied the vibration of a rotating spindle carrying multiple flexible disks mounted on a flexible housing-stator assembly through ball bearings or hydrodynamic bearings. They measured the natural

---

N. Khader (✉)

Department of Mechanical Engineering, Jordan University of Science & Technology (JUST), P.O. Box 3030, Irbid 22110, Jordan
e-mail: nkhader@just.edu.jo

frequencies of a ball bearing spindle with different housing configurations to verify the presented mathematical model. Hili et al. [8] analyzed the free vibration of a spinning disk-shaft system using finite element method and evaluated the effect of rotor speed, disk flexibility, and boundary conditions on the natural frequencies of the system.

When the flexible disk carries flexible blades, as it is the case in gas turbine engine's compressors and turbines, coupling between disk and shaft modes is influenced by blade vibrations, and blade stagger angle is an important parameter which affects the coupling between bladed-disk and shaft vibrations. This subject has been addressed by some researchers, for example, Chun and Lee [9] combined the substructure synthesis approach and the assumed modes method to investigate bladed-disk-shaft vibration. They employed the developed approach to evaluate the effect of stagger and pretwist angles on the vibrational modes of the complete assembly. Yang and Huang [10] examined the influence of disk flexibility and blade stagger angle on the coupling behavior of flexible shaft-flexible disk-flexible blade system. Khader et al. [11] presented a theoretical model based on the assumed modes method to examine the coupled multiple disk-flexible shaft system, and compared theoretical results with the experimentally determined natural frequencies, which were identified from the peaks of the obtained Frequency Response Functions (FRF), relating a single measured response with a single excitation from an impact hammer. It is known that the considered system has repeated frequencies, and the single input/single output scheme is not the appropriate choice, and one has to employ a MIMO estimation scheme to predict the modal parameters of such systems, which was later [12] employed to estimate modal parameters of the coupled vibration of a flexible disk-flexible shaft system from theoretically generated FRF matrix, obtained from simulated excitation and response data.

The present work simulates multi reference testing of a flexible shaft carrying more than one flexible disk. Impulse forces are assumed to excite the system at a number of input points N_i, and the resulting response at a number of output points N_o is calculated. Random noise is added to the calculated response in order to simulate actual vibration measurements. The assumed excitations and corresponding response are used to estimate $N_o x N_i$ FRF matrix. The associated Impulse Response Function (IRF) matrix is obtained by IFFT. MIMO modal parameter estimation algorithms, based on UMPA low order, (in both time and frequency domains), as well on an UMPA high order (in the frequency domain) formulation [13–15], are employed to estimate the desired modal parameters of the considered system.

The considered simulation is based on the theoretical model described in [11], where Lagrange's equation was combined with the assumed modes method to derive the governing equations of motion for the multiple flexible disk shaft system. The obtained results are found to be in excellent agreement with results from TMA.

20.2 Theoretical Analysis

20.2.1 Frequency Response Function Matrix of the Multiple Disk Shaft System

The examined rotor consists of two flexible disks, attached to a fixed-free flexible shaft. The shaft is modeled by a slender beam with circular cross section and uniformly distributed mass and stiffness. The flexible disk is modeled by an annular thin plate, with uniformly distributed mass and bending rigidity, and clamped at its inner radius to the outer radius of the shaft, as shown in Fig. 20.1.

Motion of the considered flexible disk-flexible shaft structure is discretized by application of the assumed mode method, where the flexible deformation of the disk or shaft is represented by summation of a number of time-dependent generalized coordinates, multiplied by assumed functions, as given bellow:

$$U_s(z, t) = \sum U_m(z) a_m(t) \tag{20.1}$$

$$V_s(z, t) = \sum V_m(z) b_m(t) \tag{20.2}$$

$$w(r, \theta, t) = \sum_m [w_m(r) \sin \theta \; q_{ms}(t) + w_m(r) \cos \theta \; q_{mc}(t)] \tag{20.3}$$

Mode shapes of individual flexible disk or flexible shaft are taken as the assumed functions. The assumed mode method is combined with Lagrange's equation $\frac{d}{dt}\left(\frac{\partial L}{\partial \dot{q}_j}\right) - \left(\frac{\partial L}{\partial q_j}\right) = Q_j$ to derive the governing equations of motion for the complete system, where $L = (T - U)$ and q_j, Q_j, T, U are the j-th generalized coordinate, the j-th generalized force, total kinetic energy,

The considered two-disk shaft system
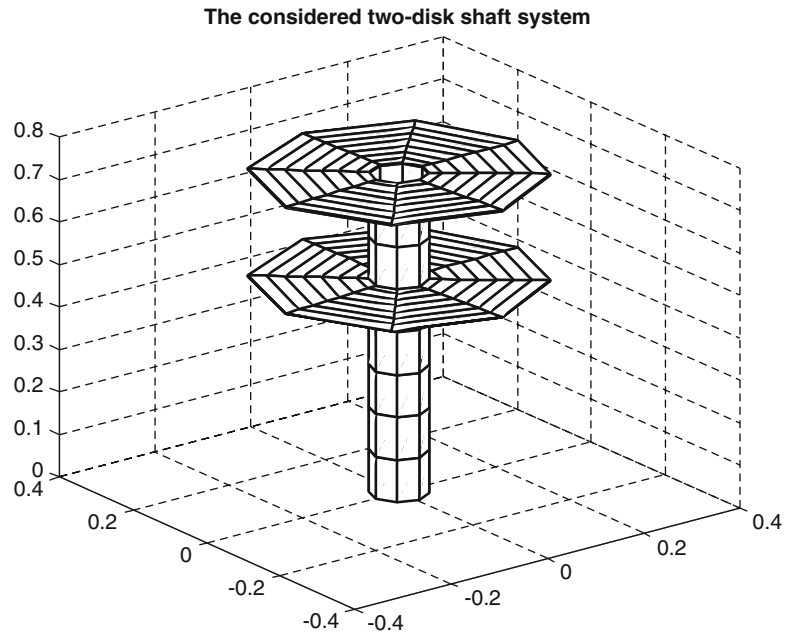
and total strain energy, respectively. With assumed proportional damping, equations of motion of the considered system are expressed in the following matrix form:

$$[M]\left\{\ddot{q}\right\} + [C]\left\{\dot{q}\right\} + [K]\{q\} = \{Q\} \tag{20.4}$$

Where $[M]$, $[C]$, $[K]$, and $\{Q\}$ are the mass matrix, damping matrix, stiffness matrix, and vector of the generalized forces, respectively. Details of the derivation are given in [11].

The FRF matrix, which relates the generalized coordinates to the generalized forces, can be expressed by:

$$[H]_{qq} = \left[K + i\omega C - \omega^2 M\right]^{-1} \tag{20.5}$$

Knowing that the generalized forces are related to the physical forces by the transformation $\{Q\} = [\Psi_{in}]\{f\}$, or in extended form:

$$
\left\{
\begin{matrix}
\left\{ \begin{matrix} Q_{a_1} \\ Q_{a_2} \\ \vdots \end{matrix} \right\} \\
\left\{ \begin{matrix} Q_{b_1} \\ Q_{b_2} \\ \vdots \end{matrix} \right\} \\
\left\{ \begin{matrix} Q_{qc1} \\ Q_{qc2} \\ \vdots \end{matrix} \right\} \\
\left\{ \begin{matrix} Q_{qs1} \\ Q_{qs2} \\ \vdots \end{matrix} \right\}
\end{matrix}
\right\}_{N_q x 1}
=
\begin{bmatrix}
\Psi_{af_x} & 0 & \Psi_{af_d} \\
0 & \Psi_{bf_y} & \Psi_{bf_y} \\
0 & 0 & \Psi_{q_c f_d} \\
0 & 0 & \Psi_{q_s f_d}
\end{bmatrix}_{N_q x N_i}
\left\{
\begin{matrix}
\left\{ \begin{matrix} f_{x1} \\ f_{x2} \\ \vdots \end{matrix} \right\} \\
\left\{ \begin{matrix} f_{y1} \\ f_{y2} \\ \vdots \end{matrix} \right\} \\
\left\{ \begin{matrix} f_{d1} \\ f_{d2} \\ \vdots \end{matrix} \right\}
\end{matrix}
\right\}_{N_i x 1},
$$

where

$$\Psi_{af_x} = \begin{bmatrix} U_1\,(z_1) & U_1\,(z_2) & \cdots \\ U_2\,(z_1) & U_2\,(z_2) & \cdots \\ \vdots & \vdots & \ddots \end{bmatrix}_{N_a x(N_{xs})_i} \quad ; \Psi_{bf_y} = \begin{bmatrix} V_1\,(z_1) & V_1\,(z_2) & \cdots \\ V_2\,(z_1) & V_2\,(z_2) & \cdots \\ \vdots & \vdots & \ddots \end{bmatrix}_{N_b x\left(N_{ys}\right)_i}$$

$$\Psi_{af_d} = \begin{bmatrix} -(r\cos(\theta))_1 V_1^{'}\,(z_d) & -(r\cos(\theta))_2 V_1^{'}\,(z_d) & \cdots \\ -(r\cos(\theta))_1 V_2^{'}\,(z_d) & -(r\cos(\theta))_2 V_2^{'}\,(z_d) & \cdots \\ \vdots & \vdots & \ddots \end{bmatrix}_{N_a x(N_d)_i}$$

$$\Psi_{bf_d} = \begin{bmatrix} -(r\sin(\theta))_1 U_1^{'}\,(z_d) & -(r\sin(\theta))_2 U_1^{'}\,(z_d) & \cdots \\ -(r\sin(\theta))_1 U_2^{'}\,(z_d) & -(r\sin(\theta))_2 U_2^{'}\,(z_d) & \cdots \\ \vdots & \vdots & \ddots \end{bmatrix}_{N_b x(N_d)_i}$$

$$\Psi_{q_c f_d} = \begin{bmatrix} (w_1\,(r)\cos(\theta))_1 & (w_1\,(r)\cos(\theta))_2 & \cdots \\ (w_2\,(r)\cos(\theta))_1 & (w_2\,(r)\cos(\theta))_2 & \cdots \\ \vdots & \vdots & \ddots \end{bmatrix}_{N_{q_c} x(N_d)_i}$$

$$\Psi_{q_s f_d} = \begin{bmatrix} (w_1\,(r)\sin(\theta))_1 & (w_1\,(r)\sin(\theta))_2 & \cdots \\ (w_2\,(r)\sin(\theta))_1 & (w_2\,(r)\sin(\theta))_2 & \cdots \\ \vdots & \vdots & \ddots \end{bmatrix}_{N_{q_s} x(N_d)_i}$$

Similarly, the physical dof can be expressed in terms of the generalized coordinates as:
$\{x\} = [\Psi_{out}]\{q\}$, or in the extended form:

$$\left\{ \begin{Bmatrix} u_1 \\ u_2 \\ \vdots \end{Bmatrix} \\ \begin{Bmatrix} v_1 \\ v_2 \\ \vdots \end{Bmatrix} \\ \begin{Bmatrix} w_1 \\ w_2 \\ \vdots \end{Bmatrix} \right\}_{N_o x1} = \begin{bmatrix} [\Psi_{ua}] & [0] & [0] & [0] \\ [0] & \Psi_{vb} & [0] & [0] \\ [\Psi_{wa}] & [\Psi_{wb}] & [\Psi_{wq_c}] & [\Psi_{wq_s}] \end{bmatrix}_{N_o x N_q} \left\{ \begin{Bmatrix} a_1 \\ a_2 \\ \vdots \end{Bmatrix} \\ \begin{Bmatrix} b_1 \\ b_2 \\ \vdots \end{Bmatrix} \\ \begin{Bmatrix} q_{c1} \\ q_{c2} \\ \vdots \end{Bmatrix} \\ \begin{Bmatrix} q_{s1} \\ q_{s2} \\ \vdots \end{Bmatrix} \right\}_{N_q x1} ,$$

where

$$\Psi_{ua} = \begin{bmatrix} U_1\,(z_1) & U_2\,(z_1) & \cdots \\ U_1\,(z_2) & U_2\,(z_2) & \cdots \\ \vdots & \vdots & \ddots \end{bmatrix}_{(N_{sx})_o x N_a} \quad ; \Psi_{vb} = \begin{bmatrix} V_1\,(z_1) & V_2\,(z_1) & \cdots \\ V_1\,(z_2) & V_2\,(z_2) & \cdots \\ \vdots & \vdots & \ddots \end{bmatrix}_{(N_{sy})_o x N_b}$$

$$\Psi_{wa} = \begin{bmatrix} -(r\cos(\theta))_1 V_1'(z_d) & -(r\cos(\theta))_1 V_2'(z_d) & \cdots \\ -(r\cos(\theta))_2 V_1'(z_d) & -(r\cos(\theta))_2 V_2'(z_d) & \cdots \\ \vdots & \vdots & \ddots \end{bmatrix}_{(N_d)_o x N_a}$$

$$\Psi_{wb} = \begin{bmatrix} -(r\sin(\theta))_1 U_1'(z_d) & -(r\sin(\theta))_1 U_2'(z_d) & \cdots \\ -(r\sin(\theta))_2 U_1'(z_d) & -(r\sin(\theta))_2 U_2'(z_d) & \cdots \\ \vdots & \vdots & \ddots \end{bmatrix}_{(N_d)_o x N_b}$$

$$\Psi_{wq_c} = \begin{bmatrix} (w_1(r)\cos(\theta))_1 & (w_1(r)\cos(\theta))_2 & \cdots \\ (w_2(r)\cos(\theta))_1 & (w_2(r)\cos(\theta))_2 & \cdots \\ \vdots & \vdots & \ddots \end{bmatrix}_{(N_d)_o x N_{q_c}}$$

$$\Psi_{wq_s} = \begin{bmatrix} (w_1(r)\sin(\theta))_1 & (w_1(r)\sin(\theta))_2 & \cdots \\ (w_2(r)\sin(\theta))_1 & (w_2(r)\sin(\theta))_2 & \cdots \\ \vdots & \vdots & \ddots \end{bmatrix}_{(N_d)_o x N_{q_s}}$$

Where N_a, N_b, N_{q_c}, and N_{q_s} are number of generalized coordinates a, b, q_c, and q_s, respectively. $(N_{sx})_i$, and $(N_{sy})_i$ are number of excitation points on the shaft along X and Y directions, respectively, and $(N_d)_i$ is the out-of-plane excitation disk points.

Using the given above relationships between the generalized coordinates and generalized forces on one side, and the physical coordinates and physical excitation forces, on the other, one can write the required FRF matrix that relates the response at N_o output points $\{X\}_{N_o x1}$ with the excitations at N_i input points $\{F\}_{N_i x1}$ in the form:

$$\begin{Bmatrix} X_1 \\ X_2 \\ \vdots \\ \vdots \\ X_{N_o} \end{Bmatrix}_{N_o x1} = \begin{bmatrix} H_{11} & \cdots & \cdots & \cdots & H_{1N_i} \\ H_{21} & & & & \vdots \\ \vdots & & & & \vdots \\ \vdots & & & & \vdots \\ H_{N_0 1} & \cdots & \cdots & \cdots & H_{N_o N_i} \end{bmatrix}_{N_o \times Ni} \begin{Bmatrix} F_1 \\ F_2 \\ \\ \\ F_q \end{Bmatrix}_{Ni \times 1} \tag{20.6}$$

This FRF matrix or the IRF matrix obtained by the Inverse Fast Fourier Transform (IFFT) can be subsequently analyzed to extract the desired modal parameters of the considered system.

20.2.2 Modal Parameters of the Multiple Disk Shaft System

An FRF matrix that relates N_o output and N_i input points is estimated as discussed above. The output points consist of a number of shaft points N_{so} with two orthogonal deformations considered at each point, and $(N_{do})_k$ out-of-plane response points for the k-th disk. Similarly, the input points consist of N_{si} shaft excitation points and $(N_{di})_k$ out-of-plane excitation points for the k-th disk. The Complex Mode Indicator Function (CMIF) [19] of the estimated FRF matrix will be employed in the Modal Parameter Estimation (MPE) of the considered structure. The CMIF is a plot of the singular values (Σ_k) of the FRF matrix, obtained from Singular Value Decomposition (SVD) of the FRF matrix for each spectral line

$$[H(\omega_k)]_{(N_o xN_i)} = [U_k]_{(N_o xN_i)} [\Sigma_k]_{(N_i xN_i)} [V_k]_{(N_i xN_i)}^H \tag{20.7}$$

Where $[U_k]_{(N_o \times N_i)}$ is the matrix of left singular vectors, $[\Sigma_k]_{(N_i \times N_i)}$ diagonal matrix of the singular values, and $[U_k]_{(N_o \times N_i)}$ is the matrix of right singular vectors, at ω_k. Peaks in the CMIF curves occur at the damped natural frequencies of the considered structure, and the left and right singular vectors associated with these peaks give approximation to the corresponding mode shapes and modal participation factors, respectively.

The CMIF was initially developed to aid in estimating the minimum model order in the modal parameter extraction algorithm. It was later extended to a spatial modal parameter estimation algorithm [20]. Since the left $[U_k]_{(N_o \times N_i)}$ and right $[V_k]_{(N_o \times N_i)}$ singular vectors are approximation of the modal vectors and participation factors, as mentioned above, they can be used as a spatial filter, which transforms the FRF matrix from physical to modal coordinates and results in a scalar function of the frequency, known as the Enhanced Frequency Response Function (eFRF) [20]. Poles and modal scaling can be estimated from the properly scaled eFRF for each mode using a single dof frequency domain algorithm. Similarly, a multi dof estimation algorithm, known as Enhanced Mode Indicator Function (EMIF) [21], was developed as an extension of the described above CMIF/eFRF algorithm. The EMIF is formulated based on a low order frequency domain UMPA model [13, 14] with matrix coefficients to estimate system poles in a selected frequency band. The SVD of the FRF matrix is computed in the considered frequency band, and the resulting left singular vectors $[U]_{N_b \times N_i}$ are used as a spatial filter to transform the FRF matrix to a new FRF $\left[e\tilde{H}(\omega)\right]_{N_b \times N_i}$ matrix of virtual measurements, equal to the number of poles in the frequency band, given by

$$\left[e\tilde{H}(\omega)\right]_{N_b \times N_i} = [U]^T_{N_b \times N_o}[H(\omega)]_{N_o \times N_i} \tag{20.8}$$

This set of eFRFs is used with a low order frequency domain UMPA model [13, 14] for parameter estimation.

$$\sum_{k=0}^{2}\left[(i\omega)^k[\alpha_k]_{N_b \times N_b}\right]\left[e\tilde{H}(\omega)\right]_{N_b \times N_i} = \sum_{k=n_l}^{n_u+2}\left[(i\omega)^k\left[\tilde{\beta}_k\right]\right]_{N_b \times N_i} \tag{20.9}$$

Where $[\alpha_k]_{N_b \times N_b}$ and $\left[\tilde{\beta}_k\right]_{N_b \times N_i}$ are the UMPA coefficient matrices

Thus, the response space is condensed to produce N_b poles without computational modes, and the effect of out of band modes can be accounted for by introducing residual terms in the numerator polynomial.

Along the EMIF frequency domain algorithm, a time domain algorithm, the Eigensystem Realization Algorithm (ERA) is also used to extract the desired modal parameters of the considered structure. For this reason, the Impulse Response Function (IRF) matrix was estimated as the Inverse Fast Fourier Transform (IFFT) of the available FRF matrix. The ERA algorithm was originally developed by NASA [22, 23] to constructs a state space model from Multiple Input/Multiple Output (MIMO) test data. This algorithm can be formulated as a time domain first order UMPA model [13, 14]

$$[\alpha_0][H_0] = -[\alpha_1][H_1] \tag{20.10}$$

Where $[\alpha_0]$ and $[\alpha_1]$ are the first order polynomial coefficient matrices, and $[H_0]$, and $[H_1]$ are the Hankel matrices, constructed from the IRF matrix $[h(t)]_{N_o \times N_i}$ with starting time, t_k [22]

$$[H_0] = \begin{bmatrix} h(k+0) & h(k+1) & \cdots & \cdots & \cdots & \cdots & h(k+r) \\ h(k+1) & h(k+2) & \cdot^{\cdot^\cdot} & & h(k+r) & h(k+r+1) \\ \vdots & \cdot^{\cdot^\cdot} & & \cdot^{\cdot^\cdot} & \cdot^{\cdot^\cdot} & & \vdots \\ h(k+s-1) & & & & & h(k+r+s-1) \end{bmatrix}_{(N_o+s) \times (N_i+s)}$$

$$[H_1] = \begin{bmatrix} h(k+1) & h(k+2) & \cdots & \cdots & \cdots & \cdots & h(k+r+1) \\ h(k+2) & h(k+3) & \cdot^{\cdot^\cdot} & & h(k+r+1) & h(k+r+2) \\ \vdots & \cdot^{\cdot^\cdot} & & \cdot^{\cdot^\cdot} & \cdot^{\cdot^\cdot} & & \vdots \\ h(k+s) & & & & & h(k+r+s) \end{bmatrix}_{(N_o+s) \times (N_i+s)}$$

It is possible to normalize equation 10 above by assuming $[\alpha_0] = [I]$ or $[\alpha_1] = [I]$, which will take forms $[I][H_0] = -[\alpha_1][H_1]$ or $-[\alpha_0][H_0] = [I][H_1]$, respectively. Eigenvalues of the coefficient matrices $[\alpha_0]$ and $[\alpha_1]$ are related to system eigenvalues $\lambda_r = \sigma_r + j\omega_r$ as

$$\sigma_r = \mathrm{Re}\left(\frac{\ln z_r}{\Delta t}\right), \text{ and } \omega_r = \mathrm{Im}\left(\frac{\ln z_r}{\Delta t}\right)$$

20.3   Results and Discussion

A fixed free flexible shaft carrying two flexible annular disks, shown in Fig. 20.1 is considered. The geometric and material properties of shaft-disk system are:

$$E_{disk} = E_{shaft} = 200\,Gpa; v_{disk} = v_{shaft} = .3; \rho_{disk} = \rho_{shaft} = 7800\,kg/m^3;$$

$$\left(\frac{R_{in}}{R_{out}}\right)_{disk} = 0.2; (R_{out})_{disk} = 0.25\,m; h_{d1} = 0.002\,m;$$

$$h_{d2} = 0.0025\,m; Z_{d1} = 0.5\,m; Z_{d2} = 0.75\,m;$$

$$L_{shaft} = 0.75\,m; (R_{out})_{shaft} = 0.05\,m; (R_{in})_{shaft} = 0.048\,m;$$

Where h_{dk} and Z_{dk} are thickness and spanwise position of the k-th disk.

An FRF matrix, which relates 126 response and 8 input points, is estimated as discussed above. The response points consist of 7 shaft points with two orthogonal dof for each point, and 56 out-of-plane response points for each disk. These points are located at the intersections of 8 radial and 7 circular lines. The input (reference) points consist of four out-of-plane excitation for each disk. Four driving and three non -driving FRF functions are shown in Figs. 20.2 and 20.3.
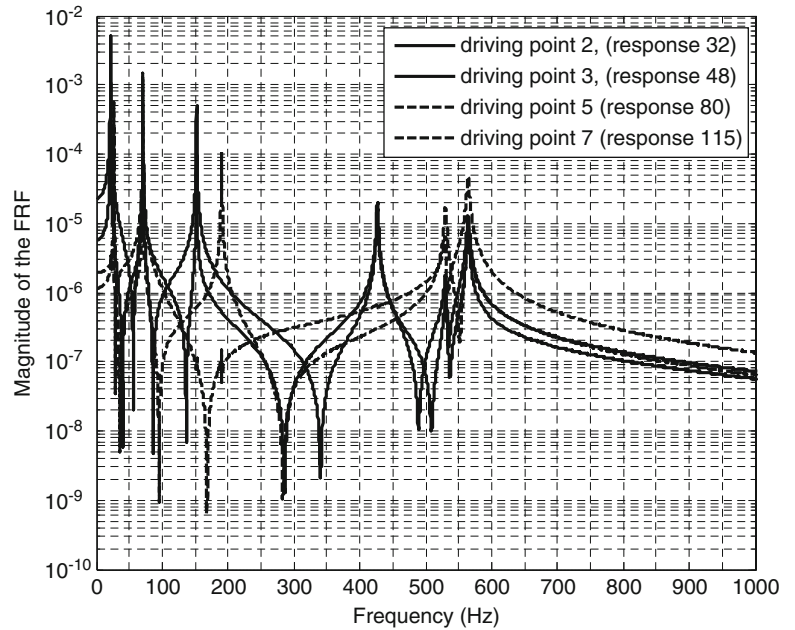
Fig. 20.2 Sample driving point FRFs

Fig. 20.3 Sample of non-driving points FRFs
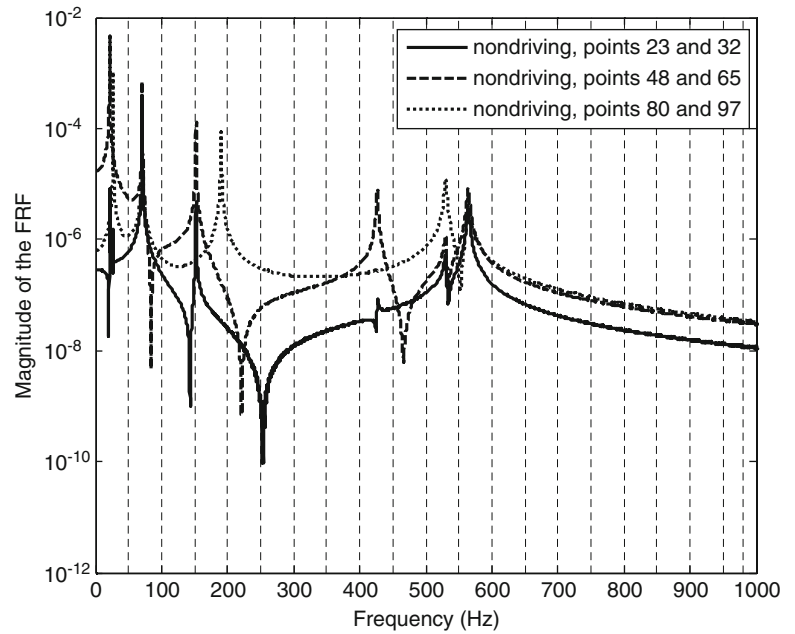
Fig. 20.4 CMIF of the FRF with 8 references
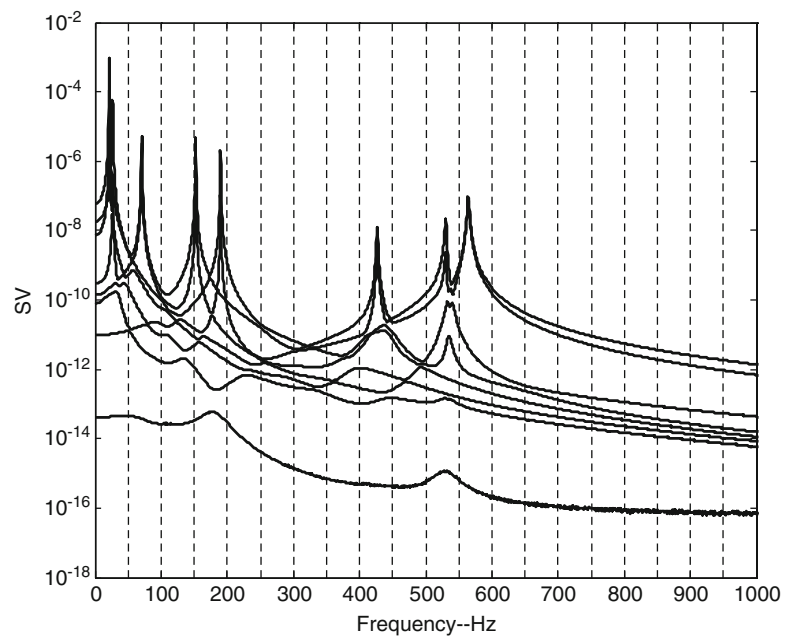
The CMIF of the estimated FRF matrix is shown in Fig. 20.4. Since the considered system consists of circular symmetric flexible disks and a flexible shaft with identical properties along the two orthogonal directions, it is expected to have repeated frequencies, which is clear in the CMIF plot, where two curves have peaks at the same frequency. An interactive code was written to select frequency bands, and apply the EMIF to estimate the poles of the structure in such bands. Figures 20.5 and 20.6 show the frequency bands, used to estimate the repeated first and second modes, and the repeated seventh and eighth modes, respectively.

Fig. 20.5 CMIF with frequency band used to estimate the repeated first two modes
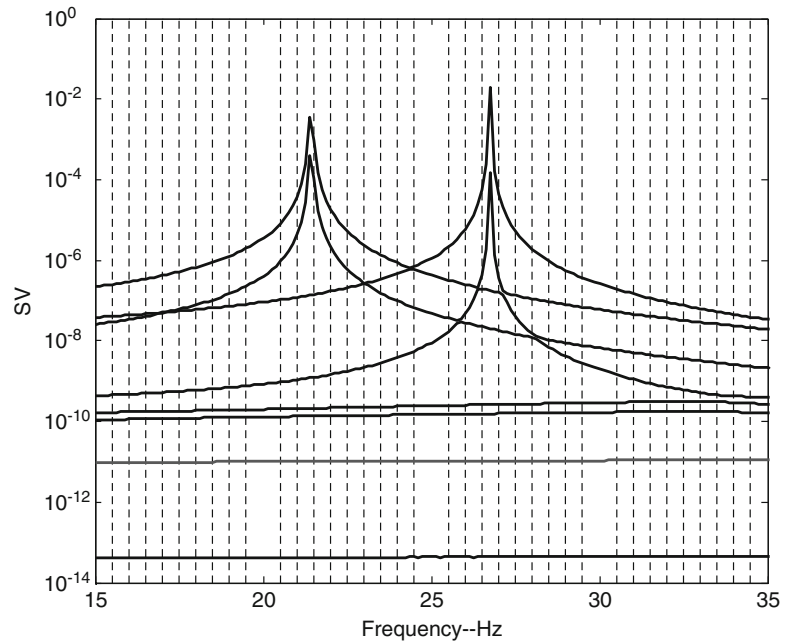
Fig. 20.6 CMIF with frequency band used to estimate the 7th and 8th repeated modes
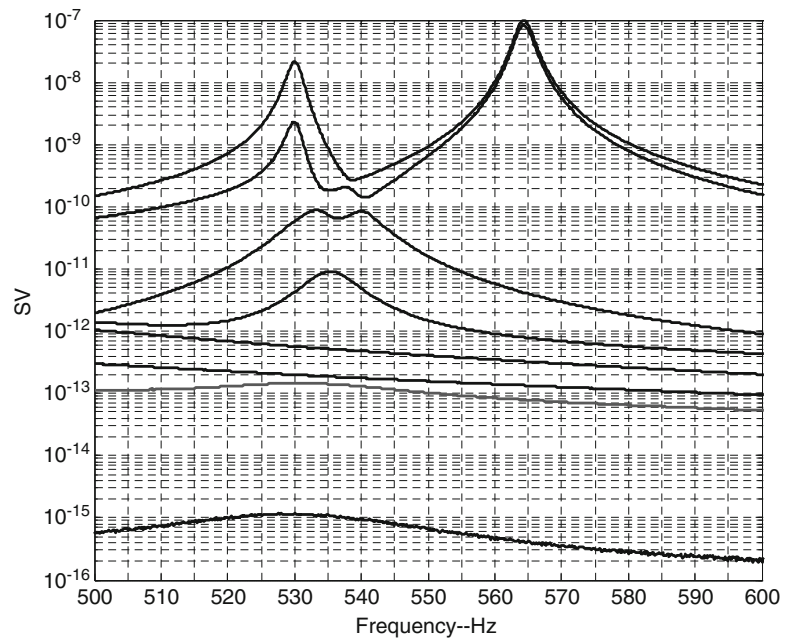
The resulting modal frequencies from the EMIF are listed in Table 20.1, along with results from the time domain ERA method, where the Hankel matrix was constructed from the IRF matrix. Results from this first order (state space) time domain method was calculated in two ways, one according to the original theory developed in [22], the other was based on the UMPA formulation [13, 14]. In the UMPA formulation, the Modal Assurance Criteria (MAC) [16] was used with the two solutions from assuming $[\alpha_0] = [I]$ and $[\alpha_1] = [I]$ to separate structural modes from the computational ones. The corresponding results from high order frequency domain with Forsyth Orthogonal Polynomials as well as from Theoretical Modal Analysis (TMA) are included in Table 20.1 for comparison.

Table 20.1 Resulting modal frequencies of the considered multiple dish shaft system in Hz

Mode #	ERA UMPA	ERA (Juang)	UMPA (LO- Frequency)	UMPA (HO- Frequency)	TMA
1	21.42	21.42	21.42	21.42	21.42
2	0.00	21.42	21.42	21.42	21.42
3	26.74	26.74	26.74	26.73	26.74
4	26.74	26.74	26.75	26.74	26.74
5	70.78	70.78	70.76	70.78	70.78
6	70.78	70.78	70.78	70.78	70.78
7	152.19	152.19	152.19	152.16	152.19
8	152.19	152.19	152.20	152.19	152.19
9	190.17	190.17	190.17	159.03	190.17
10	190.17	190.17	190.17	190.16	190.17
11	426.74	426.75	426.65	426.74	426.74
12	426.74	426.75	426.83	426.75	426.74
13	530.12	530.11	529.53	524.85	530.12
14	530.12	530.12	532.29	526.45	530.12
15	547.23	564.33	564.39	563.92	564.34
16	564.34	564.33	564.58	564.23	564.34

Fig. 20.7 Mode shape of the coupled vibration with frequency of 21.42 Hz

Mode shape at frequency 21.42 Hz
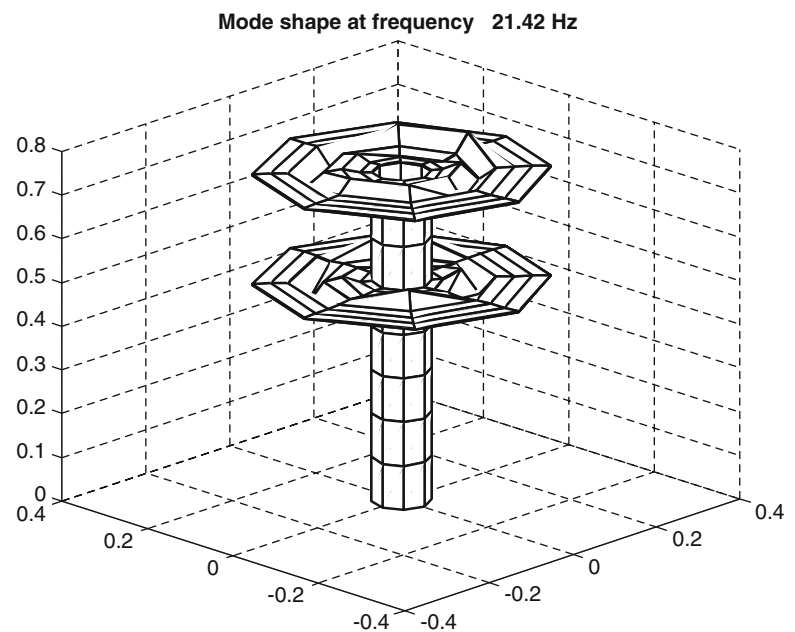
Examples of the obtained mode shapes are shown in Figs. 20.7, 20.8, 20.9, and 20.10, where the coupling between individual components is obvious. This confirms the need to consider the complete system rather than individual components for accurate prediction of the modal parameters.

20.4 Conclusions

The coupled natural frequencies and mode shapes of a two-flexible disk-flexible shaft are estimated from theoretically generated multiple input/multiple output FRF matrix, which is the appropriate scheme to estimate repeated modes. The assumed modes method and Lagrange's equation are employed in the theoretical analysis. Low order frequency domain

Fig. 20.8 Mode shape of the coupled vibration with frequency of 70.78 Hz

Mode shape at frequency   70.78 Hz
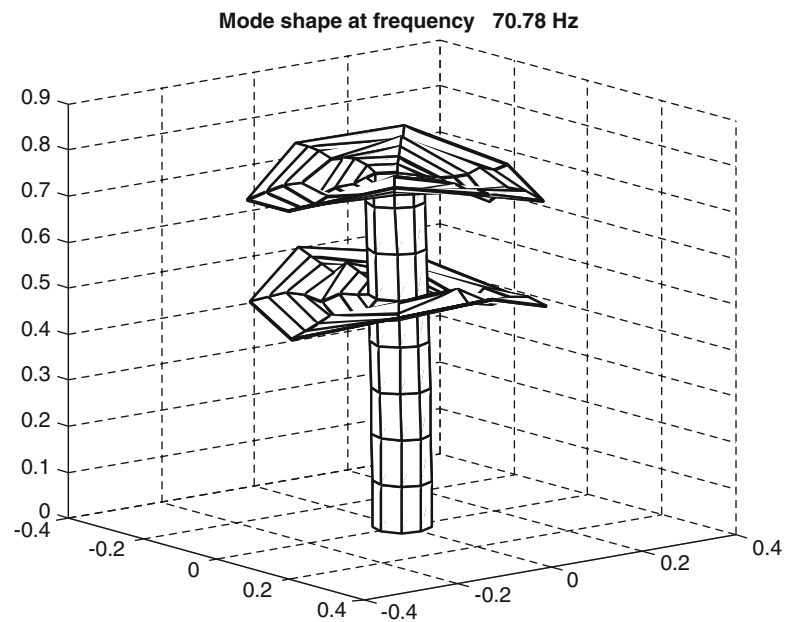
Fig. 20.9 Mode shape of the coupled vibration with frequency of 530.1 Hz

Mode shape at frequency   530.1 Hz
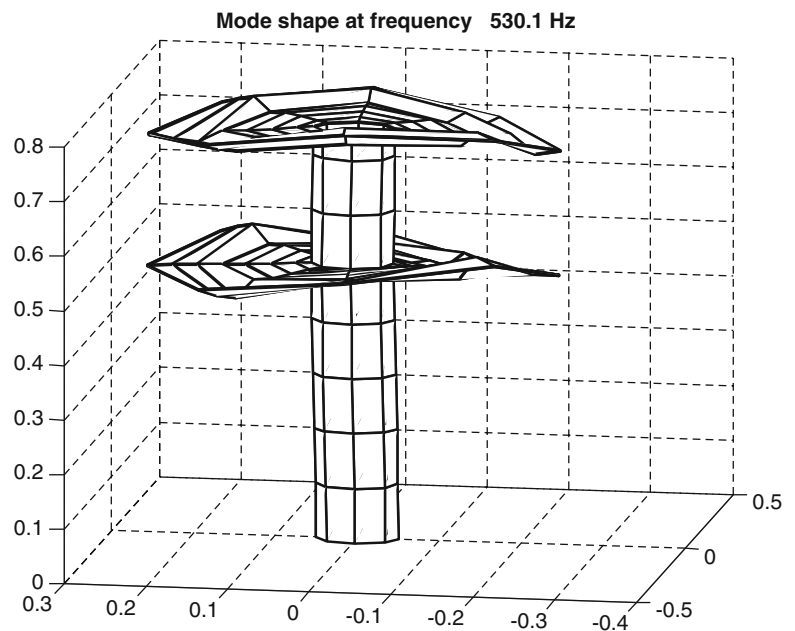
EMIF and a high order frequency domain with Forsyth Orthogonal Polynomials were used to extract the desired parameters from the FRF matrix. The low order time domain ERA algorithm based on both its original form and on the UMPA formulation was used to estimate modal parameters from the corresponding IRF matrix. The estimate results from FRF and IRF matrices are found to be in excellent agreement with similar results obtained from Theoretical Modal Analysis. The presented work lays the background to estimate these modal parameters from experimentally obtained data, which is scheduled to take place at JUST soon. Since the considered structure is found mainly in rotating machine, rotational effects will be presented in further work.

Fig. 20.10 Mode shape of the
coupled vibration with frequency
of 564.3 Hz
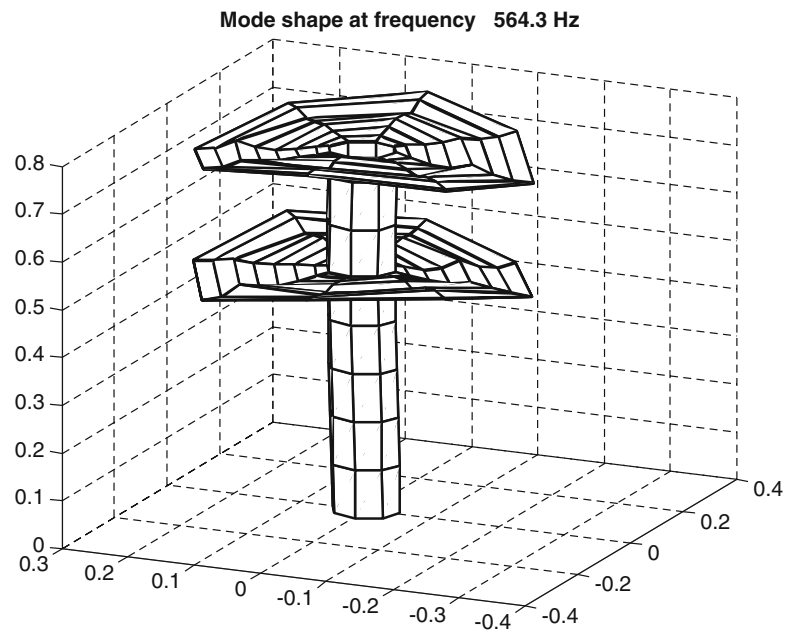
Mode shape at frequency 564.3 Hz

References

1. Shahab AS, Thomas J (1987) Coupling effect of disk flexibility on the dynamic behavior of multi disk-shaft system. J Sound Vib 114(3): 435–446
2. Wu F, Flowers GT (1992) A transfer matrix technique for evaluating the natural frequencies and critical speeds of a rotor with multiple flexible disks. J Vib Acoust 114:242–248
3. Lee CW, Jia HS, Kim CS, Chun SB (1997) Tuning of simulated natural frequencies for a flexible shaft-multiple flexible disk system. J Sound Vib 207(4):435–451
4. Lee C-W, Chun S-B (1998) Vibration analysis of a rotor with multiple flexible disks using assumed modes method. J Vib Acoust 120:87–94
5. Jia HS (1999) On the bending coupled natural frequencies of a spinning, multispan Timoshenko shaft carrying elastic disks. J Sound Vib 221:623–649
6. Jang GH et al (2002) Free vibration analysis of a spinning flexible disk-spindle system supported by ball bearing and flexible shaft using the finite element method and substructure synthesis. J Sound Vib 251(1):59–78
7. Shen J-Y, Tseng C-W, Chen IY (2004) Vibration of rotating disk/spindle system with flexible housing/stator assemblies. J Sound Vib 271: 725–756
8. Hili MA, Fakhfakh T, Haddar M (2007) Vibration analysis of a rotating flexible shaft-disk system. J Eng Math 57:351–363
9. Chun SB, Lee CW (1996) Vibration analysis of shaft-bladed disk system by using substructure synthesis and assumed mode method. J Sound Vib 189(5):587–608
10. Yang CH, Huang SC (2007) The influence of disk's flexibility on coupling vibration of shaft–disk–blades systems. J Sound Vib 301(20):1–17
11. Khader N, Atoum A, Al-Qaisia A (2007) Theoretical and experimental modal analysis of multiple flexible disk-flexible shaft system. Paper Presented at 2007 SEM annual Conference, June 3–6, Springfield, Massachusetts, USA (2007)
12. Khader N (2012) "Modal parameters of a flexible disk-flexible shaft system from simulated data" Int. J Vehicle Noise Vib 8(1):60–73
13. Allemang RJ, Brown DL (1998) A unified matrix polynomial approach to modal identification. J Sound Vib 211(3):301–322
14. Phillips AW, Allemang RJ (2004) The unified matrix polynomial approach to understanding modal parameter estimation: an update. Proceedings, International Conference on Noise and Vibration Engineering, Katholieke Universiteit Leuven, Belgium
15. Brown DL, Phillips AW, Allemang RJ (2005) A first order extended state vector expansion approach to experimental modal parameter estimation. Proceedings, International Modal Analysis Conference (2005)
16. Allemang RJ (2003) The modal assurance criterion–twenty years of use and abuse. J Sound Vib 37(8):14–23
17. Shin CY et al (1988) A frequency domain global parameter estimation method for multiple reference frequency response measurements. Mech Syst Signal Process 2(4):349–365
18. der Auweraer V, Leuridan J (1987) Multiple input orthogonal polynomial parameter estimation. Mech Syst Signal Process 1(3):259–272
19. Shih CY, Tsuei YG, Allemang RJ, Brown DL (1988) Complex mode indication function and its application to spatial domain parameter estimation. J Mech Syst Signal Process 2(4):367–372, Academic Press Limited

20. Allemang RJ, Brown DL (2006) A complete review of the complex mode indicator function (CMIF) with applications. Proceedings, International Conference on Noise and Vibration Engineering (ISMA), Katholieke Universiteit Leuven, Belgium, 38 pp
21. Li S, Fladung WA, Phillips AW, Brown DL (1998) Automotive applications of the enhanced mode indicator function parameter estimation method. Proceedings, International Modal Analysis Conference, pp. 36–44
22. Juang J-N, Pappa RS (1985) An eigensystem realization algorithm for modal parameter identification and model reduction. AIAA J Guidance Control Dyn 8(4):620–627
23. Juang JN (1987) Mathematical correlation of modal parameter identification methods via system realization theory. J Anal Exp Modal Anal 2(1):1–18

Chapter 21
System Identification of an Isolated Structure Using Earthquake Records

Ruben L. Boroschek, Antonio A. Aguilar, and Fernando Elorza

Abstract The growing interest of investors and stakeholders in protecting building contents and operation beyond the goals of current seismic design codes is generating an increased demand for the use of nonconventional seismic protection systems such as base isolation and energy dissipation devices. This paper focuses on the application of seismic identification techniques on earthquake records obtained in the first Chilean Base Isolated Building. Seismic responses recorded in this structure located in the capital city of Chile, range in Magnitude from 4 to 8.8. This last earthquake corresponds to the sixth largest event recorded in the world and identification results are preliminary presented here. Due to the strong nonlinear elastic response of the base isolation system, classical linear identification methods present poor results. Several procedures to identify the response are presented, including window the response data and nonlinear identification. Basic modal parameters like natural frequency and modal damping ratios are obtained as a function of response amplitude indicating the great benefit of the isolation system and the relevance of developing appropriate identification techniques for this type of highly nonlinear systems. Building isolation system performance is reflected in modal parameters variations observed in the analysis.

Keywords Structural health monitoring • Nonlinear identification • Earthquakes • Base isolation

21.1 Introduction

After the 27th February, 2010 Chilean earthquake, a renewed and increasing interest in additional seismic protection seismic in buildings was born in investors, stakeholders and structural engineering. Because of this several systems, like energy dissipating devices and base isolation, have been incorporated in new constructed structures. In high seismic countries, like Chile, recurrent damage due to low level earthquake in non-structural components is common. In severe earthquakes the structural and nonstructural is extremely large. As an example the Magnitude 8.8 event caused economic losses exceeding US$30 billion. A high percentage of these losses resulted from damage to nonstructural systems and components, such as architectural elements, building contents, and electric and mechanical equipment [1]. The increase use of these systems that are inherently nonlinear poses a challenge to Structural Health Monitoring. In this article we present an example of an isolated structure that has been instrumented for more than 20 years. The main characteristics of the isolated structure is presented together with possible isolator models and procedures to identify their nonlinear characteristics.

R.L. Boroschek (✉)
Civil Engineering Department, University of Chile, Blanco Encalada 2002, Santiago, Chile
e-mail: rborosch@ing.uchile.cl

A.A. Aguilar
Ruben Boroschek y Asociados Ltda., Luis Thayer Ojeda 0127, Of. 1002, Providencia, Santiago, Chile
e-mail: antonio.aguilar@rbasoc.cl

F. Elorza
University of Chile, Blanco Encalada 2002, Santiago, Chile
e-mail: florza@ing.uchile.cl

21.2 Building and Instrumentation Description

The Andalucia Condominium is the first seismic base isolation structure in Chile [2] and it is the result of research work performed at the University of Chile. It is a 4 story concrete and masonry structure designed for low income families. The building rest on top of eight high damping rubber bearing located at ground level, Fig. 21.1. To understand the behavior of the structure two identical building, the base isolated and one of fixed base building, were instrumented with an accelerometer array.

The building has a typical floor of 10×6 m of surface. The weight of structure is of 1,630 kN. The first level is constructed with reinforced concrete and the other three levels are of masonry. The slab thickness is 10 cm, except for the roof, which is structured with wood trusses. The isolators have a 31.5 cm diameter, 32 cm height and 6.7 mm of rubber sheet thickness. Four of these isolators are located in each corner of the building and two at the center of each longer side.

The instrumentation consists of triaxial accelerometers with common triggering. The recording system has a 12 bit analog to digital converter so it is limited to earthquake events only. Figure 21.1 show the position of accelerometers C, L and F. Signals registered from C and F sensors are presented in this paper, Table 21.1. Sampling frequency is 200 samples per second.
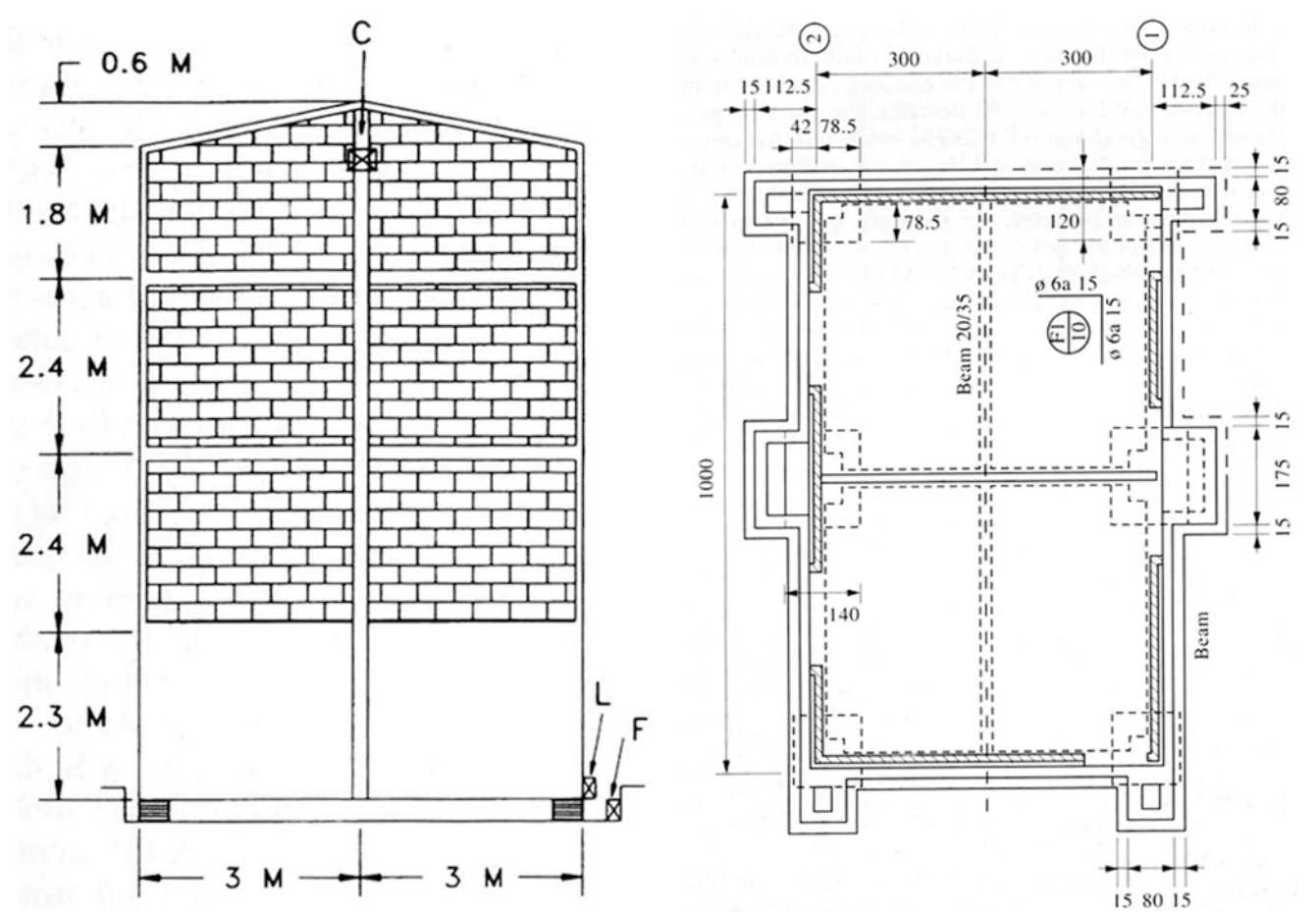
Fig. 21.1 Andalucía building drawings

Table 21.1 Sensors direction

Channel	Direction	Level
1	EW	Ground
2	NS	
3	UD	
4	EW	4th
5	NS	
6	UD	

21.3   Seismic Events Records

Several records have been obtained in the Andalucia Buildings. The largest seismic event recorded is the February 27th, 2010 Chile earthquake. Despite the M_w 8.8 magnitude, the earthquake did not cause any damage to the isolated structure or its contents. Figure 21.2 shows the recorded data. The strong motion phase lasts about 60 s. The peak accelerations at ground level were 0.30 g and 0.18 g in the horizontal and vertical directions, respectively. The maximum horizontal acceleration recorded within the isolated building was 0.22 g. In the vertical direction amplification was observed since the maximum acceleration recorded at the top building level was 0.29 g.

21.4   Models and Identification Methods

As in typical structure there is a need to validate the structural response of isolated systems as well as the device behavior. The basic characteristic of elastomeric isolators is its strong nonlinear elastic behavior. Also they are strongly influence by temperature, aging and vertical pressure. The basic recording system shall consider accelerometers below and on top of the isolation system and throughout the structure and displacement meters at the interface. In order to correlate the parameters with environmental variable a meteorological station is recommended.

Several models have been considered for the identification of elastomeric isolated structures. Some of these models are presented below.

21.4.1   Kelvin Voight Model and Maxwell Model

The viscoelastic model can be represented by damping and stiffness connected in parallel or in series. The equation of motion for the Kelvin Voight model, parallel system, is presented in Eq. 21.1. If the model is represented with these components in series, it is call the Maxwell model. The equation of motion in this case is given by Eq. 21.2.

$$C\,\dot{u} + K\,u = f \tag{21.1}$$

$$K\,\dot{u} = \frac{K}{C} \times f + \dot{f} \tag{21.2}$$

With C = damping, K = stiffness, f = Excitation and u = displacement. Both models correspond to the most basic representations of a viscoelastic isolator. An extension of these models corresponds to a *linear model of three parameters*. In this case the viscoelastic model can be represented by a damper and a spring connected in series with an additional spring
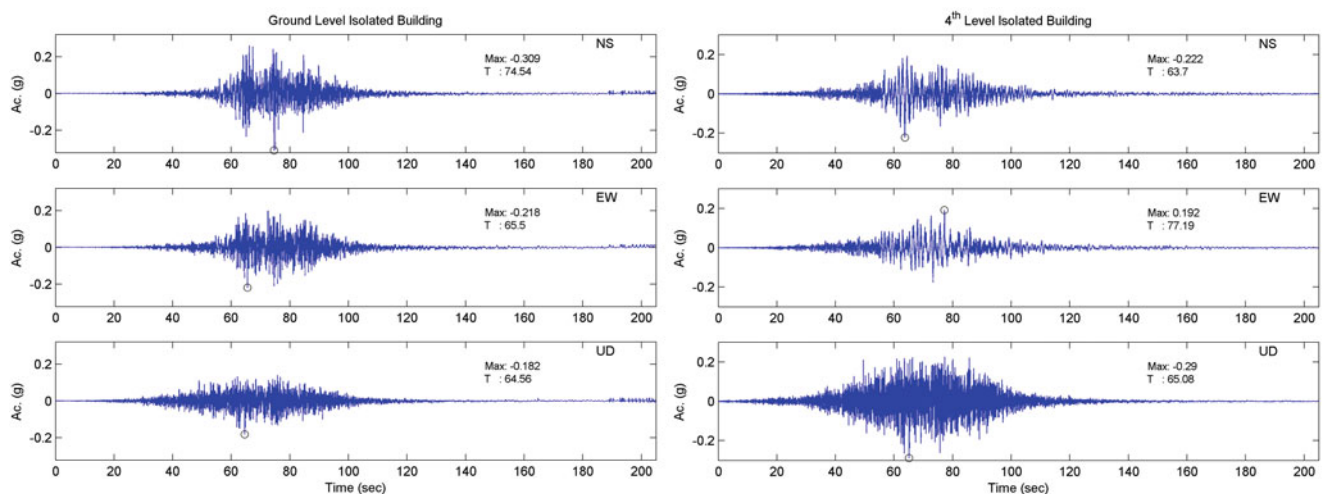
Fig. 21.2   February, 2010 earthquake acceleration records

connected in parallel. The equation of motion in this case is given by Eq. 21.3:

$$K_2 \left[u + \left\{ C \; \frac{[K_1 + K_2]}{K_1 \, K_2} \right\} \dot{u} \right] = f + \frac{C}{K_1} \, \dot{f} \tag{21.3}$$

21.4.2 Non-Linear Elastic Model

A non-linear elastic model can be assumes that both damping and stiffness. In this case the stiffness can be represented by a linear and cubic relation to displacement, and with two springs in parallel, [3], Eq. 21.4:

$$F_s = K_1 \, u + \left[\frac{K_2 - K_1}{3 \, u_0^2} \right] \times u^3 \tag{21.4}$$

The force associated with the non-linear damping can have a similar form, Eq. 21.5:

$$C_a = C_1 \, \dot{u} + \left[\frac{C_2 - C_1}{3 \, \dot{u}_0^2} \right] \times \dot{u}^3 \tag{21.5}$$

Where u_0 = characteristic displacement and $\dot{u}_0$ = characteristic velocity.
Considering Eqs. 21.4 and 21.5, the equation of motion in this case is given by:

$$C_1 \, \dot{u} + \left(\frac{C_2 - C_1}{3 \, \dot{u}_0^2} \right) \dot{u}^3 + k_1 \, u + \left(\frac{K_2 - K_1}{3 \, u_0^2} \right) u^3 = f \tag{21.6}$$

21.4.3 Bouc-Wen Models

The Bouc-Wen model, [4] is constructed considering a complex function of the stiffness component as a restorative force of the isolator. The equation of motion for a SDOF system is given by the Eq. 21.7:

$$C \, \dot{u} + q = f \tag{21.7}$$

In which C = Damping Matrix, u = Displacement, q = Restoring force and f = Excitations. The restoring force is expressed as:

$$q = \alpha \, K + (1 - \alpha) \; K \, Z \tag{21.8}$$

Where Z can be obtained from a differential equation that considers the time derivative of Z an its modulus, as given by Eq. 21.9:

$$\dot{Z} = A \, \dot{u} - \beta \, \dot{u} \, |Z|^n + \gamma \; |\dot{u}| \; |Z|^{n-1} Z \tag{21.9}$$

21.4.4 Biaxial Hysteretic Restoring Force Model

In order to consider the influence between two orthogonal horizontal directions in the isolator response, a modified Bouc Wen model can be used [5]. The equation of motion of a 2-DOF system subject to two-dimensional excitations is given by Eq. 21.10:

$$[M] \left\{ \begin{matrix} \ddot{u}_x \\ \ddot{u}_y \end{matrix} \right\} + [C] \left\{ \begin{matrix} \dot{u}_x \\ \dot{u}_y \end{matrix} \right\} + \left\{ \begin{matrix} q_x \\ q_y \end{matrix} \right\} = \left\{ \begin{matrix} f_x \\ f_y \end{matrix} \right\} \tag{21.10}$$

In which [M] = Mass Matrix, [C] = Damping Matrix, u_x, u_y = Orthogonal displacements, q_x, q_y = Restoring forces and f_x, f_y = Orthogonal excitations. The restoring force vector is expressed as shown in Eq. 21.11:

$$\begin{Bmatrix} q_x \\ q_y \end{Bmatrix} = \alpha \ [K] \begin{Bmatrix} u_x \\ u_y \end{Bmatrix} + (1 - \alpha) \ [K] \begin{Bmatrix} Z_x \\ Z_y \end{Bmatrix} \tag{21.11}$$

Where [K] = initial stiffness matrix, α = post yielding stiffness ratio and Z_x, Z_y = Hysteretic dimensionless components of the restoring force. In this case, Z_x and Z_y are described by the following differential equations, Eqs. 21.12 and 21.13.

$$\dot{Z}_x = A \ \dot{u}_x - \beta \ |\dot{u}_x \ Z_x| \ Z_x - \gamma \ \dot{u}_x \ Z_x^2 - \beta \ |\dot{u}_y \ Z_y| \ Z_x - \gamma \ \dot{u}_y \ Z_x \ Z_y \tag{21.12}$$

$$\dot{Z}_y = A \ \dot{u}_y - \beta \ |\dot{u}_y \ Z_y| \ Z_y - \gamma \ \dot{u}_y \ Z_y^2 - \beta \ |\dot{u}_x \ Z_x| \ Z_y - \gamma \ \dot{u}_x \ Z_x \ Z_y \tag{21.13}$$

Where A, β *and* γ are dimensionless constants.

21.4.5 Multiple Shear Spring Models

A bidirectional model is also constructed from several shear trilinear springs arranged in a circle [6, 7]. Each spring has its own specific characteristic of initial stiffness, secondary stiffness, and yield displacement.

$$\begin{aligned} \Delta x_{ew} &= x_{ew}(t) - x_{ew} \ (t - 1) \\ \Delta x_{ns} &= x_{ns}(t) - x_{ns} \ (t - 1) \end{aligned} \tag{21.14}$$

Where Δx_{ns} and Δx_{ew} are equal to NS and EW displacement at time t. The total restoring force can be evaluated by the equations system Eqs. 21.15 and 21.16:

$$\begin{bmatrix} \Delta R_{ew} \\ \Delta R_{ns} \end{bmatrix} = \sum_{i=1}^{N} k_i'(t) \begin{bmatrix} cos^2\theta_i & cos\theta_i \ sin\theta_i \\ cos\theta_i \ sin\theta_i & sin^2\theta_i \end{bmatrix} \begin{bmatrix} \Delta x_{ew} \\ \Delta x_{ns} \end{bmatrix} \tag{21.15}$$

$$\vartheta_i = \tfrac{\pi}{N} (i - 1) \ \ (i = 1, 2 \cdots, N)$$
$$Uy' = \frac{\sum_{i=1}^{N} cos^2 (\vartheta_i)}{\sum_{i=1}^{N} |cos (\vartheta_i)|} Uy \ \ k' = \frac{1}{\sum_{i=1}^{N} |cos^2 (\vartheta_i)|} k \tag{21.16}$$

Here, ΔR_{ew} and ΔR_{ns} are equals to increments of restoring forces along the EW and NS directions, $k_i'(t)$ = stiffness of i-th spring at time t, N is the number of shear springs, and ϑ_i is the angle between the EW axis and the i-th spring, Uy' = yield displacement and k' = each shear spring.

21.5 Identification Isolation Bearing with No-Linear Behavior

Common system identification methods that consider Linear Time-Invariant systems have been apply to traditional [8] and base isolated structures despite its nonlinear response. This section presents different analysis methods that have been used for isolation systems.

Stewart and other [9] described the seismic response and the system identification procedures used for four buildings in Los Angeles Area subjected to several earthquake events. The earthquake events produce accelerations lower than 0.21 g. For

the identification, they used basic frequency response function techniques, like peak peaking, and two parametric techniques proposed by Safak:

- Cumulative error method (CEM): The transfer function is estimated by minimizing cumulative error for the entire history [10].
- Recursive prediction error method (RPEM): The transfer function is determined by recursively minimizing error for each time step, using time windows [11, 12].

The transfer function is given by Eq. 21.17:

$$H(q) = \frac{B(q)}{A(q)} \tag{21.17}$$

Because the systems dynamic are always contaminated by noise, it includes two lineal filters representing the systems dynamic and noise dynamic. The signal and the noise are represented by Eq. 21.18, where $y_s(t) =$ equation for the signal and $y_n(t) =$ equation for the noise. These are combined as presented in Eq. 21.19. Then, considering a time k delay between input and output, from Eqs. 21.20 and 21.21, an estimator could be constructed as in Eq. 21.22, this allows to define an error objective function, Eq. 21.24, that depends on a set of parameters denoted by ϑ, Eq. 21.23.

$$y_s(t) = \frac{B(q)}{A(q)\ F(q)} \quad y_n(t) = \frac{C(q)}{A(q)\ D(q)}\ e(t) \tag{21.18}$$

$$y(t) = y_s(t) + y_n(t) \tag{21.19}$$

$$A(q)y(t) = q^{-k}\frac{B(q)}{F(q)}x(t) + \frac{C(q)}{D(q)}e(t) \tag{21.20}$$

$$y(t) = \left[1 - \frac{D(q)A(q)}{C(q)}\right]y(t) + q^{-k}\frac{D(q)B(q)}{C(q)F(q)}x(t) + e(t) \tag{21.21}$$

$$E[y(t)] = \widehat{y}(t,\vartheta) = \left[1 - \frac{D(q)A(q)}{C(q)}\right]y(t) + q^{-k}\frac{D(q)B(q)}{C(q)F(q)}x(t) \tag{21.22}$$

$$\vartheta = \left(a_1, \cdots, a_{na}, b_1 \cdots, b_{nb}, c_1 \cdots, c_{nb}\ d_1 \cdots, d_{nb}, f_1 \cdots, f_{nb}\right)^T \tag{21.23}$$

$$\varepsilon(t,\vartheta) = y(t) - \widehat{y}(t,\vartheta) \tag{21.24}$$

The least squares method is used as criteria for measuring errors. The total error in time t includes a weighting factor, as is observed in Eqs. 21.25 and 21.26.

$$V(t,\vartheta) = \frac{1}{2}\gamma(t)\sum_{s=1}^{t}\beta(t,s)\ \varepsilon^2(s,\vartheta) \tag{21.25}$$

$$\gamma(t)\sum_{s=1}^{t}\beta(t,s) = 1 \tag{21.26}$$

Where $\beta(t,s)$ corresponds to the weighting factor and $\gamma(t)$ is the normalization factor. The model that minimizes the total estimation error is given by Eqs. 21.27–21.30.

$$\frac{d}{d\vartheta} V(t,\vartheta) = 0 \tag{21.27}$$

$$\vartheta(t) = \vartheta(t-1) + \gamma(t) \ R^{-1}(t)\psi(t)\varepsilon(t) \tag{21.28}$$

$$R(t) = R(t-1) + \gamma(t) \left[\psi(t)\psi(t)^T - R(t-1)\right] \tag{21.29}$$

$$\psi(t) = \frac{d\varepsilon(t,\vartheta)}{d\vartheta} = \frac{dy(t,\vartheta)}{d\vartheta} \tag{21.30}$$

Yoshimoto et al. [13] used the *Multivariable Output Error State Space* (*MOESP*) method in a base isolated building under small shaking levels. MOESP is a method that obtains state space matrices from input and output data using Hankel and Toeplitz matrices and time windows analysis. The model is described by Eq. 21.31. This system is solved for each time window determining the modal properties of the system.

$$\begin{aligned} x_{k+1} &= A \ x_k + B \ u_k \\ y_k &= C_k x_t + D \ u_k \end{aligned} \tag{21.31}$$

Furukawa et al. [6] use the *Prediction Error Method* and a nonlinear isolator model derived by Wada. The method considers a restoring force as a function of parameter vector (ϑ). The system discrete-time state space is given by Eq. 21.32:

$$\begin{aligned} x_{k+1} &= A_d(\vartheta,t) \ x_k + B_d(\vartheta,t) \ u_k + w_k \\ y_k &= C(\vartheta,t) \ x_k + v_k \end{aligned} \tag{21.32}$$

Where x_k is the state vector at k, y_k the Output of the system at k, w_t the Gaussian process noise at k, v_t = Gaussian measurement noise k, and A_d, B_d = Matrices, and C_d = observation process noise matrix. Introducing an estimator for the Gaussian noise and measurement depending of a Kalman gain Eq. 21.32 is transformed to Eq. 21.33.

$$\begin{aligned} \widehat{x}_{k+1} &= A_d(\vartheta,t) \ x_k + B_d(\vartheta,t) \ u_k + K \left[y_k - C_d\widehat{x}_k\right] \\ \widehat{y}_k &= C_d \widehat{x}_k \end{aligned} \tag{21.33}$$

In which $\widehat{x}_k$ = state vector expectations at k, $\widehat{y}_k$ = Output of the system expectations at k, and K = Kalman gain. As well as the last methods, a prediction error vector ε and prediction error matrix E are defined, as is shown in Eqs. 21.34 and 21.35.

$$\varepsilon(k,\vartheta) = y_k - \widehat{y}_k, \ E(\vartheta) = \begin{bmatrix} \varepsilon(1,\vartheta) \\ \varepsilon(2,\vartheta) \\ \vdots \\ \varepsilon(N,\vartheta) \end{bmatrix}_{Nxny} \tag{21.34}$$

$$J(\vartheta) = \det\left\{\frac{1}{N}\left[E(\vartheta)^T E(\vartheta)\right]\right\} \rightarrow \min \tag{21.35}$$

Then, the Gauss-Newton method is used to search for the best parameter, as is described in the process represented by Eqs. 21.36–21.38.

$$\vartheta^{k+1} = \vartheta^k + \alpha \, \Delta \vartheta^k \tag{21.36}$$

$$\Delta \vartheta^k = \left[\Phi^T W \Phi \right]^{-1} \Phi^T \left(y - \widehat{y} \right) \tag{21.37}$$

$$\Phi = \begin{bmatrix} \frac{\partial \widehat{y}_1}{\partial \vartheta_1} & \cdots & \frac{\partial \widehat{y}_1}{\partial \vartheta_d} \\ \vdots & & \vdots \\ \frac{\partial \widehat{y}_N}{\partial \vartheta_1} & \cdots & \frac{\partial \widehat{y}_N}{\partial \vartheta_d} \end{bmatrix} \tag{21.38}$$

where W = weighting matrix or the inverse of prediction-error covariance matrix.
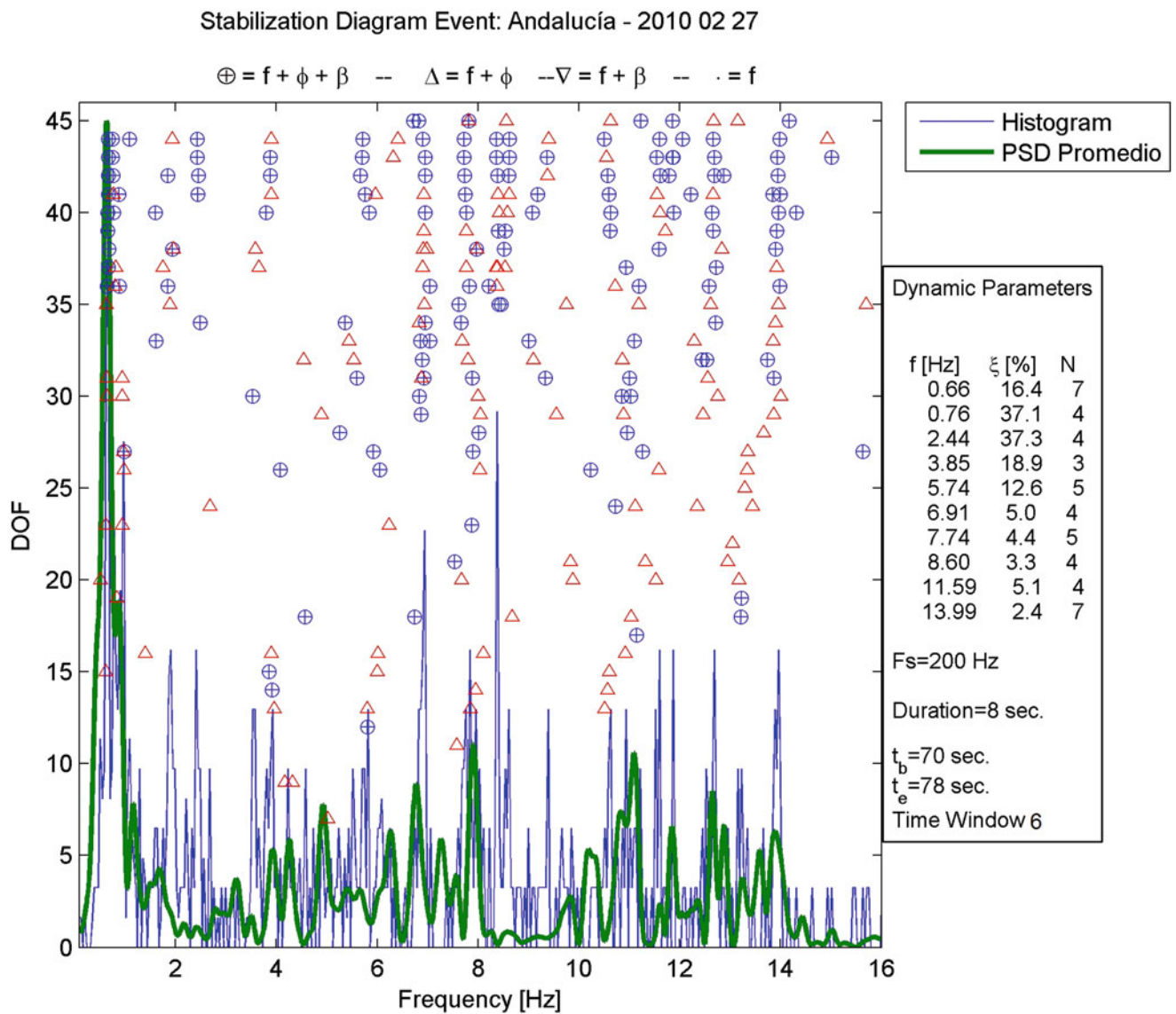
Fig. 21.3 Stabilization diagram. 70–78 s frame of event

21.6 Modal Properties Identification Results

The window MOESP technique was used to identify the modal properties of the structure. The identification process was performed considering the time frame from 30 to 110 s in time windows of 8 s long. The main time intervals evaluated are from 30 to 38 s, 70 to 78 s, and 110 to 118 s, respectively. This procedure allows the identification of variations of structure's modal properties between time windows selected, considering different accelerations amplitudes situations. Figure 21.3 shows the high non-linearity of the dynamic system when the acceleration amplitude increase with the earthquake demand, time frame of 70–78 s of the response. The figure clearly shows the variations in poles definition, and a high variability even with a short time frame.

Table 21.2 resumes identified properties for main windows evaluated. The increase of structural flexibility is notorious in the 70–78 s interval, when the event presents the highest amplitude of acceleration. The same could be observed in the case of modal damping ratios. There is a notorious increment in their value for higher demand, reaching a 50 % of damping. The structure suffered no damage during the earthquake. Figure 21.4 gives a comparison between the model of the identification method.

Table 21.2 Modal properties identified

Modal frequencies (Hz)			Modal damping ratios (%)		
30–38 s	70–78 s	110–118 s	30–38 s	70–78 s	110–118 s
1.86	0.62	1.89	2.7	23.7	22.3
2.23	0.78	2.00	12.7	41.8	–
2.99	2.34	3.06	17.9	50.5	19.9
14.11	16.42	18.63	3.9	3.0	2.3
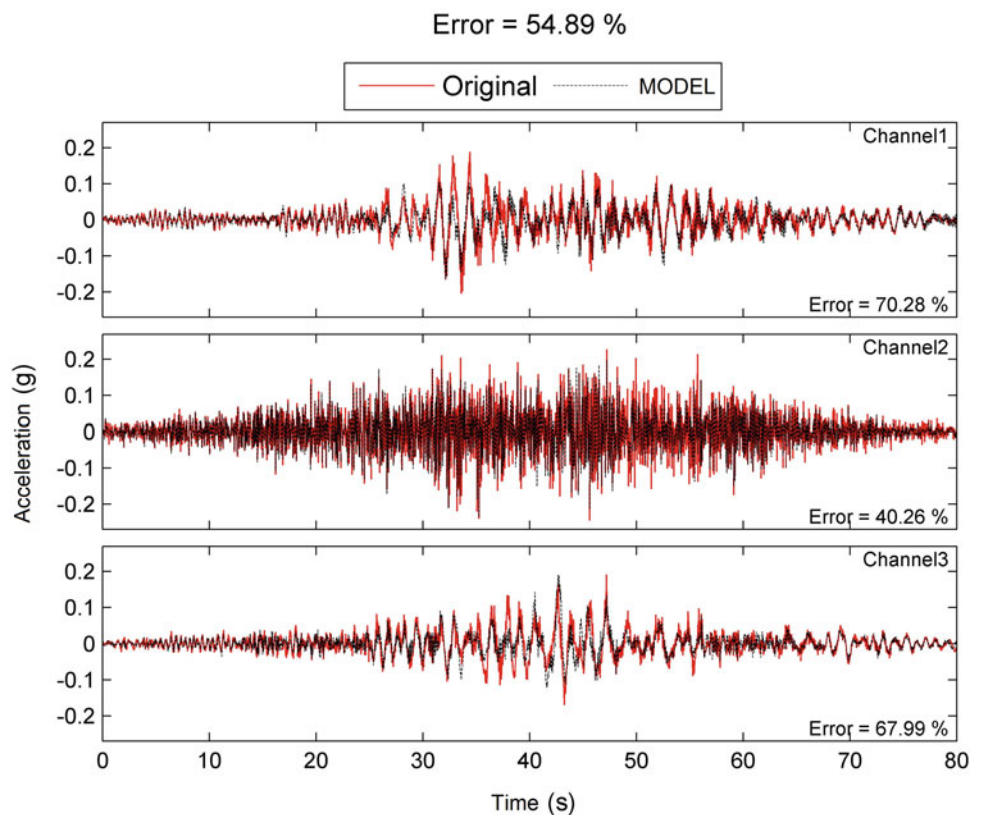
Fig. 21.4 Comparison between original output data and the modeled by the identification method

21.7   Conclusion

The analysis shows the variations of the modal frequencies and damping ratios identified, for each time window of analysis. It could be observed that the first modal frequencies strongly depend on the amplitude of vibration. For example, the natural period at the beginning of the strong motion phase is 0.54 s and gets longer during the second time window, between 70 and 78 s, achieving a value of 1.61 s. It is important to note that after the earthquake the structure recovered the dynamic properties it had before the earthquake. Modal damping ratios show that, at the same time that the natural frequencies changes damping ratios change too. In the case of the isolated structure, the high damping ratio is associated with the first modes.

References

1. Miranda E, Mosqueda G, Retamales R, Peckan G (2010) Performance of nonstructural components during the February 27, 2010 Chile earthquake. Earthquake Spectra 28(S1):S453–S471
2. Boroschek K, Retamales R, Aguilar A (2012) Seismic response of isolated structures subjected to Mw 8.8 Chile earthquake of February 27, 2010. Seminar in Technological Advances and lessons learned in the last large earthquakes and tsunamis. CISMID. Paper No M-2. Lima, Perú, 17-18 de Agosto, 2012
3. Soto J (2000) Mathematical Models for elastomeric specimens and isolators. M.S. thesis Civil Engineering. University of Chile (in Spanish)
4. Wen YK (1976) Method for random vibration of hysteretic systems. J Eng Mech 102(2):249–263
5. Park YJ, Wen YK, Ang H-S (1986) Random vibration of hysteretic systems under bi-directional ground motions. Earthquake Eng Struct Dyn 14:543–557
6. Furukawa T, Ito M, Izawa K, Noori M (2005) System identification of base-isolated building using seismic response data. J Eng Mech 131:268–275
7. Wada A, Kinoshita M (1985) Elastic plastic dynamic 3-dimensional response analysis by using multiple shear spring model Part 1 and Part 2. Summaries of technical papers of annual meeting, Architectural Institute of Japan, Structure I, Tokai, Japan, 313–316 (in Japanese)
8. Van Overschee P, De Moor B (1996) Subspace identification of linear systems: theory, implementation, applications. Kluwer Academic Publishers, Boston, MA
9. Stewart J, Conte J, Aiken I (1999) Observed behavior of seismically isolated building. J Struct Eng 125(9):955–964
10. Safak E (1991) Identification of linear structures using discrete-time filters. J Struct Eng 117(10):3064–3085
11. Safak E (1989) Adaptive modeling, identification, and control of dynamic structural systems. I: Theory. J Eng Mech 115(11):2386–2405
12. Safak E (1989) Adaptive modeling, identification, and control of dynamic structural systems. II: Applications. J Eng Mech 115(11):2406–2426
13. Yoshimoto R, Mita A, Keiichi Okada K (2005) Damage detection of base-isolated buildings using multi-input multi-output subspace identification. Earthquake Eng Struct Dyn 34:307–324
14. Moroni M, Sarrazin M, Boroschek R (1998) Experiments on a base-isolated building in Santiago, Chile. Eng Struct 20(8):720–725

Chapter 22
Design of an Inertial Measurement Unit for Enhanced Training

M. Bassetti, F. Braghin, F. Castelli Dezza, and F. Ripamonti

Abstract During training, athletes are evaluated by their trainer in a subjective way. It is hard task to appreciate improvements between two different performances of the same athlete, particularly if carried out at different places and times or if referred to different tests. Moreover, in team sports, like soccer, football and basket, to follow and evaluate each athlete could be very demanding for the trainer. This paper presents the work done to design a wearable, light-weight and rugged inertial measurement unit designed to collect and analyze data. Inertial measurements are correlated with the athlete's position too. Some results are presented and discussed.

Keywords Sport • GPS and MEMS-IMU integrated system • Embedded systems • Microprocessor and transceivers • Inertial sensor systems

22.1 Introduction

Every discipline of sport has its own techniques for performance analysis. The requirements for such methods depend on the discipline's motion, ergonomic constraints and cost related to the discipline. For example, for disciplines implying fast body motion of longer duration, the investigation of the trajectory is of utmost importance. Anyway, athletes and coaches are not only interested in the positions and velocities, but also in the motion analysis of segments of the human or the orientation of equipment [1, 2]. Furthermore, sometimes the knowledge of position serves as a base for comparing other performance criteria (e.g. heart rates, rotations per minute) [3]. For these reasons, it is very important to correctly assess the accuracy of monitoring systems. High positioning accuracy is crucial only for few applications where small trajectory differences can be important (e.g. slalom in Alpine skiing). Moreover in many disciplines the trajectory shape (meaning high relative accuracy) is of greater importance than the absolute positioning accuracy. This is true also for energy transfer computations where sports professionals are more interested in relative changes rather than absolute values.

Starting from these considerations, the application of low-cost GPS receivers integrated with micro-electro-mechanical system (MEMS) inertial measurement unit (IMU) allows, in many applications, an accurate and continuous observation of position, velocity and orientation which opens new possibilities for monitoring of athletes' performance [4–6].

The aim of this paper is to design of a miniature Inertial Measurement Units (IMU) based on MEMS inertial sensors. In the past decade indeed the cost, power consumption, weight and size of MEMS IMUs have motivated the use of miniature versions in a variety of applications such as personal digital assistants, smart phones, gaming and monitoring devices [7, 8]. The idea is to embed the measurements system directly in the sport equipment (e.g. the athletes' T-shirt) exploiting its low mass and small dimensions. The designed device consists of a complete six degree-of-freedom (dof) IMU composed of MEMS accelerometers and angular rate gyros with an integrated microprocessor and SD card for storing data. The experiments, carried out at the AC Milan training centre (Milanello), reveal that the designed device returns accurate results if compared to commercial and professional devices. These achievements yield a highly accurate, portable, and inexpensive sensor system to support athletes' real-time monitoring or off-line analysis and assessment of their performance.

M. Bassetti (✉) • F. Braghin • F.C. Dezza • F. Ripamonti
Department of Mechanical Engineering, Politecnico di Milano, Via La Masa 1, 20156 Milan, MI, Italy
e-mail: marco.bassetti@polimi.it

22.2 The Designed IMU

In Fig. 22.1 the Inertial Measurement Unit (IMU) board is shown. The board includes a microcontroller, a 3-axis MEMS accelerometer, two MEMS gyroscopes and an SD-card slot. Moreover there is all the electronics required for charging the included LiPo battery as well as a GPS receiver and an antenna.

The sensor node "intelligence" is provided by a dsPIC33F microcontroller from Microchip® Technology Inc. The use of this Digital Signal Controller (DSC) represents the best compromise for low power consumption, hardware reliability and firmware ruggedness. It is able to run up to 40 MIPS operation (@3.0–3.6 V) within a broad temperature range (−40 °C to +125 °C) and has a modified Harvard architecture, C compiler optimized instruction set with 16-bit wide data path and 24-bit wide instructions. It has an internal flash program memory capable of up to 256 Kbytes and a data SRAM of up to 30 Kbytes (including 2 Kbytes of DMA RAM).

The 3-axis MEMS accelerometer is produced by Analog Devices® and has a sensing range of ±16 g, low power consumption (350 μA) and small package (4 mm × 4 mm × 1.45 mm). The bandwidth of the sensor is up to 1,600 Hz along both X and Y axes and up to 550 Hz along Z axis. Being capacitive, the accelerometer is able to measures also static accelerations.

The two 2-axis MEMS gyroscopes are produced by ST Microelectronics. They are pitch/roll and pitch/yaw, both able to measure angular velocity up to ±300°/s.

The output signals of the MEMS accelerometer and gyroscopes are digitalized by the Analog-to-Digital Converter (ADC) of the microcontroller and stored in the SD memory according to a protocol developed for the purpose. Note that it is very important to have a sensor with optimal thermal performances: the offset vs. temperature performance of the adopted accelerometer is equal to ±1 mg/°C and its sensitivity change due to temperature is equal to ±0.001 %/°C.

All three measured accelerations and all three angular velocities are sent to the dsPIC33F microcontroller that low pass filters them to avoid aliasing with a first order Butterworth filter having cut-off frequency equal to

$$f_{-3db} = \frac{1}{2\pi \, (1k\Omega) \times C_{x,y,z}} = 1600 Hz \tag{22.1}$$

(being $C_{x,y,z}$ equal to 100 nF) and samples them simultaneously at 16 kHz with a resolution of 12 bits sequentially. Every channel is acquired with a buffer of 16 samples, acting as window filter. Finally, all three acceleration signals are sequentially decimated to 500 Hz and stored in the SD flash memories.

The microcontroller runs a microkernel that serves all the tasks (i.e. acquisition and storage, communication to an external PC, erase of flash memory). The firmware can be updated via USB connection thanks to a dedicated boot loader. Note that, during the acquisition and storage task, the microcontroller manages the reading and writing procedures, avoiding the overwriting of the saved data while, during the communication task, it handles all the functions useful to transfer data from the sensor node to the external PC. The data are provided in raw binary format.

The board includes also an integrated GPS receiver with its antenna. The GPS receiver used is made by U-Blox® and is characterized by small size and low power consumption (35 mA @ 3.3VDC). Information are collected, the acquired NMEA messages are parsed by the microcontroller and then stored into the SD flash memory.

The developed IMU has been tested and the results have been compared with two professional devices provided by AC Milan:
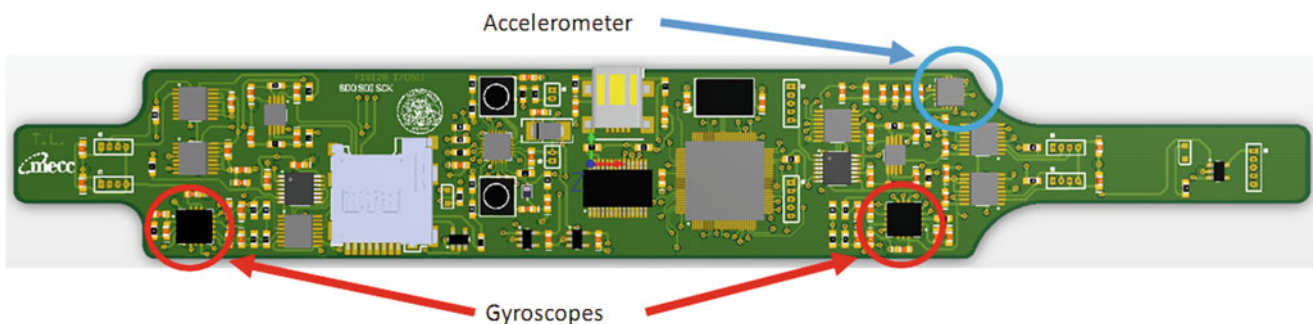
Fig. 22.1 The Polimi IMU

- *Adidas Catapult*: an IMU able to return several information about the test. In particular, among the others, the three accelerations (forward, sideway and up) and the three angular velocities will be collected for the benchmark. Data are collected with a sampling frequency equal to 100 Hz.
- *GPS Sport*: a GPS system returning information about the athlete's position, elapsed time, covered distance . . . Data are collected with a sampling frequency equal to 5 Hz.

22.3 The Experimental Results

22.3.1 Experimental Setup

Experimental tests have been carried out at the AC Milan training centre (Milanello). Figure 22.2 shows the satellite map of the facility as well as the base of the measurement campaign. Three different tests have been performed:

- Test 1: the GPS system has been calibrated by walking along the football pitch and stopping for few seconds at the four corners (Fig. 22.3). Moreover a soft running along the reference trajectory reported in Fig. 22.3 has been carried out.
- Test 2: four reverse direction exercises have been performed, (reference trajectories are shown in Fig. 22.4) considering a change of the sprint direction respectively of 135°, 90°, 45° and 180°.
- Test 3: a bike tour around the training centre.

For tests 1 and 2, the IMUs are placed on the athlete back. The reference system is shown in Fig. 22.5. In test 3, instead, the IMUs are placed on the rear luggage rack of the bike and the reference system is shown in Fig. 22.5.

Fig. 22.2 The AC Milan training centre (Milanello)
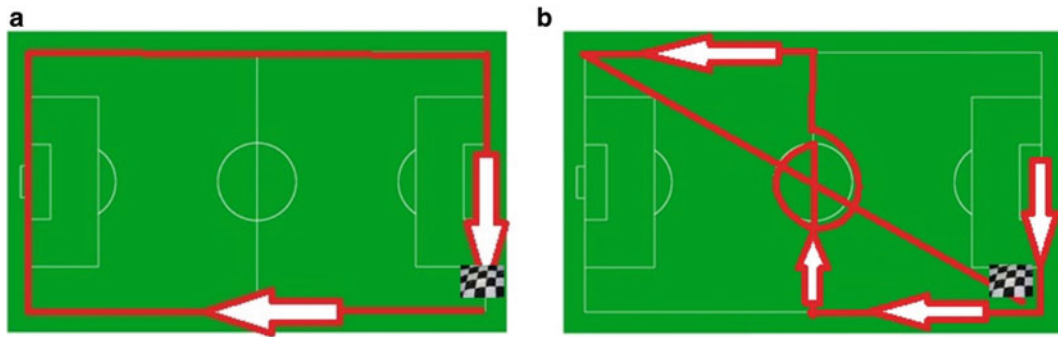
Fig. 22.3 The Test 1 reference trajectories for the GPS (**a**) and the IMU (**b**) calibration

Fig. 22.4 The Test 2 (sprints and changes of direction) reference trajectories
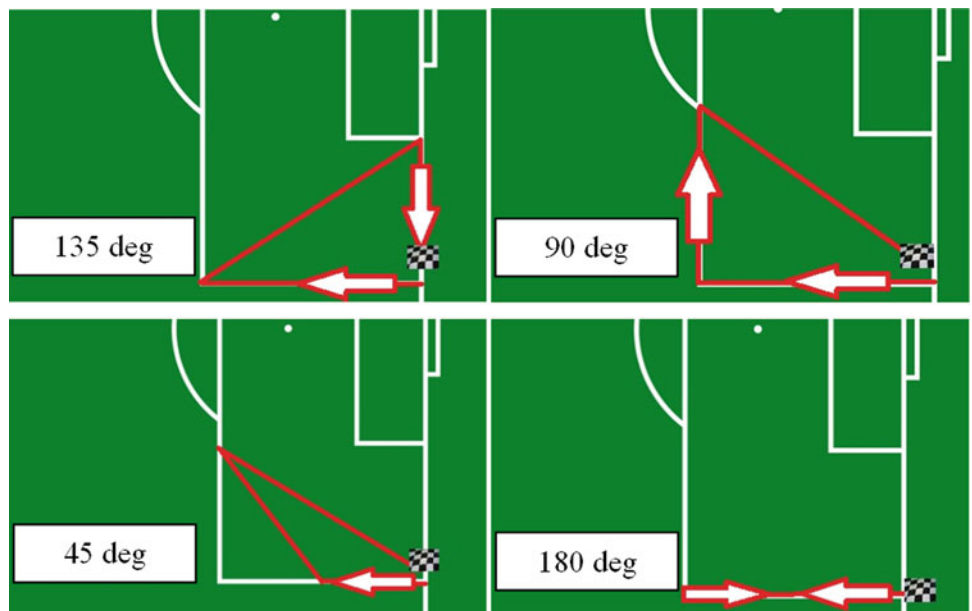
Fig. 22.5 The IMUs reference system in for the Test 1 and 2, with the IMUs on the back of the athlete (**a**), and the Test 3, with the IMUs on the rear luggage rack of the bike (**b**)
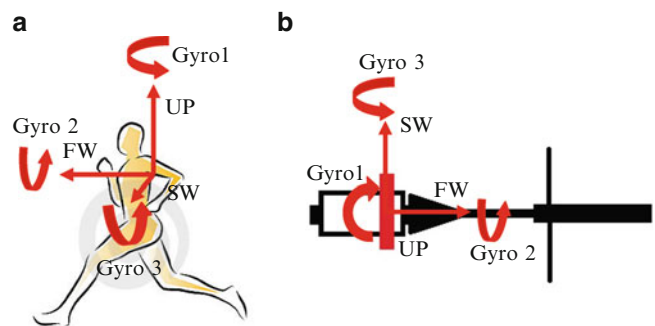
Fig. 22.6 The Test1 GPS result

22.3.2 Test 1: GPS and IMU Calibration

As previously introduced this test has been performed to calibrate the GPS and to test the IMU performance in soft and constant running condition. In Fig. 22.6 the GPS results in terms of athlete's position are reported while the trajectories described in Fig. 22.3 are followed. During the first part of the test the average walking speed is about 4 km/h, while in the second part it rises at about 10 km/h. For the second part of the test the IMUs data are collected and compared (Fig. 22.7).

A good agreement between the two measurement systems can be observed. However small differences are present and are mainly due to:

- the position of Polimi and Catapult IMUs is slightly different; this mainly affects the measured acceleration
- the different sampling frequencies, 100 Hz for Catapult IMU and 500 Hz for Polimi IMU. In fact the higher sampling frequency adopted by Polimi IMU allows to register a wider harmonic content and consequently the peak levels in the time histories are generally higher; also the signal post-processing is of relevance: the signals acquired by Polimi IMU were filtered using a sixth order Butterworth low pass filter having a cut-off frequency equal to 100 Hz while Catapult signals were filtered using an unknown low pass filter.

22.3.3 Test 2: Sprints and Changes of Direction

Dealing with the athlete's accelerations and angular velocities, the second test is more interesting. During this test the trajectory is measured with the GPS system (Fig. 22.8). It can be compared with the target summarized in Fig. 22.4 showing the high performance and accuracy of the proposed system.
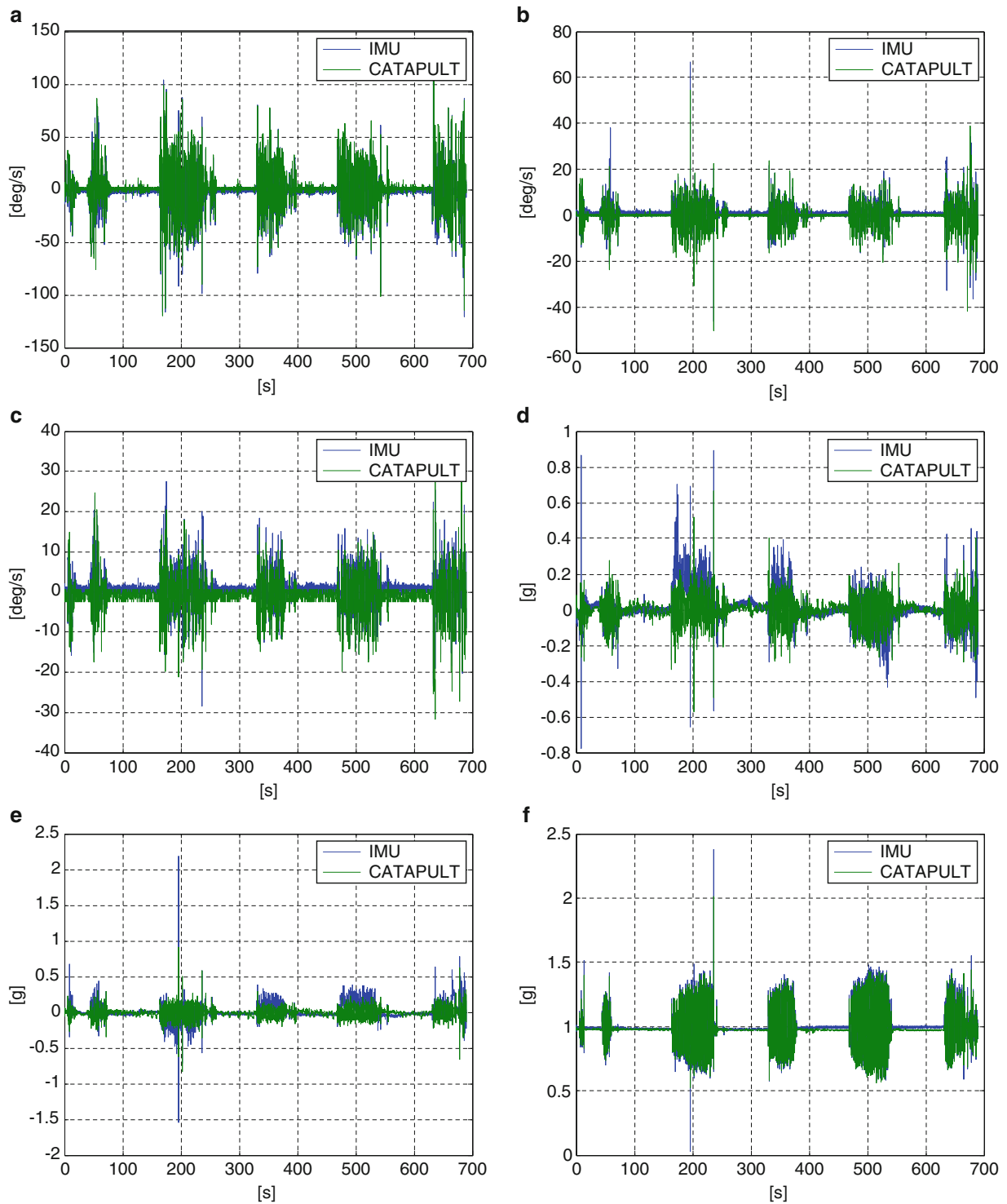
Fig. 22.7 The Test1 IMU results; the Gyro1 (**a**), Gyro2 (**b**), Gyro3 (**c**), Acceleration SW (**d**), Acceleration FW (**e**) and Acceleration UP (**f**) time histories

Fig. 22.8 The Test2 GPS result

Also for this test the two IMUs are compared (Fig. 22.9) and considerations very similar to ones done for the first test can be drawn. However, in this second case, both the accelerometers and gyroscopes identify higher values due to the sprints and the quick changes of direction. Among the others, as expected, the angular velocities around the vertical axis (Gyro1) and the vertical accelerations are particularly high. Also the forward accelerations due to the sprints are significant (up to 4 g).

22.3.4   Test 3: Endurance Test

The last test is performed with the athlete riding a bike in the Milanello training centre for about 15 min covering a distance of 4 km. The ride is registered by the GPS unit and it is shown in Fig. 22.10. The average speed is approximately 16 km/h, but peak values of 25–30 km/h are reached. The IMUs data are reported in Fig. 22.11.

Also for this test, the highest value, in terms of angular velocity, is measured around the vertical axis (Gyro1) and the highest acceleration is obtained in the vertical direction (component UP), mainly due to the terrain roughness.

22.4   Conclusions

In this paper a miniature Inertial Measurement Units (IMU) based on MEMS inertial sensors and designed for sport applications (low mass and small dimensions) is presented. The main features of the device are described and a benchmark experimental campaign is carried out in collaboration with AC Milan.
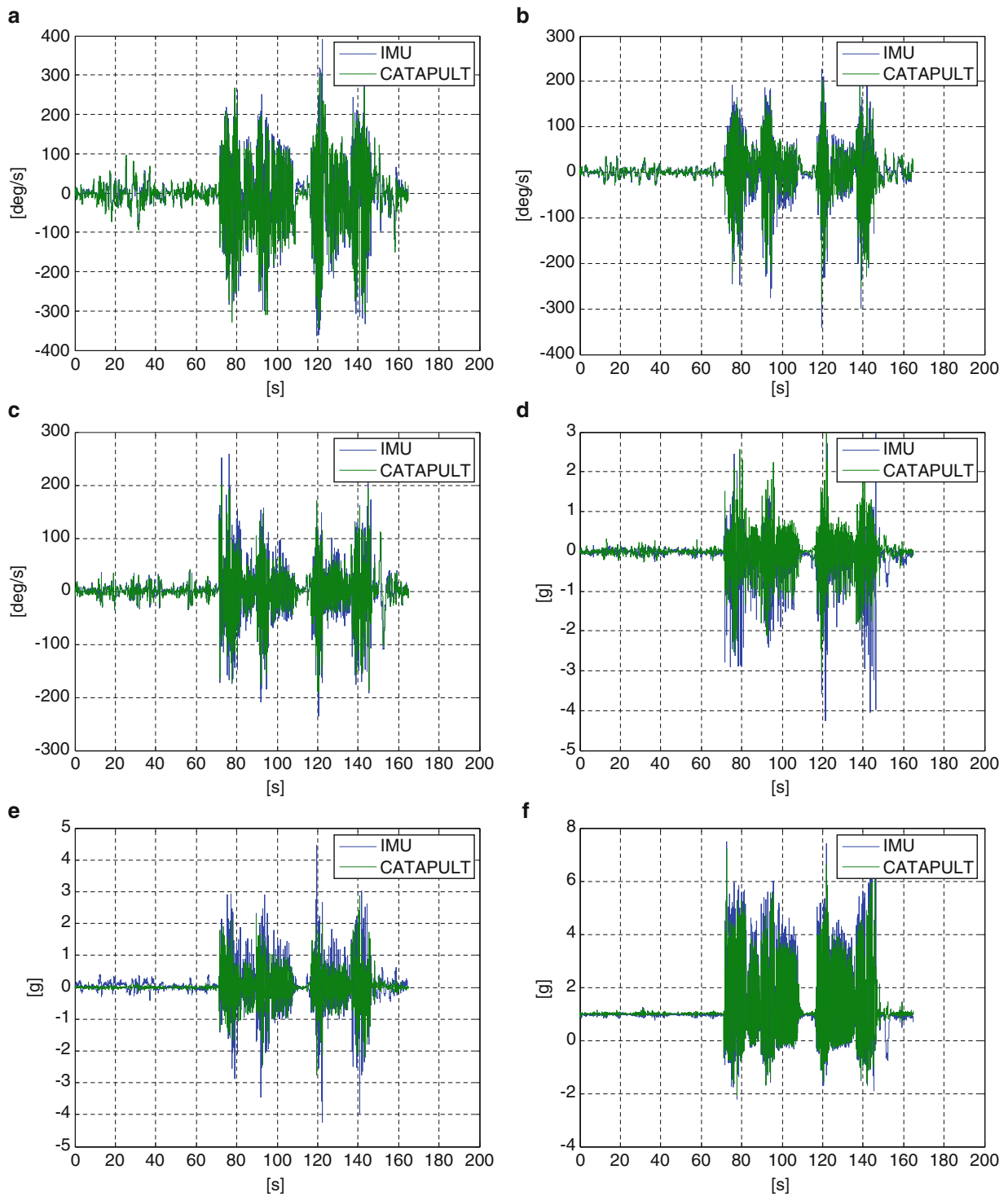
Fig. 22.9 The Test2 IMU results; the Gyro1 (**a**), Gyro2 (**b**), Gyro3 (**c**), Acceleration SW (**d**), Acceleration FW (**e**) and Acceleration UP (**f**) time histories

Fig. 22.10 The Test3 GPS result

The experiments show a good agreement between the designed IMU and professional devices used to monitor the athletes' performance in terms of position, acceleration and angular velocity. Starting from the collected data it is possible to develop algorithms, specific for several different sport applications such as soccer, football or basketball, for the athletes' real-time monitoring during training and the off-line calculation of parameters for the assessment of their performance.
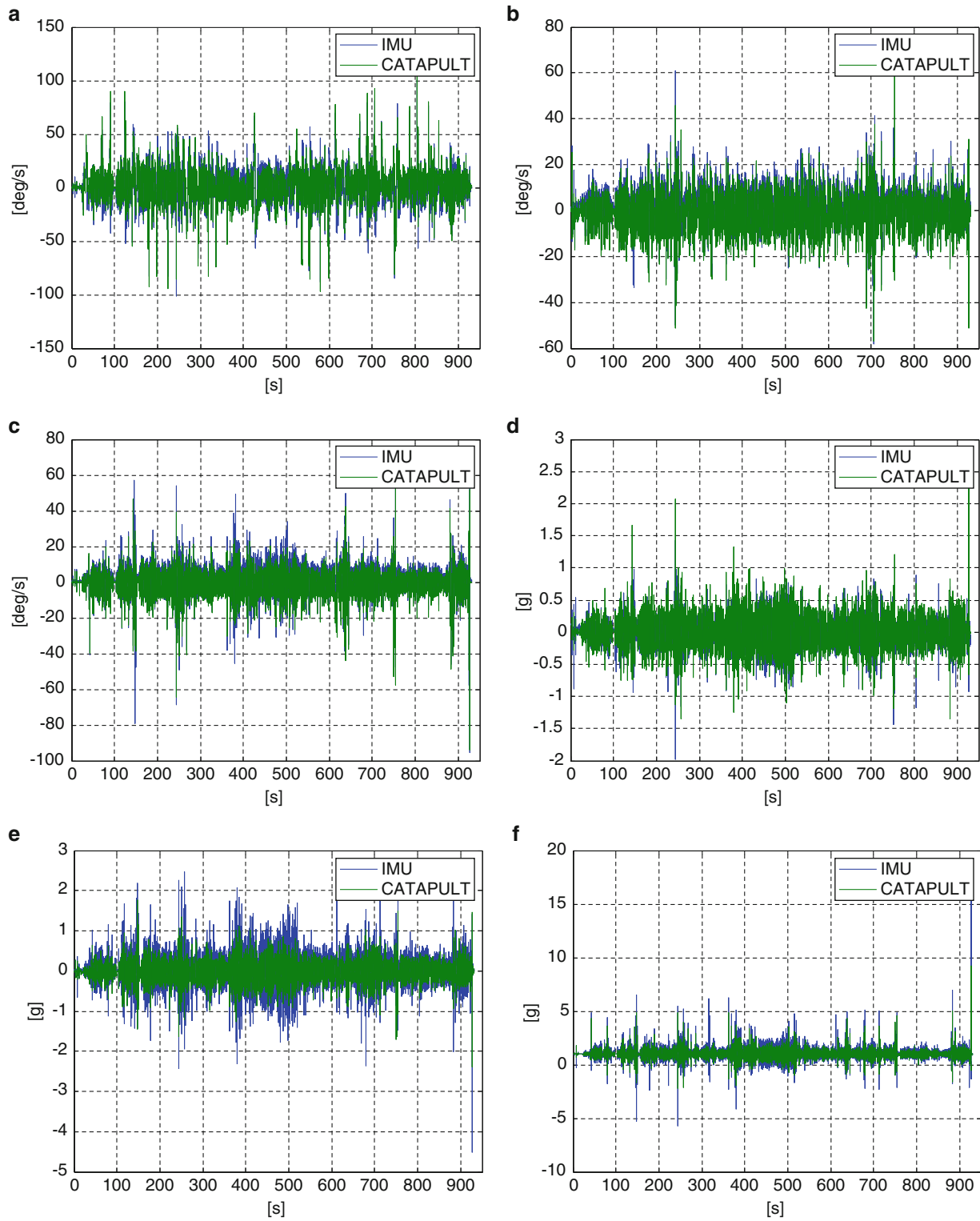
Fig. 22.11 The Test3 IMU results; the Gyro1 (**a**), Gyro2 (**b**), Gyro3 (**c**), Acceleration SW (**d**), Acceleration FW (**e**) and Acceleration UP (**f**) time histories

References

1. Waegli A, Skaloud J, Tomé P, Bonnaz J-M (2007) Assessment of the integration strategy between GPS and body-worn MEMS sensors with application to sports. 20th international technical meeting of the Satellite Division of The Institute of Navigation 2007 ION GNSS 2007, 2, pp. 2075–2084
2. Waegli A, Guerrier S, Skaloud J (2008) Redundant MEMS-IMU integrated with GPS for performance assessment in sports. Record - IEEE PLANS, Position location and navigation symposium, art. no. 4570079, pp. 1260–1268
3. Waegli A, Skaloud J (2009) Optimization of two GPS/MEMS-IMU integration strategies with application to sports. GPS Solutions 13(4):315–326
4. Bergamini E, Picerno P, Pillet H, Natta F, Thoreux P, Camomilla V (2012) Estimation of temporal parameters during sprint running using a trunk-mounted inertial measurement unit. J Biomech 45(6):1123–1126
5. Kong X, Li J, Du Y (2010) Method of coordinate system unity in MEMS-IMU/GPS integrated navigation system. Chin J Sensor Actuator 23(4):522–524
6. Bonnet V, Mazza C, Fraisse P, Cappozzo AR-t (2013) estimate of body kinematics during a planar squat task using a single inertial measurement unit. IEEE Trans Biomed Eng 60(7):1920–1926, Art. no. 6450063
7. Chang H-W, Georgy J, El-Sheimy N (2012) A low cost multi-sensors navigation solution for sport performance assessment. 25th international technical meeting of the Satellite Division of the Institute of Navigation 2012, ION GNSS 2012, vol. 5, pp. 3791–3798
8. King K, Yoon SW, Perkins NC, Najafi K (2008) Wireless MEMS inertial sensor system for golf swing dynamics. Sensors Actuators A Phys 141(2):619–630

Chapter 23
A Parameter Optimization for Mode Shapes Estimation Using Kriging Interpolation

Minwoo Chang and Shamim N. Pakzad

Abstract A parametric study of Kriging interpolation for Optimal Sensor Placement (OSP) is presented in this paper. A Kriging model uses geostatistical information to interpolate and extrapolate the values for unobserved locations with a weighted sum of known neighbors. The accuracy of mode shape estimates is evaluated by Modal Assurance Criteria (MAC), compared to the target mode shapes. The performance of OSP is enhanced by the Kriging results. For the quality estimation of mode shape, a parametric study is conducted in this paper. The Kriging model is composed of linear regression model with random error which is assumed as a realization of a stochastic process. A Gaussian function is used to characterize the covariance function between two random errors in terms of their relative distance. Three parameters are involved to define covariance function: regression model order and two amplification parameters. The parameter optimization approach aims at OSP solution with the minimum number of sensors. The effect of parameters is evaluated using numerically simulated harmonic modes, and modes from Northampton Street Bridge (NSB). Modified Variance (MV) is used to rank the signal strength at candidate sensing locations. The results show that the accuracy of estimated mode shapes is dependent on the eigenvalue of covariance matrix and the number of sensors can be minimized when the Kriging model is optimally designed.

Keywords Optimal sensor placement • Kriging • Modal assurance criteria • Modified variance • Wireless sensor network

23.1 Introduction

Optimal Sensor Placement (OSP) is a common issue for all engineering systems such as mechanical, aerospace, and structural, which require the posterior monitoring to maintain their performance [1–3]. From a set of observations, the indices can be extracted to quantify the systems' performance and modal parameters can be updated to reflect the behavior of existing systems. In particular, the effect of OSP is significant for structural systems, since the scale of civil infrastructure is much larger than other engineering problems. The traditional sensor networks, represented by wired sensors, are costly and physically limited to properly place them on large scale structures. Although the recent development of Wireless Sensor Networks (WSN) have facilitated the possibility of vibration monitoring with densely located sensors [4–6], the costly process for data transmission is inevitable and an optimum number of sensors is a more effective solution for practical Structural Health Monitoring (SHM).

The main objective of OSP is to formulate the sensor configuration to detect significant changes representing structural damage based on the evaluation of the signal strength at sensing locations [3, 7]. Additionally, the use of OSP reduces the cost by eliminating collecting large volume of redundant sensor data as well as managing the number of sensors. Effective Independence (EI) method [1], one of the widely used OSP techniques, examines the error of unbiased estimator using target mode shapes. For a variation of EI, modal frequency and modal mass are additionally used to quantify signal strength in EI-Driving Point Residue (DPR) [8] and Kinetic Energy [9] methods, respectively. Alternatively, the methods to search principal component in target mode shape matrix have been developed using correlation [10] and covariance [11] of mode

M. Chang (✉) • S.N. Pakzad
Department of Civil and Environmental Engineering, Lehigh University, 117 ATLSS Drive, Bethlehem, PA 18015, USA
e-mail: mic307@Lehigh.edu; pakzad@Lehigh.edu

shape matrix. In order to expand the applicability of previously developed variance method [11], Modified Variance (MV) method is introduced in which the computational time to define the best sensor configuration is much reduced [7].

In order to provide an automatic guideline for optimal sensor configuration, a framework, based on Modal Assurance Criteria (MAC) comparison, is introduced and serves to decide the minimum number of sensors on most informative locations [7]. The estimated mode shapes using interpolation/extrapolation techniques are compared to the target mode shapes using MAC to analyze the compatibility of a chosen sensor configuration. The polynomial functions are facilitated in many engineering problems and have shown reliable estimation results [12]; however, the boundary conditions should be known for satisfying the continuity of piecewise components. Alternatively, Kriging method, which is a geostatistical estimator of the unknown values at unobserved locations, can be used with only geometric information at candidate sensor locations to resolve the need for boundary conditions [13]. In order to define Kriging model, the error of mode shape function is assumed as random and its covariance is mathematically designed with several parameters.

This paper aims to investigate Kriging technique and to observe the effect of associated parameters for accurate mode shape estimation. Two examples are used to demonstrate optimal sensor configurations. EI and MV methods are investigated to quantify the signal strength at candidate sensor locations. The results of OSP are used to estimate the mode shapes for all candidate sensor locations.

23.2 Framework for Optimal Sensor Configuration

A framework to design optimal sensor configuration is introduced in [7]. The framework is comprised of two sub-tasks: (1) estimation of signal strength at each sensing node and (2) MAC comparison between target modes and estimated modes from a set of optimal sensor configuration. The target mode information is used to define the best sensor locations depending on the number of sensors. For a particular set of sensor configuration, the mode shapes are estimated for the unobserved locations using interpolation/extrapolation techniques. The MAC between exact mode shape and estimated from a set of optimal sensors is calculated. The best sensor configuration is defined when the minimum MAC amongst all target modes is beyond the threshold; otherwise the next sensor configuration with an additional sensor is selected and this procedure is repeated until the constraint for the MAC threshold is satisfied.

23.2.1 Optimal Sensor Placement (OSP) Methods

In this study, two OSP methods, Effective Independence (EI) [1] and Modified Variance (MV) [7], are investigated to quantify the signal strength at candidate sensor locations depending on the target modes. These two methods are convenient to implement since the methods require only the target mode shape information and are computationally inexpensive. The following is a brief description for each method.

Effective Influence (EI): An unbiased estimator of modal contribution parameter is defined as a function of target modes. The numeric deployment of error covariance between the exact modal contribution parameter and the unbiased estimator is the inverse of Fisher information matrix which is the expected value of the observed information. The Effective Independence Distribution (EID) vector is introduced to quantify the contribution of the candidate sensor locations. A sensor location noted with a lowest index of EID is discarded from the candidate locations and this procedure is repeated to determine the priority of sensor locations.

Modified Variance (MV): The covariance of target mode shape matrix is used to quantify the signal strength of candidate sensor locations. In order to prevent the irregularity in covariance due to sign convention and to increase independency of modal information at nodes, the target mode shape matrix is transformed by attaching the negative of mode shape matrix to the original. The unbiased estimator of mode shape function at unobserved locations is defined as a function of covariance matrix. The error of this estimator can be minimized when the determinant of covariance of observed locations is maximized. For the practical implementations, a *pc* index is introduced, considering the dispersion of off-diagonal components. Similar to EI method, a sensor location with lowest signal strength is tossed from the candidate sensor locations.

23.2.2 Kriging

Kriging is a geostatistical estimator to infer the random values at unobserved locations where the signal response can be estimated using weighted sum of known values at neighbors [14]. The shape function is initially estimated by the sum of a linear regression model and random error as:

$$y_i = p(x_i)^T a + z(x_i) \tag{23.1}$$

In Eq. 23.1, y_i is a modal ordinate at x_i; $p(x_i)$ is a set of non-linear bases, for example $p(x_i) = \begin{bmatrix} 1 & x_i & x_i^2 \end{bmatrix}$ for a quadratic basis; a denotes a coefficient vector which minimizes the random error $z(x_i)$. The covariance of the error is defined by the correlation between two sensor locations, with high correlation for closely spaced sensors. The correlation function is frequently expressed by using Gaussian functions in which two parameters are involved.

$$R(x_i, x_j) = \alpha \exp\left(-\theta r_{ij}^2\right) \tag{23.2}$$

In Eq. 23.2, α and θ are the amplification parameters and r_{ij} is the physical distance between x_i and x_j. Considering that the a is canceled out for the mode shape estimation, the order of the basis and correlation parameter θ, need to be designed for Kriging model. The details to estimate mode shapes are presented in [13, 15].

23.3 Case Studies

Two examples are used to verify the effectiveness of the framework to formulate the sensor configuration and to observe the effect of two parameters. In a numerically simulated shear building model, the effect of Kriging parameters is investigated and the best sensor configuration is found. Amongst the parameters, the effect of the order of basis and correlation parameter θ are considered since α does not affect the mode shapes estimation. In the second example, the modal parameters estimated from the response from the Northampton Street Bridge (NSB) are used to optimize sensor configuration depending on the number of target modes and applied OSP methods.

23.3.1 Shear Building Model

A 19-DOF simply supported beam is used to simulate modal parameters as shown in Fig. 23.1 (first five vibration modes). Kriging can be used effectively to interpolate the mode shapes since it does not require the continuity at the top of the shear building model. EI and MV methods are applied to determine the sensor location priority chart. In order to define the number of sensors, MAC of 0.95 for all target modes are set as a constraint.

For harmonic mode shapes, the minimum number of sensors is determined, which is equal to the number of target modes. For example, the changes of the optimal number of sensors and corresponding determinant of correlation matrix are illustrated in Fig. 23.2a. The constant basis for correlation is used. In this figure, the optimal number of sensors decreases
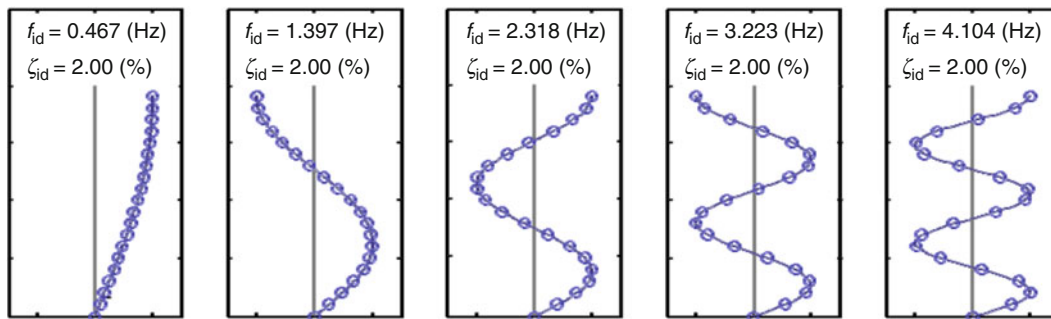
Fig. 23.1 First five mode shapes in 19DOF model with natural frequency and damping ratio
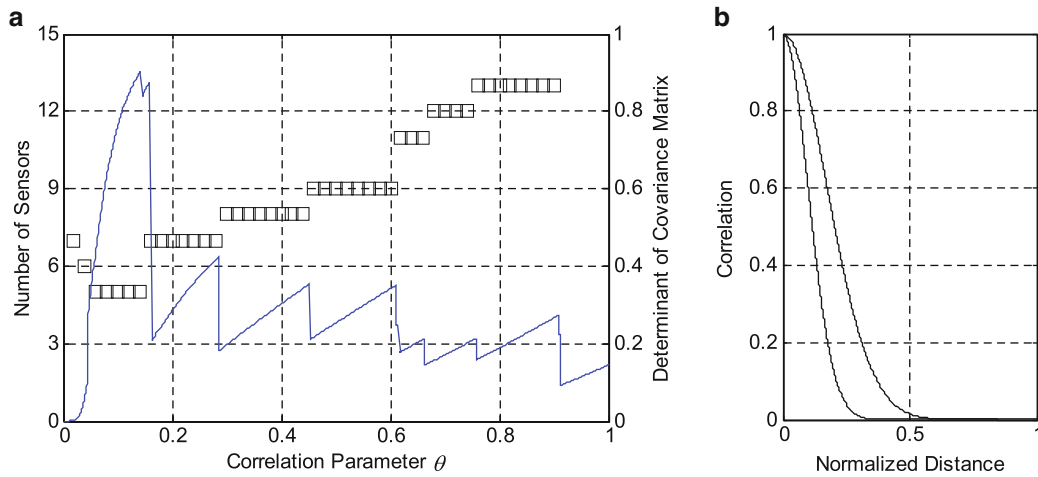
Fig. 23.2 Effect of correlation parameter to minimize number of sensors when five modes are targeted. (**a**) Number of sensors and determinant of target modes (**b**) Feasible range of correlation functions

Fig. 23.3 Ranges of optimal coefficient parameter for three orders of basis
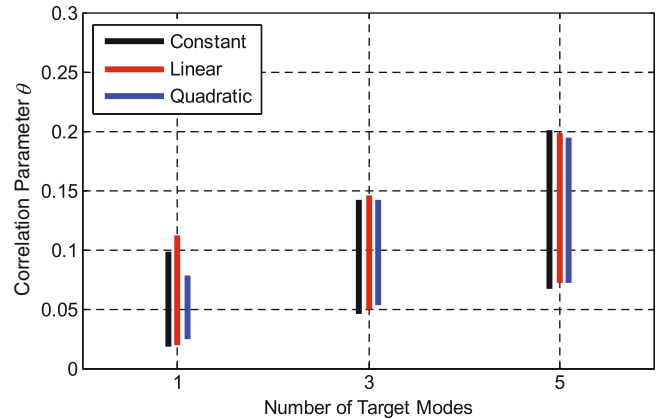
rapidly for $\theta < 0.46$ and increases as the correlation parameter increases. In particular, the feasible range of θ is determined between (0.046 and 0.142) for which five sensors are determined as an optimal solution. The determinant of correlation function is discontinuous when the sensor configuration changes. The feasible range of correlation function is plotted in Fig. 23.2b, indicating the high correlation for closely located sensors and the random errors are almost independent when the normalized distance between two sensor locations is larger than the half of height of the structure.

Further investigation is conducted to evaluate the effect of the order of basis. The basis for the one dimensional problem is determined as power series of candidate sensor location; for example, [1] for constant basis, [1 x_i] for linear basis, and [1 x_i x_i^2] for quadratic basis can be used. Although the increase of order requires additional computational cost, it does not necessarily improve the quality of estimated mode shape and reduce the number of sensors. Figure 23.3 shows the feasible ranges of correlation parameter θ when the numbers of target modes are varied. For all cases, the optimal numbers of sensors are the same with the number of target modes. The higher orders of basis are excluded in this figure since the optimal numbers of sensors are larger than the optimal number of target modes. In general, the linear basis slightly expands the feasible range of correlation parameter and the high order shows negative effect to search the best sensor configuration.

23.3.2 Northampton Steel Bridge

The ambient vibration response of Northampton Street Bridge (NSB) was measured using Wireless Sensor Network (WSN) and used to identify modal parameters in vertical responses [16]. A total of 21 wireless sensor units (18 on the North Side and three on the South Side) measure the ambient vibration of the bridge (Fig. 23.4). Structural Modal Identification Toolsuite (SMIT) [17] is used to identify seven structural modes under 10 Hz frequency range. The modal ordinates for sensors on south sides are used to distinguish the type of modes (vertical and torsional).
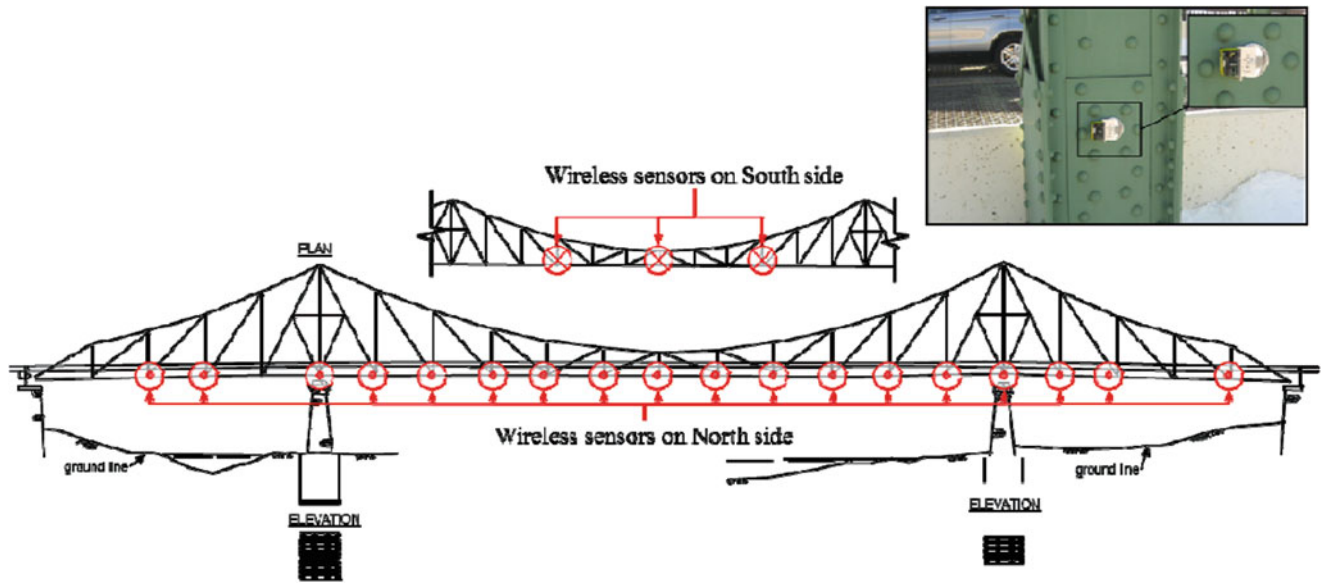
Fig. 23.4 Wireless sensor network in Northampton Street Bridge

Fig. 23.5 Optimal numbers of sensors versus correlation parameter
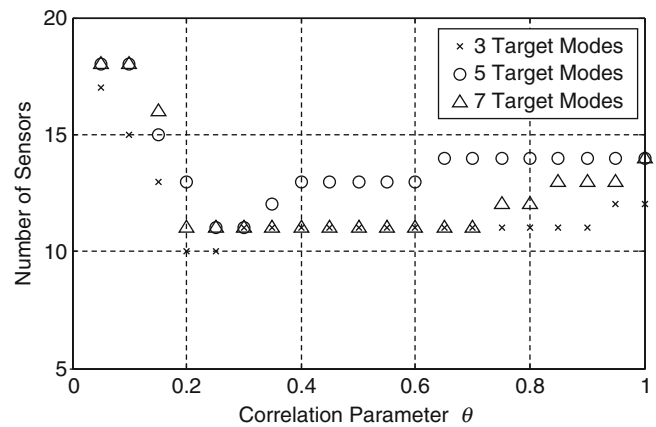
The optimal numbers of sensors to observe three, five, and seven target modes are plotted versus correlation parameter when MV method is employed (Fig. 23.5). Similar to the shear structure model, the number of sensors decreases rapidly first; then increases as the correlation parameter increases. For this example, very small range of correlation parameter is available for the optimal solution. In general, the numbers of sensors required to observe several sets of target modes are similar due to the complex mode shapes caused by two piers in the middle of bridge and the insufficient information of low number of target modes.

The optimal numbers of sensors for EI and MV methods are plotted (Fig. 23.6). For both methods, the required sensors are similar when the targeted modes are larger than four. As reported in [7], the insufficient information in target mode shape matrix results in the false estimation of signal strength and requires more sensors even though the fewer number of modes are targeted. EI and MV methods show similar performance to optimize the number of sensors regardless of the number of target modes.

In order to observe the way to determine sensor locations for each OSP method, the step by step procedures are tabulated when seven modes are targeted (Table 23.1). EI method detects two highest signal strengths at the end of the bridge while MV method evaluates highest signal strength at the middle. The sensors are almost uniformly spaced when the seventh sensor location, which is the minimum number of sensors when the rank of seven for target mode shape matrix is chosen. Since it fails to estimate MAC of 0.95, extra sensor locations are added for the optimal sensor configurations. For this particular example, the performance of MV (11 sensors) is better than EI (12 sensors). The sensor configurations become the same when 12 sensor locations are selected.

Fig. 23.6 Optimal numbers of sensors versus number of target modes for EI and MV methods
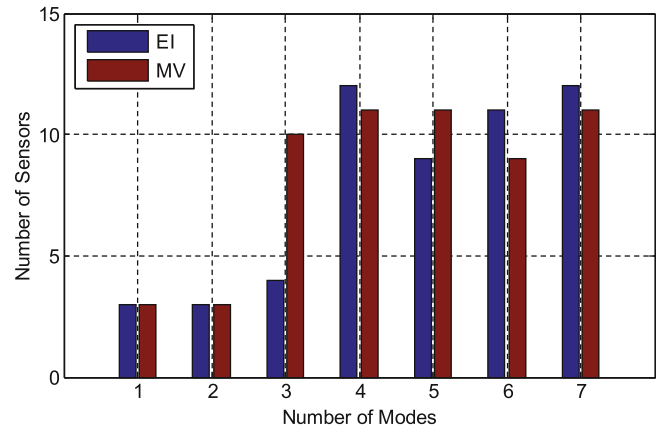
Table 23.1 Sensor configuration comparison for NSB between EI and MV methods

23.4 Conclusion

In this study, the effects of Kriging parameters, the order of basis for mode shape estimator and the correlation parameter for random error are investigated. Kriging model can be used to estimate the mode shape effectively since it utilizes the geometry information whereas other methods such as Spline require continuity condition at the boundaries.

Two applications are used to observe the effect of the Kriging parameters. A 19-DOF shear structure model shows the effect of the order of basis function is insignificant and low order is recommended to reduce the computational cost. The correlation parameter needs to be carefully selected. The feasible range for the correlation parameter always exists, which requires further research for the automatic search for the best sensor configuration. The modal parameters for NSB from a set of ambient vibration response are used for optimal sensor configuration. In general, the feasible range of correlation parameter is shorter than shear structure. Due to the complexity in mode shapes and insufficient information in target mode matrix, many sensors are required. The EI and MV methods are used to quantify the signal strength. Both show similar sensor configuration with almost uniform spacing.

References

1. Kammer DC (1990) Sensor placement for on-orbit modal identification and correlation of large space structures. Proceedings of American Control Conference, San Diego, CA, 23–25 May, 1990, pp 2984–2990
2. Yao L, Sethares WA, Kammer DC (1992) Sensor placement for on-orbit modal identification of large space structure via a genetic algorithm. IEEE international conference on Systems Engineering, Kobe, Japan, 17–19 September 1992, pp 332–335
3. Laory I, Hadj Ali NB, Trinh TN, Smith IF (2012) Measurement system configuration for damage identification of continuously monitored structures. J Bridg Eng 17(6):857–866
4. Spencer BF, Ruiz-Sandoval ME, Kurata N (2004) Smart sensing technology: opportunities and challenges. Struct Control Health Monit 11(4):349–368
5. Lynch JP, Loh KJ (2006) A summary review of wireless sensors and sensor networks for structural health monitoring. Shock Vib Digest 38(2):91–130
6. Pakzad SN, Fenves GL (2008) Statistical analysis of vibration modes of a suspension bridge using spatially dense wireless sensor network. J Struct Eng 135(7):863–872
7. Chang M, Pakzad S (2014) Optimal sensor placement for modal identification of bridge systems considering number of sensing nodes. J Bridge Eng. doi:10.1061/(ASCE)BE.1943-5592.0000594
8. Papadopoulos M, Garcia E (1998) Sensor placement methodologies for dynamic testing. AIAA J 36(2):256–263
9. Heo G, Wang ML, Satpathi D (1997) Optimal transducer placement for health monitoring of long span bridge. Soil Dyn Earthquake Eng 16(7):495–502
10. Carne TG, Dohrmann CR (1995) A modal test design strategy for model correlation. Proceedings of the 13th international modal analysis conference, Nashville, TN, 13–15 February, 1995
11. Meo M, Zumpano G (2005) On the optimal sensor placement techniques for a bridge structure. Eng Struct 27:1488–1497
12. Ahlberg JH, Nilson EN, Walsh JL (1967) The theory of splines and their applications. Academic, New York, NY
13. Sacks J, Welch WJ, Mitchell TJ, Wynn HP (1989) Design and analysis of computer experiments. Stat Sci 4(4):409–423
14. Matheron G (1963) Principles of geostatistics. Econ Geol 58(8):1246–1266
15. Belytschko T, Lu YY, Gu L (1994) Element-free Galerkin methods. Int J Numer Meth Eng 37(2):229–256
16. Chang M, Pakzad SN, Leonard R (2012) Modal identification using smit. In Topics on the dynamics of civil structures, vol 1. Springer, New York, NY, pp 221–228
17. Chang M, Pakzad SN (2013) Observer Kalman filter identification for output-only systems using interactive structural modal identification toolsuite (SMIT). J Bridge Eng. DOI: 10.1061/(ASCE)BE.1943-5592.0000530

Chapter 24
Determination of Principal Axes of a Wineglass Using Acoustic Testing

Huinam Rhee, Sangjin Park, Junsung Park, Jongchan Lee, and Sergii A. Sarapuloff

Abstract A general methodology to determine the principal axes of an arbitrary quasi-axi-symmetric resonator oscillating at its low-frequency flexural modal pair has been proposed. For an ideal axi-symmetric case, such a structure has two degenerated modes with identical eigen frequencies and similar modal shapes distinguished by their angular orientation only. However, in reality, due to a small non-uniformity of the structure, the structure has two specific directions corresponding to slightly-different modal properties. This paper describes a simple mathematical method to determine the principal axes using acoustic signals of the structure's free oscillations in air. An ordinary wineglass was chosen to verify the methodology. An impulse was applied to the wineglass in an arbitrary direction that generates a beating, and the oscillatory data were acquired by a pair of microphones located in a vicinity of the shell rim to estimate its principal axes using the proposed method. The accuracy of this approach was verified by additional tests, in which impacts were applied along the calculated principal axes to show that there is no beating. This method can be applied for initial tuning of an imperfect shell resonator and can be generalized for a fine tuning of a gyroscopic resonator.

Keywords Principal axis • Frequency mismatch • HRG • CRG • Tuning

24.1 Introduction

HRG (Hemispherical Resonator Gyroscope) and CRG (Cylindrical Resonator Gyroscope) are modern types of Coriolis' resonator gyroscopes [1] using Bryan's effect [2] in cantilevered elastic shells. To measure any input angle of turn or an angular rate enough accurately, such resonators need to have an extremely high Q-factor as well as a perfectly-homogeneous structure and properties. However, a real resonator is not fabricated precisely. Hence, it has two specific axes with slightly-different modal properties. They result in an output drift of the sensor; so, a false output signal can be read-out without any input rotation [3]. If the difference of the modal properties is enough small, the small mismatch of the eigen frequencies can be compensated and stabilized electronically [4, 5]. Anyway, a rough tuning of the frequencies of the resonator has to be performed to avoid further degradation of performance (due to high control voltages, associated non-linearities, etc.). Thus, first of all, principal conservative axes of operating modal pair have to be found for an initial rough tuning of the resonator.

Actually, such a fine tuning of gyroscopic resonators has to be done *in vacuo* using precise capacitive measurement technique (e.g., AFR and PFR characteristics of forced oscillations described in very details in [6]). However, a preliminary characterization and ranging of numerous uncoated resonators and their rough tuning by simple tools and free oscillations in air often looks reasonable. Anyway, acoustic measurement technique is definitely useful for educational purposes at university. For such tests in air, we can neglect differences between conservative and dissipative principal axes of a high-Q resonator and estimate locations of its conservative principal axes only. The proposed acoustic testing technique can be used for measurements of spectra and mismatches, studies of fixture conditions, rough tuning, rough estimation of noises of a resonator, etc.

H. Rhee (✉) • S. Park • J. Park • J. Lee • S.A. Sarapuloff

Mechanical & Aerospace Engineering, Sunchon National University, 50 Maegok-dong, Sunchon, Junnam 540-742, Republic of Korea
e-mail: hnrhee@sunchon.ac.kr

24.2 Dynamic Characteristics of a Wineglass

To show proposed way of acoustic testing a simple experimental set-up (Fig. 24.1) was used. It contained: a common wineglass fixed at a table, two identical microphone sensors (IEPE type, with scale factors difference less than 0.2 %), and an impact hammer (with 0.1 mm-diameter metal cap). Two microphone sensors were positioned along normals to the shell midsurface at the same air gaps (about 3 mm) from the glass rim (at approximately ± 1 mm from the edge) and at 45°-angle between each other (angular errors is about $\pm 1°$). A wineglass was excited by a normal impulse of a hammer at a direction where the first microphone was positioned at the opposite site of the resonator.

Figure 24.2 presents the result of impulse excitation responses of the wineglass. There are also more detailed characteristics in narrow resonant ranges of the second flexural modes of the wineglass (with frequency resolution 0.38 Hz). The eigen frequencies are 501.5 and 513.0 Hz, and, so, their mismatch is 11.5 Hz. This phenomenon is known as a mismatch of eigen frequencies, and the main reasons are revealed as a non-uniformity of inertial and stiffness properties (asphericity, thickness variations, density and elastic non-homogeneities, initial stresses, imperfect edges, etc.) into circumferential directions of the shell of the wineglass [3]. The mean Q-factor of the mentioned modal pair is about 1,730.
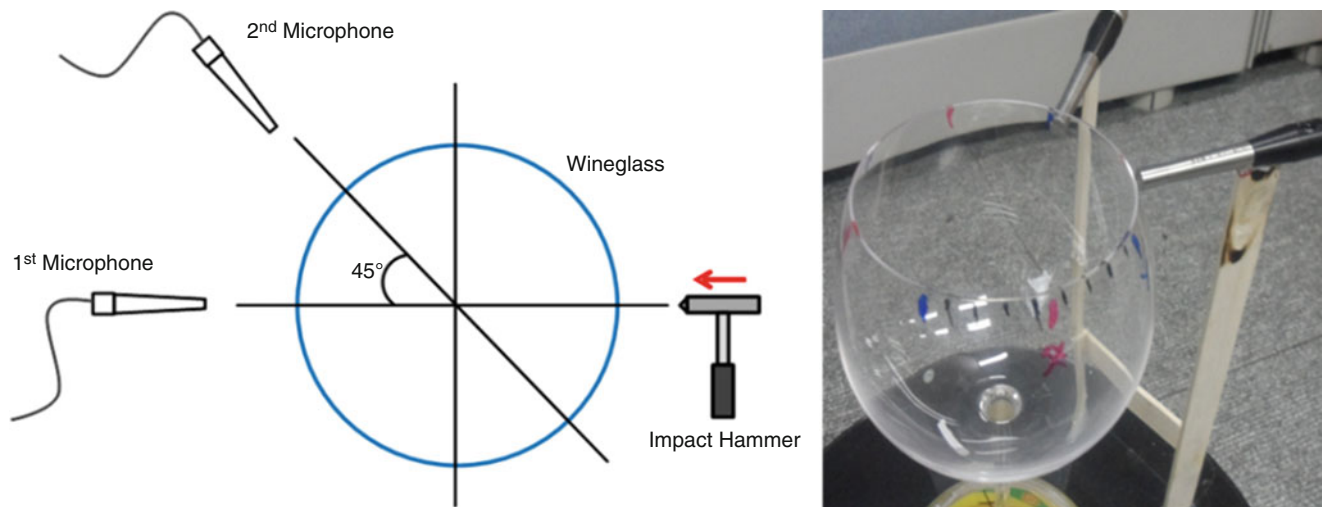
Fig. 24.1 Experimental set-up for acoustic testing of a wineglass resonator
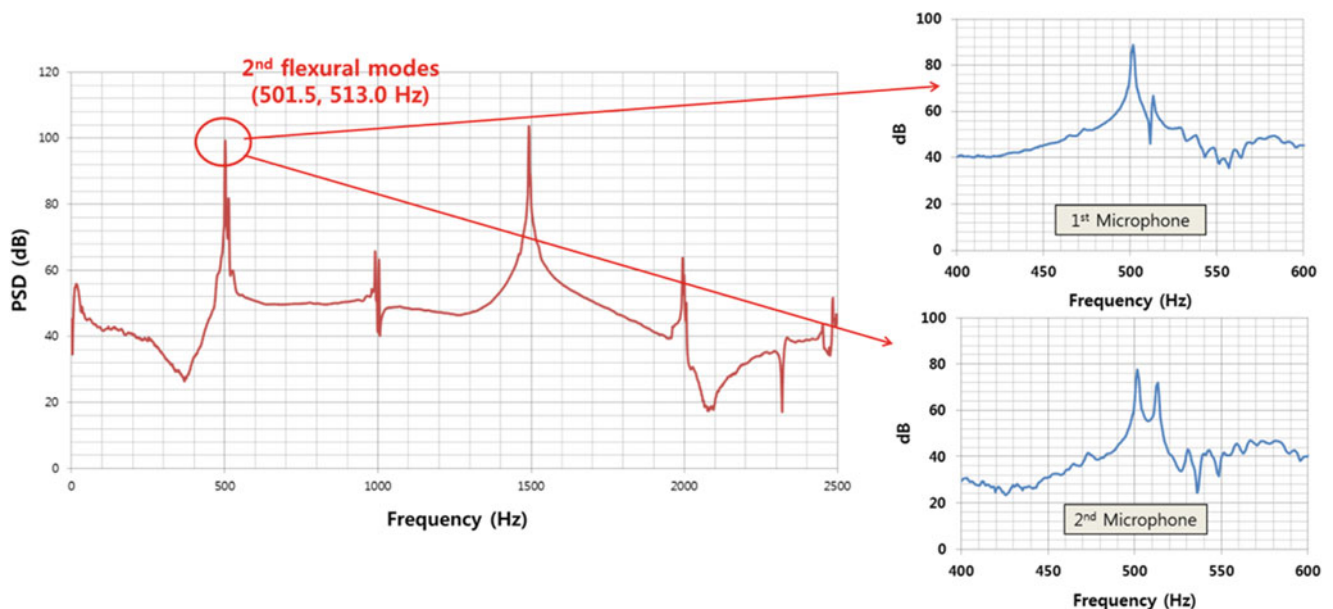
Fig. 24.2 Impulse excitation response characteristics of a wineglass

24.3   Methodology to Determine the Principal Axes

Paired nth flexural modes of a wineglass can be assumed as free oscillations of a two-DOF system (so-called, an equivalent or generalized model). If the system is supposed as no damping system and the resonator's natural frequencies are slightly-different at a set of axes $Ox'y'$, the equations of free oscillations for this imperfect resonator are

$$
\begin{aligned}
\ddot{x}'(t) + \omega_1^2\, x'(t) &= 0, \\
\ddot{y}'(t) + \omega_2^2\, y'(t) &= 0.
\end{aligned}
\tag{24.1}
$$

These equations are for the case when the modal axes of the oscillator coinciding with coordinate axes exactly. If the principal axes of the resonator do not correspond to coordinate axes, the schematic of its equivalent planar oscillator can be drawn like Fig. 24.3.

The components at normal coordinate basis $Ox'y'$, and at Oxy -frame (where the forces will be applied and readouts are placed) are related to each other by the following coordinate transformation

$$
\begin{pmatrix} x' \\ y' \end{pmatrix} = \begin{pmatrix} \cos\theta_\omega & \sin\theta_\omega \\ -\sin\theta_\omega & \cos\theta_\omega \end{pmatrix} \begin{pmatrix} x \\ y \end{pmatrix},
\tag{24.2}
$$

where θ_ω is an angle between the principal axis of the system and Oxy-axes and this angle is defined in respect to the configuration plane (x, y), so, in the physical space (XYZ) of a shell resonator, it corresponds to the angle $\frac{\theta_\omega}{n}$ (here n is a modal number). Substituting this transformation into the equations of motion (24.1) for $Ox'y'$-components, the equations of motion in terms of Oxy-components get the form [3, 5, 6]

$$
\begin{aligned}
\ddot{x}(t) + \tfrac{\omega_1^2+\omega_2^2}{2} x(t) + \tfrac{\omega_1^2-\omega_2^2}{2}\,(\,x(t)\cos 2\theta_\omega + y(t)\sin 2\theta_\omega\,) &= 0, \\
\ddot{y}(t) + \tfrac{\omega_1^2+\omega_2^2}{2} y(t) - \tfrac{\omega_1^2-\omega_2^2}{2}\,(-x(t)\sin 2\theta_\omega + y(t)\cos 2\theta_\omega\,) &= 0.
\end{aligned}
\tag{24.3}
$$

The solutions of these equations in Oxy coordinates are

$$
\begin{aligned}
x(t) &= Re\left\{ A_* e^{(i\omega_1 t)}\cos\theta_\omega - B_* e^{(i\omega_2 t)}\sin\theta_\omega \right\}, \\
y(t) &= Re\left\{ A_* e^{(i\omega_1 t)}\sin\theta_\omega + B_* e^{(i\omega_2 t)}\cos\theta_\omega \right\}.
\end{aligned}
\tag{24.4}
$$

Let X1 and X2 be the first and second terms in the solution $x(t)$ and Y1, Y2 be the same types of terms in the solution for $y(t)$. If these solutions $x(t)$ and $y(t)$ are in-phase (i.e., complex amplitudes A_*, B_* are the real quantities A, B) and they have been extracted from the measured data, an angle between the principal axes of modal pair and Oxy-axes can be calculated using one of the following relations

$$
\frac{X1}{Y1} = \frac{Re\left\{ Ae^{i\omega_1 t}\cos\theta_\omega \right\}}{Re\left\{ Ae^{i\omega_1 t}\sin\theta_\omega \right\}} = \cot\theta_\omega, \qquad \frac{X2}{Y2} = -\frac{Re\left\{ Be^{i\omega_2 t}\sin\theta_\omega \right\}}{Re\left\{ Be^{i\omega_2 t}\cos\theta_\omega \right\}} = -\tan\theta_\omega.
\tag{24.5}
$$
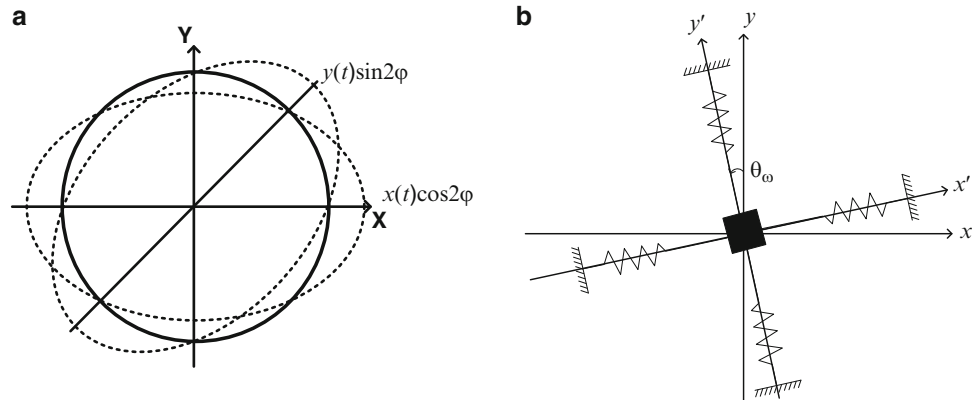
Fig. 24.3 Flexural modal pair $(n = 2)$ of a shell resonator (**a**) at OXY-frame, and schematic of an equivalent planar oscillator (**b**) at Oxy-frame, having a mismatch of the eigen frequencies
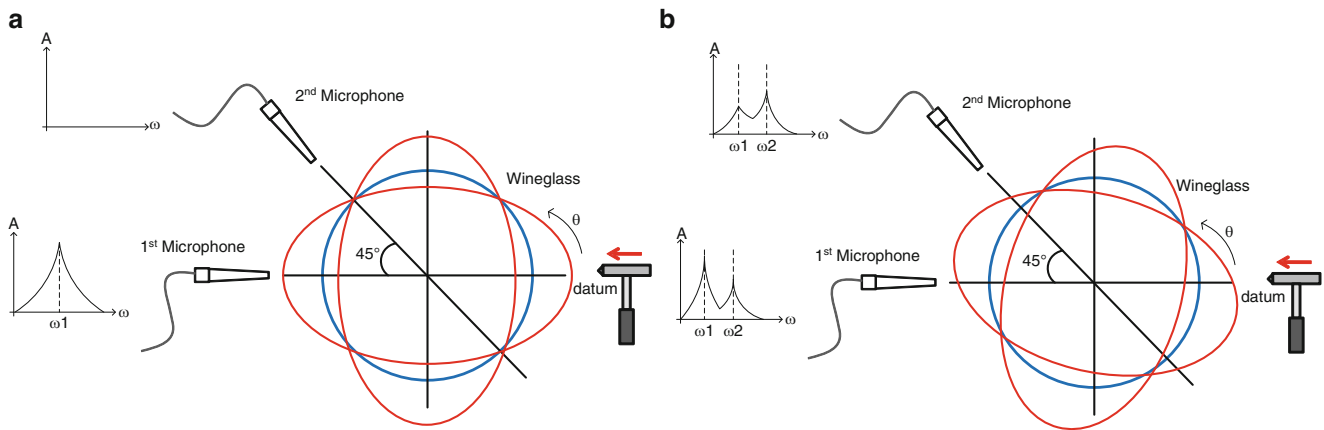
Fig. 24.4 Schematic diagrams of acoustic testing for confirmation of principal axes

Table 24.1 Principal axis angles obtained by the proposed method

$\theta_{\omega\,(1)}$	$\theta_{\omega\,(2)}$	$\theta_{\omega\,(2)} - \theta_{\omega\,(1)}$
11.09°	12.16°	1.1°

24.4 Acoustic Testing to Verify the Methodology

In order to verify the proposed approach, acoustic testing has been performed. Figure 24.4 shows a schematic diagram of the acoustic testing for confirmation of principal axes. Figure 24.4a tells that the principal axes of a wineglass coincide with the readout axes (that is a highly-uncommon case), and, so, the principal axes of a wineglass can be determined directly. Contrary, Fig. 24.4b signifies that principal axes of a wineglass do not correspond to the readout axes.

Magnitudes of the amplitudes with respect to each frequency component can be acquired from spectra of acoustic signals measured simultaneously at two microphone sensors. An angle between principal axes of a wineglass oscillating at the flexural modes and readout axes can be calculated using the methodology proposed in this paper. E.g., according to the calculation results for a wineglass sample studied, the principal axis of the first normal component of the second flexural modal pair is positioned at approximately $11.5 \pm 0.5°$ from the readout axes as shown in Table 24.1, where $\theta_{\omega\,(1)}$ and $\theta_{\omega\,(2)}$ mean the angular orientations of the principal axis with respect to the impact direction and are calculated by the first and second equations of Eq. 24.5, respectively.

The two equations in Eq. 24.5 generates different results (10 % relative deviation each other). For such a simplified measurement, there may be different reasons of errors as follows: a phase shifts between the measured signals, inaccuracy of distance between microphone sensor and a wineglass rim, aerial crosstalk between microphones, intrinsic errors of the microphone sensing and influence of room noises, a mismatch of Qs and a dissipative coupling inside the second flexural modes due to a mismatch between the principal axes of frequencies and those of damping, etc.

Figure 24.5 shows impulse excitation responses to verify the calculation by an additional acoustic testing. This data shows only a single component, that is, no beating exists contrary to Fig. 24.2. This tells that the wineglass is excited along the direction of principal axes. Thus, the proposed methodology is reasonably proven.

24.5 Conclusions

A simplified mathematical approach to determine the principal axes of a flexural modal pair for a wineglass resonator using its oscillating in air has been proposed, and an acoustic testing to verify the proposed methodology has been performed. The results of this paper form a good basis for a more detail study of the frequency tunings and acoustic diagnostics for a party of real gyroscopic resonators made from high-purity quartz glass, taking into account its dissipative mismatch and coupling too.
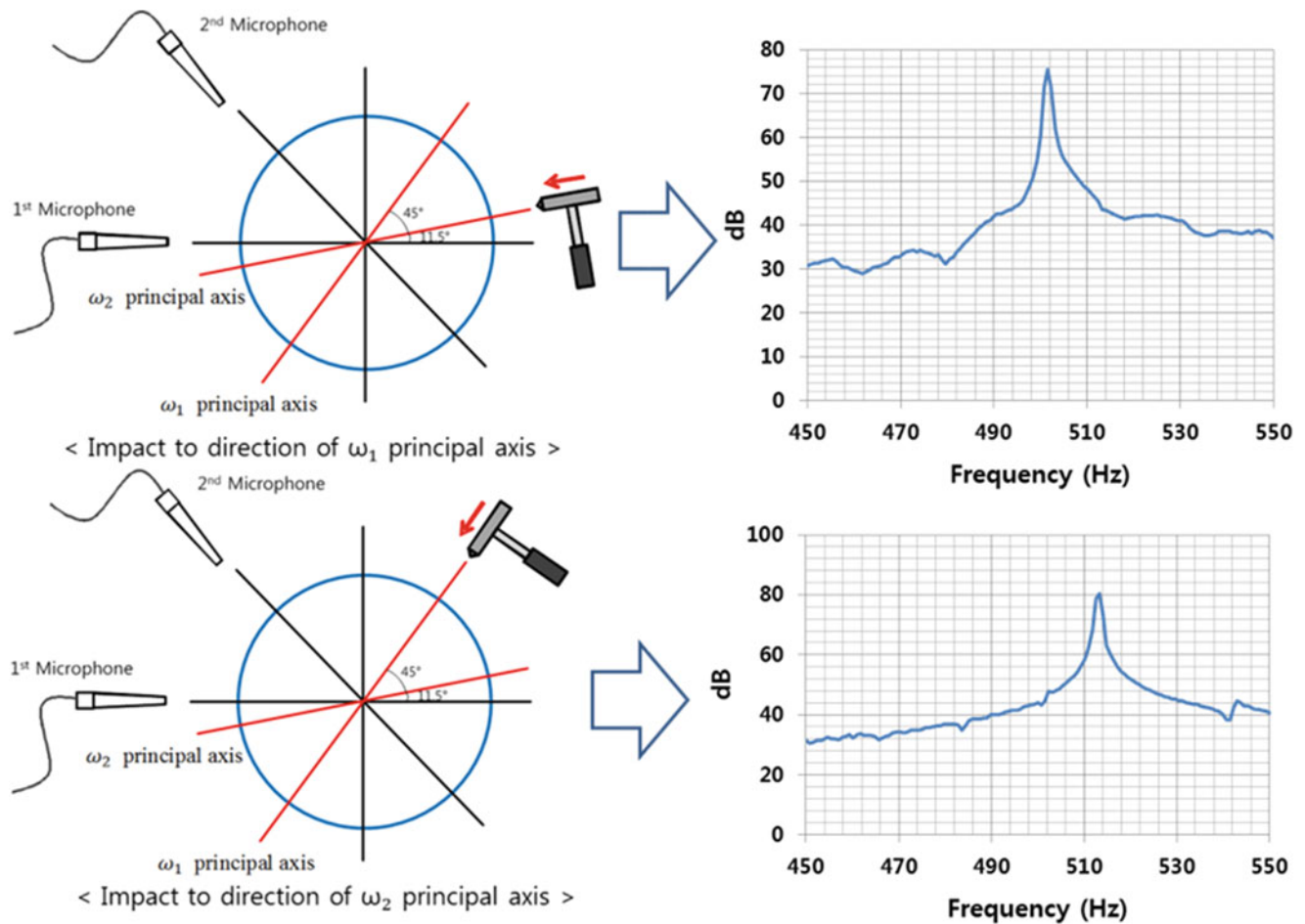
Fig. 24.5 Impulse excitation response along the principal axes calculated by the proposed method

References

1. IEEE Standard #528-2001 for inertial sensor terminology (2001) IEEE Aerospace and Electronic Systems Society
2. Bryan GH (1890) On the beats in the vibrations of a revolving cylinder or bell. Proc Camb Philos Soc VII:101–111
3. Sarapuloff SA, Kisilenko SP, Iosifov AO (1988) Rotation influence on dynamics of an imperfect hemispherical resonator. Collection of sc. papers on mechanics of gyroscopic systems (MGS). Issue 7. Kyiv, Ukraine. pp 59–66
4. Sarapuloff SA (1993) Stabilization of oscillations under principal parametric resonance in gyroscopic systems with conservative and dissipative couplings. Collection of sc. papers on mechanics of gyroscopic systems (MGS). Issue 12. Kyiv, Ukraine. pp 65–74
5. Lynch DD (1995) Vibratory gyro analysis by the method of averaging. Proceedings of the second Saint-Petersburg international conference on gyroscopic technology & navigation. St.-Petersburg, RF, May 1995. pp 24–25
6. Sarapuloff SA et al (1989) Frequency characteristics of imperfect shell resonator //reporters of the higher education establishments. Ser. Instrument-Making ("Izvestiya VUZov. Priborostroyeniye"), vol. XXXII, No.6. St.-Petersburg. pp 34–40

Chapter 25
Remote Placement of Magnetically Coupled Ultrasonic Sensors for Structural Health Monitoring

Nipun Gunawardena, John Heit, George Lederman, Amy Galbraith, and David Mascareñas

Abstract In this work we develop an intelligent remote sensor placement system for standoff deployment of magnetically coupled ultrasonic sensors for structural health monitoring applications. Currently there exists significant legacy infrastructure that requires monitoring. Sensors often need to be accurately placed in hard-to-reach locations which are exposed to harsh environmental conditions, all while ensuring adequate mechanical coupling between the sensor and the structure. Installing these sensors is a task which is time consuming, expensive, and dangerous. In this paper, we develop an intelligent pneumatic remote sensor placement system meant to be integrated with commercially available multicopters. It is designed to accurately deploy sensor nodes from a standoff distance. To achieve this it will calculate the required trajectory and energy requirements to ensure proper placemen as well as coupling between the node and the structure without damaging the sensor package or the structure in the process. This work leverages recent advances in computer vision and commercially available multicopters to align the remote sensor placement system with the point of attachment on the structure. This technology will reduce the barriers associated with the deployment of large scale sensor networks in the field of structural health monitoring.

Keywords Structural health monitoring • Multicopter • Computer vision • Pneumatic cannon

25.1 Introduction

Structural Health Monitoring (SHM) can be used to detect damage in structures of all types, ranging from large bridges and buildings, to dynamic mechanical structures in aerospace and robotics [1]. There is particular demand to use SHM to monitor the state of our aging national infrastructure. According to the American Society of Civil Engineers' 2013 Report Card for America's Infrastructure, more than 65,000 bridges across the United States are structurally deficient [2]. Many of these bridges require more frequent assessment than the federally mandated bi-annual visual inspection, but both visual inspection and manually installing sensors are expensive and expose workers to considerable risk. When the state of California retrofitted 21 toll bridges with sensors, it cost on average more than $300,000 per bridge [3].

In this paper we propose a novel technique for remotely placing sensor nodes for structural applications using an unmanned aerial system (UAS) coupled with a pneumatic placement device. Recent advancements in computing power, computer vision, and control algorithms for multicopter vehicles have made it possible to package a lightweight, efficient, and low-cost device for deploying sensor packages. By utilizing these technologies, an aerial vehicle could safely and accurately deploy many sensor packages for a fraction of the cost and risk of existing systems. Previous work has been done deploying sensor nodes from a UAS, however the nodes have simply been dropped from the multi-copter [4]. By launching the devices, we can fix the sensor node on the side or bottom of a structure, and we can achieve considerably higher precision in every orientation.

N. Gunawardena • J. Heit
Department of Mechanical Engineering, University of Utah, Salt Lake City, UT 84102, USA

G. Lederman
Department of Civil and Environmental Engineering, Carnegie Mellon, Pittsburgh, PA 15213, USA

A. Galbraith • D. Mascareñas (✉)
Los Alamos National Laboratory, Los Alamos, NM, USA
e-mail: dmascarenas@lanl.gov

UASs have been used previously for Structural Health Monitoring purposes, in particular, visual inspection [5]. Visual inspection is a far simpler application, as the UAS does not have to handle the recoil associated with sensor placement. Visual inspection is not a permanent solution for long term monitoring unless the UAS is dedicated to the particular site.

The device we present in this paper has numerous applications outside of structural health monitoring. Among them are environmental monitoring in inaccessible climates such as near the polar ice caps or active volcanos, monitoring sensitive equipment in the wake of natural disasters like nuclear power plant accidents. In this paper we present our design and simulation of the pneumatic sensor placer, the multicopter and its control system along with testing of the individual hardware and software components. Our short-term (1–2 years) goal is to semi-autonomously deploy and install multiple sensor packages at a distance of 100 m away from the intended target while achieving an accuracy of ± 2 m of the intended target.

25.2   Remote Sensor Placement Device

The proposed remote sensor placement device can best be summarized as an intelligent, pneumatically powered launcher. Pneumatic power was selected for placing sensor nodes because it is relatively simple to modulate the amount of energy used to propel the sensor package. It is also convenient because it simplifies the mechanical design of the system when trying to launch multiple sensor packages during a single flight. The system consists of five main components: the storage tank, charge solenoid, charge tank, firing solenoid, and barrel. The conceptual sequence for propelling the sensor node is as follows. At the beginning of the firing sequence, the storage tank is the only component under pressure. To initiate the firing sequence, the charge solenoid is opened while the firing solenoid remains closed. This allows gas to flow into the charge tank. Once the charge tank is at the appropriate pressure the charging solenoid closes. The firing solenoid then waits for the command to fire the sensor node. Once the firing command is received, the firing solenoid opens, pressurizing the volume behind the sensor package and propels it forward. The abstract diagram of this process is shown in Fig. 25.1.
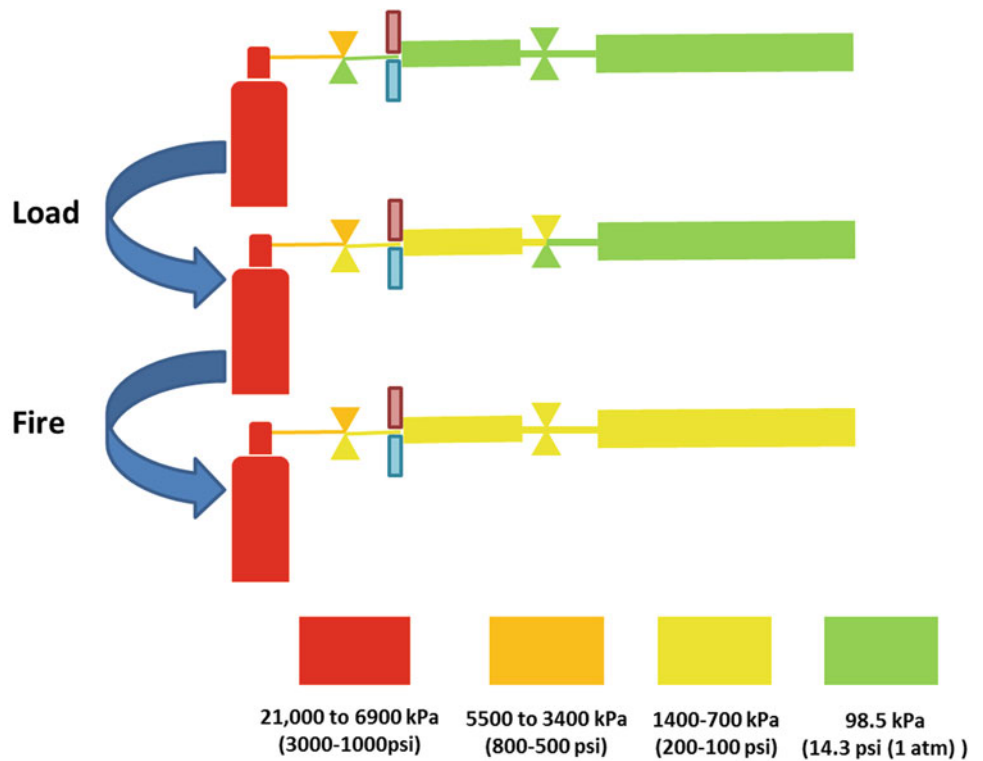
Fig. 25.1 Schematic Firing Sequence of the pneumatic remote sensor placement device

25.3 Internal Ballistics Models

In order to design an remote sensor placement device capable of delivering sensor packages with just the right amount of energy to get them to the appropriate location and install correctly without damaging them in the process requires that we have a solid understanding of how the initial charge tank pressure influences the internal ballistics and exit velocity of the sensor package from the barrel. It also informs the physical design of the gas gun for various sensor sizes, shapes, and weights. In order to put some bounds on the gas gun performance several different models were used to provide information on the internal ballistics. The models were based on isothermal expansion, adiabatic expansion, the work-energy theorem, and Newtonian dynamics [6, 7]. A comparison of predicted sensor package velocity plotted against barrel length for each of the four models is shown in Fig. 25.2. The isothermal model is shown in Eq. 25.1 and Fig. 25.3. This model assumes isothermal expansion of an ideal gas located in a volume directly behind the projectile. The adiabatic model is shown in Eq. 25.2 and Fig. 25.4. This model assumes adiabatic expansion of a diatomic gas located directly behind the projectile. A simple calculation based on the work-energy theorem was used to define the upper bound of the exit velocity. In order to set an upper bound on velocity, the model assumes a constant pressure behind the projectile as it moves down the barrel. All three models make critical assumptions that heavily affect the exit velocity of the projectile. This includes not accounting for the flow constriction of a valve, transients associated with the valve opening, neglecting the volume between the projectile and valve (Fig. 25.5).
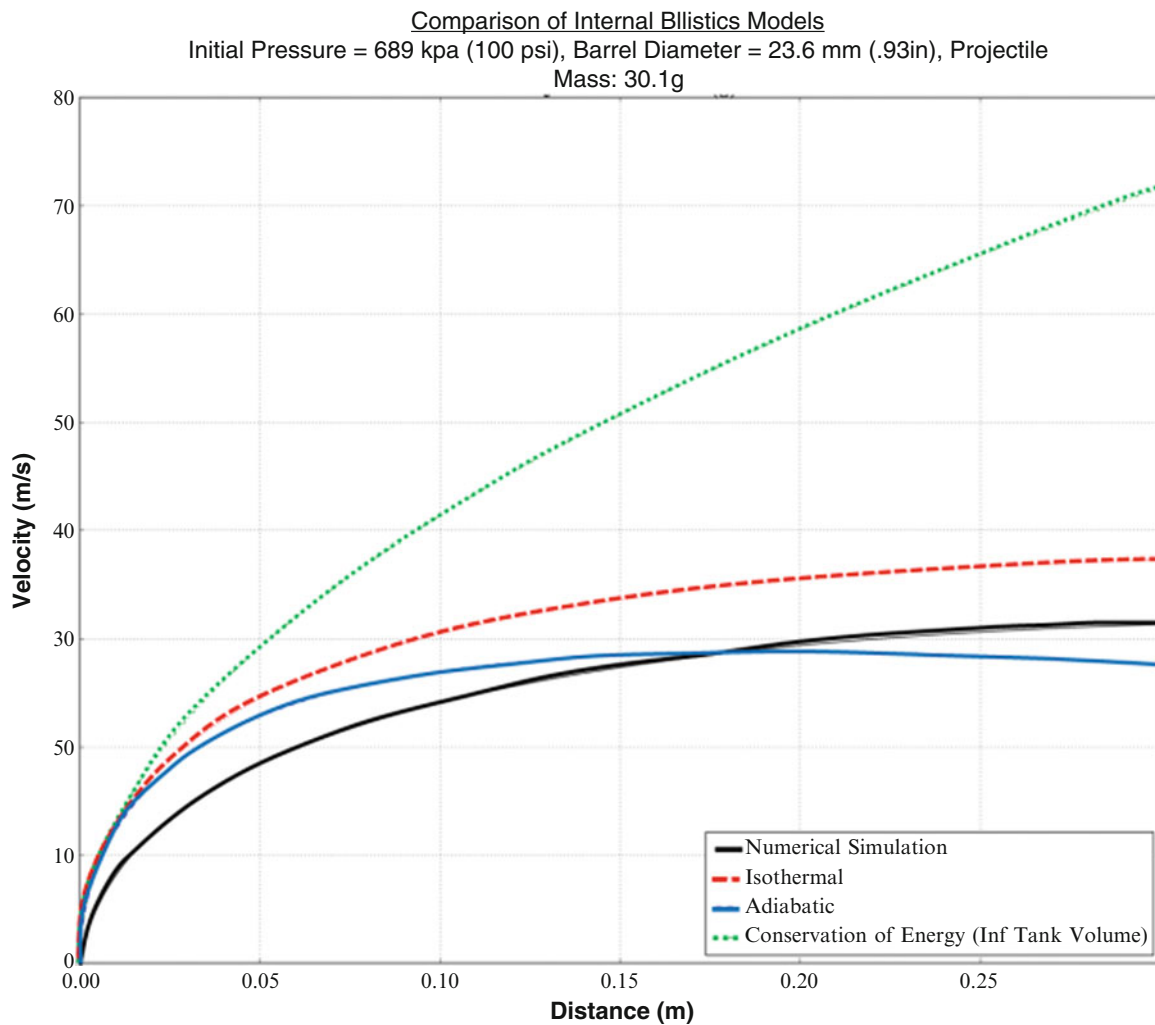
Fig. 25.2 This plot shows the velocity of the sensor package as it travels through the barrel of the remote sensor placement device as predicted by the four internal ballistic models

Fig. 25.3 Diagram for the
Isothermal expansion model of
the gas gun
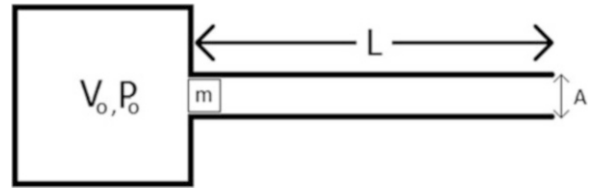
Fig. 25.4 Diagram for the
adiabatic model of the gas gun
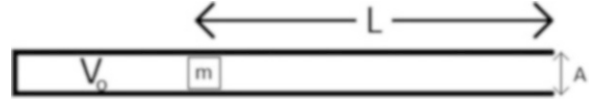
Fig. 25.5 Diagram for the
complete model of the gas gun.
This includes the valve flow
characteristics
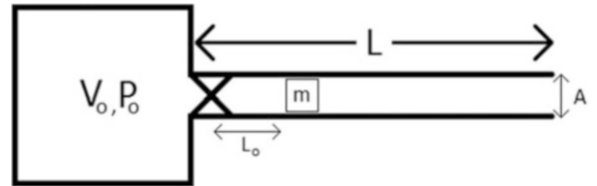
$$V_{is} = \sqrt{\frac{2}{m} * \left(P_o * V_o * \ln\left(1 + \frac{A * L}{V_o}\right) - A * L * P_{atm} \right)} \tag{25.1}$$

$$V_a = \sqrt{\frac{2}{m} * \left(\frac{P_o * V_o}{\gamma - 1} * \left(1 - \left(\frac{V_o}{A * L + V_o}\right)^{\gamma - 1}\right) - A * L * P_{atm} \right)} \tag{25.2}$$

To account for some of the assumptions made in the other models an expanded version of the Newtonian model used in
[7] was implemented. The system was defined by a set of eight first order differential equations. The Eqs. 25.3–25.10 can be
numerically integrated for each of the eight states in time.

$$\dot{X}_p = V_p + V_q \tag{25.3}$$

$$\dot{V}_p = \frac{A}{m} \left(P_b - P_{atm} - 0.5 * C * \rho * V_p^2 \right) \tag{25.4}$$

$$\dot{P}_b = \frac{Q * K * T - P_b * A * V_p}{A * (L_o + X_p)} \tag{25.5}$$

$$\dot{P}_t = -\frac{Q * K * T}{V_p} \tag{25.6}$$

$$\dot{N}_b = Q \tag{25.7}$$

$$\dot{N}_t = -Q \tag{25.8}$$

$$\dot{X}_q = V_q \tag{25.9}$$

$$\dot{V}_q = -\frac{A}{m} * (P_b - P_{atm}) \tag{25.10}$$

Where the states X_p and V_p are the position and velocity of the projectile, P_b and P_t are the pressures in the barrel and tank, N_b and N_t are the number of molecules in the barrel and tank and, X_q and V_q are the position and velocity of the quadcopter.

In Eqs. 25.5–25.8, Q is the molecular flow rate through the valve. This is defined by the piecewise function:

$$If : 2 * P_b < P_t \qquad Q = 0.471 * B * C_v * P_t * \sqrt{\frac{1}{T}} \tag{25.11}$$

$$else : \qquad Q = B * C_v * P_t * \left(1 - \frac{2}{3}\left(1 - \frac{P_B}{P_t}\right)\right) * \sqrt{\frac{\left(1 - \frac{P_b}{P_t}\right)}{T}} \tag{25.12}$$

Here C_v is the solenoid valve flow coefficient. To account for the transient of the solenoid valve a linear function was assumed for the flow coefficient defined as:

$$If \ t < t_c : \qquad C_v = C_{vm} * \frac{t}{t_c} \tag{25.13}$$

$$Else : \qquad C_v = C_{vm} \tag{25.14}$$

The remaining constants are defined as follows: A is the cross sectional area of the projectile, m is the mass of the projectile, C is the coefficient of drag, ρ is the density of air, K is the conversion factor from L/min to Molecules/second, T is the temperature of the air, L_0 is the initial distance between the projectile and valve, and C_{vm} is the maximum flow coefficient of the valve.

25.3.1   External Ballistics Modeling

Once the exit velocity of the projectile is known the external ballistics need to be accounted for in order to successfully predict the flight path. This was modeled with a simple drag coefficient shown in Eq. 25.15.

$$F_d = 0.5 * A * C * \rho * V^2 \tag{25.15}$$

25.3.2   Combine Internal Modeling and Inverse Problem

For the final implementation running on-board the multicopter it would be best if Eqs. 25.3–25.15 did not have to be numerically integrated for each given set of initial conditions. To avoid repeatedly solving the computationally intense equations the equations were numerically integrated offline over a range of initial pressure values beforehand, and curve fit using a simple power function as shown in Eq. 25.16. This power function can then be quickly solved right before the projectile needs to be fired.

$$y = Ax^b + c \tag{25.16}$$

25.3.3   Bench Test Setup

To characterize the system and validate the model of the internal ballistics a bench top prototype of the gas gun was built as shown in Fig. 25.6. We selected lightweight plastic components wherever possible to minimize the final weight of the gas gun. We used Nitra Pneumatic Push to Connect Fittings and Polyurethane Tubing to link the various components, all rated

Fig. 25.6 The initial bench top prototype of the remote sensor placement device
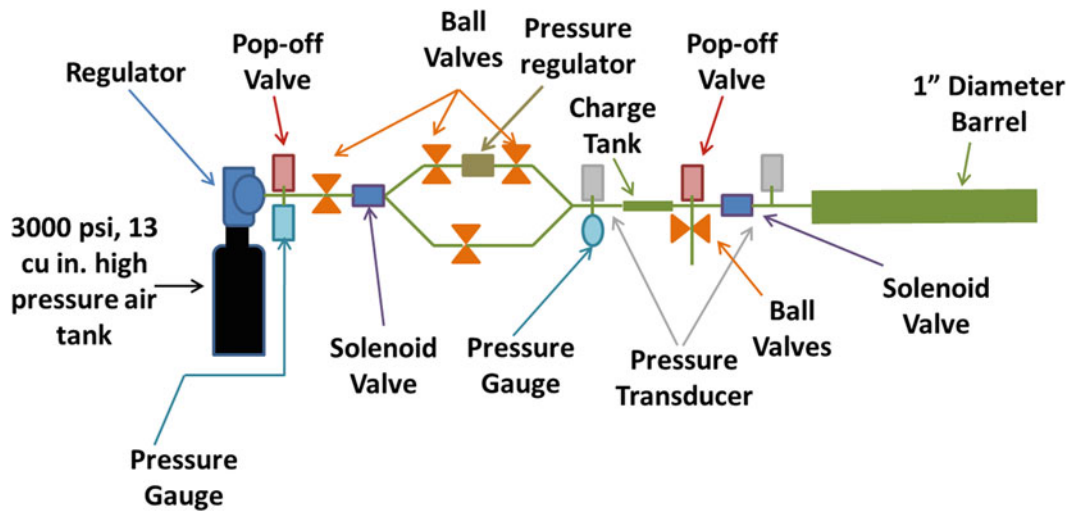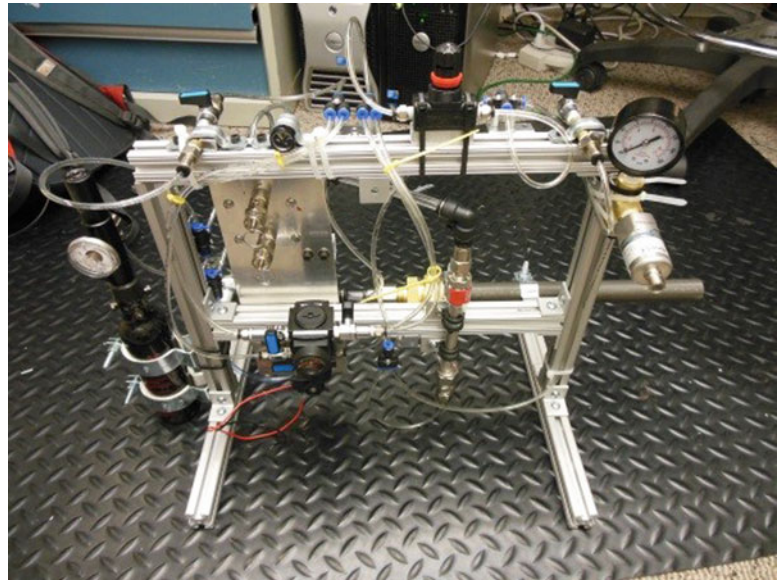
Fig. 25.7 Schematic of the gas gun designed for initial testing and model verification

at 150 psi (1.03 MPa). We used the 2P025 plastic solenoids from Sizto Technology Corporation, Prosense SPT25 pressure transducers from Automation Direct and a pressure regulator rated up to 250 psi from Ingersoll Rand. We wrote a simple interface in PyQT which controlled an Arduino Mega, which in turn measured the output from the pressure transducers and actuated the solenoids.

In this iteration of the gas gun, the charge tank was given two paths through which the charge tank could be pressurized. Figure 25.7 gives a schematic showing the layout. One of the paths contained a pressure regulator, while the other path bypassed this regulator. This allowed for controlling the pressure in the charge tank either with the pressure regulator or by opening the solenoid for a limited amount of time. This allowed us to perform different types of experiments to tune the electro-mechanical-pneumatic characteristics of the remote sensor placement device.

The experimental gas gun was placed inside a testing chamber made of 9.5 mm (3/8″) aluminum plate to ensure that the projectile could be contained. We used the pressure transducers to measure both the rate at which the charge tank filled and discharged, and the chronograph to measure the speed at which the projectile leaves the barrel. To slow down the projectile prior to impact, we placed strips of heavy fabric beyond the chronograph. A 12.7 mm (½″) steel plate was placed at the end of the chamber for additional safety.
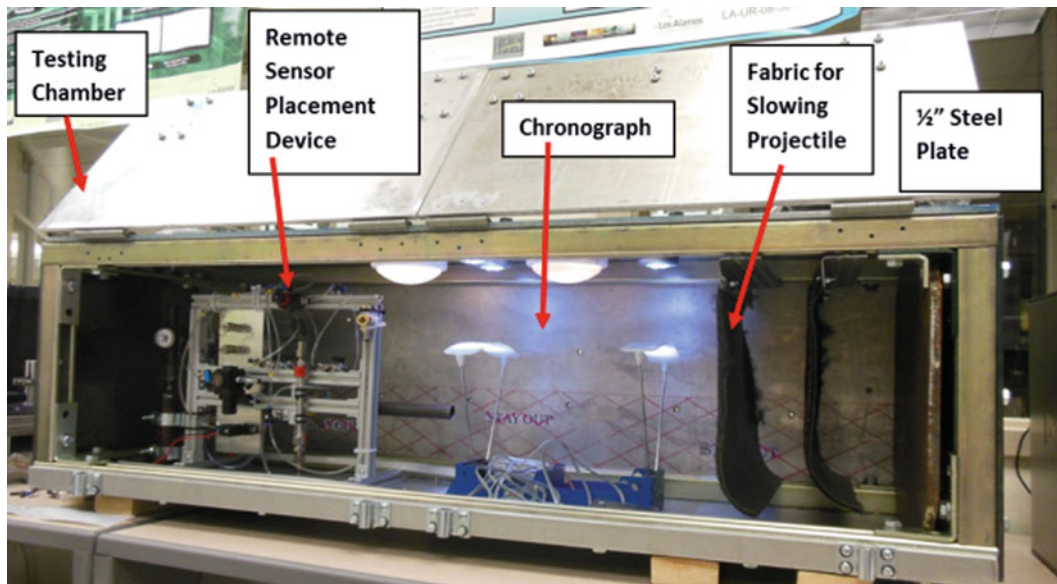
Fig. 25.8 Benchtop remote sensor placement device inside the testing chamber

The sensor package exit velocities achieved by the prototype remote sensor placement device were about an order of magnitude lower than the models predicted. It was determined that this discrepancy was caused by the solenoid valves. As a result of the initial testing the device was redesigned to use a quick exhaust valve rated to 120 psi. After this change was made the resulting velocities were on the same order of magnitude as the models predicted. Future work will give more in-depth information on the performance of the remote sensor placement device (Fig. 25.8).

25.3.4 Sensor Package

We designed an ABS plastic sensor package which could be launched from a $1''$ OD pipe with a neodymium magnetic tip. The magnetic tip was used to provide coupling for an ultrasonic/impedance sensor. This iteration contained a U-blox GPS module, a modified XBee radio, a switch and a lithium polymer battery (Fig. 25.9). The ABS casing was prototyped using a MakerBot 3D printer. The whole package including casing, magnet, electronics, and streamer weighs 21 g. We found that the streaming pink tail shown in Fig. 25.9 provided better inflight stability than a rigid fin type projectile. This streamer also proved a useful feature for the computer vision algorithm to detect the location of the deployed package from the camera on the quadcopter.

25.3.5 Computer Vision

25.3.5.1 Concept

While it is possible to manually control the multicopter during its mission, including autonomous elements in the multicopter control software would reduce operator load significantly. One method of autonomy that can be implemented is object tracking for the purpose of aiming the remote sensor placement device. Once the multicopter is in the general area of interest, the operator can select an object a user interface to direct the multicopter to fly closer to the object autonomously using an object tracking algorithm.
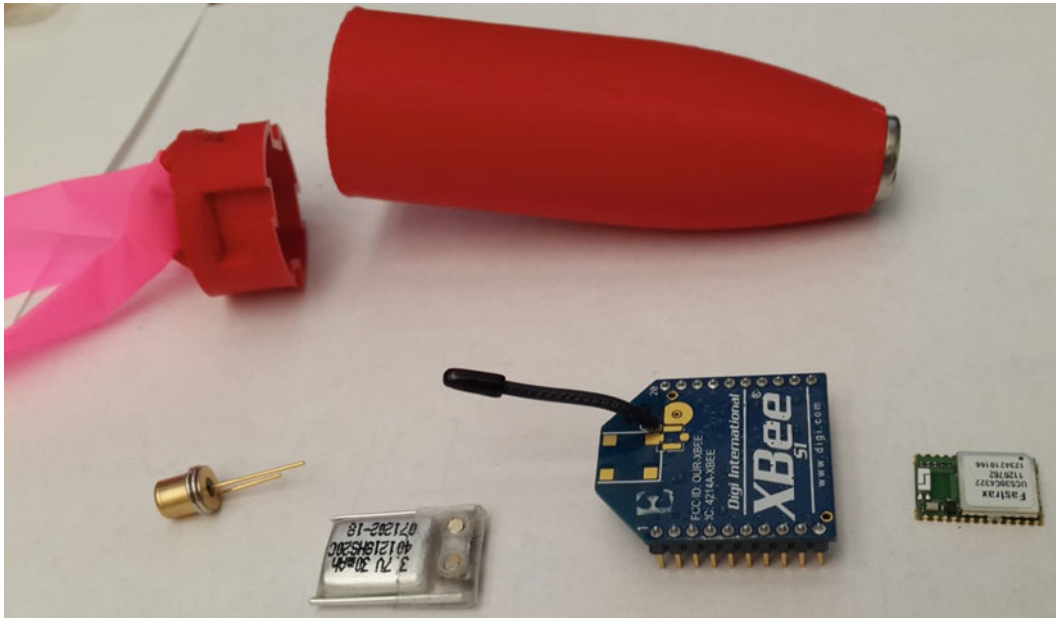
Fig. 25.9 Prototype sensor package with GPS, radio, lithium battery and magnetic switch

25.3.5.2 Object Tracking Methods

There are many different methods that can be used to track objects in real-time video. The criteria for selecting an appropriate method should be based on robustness to large changes in scale as well as shape. It should also be able to run efficiently on low-powered computing systems that can be included on the multicopter. Based on these criteria, the two main tracking methods considered were feature-detection based tracking and color based tracking.

25.3.5.3 Feature Based Tracking

In keypoint detection based tracking, the user selects a region of interest (ROI) within the video frame. From that ROI, features are detected using a feature detection algorithm. The detected features can be corners, edges, or blobs in the image, and will depend on the algorithm used. The detected features are then described using a feature description algorithm. In feature description, the features from the previous step are reduced to a vector that can be easily compared with other features. After the features from the ROI are described and saved, they are compared to the features detected in succeeding frames of the video. Using various norms of the feature descriptor vector, the features can be matched.

While SIFT (Scale-Invariant Feature Transform) and SURF (Speeded Up Robust Features) are the well-known feature detection algorithms [8], FAST (Features from Accelerated Segment Test) was implemented for this application [9, 10]. This was done because FAST is much quicker than SIFT and SURF, and also works better with the FREAK feature descriptor [11]. Once FAST is run on the ROI, the FREAK (Fast Retina Keypoint) algorithm is used to describe the features returned by FAST. SIFT and SURF can also be used as feature descriptors, but FREAK was chosen for its speed. Finally, the feature matching was performed with a brute force matcher comparing the Hamming distance of each vector.

Unfortunately, the results from the feature-based matching were less than satisfactory. There are many reasons for this. First, when using the OpenCV libraries, the FAST/FREAK combination produced a large amount of false-positive matches. Even if this problem were to be fixed, there would still be other problems. While FAST and FREAK are relatively scale invariant, they are not scale invariant to the extent that this application requires. Since the features detected on the target are the same size regardless of the distance to the target, the features will disappear if the target gets too close to the camera. This also means that any features detected on small targets will be few in number. Finally, there are hardware limitations on feature-detection algorithms. Feature detection algorithms can be slow on a desktop computer with high-resolution video; they will definitely be slow on the embedded systems included on the multicopter. Feature detection algorithms are also

Fig. 25.10 Image processing
chain for tracking targets
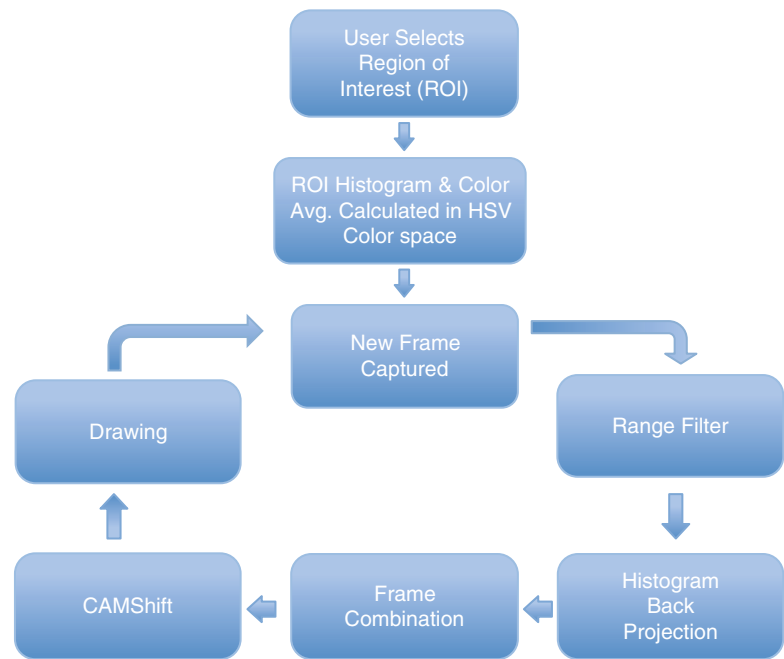
easily affected by blur, which can be introduced into the image through slow autofocusing, fast movements, or vibrations. All three of those are modes that can be expected at some point on the multicopter. Due to these reasons feature based tracking had to ultimately be abandoned.

25.3.6   Color Based CAMShift Tracking

Since feature based tracking did not work, focus was shifted to color based tracking with the aid of Continuously Adaptive Meanshift (CAMShift). As before, the user selects an ROI from the video. The ROI is converted to the HSV colorspace and the mean, standard deviation, and histogram is calculated for the hue and saturation channels. This data is saved for use during the rest of the video. The location of the region of interest is also saved for use in the succeeding frame.

For each frame following the selection of the ROI, a certain number of actions are taken. First, the frames hue and saturation channels are passed through a range filter. In the range filter, any pixel that is greater than one standard deviation away from the mean hue value is marked as a zero, and any pixel within the one standard deviation is marked as a one. This is done to the saturation channel as well. Both binary image outputs are combined using a bitwise-and operation, and the combined image is saved for later use. The purpose of the range filter is to remove any pixels that are obviously not present in the ROI.

After the range filter, a back projection of the frame is calculated based on the ROI. The output of the back projection calculation is a grayscale image the same size as the frame, where the brightness of each pixel corresponds to the probability that the frame pixel was present in the ROI. This is done to the hue and saturation channel of the frame, resulting in two grayscale output images. The two output images are combined using a bitwise-and operation, and then combined with the output of the range filter with another bitwise-and operation. This image is then passed into CAMShift.

The CAMShift algorithm is used to find the "center of mass" and "size" of a group of pixels [12]. The input of camshaft is rectangle containing the group of pixels that need the size and center of mass calculated, and the output is another rectangle centered on the group of pixels. On the first frame that CAMShift is run, the input rectangle is the ROI. On all the succeeding frames, the input rectangle for CAMShift is the output rectangle from the previous frame. In this implementation of CAMShift, the combined output from the range filter and back projection supply the group of pixels to be tracked. Once the CAMShift output is calculated, the tracked object location and size is known. This information can be used to draw a marker on the frame for operator inspection, and/or control the Quadcopter. An algorithm flowchart can be seen below in Fig. 25.10. Figure 25.11 shows an example of the tracker being used on data collected at the testing site.

Fig. 25.11 CAMshift Demo demonstrated on data collected at the testing facility

25.3.7 Algorithm Improvements

Since the CAMShift algorithm only needs a group of pixels to operate on, its effectiveness depends on how well the filtering steps that precede it can turn the object of interest into a group of pixels [12]. This means that possible improvements are made on the filtering steps. For example, if there are many colors present in the region of interest, the hue standard deviation will be large, leading to an ineffective range filter. Adding steps to account for multiple colors will improve the range filter, which in turn will improve the tracking.

Another way to improve the image that is passed into CAMShift is by changing the way the filtered frames are combined. As of now, all output frames are combined using a bitwise-and operation. If a better way to combine the frames was devised, the tracking could be improved.

25.3.8 Implementation Improvements

The tracking algorithm has been implemented on a desktop computer utilizing OpenCV in C++ with acceptable performance. It has also been implemented on a Samsung Galaxy S4 Android phone using OpenCV for Android. Since the phone is what will actually be on the multicopter, it is important for the tracking algorithm to run efficiently. As of now, when running at 1920×1080 resolution, the tracking algorithm runs at approximately three frames per second. However, as the resolution is lowered, the frame rate increases, and 15 fps can easily be achieved. There are a couple options to make the algorithm more efficient: improve the algorithm, and make the android implementation more efficient. Adding more memory management to the code will speed up the tracking process.

25.4 Multicopter

25.4.1 Control

All computing for this device is done onboard, with the ultimate goal being a fully autonomous senor placement system. For our master computer we used a Samsung Galaxy S4 smartphone. We captured images from its camera and ran the computer vision algorithms directly on the phone. To control the flight of the UAS we used an ArduPilot APM 2.5 along

Fig. 25.12 Tuning the PID loops with the multicopter inside a safety cage
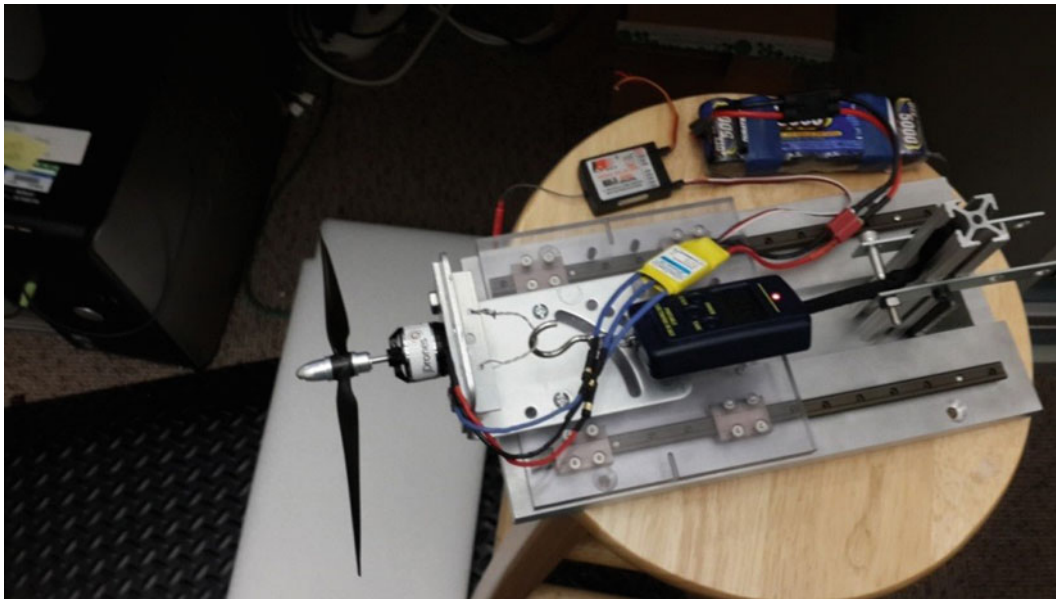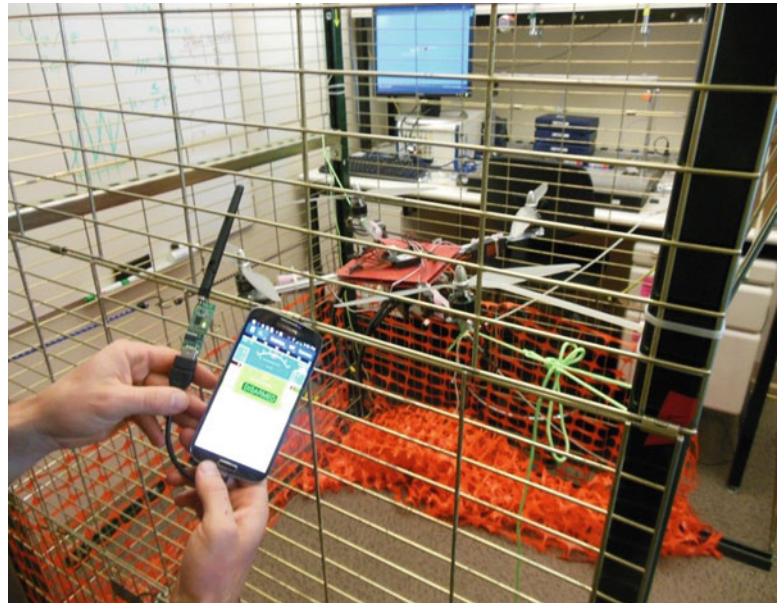
Fig. 25.13 Test setup to measure the lift capacity of motor and propeller combinations

with its inertial sensors, compass and UBlox GPS module. This device communicated with a base station computer through a 915 MHz wireless telemetry kit, and to a FS-TH9x transmitter through the FS-TH9x's dedicated receiver. To control the pneumatic placer, we used an Arduino Mega 2560 board. Together, these three devices (Galaxy S4, ArduPilot and Arduino Mega) formed the intelligence of our remote sensor placement system.

The response of the multicopter to a transient load was simulated using Corke's Robotics Toolbox [13]. A safety cage was built for the purpose of providing a space to tune the multicopter PID loops used in the Arducopter autopilot. Based on the initial tuning we expect the pre-set conditions for the Arducopter are suitable for the expected loads, although additional adjustment may be required when the remote sensor placement device is mounted to the quadrotor (Fig. 25.12).

During the multicopter design phase it was also necessary to characterize the propellers and motors in order to get some idea of the lifting capability of the multicopter. A test fixture was built to measure the thrust from each motor configuration using a digital fish scale (Fig. 25.13). We tried a smaller and larger motor, along with a variety of propeller sizes. The results are shown in Table 25.1. The smaller motor was the most power efficient in terms of thrust to power ratio. In our particular

Table 25.1

Blade size (in.)	Motor mass (g)	Current (A)	Voltage (V)	Power (W)	Thrust (N)	Thrust to weight (N/g)	Thrust to power (N/W)
10	105	6.8	7.8	53.0	3.53	0.034	0.067
14	360	27	15.6	421	15.7	0.044	0.037
16	360	44	15.6	686	24.5	0.068	0.036

application, we are not concerned with flight time, so we selected motor configuration based on the thrust to weight ratio of the motor itself. For our battery we selected a 7800 mAh 5 cell lithium polymer battery (18.5 V) from Thunder Power RC with a mass of 858 g.

25.5   Conclusion

This paper presents the initial design work toward building a remote sensor placement device. This is part of a larger ongoing research effort. This project epitomizes system-level engineering; the selection and integration of various software and hardware packages to achieve a unique sensor placement capability. Although we tried to use off the shelf components wherever necessary, often we had to modify components (e.g. cutting off parts of the XBee radio to decrease its size) so that they would work in this unusual application. Similarly when dealing with the software, some traditional tracking algorithms were too slow to run on the Android so we opted for the more efficient color tracking algorithms, then we optimized the algorithms for our needs.

Future work on this system will focus on testing and tweaking the system for better operational behavior. Progress could be made by increasing accuracy of the pneumatic placer by perhaps adding a gimbal, and increasing the number shots that can be fired on one flight. Additionally, progress could be made on improving up the computer vision algorithms to increase reliability and speed.

Ultimately we believe that this device may become integral in the installation of many monitoring systems. It will offer precise and economical placement of sensors in a rapid and scalable fashion. This device will facilitate widespread sensor deployment to collect more information about the physical world.

References

1. Farrar C, Worden K (2013) Structural health monitoring: a machine learning perspective. Wiley, New York
2. ASCE (2013) 2013 Report card for America's infrastructure. http://www.infrastructurereportcard.org/bridges/. Accessed 14 Aug 2013
3. Kottapalli VA, Kiremidjiana AS, Lynch JP, Carryerb E, Kenny TW, Law KH, Leia Y (2003) Two-tiered wireless sensor network architecture for structural health monitoring. Smart Struct Mater. doi:10.1117/12.482717
4. Corke P, Hrabar S, Peterson R, Rus D, Saripalli S, Sukhatme G (2004) Autonomous deployment and repair of a sensor network using an unmanned aerial vehicle. IEEE international conference on robotics and automation, New Orleans, 26 Apr–1 May
5. Lattanzi D, Miller G (2013) A prototype imaging and visualization system for robotic infrastructure inspection. ASCE Structural Engineering Institute's Structures Congress, Pittsburgh, PA, 2–4 May
6. Mungan C (2009) Internal Ballistics of a pneumatic potato cannon. Eur J Phys 30(3):453–457
7. Rohrbach Z (2012) Modeling the exit velocity of a compressed air cannon. Am J Phys 80:24–27
8. Yilmaz A, Javed O, Shah M (2006) Object tracking: a survey. ACM Comput Surv 38(4):7–9
9. Rosten E, Drummond T (2005) Fusing points and lines for high performance tracking. Tenth IEEE international conference on Computer Vision, ICCV 2005 2:1508–1515
10. Rosten E, Drummond T (2006) Machine learning for high-speed corner detection. Computer Vision–ECCV 2006, pp 430–443
11. Alahi A, Oritz R, Vandergheynst P (2012) Freak: fast retina keypoint. Computer Vision and Pattern Recognition (CVPR), 2012 IEEE Conference on
12. Bradski GR (1998) Real time face and object tracking as a component of a perceptual user interface. Applications of Computer Vision, 1998, WACV'98, Proceedings, Fourth IEEE Workshop on
13. Corke P (2011) Robotics, vision and control. Springer, Berlin. ISBN 36412201431

Chapter 26
Modular System for High-Speed 24-Bit Data Acquisition of Triaxial MEMS Accelerometers for Structural Health Monitoring Research

Brianna Klingensmith, Stephen R. Burgess, Thomas A. Campbell, Peter G. Sherman, Michael Y. Feng, Justin G. Chen, and Oral Buyukozturk

Abstract A hardware system has been developed to obtain data from multiple MEMS triaxial accelerometers for structural health monitoring research. The system can be easily configured for a single accelerometer or up to as many as 120 triaxial accelerometers with 24-bit data sampled up to a 2 kHz rate simultaneously. The system is modular where each module consists of an electrical board that supports up to eight accelerometers. Each module powers the accelerometers, conditions the analog output from the accelerometers, and performs analog-to-digital conversion. In addition, the module has an FPGA that timestamps and packetizes the digital data. The data from each module is transmitted to a host computer using serial communication through a USB virtual COM port. A LabVIEW application on a host computer logs and processes the data, although any software that can perform serial communication and data parsing, e.g. MATLAB, can be utilized. In the case of a single module with eight accelerometers, a single laptop computer can be used for both electrical power and user interaction making an ideal setup for measurements in the field.

Keywords MEMS accelerometer • Distributed sensor network • 24-bit resolution • Synchronization • LabVIEW

26.1 Introduction

The Massachusetts Institute of Technology Energy Initiative (MITEI) Distributive Sensing program is a collaboration between MIT CSAIL and MIT Civil Engineering and Draper Lab to develop a cutting edge structural health monitoring system for the oil and gas industry.

Draper's role was to implement a ∼100 MEMS accelerometer network for a laboratory-scale structure. The MIT teams focused on damage detection algorithms and helped develop the requirements for the accelerometer network such as sampling rate. MEMS accelerometers were chosen over integrated electronic piezoelectric (IEPE) accelerometers for their low cost and low power. The laboratory-scale structure is shown in Fig. 26.1, and the Draper accelerometer package is shown in Fig. 26.2.

This paper will focus on the MEMS accelerometer network.

26.2 Requirements and Network Architecture

The MEMS accelerometers were the STMicro LIS344ALH triaxial accelerometer incorporated into a Draper designed and built package. This accelerometer had a specified noise density of 50 $\mu g/\sqrt{Hz}$; we chose a 1 kHz bandwidth (0–1 kHz), so the noise would be 1.6 mg which dictated a 24-bit analog-to-digital resolution requirement. Based on the

B. Klingensmith • S.R. Burgess • T.A. Campbell • P.G. Sherman • M.Y. Feng (✉)
The Charles Stark Draper Laboratory, Inc., 555 Technology Square, Cambridge, MA 02139, USA
e-mail: mfeng@draper.com

J.G. Chen • O. Buyukozturk
Department of Civil & Environmental Engineering, The Massachusetts Institute of Technology, 77 Massachusetts Avenue, Cambridge, MA 02139, USA

Fig. 26.1 Laboratory-scale structure with MEMS accelerometer network installed. Each structural member is 60 cm in length; therefore, the structure's dimensions are 180 cm height by 120 cm width by 60 cm depth
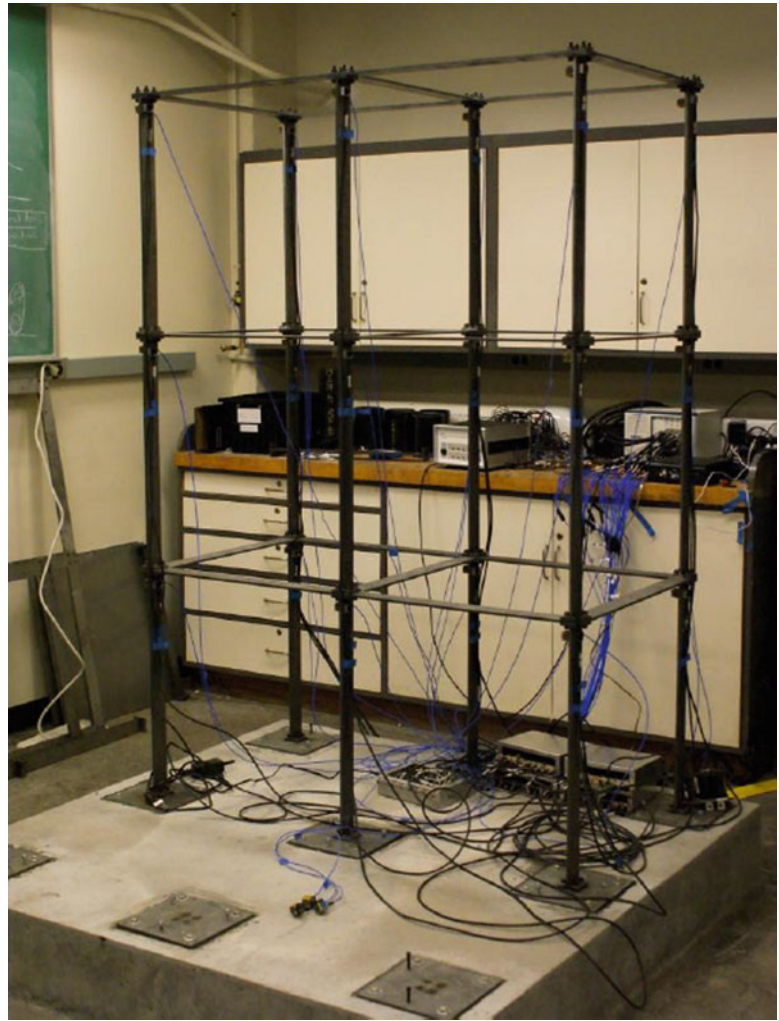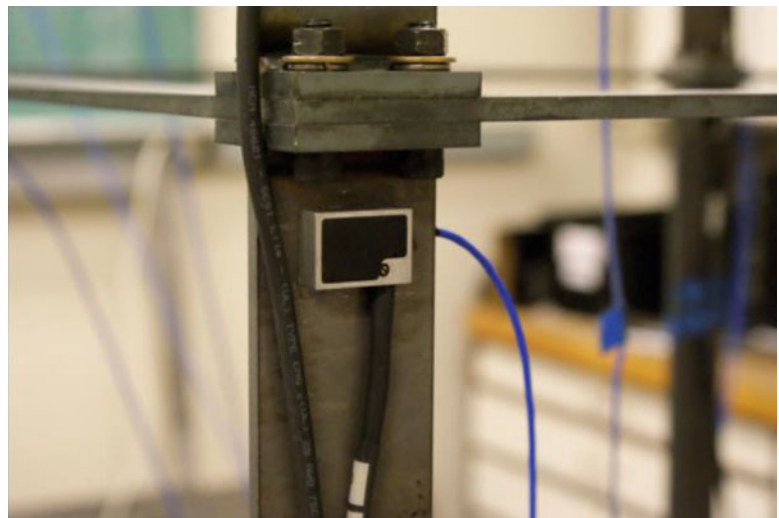

Fig. 26.2 Draper accelerometer assembly installed on lab structure

largest laboratory structure configuration planned, the network had to accommodate up to 120 triaxial accelerometers. To measure the propagation of waves through the structure, accelerometer outputs were synchronized to within 0.1 ms. Lastly, the MIT CEE team established the requirement to monitor structural modes up to 1 kHz necessitating a sampling rate of at least 2 kHz per channel. These requirements are summarized in Table 26.1.

Table 26.1 Requirements

	Value	Driver
ADC resolution	24-bit	ADC resolution to be below noise floor of accelerometer
Sampling frequency	2,000 Hz	Sense modal frequencies up to 1 kHz
# of triaxial accelerometers	120	Size of laboratory structure
Data synchronization	0.1 µs	Sense mechanical wave propagation across structure
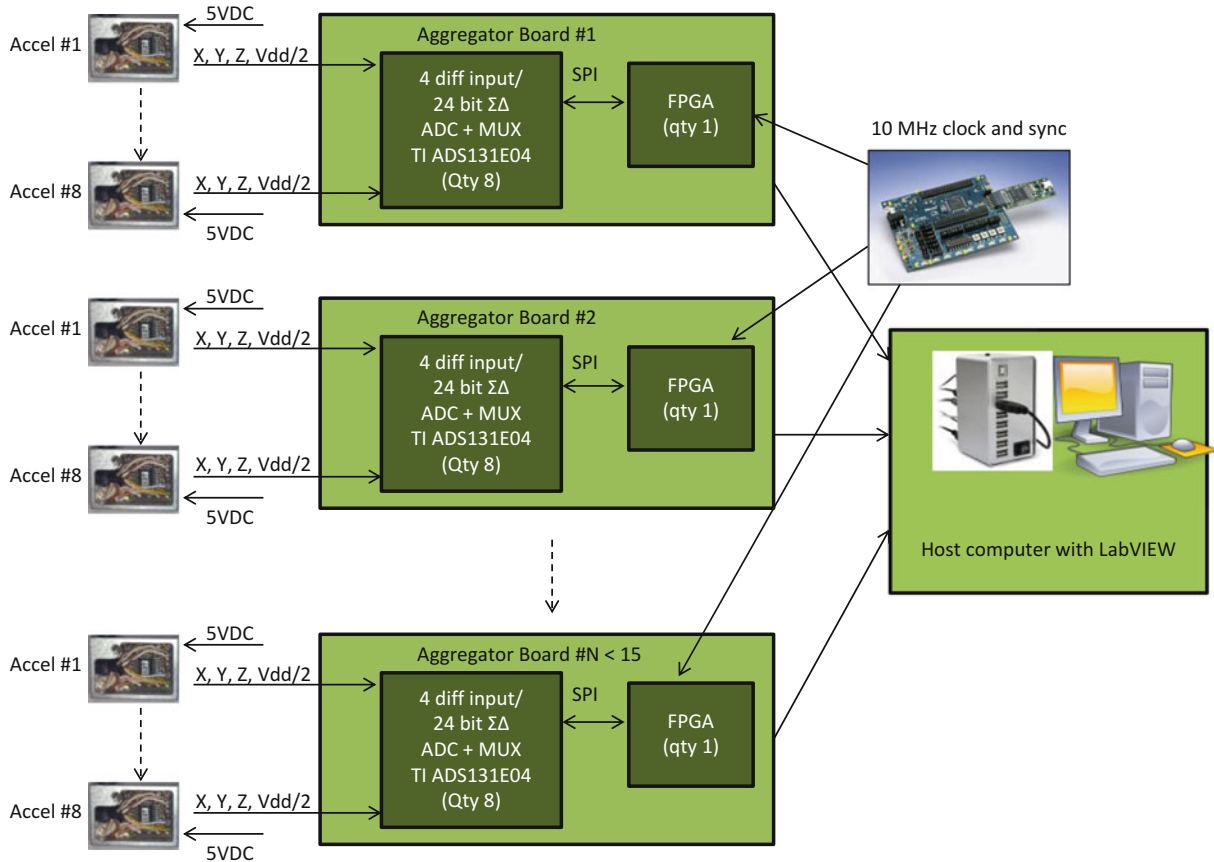
Fig. 26.3 Modular architecture for accelerometer network. Each aggregator board accommodates eight accelerometers and can be added to grow the size of the network. Single clock for data synchronization is also shown

To meet these requirements, we developed a modular architecture where the basic building block was a custom electronics board called the MITEI Aggregator Board. The MITEI Aggregator Board conditions and digitizes 3-axis analog accelerometer signals from up to eight accelerometers. The digitized accelerometer data is then time stamped, packetized, and transmitted via USB 2.0 to a host PC for analysis. To network more than eight accelerometers, two or more aggregator boards are timed with a single 10 MHz clock for synchronization, and each aggregator board connects to the host PC separately via an individual USB2.0 cable. We tested a network size of 15 aggregator boards, i.e. 120 accelerometers, although this is not necessarily the upper limit. However, USB limitations and PC limitations on handling the data flow, i.e. writing the data to files quickly enough, eventually limit the network size. This architecture is depicted in Fig. 26.3.

26.3   Aggregator Board Overview

The fundamental building block of the modular network system is the aggregator board which is comprised of three sections:

- an analog front end section,
- an analog-to-digital converter (ADC) section,
- and a digital section composed of an FPGA and a UART/USB bridge.
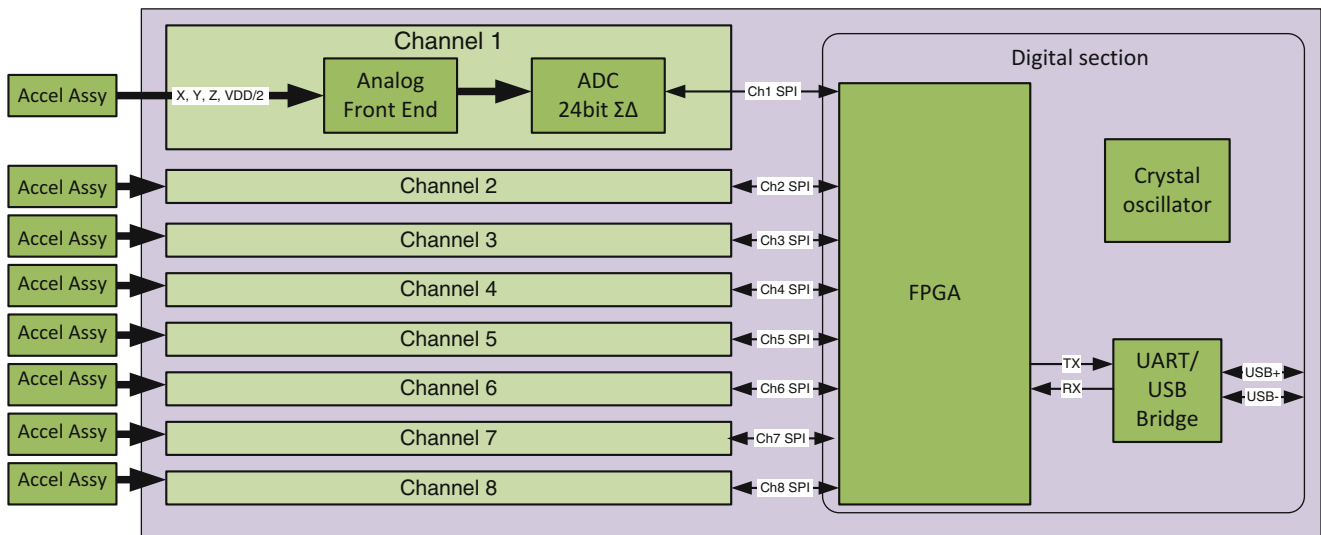
Fig. 26.4 MITEI aggregator board functional block diagram

Each of these sections is shown in the functional block diagram in Fig. 26.4.

There are eight individual subsections of the analog front end channel, one per accelerometer assembly. Each front end subsection receives signals from each axis (X, Y, Z) as well as a common reference signal (Vdd/2) from its respective accelerometer assembly. It provides scaling, single ended to differential conversion, and filtering of each signal.

There are also eight individual subsections of the ADC section. Each subsection consists of a 4-channel, differential, 24 bit delta-sigma, simultaneous sampling analog-to-digital converter integrated circuit (IC) along with supporting electronics. Each subsection digitizes the analog signals output from the front end.

Lastly, the digital section consists of one FPGA, its supporting electronics, a crystal oscillator and a UART/USB bridge IC. This section is responsible for controlling analog-to-digital conversion, aggregating, and transmitting the outputs from all eight ADC subsections to a PC via USB 2.0.

26.4 Front End Section Design

The main requirement of the front end circuitry is the conditioning of the incoming accelerometer signals to take advantage of the full dynamic range of the ADC as well as to filter out as much noise as possible The LIS344ALH accelerometers can sense up to ± 6 g and have a nominal scale factor of 0.22 V/g. This means that the full range of the accelerometer output is from 0.33 V (-6 g) to 2.97 V ($+6$ g), with 0 g at 1.65 V. The ADC IC, the ADS131E04, only accepts inputs between 0 V and 2.5 V.

To fit the accelerometer output into the ADC input range, the front end section scales the accelerometer output. In addition, the front end circuitry provides the inverse of the accelerometer output for use in the differential input to the ADC. This also makes 0 g correspond to 0 V input at the ADC.

Assuming the nominal scale factor of 0.22 V, the front end circuitry converts the acceleration, a, with units of g's to an analog voltage input to the ADC section, $INP - INN$, as follows:

$$INP - INN = 0.3636a$$

which provides an input range of -2.18 V to 2.18 V to the ADC section corresponding to -6 g to $+6$ g.

26.5   ADC Section Design

The ADC section was based on the Texas Instruments ADS131E04 analog-to-digital converter IC. The ADS131E04 contains four separate converters that simultaneously sample its four analog inputs. It is a 24 bit delta-sigma converter that allows selectable data rates from 1 up to 64 kHz, contains a programmable gain amplifier, and operates off of a single 3.3 V supply. It is configured and sampled through a Serial Peripheral Interface (SPI).

26.6   Digital Section Design

The digital section consists of an FPGA (Actel IGLOO AGLN250V2-VQG100), its supporting electronics, a 20 MHz crystal oscillator and a high speed UART/USB bridge (Exar XR21V1410). The FPGA provides sample timing and control to all eight ADC's and processes and packages all accelerometer samples. The FPGA then transmits the packaged data at a predetermined rate in RS422 format to the UART/USB bridge. The UART/USB bridge retransmits the data in USB 2.0 format to a USB hub connected to a PC.

The digital section can use the 20 MHz on-board crystal oscillator as the clock when only one aggregator board is in use or a separate 10 MHz off-board clock that is shared by multiple aggregator boards for data synchronization.

26.7   Noise Measurements

To assess the noise of the system and ensure that all components of the MITEI Aggregator Board remain below the noise floor of the LIS344ALH, the following tests were completed:

26.7.1   Front End Breadboard Noise

Before fabricating the MITEI Aggregator Board, a quick-turn breadboard was designed to assess the pieces of the front end circuitry used to tailor the accelerometer output to the ADC input; it did not include the anti-alias stage. Two sets of noise measurements were taken on the output of each axis of the breadboard. The accelerometer was connected to the inputs of each axis for the first set of measurements and then was disconnected for the second. Figure 26.5 shows the two noise measurements for the X-axis. The Y and Z axis were comparable to X, therefore, they are not shown in the following figure:

The resonant frequency of the accelerometer is 1.8 kHz, and the accelerometer package has a low pass filter with a front 1 kHz cutoff on the accelerometer output. Therefore, the noise was examined at 1 kHz. It is believed that the noise spike near 8 kHz on the breadboard is due to the fact that the op-amps used in the front circuitry are auto-zeroing chopper-stabilizer parts that utilize an oscillator in order to perform the auto-zeroing function. This spike should be greatly attenuated when the anti-alias stage is in place.

The LIS344ALH accelerometer has a nominal noise density of 50 $\mu g/\sqrt{Hz}$ which corresponds to 11 $\mu V/\sqrt{Hz}$ when multiplying by the 0.22 V/g scale factor. The actual test data shows a lower value of 7 $\mu V/\sqrt{Hz}$. This demonstrates that the noise of the front end electronics (excluding the anti-alias stage) should not reach the noise floor of the accelerometer outputs and, therefore, not introduce additional noise into the measured signals.

26.7.2   MITEI Aggregator Board Noise

For the complete MITEI Aggregator Board, two accelerometers were connected to channels 1 and 2 of a single Aggregator Board; both accelerometers were fixed to a mechanically isolated stone slab to minimize input acceleration. Channel 0's X, Y, and Z inputs were shorted to Vdd/2 (1.65 V) corresponding to 0 g. In this configuration, 10 minutes of data were recorded from these three channels at 2 kHz. The noise density values were calculated for channels with and without a sensor attached and are shown in Table 26.2.
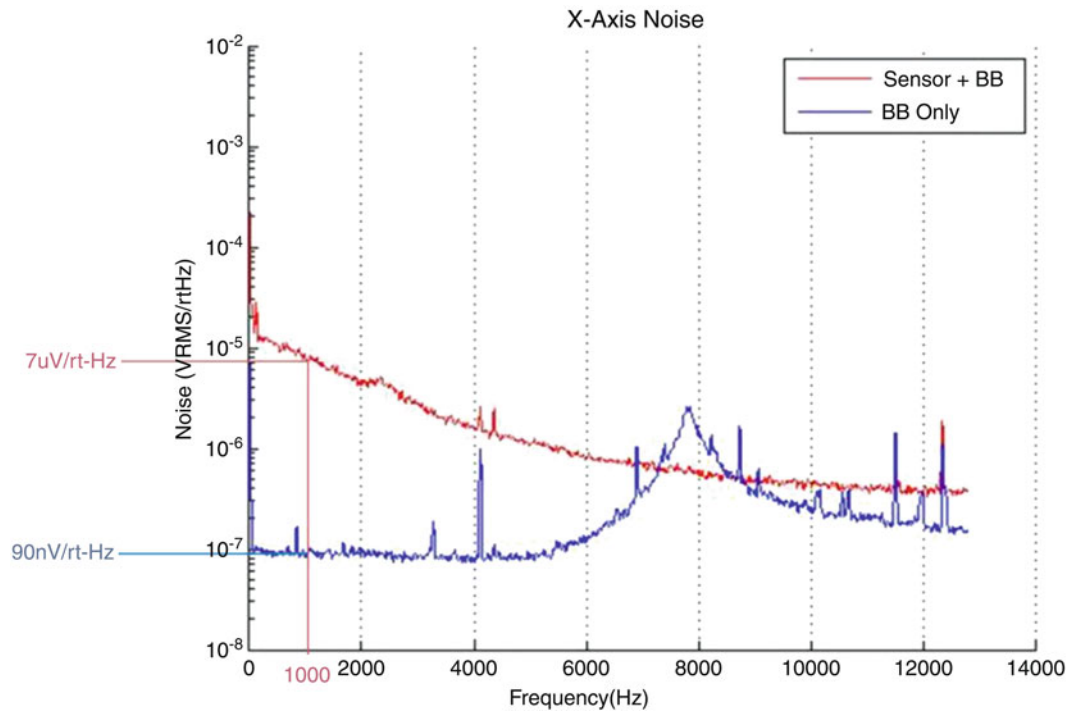
Fig. 26.5 Breadboard front end X-axis noise. *BB*: breadboard

Table 26.2 Calculated noise measurements

System component	Noise density
Breadboard	90 nV/$\sqrt{Hz}$
Breadboard + sensor	7 μV/$\sqrt{Hz}$
Sensor (based on datasheet)	11 μV/$\sqrt{Hz}$
Aggregator board (channel 0)	112.3 nV/$\sqrt{Hz}$
Aggregator board + sensor (ch 1 or 2)	4.17 μV/$\sqrt{Hz}$

For the full aggregator board, the calculated noise density with the sensor disconnected from the electronics is over an order of magnitude lower than with the sensor connected. This demonstrates that the noise of Aggregator electronics (Sects. 26.4–26.6) will not exceed the noise floor of the accelerometer outputs and, therefore, not add noise into the measured signals (Table 26.2).

26.8 Power

The aggregator board only needs 5VDC for power. This can be done in two ways: a power jack that accepts an AC-DC power supply or a modified USB cable plugged into an eight pin connector on the board. The modified USB cable enables a laptop to simultaneously power and host a single aggregator board making it ideal for field use. The following table lists power measurements for a single aggregator board with and without its full complement of eight sensors (Table 26.3).

26.9 LABVIEW GUI for Host PC

Each aggregator board is connected to a single host PC via USB2.0 cables and is recognized as a virtual COM port on the PC. A LabVIEW program reads the data packets being streamed from each aggregator board as serial data and then writes the data to files on the hard drive. Because the aggregator board transmits the data to the host PC as serial data, any software package capable of serial communicable, e.g. MATLAB, can be used on the host PC. The MIT team then accesses the data files on the host PC. Figure 26.6 shows the LabVIEW GUI.

Table 26.3 Power measurements

System component	Power
Aggregator board	775 mW
Aggregator board + eight accelerometers	800 mW
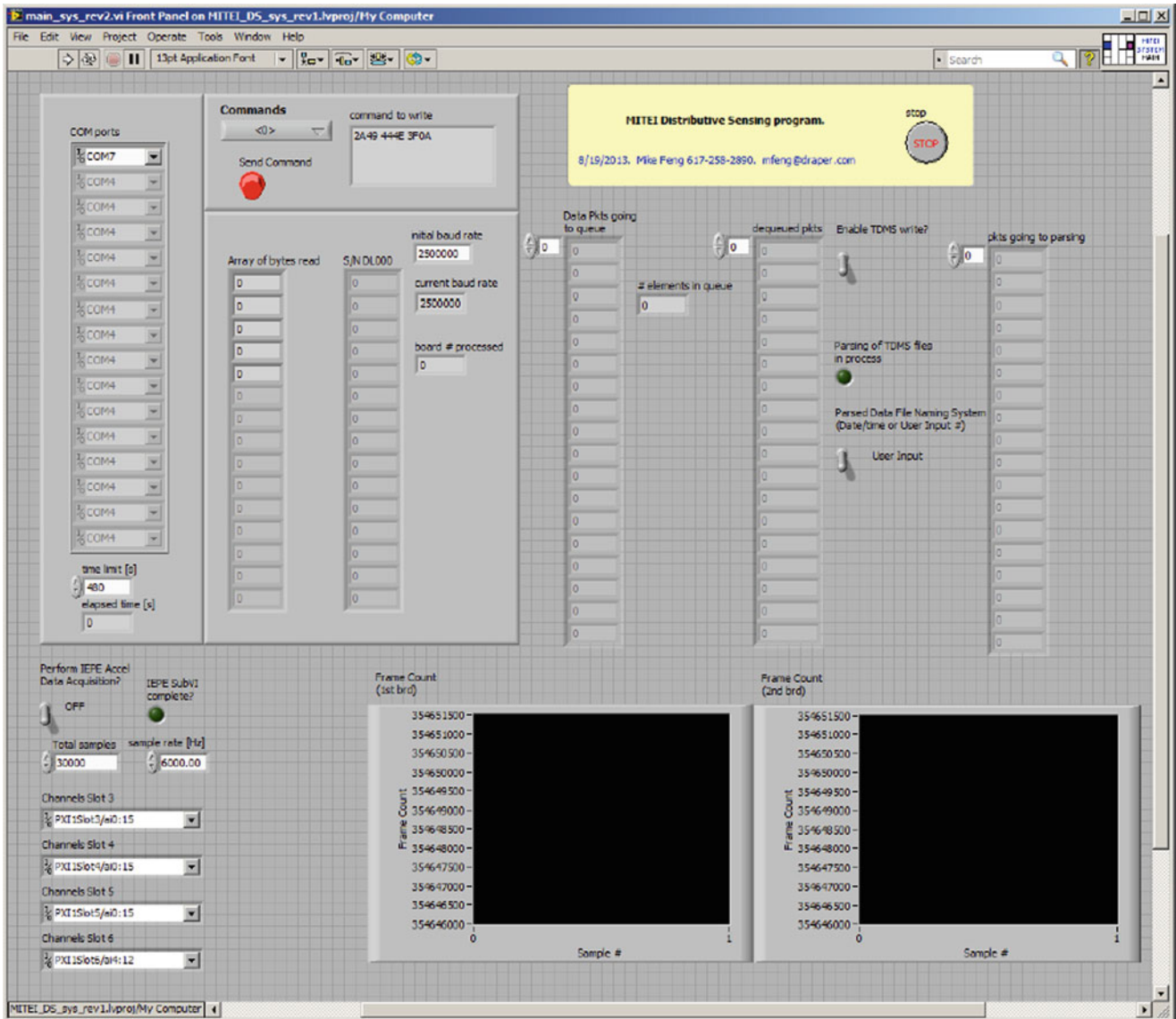
Fig. 26.6 LabVIEW GUI for host PC. Each aggregator board is a separate COM port (*upper left corner*)

26.10   Conclusions

A modular network of up to 120 MEMS accelerometers has been developed around a custom electronics board that features very high 24-bit ADC resolution and 0.1 microsecond synchronization. The selected ADC component also provides simultaneous sampling of all channels. Testing has shown overall noise is only limited by the noise inherent in the MEMS accelerometers. When only a single aggregator board accommodating up to eight accelerometers is in use, a single laptop can supply power and serve as the host PC which is useful for field work. For networks of greater than eight accelerometers,

the network is easily extended by adding multiple aggregator boards up to a total of 120 accelerometers. The aggregator board(s) streams the data to a single host computer where any number of software packages can be used to read the data and write it to a file for postprocessing.

Chapter 27
Mode Shape Comparison Using Continuous-Scan Laser Doppler Vibrometry and High Speed 3D Digital Image Correlation

David A. Ehrhardt, Shifei Yang, Timothy J. Beberniss, and Matthew S. Allen

Abstract Experimental structural dynamic measurements are traditionally obtained using discrete sensors such as accelerometers, strain gauges, displacement transducers, etc. These techniques are known for providing measurements at discrete points. Also, a majority of these sensors require contact with the structure under test which may modify the dynamic response. In contrast, a few recently developed techniques are capable of measuring the response over a wide measurement field without contacting the structure. Two techniques are considered here: continuous-scan laser Doppler vibrometry (CSLDV) and high speed three dimensional digital image correlation (3D-DIC). The large amount of measured velocities and displacements provide an unprecedented measurement resolution; however, they both require post processing to obtain measurements. In this investigation, the frequency response function of a clamped-clamped flat beam will be determined using a modal hammer test, CSLDV, and high speed 3D-DIC. The mode shapes of the beam determined by each of these experimental methods will then be compared to assess the relative merits of each measurement approach.

Keywords Continuous scan laser • Digital image correlation

27.1 Introduction

The development of full-field measurement techniques has received much attention as the design of high-performance light weight structures has advanced. There is an increasing need for experimental techniques capable of measuring the response at a large number of measurement degrees of freedom without modifying the structural response significantly, and techniques such as Continuous-Scan Laser Doppler Vibrometry (CSLDV) and high-speed Three Dimensional Digital Image Correlation (high-speed 3D-DIC) have been developed to meet this need. Both CSLDV and high-speed 3D-DIC are capable of measuring the response at thousands of points across the surface of the test specimen with good accuracy. However, these techniques involve additional processing to extract velocities or displacements when compared with traditional measurement techniques.

Measurements from CSLDV are more challenging to process than traditional Laser Doppler Vibrometer (LDV) measurements because in CSLDV, the measurement point is continuously moving during the measurement, so the system must be treated as time-varying. The benefit provided by the continuously moving measurement point is an increased measurement resolution with a drastically decreased measurement time when compared with a traditional LDV measurements, which must remain at a measurement location for a prescribed length of time. Various algorithms have been devised to determine the mode shapes of the test piece along a continuously moving laser scan path. For example, Ewins et al. treated the operational deflection shape as a polynomial function of the moving laser position [1–5]. They showed that sideband harmonics appear in the measured spectrum, each separated by the scan frequency, and that the amplitudes of the sidebands can be used to determine the polynomial coefficients. Allen et al. later presented a lifting approach for impulse response measurements [6, 7]. The lifting approach groups the responses at the same location along the laser path. Hence, the lifted responses appear to be from a set of pseudo sensors attached to the structure, allowing conventional modal analysis routines to extract

D.A. Ehrhardt (✉) • S. Yang • M.S. Allen
Department of Engineering Physics, University of Wisconsin-Madison, 535 Engineering Research Building, 1500 Engineering Drive, Madison, WI 53706, USA
e-mail: dehrhardt@wisc.edu

T.J. Beberniss
Structural Sciences Centers, Aerospace Systems Directorate, Air Force Research Laboratory, Wright-Patterson AFB, Dayton, OH 45433, USA

modal parameters from the CSLDV measurements. Recently, algorithms based on Linear Time Periodic (LTP) system theory [8–11] were used to derive input–output transfer functions from CSLDV measurements allowing virtually any input to be used with CSLDV. These algorithms will be used in this investigation to identify the natural frequencies and modes shapes of a clamped-clamped beam.

Displacements measured with 3D-DIC are challenging to obtain since each individual measurement point has to be matched in each image from each camera for the duration of the experiment. For sample rates greater than 100 fps, this requires an additional step of post processing. Schmidt et al. [12] presented early work on the use of high-speed digital cameras to measure deformation and strain experienced by test articles under impact loadings. Tiwari et al. [13] used two high-speed CMOS cameras in a stereo-vision setup to measure the out of plane displacement of a plate subjected to a pulse input. Results compared favorably with work previously published and showed the capability of the 3D-DIC system in a high-speed application, although over a short time history. Niezrecki et al. [14], Helfrick et al. [15], and Warren et al. [16] obtained mode shapes using 3D-DIC with different test articles using discrete measuring points. Niezrecki et al. and Helfrick et al. also combined accelerometers, vibrometers, and dynamic photogrammetry to compare results obtained with DIC analyzed at discrete measurement locations. Each technique provided complimentary between all measurement techniques showing the capability of 3D-DIC, although 3D-DIC was not processed along the entire surface. Since 3D-DIC has the capability to measure hundreds of 3D displacements on a surface, a further comparison can be made with full field measurements; however handling the large amount of data in conjunction with the image files can prove to be difficult.

In this investigation, CSLDV and high-speed 3D-DIC are used to measure the linear dynamic response of a 9″ mild steel clamped-camped beam. For comparison, the response of the specified beam is measured when it is excited with a steady state sinusoid at the first three measured natural frequencies and when it is excited with a band limited random excitation from 10 to 800 Hz. To process measurements from CSLDV, both the harmonic transfer function and harmonic power spectrum will be used to identify mode shapes of the clamped-clamped beam under the sinusoidal and random excitation, respectively. Displacements measured by 3D-DIC are processed using a commercial software Aramis [17] and its Real Time Sensor program [18]. In both CSLDV and 3D-DIC, mode shapes and natural frequencies are extracted from the assembled transfer function using peak picking for the steady state excitation and the Algorithm of Mode Isolation (AMI) [19] for the random excitation.

27.2 Measurements

27.2.1 CSLDV Theory/Mode Shape Extraction Description

The CSLDV measurements were acquired using a periodic scan pattern, e.g., a line as shown in Fig. 27.1, so the measurements appear to be from a linear time periodic (LTP) system because the measurement location is moving periodically [19].

In this work, the harmonic transfer function and harmonic power spectrum concepts from LTP systems theory will be employed to process CSLDV measurements in order to extract the modal parameters of the beam. These algorithms are completely analogous to the transfer function and power spectrum of linear time invariant (LTI) systems; both the harmonic transfer function and harmonic power spectrum can be written in a modal summation form in terms of the modal parameters of the clamped beam. Therefore the well-established LTI modal identification routines can be used to process CSLDV measurements.
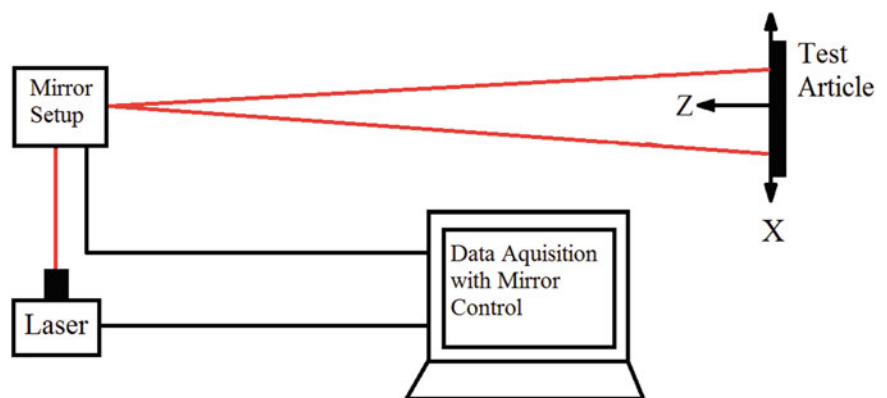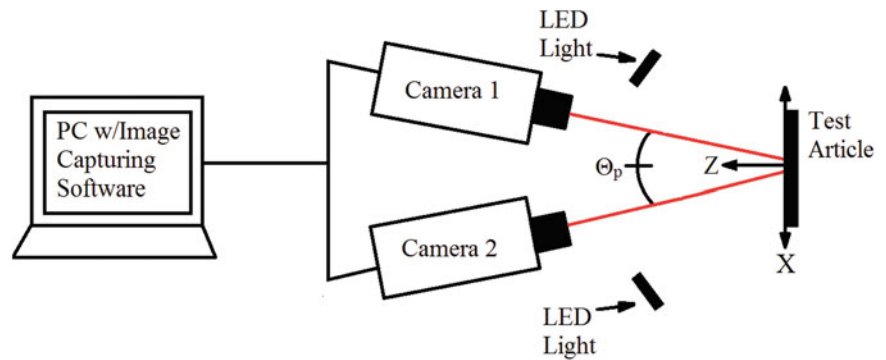

Fig. 27.1 CSLDV system diagram: the laser beam was redirect by a pair of mirror to continuously scan on the test article

Fig. 27.2 3D-DIC system diagram. The 3D-DIC system diagram shows Camera 1 (left camera) and Camera 2 (right camera) set to a specified pan angle, Θ_p

However, there are two notable differences. First, the mode vectors ψ_r of an LTI system describe the spatial pattern of deformation of a mode over the set of measurement points. In contrast, when using CSLDV to measure mode shapes of a structure, one has a moving measurement point. The location of that point is expanded in the processing step so that the mode vectors $\overline{\mathbf{C}}_{r,l}$ end up consisting of a vector of the Fourier coefficients $\overline{C}_{r,n}$ that describe the time periodic spatial deformation pattern along the scan path, $C(t)\psi_r = \sum_{n=-\infty}^{\infty} \overline{C}_{r,n} e^{jn\omega_A t}$, where $C(t)$ is an output vector indicating the location where the response is being measured at any instant, and ω_A is the laser scanning frequency. Second, an LTP system theoretically has an infinite number of peaks for each mode. Each peak occurs near the imaginary part of the Floquet exponent λ_r plus some integer multiple of the fundamental frequency ω_A. If the observed mode shapes $C(t)\psi_r$ are constant in time (the laser is stationary), $\overline{\mathbf{C}}_{r,l}$ would contain only one nonzero term, and the system reduces to the familiar linear time invariant system. Note that one needs to fit a peak to each harmonic of each mode to obtain a best estimate of the mode vector [20].

The harmonic transfer function and harmonic power spectrum are readily derived by defining an exponentially modulated periodic signal and then using the general solution for the response of a linear time varying system. The readers are referred to [19] for more details about the derivation.

27.2.2 DIC Theory/Mode Shape Extraction Description

To accurately measure 3D displacements with DIC, a setup using two cameras is used to image the test article as it deforms. As shown in Fig. 27.2, the two cameras are placed at a specific distance along the Z-axis from the test article to allow the surface to be captured simultaneously in each camera and establish a field of view. A pan angle, Θ_p, is specified based on a desired depth of view or range of out-of-plane displacements expected. Once the stereo camera setup is assembled and fixed, photogrammetric principles of triangulation and bundle adjustment are used to establish each camera's position and the experimental measurement volume by capturing images of a known pattern or calibration panel [21]. With this calibration, displacement accuracy is not limited to the pixel size of the imaged surface of the test specimen, but instead allows for accuracies on the sub pixel level (e.g. 0.01 pixels). Additionally, in-plane deformations are measured with a greater accuracy when compared with purely out-of-plane deformations. Prior to testing, a high-contrast random gray-scale pattern is applied to the measurement surface so facets from each image can be matched. As detailed in [21], triangulation of the facet and surface matching is used to determine the coordinate value of each measurement point.

27.3 Experimental Setup

27.3.1 Beam Description

The device under test for this investigation is a precision-machined flat feeler gauge made from high-carbon, spring-steel in a clamped-clamped configuration. As summarized in Table 27.1, the tested beam had an effective length of 9 in., a nominal width of 0.5 in., and a thickness of 0.03 in. Prior to clamping, the beam was painted with a white base coat and a speckle pattern was applied using a marker to allow for tracking positions with the 3D-DIC system. Once the beam had dried, a strip

Table 27.1 Beam geometric and
material properties

Length = 9 in.	Width = 0.5 in.	Thickness = 0.031 in.
E = 29.7 Mpsi	G = 11.6 Mpsi	Rho = 7.36×10^{-4} lb-s^2/in^4
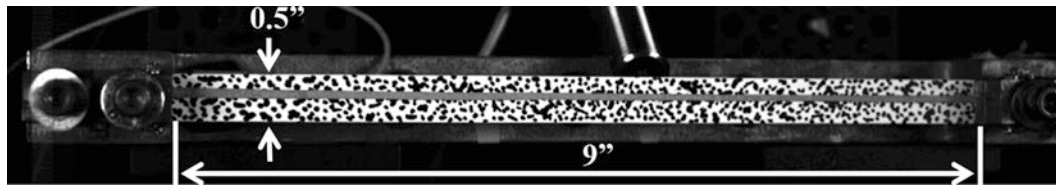
Fig. 27.3 Beam specimen

of retro-reflective tape was added to increase feedback for the CSLDV. The final prepared beam is shown in the clamping fixture in Fig. 27.3. The clamping force was provided by the two 6.35-28 UNF-2B bolts located on the inside of the clamping fixture, which is the same fixture used in [22]. Both inside bolts were tightened to 90 in.-lbs; however, the outer bolts were not tightened to the full 90 in.-lbs due to the noticeable deformation of the beam during clamping. Static 3D-DIC images were captured during clamping to quantify any initial deflection seen. It is noted that the 3D-DIC deformation measurements during clamping are approaching the noise floor of the system for this field of view; however, maximum deformations measured during clamping are below 25 % of the beam thickness. Since 3D-DIC is sensitive to small deformations, the beam was driven at the largest force that allowed a linear response. This force was determined by incrementally increasing the input force level while monitoring damping. When damping increased a measurable amount, the force was decreased to the previous forcing level. The maximum resulting response was 62 % of the beam thickness.

27.3.2 Experimental Setup

Figure 27.4 shows the experimental setup. The continuous-scan mechanisms were built using a Polytec OFV-552 fiber optic laser vibrometer with a sensitivity of 125 mm/s/V and the same external mirror system that was used in [19, 23, 24]. It is worth noting that a fiber optic laser such as this has not been used with CSLDV in any of the authors' previous works. The external mirror system consisted of two galvanometer scanners in closed-loop control; each scanner had a position detector that measured the instantaneous rotational angle, allowing precise and accurate control of the laser position. The control and data acquisition system was built using a National Instruments PXI system. A LabVIEW program was developed to integrate several the features including the function generator, data acquisition, and signal processing.

The 3D-DIC system includes two Photron, high speed 12-bit CMOS cameras (model Fastcam SA5 775K-M3K). Each camera has onboard 32GBs of memory with a maximum resolution of $1,024 \times 1,024$ pixels. For this experimental setup, images of 832×144 pixels were used. All static displacements were calculated using a commercial 3D-DIC software Aramis [17], while dynamic displacements were calculated using a software extension of Aramis called IVIEW Real Time Sensor [18]. In order to minimize the heat generated and remove the 60 Hz noise produced by halogen lamps typically used in high-speed DIC systems, two panel, 100×100 LED lights were used. The cameras and the data acquisition system were simultaneously started using an external TTL trigger.

As previously stated, Aramis in combination with the Real Time Sensor module is used to post-process the images and extract the measured displacements. Due to limited processing time with the 3D-DIC software, only two rows of 41 points along the beam were selected to be processed for this investigation. One row of measurement points is located above the laser scan retro reflective tape shown in Fig. 27.3 and the other is below the tape. A maximum of 2,500 points in a 2D grid across the surface of the beam could have been processed if time permitted. Also, since all images were stored, the data can be reprocessed to obtain a denser measurement grid if needed. A 250 mm × 200 mm calibration panel was used to establish the measurement volume and lead to a calibration deviation of 0.02 pixels or 0.007 mm based on the field of view. To process the displacements, a facet size of 20 pixel × 20 pixel was used. After processing the recorded images and obtaining the displacements, the frequency response function (FRF) was calculated from the auto and cross spectrum determined using the Fourier transform in MATLAB. Using peak picking, the imaginary part of the FRFs for the steady state response was used to determine the mode shapes. AMI was used to extract the mode shapes and natural frequencies from the random response data after 45 averages with a block size of 5,000 samples and a 50 % overlap.

The steady state sinusoidal input was provided by a magnetic driver with a Piezo Amplifier in line with a Wavetek Variable Phase Synthesizer. To measure the force provided by the magnetic driver, a force transducer measured the reaction
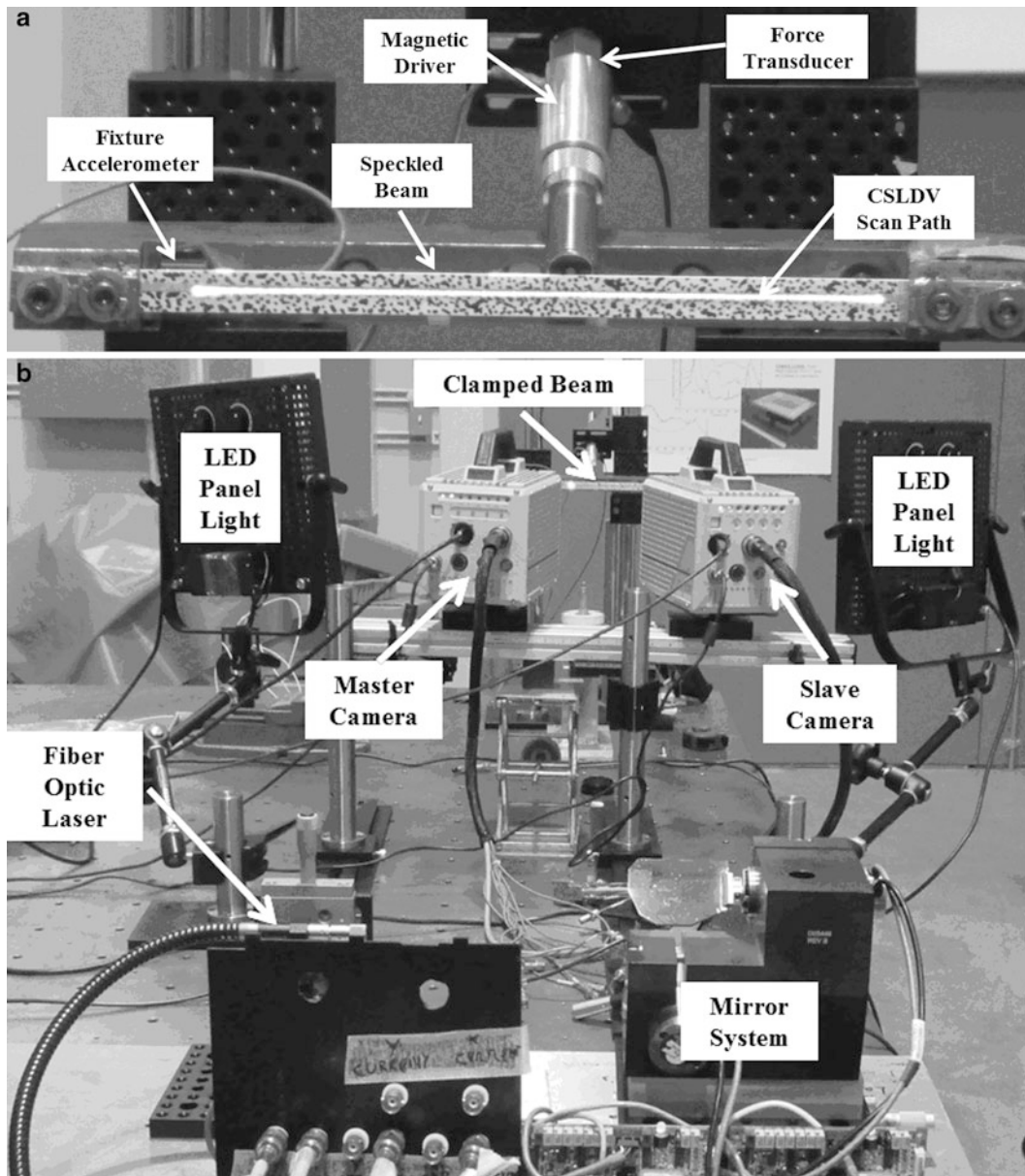
Fig. 27.4 Experimental setup. (**a**) Close up of clamped beam, (**b**) Complete experimental setup

force between the magnetic driver and the frame to which it was mounted. In addition to the steady state experiments at the natural frequencies of the beam, a band limited random excitation was used over the range of 10–800 Hz. The same magnetic driver was used to provide the band limited random excitation.

Prior to sinusoidal and random excitation testing, a modal survey was performed using a modal hammer and a single point laser to establish the natural frequencies and damping ratios of the clamped-clamped beam. The first three identified natural frequencies were used as driving frequencies for the steady state sinusoidal tests. For steady state experiments, the CSLDV system scanned the surface of the beam at 3 Hz with a sampling frequency of 5,120 Hz. The total scan time was 2 min. The high-speed 3D-DIC system captured 40,000 images at 2,000 fps. The total measurement time was 20 s, but an additional 10 min was needed to download the images from the cameras. For the random excitation experiment, the CSLDV system scanned the surface of the beam at 9 Hz with a sampling frequency of 5,120 for a duration of 15 min. The high-speed 3D-DIC system captured 120,000 images at 5,000 fps, and an additional 40 min was needed to download all images from the cameras. The input signals were not recorded in these tests, so the longer time histories used for these tests allowed for more averaging to reduce the noise and variability in the response due to the random input force.

27.4   Results

27.4.1   Modal Hammer Test

A single input and single output modal hammer test was performed on the beam to identify the first three natural frequencies and document any frequency shifts during testing. Pre- and postexcitation modal hammer tests for the steady state sine experiments showed a small frequency shift of 0.5 Hz for the first three modes of the beam. Similarly a frequency shift of 2 Hz, 2.5 Hz, and 3.5 Hz was observed for modes 1, 2, and 3 for the pre- and postexcitation modal hammer tests for the random experiments. Since the temperature difference between the beam and the fixture remained less than 1 °C for all tests, the larger observed frequency shifts in the random excitation experiment were concluded to be a result of a change in boundary conditions, perhaps due to the clamped ends of the beam slightly slipping as it was excited. The clamed beam has been shown to be very sensitive to slight temperature changes [22], which could account for some of the observed shift in natural frequencies. The average of each natural frequency identified with the modal hammer tests was compared with the natural frequencies identified using CSLDV and high-speed 3D-DIC and the results are shown in Table 27.2. The computed MAC values for the mode shapes determined from testing are also shown in Table 27.2, but will be discussed later. The maximum difference between the natural frequencies measured by each method was 2.6 % although most differed by less than 1 %. It is worth noting that the percent difference between the natural frequencies measured with CSLDV and 3D-DIC were within the observed percent change between the pre- and postmodal tests, leading to the conclusion that test setup variability is a major part in the differences between the identified natural frequencies.

27.4.2   Mode Shape Comparison: Sine Dwell Experiments

As previously mentioned, the beam was driven at each of the first three identified natural frequencies and the steady state response was measured using both CSLDV and high-speed 3D-DIC. Figure 27.5a shows an example of the spectrum from the CSLDV signal with the laser scanning at 3 Hz when the beam was driven at 71.3 Hz. The sideband harmonics higher than the 6th order are buried in the noise floor and hence no harmonics above the 6th order were used when construction the mode shape. The harmonic transfer function was computed using $n = -8{:}8$ to assure that all of these harmonics were captured. Figure 27.5b shows the magnitude and phase of the Fourier coefficients obtained by peak picking at 71.3 Hz versus the harmonic order. Note that there is a small phase error (about 0.5°) between any neighboring peaks which could be caused by the mirror phase delay [25]. These Fourier coefficients for harmonics of $n = -6{:}6$ were then used to construct the mode shape along the laser path. The second and third bending mode shapes were reconstructed using the Fourier coefficients for harmonics $n = -10$ to 10 and $n = -15$ to 15, respectively.

Figure 27.6 compares the mode shapes obtained by CSLDV and DIC for the three steady state experiments. Figure 27.6a contains the mode shape at 71.3 Hz and shows the difference between the mode shapes measured with CSLDV and the upper and lower row of measurement points obtained with high-speed 3D-DIC. Similarly, Fig. 27.6b, c shows the mode shapes at 205.5 Hz and 411.4 Hz. The MAC values between each of the DIC rows and the CSLDV shapes are shown in Table 27.2 along with the frequency errors previously discussed. Separate MAC values were computed for the upper and lower row of computed 3D-DIC measurement points compared with CSLDV to show the consistency of 3D-DIC measurements across the entire surface of the beam. It is noted that MAC values for modes 1 and 2 are above 0.99 showing excellent correlation

Table 27.2 Modal comparison

|	Mode	f_n AVG modal hammer test, Hz	% Change between pre- and postexperiment modal hammer tests	f_n CSLDV, Hz	% Error CSLDV	f_n DIC, Hz	% Error DIC	MAC upper	MAC lower
Sinusoidal	1	71.75	−0.70	71.24	−0.7112	71.30	−0.6269	0.9993	0.9997
	2	204.35	−0.49	204.33	−0.0117	204.50	0.0747	0.9968	0.9994
	3	411.45	−0.12	411.05	−0.0972	411.39	−0.0134	0.5381	0.7762
Random	1	72.15	−2.82	73.99	2.5554	73.00	1.1712	0.9988	0.9990
	2	204.85	−1.23	205.03	0.0864	205.35	0.2420	0.9984	0.9990
	3	412.05	−0.85	411.94	−0.0268	414.63	0.6260	0.9891	0.9883
	4	675.9	−0.52	675.58	−0.0471	676.38	0.0716	0.9376	0.9583
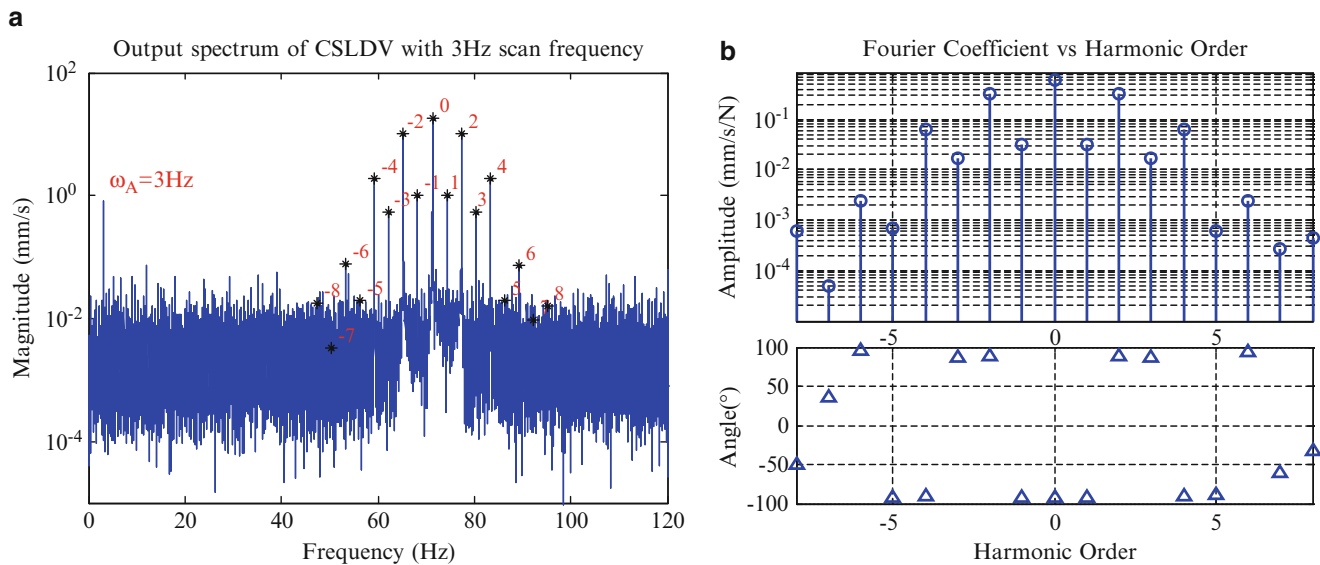
Fig. 27.5 Output spectrum for CSLDV

between CSLDV and high-speed 3D-DIC; however, due to the small displacements measured at 411.4 Hz, high-speed 3D-DIC begins to exhibit larger errors in the mode shape, which is shown in Fig. 27.6c, leading to MAC values 0.5381 and 0.7762. Additionally an asymmetry in the mode shape, where a larger amplitude of displacement is observed on the left end of the beam, is seen in mode 2 and 3, which is believed a result of asymmetry of the boundary conditions or an initial curvature in the beam that is below the measurable range of the 3D-DIC system. In either case, the asymmetry is undetectable until the dynamic response is observed with the large measurement resolution.

It is also important to note that while the smooth nature of the CSLDV mode shapes seems to suggest that they are infallible, they are in fact an approximation of the true mode shapes obtained by expanding them in a Fourier series of the time-varying scan pattern. As mentioned previously, 13 clearly dominant harmonics (i.e. $n = -6$ to 6) were observed for the first mode. The neglected harmonics were at least a few orders of magnitude smaller than the dominant ones, so one would be inclined to have high confidence in that shape. For example, if $n = -8$ to 8 were used to reconstruct the first bending mode shape, the maximum change in the shape is only 0.068 % with respect to the shape reconstructed using $n = -6$ to 6. Furthermore, because the laser is scanning along a line with CSLDV, when the measurements are noisy, the mode shapes measured on the forward and backward parts of the sweep tend to differ giving an indication of the error. Here, the forward and backward sweeps overlay completely suggesting that the shapes were quite accurate.

27.4.3 Natural Frequencies and Damping/Mode Shapes from Random Excitation

Band limited random noise over the range of 10–800 Hz was used to excite the first 4 modes of the clamped-clamped beam. For this experiment, a 9 Hz scan frequency was found to be preferable to help prevent the neighboring harmonics of each mode from blending together. The actual scan frequency ends up varying a little from what is commanded, for example, the scan frequency measured in the mirror displacement signals for this case was 9.0007 Hz. An accurate scan frequency is critical in this process since the phase error may accumulate especially when the time histories are long. The following plots show are the force spectrum and the output power spectrum (Fig. 27.7).

The random response data measured with the CSLDV and high-speed 3D-DIC was processed using AMI to identify the natural frequencies and mode shapes. For CSLDV, this included mode shapes from all identified sidebands, and the following figures show the fitted composite harmonic power spectrum around 73 Hz. For high-speed 3D-DIC, the response data was averaged 45 times with a block size of 5,000 samples and a 50 % overlap. The resulting response spectrums were then loaded into AMI to extract natural frequencies and mode shapes (Fig. 27.8).

The identified mode shapes obtained from the band limited random excitation are compared in Fig. 27.9. Figure 27.9a, b is the comparison of the identified modes at 72.15 Hz and 205.4 Hz between CSLDV and high-speed 3D-DIC, the mode shapes agree well, with computed MAC values above 0.99 for both modes. Figure 27.9c shows the third mode at 414.6 Hz, which has computed MAC values of 0.9891 and 0.9883. The measured random excitation was shown to excite the 3rd mode
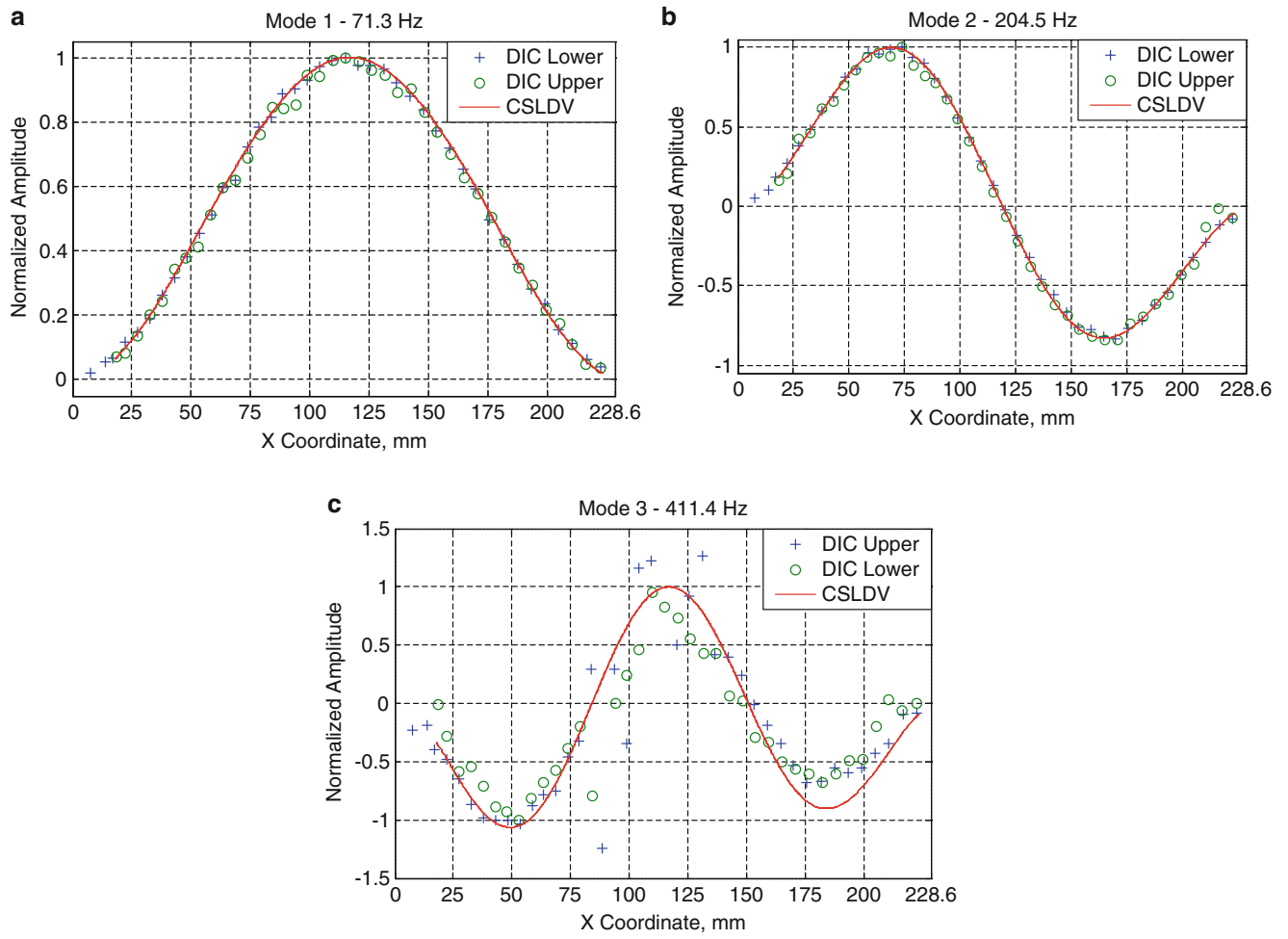
Fig. 27.6 Modes shapes from steady state excitation. (**a**) Mode 1 at 71.3 Hz, (**b**) Mode 2 at 204.5 Hz, and (**c**) Mode 3 at 411.4 Hz
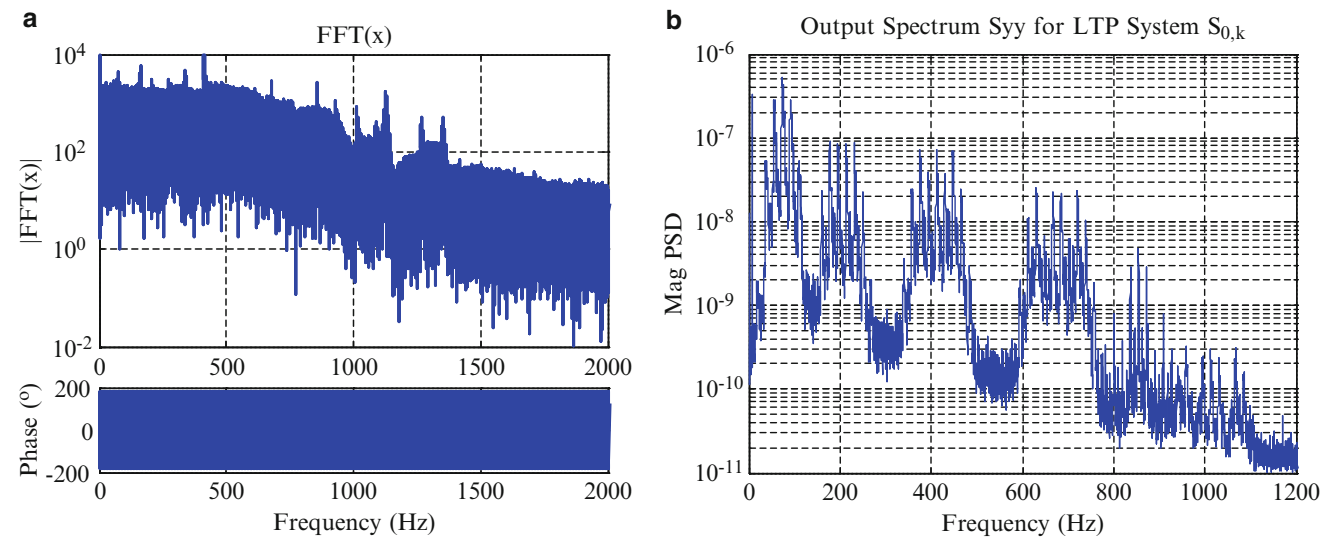

Fig. 27.7 Force spectrum and output power spectrum

Fig. 27.8 Results of AMI mode isolation of the composite harmonic power spectrum from CSLDV measurement
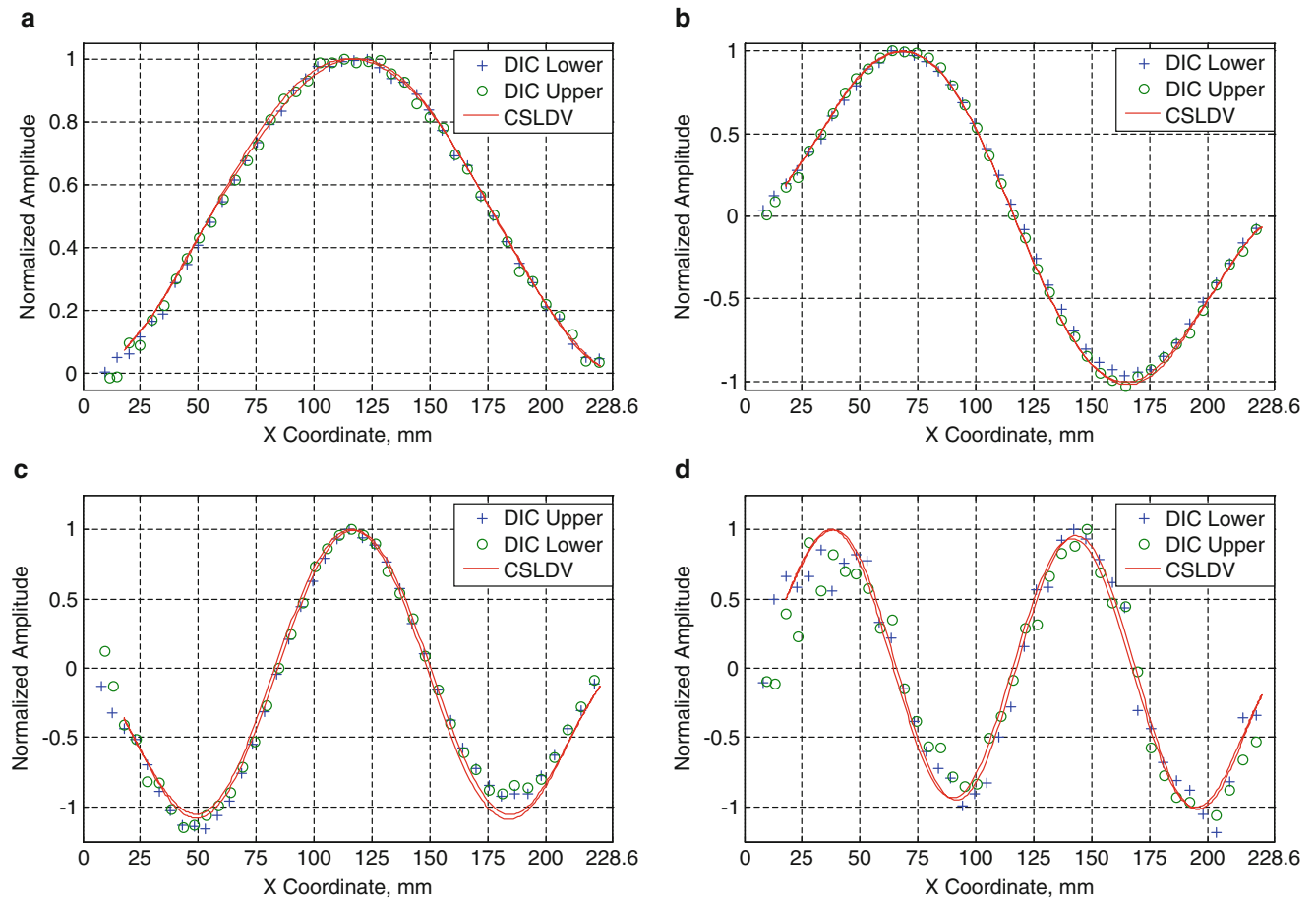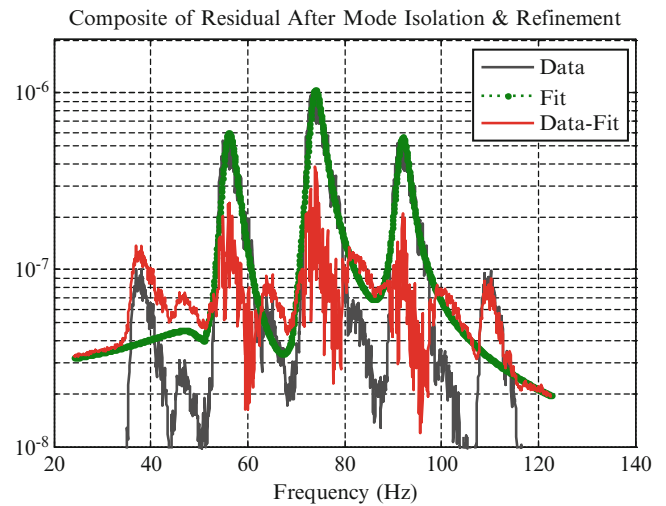

Fig. 27.9 Modes shapes from random excitation. (**a**) Mode 1 at 74.5 Hz, (**b**) Mode 2 at 205.4 Hz, (**c**) Mode 3 at 414.6 Hz, and (**d**) Mode 4 at 676.4 Hz

better than the use of a steady state sine wave as exhibited by the shape comparison and MAC value. Also, the asymmetry seen in the steady state sine dwell was seen with high-speed 3D-DIC; however, CSLDV did not capture the same asymmetry which could be a result of the shifting frequencies or expected shifting boundary conditions. Results of mode 4 are shown in Fig. 27.9d and computed MAC values of 0.9376 and 0.9583 were obtained for lower and upper 3D-DIC measurement locations, respectively. Again, as higher frequencies are measured, the smaller displacements lead to a greater observed noise with 3D-DIC as observed in the plot of mode 4.

27.5 Conclusion

Modes shapes and natural frequencies of a clamped-clamped flat steel beam were identified using CSLDV and high speed 3D-DIC. Natural frequencies were also identified using single-input single-output modal hammer testing for comparison with CSLDV and high speed 3D-DIC. A maximum frequency error of 2.56 % for CSLDV and 1.17 % for high speed 3D-DIC was observed when compared with the modal hammer tests. Throughout testing, single-input-single-output modal hammer tests showed that the natural frequencies shifted a maximum of 2.8 %. So, it is concluded that the frequency error between the modal hammer tests compared with CSLDV and 3D-DIC is largely due to the experimental setup instead of the measurement techniques. Additionally, inconsistencies with the clamped boundary conditions were identified with an asymmetry seen in the second and third mode shapes as measured with both CSLDV and 3D-DIC. Measurement error is dismissed as a cause since each measuring technique independently identified the asymmetry from the sinusoidal excitation test. For the random excitation experiment, the mode shape difference in the second and third mode is concluded to be from changing experimental conditions throughout the test since CSLDV and 3D-DIC are not measured simultaneously. Future work with an improved experimental setup is needed for further comparison, but it is shown that both techniques exhibit the ability to capture a high spatial resolution measurement of the clamped-clamped beam when subjected to steady state sinusoidal and band limited random excitations.

CSLDV was able to measure 1,708 points for the steady state sine excitation and 570 points for the random excitation. However, the information in the measurement is not governed by the number of points used to define the shape but by the number of Fourier coefficients that can be identified to describe the time-varying shape. In fact, decreasing the sample rate, and hence the number of points, has sometimes been found to increase the resolution of the measurement. An additional consideration with CSLDV is the measurement grid, which is dependent on the choice of a periodic scan signal and by the location of the laser on the surface, which is determined by a curve fit of the stepped galvo-motor signal. If a more complex 2-D grid of measurement locations is required, patterns following a Lissajous curve would be needed and testing time will increase. One benefit CSLDV has over high-speed 3D-DIC is the ability to measure at large stand off distances and maintain accuracy over larger test specimens; however, the maximum stand off distance is laser dependent and the measurement is limited to motion along the scan path and in the direction of the incident laser beam. Current LDVs clearly have much higher measurement resolution than DIC, down to tens of nanometer/second velocities or picometer displacements. Some of that resolution can be lost to speckle noise when scanning in a CSLDV mode, and yet in this study CSLDV was still clearly preferable for higher modes where the displacements were small.

High speed 3D-DIC was computed with two rows of 41 points for both excitations; however, a denser measurement grid can be obtained if needed since the images were stored. For the given field of view and beam geometry, 2,500 points can be computed in a 2D grid across the surface of the beam and the measurement resolution is independent of measurement duration or excitation type. (In CSLDV, the spatial information is captured in empty regions of the frequency band, and hence one must consider the input type, scan frequency, speckle noise, and the properties of the system to successfully capture measurements.) The spatial resolution of the acquired mode shape measured with high speed 3D-DIC is dependent on the stand off distance and the camera resolution; therefore, if more accurate measurements are needed, the camera setup needs to be moved closer to the test specimen, or a higher resolution camera is needed. Additionally, since high frequencies correspond to smaller displacements, high-speed 3D-DIC loses ability to measure mode shapes at higher frequencies. 3D-DIC mode shapes do appear nosier when compare with those measured with CSLDV; however, this is largely due to the fact that each measurement point is independent and subject to speckle pattern variations instead of dependent on a periodic signal. One benefit high-speed 3D-DIC has over CSLDV is the ability to provide a 2D grid of measurement points equally spaced across the specimen surface that measures the three dimensional deformations providing near full-field measurements in all deformation axes. Indeed, with 3D-DIC one can capture the in-plane motions of the surface even more accurately than the out-of-plane motions, whereas CSLDV can only capture the motion along the axis of the incident laser beam.

Both techniques can provide dense measurements along surfaces, as long as each technique can "see" the surface. To provide accurate measurements, both techniques require surface preparation, unless the material used for the test piece fulfills specific requirements (e.g. a random pattern for 3D-DIC and a sufficiently reflective pattern for CSLDV). For DIC, this surface preparation is especially important when response levels are small, or in a structure's linear range. For CSLDV, surface preparation becomes more important when the vibration amplitude becomes small relative to speckle noise, and also as the laser standoff distance (or field of view) increases.

Finally, this study has illustrated that when full-field velocities or displacements are measured rather than simply motion at a few points, inconsistencies in the dynamic behavior (e.g. asymmetries in mode shapes) of the structure under test can be identified and provide insight to modeling and predicting dynamic behavior. Here, the CSLDV and DIC shapes revealed asymmetry in the 2nd and 3rd bending mode shapes which was probably due to (unmodeled) asymmetry in the boundary conditions. If a traditional test were performed with only a few measurement points, one would not be likely to detect this, nor would they have sufficient information to update the model to account for it.

References

1. Schwingshackl CW, Stanbridge AB, Zang C, Ewins DJ (2007) Full-field vibration measurement of cylindrical structures using a continuous scanning LDV technique. Presented at the 25th international modal analysis conference (IMAC XXV), Orlando, Florida, 2007
2. Stanbridge AB, Ewins DJ (1999) Modal testing using a scanning laser Doppler vibrometer. Mech Syst Signal Process 13:255–270
3. Stanbridge AB, Martarelli M, Ewins DJ (2004) Measuring area vibration mode shapes with a continuous-scan LDV. Measurement 35:181–189
4. Martarelli M (2001) Exploiting the laser scanning facility for vibration measurements. Ph.D., Imperial College of Science, Technology & Medicine, Imperial College, London
5. Stanbridge AB, Khan AZ, Ewins DJ (2000) Modal testing using impact excitation and a scanning LDV. Shock Vib 7:91–100
6. Allen MS (2009) Frequency-domain identification of linear time-periodic systems using LTI techniques. J Comput Nonlinear Dynam. 4(4). DOI 10.1115/1.3187151
7. Yang S, Sracic MW, Allen MS (2012) Two algorithms for mass normalizing mode shapes from impact excited continuous-scan laser Doppler vibrometry. J Vib Acoust 134:021004
8. Wereley NM (1991) Analysis and control of linear periodically time varying systems. Ph.D., Department of Aeronautics and Astronautics, Massachusetts Institute of Technology, Cambridge
9. Wereley NM, Hall SR (1991) Linear time periodic systems: transfer functions, poles, transmission zeroes and directional properties. In: Presented at the proceedings of the 1991 American control conference, Boston, MA, USA, 1991
10. Wereley NM, Hall SR (1990) Frequency response of linear time periodic systems. Proceedings of the 29th IEEE Conference, Honolulu, HI, USA, pp 3650–3655 DOI:DOI 10.1109/CDC.1990.203516
11. Yang S (2013) Modal identification of linear time periodic systems with applications to continuous-scan laser Doppler vibrometry. Ph.D., Engineering Physics, University of Wisconsin-Madison
12. Schmidt TE, Tyson J, Galanulis K, Revilock DM, Melis ME (2005) Full-field dynamic deformation and strain measurements using high-speed digital cameras, Proceedings of the SPIE, pp 174–185, DOI 10.1117/12.567142
13. Tiwari V, Sutton MA, Shultis G, McNeill SR, Xu S, Deng X, Fourney WL, Bretall D (2009) Measuring full-field transient plate deformation using high speed imaging systems and 3D-DIC. In: Proceedings of the society for experimental mechanics annual conference, Albuquerque, 2009
14. Niezrecki C, Avitabile P, Warren C, Pingle P, Helfrick M (2010) A review of digital image correlation applied to structural dynamics. Am Inst Phys Conf Proc 1253:219–232
15. Helfrick M (2011) 3D digital image correlation methods for full-field vibration measurement. Mech Syst Signal Process 25:917–927
16. Warren C, Niezrecki C, Avitabile P, Pingle P (2011) Comparison of FRF measurements and mode shapes determined using optically image based, laser, and accelerometer measurements. Mech Syst Signal Process 25:2191–2202
17. GmbH (2011) Aramis, 6.3.0 edn. Braunschweig, Germany
18. GmbH (2011) IVIEW real time sensor, 6.3.0 edn. Braunschweig, Germany
19. Yang S (2013) Modal identification of linear time periodic systems with applications to continuous-scan laser Doppler vibrometry. Ph.D., Engineering Physics, University of Wisconsin-Madison
20. Yang S, Allen MS (2012) Output-only modal analysis using continuous-scan laser Doppler vibrometry and application to a 20 kW wind turbine. Mech Syst Signal Process 31:2011
21. Sutton MA, Orteu JJ, Schreier H (2009) Image correlation for shape, motion, and deformation measurements: basic concepts, theory, and applications. Springer New York, DOI 10.1007/978-0-387-78747-3
22. Gordon RW, Hollkamp JJ, Spottswood SM (2003) Non-linear response of a clamped-clamped beam to random base excitation. Presented at the VIII international conference on recent advances in structural dynamics, Southampton, United Kingdom, 2003
23. Gasparoni A, Allen MS, Yang S, Sracic MW, Castellini P, Tomasini EP (2010) Experimental modal analysis on a rotating fan using tracking-CSLDV. Presented at the 9th international conference on vibration measurements by laser and noncontact techniques, Ancona, Italy, 2010
24. Yang S, Allen MS (2012) A lifting algorithm for output-only continuous scan laser Doppler vibrometry. Presented at the 53rd AIAA structures, structural dynamics, and materials conference, Honolulu, Hawaii, 2012
25. Martin P (2010) Uncertainty due to speckle noise in laser vibrometry. Doctor Thesis, Wolfson School of Mechanical and Manufacturing Engineering, Loughborough University

Chapter 28
Triaxial Accelerometer, High Frequency Measurement and Temperature Stability Considerations

Thomas Petzsche, Andy Cook, and Marine Dumont

Abstract Many applications such as operational, environmental, structural or durability testing require increasingly more triaxial IEPE accelerometers with higher frequency operation in the three orthogonal directions. The new, novel mounting for Kistler miniature PiezoStar® and Piezoceramic Triaxial cube accelerometer families offer a practical solution. Additionally, in certain applications that require ultra-low sensitivity temperature coefficient, Piezostar® offers a practical solution when piezoceramic sensors do not satisfy the application needs.

The seismic elements of these IEPE triaxial accelerometer families have inherent benefits resulting in high resonance frequency where the sensor design provides stud mounting for each orthogonal axis with threaded holes on three sensor faces. The calibration methodology will be reviewed supporting frequencies up to 20 kHz, without additional mechanical fixtures, which can impact precision measurements.

Ultra-low sensitivity temperature coefficient is achieved with PiezoStar® IEPE accelerometers and will be demonstrated as well as a comparison between more traditional quartz and ceramic sensing elements. PiezoStar® IEPE accelerometers provide less than 1.5 % sensitivity change between −55 °C and 165 °C, as well as inherent long term stability of a piezoelectric crystal.

Keywords PiezoStar • Accelerometer • Thermal stability • High frequency • Vibration

28.1 Introduction

28.1.1 High Frequency Response Characterization in Each Orthogonal Axis

According to ISO EN DIN 16063 standard series [1], the calibration of the frequency response of an accelerometer is performed by primary laser or secondary comparison calibration methods. The characterization of the frequency response above 2–3 kHz becomes more complicated for triaxial accelerometers because of required mechanical adaptions to the reference side of a back-to-back standard. Direct mounting is not possible in the x- and y-direction. Even if Beryllium is used as the material in making the adapters, they are still too flexible. And going further, if the highest ratio between elastic stiffness and density of any materials is used, the relative motion between the coupling area of the unit under test (UUT) and the reference accelerometer is still an issue as both amplitudes cannot be identical. This is illustrated in Fig. 28.1.

The frequency response of a sensor along X and Y axes at higher frequencies will then be limited by the calibration mounting fixture. Therefore, due to the limits of the calibration mounting fixture, specifications for high frequency must be noted more conservatively. An estimation of the frequency response in the upper end can often be performed with a resonance excitation of the seismic element (Fig. 28.7).

T. Petzsche
Kistler Instrumente GmbH, 73760 Ostfildern, Germany

A. Cook • M. Dumont (✉)
Kistler Instruments Inc., 75 John Glenn Drive, Amherst, NY 14228-2171, USA
e-mail: marine.dumont@kistler.com

Fig. 28.1 View of a triaxial
accelerometer as UUT.
Mechanical adapter fixed to the
calibration shaker air bearing
armature. Built-in reference
standard

Reference Face UUT

Reference Face Reference

Shaker with Air Bearing Armature
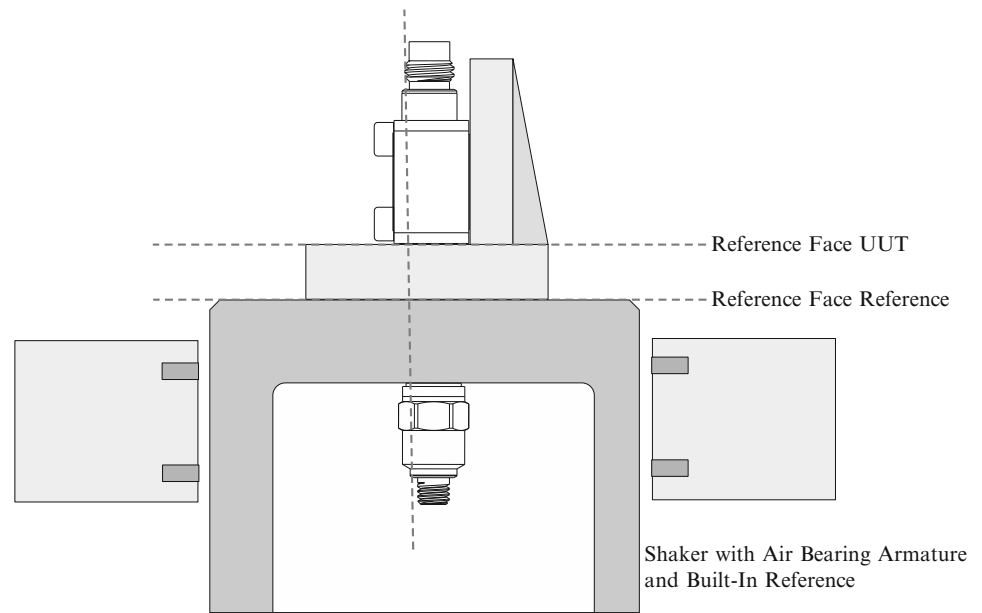and Built-In Reference

Fig. 28.2 Mounting adapters used to calibrate the z-axis (*left*) and the x- and y-axes (*right*) of a triaxial accelerometer Kistler type 8793A500 (*center*)

Figures 28.2 and 28.3 show a Kistler triaxial accelerometer type 8793A500 and the calibration mounting adaptors that are used with a back-to-back reference standard for different axes on a TIRA S514-C calibration shaker. Figure 28.4 shows an overview of the obtained frequency responses up to 2 kHz (x- & y-axes) and to 10 kHz (z-axis). It is obvious that the results of the frequency response in the x-axis and y-axis are mostly influenced by the relative motion between the UUT and B-t-B reference side. In these two axes, the frequency response can be measured only up to 2 kHz. Some improvements can only be achieved by the use of Beryllium mounting adaptors of optimized design. This will be costly for a very slight improvement at higher frequencies. In addition, these adaptors would not just be expensive and time consuming to manufacture, but they would also be problematic from the toxicological point of view.

Another common design found in triaxial accelerometers is a cube shaped housing with only a z-axis mounting hole. Calibration of this design of sensor consists of stud mounting the z-axis and adhesively mounting the x-axis and y-axis. The y-axis is mounted, like the z-axis, through the base and into the mounting point of the element post. The x-axis, on the other hand, is adhesively mounted on the cover of the sensor. Figure 28.5 shows the problematic nature of mounting on the x-axis cover. This type of calibration yields a similar frequency response in the y- and z-axes, but an x-axis response that is considerably lower, like that seen when using a calibration mounting adapter. Figure 28.6 shows the frequency responses of the three axes of a piezoceramic triaxial accelerometer utilizing this type of calibration mounting. Again, a conservative frequency response specification needs to be used for the x-axis due to the available calibration method.

As an alternative to alleviate this issue, the characterization of the resonance frequency in the mounted state can be used as an estimation. This method is described in the ISO 5247-14 and -22 and will also be part of a new standard ISO 16063-32 [2, 3]. A rule of thumb is that the 5 % frequency response deviation point of the sensor at high frequency is approximately
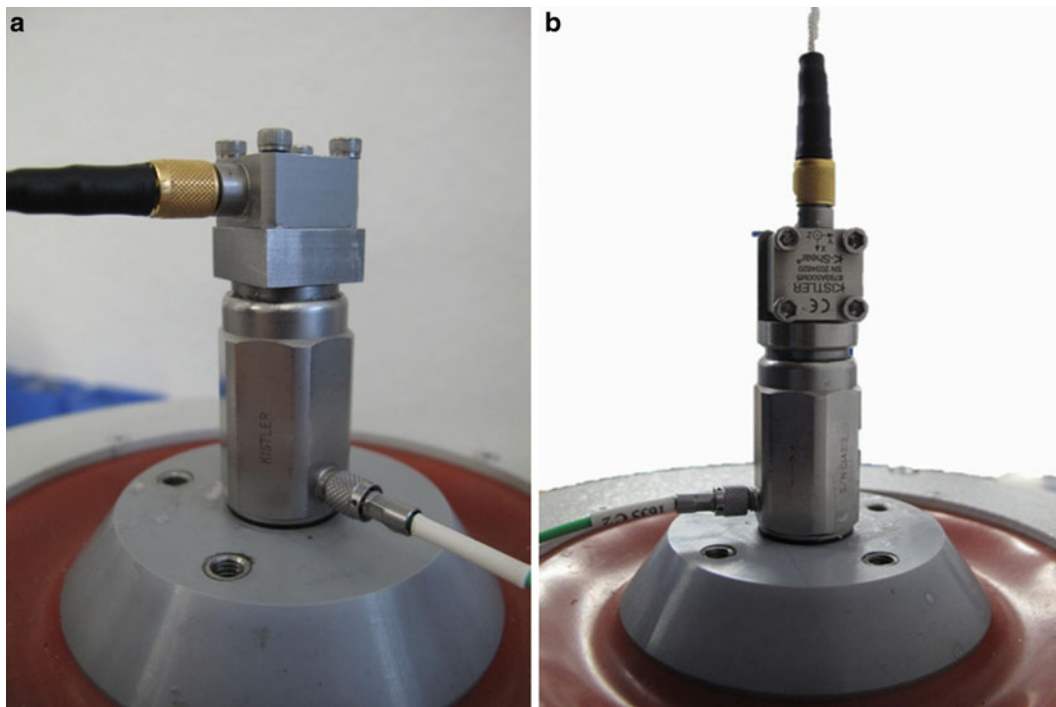
Fig. 28.3 Mounting a Kistler 8793A500 triaxial accelerometer in z-axis (**a**. *left*) and x-axis (**b**. *right*) to the reference side of a back-to-back reference sensor Kistler 8076K

20 % of the mounted resonance frequency. It can be deviated out of the theory of the seismic accelerometer frequency response [4, 5]. This practice offers an alternative method to estimate the frequency response of a sensor used in testing. Figure 28.7a–c shows this test and results.

In order to solve this problem, triaxial accelerometers have been designed by Kistler which incorporate stud mounting for each orthogonal axis. This is achieved by supplying threaded holes on three sensor faces. This concept has been used for the past 10 years and is currently available in three Kistler sensor families: 8762A, 8763B, 8766A (Fig. 28.8).

Along with the advantage of three mounting holes, the very rigid crystal element made from PiezoStar® allows measurements up to 10–12 kHz ($\pm$5 %) with mounted resonance frequencies up to 70 kHz. As the measurement uncertainty for the sensitivity is much higher beyond 10 kHz, the data sheet specifies an upper frequency response value of 10 kHz with $\pm$5 % sensitivity deviations referenced to a specified frequency. This design principle allows a frequency response of 0.5 Hz to 10 kHz and offers a generic use of these sensors in a very wide frequency range where quite often two sensors would have been used in the past.

In the following example, a Kistler type 8766A500AB was tested for frequency response from 5 Hz to 50 kHz. The amplitude and phase responses are shown for the x- and z-axes in Fig. 28.9. In Fig. 28.9a, the sensitivity deviation was referenced to its sensitivity taken at a frequency of 160 Hz. The results for the y-axis are qualitatively identical to the z-axis. We can observe some minor resonances above 10 kHz with less than 7 % sensitivity deviation. The rest of the spectrum is linear and the slope of the entire frequency response is nearly zero percent, as opposed to the response of soft piezoelectric ceramic element material coupled with an internal charge amplifier. The frequency response in Fig. 28.6 shows this sloped response. Frequency response and phase between axes match very closely over the entire frequency range.

Figure 28.10 shows a Kistler 8766A500AB mounted on a SPEKTRA SE-09 calibration shaker with a single stud. In this setup, the reference sensor is integrated into the shaker armature. Both reference faces of the UUT as well as the reference sensor are assembled directly together and a relative motion is almost impossible. The calibration equipment being used was traceable to an NMI up to 20 kHz frequencies. In our case the reference standard frequency response has been modeled with a 70 kHz resonance at 20 dB amplitude. The overall measurement uncertainty for the UUT is 1 % up to 1.25 kHz, 2 % from 1.25 kHz to 5 kHz and 3 % from 5 kHz to 10 kHz, using $k = 2$ (95 % coverage factor). The result above 20 kHz is then purely qualitative due to the fact that an uncertainty cannot be specified. The occurrence of additional smaller resonances below the main resonance and the deviations from the ideal frequency response may have a different cause than the UUT; i.e. rocking motions of the shaker armature in relation to a cross axis sensitivity of the UUT as one possibility. But these potential error sources have not been subjected to detailed investigations.
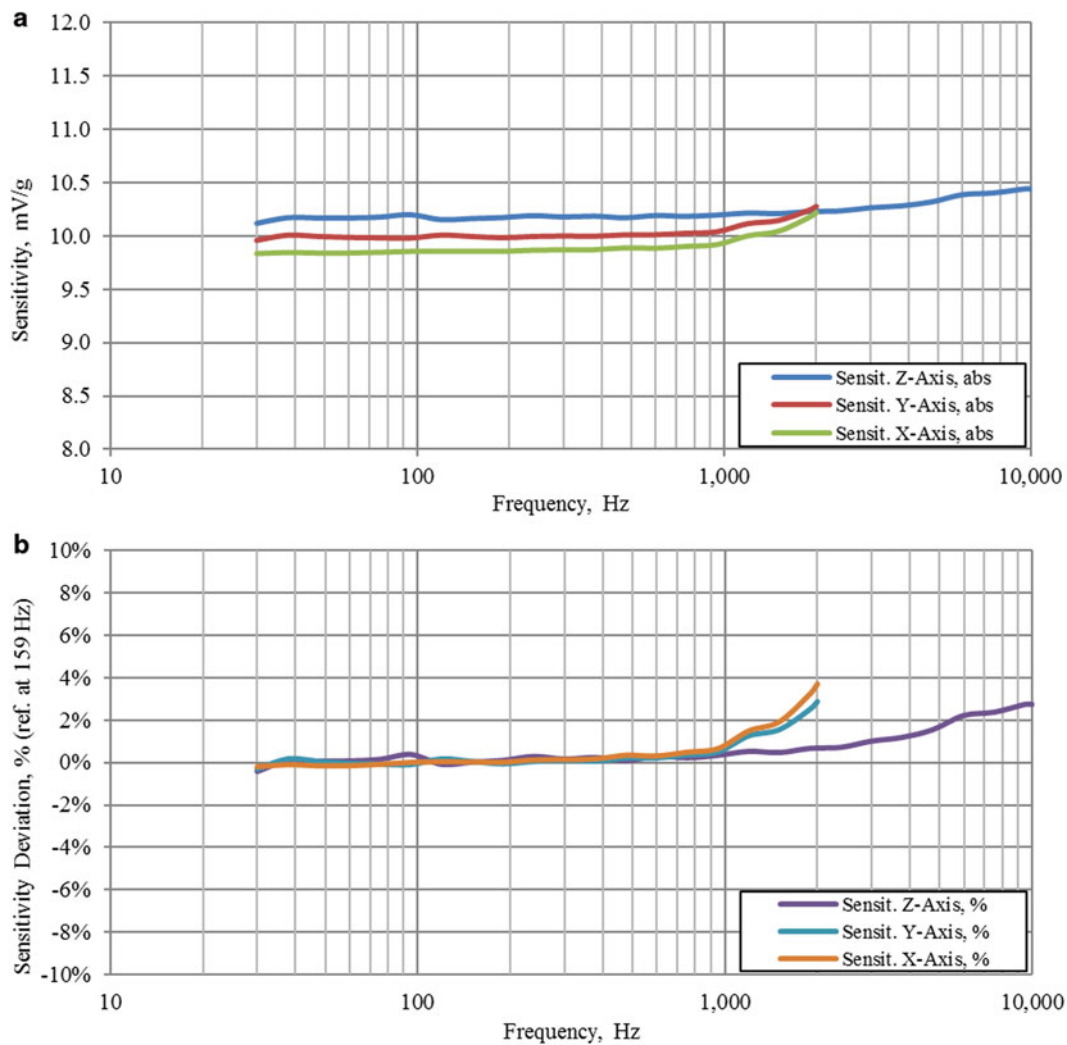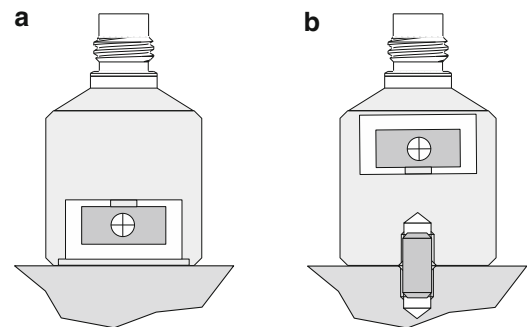
Fig. 28.4 (**a**, **b**) Frequency response of an accelerometer Kistler type 8793A500 calibrated in x-, y- and z-axes from 30 Hz to 2 kHz and 30 Hz to 10 kHz, respectively

Fig. 28.5 Triaxial sensor design which requires adhesive mounting on cover of x-axis (**a**) versus triaxial sensor design which allows stud mounting of x-axis (**b**)

28.1.2 Low Sensitivity Temperature Coefficient and High Stiffness Properties of PiezoStar® Crystals

Kistler Instruments grows a family of synthetic single crystals in-house, that have very unique properties [6]. The PiezoStar® family of crystals have improved at least two different important accelerometer properties. First, a low *temperature coefficient of the sensitivity* has been achieved with deviations less than 1.5 % over the entire temperature range from −55 °C up to 165 °C. Some accelerometers are available in a cryogenic version which can measure in temperatures down to −196 °C.
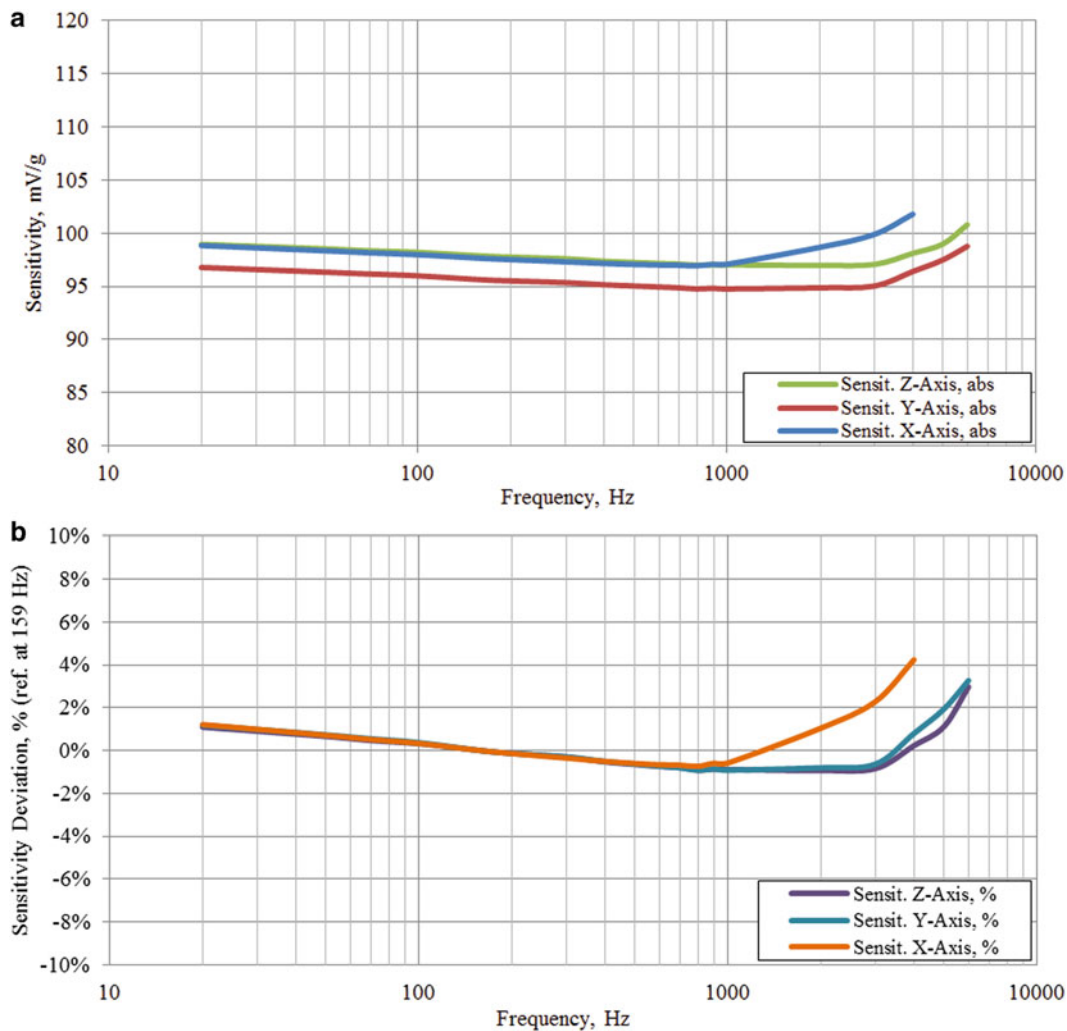
Fig. 28.6 (**a**, **b**) Frequency response of a piezoceramic accelerometer calibrated in x-, y- and z-axes from 20 Hz to 4 kHz and 20 Hz to 6 kHz, respectively

Some sensors have even been proven to perform excellently down to −246 °C as well. All the PiezoStar® accelerometers are IEPE sensors with a constant current line drive (CCLD) concept. This major improvement in the thermal sensitivity, compared to quartz or piezoceramic is shown in Fig. 28.11.

Vibration testing under temperatures, such as in combined climate and vibration testing in environmental simulation, product durability, modal testing under changing temperature or exhaust systems tests, may benefit from this specification. No additional effort will be necessary to compensate for any sensitivity change due to steady state temperature changes during testing such as sensors integrated in a shaker control loop in a thermal chamber.

The second unique property of PiezoStar® that is useful in accelerometer design is the increased charge output yielding a higher sensitivity than quartz while using same sized element masses. In turn, this permits a Piezostar® IEPE accelerometer to use much less mass than a quartz based IEPE accelerometer and attain the same standard sensitivity. Less element mass equates to higher mounted resonance frequencies, better frequency response and allows smaller overall housing designs. When comparing to soft PZT-piezoceramic based accelerometers, Piezostar® accelerometers offer a flat frequency response, long term stability, and a much better thermal coefficient of sensitivity.

Compression mode sensors showing high base strain sensitivity or thermal transient response have been used in the early days as a control accelerometer for electro dynamic shakers. Presently we can refer to those up to date shear mode accelerometers with crystal elements exempt of these undesired properties. Such solutions allow cost effective test equipment investments by offering a multiple use generic accelerometer for many different applications without the need of a variety of different sensor designs.
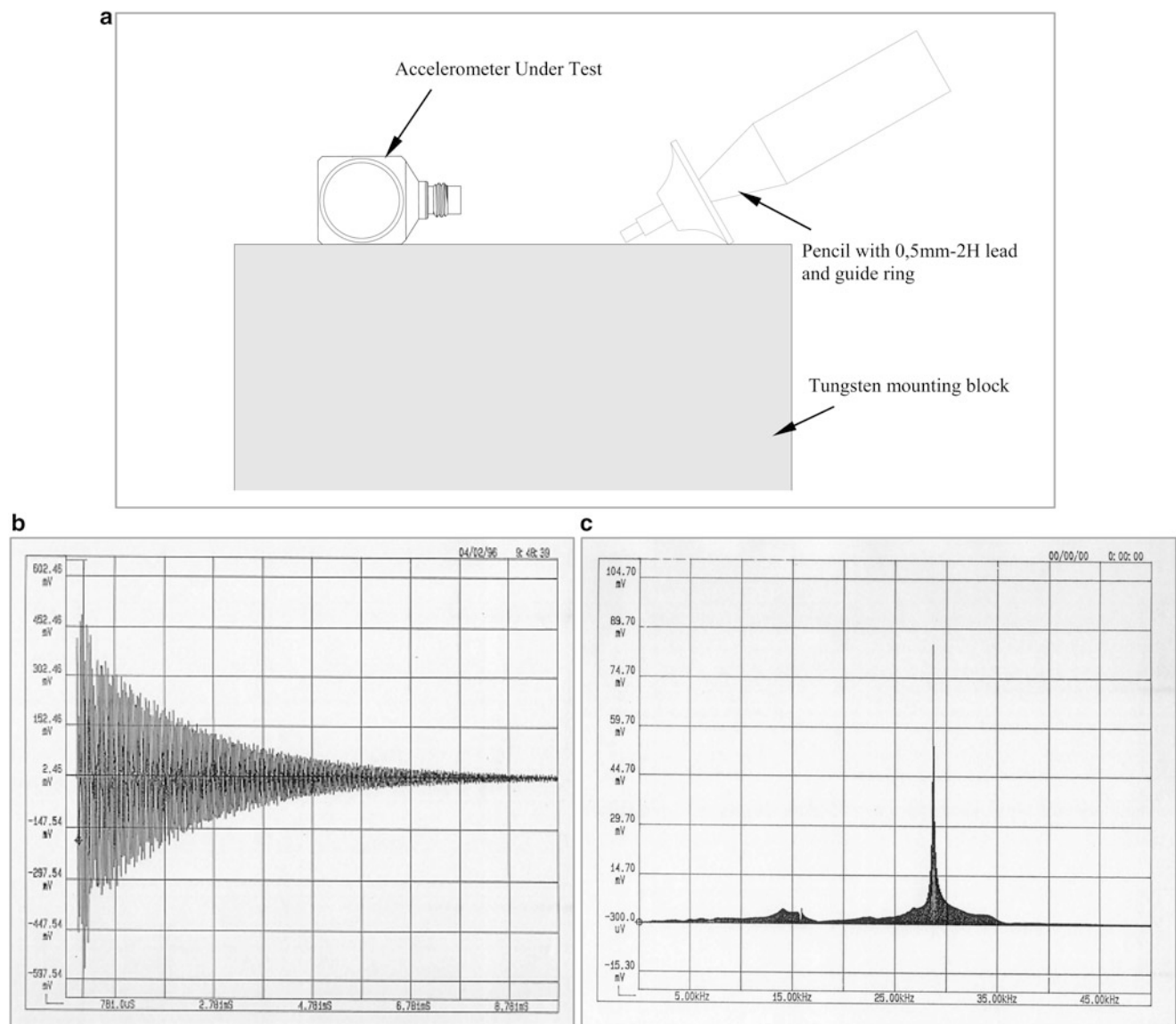
Fig. 28.7 (**a**) Characterization by lead breaking of the resonance frequency of an Acoustic Emission Sensor mounted on a tungsten cube (so called HSU-NIELSON according to ASTM E976-10) [8]. (**b**, **c**) Analysis of the transient response with FFT
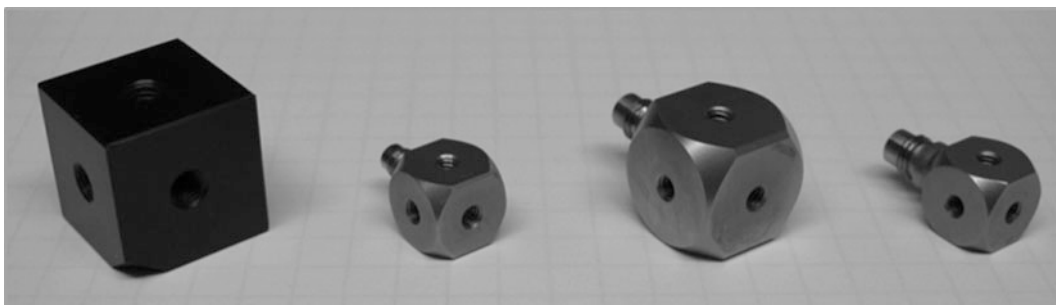
Fig. 28.8 New generation of triaxial accelerometers KISTLER type 8672A, 8763B (ceramic shear), 8766A50 and 8766A500BH (PiezoStar®) for a measurement range of 5–2,000 g
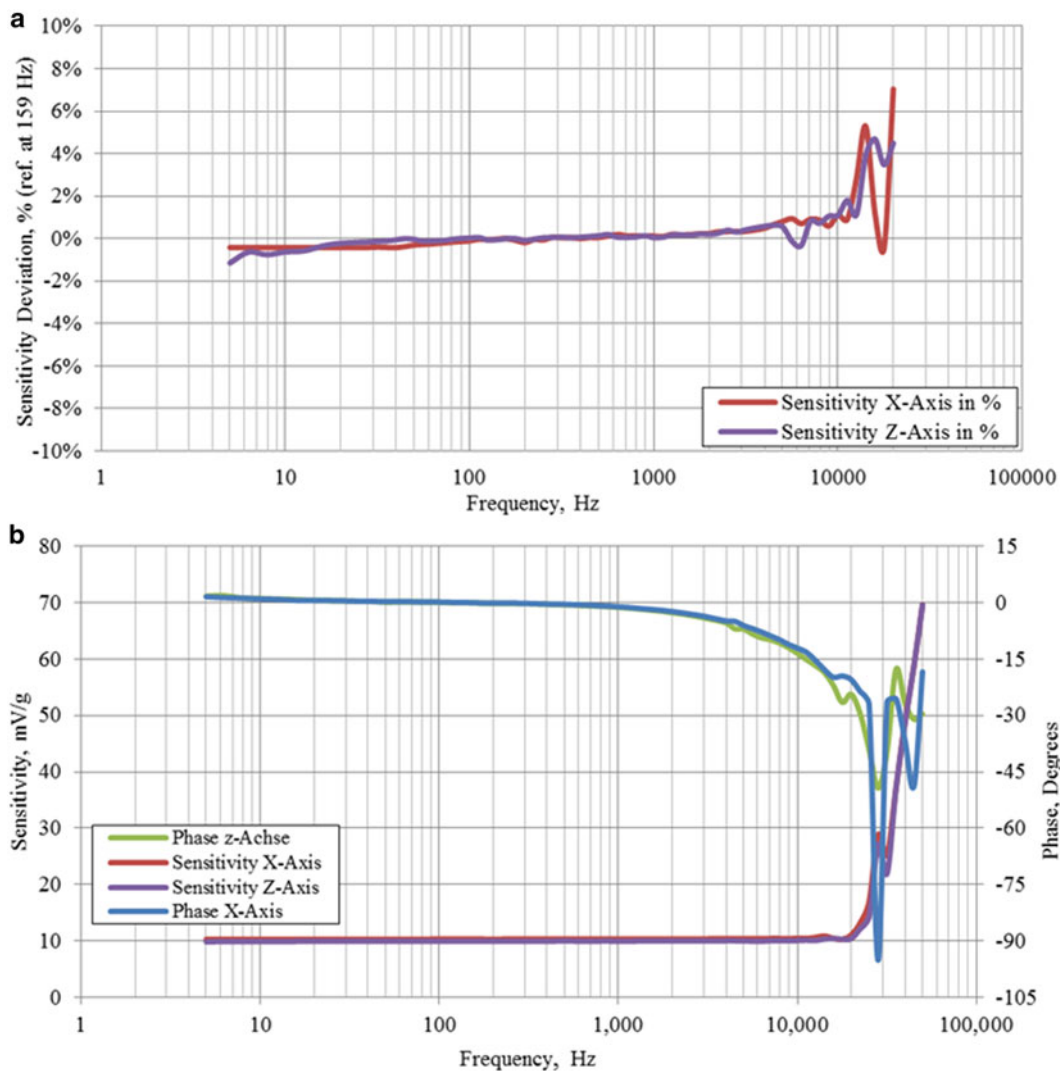
Fig. 28.9 (**a**) Frequency response of a Kistler 8766A500AB triaxial accelerometer along x and z axes directly mounted to reference. (**b**): Frequency response in phase and sensitivity of a Kistler 8766A500AB triaxial accelerometer along x and z axes directly mounted to reference. See Fig. 28.10a for mounting configuration along x-axis
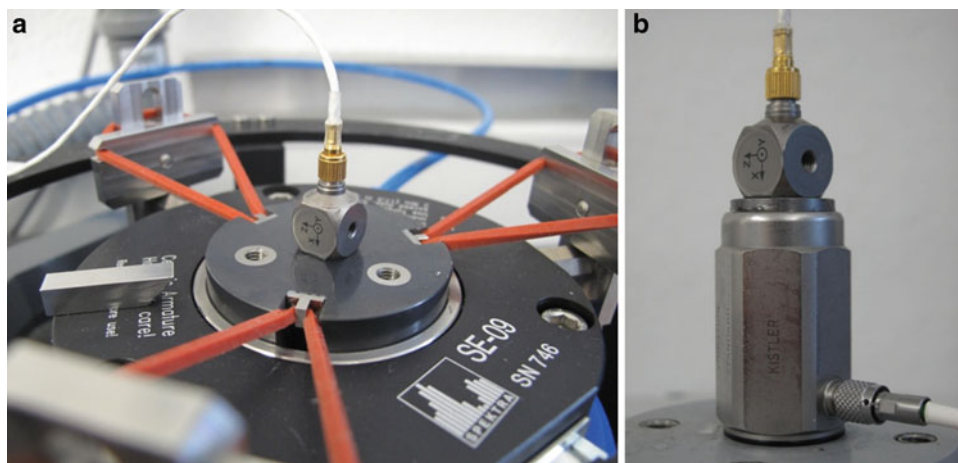
Fig. 28.10 UUT Kistler type 8766A500AB mounted in X-direction on the armature of a SPEKTRA SE-09 air bearing shaker (**a. left**, results in Fig. 28.9) and on the reference face of a "back-to-back" reference accelerometer Kistler type 8076K (**b. right**)
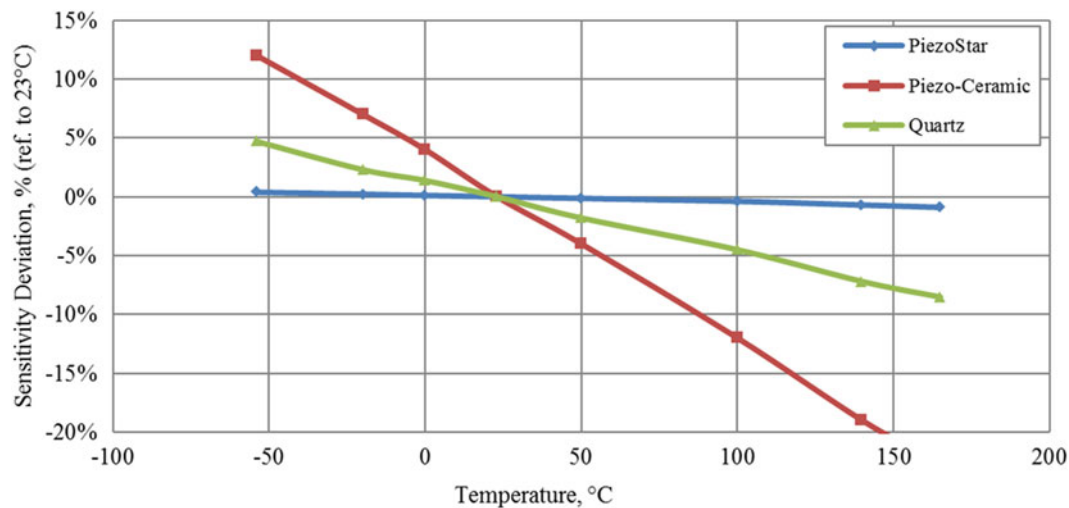
Fig. 28.11 Thermal coefficient of sensitivity for typical piezoelectric materials used in IEPE-accelerometers within a −55 °C to 165 °C temperature range

28.2 Summary

New mechanical design and piezoelectric sensing elements allows us to push the limits of Triaxial IEPE accelerometers. Very wide frequency range in the three orthogonal axes and less than 0.004 %/K thermal sensitivity shift can now be achieved. Because of the characterization of frequency response of those new mechanical designs with integral threads on three faces, we can observe a flat sensitivity over the entire frequency spectrum. This low mass solution appears to be very versatile covering many different applications where formerly several type numbers would have been needed. Finally, the possibility of mounting these sensors in any direction simplifies everyday work during installation.

References

1. Methods for the calibration of vibration and shock transducers: DIN EN ISO 16063-1x und DIN EN ISO 16063-2x; Kalibrierung von Beschleunigungsmessgeräten nach dem Vergleichsverfahren Richtlinie DAkkS-DKD-R 3-1, Teil 1 und 3
2. Kistler Doc e-08.07, Testing of acoustic emission sensors according to HSU-NIELSEN ASTM Std. E976-1984
3. Accelerometer resonance testing described in DIN EN ISO 5743-xx and DIN EN ISO 16063-3: methods for the calibration of vibration and shock pick-ups ISO 5347-14:1993, part 14: resonance frequency testing of undamped accelerometers on a steel block; ISO 5347-22:1993, part 19: accelerometer resonance testing. Methods for the calibration of vibration and shock transducers: ISO DIS 16063-32 "Methods for the calibration of vibration and shock transducers—part 32: resonance testing (Revision for ISO 5347-14:1993)
4. Handbuch der Mess- und Automatisierungstechnik in der Produktion, Hsg.: H.-J. Gevatter, U. Grünhaupt: Abschn. 4: Beschleunigung, Th. Petzsche u. H. Müller; Springer Verlag, 2006
5. Endevco. Handbook of shock and vibration measurement technology; Endevco, San Juan Capistrano, CA, USA
6. PiezoStar® Kristalle—Eine neue Dimension in der Sensortechnik; Dr. Claudio Cavalloni, Dr. Roland Sommer, Sonderdruck der Kistler Instrumente AG, Winterthur, 920-240d-07.03
7. Kistler data sheets to the data sheets type 8762A, 8763B, 8766A50 and 8766A250/500
8. ASTM E976-10 standard guide for determining the reproducibility of acoustic emission sensor response

Chapter 29
Laser Speckle in Dynamic Sensing Applications

Will Warren, Logan Ott, Erynn Elmore, Erik Moro, and Matt Briggs

Abstract Laser velocimetry is used as a measurement technique across a variety of fields including mechanical vibration and flow research, medical diagnostics and shock physics. In modern photon Doppler velocimetry (PDV) applications, the perception is that laser speckle pollutes the measured signal, sometimes destroying useful data. Recent experiments suggest the possibility of exploiting speckle to measure transverse speeds, thereby gaining information about surface dynamics across an additional degree of freedom. In this report, we examine the influence of axial displacement and probe characteristics on speckle velocimetry measurement capabilities.

Keywords Laser speckle • Laser Doppler • Velocimetry • Heterodyne • Surface dynamics

29.1 Introduction

Photon Doppler velocimetry (PDV) plays a central role in shock physics research where the method is used to observe high-speed phenomena; explosively driven objects traveling at speeds on the order of several km/s. The technique is heterodyne and yields velocity measurements along a monochromatic beam's optical path. Surfaces moving in the axis of the beam induce a Doppler-shift on returned light that, when combined with the reference field, produces a beat frequency from which velocity may be resolved. Measurement resolution is related to the wavelength of the incident laser beam [1] allowing infrared lasers to capture surface dynamics at nanosecond time scales. Dolan et al. [2] use multiple beams to measure velocities up to 48 km/s, and a typical digitizer will easily measure beyond 10 km/s.

While PDV is robust, highly-accurate and easily implemented, the technique is sensitive to speckling of backscattered light. Laser speckle is unavoidable in most PDV applications, resulting in periodic signal drop outs and large-amplitude intensity fluctuations which can obstruct the desired signal. Typically seen as an undesirable consequence of coherent light interference, speckle may be exploited to obtain information about lateral surface dynamics. Moro and Briggs [6] experimentally demonstrate the simultaneous measurement of axial velocity and transverse speed with a standard, single-beam PDV architecture. The results of their study indicate that speckle velocimetry is feasible in the context of PDV and calls for further detailed analysis. In this paper we attempt to further characterize speckle velocimetry performance by testing multiple optical probes over a range of velocities and axial displacements. Since PDV is inherently used to gather data from surfaces moving along the laser beam and through the focal length it is of particular interest to understand how speckle dynamics influence speckle velocimetry measurements near the beam focal point.

W. Warren
Department of Mechanical Engineering, University of California — San Diego, CA 92093, USA

L. Ott
Department of Engineering Physics, Fort Lewis College — Durango, CO 81301, USA

E. Elmore
Department of Computer Science, Alabama Agricultural and Mechanical University — Huntsville, AL 35811, USA

E. Moro (✉) • M. Briggs
WX-4, Los Alamos National Laboratory — Los Alamos, NM 87545, USA
e-mail: moro@lanl.gov

29.2 Background

Speckle is produced from the scattering of monochromatic light off of a surface whose face-height variation is large with respect to the source wavelength. A resulting set of coherent, de-phased wave fronts extend outward from the surface, combining to form a spatially unordered interference pattern in three-dimensional space. The simulated cross section of such a speckle pattern may be seen in Fig. 29.1a. Both a well-developed theory [3] and experimental results show that speckle is a stationary random process and that it exhibits trends which contain information about surface dynamics. Pure lateral translation of the illuminated surface with respect to the optical beam axis results in corresponding translation of the speckle pattern.

Iwai et al. [5] estimate the lateral speed of an illuminated surface by measuring the time required for the resulting speckle pattern to become uncorrelated at a fixed observation point. They show that time-varying speckle-intensity fluctuations produced from lateral translation decay with a characteristic correlation time, $\tau_{c\perp}$, that is inversely proportional to speed. Assuming that a point measurement is taken from a translating speckle pattern in the far field diffraction region, lateral surface displacement is given by the beam waist, ω_0.

$$| v_\perp | = \frac{\omega_0}{\tau_{c\perp}} \tag{29.1}$$

A physical interpretation of this concept is that the speckle pattern's coarse spatial structure, consisting of bright and dark volumes, passes through the observation point producing time-varying intensity fluctuations; as the speckle pattern translates with increased speed the intensity fluctuations contract. Temporal decoherence for a purely translating speckle pattern in the far field diffraction region is described by the normalized autocorrelation function. The shape of the autocorrelation function has been derived for a physical model with this particular free-space geometry and is given by the following expression.

$$\gamma_\perp(\tau) = \exp\left(\frac{-\tau^2}{\tau_{c\perp}^2}\right) \tag{29.2}$$

Loss of coherence is taken at a $\frac{1}{e}$ threshold where e is the base of the natural logarithm. For experimental data sets, a Hilbert transform was used to produce an envelope around the normalized autocorrelation function and the theoretical model given in Eq. (29.2) was subsequently fit to the envelope using least squares approximation. Experimental and theoretical autocorrelation functions are shown in Fig. 29.1b.
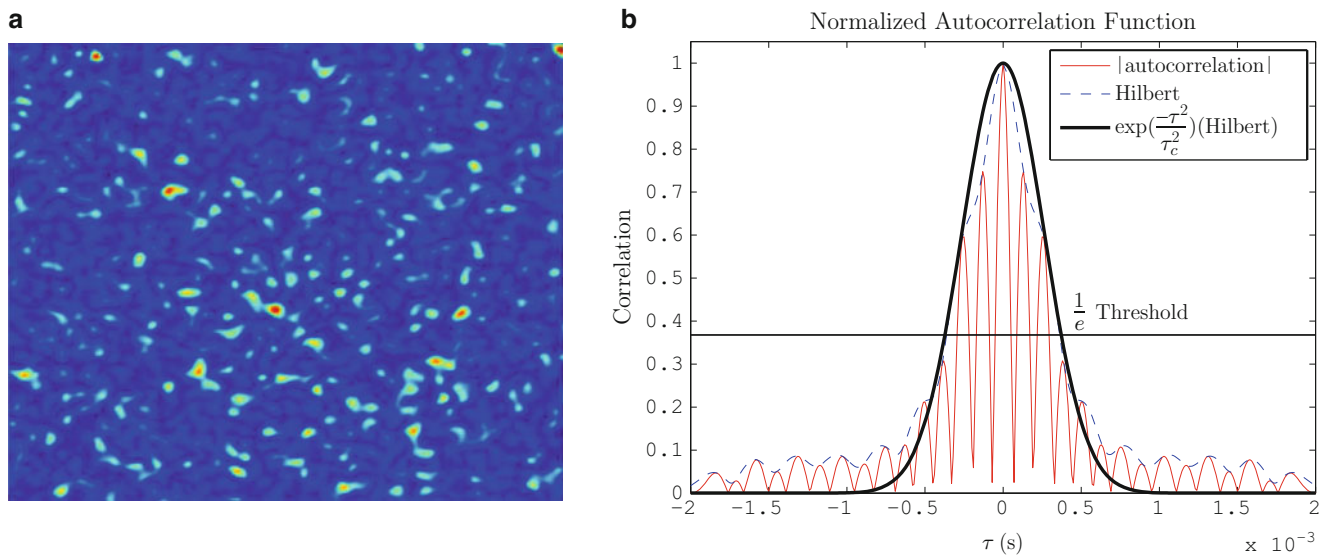

Fig. 29.1 Temporal decoherence of a speckle pattern is described by the normalized autocorrelation function in (**b**). Correlation time (τ_c) is given by the width of the curve between zero and the point where it falls below $\frac{1}{e}$. (**a**) Speckle pattern; (**b**) autocorrelation

In application, one must employ a detecting element of finite size to measure the intensity of a speckle field. For PDV applications this detecting element is simply the aperture of the optical probe receiving backscattered light. The relative size of the aperture with respect to the speckle pattern spatial granularity influences the shape of the normalized autocorrelation function. Iwai et al. [4] report that for a Gaussian circular aperture of radius r the correlation time will vary according to the speckle pattern's coarseness as follows

$$\tau_c = \frac{1}{\mid v \mid \left(\frac{1}{\omega} + \frac{(1+z/\rho)^2}{r^2 + r_c^2} \right)^{1/2}} \tag{29.3}$$

where ω, r and r_c are radii of the illuminated beam spot, aperture and average speckle, respectively, and ρ is the beam's radius of curvature at the point of incidence. The experiments contained herein assume that intensity measurements are taken at a single point.

29.3 Experiment

The experimental configuration, shown in Fig. 29.2, resembles a typical PDV setup. Laser light is directed through a focusing probe onto a diffusing surface. Backscattered light falling back onto the probe aperture is routed through a circulator to a Thor Labs DET01CFC photo detector, which produces an electrical signal. Finally, the signal is digitized by a Tektronix oscilloscope. Lasers are passed through fiber optic cable to maximize efficiency and simplify fielding. A Gaussian beam consisting of 1,550 nm wavelength monochromatic light is directed onto an aluminum disk whose rotation is orthogonal to the optical beam axis. This geometry ensures lateral translation of the speckle pattern. Infrared lasers at 1,550 nm are commonly used because optical fibers and related components transmit with low-loss at these wavelengths. The surface of the aluminum disk is treated with 600 grit sandpaper to produce 15 μm surface features which, at an order of magnitude larger than the laser wavelength, ensure diffusely backscattered light. The aluminum disk is driven by a variable-speed DC motor and a rotary encoder with 3.6° resolution is mounted to the motor to provide ground truth speed measurements.

The laser used for this experiment is limited to 5 mW of power output while typical PDV configurations incorporate probes whose power output is one Watt or less. As a result, a higher level of photo detector impedance is required to achieve a reasonable signal-to-noise ratio from the weak light returns. This constraint influences the sensor's frequency response, effectively limiting measurement capabilities to frequencies below 33 kHz. It follows that the maximum lateral velocity that can be reliably tested with this configuration was found to be near 1 m/s.

To study the influence of offset distance on speed measurements a series of observations is taken for the aluminum disk set at different axial displacements and a constant angular velocity. Care is taken in aligning the laser to ensure consistent beam placement at a 12.5 ± 0.5 mm radius from the disk's center of rotation for each observation. Both a collimating and focusing probe are employed to study the effect of beam characteristics on speed estimation capabilities. The focusing probe's beam waist is 81 μm with a focal length of 40 mm while the collimating probe's related properties are 195 μm and 100 mm, respectively. In a second experiment the aluminum disk is fixed at an offset distance of 20 mm and the angular velocity is varied over a series of observations. Again, this procedure is carried out for each probe. One million samples are collected for each observation, providing sufficient data to build a speed estimate distribution and establish error bounds. The normalized autocorrelation function is generated from a 50,000 data point window.
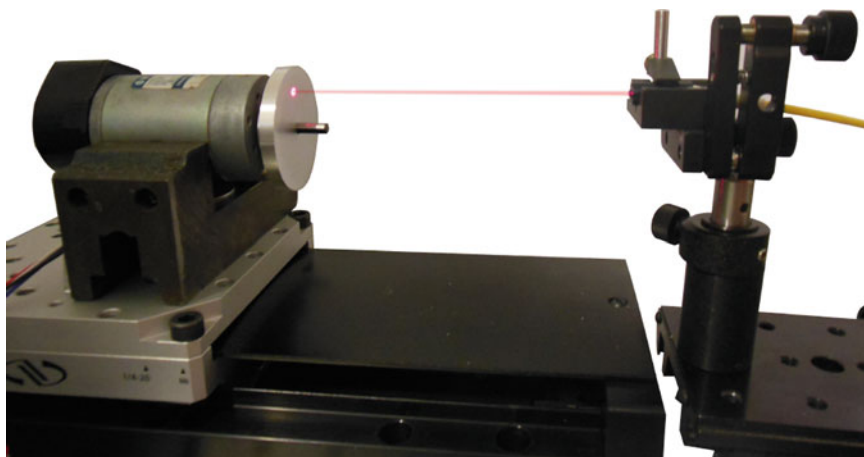

Fig. 29.2 An aluminum disk whose rotation is orthogonal to the optical beam axis is fixed atop a linear slider which is used to gather data across a range of axial displacements. A rotary encoder is used to acquire ground truth velocity measurements

29.4   Results

Experimental results show agreement with the theoretical model far from the focal point and for a range of lateral speeds. In Fig. 29.3a, c, speed estimates deviate no more than 20% from the ground truth measurements recorded by our rotary encoder and only stray beyond this bound near the photo detector band-limit. Also notice that the estimates linearly scale in proportion to the ground truth when below the photo detector band-limit. The beam waists of the probes used to generate these two data sets vary by 150%, yet both probes provide relatively accurate estimates of lateral surface speed according to Eq. (29.1). Possible explanations for estimation errors include optical aberrations changing the effective beam waist, speckle dynamics influencing τ_c and various experimental uncertainties.

Speckle dynamics clearly influence speed estimates near the focal point of the focusing probe as can be seen in Fig. 29.3b at an offset distance of 40 mm and average lateral speed of 0.65 m/s. However, the increase in coherence time is unexpected as speckle boiling should typically increase a speckle pattern's temporal variation and therefore it's average frequency content. It is possible that the up-shift in frequency content due to boiling, when passed through the transfer function of our high-impedance photo detector, resulted in a net reduction in the dominant frequency within the measured signal. Far from the focusing probe's focal point the coherence time remains static, uniformly within 10% of its theoretical value.

In Fig. 29.3d, coherence time fluctuations of 60% were measured over a range of axial displacements surrounding the collimating probe's 100 mm focal length before leveling off at distance of 125 mm. This result indicates that boiling is not closely constrained to the focal point as was found for the focusing probe. Such a contrast in behavior can possibly be explained by each beam's radius of curvature, $\rho(z)$: for the focusing probe $\rho(z)$ sharply approaches ∞ at the focal point, while the collimating probe is designed such that $\rho(z) \approx \infty$ over the whole axis of propagation. Since the collimating probe
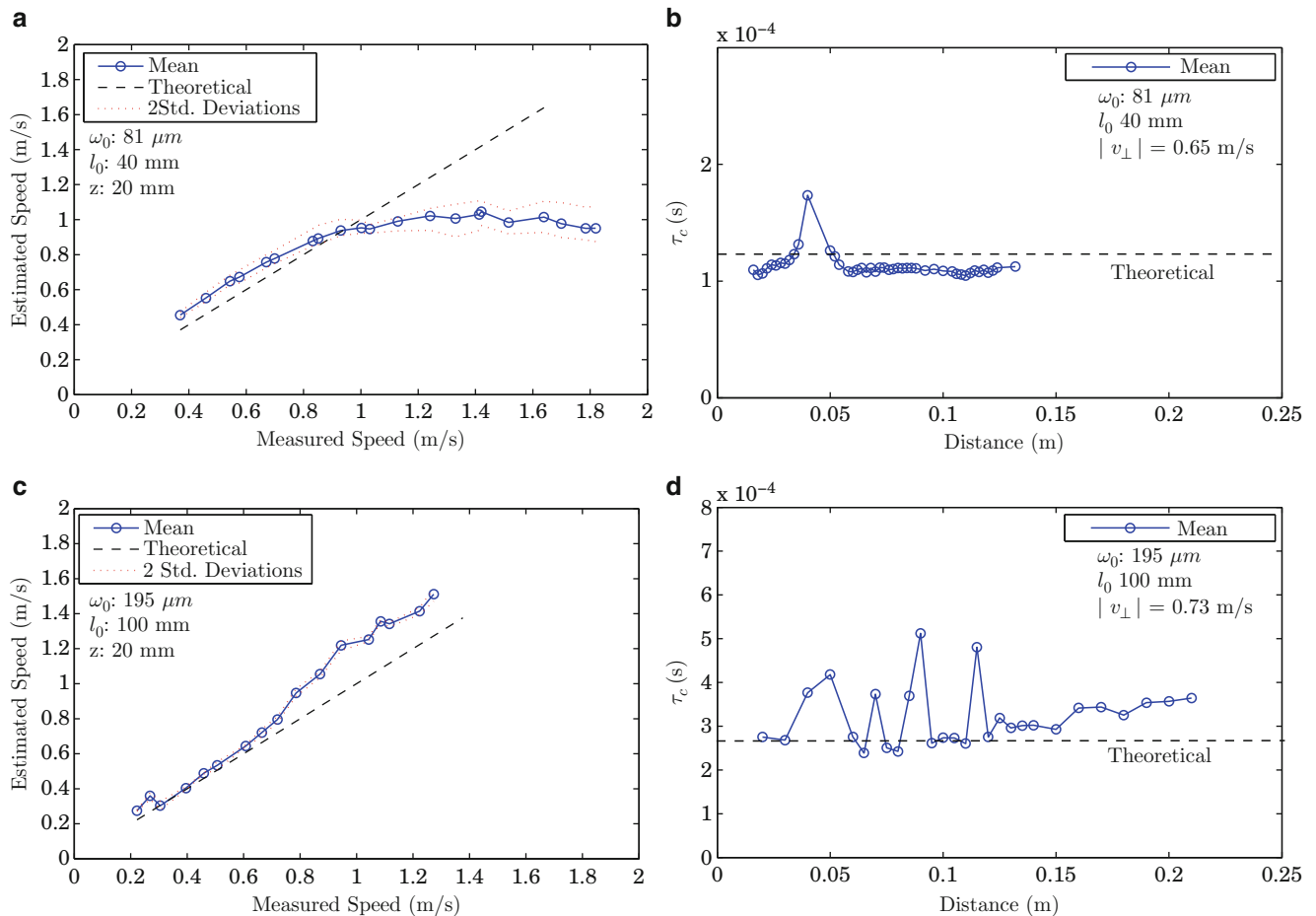
Fig. 29.3 Processed experimental data for focusing (**a**), (**b**) and collimating (**c**), (**d**) probes. Speed estimates in (**a**) roll-off at the photo detector's band-limit

is not perfect, there will inherently be a range of axial displacements where $\rho(z) \ll \infty$ before and beyond the focal point. It is in these regimes where boiling does not dominate the coherence time and our experimental data shows closer agreement with the theoretical model.

29.5   Conclusions

Our experiments have shown that reasonable lateral speed estimates may be produced from laser speckle in the case of pure lateral translation of a diffusing surface. Despite significant signal-to-noise limitations due to the use of a 5 mW laser, speed estimates were within 20% of the ground truth for collimating and focusing probes operating below the photo detector band-limit on surfaces that were far from the focal point. It is likely that lasers used in most PDV applications would produce improved results due to their increased power output.

Axial displacement was found to significantly influence speed measurements in regimes where boiling is believed to dominate. By studying the behavior of both a focusing and collimating probe, we posit that the dimension of these boiling regimes may be related to the beam's radius of curvature. To be more specific: boiling may dominate speckle dynamics when the beam radius of curvature is close to ∞ at the point of incidence. The details of such a relationship will be explored in future work.

References

1. Briers JD (1996) Laser doppler and time-varying speckle: a reconciliation. JOSA A 13(2):345–350
2. Dolan DH, Lemke RW, McBride RD, Martin MR, Harding E, Dalton DG, Blue BE, Walker SS (2013) Tracking an imploding cylinder with photonic doppler velocimetry. Rev Sci Instrum 84(5):055102–055102
3. Goodman JW (1975) Statistical properties of laser speckle patterns. In: Laser speckle and related phenomena, pp 9–75. Springer, Berlin
4. Iwai T, Takai N, Asakura T (1981) The autocorrelation function of the speckle intensity fluctuation integrated spatially by a detecting aperture of finite size. J Mod Opt 28(10):1425–1437
5. Iwai T, Takai N, Asakura T (1982) Dynamic statistical properties of laser speckle produced by a moving diffuse object under illumination of a gaussian beam. JOSA 72(4):460–467
6. Moro EA, Briggs ME (2013) Note: Simultaneous measurement of transverse speed and axial velocity from a single optical beam. Rev Sci Instrum 84(1):016110–016110

Chapter 30
Sensor Placements for Damage Localization with the SDLV Approach

D. Bernal, Q. Ma, R. Castro-Triguero, and R. Gallego

Abstract The SDLV approach is a technique that localizes damage by identifying loading conditions for which the damage is unobservable. The loading conditions are defined in sensor coordinates and are given by the kernel of a matrix that can be extracted from the differences in the identification between the reference and the damaged states. This paper examines the performance of two strategies to decide on the sensor locations. One is based on the idea of attaining maximum linear independence of stress fields generated from the sensor locations and the other is based on linear independence of the mode shapes at the sensor locations. In addition to these two techniques the performance of a "user selected" position is also obtained, for comparison.

Keywords Optimal sensor placements • Damage localization • Damage locating vectors

30.1 Introduction

Since the location of sensors dictate which signals are retrieved from a structure one anticipates that, for any task, there are positions that are "better" than others. The term optimal sensor placement is often used to refer to some position that is expected to maximize some objective function, although the connection of the objective function with the actual goal of the monitoring is not always clearly stated. In this paper we focus on the question of how the location of sensors affects the performance of damage localization using the SDLV approach [1]. The study is exploratory and is limited to the comparison of two strategies, namely: the Effective Independence Method (EIM) proposed in [2] and a strategy, introduced here, which we designate as the Linear Independence Stress Field (LISF). In addition to these two strategies, and in order to check the merit of the results from EIM and LISF, a user selected "reasonable" distribution is also examined. The paper reviews the SDLV localization scheme, discusses the sensor placement strategies and summarizes the results obtained.

30.2 The SDLV Approach

The SDLV approach is a technique to localize damage from the null space of changes in flexibility that applies in cases where the input cannot be measured. In the absence of a deterministic input the flexibility cannot be computed but a matrix that has a related null space can be obtained. Here we limit the presentation to an outline of the procedure from a user's perspective; details of the approach are presented in [1].

D. Bernal (✉) • Q. Ma
Northeastern University, Boston, MA, USA
e-mail: bernal@coe.neu.edu

R. Castro-Triguero • R. Gallego
University of Granada, Granada, Spain

Assume that two system identifications have been carried out, one before and one after the damage and let the subscripts u and d be used to refer to the results. With the sensors in the same locations in the reference and the damaged states one has state transition and state to output matrices $\{A_u, C_u\}$ and $\{A_d, C_d\}$. The SDLV approach uses the matrices H_p and L given by

$$H_p = \begin{bmatrix} CA^{1-p} \\ CA^{-p} \end{bmatrix} \tag{30.1}$$

$$L = \begin{bmatrix} I \\ 0 \end{bmatrix} \tag{30.2}$$

where $p = 0$, 1 or 2 for displacement, velocity or acceleration sensing, and the matrix Q given by

$$Q = -CA^{-(p+1)} H_p^+ L \tag{30.3}$$

where $H_p^+ =$ pseudoinverse of H_p.

The damage locating vectors (DLV) are the right side singular vectors of $\triangle Q^{\mathrm{T}}$ corresponding to the smallest q singular values. With the singular value decomposition of $\triangle Q^{\mathrm{T}}$ as

$$SVD\left(\Delta Q^T\right) = [U][S][V]^T \tag{30.4}$$

q is taken as

$$q = 0.5 \times \left\{ number \ of \ \gamma \ values \le 0.1 \middle| \gamma = \sqrt{\frac{s_i}{s_i\big|_{max}}} \right\} \tag{30.5}$$

where q is rounded downward if fractional.

The SDLV approach takes the DLV vectors and applies them as loads on a model of the undamaged structure to obtain the stress fields σ_j. The stress fields for each DLV vector are normalized to a maximum of unity to define the normalized stress fields (nsi), namely

$$nsi_j = \frac{|\sigma_j|}{|\sigma_j|_{max}} \tag{30.6}$$

The decision on damage location is taken from inspection of the *weighted stress index* (WSI), defined by

$$WSI = \sum_{j=1}^{q} nsi_j \tag{30.7}$$

Specifically, the elements of the potentially damaged set {PD} are taken as those for which WSI is less than 10 % of the largest value, namely

$$PD = \left\{ elements \middle| WSI \le 0.1 WSI_{max} \right\} \tag{30.8}$$

As one gathers from inspection of Eq. 30.3, in applying the SDLV approach it is necessary to ensure that the matrix H_p is full column rank. This requirement implies that the maximum system order that can be used in the calculations is twice the number of sensors. In cases where a larger number of modes are identified it is necessary to truncate and the approach is outlined next.

Let m be the number of sensors and n be the number of identified modes and assume that n > m. Let the number of modes to be retained $=$ nm.

1. Solve $A \ \Phi = \Phi \Lambda$
2. Define $A_1 = \Lambda$ and $C_1 = C\Phi$

3. Define A_t as the diagonal matrix with the first nm entries of A_1 and C_t as the first nm columns of C_1, namely

$$A_t = \begin{bmatrix} \Lambda_1 & \cdots & 0 \\ \vdots & \ddots & \vdots \\ 0 & \cdots & \Lambda_{nm} \end{bmatrix}_{nm \times nm}, \qquad C_t = \begin{bmatrix} \Phi_1 \ldots \Phi_{nm} \end{bmatrix}_{m \times nm} \tag{30.10}$$

4. Substitute A_t and C_t for A and C in Eq. 30.3 and proceed as usual.

30.3 Sensor Placement Strategies

30.3.1 Effective Independence Method

The effective independence method (EIM) presented in [2, 3] is an iterative method designed to select locations of a set of sensors based upon their contribution to the linear independence of the mode shapes. Let the measurements be expressed in the basis of the mode shapes as

$$y = \Phi Y + \omega \tag{30.11}$$

where ω is the measurement noise. The accuracy with which the modal amplitudes (Y) can be estimated from the y measurements is determined by the derivative of y with respect to Y and on the covariance of the measurement noise Σ_ω. Assuming that ω is normally distributed the Fisher Information on Y that is contained in the data is

$$I_Y = \frac{dy}{dY}^T \Sigma_\omega^{-1} \frac{dy}{dY} \tag{30.12}$$

or

$$I_Y = \alpha \cdot \Phi^T \Phi \tag{30.13}$$

where the covariance of the measurement noise has been taken as $\alpha^{-1} \cdot I$. Since the inverse of I_Y is the Cramer-Rao-Lower-Bound (CRLB) of the covariance with which the modal amplitude can be estimated it is reasonable to select the m rows of the mode shapes (sensor locations) such that the product in Eq. 30.13 has the largest determinant. The problem is seldom solved by performing the required nonlinear optimization but it is, instead, approximated by removing, one at a time, the sensor that "least contributes" to the determinant [4].

The EIM standard approach is as follows:

1. Obtain the eigenvectors Φ—select n target modes where $n \leq$ number of sensors, designate the matrix Φ_T.
2. Form $Q = \Phi_T^T \Phi$
3. Obtain the eigenvalues and eigenvectors of Q, namely, solve $Q\Psi = \Psi\Lambda$
4. Compute $E = diag(\Phi_T \Psi \Lambda^{-1} \Psi^T \Phi_T^T)$
5. Eliminate the smallest value in E as well as the corresponding row in Φ_T;
6. Repeat steps 2–5 until m positions are left.

30.3.2 Linear Independence Stress Field

Since the SDLV approach locates damage using stress fields generated by loads applied at sensor positions it appears reasonable to examine the merit of locating sensors at the positions that lead to the most linearly independent stress fields. Here we designate this sensor placement criterion as the LISF scheme. Methodology to organize the columns of a matrix in an order that makes then most linearly independent is known as the subset selection problem. Let V be a real full rank matrix. The objective is to find a column permutation matrix Π so that V is reordered as

$$V_{m \times n} \Pi = \left(V_{1m \times k} \quad V_{2m \times (n-k)} \right) \tag{30.14}$$

where V_1 contains k most linearly independent column vectors and V_2 is the rest. There are different algorithms to obtain the subset V_1. Here we use a subset selection method presented in [5] which is described next:

1. Perform a QR decomposition with column pivoting to obtain an initial permutation Π. Let the upper triangular matrix obtained be $R = \begin{pmatrix} R_k & B_k \\ 0 & C_k \end{pmatrix}$;

   Let e_i be the ith column of the identity matrix so that $C_k e_j$ is the jth column of C_k and $e_i^T R_k^{-1}$ is the ith row of R_k^{-1}.

2. While there exist i and j
3. If $\sqrt{\left(R_k^{-1} B_k \right)_{i,j}^2 + \| C_k e_j \|_2^2 \| e_i^T R_k^{-1} \|_2^2} > 1$ switch columns i and $j + k$ of R: $\tilde{R} = R \Pi_{i,j+k}$;
4. Retriangularize: $\tilde{R} = Q_{i,j+k} R$;
5. Update: $\Pi = \Pi \Pi_{i,j+k}$;
6. End while

   Obtain V_1 from $V_{m \times n} * \Pi = (V_{1m \times k} \ V_{2m \times (n-k)})$

30.4 Criterion to Compare Performance

We compare performance by illustrating the total number of structural elements that have a normalized stress field less than 10 % of the maximum. This is a reasonable metric because the SDLV approach locates the damage as elements where the stress (for the SDLV loading) is below a certain threshold.

30.5 Numerical Examination

The structure considered is the 2-D truss shown in Fig. 30.1. The mass distribution (used to compute mode shapes) is given in Table 30.1.
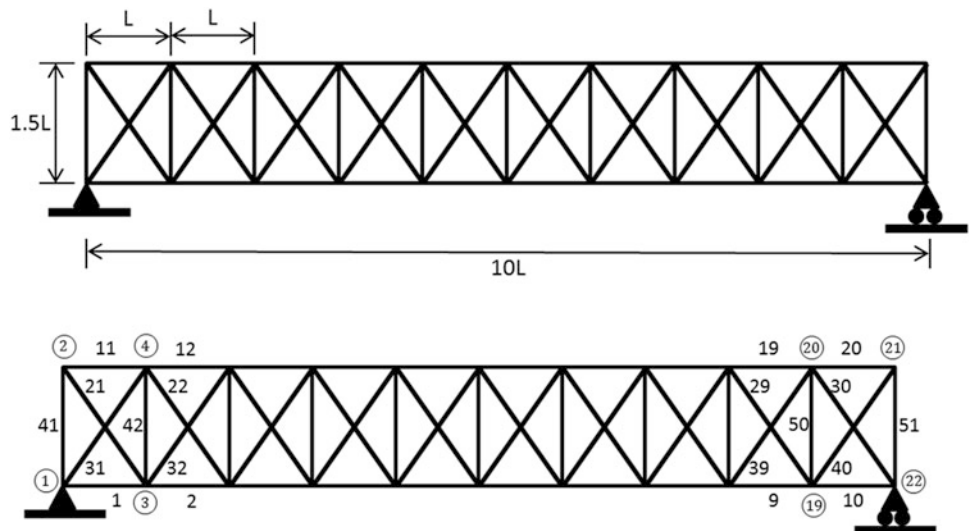
Fig. 30.1 Truss model ($A = 0.5 \text{ m}^2$, $E = 200$ GPa)

Table 30.1 Masses

Mass	0.75M	M	M	1.5M
Nodes	2, 21	1, 22	4, 6, 8, 10, 12, 14, 16, 18, 20	3, 5, 7, 9, 11, 13, 15, 17, 19

Fig. 30.2 Sensor placements
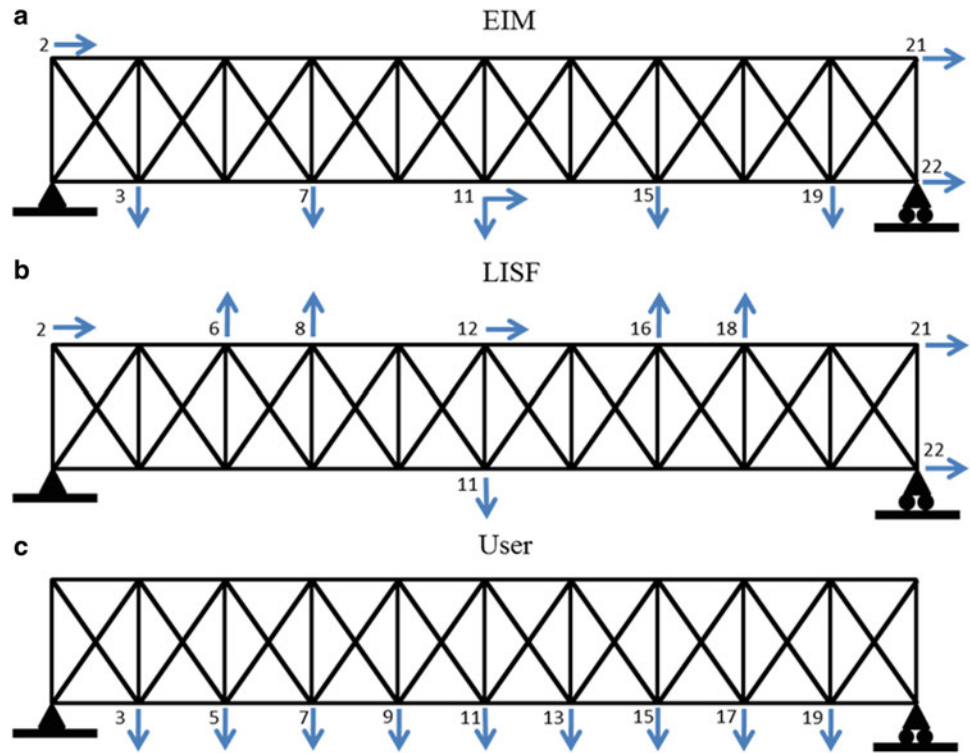
Table 30.2 Total number of potential damaged elements

Number of modes included	5	6	7	8	9
EIM	272	337	321	243	304
LISF	287	298	347	290	234
User's	355	186	113	101	101

Table 30.3 Number of cases where the damaged element was missed (out of 51)

Number of modes	5	6	7	8	9
EIM	0	3	2	6	0
LISF	0	2	4	12	0
User's	1	0	11	0	0

30.5.1 Sensor Placements Results

We select nine sensors and find that the sensor placements for the strategies considered are as shown in Fig. 30.2.

30.5.2 Damage Scenarios

We apply single damage with 50 % reduction in stiffness at each element one by one.

30.5.3 Summary of Results

Table 30.2 shows the total number elements in the potentially damaged set for the 51 different damage scenarios and Table 30.3 indicates the number of cases where the damaged element is not included in the PD set.

Finally, Fig. 30.3 shows the histogram of the ranking of the damaged element based on the WSI results.
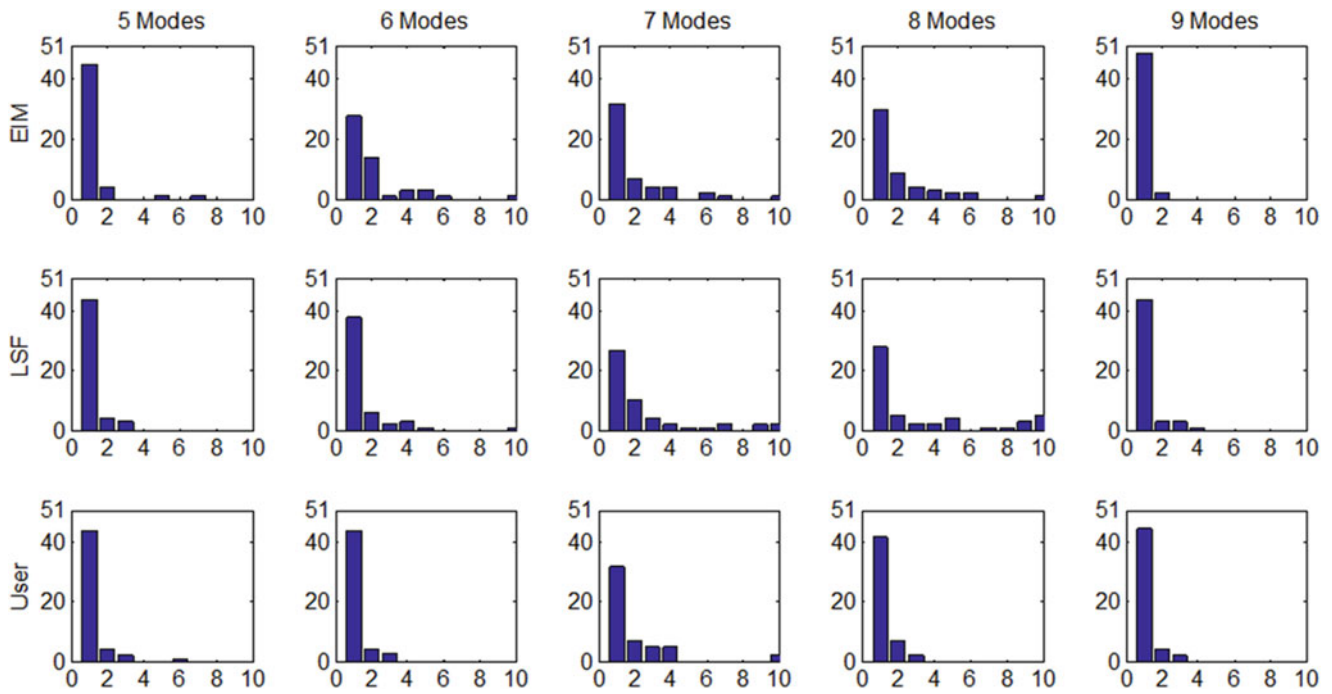
Fig. 30.3 Histogram of damaged element ranking (based on WSI)
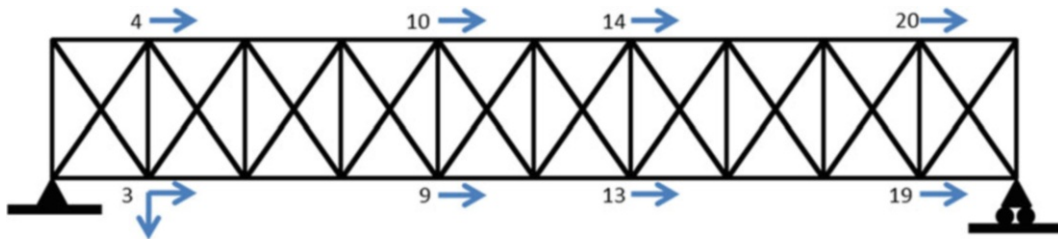
Fig. 30.4 Sensor placement deemed poor by the LSF approach

Table 30.4 Total number of potential damaged elements for the arrangement of Fig. 30.5

Number of modes	5	6	7	8	9
Sum of elements in PD sets	500	489	562	687	522

30.5.4 Discussion

The results shown do not provide evidence to suggest the superiority of EMI or the LSF. In fact, although poorer when five modes are used, the user selected distribution actually outperformed both EMI and LSF in all other cases. While we cannot offer definite assertions at this point because the examination is currently ongoing, we're under the impression that the results from the algorithm used to reorder the stress field columns are suspect.

To determine whether a position that was deemed poor by the LSF approach actually performed poorly we examined the configuration is depicted in Fig. 30.4. The results on the sum of all the elements in the potential damage set are given in Table 30.4 and, as can be seen, the arrangement does in fact perform poorly, with an increase of around 60 % in the total elements on the PD set when compared to the results in Table 30.2.

30.6   Concluding Comments

A strategy based on placing the sensors so that the stress fields that are generated by unit loads acting at each of the coordinates are as linearly independent as possible seemed to be a rational criterion for damage localization using the SDLV approach. Exploratory results obtained on a 2-D truss did not, however, provided the anticipated confirmation. As noted, it may be that the implementation of the linear stress field concept realized in the numerical example is suspect. Another reason that needs to be examined is that the approximation in the loading from modal truncation may be strongly dependent on sensor placements. Specifically, it may be that arrangement X is better than Y when the DLV is correct but in practice the reverse may be found because error from truncation in the estimation of the loading is higher in X and it may dominate the solution. Studies to clarify this matter are part of the ongoing research.

References

1. Bernal D (2006) Flexibility-based damage localization from stochastic realization results. J Eng Mech 132:651–658
2. Kammer DC (1991) Sensor placement for on-orbit modal identification and correlation of large space structures. J Guid Control Dyn 14:251–259
3. Kammer DC (1992) Effects of noise on sensor placement for on-orbit modal identification of large space structures. J Dyn Syst Meas Control 114:436–443
4. Kammer DC, Yao L (1994) Enhancement of on-orbit modal identification of large space structures through sensor placement. J Sound Vib 171(1):119–139
5. Broadbent ME, Brown M, Penner K (2010) Subset selection algorithms: randomized vs. deterministic. SIAM Undergr Res Online 3:22

Chapter 31
Diaphragm Flexibility in Floor Spectra

D. Bernal, E. Cabrera, and E. Rodríguez

Abstract When a secondary system is attached to the floor of a structure its earthquake imposed demands derive from the motion at the attachment points. Computation of these motions is typically carried out on the premise that the floor is rigid in its own plane and that the modification of the floor motion due to interaction can be neglected. While interaction can in fact be expected to be negligible for light secondary systems, it is not clear whether the flexibility of the floor slab in its own plane can have significant effects on the floor spectra at frequencies that may be relevant for the seismic review of the attachment. This paper investigates the matter using seismic response data from an instrumented building that has four sensors measuring horizontal motion in a level. Specifically, the paper computes the floor spectra for the measurements and compares them with that obtained when the input signal is reconstructed from the other accelerometers on the premise of rigid behavior. It is shown that the frequency range where the deviations become significant is sufficiently low to be of practical importance.

Keywords Diaphragms • Floor spectra • Earthquake • Secondary systems

31.1 Introduction

In the design of buildings for earthquake loads it is customary to assume that the floors can be treated as rigid in the horizontal plane. This assumption leads to an approximation of the building dynamics with a model that has only three inertial degrees of freedom per floor. A significant number of studies have been carried out to investigate the error that can result from this assumption when it comes to the distribution of the inertial forces to the lateral force resisting subsystems [1–4]. As one gathers from qualitative inspection, the assumption of a rigid floor becomes suspect as the floor aspect ratio increases or in those cases where there are large holes in the floor system that can contribute to in plane deformability. There is, of course, also the issue of building plans in the shape of L's or T's that often require special treatment. Seismic codes provide simplified guidelines indicating when the deformability of a floor system needs to be considered in the distribution of the inertial forces and when it is acceptable to treat the floor as a rigid diaphragm [5, 6]. Needless to say, the potential importance of floor deformability is not just a function of the geometry, or of the structural details of the floor, but depends also on the stiffness of the lateral load resisting systems.

This paper is concerned with floor flexibility in the horizontal plane but not from the perspective of the effect on the lateral load distribution. Instead, the focus is on the adequacy of the rigid diaphragm assumption regarding the prediction of floor spectra. The term floor spectra is used to describe the spectra associated with motions taking place at points within structures; reference to the floor coming from the fact that in the majority of cases the points of interest are in the floors. Floor spectra are or interest when equipment or some other secondary system is to be attached to a floor and it is of interest to determine the demands that it will undergo during seismic excitation of the building. In the majority of cases the secondary system is light and the interaction forces can be neglected without introducing undue error i.e. the movement at the point

D. Bernal (✉)
Northeastern University, Boston, MA, USA
e-mail: bernal@coe.neu.edu

E. Cabrera • E. Rodríguez
Santiago University of Technology, Santiago, Chile

where the item is connected to the floor is computed by analyzing the building without the attachment. Although we operate under this premise it is opportune to note that non-negligible error from neglecting interaction can arise when the natural frequency of the attachment coincides with that of some mode of the system. Our specific interest here is to inspect the adequacy of the rigid diaphragm assumption in the computation of floor spectra. In this regard the qualitatively behavior can be anticipated without the need for analysis. Namely, the measured motion will be very close to the motion predicted by the rigid floor model at low frequencies and, as the frequency increases the motions will deviate. The question of practical interest is whether or not the frequency at which the motions begin to deviate is sufficiently low to be practically relevant and also whether the magnitude of the deviations are likely to be sufficiently large to be important. It is evident that the answers to these questions depend on the specific configuration of the building and the natural frequency of the attachment. We note that the purpose here is not to provide design guidelines or adjustments to rigid floor estimates of floor spectra but simply to determine if the matter is likely relevant in buildings of typical dimensions.

31.2 Experimental Examination

The California Strong Motion Instrumentation Program (CSMIP) has a large number of instrumented buildings and there is a subset for which some levels have more than three accelerometers measuring motion in the horizontal plane. Most of these buildings have been subjected to earthquakes and the measured response provides the data that is needed to examine the range of frequencies for which the rigid floor assumption is valid. As is evident, if the floor were perfectly rigid there would only be three independent motions in the horizontal plane. A measure of the accuracy of the rigid floor assumption is thus given by comparing the response that is measured at any sensor with that which is reconstructed from the other locations. To make the comparison most transparent it is best to perform the comparison at the level of the response spectra of the signals. To explore this matter we've taken the building depicted in Fig. 31.1. Since the relative stiffness of the floor to the lateral load resisting system has a role to play we look at the lowest and highest diaphragms in this structure, namely, level #2 and the roof (level #6). We examine the response to the Chino hills earthquake and focus on the response in the N-S direction. In this direction there are three parallel sensors and it is thus possible to predict using two at a time the other sensor (on the assumption or rigid floor). The results are shown in Figs. 31.2 and 31.3. Figure 31.2 shows that at level #2 the rigid floor assumption is valid up to approximately 2 Hz and Fig. 31.3 shows that in the roof (which is stiffer in relative terms due to the increased flexibility of the lateral load resisting system) the match extends to approximately 3 Hz. These frequencies are (perhaps) surprisingly low and suggest that flexibility in the horizontal plane may be relevant in floor spectra calculations in the frequency range where most attachments are likely to resonate.

31.3 A Simplified Model

Although the discrepancies in Figs. 31.2 and 31.3 are an indication that the diaphragm is not rigid, assigning significance to the magnitude of the discrepancies is somewhat difficult because the reconstructed response cannot be assumed to be equal to the response for the rigid floor assumption. What we opted to do to gain some insight into the likely magnitude was to formulate a model of a one-story structure where the diaphragm is modeled as a beam. The schematic illustration is depicted in Fig. 31.4.

The beam itself is modeled using 100 elements and bending and shear deformations are considered. The properties assigned to the model were taken to mimic those of the floors of the building in Fig. 31.1. While it is evident that the one level model cannot capture the complexity of the motion in the actual building we checked the reasonableness of the model by confirming that the spectra of measured vs. reconstructed values, computed in the same manner as was done for the building, illustrated coincidence in approximately the same frequency band. The results for this analysis are depicted in Fig. 31.5.

31.4 Results

Having gained some confidence on the reasonableness of the beam model we then compute, with the model, the floor spectra for the flexible and the rigid diaphragm model at the centerline of the beam and plot the results in Fig. 31.6. Note that at a frequency is 5 Hz (in the second floor) the rigid floor sub-estimates the spectral amplitude by a factor of nearly 5, which needless to say, is quite large.
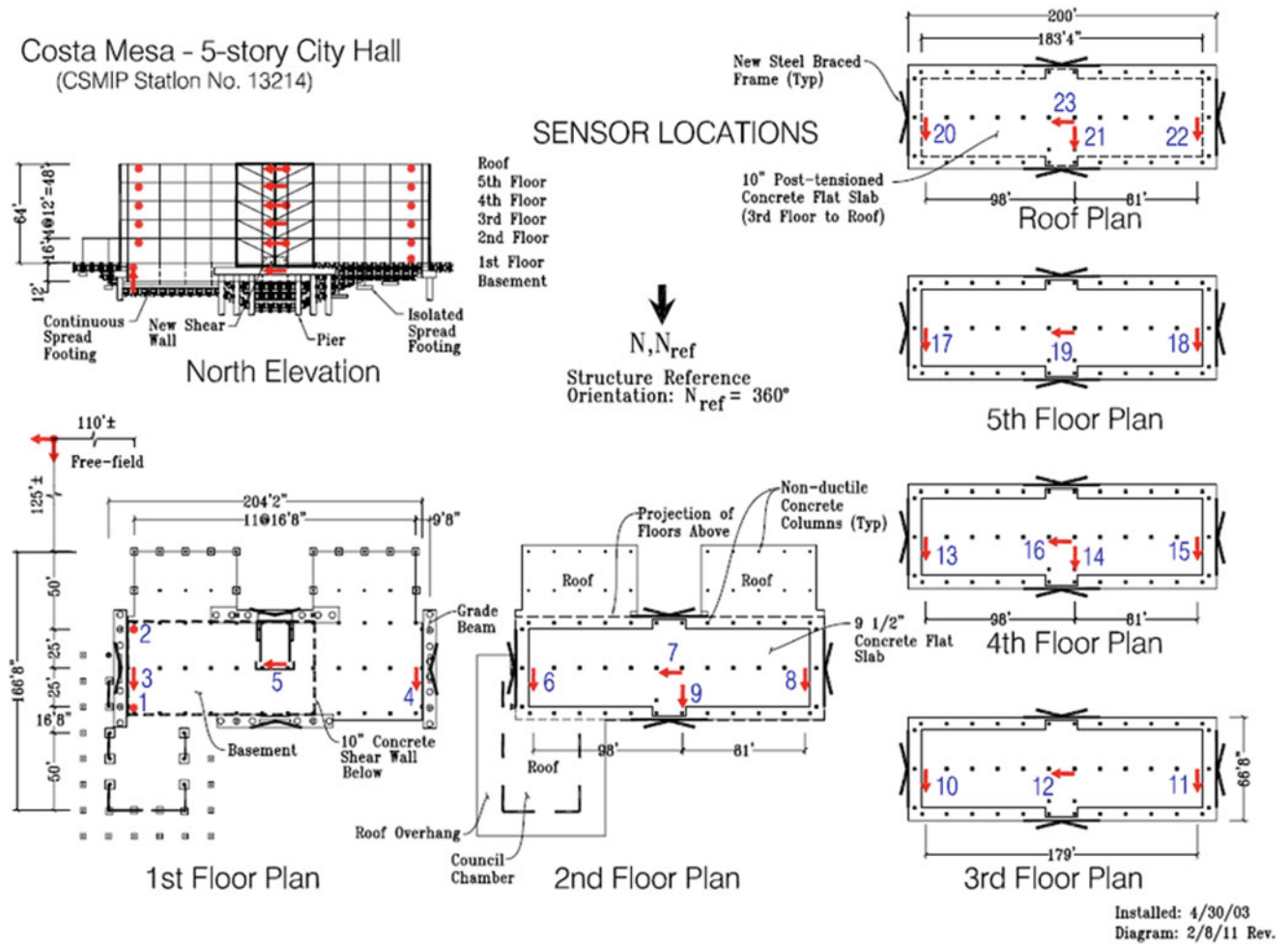
Fig. 31.1 Building selected for examination [taken with permission from the website of the California Strong motion Instrumentation Program (CSMIP)]
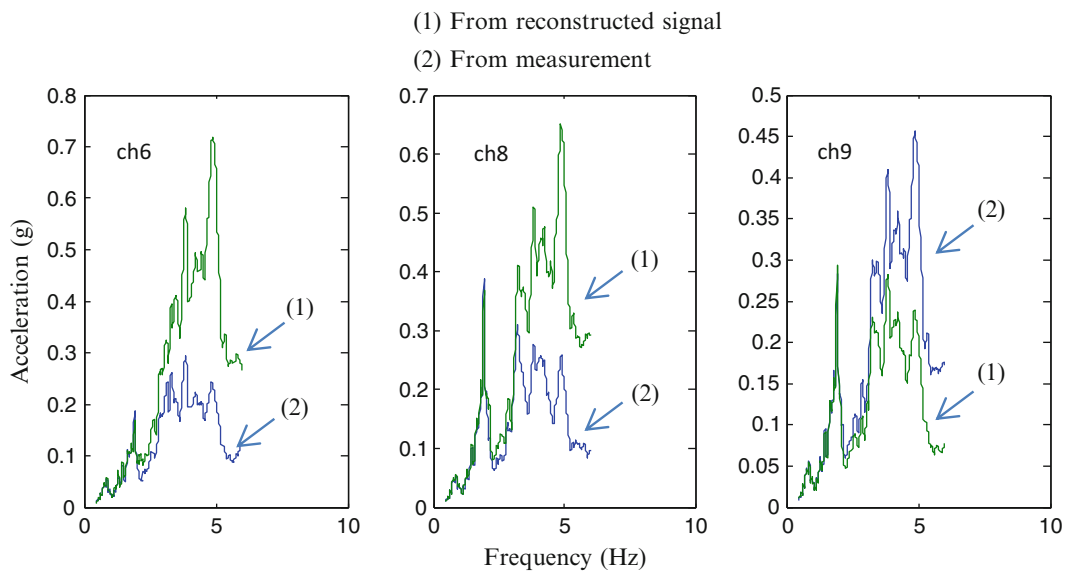

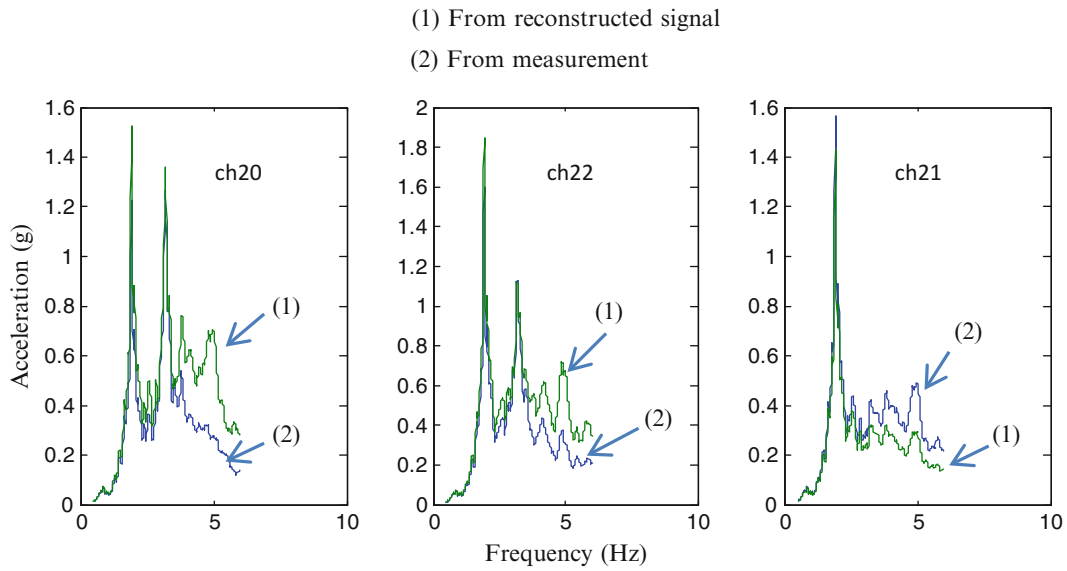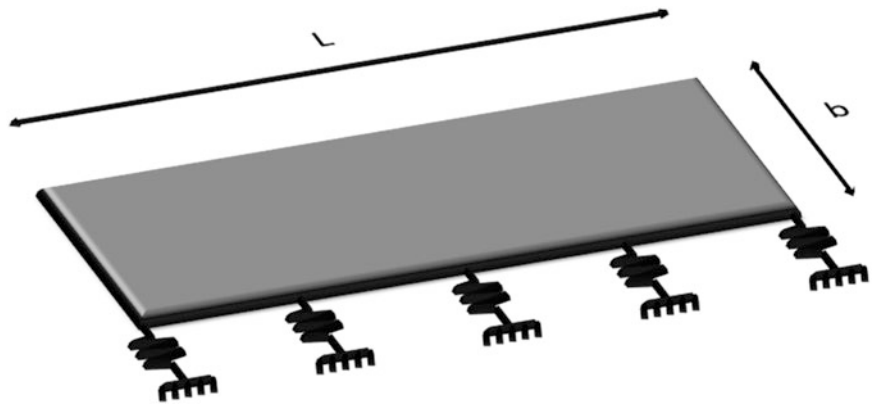**Fig. 31.2** Floor response spectra for the building of Fig. 31.1, level #2

(1) From reconstructed signal

(2) From measurement

Fig. 31.3 Floor response spectra for the building of Fig. 31.1, level #6

Fig. 31.4 Schematic illustration of a diaphragm with the lateral load resisting systems represented as springs

(1) From other sensors using RDA

(2) From measurement
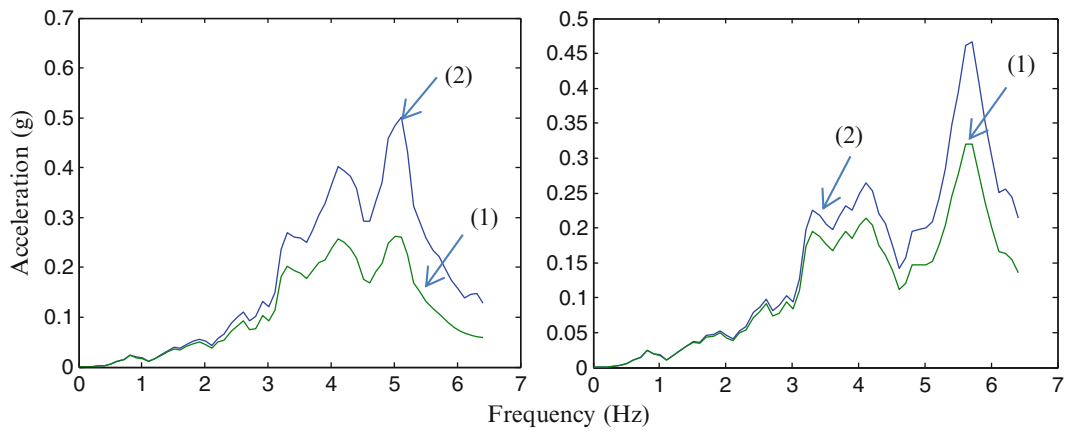
Fig. 31.5 Spectra computed at the centerline of the beam model for the diaphragm (RDA = rigid diaphragm assumption)

(1) From rigid model
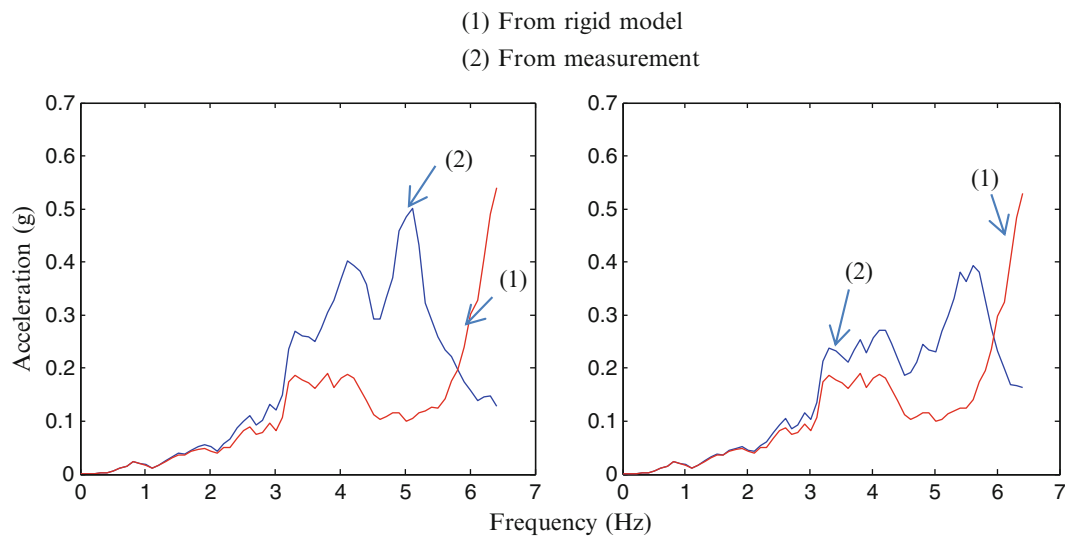
(2) From measurement

Fig. 31.6 Floor spectra for 2 % damping at the centerline of the diaphragm modeled as a beam (left = relative stiffness approximates level-2 right = approximates the roof)

31.5   Conclusions

Examination shows that floor spectra computed from measurements and from responses reconstructed on the premise of rigid floor response can differ for frequencies that are much lower than the writers anticipated prior to the analysis. In the particular building considered, whose aspect ratio is around 4, the cutoff in the lower level is found to be 2 Hz and around 3 Hz in the roof. The take away from this exploratory examination is that if one is interested in accurate floor spectra for checking some sensitive attachment then diaphragm flexibility may play an important role, even at relatively low frequencies.

References

1. Ju S, Lin M (1999) Comparison of building analyses assuming rigid or flexible floors. Struct Eng Mech 125:25–31
2. Tena-Colunga A, Abrams D (1996) Seismic behavior of structures with flexible diaphragms. Struct Eng Mech 12:439–445
3. Basu D, Jain S (2004) Seismic analysis of asymmetric buildings with flexible floor diaphragms. Struct Eng Mech 130:1169–1176
4. Jain S (1984) Seismic response of buildings with flexible floors. J Eng Mech 110:125–129
5. ASCE (2010) Minimum design loads for buildings and other structures. ASCE Standard ASCE/SEI 7-10. ASCE, Reston, VA
6. ICC. International Code Council, Inc (2009) International building code. ICC, Country Club Hills, IL

Chapter 32
Use of Zernike Polynomials for Modal Vector Correlation of Small Turbine Blades

Jonathan Salerno and Peter Avitabile

Abstract Correlation of modal data using the Modal Assurance Criterion (MAC) is difficult under the best of circumstances. This is especially true for very small structures such as turbine blades. Considering the typical geometric variation in overall blade geometry, the sensitivity of point location geometric variation can have a detrimental effect on the stated mode correlation using MAC. However, visual interpretation can indicate very similar shapes whereas MAC using detailed discrete points for a large number of points typically obtained from optical measuring systems may not yield suitable MAC values.

Recently, imaging techniques have been proven to be useful in correlating mode shapes of structures. The imaging techniques used here, specifically Zernike Polynomials (ZPs) and Zernike Moment Descriptors (ZMDs), are utilized as a mechanism to decompose modal vectors of structures that have geometric point locations that do not all accurately align with each other followed by correlating the ZMDs with a traditional MAC. Several cases are shown with analytical models to show the usefulness of the approach as well as with actual data obtained from small turbine blades tested using laser holography techniques.

Keywords Vector correlation • MAC • Zernike Polynomials

Nomenclature

p	Represents the radial order of the polynomial
q	Represents the angular frequency of the polynomial
x	X-coordinate
y	Y-coordinate
ρ	Radial vector from origin
Θ	Counter-clockwise angle from X-axis
I	Represents $\sqrt{-1}$
V	Equivalent to R and refers to Zernike Polynomials
λ_n	The normalization factor for a discrete image equivalent to the number of pixels located within the unit circle
V	Original set of non-orthogonal linearly independent functions
U	Gram-Schmidt orthogonal functions
E	Gram-Schmidt orthogonal and normalized functions
K	Indicates the function being processed
[A]	Matrix of ZPs (Each column represents a p,q set)
$\{X_K\}$	Vector of ZMDs
$\{B_K\}$	Kth Modal vector

J. Salerno • P. Avitabile (✉)

Structural Dynamics and Acoustic Systems Laboratory, University of Massachusetts Lowell, One University Avenue, Lowell, MA 01854, USA
e-mail: peteravitabile@uml.edu

32.1 Introduction

Correlation of modal data using the Modal Assurance Criterion (MAC) [1] is difficult under the best of circumstances. Difficulties in shape comparison are amplified by the identification of geometric points used to identify mode shapes. Small differences in the actual geometric point location can produce noticeable differences in the MAC results. This effect is significantly amplified in small structures where very small differences in point location are large in relation to the ratio of adjacent points describing the geometry.

This is true for very small structures such as turbine blades. For instance, in the validation of replacement turbine blades, the individual blades need to be correlated to a large group (30 or more) of similarly made turbine blades. Extraction of frequencies and mode shapes for the set of modes of concern (up to 20 or more modes), and correlation of all turbine blades in the "lot" to each other using MAC is a significant undertaking. Considering the typical geometric variation in overall blade geometry, the sensitivity of point location geometric variation can have a detrimental effect on the stated mode correlation using MAC. However, visual interpretation can indicate very similar shape whereas MAC, using detailed discrete points for a large number of points, may not yield suitable MAC values. (For these turbine blade applications, use of laser holography techniques to acquire mode shapes always produces data sets with an extremely large number of physical points to describe the entire geometry.)

Generally, thousands of physical points may not be necessary to identify the shape. A more compact description of the shape is needed. Several imaging techniques may be better suited to cast the shape information in a more compact form. The work here focuses on casting the shape information in a more compact form using Zernike Polynomials (ZPs) and Zernike Moment Descriptors (ZMDs), which were developed by Zernike [2] and primarily used in optical measurements. By utilizing ZPs, which are a defined by a set of infinite polynomials formulated over a unit circle, the modal vector can be decomposed to represent a summation of ZPs with coefficients equivalent to the ZMDs up to order 'p'. Because the ZMDs can be represented as a vector for each mode, a traditional MAC, which was developed by Allemang [1] and is a tool to determine the correlation between two vectors, is utilized to compare the ZMDs of one system to a similar system that utilizes a different portion of the pattern.

This work utilizes the documented work completed by Wang, Mottershead, and Mares [3] in examining finite element models with ZPs and ZMDs in correlating the original modal vector to that reproduced by the reconstruction from the ZMDs. Utilizing this work, a study of the utilization of ZPs and ZMDs as a resource in decomposing modal vectors of structures that do not have accurately aligned geometric point locations, and with the correlation being performed with a traditional MAC, is examined. By examining analytical and experimental case studies, this work shows advantages in using Zernike Polynomials in correlating objects with small geometric differences due to manufacturing differences when compared to a traditional MAC correlation.

32.2 Theoretical Background

The theoretical background is described in [2]. However, the majority of the theory in this section is summarized from [3] where a significant amount of work was done. This theory is summarized here for completeness of the paper.

32.2.1 Zernike Polynomials

The theory presented here for ZPs are summarized from Wang, Mottershead, and Mares [3] and are commonly available; the theory is only summarized here with details found in the references. ZPs are an infinite set of orthogonal, complex polynomials defined over the unit circle [2]. ZPs can be expressed mathematically as,

$$V_{p,q}(x, y) = V_{p,q}(\rho, \theta) = R_{p,q}(\rho) e^{iq\theta} \tag{32.1}$$

Equation 32.1 shows that the polynomials can be defined in Cartesian or Polar coordinates. The variable $R_{p,q}(\rho)$ of Eq. 32.1 is defined in [2] as,

$$R_{p,q} = \sum_{s=0}^{(p-|q|)/2} (-1)^s * \frac{(p-s)!}{s! \left(\frac{p+|q|}{2} - s\right)! \left(\frac{p-|q|}{2} - s\right)!} * \rho^{p-2s} \tag{32.2}$$

Equation 32.2 shows that for $R_{p,q}(\rho)$ the result is equivalent to $R_{p,-q}(\rho)$. ZPs have been proven to satisfy the condition for orthogonality [4],

$$\iint_{x^2+y^2\leq 1} V^*_{p,q}(x,y)\, V_{p',q'}(x,y)\, dxdy = \frac{\pi}{p+1}\delta_{p,p'}\delta_{q,q'} \tag{32.3}$$

or in polar coordinates as [5],

$$\int_0^{2\pi}\int_0^1 V^*_{p,q}(\rho,\theta)\, V_{p',q'}(\rho,\theta)\, d\rho d\theta = \frac{\pi}{p+1}\delta_{p,p'}\delta_{q,q'} \tag{32.4}$$

Equation 32.4 proves that the orthogonality condition can only be achieved in a continuous fashion or for an analog image over the unit circle. Therefore, for discrete data or a digital image the condition for orthogonality cannot be achieved but can be approximated if the discrete data is dense.

32.2.2   Zernike Moment Descriptors

The theory presented here for ZPs are summarized from Wang, Mottershead, and Mares [3] and are commonly available. ZMDs are the coefficients of ZPs that are able to reconstruct an image I(x,y). ZMDs are defined as,

$$Z_{p,q} = \frac{p+1}{\pi} \iint_{x^2+y^2\leq 1} I(x,y)\, V^*_{p,q}(x,y)\, dxdy \tag{32.5}$$

or in polar coordinates as,

$$Z_{p,q} = \frac{p+1}{\pi} \int_0^{2\pi}\int_0^1 I(\rho,\theta)\, V^*_{p,q}(\rho,\theta)\, \rho d\rho d\theta \tag{32.6}$$

For convenience Eq. 32.6 can be recast such that $V^*_{p,q}$ is real-valued, shown as,

$$Z_{p,q} = \frac{p+1}{\pi} \int_0^{2\pi}\int_0^1 I(\rho,\theta)\, R_{p,q}(\rho)\, (cos\,(q\theta) - i\,sin\,(q\theta))\, \rho d\rho d\theta \tag{32.7}$$

Equation 32.7 shows that ZMDs are the inner product of the image I(x,y) and set of complete orthogonal ZPs. Therefore, the image I(x,y) can be reconstructed by summing together the product of the ZMDs with the Zernike Polynomials [6].

$$I(\rho,\theta) = \sum_{p=0}^{\infty}\sum_q Z_{p,q} V_{p,q}(\rho,\theta) \tag{32.8}$$

Because Eq. 32.8 requires an infinite order of polynomials to accurately represent the image I(x,y), the order of the polynomial needs to be truncated to a p_{max} order such that results can be computed. However, errors are prevalent in the reconstructed image due to the truncation. In addition to the error related with utilizing a pmax order of ZPs, there is an error in approximating the double integral solution of Eq. 32.5 for a discrete image, shown as,

$$I(\rho,\theta) = \frac{p+1}{\lambda_n}\sum_{x=0}^{p-1}\sum_{p-1}^{p-1} I(x,y)\, V^*_{p,q}(x,y) \tag{32.9}$$

Equation 32.9 is necessary for an image I(x,y) that cannot be directly integrated [7]. The normalization factor replaces the π term of Eq. 32.5, because the area inside a unit circle is equivalent to π.

32.2.3 Additional Processing

To solve for the Zernike Moment Descriptors a Least Squares Solution (LSQ) is used as an error minimizing solution to a system of equations. For this study an LSQ is utilized to solve the system of equations represented by,

$$[A]\{X_K\} = \{B_K\}. \tag{32.10}$$

Prior to the formulation of the Zernike Polynomials, a system that is discretized and not defined over the entire area of a unit circle should be mapped to a unit circle. This mapping process attempts to preserve the shape features of the original structure while encompassing as much area of the unit circle as possible, to best reduce geometric errors in calculating ZPs and ZMDs [8]. This is an important step in the process and is detailed in [3].

Since, a finite number of Zernike Polynomials are being utilized in the process the orthogonality of the polynomials are lost. To maintain orthogonality, a Gram-Schmidt Orthogonalization is performed, as defined in [9].

32.2.4 Modal Assurance Criterion

The Modal Assurance Criterion (MAC) is used to determine the amount of correlation that exists between two vectors. For this study MAC is used to determine the correlation between a modal vector and the same modal vector that is reconstructed from increasing orders of GSZPs. MAC is defined as,

$$0 \le MAC_{ij} = \frac{\left[\{u_j\}^T \{e_k\}\right]^2}{\left[\{u_j\}^T \{u_j\}\right]\left[\{e_k\}^T \{e_k\}\right]} \le 1 \tag{32.11}$$

The results of a MAC produce values on a scale from zero to one. Values close to one represent strong correlation, while values close to zero represent poor correlation. The results of MAC calculations are plotted in the form of a three-dimensional matrix. Another type of MAC is a MAC which computes a MAC for all the vectors of a matrix. A MAC will be used to correlate a matrix of ZMDs for one structure and a matrix of ZMDs for a similar structure.

32.2.5 Mode Shape Decomposition

To analyze the modal information, the out of plane mode shapes of the object must be decomposed to determine the linear combination of GSZPs with coefficients equivalent to ZMDs that best represent the mode shapes. This decomposition is performed within MATLAB® [11].

To determine the appropriate order of polynomials used for each mode shape, each individual mode shape is decomposed utilizing GSZPs with the results being the ZMDs from an LSQ. This decomposition is then reconstructed to approximate the original mode shape. This reconstructed mode shape is then compared to the original mode shape utilizing a calculation of the MAC. Once the MAC calculation presents a result greater than or equal to 0.99 the appropriate order of polynomials are determined. From the order of the polynomials the number of polynomials [12] used can be calculated as,

$$\#of\ Polynomials = \frac{Order^2 + 2*Order + Order}{2} + 1 \tag{32.12}$$

Equation 32.12 determines the number of Polynomials from the Polynomial Order.

In correlating two models the same number of polynomials must be utilized such that the MAC calculation can be performed. Therefore, the maximum order of polynomials appropriate for the models being correlated are utilized in the decomposition of the mode shapes for each. Each mode shape is then decomposed in two fashions.

The first scheme for mode shape decomposition involves utilizing the full order of polynomials to decompose the mode shapes. This decomposition scheme is shown in Fig. 32.1. Figure 32.1 shows the first scheme for mode shape decomposition. Each column represents a mode of the model being analyzed with each row representing a ZMD of a (p,q) polynomial.

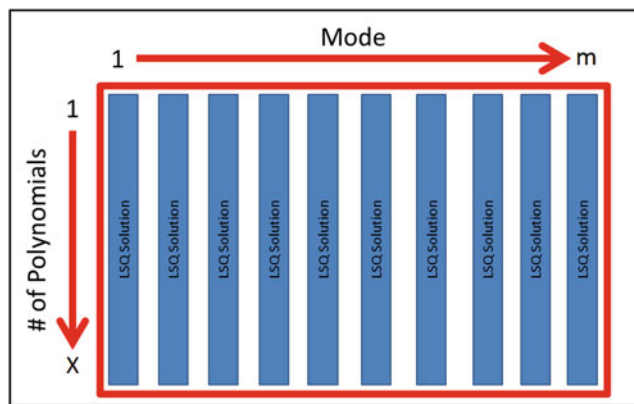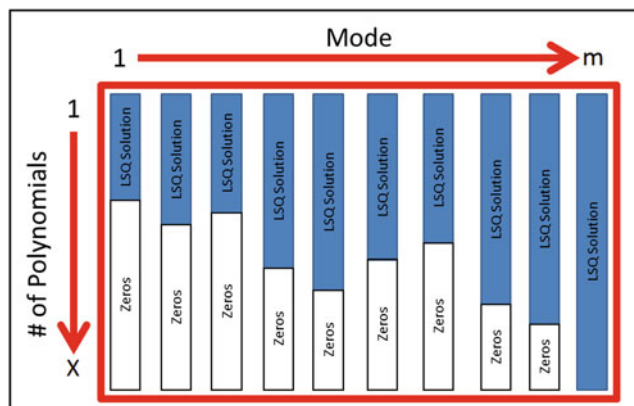**Fig. 32.1** Full order decomposition to evaluate ZMDs

Fig. 32.2 Truncated order decomposition to evaluate ZMDs

The second scheme for mode shape decomposition involves utilizing a truncated order of polynomials to decompose the mode shapes. The truncated order is determined from the initial determination of the appropriate order of polynomials for each mode shape. Prior to the LSQ the polynomials that are higher than the order appropriate for the mode shape being analyzed are zeroed out. This decomposition scheme is shown in Fig. 32.2. This figure shows the second scheme for mode shape decomposition. Each column represents a mode of the model being analyzed with each row representing a ZMD of a (p,q) polynomial. The results of these mode shape decomposition schemes are utilized in the correlation of models presented in this work. The ZMDs for each scheme and model are compared to subsequent models utilizing a MAC calculation.

32.3 Test Case Studied: Analytical

32.3.1 Model Description

For the case study analyzed, a Finite Element Model (FEM) referred to as the nominal model was created utilizing FEMAP® and processed using NX Nastran® [13]. The nominal model is used as a generic model with the subsequent model employing perturbations to the nominal model with differences between models related to length and width which mimic what is expected in a true manufacturing situation. Table 32.1 lists the parameters used for the creation of the nominal model. The nominal model is shown in Fig. 32.3; the model is fixed at the left edge. Utilizing FEMAP with Nastran NX, an eigensolution was computed for the nominal model; the results of the eigensolution for out of plane mode shapes of the nominal model are shown in Fig. 32.4.

Considering the subsequent models are similar to the nominal model with length and width differences, the mode shape results of the eigensolution are considered to be similar for the subsequent models. Notice as the mode shapes increase in frequency the shape becomes more complex and this becomes the problem when performing a MAC between two blades that have small geometry differences; each individual point on the structure will have differences in the actual shape value distorting the MAC but visually the mode shapes are very similar to one another.

Table 32.1 Nominal model parameters

Length [in.]	5.5
Width [in.]	3.5
Thickness [in.]	0.2
Number of elements (length)	110
Number of elements (width)	70
Number of nodes	7,881
Element dimensions (fixed) [in. $\times$ in.]	0.05×0.05
Material	Aluminum
Density [lb/in^3]	2.53881 E-4
Young's Modulus [ksi]	9,900

Fig. 32.3 FEMAP model of nominal model (*triangles* represent fixed boundary condition)
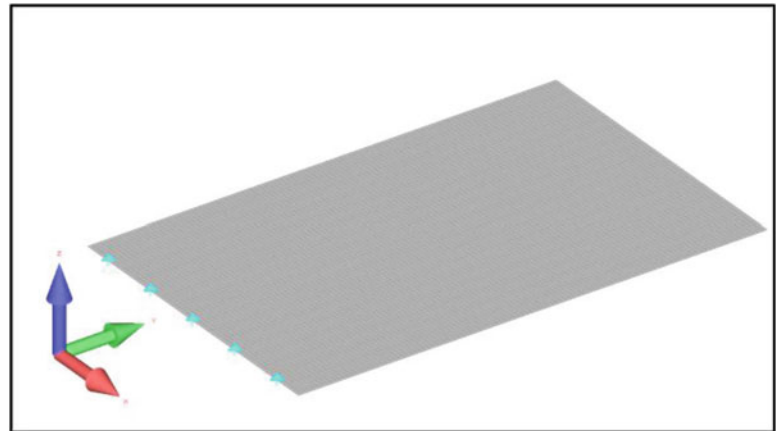
32.4 Nominal Model with Two Element Width and Height Difference

The decomposition of the nominal model is compared to the decomposition of a model with similar parameters to the nominal model, but with a length of 5.4 in. and a width of 3.4 in. (compared to the nominal length of 5.5 in. and width of 3.5 in.). An overlay of the models to display the difference in dimensions is shown in Fig. 32.5.

Utilizing a traditional MAC calculation, the correlation between the modal vectors of the nominal model and the modal vectors of the smaller model were determined. The calculation of a MAC can only be performed if the geometric points of both models are aligned, therefore various MAC calculations can result. Multiple geometric alignments were examined and are shown in Fig. 32.6. Because of the axisymmetric nature and simplicity of the systems, the results of certain alignments are identical. Specifically, Alignments 1 & 4, and Alignments 2 & 3 produce identical results. Therefore, to not reiterate information, the MAC calculation that results from Alignments 1, 2, 5, and 6 are shown in Fig. 32.7a–d, respectively. Figure 32.7 shows very clearly that as the mode number increases, and therefore the complexity of the mode shape increases, the MAC utilizing geometric alignments shows degradation. Utilizing the results of the geometric alignment MAC as a reference, the ZMDs for each model are correlated with a MAC. The results for these MAC calculations are shown in Fig. 32.8a, b.

Figure 32.8 shows that utilizing 276 terms compared to the 7,521 nodes utilized in the Modal Vector MAC, a high level of correlation is achieved for the Zernike decomposition of each model's mode shapes. These results also show low correlation on the off diagonals, which is expected. The differences between the full (a) and truncated (b) Zernike vectors are related to the LSQ. An important note is that the 24th, 25th, 36th, and 37th modes show a low correlation in respect to the other modes. This result can be associated to actual differences in the mode shape.

Comparing the results of Fig. 32.7 to those of Fig. 32.8, the MAC of a matrix of ZMDs are shown to be capable of correlating mode shapes, while not degrading at higher modes unlike a traditional MAC, which has been shown to degrade depending on geometric alignment. This lack of degradation of the ZMDs is due to the inherent similarity of the mode shapes and that during the decomposition of the mode shapes, the same GSZPs are utilized to decompose each shape.

In addition to this case, additional cases were examined in [14]. One case included the decomposition of the nominal model compared to the decomposition of the nominal model with a perturbation resulting in one element less in the width and the same height. This comparison showed similar results to those shown in this paper, where the MAC of the ZMDs resulted in a higher correlation. A case comparing two of the same models, but one with far fewer points describing the mode shapes, resulted in a correlation that steadily degraded as the mode number increased due to the lack of mode shape

Fig. 32.4 Nominal model out of
X-Y plane mode shapes 1–38
(*Numbered L–R*, *top–bottom*)
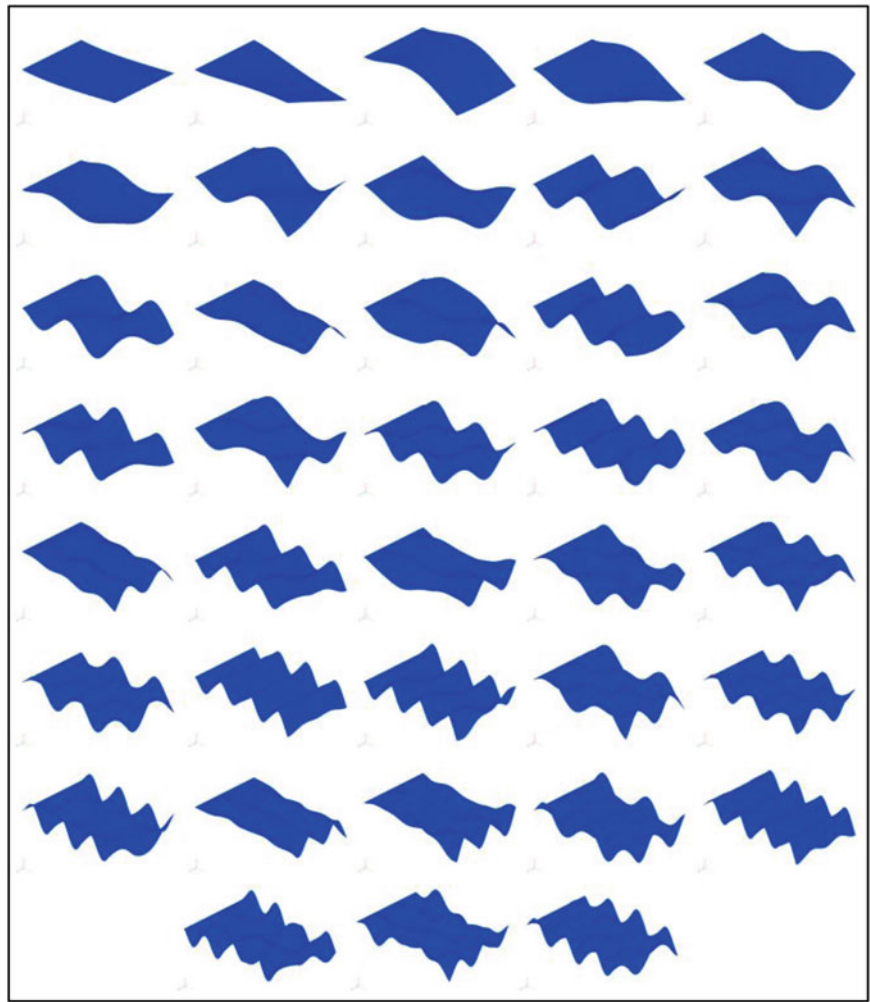
description, for the model with fewer points. Another case involved comparing two of the same models, but each utilizing a different set of points. A series of cases were examined where the aspect ratio of the models were adjusted. The aspect ratio of the models is considered to be the proportionality between the larger dimension to the smaller dimension. The results of these cases showed that as the aspect ratio from one model to the next started to differ the correlation utilizing ZMDs shows degradation due to the lack of similarity between sectors created during the coordinate mapping.

32.5 Test Case Studied: Experimental

32.5.1 Structure Description

Experimental test results were correlated using the Zernike decomposition of the mode shapes examined. The experimental test results were obtained from the testing of two large IGT turbine blades with dimensions approximately equal to a chord length of 5 in. and a height of 11 in. These blades were not part of an official correlation study and therefore the data is not expected to be of the highest quality but were specimens that provided data that could be used without restriction. The blades were tested utilizing Laser Holography with an excitation provided by an acoustic horn. The approximate fixturing for the blades and an image of one of the blades tested are shown in Fig. 32.9. The test results for these blades were kindly provided by an un-named anonymous blade manufacturer.

The test results for one IGT Turbine Blade (Referred to as IGT Turbine Blade 1) were correlated to a similar turbine blade with manufacturing differences (Referred to as IGT Turbine Blade 2). The mode shapes pertaining to IGT Turbine Blades

Fig. 32.5 Comparison of dimensions for nominal model (7,881 nodes) to 5.4″× 3.4″ model (7,521 nodes)
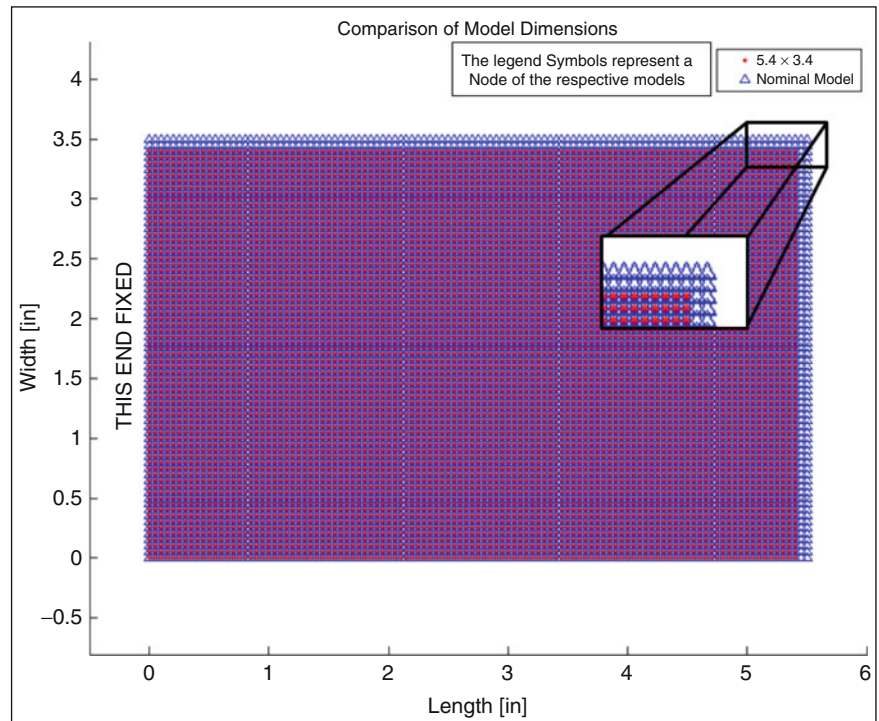
Fig. 32.6 Representation of geometric alignment for node pairing of nominal model to 5.4″× 3.4″ model (The points encompassed and on the *blue/thicker line* are paired for the correlation)
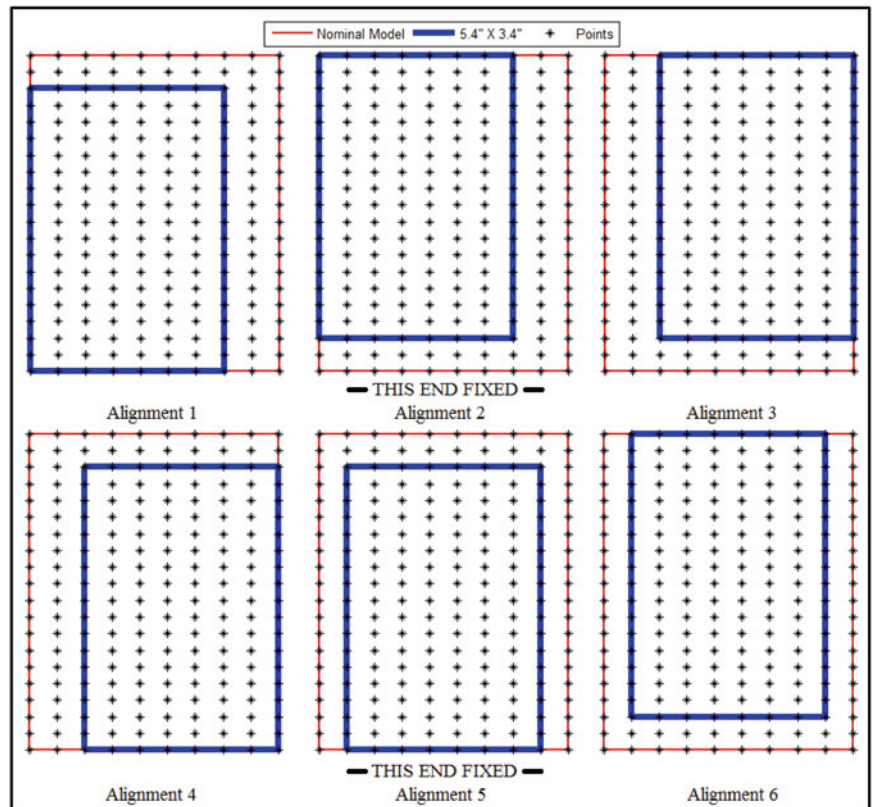
1 & 2 are shown in Fig. 32.10a, b. A comparison of the geometries for each turbine blade is shown in Fig. 32.11. Figure 32.11 shows that the data points for each blade differ; specifically, Blade 1 has 162,504 data points and Blade 2 has 165,564 data points. Therefore, to utilize a traditional MAC calculation, an alignment was necessary and various cases were examined.
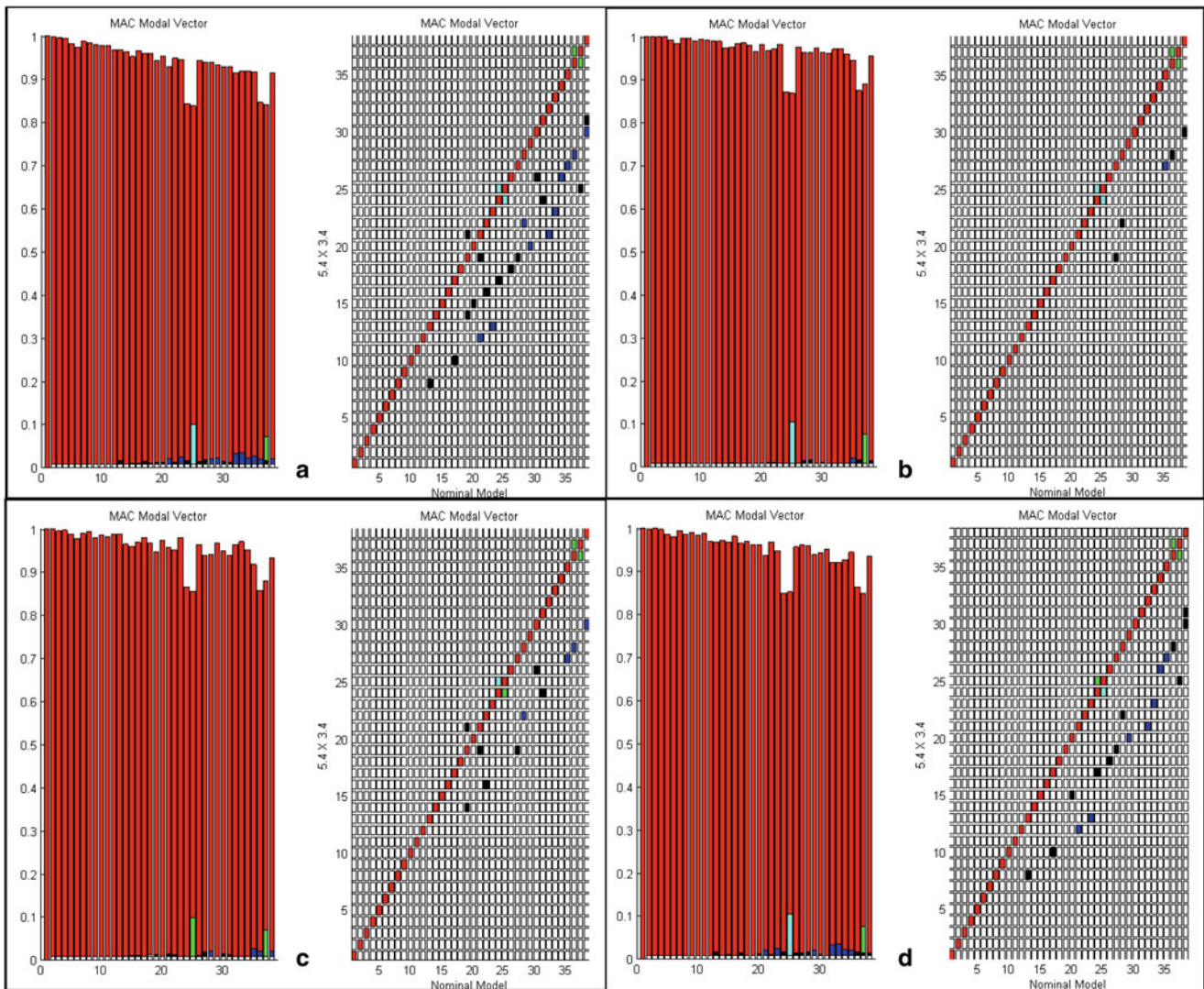
Fig. 32.7 Modal vector MAC calculation for various alignments of nominal model to $5.4'' \times 3.4''$ model (**a**) alignment 1 (**b**) alignment 2 (**c**) alignment 5 (**d**) alignment 6

32.5.2 Correlation of IGT Blade 1 to IGT Blade 2 Alignment 1

The alignment utilized for this correlation shall be referred to as Alignment 1 and is shown in Fig. 32.12. Alignment 1 clearly omits many of the points pertaining to Blade 2, and some of Blade 1. However, three of the four edges of the blades are matched up, which should allow for a high correlation. The MAC that results from Alignment 1 is shown in Fig. 32.13. Utilizing the resultant MAC, a comparison to the GSZPs MAC was performed. The comparison performed involved the subtraction of the MAC of Alignment 1 from the GSZPs MAC utilizing only the modes of high correlation, the modes of high correlation are shown in Fig. 32.14. The results showing the difference are shown in Fig. 32.15 with the vertical axes equivalent to 0.2 and −0.2 to best present the results. If a positive number is shown, the GSZP MAC was higher by that value, while a negative number shows the Modal MAC of Alignment 1 being higher by the absolute value of that number. Figure 32.15 shows that the GSZP MAC is considerably higher than the Alignment 1 Modal MAC for a majority of the modes with high correlation, along with having a higher average MAC (GSZP = 0.8152 [full] or 0.8163 [trunc]; Modal = 0.7618). Additionally, the amount of data being correlated drops from over 100,000 to approximately 230, which is a drastic reduction of over 99 % that preserves the modal data to a high degree and requires no alignment of the nodes.
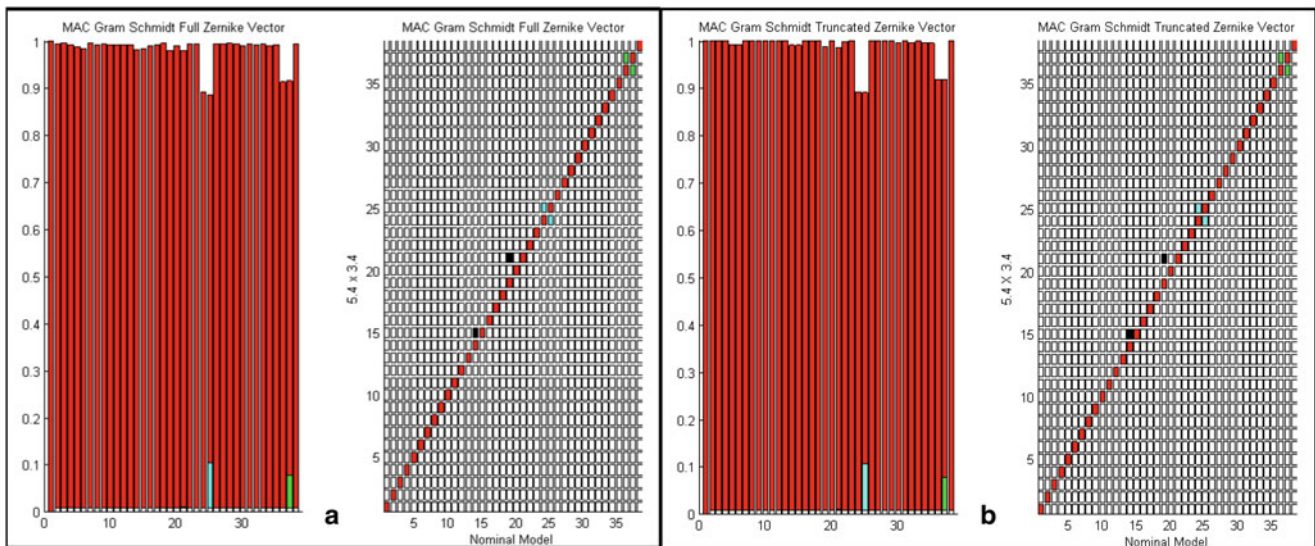
Fig. 32.8 (**a**) MAC of 22 orders of ZMDs for nominal model to $5.4'' \times 3.4''$ model [*full*] (**b**) MAC of 22 orders of ZMDs for nominal model to $5.4'' \times 3.4''$ model [*truncated*]

Fig. 32.9 IGT turbine blade testing configuration
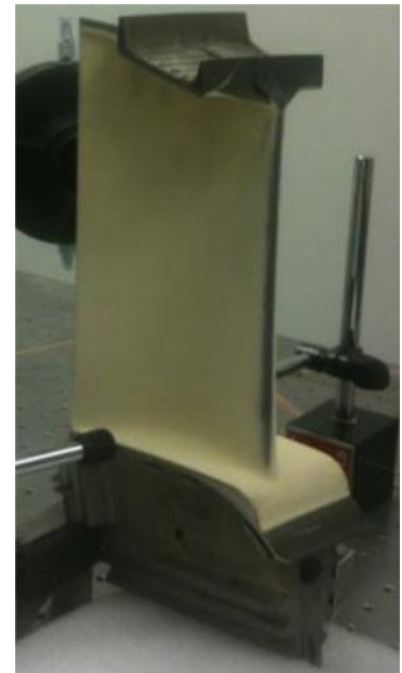
32.5.3 Correlation of IGT Blade 1 to IGT Blade 2 Alignment 2

The alignment utilized for this correlation shall be referred to as Alignment 2 and is shown in Fig. 32.16. Alignment 2 also omits many points pertaining of Blade 2, and some of Blade 1. However, the points selected as node pairs occupy a central region and are not biased towards a particular edge. The MAC that results from Alignment 2 is shown in Fig. 32.17. Utilizing the resultant MAC, a comparison to the GSZPs MAC was performed.

The comparison performed involved the subtraction of the MAC of Alignment 2 from the GSZPs MAC utilizing only the modes of high correlation (Fig. 32.14), because the difference between these terms is the most important. The results showing the difference are shown in Fig. 32.18 with the vertical axes equivalent to 0.05 and −0.05 to best present the results. If a positive number is shown, the GSZP MAC was higher by that value, while a negative number shows the Modal MAC of Alignment 2 being higher by the absolute value of that number.
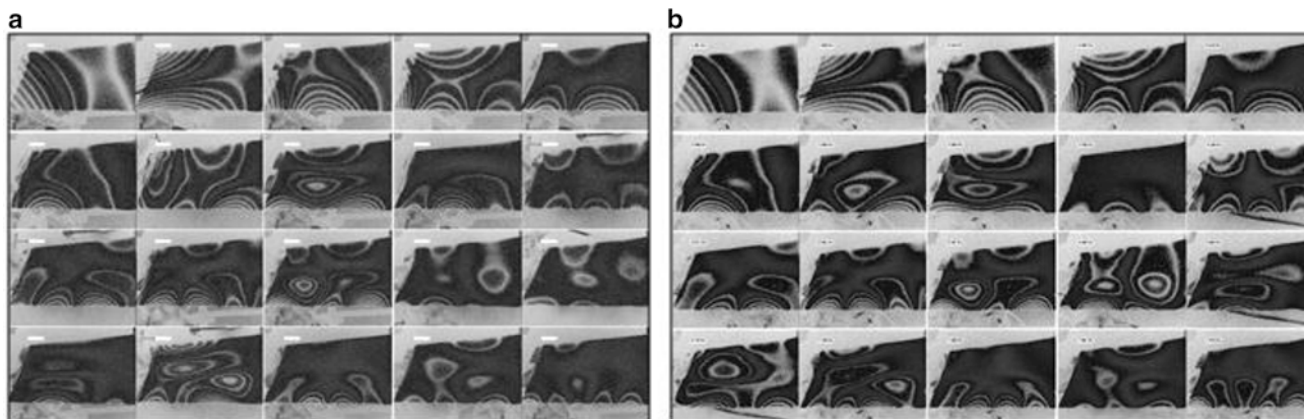
Fig. 32.10 IGT turbine blade mode shapes 1–20 (*numbered L–R*, *top–bottom*) (**a**) IGT turbine blade 1 (**b**) IGT turbine blade 2

Fig. 32.11 Comparison of IGT turbine blade test points (highly exaggerated)
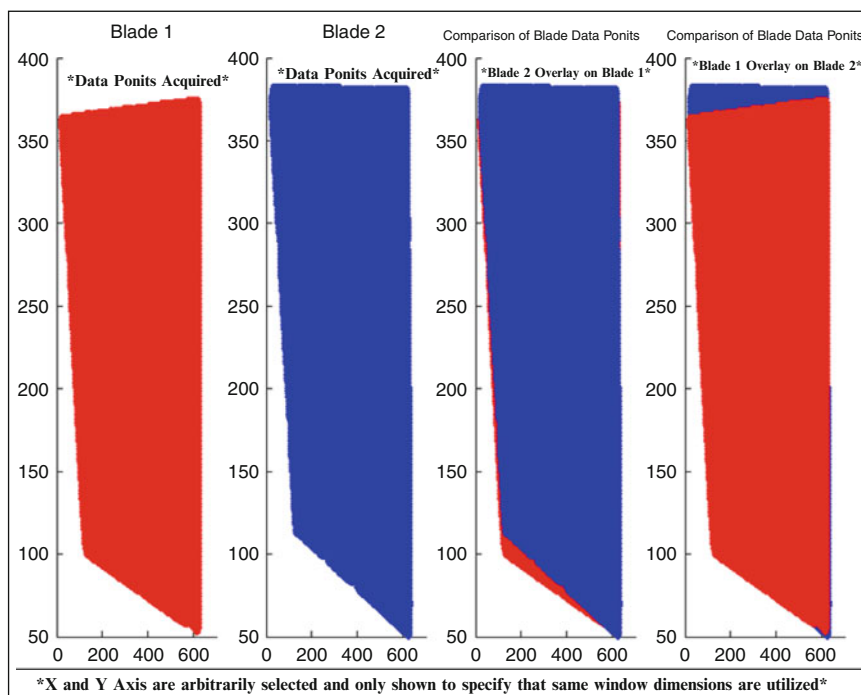
Figure 32.18 shows that the differences between the GSZP MAC and the Alignment 2 Modal MAC are fluctuating for the modes with high correlation; however, the Alignment 2 Modal MAC has a higher average MAC (GSZP = 0.8152 [full] or 0.8163 [trunc]; Modal = 0.8202), which suggests better correlation. But, the amount of data being correlated still drops from over 100,000 to approximately 230, which is a drastic reduction of over 99 % that still preserves the modal data to a high degree and requires no alignment of the nodes.

32.5.4   Correlation of IGT Blade 1 to IGT Blade 2 Alignment 3

The alignment utilized for this correlation shall be referred to as Alignment 3 and is shown in Fig. 32.19. Alignment 3 omits many of the points pertaining to both Blades 1 and 2 in an attempt to match three of the four edges. The MAC that results from Alignment 3 is shown in Fig. 32.20. Utilizing the resultant MAC, a comparison to the GSZPs MAC was performed. The comparison performed involved the subtraction of the MAC of Alignment 3 from the GSZPs MAC utilizing only the modes of high correlation (Fig. 32.14), because the difference between these terms is the most important. The results showing the difference are shown in Fig. 32.21 with the vertical axes equivalent to 0.05 and −0.05 to best present the results. If a
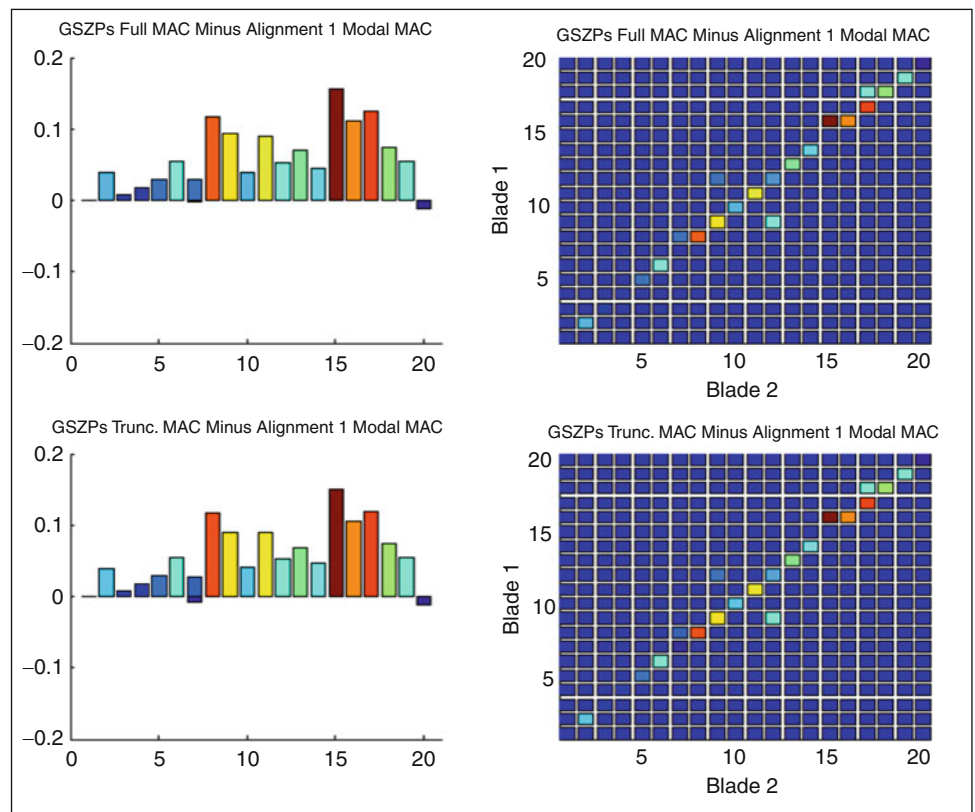
Fig. 32.12 Turbine blade
experimental data alignment 1
[nodes used for MAC = 155,701]
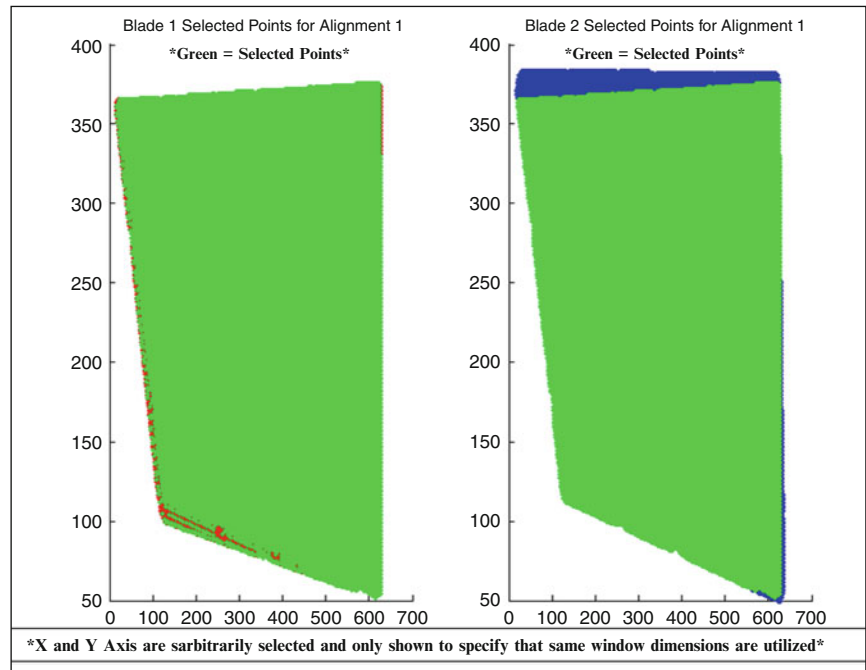
Fig. 32.13 Modal vector MAC
calculation for alignment 1
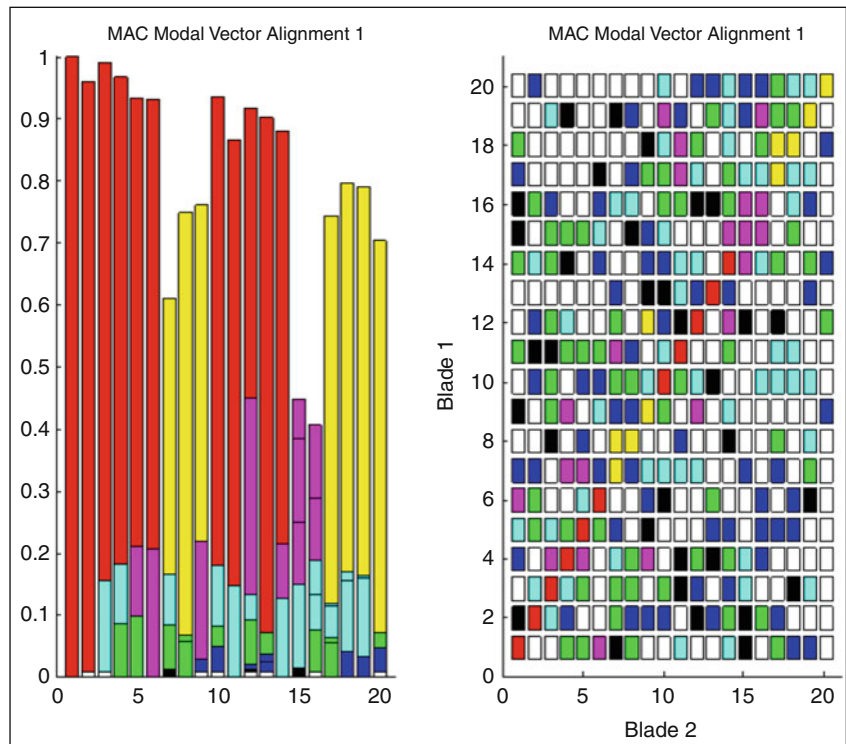
positive number is shown, the GSZP MAC was higher by that value, while a negative number shows the Modal MAC of Alignment 3 being higher by the absolute value of that number. Figure 32.21 shows that the Alignment 3 Modal MAC is higher than the GSZP MAC for a majority of the modes with high correlation, along with having a higher average MAC (GSZP = 0.8152 [full] or 0.8163 [trunc]; Modal = 0.8207). Once again, the amount of data being correlated drops from over 100,000 to approximately 230, which is a drastic reduction of over 99 % that preserves the modal data to a high degree and requires no alignment of the nodes.

Fig. 32.14 Modes of high correlation when correlating IGT turbine blade 1 to IGT turbine blade 2
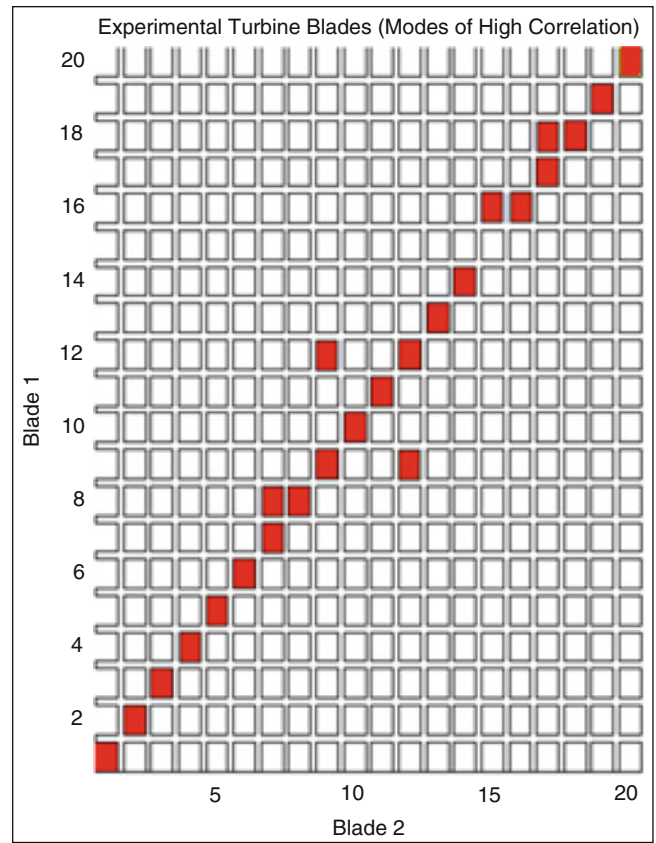
Fig. 32.15 Difference between MAC of GSZPs matrix and alignment 1 modal MAC for modes of high correlation (Fig. 32.14)
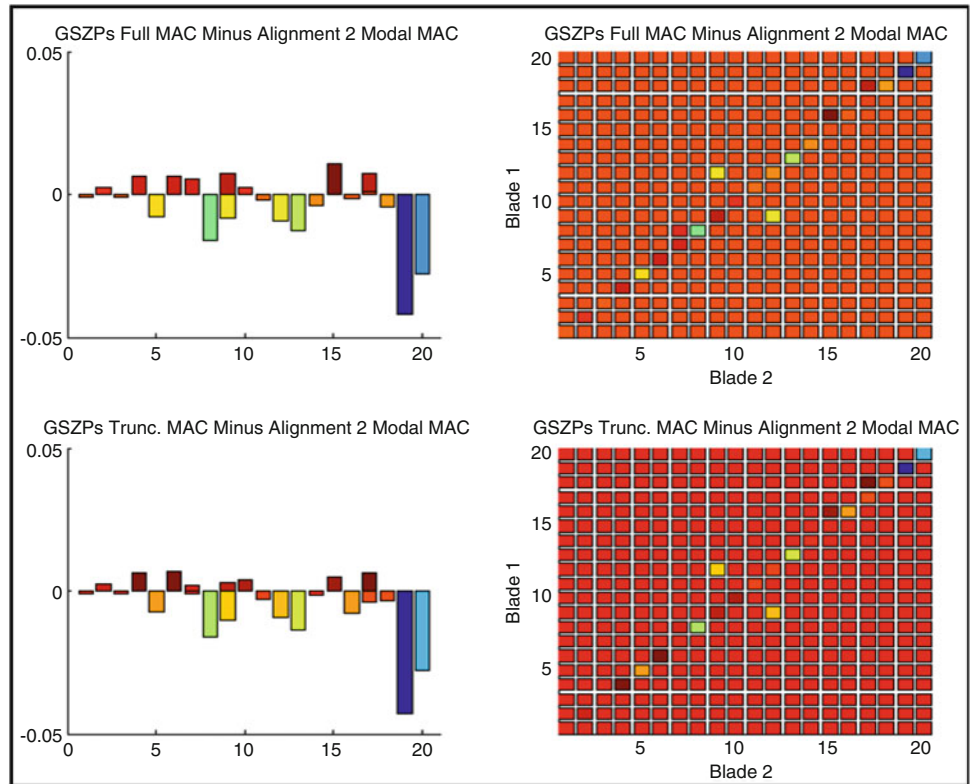
Fig. 32.16 Turbine blade
experimental data alignment 2
[nodes used for MAC = 159,260]
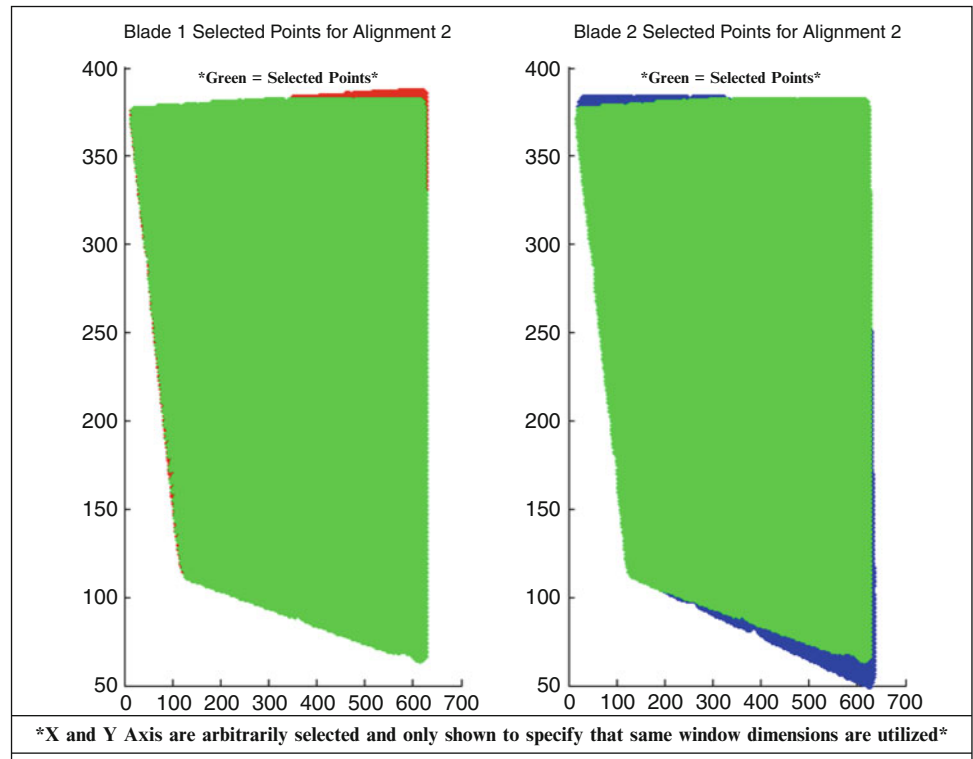
Fig. 32.17 Modal vector MAC
calculation for alignment 2
[average MAC of modes with
high correlation = 0.8202]
(Fig. 32.14)
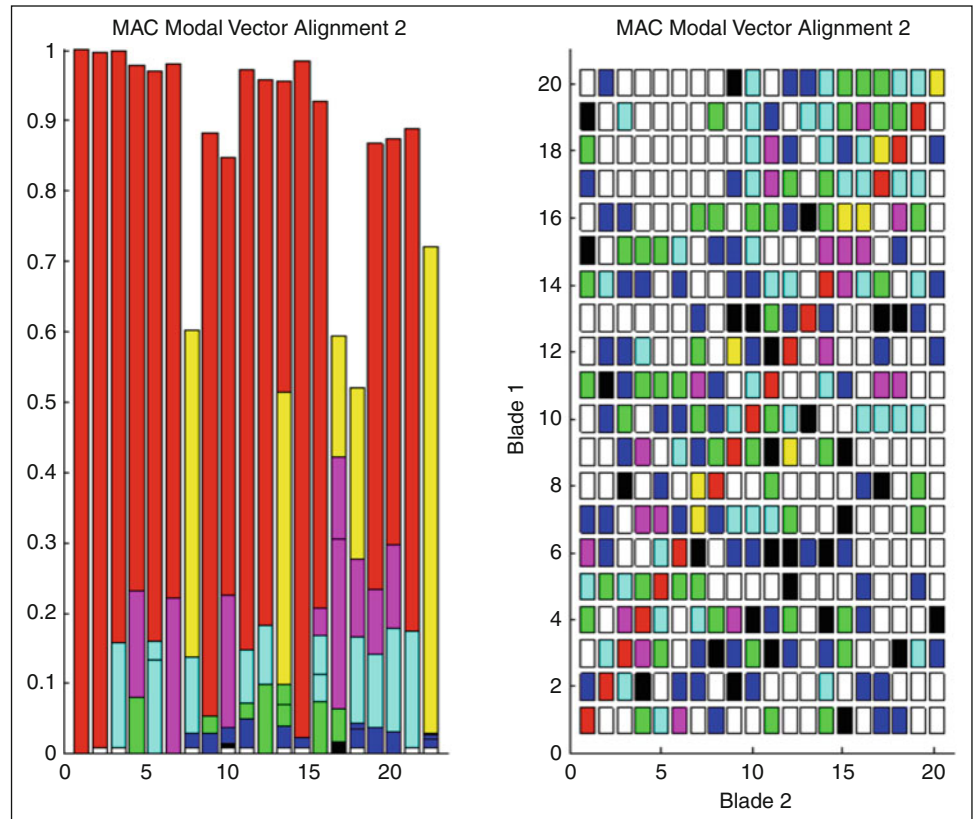
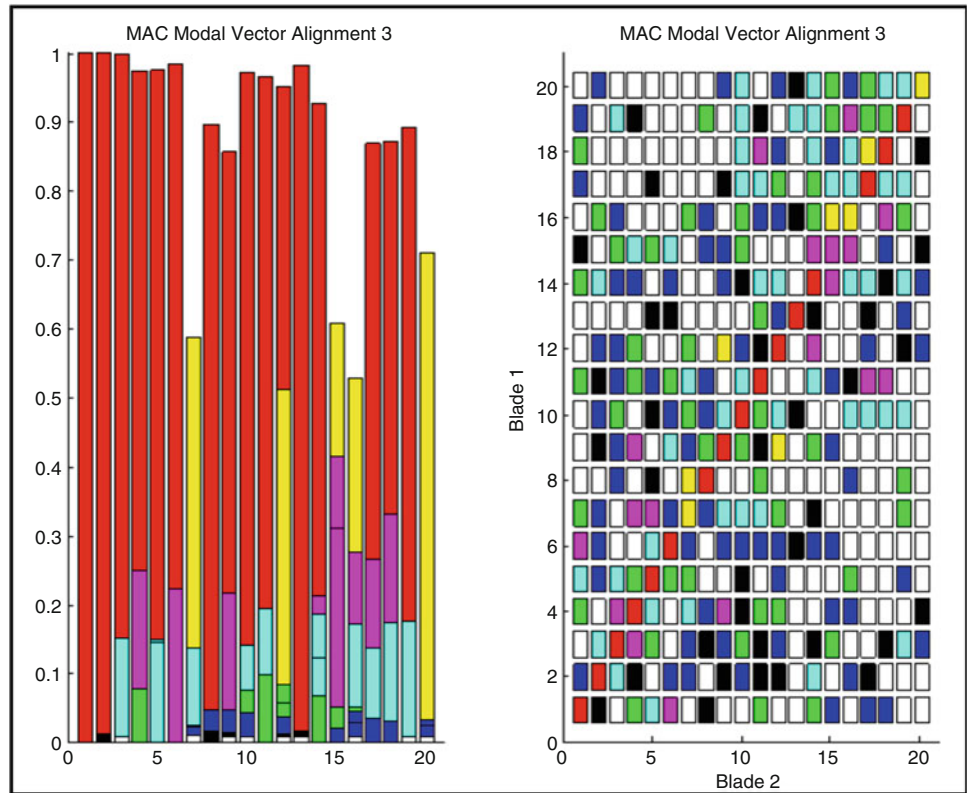**Fig. 32.18** Difference between MAC of GSZPs matrix and alignment 2. Modal MAC for modes of high correlation (Fig. 32.14)

Fig. 32.19 Turbine blade experimental data alignment 3 [nodes used for MAC = 158,231]
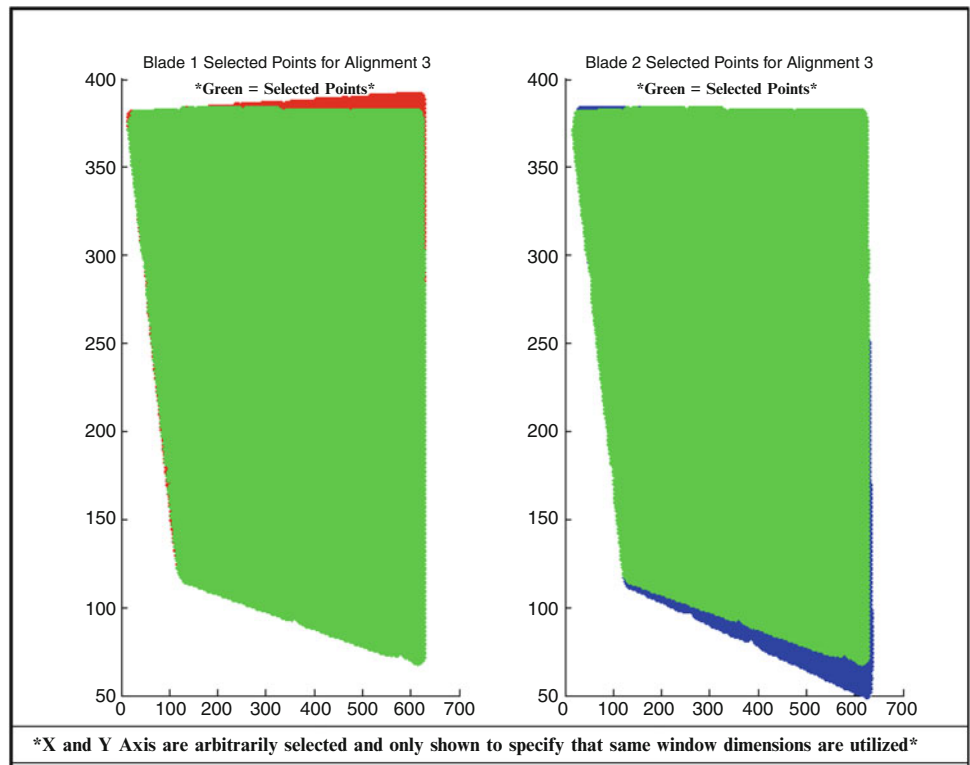
32.5.5   Comparison of Results

Obviously, only a few alignments considered were presented in this paper for illustration purposes and due to space restrictions. Many iterations of alignments were performed to obtain an optimal and suboptimal configuration shown here.

Fig. 32.20 Modal vector MAC calculation for alignment 1 [average MAC of modes with high correlation = 0.8207] (Fig. 32.14)

Fig. 32.21 Difference between MAC of GSZPs matrix and alignment 3. Modal MAC for modes of high correlation (Fig. 32.14)
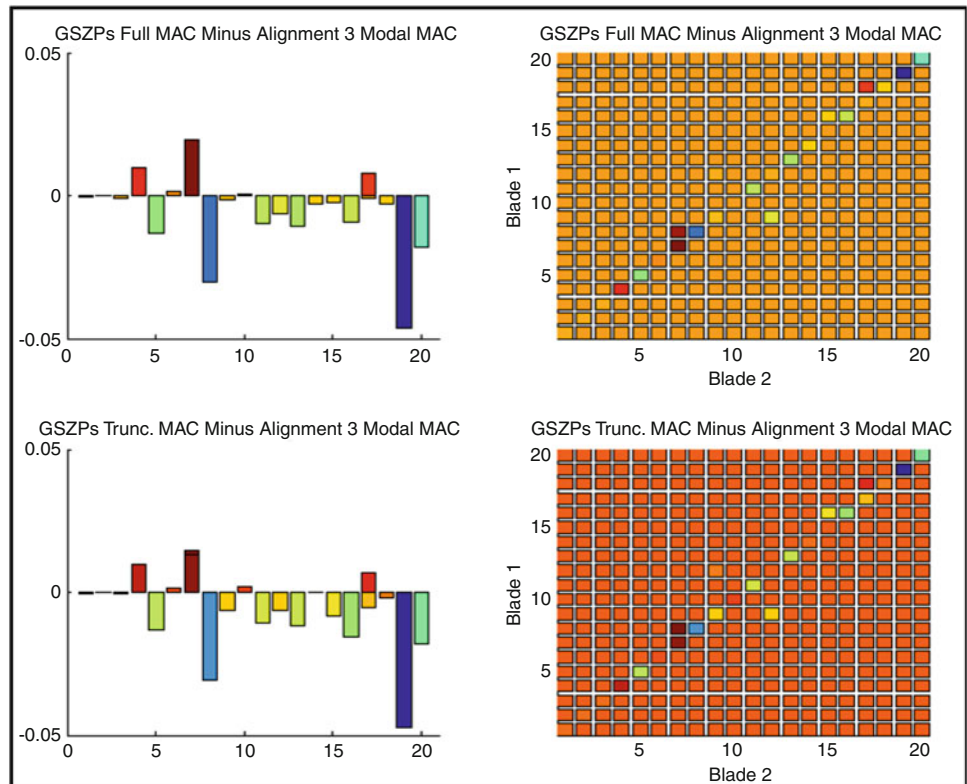
The issue is that the blades differ in size and many different alignments need to be considered using the traditional MAC with the large number of data points obtained with the laser holography approach. The alignments used1 also varied the amount of nodes paired and the respective locations of the nodes. These alignments resulted in different correlations as seen with the analytical cases shown. Specifically, depending on the alignment utilized and the mode shapes being analyzed, no

Table 32.2 Comparison of average MAC GSZP and alignments

	Average MAC		% Error	
	Full set	Truncated set	Full set	Truncated set
GSZP	0.8153	0.8165	—	—
Alignment 1	0.7618		−6.562	−6.699
Alignment 2	0.8202		0.601	0.453
Alignment 3	0.8207		0.662	0.514

one alignment was adequate in producing the highest correlation for the mode shapes. However, the GSZPs were able to achieve results that were essentially equivalent to those produced by alignments optimized for a high correlation, as shown in Table 32.2 with no regard for the specific alignment of the two blades. Additionally, the GSZPs were able to reduce the number of effective points needed in the correlation by over 99 %. The cases presented clearly illustrate the usefulness of the approach.

32.6   Conclusion

The traditional Modal Assurance Criteria (MAC) results present difficulties when a very large number of points exist and no one geometric correlation is known; the MAC results are very sensitive to the geometric alignment used for the comparison of modes. This is compounded when many different test specimens need to be evaluated that have small manufacturing differences such as those observed with the turbine blades studied in this work.

This paper presented a methodology for correlating modal vectors of turbine blade like structures (that inherently have manufacturing differences) utilizing Zernike Polynomials. The results show that the proposed approach is inherently better than the results obtained from a traditional MAC and the difficulty with geometric alignment is overcome by the approach.

The results also show that for a correlation utilizing a traditional MAC, multiple different correlations occur. However, by utilizing Zernike Polynomials in the correlation method described, a single correlation results for a particular blade pair. Another very significant benefit is that the large number of data points obtained is effectively reduced to retain the important features related to each of the particular modes of the structure; this allows for dramatically reduced size of the modal vector description. Although there is still additional effort required for this methodology to be widely used, the initial results and cases described in this paper show very good results overall and warrant additional investigations.

While this paper presented results for a turbine blade application, the approach using Zernike Polynomials will have application to many different types of structures and applications.

References

1. Allemang R, Brown D (1982) A correlation coefficient for modal vector analysis. First international modal analysis conference, Orlando, Florida, November 1982
2. Zernike F (1934) Beugungstheorie des schneidenverfahrens und seiner verbesserten form, der phasenkontrastmenthode (Diffraction theory of the cut procedure and its improved form, the phase contrast method). Physica 1:689–704
3. Weizhuo W, Mottershead JE, Mares C (2009) Mode-shape recognition and finite element model updating using the Zernike moment descriptor. Mech Syst Signal Process 23:2088–2112
4. Hew P (1996) Orthogonal functions on the unit disk having invariance in form. The University of Western Australia. http://citeseerx.ist.psu.edu/viewdoc/summary?doi=10.1.1.51.5351
5. Pawlak M, Liao SX (2002) On the recovery of a function on a circular domain. IEEE Trans Inform Theor 48:2736–2753
6. Khotanzad A, Hong YH (1990) Invariant image recognition by Zernike moments. IEEE Trans Pattern Anal Mach Intell 12:489–497
7. Hwang S-K, Kim W-Y (2006) A novel approach to the fast computation of Zernike moments. Pattern Recogn 39:2065–2076
8. Wee C-Y, Paramesran R (2007) On the computational aspects of Zernike moments. Image Vis Comput 25:967–980
9. The Gram-Schmidt Algorithm (2013) http://www.math.hmc.edu/calculus/tutorials/gramschmidt/. Accessed 5 Feb 2013
10. Tripoli N. The Zernike Polynomial. Department of ophthalmology, University of North Carolina at Chapel Hill, NC, USA
11. MATLAB R2010a, The MathWorks Inc., Natick, MA. http://scholar.google.com/scholar_url?hl=en&q=http://www.optikon.com/en/articles/keratron_023/media/TheAberrometers_2003_Tripoli%2520(Zernike%2520Polynomials).pdf&sa=X&scisig=AAGBfm0QLAkBR05PEhSTtyEeaq5JPUXsxQ&oi=scholarr
12. Standards for reporting the optical aberrations of eyes. http://www.opt.indiana.edu/vsg/library/vsia/vsia-2000_taskforce/tops4_2.html. Accessed 22 Jan 2013
13. FEMAP With NX Nastran V10.2, Siemens Inc., Munich, Germany
14. Salerno J (2013) Use of Zernike Polynomials for modal vector correlation applications. Master's thesis, University of Massachusetts Lowell, May 2013

Chapter 33
Modeling of Flexible Tactical Aerospace Vehicle for Hardware-in-Loop Simulations

Yadunath Gupta, Pulak Halder, and Siddhartha Mukhopadhyay

Abstract Tactical aerospace vehicles with slender body configuration undergo deformations due to aerodynamic and propulsive loads during flight. These deformations have considerable effects on flight dynamics. Sensors which provide feedback to the control system measure the combined effect of rigid body motion and motion caused by structural deformations at sensor locations. Thus control commands may also be influenced by structural deformations. This control-structure interaction can lead to excessive oscillations in the vehicle or even structural failure. Such situation can be avoided using either gain stabilization or phase stabilization in control design depending on mode frequency with respect to autopilot bandwidth. Extensive simulation is needed for validation of control design. Though due to computational complexity in flexibility dynamics, simulations are performed in non-real time, but it cannot encompass the effects of computational and communication delays which have significant effect in phase stabilization. Thus realization of entire vehicle dynamics including flexibility is needed in real-time (HIL Simulation). This research demonstrates a new model based approach for the same using MATLAB/SIMULINK and OPAL-RT/RT-LAB. HIL Simulations with present model precisely reproduce the results of previous flight failures due to divergent bending vibrations, which was not achieved using rigid body model alone. The advantage of this research is to facilitate not only the validation of control software and embedded hardware with advanced processors, but also its interaction with new generation composite airframes having significant uncertainty in flexibility characteristics.

Keywords Hardware-in-loop simulation • Flexible aerospace vehicle • Mathematical modelling • Model based design • Equations of motion

Nomenclature

$v(x,t), w(x,t)$	Elastic displacement along y and z axis.
$\phi_{y_i}(x), \phi_{z_i}(x)$	ith mode shape for pitch and yaw bending.
$\phi'_{y_i}(x), \phi'_{z_i}(x)$	ith mode slope for pitch and yaw bending.
$q_{y_i}(t), q_{z_i}(t)$	Generalized coordinate along y and z axis associated with ith bending mode.
η	Coordinate measured aft from gimbal point along the centre line of nozzle.
$\vec{V}_P, \vec{V}_{P_e}$	Inertial velocity vector of a point on the centre line of deformed vehicle structure and nozzle.
x_{cg}	x coordinate of centre of gravity (c.g.) of the complete vehicle.
V_x, V_y, V_z	Components of inertial velocity of the vehicle c.g.
p, q, r	Components of angular rates about vehicle c.g.
δ, γ	Nozzle deflection angles in pitch and yaw plane.

Y. Gupta (✉)
Department of Aerospace Engineering, IIT Kharagpur, West Bengal 721 302, India
e-mail: yadunathkgp@gmail.com

P. Halder
Research Centre Imarat, DRDO, Hyderabad, Andhra Pradesh 500 069, India

S. Mukhopadhyay
Department of Electrical Engineering, IIT Kharagpur, West Bengal 721 302, India

l, l_e	Length of the vehicle structure and the nozzle.
E	Kinetic energy of the complete vehicle.
t	Time
$U_{F_x}, U_{F_y}, U_{F_z}$	Components of force due to potential energy.
$U_{M_x}, U_{M_y}, U_{M_z}$	Components of moment about c.g. due to potential energy.
$F_{A_x}, F_{A_y}, F_{A_z}$	Components of aerodynamic force.
M_{A_y}, M_{A_z}	Aerodynamic moments about y and z axis.
$F_{P_x}, F_{P_y}, F_{P_z}$	Components of propulsive force.
M_{P_y}, M_{P_z}	Propulsive moments about y and z axis.
$Q_{A_{y_i}}, Q_{A_{z_i}}$	Generalized aerodynamic forces along y and z axis associated with ith bending mode.
$Q_{P_{y_i}}, Q_{P_{z_i}}$	Generalized propulsive forces along y and z axis associated with ith bending mode.
U_g	Gravitational potential energy
U_p	Strain energy
U	Total potential energy of the complete vehicle.
D	Rayleigh's dissipation function.
m_{y_i}, m_{z_i}	Generalized masses associated with ith mode of pitch and yaw plane bending.
ξ_{y_i}, ξ_{z_i}	Damping ratios associated with ith mode of pitch and yaw plane bending.
ϕ, θ, ψ	Euler angles.
h	Height of c.g. in earth fixed frame.
h_P, h_{P_e}	Height of any point on vehicle structure and nozzle in earth fixed frame.
m_t	Total mass of the complete vehicle.
m_e	Nozzle mass
g	Acceleration due to gravity
S_e, I_e	First and second mass moments of nozzle about the gimbal point.
$V_{P/w}$	Velocity of a point on vehicle structure relative to wind.
$V_{m/w}$	Velocity of c.g. relative to wind.
α, β	Angle of attack and side slip angle of undeformed vehicle in no wind condition.
α_w, β_w	Angle of attack and side slip angle due to wind velocity.
α_P, β_P	Local angle of attack and side slip angle of any point on vehicle structure.
α_T	Total angle of attack of undeformed vehicle.
M	Mach number
c_{d_α}	Slope of local drag coefficient w.r.t. angle of attack.
c_{n_α}	Slope of local normal force coefficient w.r.t. angle of attack.
Q	Dynamic pressure
S	Reference surface area
T_e	Thrust
I_{yy}, I_{zz}	Mass moment of inertia of the vehicle about z and y axis.
x_{ins}	x coordinate of the sensor location.
a_y, a_z	Components of c.g. acceleration along y and z axis.
$a_{y,ins}, a_{z,ins}$	Accelerations measured by sensor along y and z axis.
q_{ins}, r_{ins}	Angular rates measured by sensor about y and z axis.
$(\dot{})$	Derivative w.r.t. time.
$(\ddot{})$	Double derivative w.r.t. time.

33.1 Introduction

In an aerospace vehicle designed for defence applications, such as a tactical aerospace vehicle, covertness is one of the primary requirements. Detection by radars mainly depends on the cross sectional area of the vehicle. Thus to reduce the radar visibility, vehicles are designed to have slender body configuration. Slender bodies also have the advantage of low pressure drag. But this design has led to the appearance of structural flexibility in these vehicles. Vehicles undergo structural deformation due to the effects of aerodynamic and propulsive loads acting on the vehicle during flight. These deformations have considerable effects on flight dynamics [1]. The sensors mounted on the vehicle which provide feedback to the control system measure the angular and translational motion, and their outputs indicate the combined effect of rigid body motion and
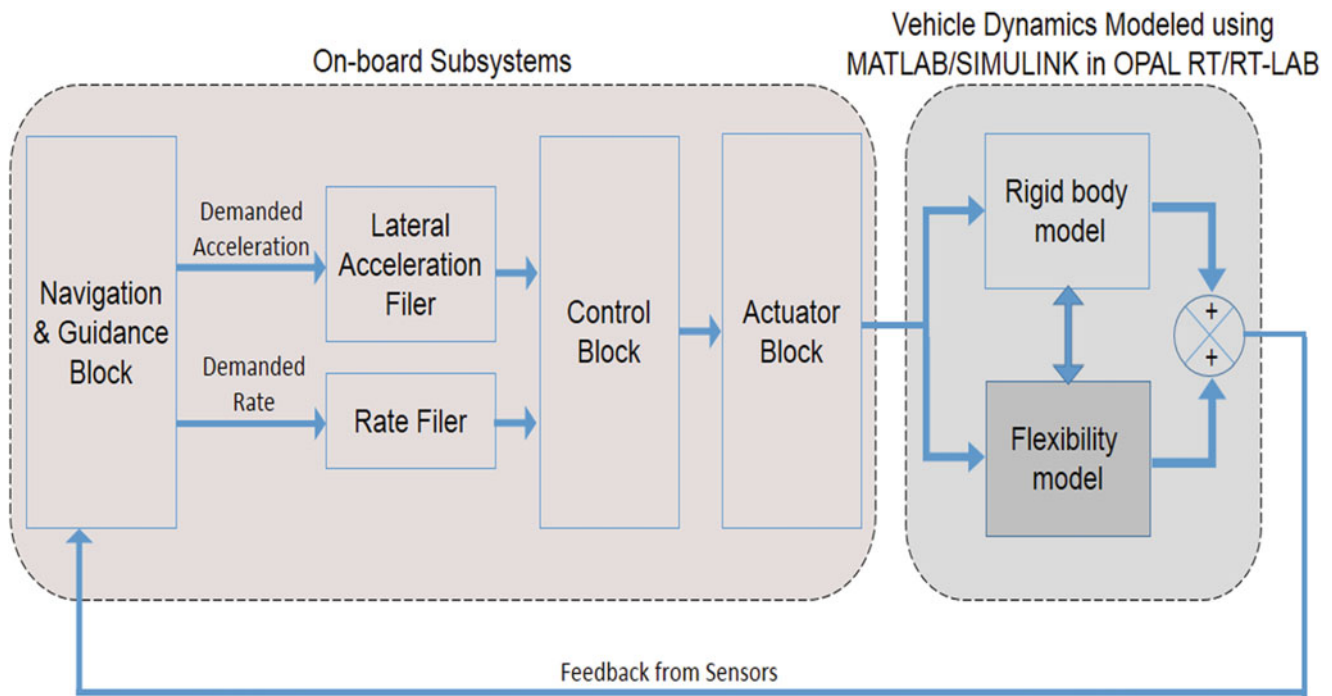
Fig. 33.1 Block diagram of the hardware-in-loop simulation model

motion caused by structural deformations at the sensor locations. Thus the command signals generated by the control system are also influenced by the structural deformations. This effect is known as control-system/structural-flexibility interaction. Such an interaction can excite bending vibrations in the vehicle and may lead to excessive oscillations or even structural failure. Thus to avoid such a situation, control structure interaction must be minimized. This can be done in two ways. First, the sensor signals at the natural frequencies of vibration can be blocked so that the controller does not respond to the feedback due to structural deformation (known as structural feedback). This method, called gain stabilization, depends upon structural damping for energy removal and is used to avoid excessive oscillations due to high frequency modes. The primary task of the control system is to direct the vehicle to a desired set of states by controlling its gross motion. To do so effectively, the controller has to supply energy in a band of frequencies determined by control and guidance requirements. In general one or more of the lowest frequency modes are not sufficiently separated from this band to permit gain stabilisation. The alternative, phase stabilization, is to design the controller so that control forces are phased to remove energy from the modes. Most designs employ both methods, with phase stabilization of low frequency modes and gain stabilization of higher frequency modes.

Once a controller is designed, extensive preflight analysis and simulation is required as detecting anomalies in the design prior to actual flight tests leads to significant cost and time savings. The efficacy of such simulation depends on how realistically the simulation mimics the real-life operation of the vehicle. This necessitates an accurate mathematical modeling of entire vehicle dynamics including flexibility effects. Because of the high computational complexity in flexible dynamics, common validation practice is to simulate the rigid body dynamics in real time and flexible body dynamics in non-real time. But in case of phase stabilized low frequency modes, effects of computational and communication delays which cannot be accurately characterized using non-real time simulations, are significant. Thus simulation of flexible vehicle dynamics must be done in real time including hardware in the loop.

Previously, Karkee et al. [2] have used distributed architecture and multi-rate modeling for real-time simulation of off-road vehicles. Elmqvist et al. [3] have described the capabilities of Dymola and Modelica modeling language for real-time simulation of detailed vehicle and powertrain dynamics. Schmidt et al. [4] have discussed the techniques of real-time simulation for flexible aircraft. Number of techniques for modeling the dynamics of complex flexible structures are reported in [5–10]. This research demonstrates a new model based approach for real-time simulation of the dynamics of flexible aerospace vehicles. Furthermore, this modeling technique allows for the flexible degrees of freedom to be added to an existing model of vehicle's rigid body dynamics. The equations of motion are programmed using MATLAB/SIMULINK® environment, and RT-LAB real-time simulator from OPAL-RT is used for simulation. A top level block diagram of the simulation model is shown in Fig. 33.1. Multi-rate modeling is employed to optimize the computational requirements.

The advantage of this research is to facilitate not only the validation of control software and embedded hardware with advanced processors, but also its interaction with new generation composite airframes having significant uncertainty in flexibility characteristics.

In Sect. 33.2, the governing equations and expressions for force and moments are derived. Simulations of the flight of a representative aerospace vehicle are carried out for three different cases and the results are presented in Sect. 33.3. Conclusion is given in Sect. 33.4.

33.2 Mathematical Model

In this section, equations of motion and bending of an aerospace vehicle are derived. The expressions of the forces and moments due to gravitational, aerodynamic and propulsive loads are also computed. Motion is referenced to the mean axis system which is a non-inertial reference frame moving with the body, as described by Waszak et al. [6]. This axis system is referred to as "body frame" from hereafter and is shown in Fig. 33.2 along with the ground fixed inertial frame. This axis system is the coordinate frame with respect to which the elastic deformations contribute no translational or rotational momentum. Bending of the vehicle structure is approximated by the centre-line deflection of an equivalent free–free beam with non-uniform mass and stiffness properties. The elastic displacement of the vehicle structure along y and z-axis is given by $v(x, t)$ and $w(x, t)$ respectively. Using mode summation method, the deflection at a point can be approximated as:

$$v(x, t) = \sum_{i=1}^{n} \phi_{y_i}(x) q_{y_i}(t) \tag{33.1}$$

$$w(x, t) = \sum_{j=1}^{n} \phi_{z_j}(x) q_{z_j}(t) \tag{33.2}$$

Mode shapes $\phi_{y_i}(x)$, $\phi_{z_j}(x)$ are functions solely of the mass and stiffness properties exhibited at a particular time in the trajectory. Mode shapes are considered to be known from the finite element analysis or ground resonance test of the vehicle. It is assumed that the mode shapes are computed with engine mass decoupled (removed) from the vehicle structure and they are normalized with respect to the tail. Dynamical effects of the engine mass are included through inertial coupling in the equations of motion. The generalised coordinates $q_{y_i}(t)$, $q_{z_j}(t)$ represent the independent degrees of freedom. Positive value of a generalised coordinate represents positive tail deflection along the corresponding axis.
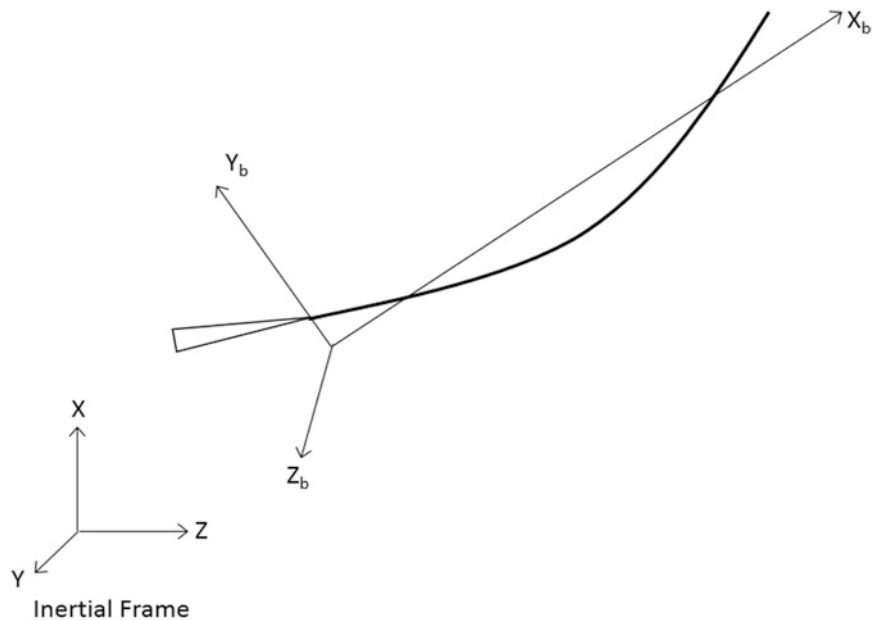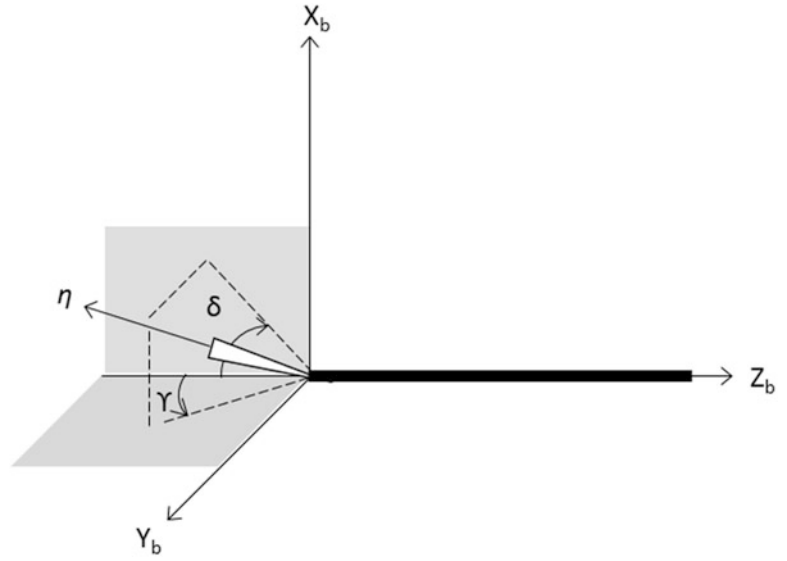

Fig. 33.2 Inertial frame and body frame of reference

Fig. 33.3 Nozzle fixed axis and deflection angles

In case of the vehicle considered for study, control forces are produced by swivelling the nozzle of the engine by angles δ and γ in pitch and yaw plane respectively, in response to the commands provided by the autopilot. Positive deflection of nozzle produces negative transverse force in the corresponding plane. The nozzle fixed axis η and the deflection angles are shown in Fig. 33.3. Effects of propellant sloshing are not considered in the derivation.

The derivation of the equations of motion is based on the variational procedure adopted from [5].

33.2.1 Lagrange's Equations

The general form of Lagrange's equations for motion referenced to an inertial frame has been derived in [11]. These equations are transformed to a form which is valid in rotating reference frame using the transformation as given in [12]. After the transformation, Lagrange's equations for the rigid body degrees of freedom (translation in x, y and z, and rotation about y and z) have the following form:

$$\frac{d}{dt}\left(\frac{\partial E}{\partial V_x}\right) + q\frac{\partial E}{\partial V_z} - r\frac{\partial E}{\partial V_y} + U_{Fx} = F_{Ax} + F_{Px} \tag{33.3}$$

$$\frac{d}{dt}\left(\frac{\partial E}{\partial V_y}\right) + r\frac{\partial E}{\partial V_x} + U_{Fy} = F_{Ay} + F_{Py} \tag{33.4}$$

$$\frac{d}{dt}\left(\frac{\partial E}{\partial V_z}\right) - q\frac{\partial E}{\partial V_x} + U_{Fz} = F_{Az} + F_{Pz} \tag{33.5}$$

$$\frac{d}{dt}\left(\frac{\partial E}{\partial q}\right) + V_z\frac{\partial E}{\partial V_x} - V_x\frac{\partial E}{\partial V_z} + U_{My} = M_{Ay} + M_{Py} \tag{33.6}$$

$$\frac{d}{dt}\left(\frac{\partial E}{\partial r}\right) + V_x\frac{\partial E}{\partial V_y} - V_y\frac{\partial E}{\partial V_x} + U_{Mz} = M_{Az} + M_{Pz} \tag{33.7}$$

Lagrange's equations for bending degrees of freedom do not change when transformed and have the form

$$\frac{d}{dt}\left(\frac{\partial E}{\partial \dot{q}_{yi}}\right) - \frac{\partial E}{\partial q_{yi}} + \frac{\partial D}{\partial \dot{q}_{yi}} + \frac{\partial U}{\partial q_{yi}} = Q_{Ayi} + Q_{Pyi} \tag{33.8}$$

$$\frac{d}{dt}\left(\frac{\partial E}{\partial \dot{q}_{zj}}\right) - \frac{\partial E}{\partial q_{zj}} + \frac{\partial D}{\partial \dot{q}_{zj}} + \frac{\partial U}{\partial q_{zj}} = Q_{Azj} + Q_{Pzj} \tag{33.9}$$

Here D, the Rayleigh's dissipation function, accounts for viscous damping in the system. It has been assumed to be of the following form:

$$D = \sum_{i=1}^{n} m_{y_i} \xi_{y_i} \omega_{y_i} \dot{q}_{y_i}^2(t) + \sum_{j=1}^{n} m_{z_j} \xi_{z_j} \omega_{z_j} \dot{q}_{z_j}^2(t) \tag{33.10}$$

33.2.2 Kinetic Energy

It is assumed that the mass of the vehicle is distributed along its structural centre line. Thus the total kinetic energy of the vehicle is equal to the integration of kinetic energies of the particles over the length of the vehicle. The vehicle is assumed to be roll controlled, so the roll rate and roll angle are taken to be zero. The inertial velocity of a point on the centre line of vehicle structure can be expressed as:

$$\vec{V}_P = \begin{bmatrix} V_{Px} \\ V_{Py} \\ V_{Pz} \end{bmatrix} = \begin{bmatrix} V_x - \dot{x}_{cg} + q \sum_{j=1}^{n} \phi_{z_j} q_{z_j} - r \sum_{i=1}^{n} \phi_{y_i} q_{y_i} \\ V_y + \sum_{i=1}^{n} \phi_{y_i} \dot{q}_{y_i} + r(x - x_{cg}) \\ V_z + \sum_{j=1}^{n} \phi_{z_j} \dot{q}_{z_j} - q(x - x_{cg}) \end{bmatrix} \tag{33.11}$$

And the inertial velocity of a point on the nozzle is:

$$\vec{V}_{Pe} = \begin{bmatrix} \left\{ \begin{array}{l} V_x - \dot{x}_{cg} + \eta\left(q\gamma + \dot{\gamma}\gamma - r\delta + \dot{\delta}\delta\right) + q \sum_{j=1}^{n} \phi_{z_j}(0)q_{z_j} - r \sum_{i=1}^{n} \phi_{y_i}(0)q_{y_i} - \eta \sum_{j=1}^{n} \phi'_{z_j}(0)\left(qq_{z_j} + \dot{\gamma}q_{z_j} + \right. \\ \left. \gamma\dot{q}_{z_j}\right) + \eta \sum_{i=1}^{n} \phi'_{y_i}(0)\left(rq_{y_i} - \dot{\delta}q_{y_i} - \delta\dot{q}_{y_i}\right) + \eta \sum_{j=1}^{n}\sum_{l=1}^{n} \phi'_{z_j}(0)\phi'_{z_l}(0)\dot{q}_{z_j}q_{z_l} + \eta \sum_{i=1}^{n}\sum_{k=1}^{n} \phi'_{y_i}(0)\phi'_{y_k}(0)\dot{q}_{y_i}q_{y_k} \end{array} \right\} \\ V_y - r\left(\eta + x_{cg}\right) + \eta\dot{\delta} + \sum_{i=1}^{n} \phi_{y_i}(0)\dot{q}_{y_i} - \eta \sum_{i=1}^{n} \phi'_{y_i}(0)\dot{q}_{y_i} \\ V_z + q\left(\eta + x_{cg}\right) + \eta\dot{\gamma} + \sum_{j=1}^{n} \phi_{z_j}(0)\dot{q}_{z_j} - \eta \sum_{i=1}^{n} \phi'_{z_j}(0)\dot{q}_{z_j} \end{bmatrix}$$

$$\tag{33.12}$$

So the kinetic energy of the complete vehicle can be written as:

$$E = \int_0^l \left(\frac{1}{2}m(x,t)V_P^2\right) dx + \int_0^{l_e} \left(\frac{1}{2}m(\eta)V_{Pe}^2\right) d\eta \tag{33.13}$$

33.2.3 Potential Energy

Derivation of gravitational potential energy requires transformation between the body frame and the earth fixed (x-Vertically up, y-South, z-East) frame of reference. Vehicle's attitude with respect to earth fixed frame is known through Euler angles ϕ, ψ, θ in that order about $x, z,$ and y axis respectively. The transformation matrix from earth fixed frame to body frame has the form

$$T_{EB} = \begin{bmatrix} \cos\psi\cos\theta & \cos\phi\sin\psi\cos\theta + \sin\phi\sin\theta & \sin\phi\sin\psi\cos\theta - \cos\phi\sin\theta \\ -\sin\psi & \cos\phi\cos\psi & \sin\phi\cos\psi \\ \cos\psi\sin\theta & \cos\phi\sin\psi\sin\theta - \sin\phi\sin\theta & \sin\phi\sin\psi\sin\theta + \cos\phi\cos\theta \end{bmatrix} \tag{33.14}$$

And transformation matrix from body frame to earth fixed frame is

$$T_{BE} = T'_{EB} \tag{33.15}$$

Now the position of any point P on the vehicle with respect to its cg in earth fixed frame can be written as

$$\begin{bmatrix} x \\ y \\ z \end{bmatrix}_P = T_{BE} \begin{bmatrix} x - x_{cg} \\ \sum\limits_{i=1}^{n} \phi_{y_i} q_{y_i} \\ \sum\limits_{j=1}^{n} \phi_{z_j} q_{z_j} \end{bmatrix} \tag{33.16}$$

So the vertical height of P from the origin of earth fixed frame will be

$$h_P = h + x_P \tag{33.17}$$

Similarly position of any point P_e on the nozzle with respect to cg of the vehicle in earth fixed frame is

$$\begin{bmatrix} x \\ y \\ z \end{bmatrix}_{P_e} = T_{BE} \begin{bmatrix} -(\eta + x_{cg}) \\ \sum\limits_{i=1}^{n} \phi_{y_i}(0)q_{y_i} + \eta \left(\delta - \sum\limits_{i=1}^{n} \phi'_{y_i}(0)q_{y_i} \right) \\ \sum\limits_{j=1}^{n} \phi_{z_j}(0)q_{z_j} + \eta \left(\gamma - \sum\limits_{j=1}^{n} \phi'_{z_j}(0)q_{z_j} \right) \end{bmatrix} \tag{33.18}$$

So the vertical height of P_e from the origin of earth fixed frame will be

$$h_{P_e} = h + x_{P_e} \tag{33.19}$$

The gravitational potential energy of the complete vehicle can be written as

$$U_g = \int_0^l m(x,t)gh_P\,dx + \int_0^{l_e} m(\eta)gh_{P_e}\,d\eta \tag{33.20}$$

On solving, it gives

$$U_g = m_t gh - g \sin \psi \left(m_e \sum_{i=1}^{n} \phi_{y_i}(0)q_{y_i} + S_e\delta - S_e \sum_{i=1}^{n} \phi'_{y_i}(0)q_{y_i} \right)$$

$$+ g \sin \theta \cos \psi \left(m_e \sum_{j=1}^{n} \phi_{z_j}(0)q_{z_j} + S_e\gamma - S_e \sum_{j=1}^{n} \phi'_{z_j}(0)q_{z_j} \right) \tag{33.21}$$

Also, the vehicle possesses strain energy due to bending which is given by

$$U_p = \frac{1}{2} \sum_{i=1}^{n} m_{y_i} \omega_{y_i} q_{y_i}^2 + \frac{1}{2} \sum_{j=1}^{n} m_{z_j} \omega_{z_j} q_{z_j}^2 \tag{33.22}$$

Thus the total potential energy of the vehicle is

$$U = U_g + U_p \tag{33.23}$$

Hence, the terms in Lagrange's equations due to potential energy of the vehicle can now be calculated as

$$
\begin{bmatrix} U_{F_x} \\ U_{F_y} \\ U_{F_z} \end{bmatrix} = T_{EB} \begin{bmatrix} \partial U/\partial h \\ 0 \\ 0 \end{bmatrix} = \begin{bmatrix} m_t g \cos \theta \cos \psi \\ -m_t g \sin \psi \\ m_t g \sin \theta \cos \psi \end{bmatrix} \tag{33.24}
$$

$$
\begin{aligned}
\begin{bmatrix} U_{M_x} \\ U_{M_y} \\ U_{M_z} \end{bmatrix} &= \begin{bmatrix} \cos \theta & 0 & -\sin \theta \\ 0 & 1 & 0 \\ \sin \theta & 0 & \cos \theta \end{bmatrix} \begin{bmatrix} 0 \\ 0 \\ \partial U/\partial \psi \end{bmatrix} + \begin{bmatrix} 0 \\ \partial U/\partial \theta \\ 0 \end{bmatrix} \\
&= \begin{bmatrix} Ag \sin \theta \cos \psi + Bg \sin^2 \theta \sin \psi \\ Bg \cos \theta \cos \psi \\ Ag \cos \theta \cos \psi - Bg \sin \theta \cos \theta \sin \psi \end{bmatrix}
\end{aligned} \tag{33.25}
$$

$$
\frac{\partial U}{\partial q_{y_i}} = - \left(m_e \phi_{y_i}(0) - S_e \phi'_{y_i}(0) \right) g \sin \psi + m_{y_i} \omega_{y_i}^2 q_{y_i} \tag{33.26}
$$

$$
\frac{\partial U}{\partial q_{z_j}} = \left(m_e \phi_{z_j}(0) - S_e \phi'_{z_j}(0) \right) g \cos \psi \sin \theta + m_{z_j} \omega_{z_j}^2 q_{z_j} \tag{33.27}
$$

where

$$
A = m_e \sum_{i=1}^{n} \phi_{y_i}(0) q_{y_i} + S_e \left(\delta - \sum_{i=1}^{n} \phi'_{y_i}(0) q_{y_i} \right) \tag{33.28}
$$

$$
B = m_e \sum_{j=1}^{n} \phi_{z_j}(0) q_{z_j} + S_e \left(\gamma - \sum_{j=1}^{n} \phi'_{z_j}(0) q_{z_j} \right) \tag{33.29}
$$

33.2.4 Damping Terms

From Eq. (33.10), damping terms in the Lagrange's equations are obtained as

$$
\frac{\partial D}{\partial \dot{q}_{y_i}} = 2 m_{y_i} \xi_{y_i} \omega_{y_i} \dot{q}_{y_i} \tag{33.30}
$$

$$
\frac{\partial D}{\partial \dot{q}_{z_j}} = 2 m_{z_j} \xi_{z_j} \omega_{z_j} \dot{q}_{z_j} \tag{33.31}
$$

33.2.5 Non-conservative Forces and Moments

33.2.5.1 Aerodynamic Forces and Moments

The aerodynamic forces and moments acting on a flexible vehicle are computed below. In the present study, aerodynamic forces acting on the nozzle have been neglected.

Let α denote the angle of attack and β the side-slip angle of undeformed vehicle such that

- Counter-clockwise rotation about y axis increases β.
- Counter-clockwise rotation about z axis increases α.

The magnitude of net velocity of any point P relative to wind is assumed to be equal to that of cg of the vehicle, i.e.,

$$
V_{P/w} \approx V_{m/w} \tag{33.32}
$$

Now y component of velocity at any point P relative to wind is given as

$$V_{P/w,y} = V_{Py} - V_{wy} = \left(V_y + r\left(x - x_{cg} \right) + \sum_{i=1}^{n} \phi_{y_i} \dot{q}_{y_i} \right) - V_{wy} \tag{33.33}$$

So, the local angle of attack at P can be written as

$$\alpha_P = -\frac{V_{P/w,y}}{V_{P/w}} + \sum_{i=1}^{n} \phi'_{y_i}(x) q_{y_i} = -\frac{V_{P/w,y}}{V_{m/w}} + \sum_{i=1}^{n} \phi'_{y_i}(x) q_{y_i} \tag{33.34}$$

Substituting $V_{P/w,y}$ from Eq. (33.33), and writing

$$\alpha = -\frac{V_{Py}}{V_{m/w}} \tag{33.35}$$

$$\alpha_w = \frac{V_{wy}}{V_{m/w}} \tag{33.36}$$

Eq. (33.34) can be rewritten as

$$\alpha_P = \alpha + \alpha_w + \sum_{i=1}^{n} \phi'_{y_i}(x) q_{y_i} - \frac{1}{V_{m/w}} \left(r\left(x - x_{cg} \right) + \sum_{i=1}^{n} \phi_{y_i} \dot{q}_{y_i} \right) \tag{33.37}$$

Similarly in yaw plane

$$V_{P/w,z} = V_{Pz} - V_{wz} = \left(V_z - q\left(x - x_{cg} \right) + \sum_{j=1}^{n} \phi_{z_j} \dot{q}_{z_j} \right) - V_{wz} \tag{33.38}$$

So the local side slip angle at P can be written as

$$\beta_P = \frac{V_{P/w,z}}{V_{P/w}} - \sum_{j=1}^{n} \phi'_{z_j}(x) q_{z_j} = \frac{V_{P/w,z}}{V_{m/w}} - \sum_{j=1}^{n} \phi'_{z_j}(x) q_{z_j} \tag{33.39}$$

Substituting $V_{P/w,z}$ from Eq. (33.38), and writing

$$\beta = \frac{V_{Pz}}{V_{m/w}} \tag{33.40}$$

$$\beta_w = \frac{V_{wz}}{V_{m/w}} \tag{33.41}$$

Eq. (33.39) can be rewritten as

$$\beta_P = \beta + \beta_w - \sum_{j=1}^{n} \phi'_{z_j}(x) q_{z_j} + \frac{1}{V_{m/w}} \left(-q\left(x - x_{cg} \right) + \sum_{j=1}^{n} \phi_{z_j} \dot{q}_{z_j} \right) \tag{33.42}$$

The slopes of local axial (drag) and normal (lift) force coefficient are computed from the CFD analysis or wind tunnel testing of the vehicle. Now, it is convenient to define certain aerodynamic integrals related to these coefficients. Note that in computation of these integrals, it has been assumed that the vehicle is symmetric such that pitch and yaw bending mode shapes are same. So the following integrals are established:

$$D_\alpha = QS \int_0^l c_{d_\alpha}(x, M) dx \tag{33.43}$$

$$N_\alpha = N_\beta = QS \int_0^l c_{n_\alpha}(x, M) dx \tag{33.44}$$

$$N_q = N_r = -\frac{QS}{V_{m/w}} \int_0^l (x - x_{cg}) c_{n_\alpha}(x, M) dx \tag{33.45}$$

$$N_{q_{y_i}} = N_{q_{z_i}} = QS \int_0^l \phi'_{y_i}(x) c_{n_\alpha}(x, M) dx \tag{33.46}$$

$$N_{\dot{q}_{y_i}} = N_{\dot{q}_{z_i}} = -\frac{QS}{V_{m/w}} \int_0^l \phi_{y_i}(x) c_{n_\alpha}(x, M) dx \tag{33.47}$$

$$M_\alpha = M_\beta = QS \int_0^l (x - x_{cg}) c_{n_\alpha}(x, M) dx \tag{33.48}$$

$$M_q = M_r = -\frac{QS}{V_{m/w}} \int_0^l (x - x_{cg})^2 c_{n_\alpha}(x, M) dx \tag{33.49}$$

$$M_{q_{y_i}} = M_{q_{z_i}} = QS \int_0^l (x - x_{cg}) \phi'_{y_i}(x) c_{n_\alpha}(x, M) dx \tag{33.50}$$

$$M_{\dot{q}_{y_i}} = M_{\dot{q}_{z_i}} = -\frac{QS}{V_{m/w}} \int_0^l (x - x_{cg}) \phi_{y_i}(x) c_{n_\alpha}(x, M) dx \tag{33.51}$$

$$Q_{i,\alpha} = Q_{i,\beta} = QS \int_0^l \phi_{y_i}(x) c_{n_\alpha}(x, M) dx \tag{33.52}$$

$$Q_{i,q} = Q_{i,r} = -\frac{QS}{V_{m/w}} \int_0^l (x - x_{cg}) \phi_{y_i}(x) c_{n_\alpha}(x, M) dx \tag{33.53}$$

$$Q_{i,q_{y_k}} = Q_{i,q_{z_k}} = QS \int_0^l \phi_{y_i}(x) \phi'_{y_k}(x) c_{n_\alpha}(x, M) dx \tag{33.54}$$

$$Q_{i,\dot{q}_{y_k}} = Q_{i,\dot{q}_{z_k}} = -\frac{QS}{V_{m/w}} \int_0^l \phi_{y_i}(x) \phi_{y_k}(x) c_{n_\alpha}(x, M) dx \tag{33.55}$$

Therefore the aerodynamic forces and moments can be computed as follows

$$F_{Ax} = -QS \int_0^l c_{d_\alpha}(x, M) \alpha_T dx = -D_\alpha \alpha_T \tag{33.56}$$

$$F_{Ay} = QS \int_0^l c_{n_\alpha}(x, M)\alpha(x)dx = N_\alpha (\alpha + \alpha_w) + N_r r$$

$$+ \sum_{i=1}^n N_{q_{y_i}} q_{y_i} + \sum_{i=1}^n N_{\dot{q}_{y_i}} \dot{q}_{y_i} \tag{33.57}$$

$$F_{Az} = -QS \int_0^l c_{n_\alpha}(x, M)\beta(x)dx = -N_\beta (\beta + \beta_w) - N_q q$$

$$+ \sum_{j=1}^n N_{q_{z_j}} q_{z_j} + \sum_{j=1}^n N_{\dot{q}_{z_j}} \dot{q}_{z_j} \tag{33.58}$$

$$M_{Ay} = QS \int_0^l (x - x_{cg})c_{n_\alpha}(x, M)\beta(x)dx = M_\beta (\beta + \beta_w) + M_q q$$

$$- \sum_{j=1}^n M_{q_{z_j}} q_{z_j} - \sum_{j=1}^n M_{\dot{q}_{z_j}} \dot{q}_{z_j} \tag{33.59}$$

$$M_{Az} = QS \int_0^l (x - x_{cg})c_{n_\alpha}(x, M)\alpha(x)dx = M_\alpha (\alpha + \alpha_w) + M_r r$$

$$+ \sum_{i=1}^n M_{q_{y_i}} q_{y_i} + \sum_{i=1}^n M_{\dot{q}_{y_i}} \dot{q}_{y_i} \tag{33.60}$$

$$Q_{Ay_i} = QS \int_0^l \phi_{y_i}(x)c_{n_\alpha}(x, M)\alpha(x)dx = Q_{i,\alpha} (\alpha + \alpha_w) + Q_{i,r} r$$

$$+ \sum_{k=1}^n Q_{i,q_{y_k}} q_{y_k} + \sum_{k=1}^n Q_{i,\dot{q}_{y_k}} \dot{q}_{y_k} \tag{33.61}$$

$$Q_{Az_j} = -QS \int_0^l \phi_{z_j}(x)c_{n_\alpha}(x, M)\beta(x)dx = -Q_{j,\beta} (\beta + \beta_w) - Q_{j,q} q$$

$$+ \sum_{l=1}^n Q_{j,q_{z_l}} q_{z_l} + \sum_{l=1}^n Q_{j,\dot{q}_{z_l}} \dot{q}_{z_l} \tag{33.62}$$

33.2.5.2 Propulsive Forces and Moments

Resolving the thrust force into its components along the three coordinate axes, the forces and moments due to thrust can be written as:

$$F_{Px} = T_e \cos\left(\sqrt{\gamma^2 + \delta^2}\right) \approx T_e \tag{33.63}$$

$$F_{Py} = -T_e \left(\delta - \sum_{i=1}^n \phi'_{y_i}(0)q_{y_i}\right) \tag{33.64}$$

$$F_{Pz} = -T_e \left(\gamma - \sum_{j=1}^{n} \phi'_{z_j}(0) q_{z_j} \right) \tag{33.65}$$

$$M_{Py} = F_{Pz} x_{cg} + T_e \sum_{j=1}^{n} \phi_{z_j}(0) q_{z_j} = -T_e \left(\gamma - \sum_{j=1}^{n} \phi'_{z_j}(0) q_{z_j} \right) x_{cg}$$

$$+ T_e \sum_{j=1}^{n} \phi_{z_j}(0) q_{z_j} \tag{33.66}$$

$$M_{Pz} = -F_{Py} x_{cg} - T_e \sum_{i=1}^{n} \phi_{y_i}(0) q_{y_i} = -T_e \left(\delta - \sum_{i=1}^{n} \phi'_{y_i}(0) q_{y_i} \right) x_{cg}$$

$$- T_e \sum_{i=1}^{n} \phi_{y_i}(0) q_{y_i} \tag{33.67}$$

$$Q_{Py_i} = F_{Py} \phi_{y_i}(0) = -T_e \left(\delta - \sum_{k=1}^{n} \phi'_{y_k}(0) q_{y_k} \right) \phi_{y_i}(0) \tag{33.68}$$

$$Q_{Pz_j} = F_{Pz} \phi_{z_j}(0) = -T_e \left(\gamma - \sum_{l=1}^{n} \phi'_{z_l}(0) q_{z_l} \right) \phi_{z_j}(0) \tag{33.69}$$

33.2.6 Equations of Motion and Bending

On substituting the expressions for variables in Lagrange's equations and solving, the equations of motion and bending as given in Eqs. (33.70)–(33.76) are obtained. In order to simplify the equations, all triple product combinations of q, $\dot{q}$, r, $\dot{r}$, and zero, first and second order time derivatives of δ, γ, $\sum_{i=1}^{n} \phi_{y_i}(0) q_{y_i}$, $\sum_{i=1}^{n} \phi'_{y_i}(0) q_{y_i}$, $\sum_{j=1}^{n} \phi_{z_j}(0) q_{z_j}$, $\sum_{j=1}^{n} \phi'_{z_j}(0) q_{z_j}$ are eliminated from the final equations. Terms in the equations of linear and angular accelerations are separated into two groups: first group represents the rigid body terms and can be used to model the vehicle's rigid body dynamics. The second group represents the effects of structural flexibility on the vehicle dynamics. This group of terms can be added to any existing model of rigid body dynamics in order to include the flexible degrees of freedom in the model.

$$\dot{V}_x = \left\{ \frac{1}{m_t} \left(-D_\alpha \alpha_T + T_e - \dot{m}_t (V_x - \dot{x}_{cg}) \right. \right.$$

$$- S_e \left(\dot{q} \gamma + 2q\dot{\gamma} + \dot{\gamma}^2 + \ddot{\gamma}\gamma - \dot{r}\delta - 2r\dot{\delta} + \dot{\delta}^2 + \ddot{\delta}\delta \right) \right) - g \cos\theta \cos\psi + \ddot{x}_{cg} -$$

$$\left. qV_z + rV_y \right\} + \frac{1}{m_t} \left\{ S_e \sum_{i=1}^{n} \phi'_{y_i}(0) \left(-\dot{r} q_{y_i} - 2r\dot{q}_{y_i} + \ddot{\delta} q_{y_i} + 2\dot{\delta}\dot{q}_{y_i} + \delta\ddot{q}_{y_i} \right) \right.$$

$$- S_e \sum_{i=1}^{n} \sum_{k=1}^{n} \phi'_{y_i}(0) \phi'_{y_k}(0) \left(\ddot{q}_{y_i} q_{y_k} + \dot{q}_{y_i} \dot{q}_{y_k} \right)$$

$$+ m_e \sum_{i=1}^{n} \phi_{y_i}(0) \left(\dot{r} q_{y_i} + 2r\dot{q}_{y_i} \right) + S_e \sum_{j=1}^{n} \phi'_{z_j}(0)$$

$$\left(\dot{q} q_{z_j} + 2q\dot{q}_{z_j} + \ddot{\gamma} q_{z_j} + 2\dot{\gamma}\dot{q}_{z_j} + \gamma\ddot{q}_{z_j} \right) - S_e \sum_{j=1}^{n} \sum_{l=1}^{n} \phi'_{z_j}(0) \phi'_{z_l}(0) \left(\ddot{q}_{z_j} q_{z_l} + \right.$$

$$\dot{q}_{z_j}\dot{q}_{z_l}) - m_e \sum_{j=1}^{n} \phi_{z_j}(0) \left(\dot{q}q_{z_j} + 2q\dot{q}_{z_j} \right) \Bigg\} \tag{33.70}$$

$$\dot{V}_y = \left\{ \frac{1}{m_t} \left(N_\alpha (\alpha + \alpha_w) + N_r r + N_\delta \delta + N_{\dot\delta}\dot\delta - T_e\delta - \dot{m}_t V_y - S_e\ddot\delta \right) \right.$$

$$\left. + g \sin\psi - r \left(V_x - \dot{x}_{cg} \right) \right\} +$$

$$\frac{1}{m_t} \left\{ \sum_{i=1}^{n} \left(N_{q_{y_i}} q_{y_i} + N_{\dot{q}_{y_i}} \dot{q}_{y_i} + T_e\phi'_{y_i}(0)q_{y_i} \right) \right.$$

$$\left. - \sum_{i=1}^{n} \left(m_e\phi_{y_i}(0) - S_e\phi'_{y_i}(0) \right) \ddot{q}_{y_i} \right\} \tag{33.71}$$

$$\dot{V}_z = \left\{ \frac{1}{m_t} \left(- N_\beta (\beta + \beta_w) - N_q q + N_\gamma\gamma + N_{\dot\gamma}\dot\gamma - T_e\gamma - \dot{m}_t V_z - S_e\ddot{y} \right) \right.$$

$$\left. - g \sin\theta \cos\psi + q \left(V_x - \dot{x}_{cg} \right) \right\} +$$

$$\frac{1}{m_t} \left\{ \sum_{j=1}^{n} \left(N_{q_{z_j}} q_{z_j} + N_{\dot{q}_{z_j}} \dot{q}_{z_j} + T_e\phi'_{z_j}(0)q_{z_j} \right) \right.$$

$$\left. - \sum_{j=1}^{n} \left(m_e\phi_{z_j}(0) - S_e\phi'_{z_j}(0) \right) \ddot{q}_{z_j} \right\} \tag{33.72}$$

$$\dot{q} = \Bigg[\Big\{ M_\beta (\beta + \beta_w) + M_q q - M_\gamma\gamma - M_{\dot\gamma}\dot\gamma - T_e\gamma x_{cg} - g S_e\gamma \cos\psi \cos\theta$$

$$- \dot{I}_{yy}q - (I_e + S_e x_{cg}) \ddot{y} - S_e \left(\dot{V}_x - \ddot{x}_{cg} \right)\gamma$$

$$- 2\dot{x}_{cg}q \left(S_e + m_e x_{cg} \right) - S_e V_z \left(q\gamma + \dot\gamma\gamma - r\delta + \dot\delta\delta \right) + m_t V_z\dot{x}_{cg} \Big\}$$

$$+ \left\{ \sum_{j=1}^{n} \left(- M_{q_{z_j}} q_{z_j} - M_{\dot{q}_{z_j}} \dot{q}_{z_j} \right) \right.$$

$$+ T_e \left(\phi_{z_j}(0) + x_{cg}\phi'_{z_j}(0) \right) q_{z_j} \Big) - g \cos\psi \cos\theta \sum_{j=1}^{n} \left(m_e\phi_{z_j}(0) - S_e\phi'_{z_j}(0) \right)$$

$$q_{z_j} - \sum_{j=1}^{n} \left(\dot{m}_{z_j} qq_{z_j}^2 + m_{z_j} \dot{q}q_{z_j}^2 + 2m_{z_j} qq_{z_j}\dot{q}_{z_j} \right)$$

$$+ \sum_{i=1}^{n}\sum_{j=1}^{n} \left(\dot{m}_{y_i z_j} r + m_{y_i z_j}\dot{r} \right)$$

$$q_{y_i} q_{z_j} + m_{y_i z_j} r \sum_{i=1}^{n}\sum_{j=1}^{n} \left(\dot{q}_{y_i} q_{z_j} + q_{y_i}\dot{q}_{z_j} \right) - \left(\dot{V}_x - \ddot{x}_{cg} \right) \sum_{j=1}^{n}$$

$$\left(m_e\phi_{z_j}(0) - S_e\phi'_{z_j}(0)\right) q_{z_j}$$

$$-\sum_{j=1}^{n} \left(\left(S_e + m_e x_{cg}\right)\phi_{z_j}(0) - \left(I_e + S_e x_{cg}\right)\phi'_{z_j}(0)\right)\ddot{q}_{z_j} + S_e V_z$$

$$\left(\sum_{j=1}^{n}\phi'_{z_j}(0)\left(qq_{z_j} + \dot{\gamma}q_{z_j} + \gamma\dot{q}_{z_j}\right)\right.$$

$$-\sum_{j=1}^{n}\sum_{l=1}^{n}\phi'_{z_j}(0)\phi'_{z_l}(0)\dot{q}_{z_j}q_{z_l} - \sum_{i=1}^{n}\phi'_{y_i}(0)\left(rq_{y_i} - \delta q_{y_i} - \delta\dot{q}_{y_i}\right)$$

$$\left.-\sum_{i=1}^{n}\sum_{k=1}^{n}\phi'_{y_i}(0)\phi'_{y_k}(0)\dot{q}_{y_i}q_{y_k}\right)$$

$$\left.\left.-m_e V_z \left(q\sum_{j=1}^{n}\phi_{z_j}(0)q_{z_j} - r\sum_{i=1}^{n}\phi_{y_i}(0)q_{y_i}\right)\right\}\right]$$

$$\Big/ \left[I_{yy} + I_e + 2S_e x_{cg} + m_e x_{cg}^2\right] \tag{33.73}$$

$$\dot{r} = \left[\left\{M_\alpha\left(\alpha + \alpha_w\right) + M_r r + M_\delta\delta + M_{\dot{\delta}}\dot{\delta} + T_e\delta x_{cg} + gS_e\cos\theta\right.\right.$$

$$\left(\delta\cos\psi + \gamma\sin\psi\sin\theta\right) - \dot{I}_{zz}r + \left(I_e + S_e x_{cg}\right)\ddot{\delta}$$

$$+S_e\left(\dot{V}_x - \ddot{x}_{cg}\right)\delta - 2\dot{x}_{cg}r\left(S_e + m_e x_{cg}\right) - S_e V_y\left(r\delta - \dot{\delta}\delta - q\gamma - \dot{\gamma}\gamma\right)$$

$$\left.-m_t V_y\dot{x}_{cg}\right\} + \left\{\sum_{i=1}^{n}\left(M_{q_{y_i}}q_{y_i} + M_{\dot{q}_{y_i}}\dot{q}_{y_i}\right.\right.$$

$$\left.-T_e\left(\phi_{y_i}(0) + x_{cg}\phi'_{y_i}(0)\right)q_{y_i}\right) + g\cos\theta$$

$$\left(\cos\psi\sum_{i=1}^{n}\left(m_e\phi_{y_i}(0) - S_e\phi'_{y_i}(0)\right)q_{y_i} + \sin\psi\sin\theta\sum_{j=1}^{n}\left(m_e\phi_{z_j}(0)\right.\right.$$

$$\left.\left.-S_e\phi'_{z_j}(0)\right)q_{z_j}\right) - \sum_{i=1}^{n}\left(\dot{m}_{y_i}rq_{y_i}^2 + m_{y_i}\dot{r}q_{y_i}^2 + 2m_{y_i}rq_{y_i}\dot{q}_{y_i}\right)$$

$$+\sum_{i=1}^{n}\sum_{j=1}^{n}\left(\dot{m}_{y_iz_j}q + m_{y_iz_j}\dot{q}\right)q_{y_i}q_{z_j}$$

$$+m_{y_iz_j}q\sum_{i=1}^{n}\sum_{j=1}^{n}\left(\dot{q}_{y_i}q_{z_j} + q_{y_i}\dot{q}_{z_j}\right) + \left(\dot{V}_x - \ddot{x}_{cg}\right)\sum_{i=1}^{n}\left(m_e\phi_{y_i}(0) - S_e\phi'_{y_i}(0)\right)$$

$$q_{y_i} + \sum_{i=1}^{n}\left(\left(S_e + m_e x_{cg}\right)\phi_{y_i}(0)\right)$$

$$
-\left(I_e + S_e x_{cg}\right)\phi'_{y_i}(0)\right)\ddot{q}_{y_i} + S_e V_y \left(\sum_{i=1}^{n} \phi'_{y_i}(0)\left(r q_{y_i} - \dot{\delta}q_{y_i} - \delta\dot{q}_{y_i}\right)\right.
$$

$$
+\sum_{i=1}^{n}\sum_{k=1}^{n}\phi'_{y_i}(0)\phi'_{y_k}(0)\dot{q}_{y_i} q_{y_k}
$$

$$
-\sum_{j=1}^{n}\phi'_{z_j}(0)\left(q q_{z_j} + \dot{\gamma}q_{z_j} + \gamma\dot{q}_{z_j}\right) + \sum_{j=1}^{n}\sum_{l=1}^{n}\phi'_{z_j}(0)\phi'_{z_l}(0)\dot{q}_{z_j} q_{z_l}\right)
$$

$$
-m_e V_y \left(r\sum_{i=1}^{n}\phi_{y_i}(0)q_{y_i} - q\sum_{j=1}^{n}\phi_{z_j}(0)q_{z_j}\right)\right\}\right]
$$

$$
\Bigg/ \left[I_{zz} + I_e + 2 S_e x_{cg} + m_e x_{cg}^2\right] \tag{33.74}
$$

$$
\ddot{q}_{y_i} = \left[Q_{i,\alpha}(\alpha + \alpha_w) + Q_{i,r}r + \sum_{k=1}^{n}\left(Q_{i,q_{yk}} q_{yk} + Q_{i,\dot{q}_{yk}}\dot{q}_{yk}\right)\right.
$$

$$
-T_e\phi_{y_i}(0)\left(\delta - \sum_{k=1}^{n}\phi'_{y_k}(0)q_{yk}\right)
$$

$$
-\left(\dot{m}_{y_i} + 2m_{y_i}\xi_{y_i}\omega_{y_i}\right)\dot{q}_{y_i}
$$

$$
-m_{y_i}\left(\omega_{y_i}^2 - r^2\right)q_{y_i} - qr\sum_{j=1}^{n}m_{y_i z_j}q_{z_j} + S_e\left(\dot{V}_x - \ddot{x}_{cg}\right)
$$

$$
\phi'_{y_i}(0)\left(\delta - \sum_{k=1}^{n}\phi'_{y_k}(0)q_{yk}\right) + \left(g\sin\psi - \dot{V}_y - \left(V_x - 2\dot{x}_{cg}\right)r\right.
$$

$$
\left.+x_{cg}\dot{r} - \sum_{k=1}^{n}(1 - \delta_{ik})\phi_{y_k}(0)\ddot{q}_{yk}\right)
$$

$$
\left(m_e\phi_{y_i}(0) - S_e\phi'_{y_i}(0)\right) + \left(\dot{r} - \ddot{\delta} + \sum_{k=1}^{n}(1 - \delta_{ik})\phi'_{y_k}(0)\ddot{q}_{yk}\right)
$$

$$
\left(S_e\phi_{y_i}(0) - \right.
$$

$$
\left.\left.I_e\phi'_{y_i}(0)\right)\right] \Bigg/ \left[m_{y_i} + \phi_{y_i}(0)\left(m_e\phi_{y_i}(0) - S_e\phi'_{y_i}(0)\right)\right.
$$

$$
\left.-\phi'_{y_i}(0)\left(S_e\phi_{y_i}(0) - I_e\phi'_{y_i}(0)\right)\right] \tag{33.75}
$$

$$
\ddot{q}_{z_j} = \left[-Q_{j,\beta}(\beta + \beta_w) - Q_{i,q}q + \sum_{l=1}^{n}\left(Q_{j,q_{zl}} q_{zl} + Q_{j,\dot{q}_{zl}}\dot{q}_{zl}\right)\right.
$$

$$
-T_e\phi_{z_j}(0)\left(\gamma - \sum_{l=1}^{n}\phi'_{z_l}(0)q_{zl}\right)
$$

$$
-\left(\dot{m}_{z_j} + 2m_{z_j}\xi_{z_j}\omega_{z_j}\right)\dot{q}_{z_j}
$$

$$-m_{z_j}\left(\omega_{z_j}^2 - q^2\right)q_{z_j} - qr\sum_{i=1}^{n}m_{y_i z_j}q_{y_i} + S_e\left(\dot{V}_x - \ddot{x}_{cg}\right)\phi'_{z_j}(0)$$

$$\left(\gamma - \sum_{l=1}^{n}\phi'_{z_l}(0)q_{z_l}\right) - \left(g\cos\psi\sin\theta + \dot{V}_z\right.$$

$$-\left(V_x - 2\dot{x}_{cg}\right)q + x_{cg}\dot{q} + \sum_{l=1}^{n}\left(1 - \delta_{jl}\right)\phi_{z_l}(0)\ddot{q}_{z_l}\right)\left(m_e\phi_{z_j}(0) - S_e\phi'_{z_j}(0)\right)$$

$$-\left(\dot{q} + \ddot{\gamma} - \sum_{l=1}^{n}\left(1 - \delta_{jl}\right)\phi'_{z_l}(0)\ddot{q}_{z_l}\right)\left(S_e\phi_{z_j}(0) - \right.$$

$$\left. I_e\phi'_{z_j}(0)\right)\right] \bigg/ \left[m_{z_j} + \phi_{z_j}(0)\left(m_e\phi_{z_j}(0) - S_e\phi'_{z_j}(0)\right)\right.$$

$$\left.-\phi'_{z_j}(0)\left(S_e\phi_{z_j}(0) - I_e\phi'_{z_j}(0)\right)\right] \tag{33.76}$$

where

$$\delta_{ij} = \begin{cases} 1 & \text{if } i = j \\ 0 & \text{if } i \neq j \end{cases} \tag{33.77}$$

33.2.7 Accelerations and Angular Rates at Sensor Locations

Equations (33.76)–(33.80) can be used to get the accelerations and angular rates of the vehicle's centre of gravity. Feedback sensors mounted on the vehicle measure the local accelerations and angular rates at their location. These measurements can be related to the accelerations and angular rates of c.g. as given below:

$$a_y = \dot{V}_y + rV_x \tag{33.78}$$

$$a_{y,ins} = a_y + \left(x_{ins} - x_{cg}\right)\dot{r} + \phi_y(x_{ins})\ddot{q}_y \tag{33.79}$$

$$a_z = \dot{V}_z - qV_x \tag{33.80}$$

$$a_{z,ins} = a_z - \left(x_{ins} - x_{cg}\right)\dot{q} + \phi_z(x_{ins})\ddot{q}_z \tag{33.81}$$

$$r_{ins} = r + \phi'_y(x_{ins})\dot{q}_y \tag{33.82}$$

$$q_{ins} = q - \phi'_z(x_{ins})\dot{q}_y \tag{33.83}$$

33.3 Simulations and Results

Equations governing the flexible aerospace vehicle dynamics were programmed in MATLAB/SIMULINK® using model based design technique. This model was used for the validation of control software by carrying out simulations using RT-LAB real-time simulator with control subsystem connected in the loop. The control software is considered valid if the vehicle response is stable, i.e., the lateral acceleration and rate produced by the controller remain bounded.

The model has provisions for inclusion of any number of bending degrees of freedom. First three bending modes were considered in case of present simulations. Further, the model has been programmed such that same model can be used to simulate either rigid vehicle dynamics or flexible vehicle dynamics by setting the value of flexibility flag to 0 or 1 respectively. Time dependent input parameters were approximated by using tabulated data and linear interpolation subroutine. Effects of wind velocity are also taken into account. All aerodynamic coefficients of the vehicle were computed on-line by interpolating the local coefficients at the instantaneous mach number and integrating them over the vehicle length.

Note: The results shown in the following subsections are normalised using a suitable normalisation factor. They indicate only the stability or instability of the vehicle response and do not represent the actual values of the simulation results. A common normalisation factor is used for all the acceleration results and another common normalisation factor is used for all the angular rate results.

In this research, first the necessity of a flexible vehicle dynamics model for hardware-in-loop simulations was established. The controller of a flight which had failed immediately after launch due to excessive bending oscillations was considered. Though the results of pre-flight simulation carried out using existing rigid body model with the above mentioned controller connected in loop had shown stable vehicle response, the vehicle response was unstable during the flight test. On post-flight analysis, it was found that the filters used in the controller to suppress the structural feedback were not correctly designed, which led to the excitement of bending vibration and hence the flight failure. The pre-flight simulation was reconstructed using the model developed in this research with flexibility effects suppressed (by setting flexibility flag to 0), and identical results were obtained. Lateral acceleration and rate plots are shown in Fig. 33.4. So it was realised that rigid body simulations cannot detect various flaws in the controller which can lead to flight failures. This demonstrated the pressing need of a model of flexible vehicle dynamics for real-time simulations.

Next, a simulation was carried out with the same controller in loop, but the flexibility flag set to 1. In this case, unstable vehicle response similar to that seen during its flight test, was obtained. Plots of lateral acceleration and rate are shown in Fig. 33.5.

Finally a simulation was carried out with updated controller in the loop and flexibility flag set to 1. In the updated controller, fourth order filters for lateral acceleration and rate were used (instead of second order filters used earlier). Results of the simulation (Fig. 33.6) show a stable vehicle response with the flexibility effects taken into account.

33.4   Conclusion

In this research, a model based approach to model the dynamics of a flexible aerospace vehicle for real-time simulations has been presented. Model based approach makes debugging, parameter monitoring and modification of the model much easier as compared with conventional C-programming based approach. The model developed is used to capture through simulation, the instability in vehicle response which was observed in the flight test earlier. This instability was not detected in the real-time simulations carried out using the model of rigid body dynamics. Thus, present model will be helpful in validating controllers and preventing flight failures in the future due to the effects of structural flexibility. The research also shows that the complex computations involving the simulation of flexible vehicle dynamics can be done in real-time using the available computers. The model can be used to facilitate not only the validation of control software and embedded hardware with advanced processors, but also its interaction with new generation composite airframes having significant uncertainty in flexibility characteristics.

Fig. 33.4 Simulation results with controller of unsuccessful flight: flexible dynamics disabled. (**a**) Lateral accelerations; (**b**) angular rates
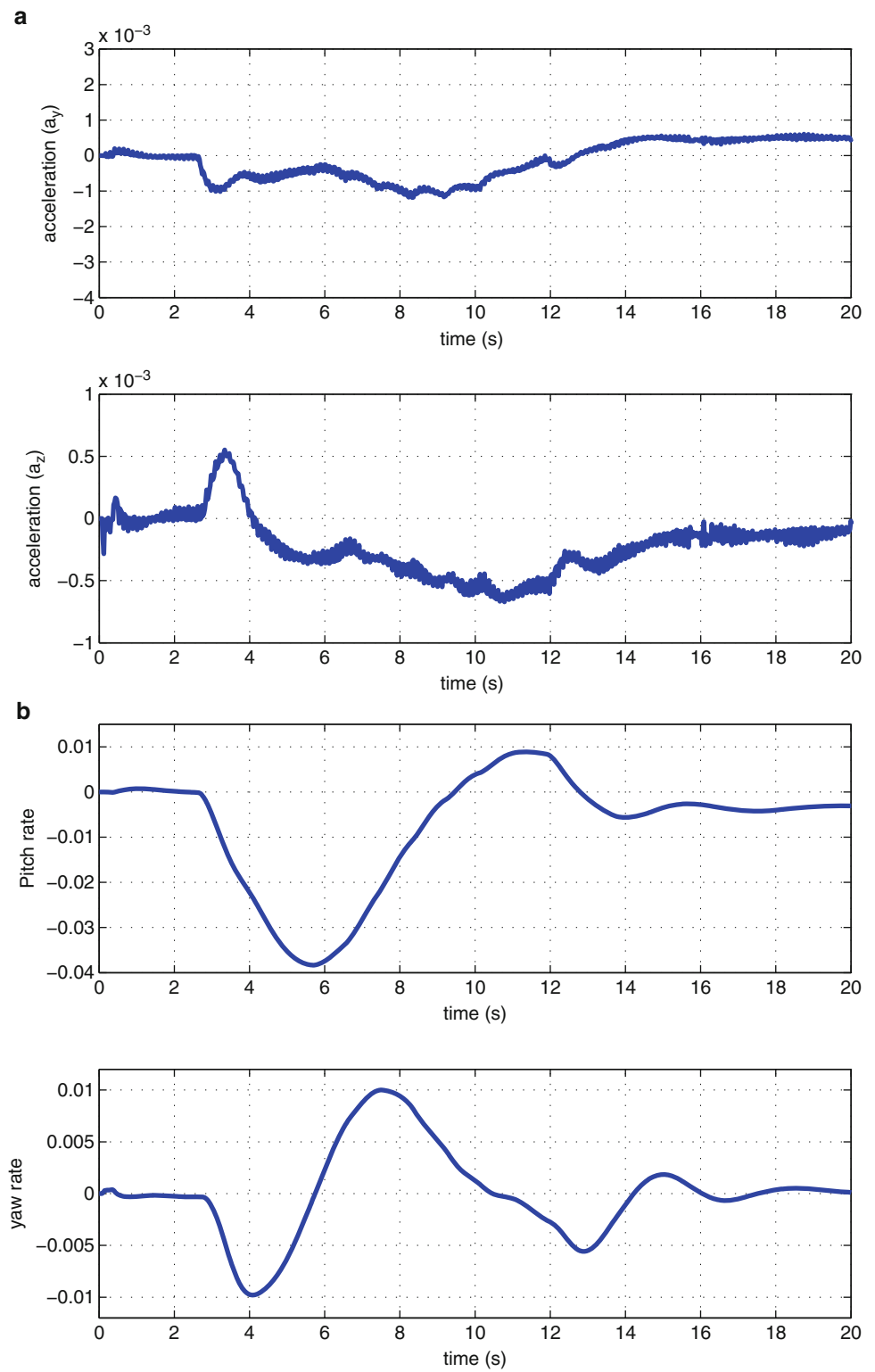
Fig. 33.5 Simulation results with controller of unsuccessful flight: flexible dynamics enabled. (**a**) Lateral accelerations; (**b**) angular rates
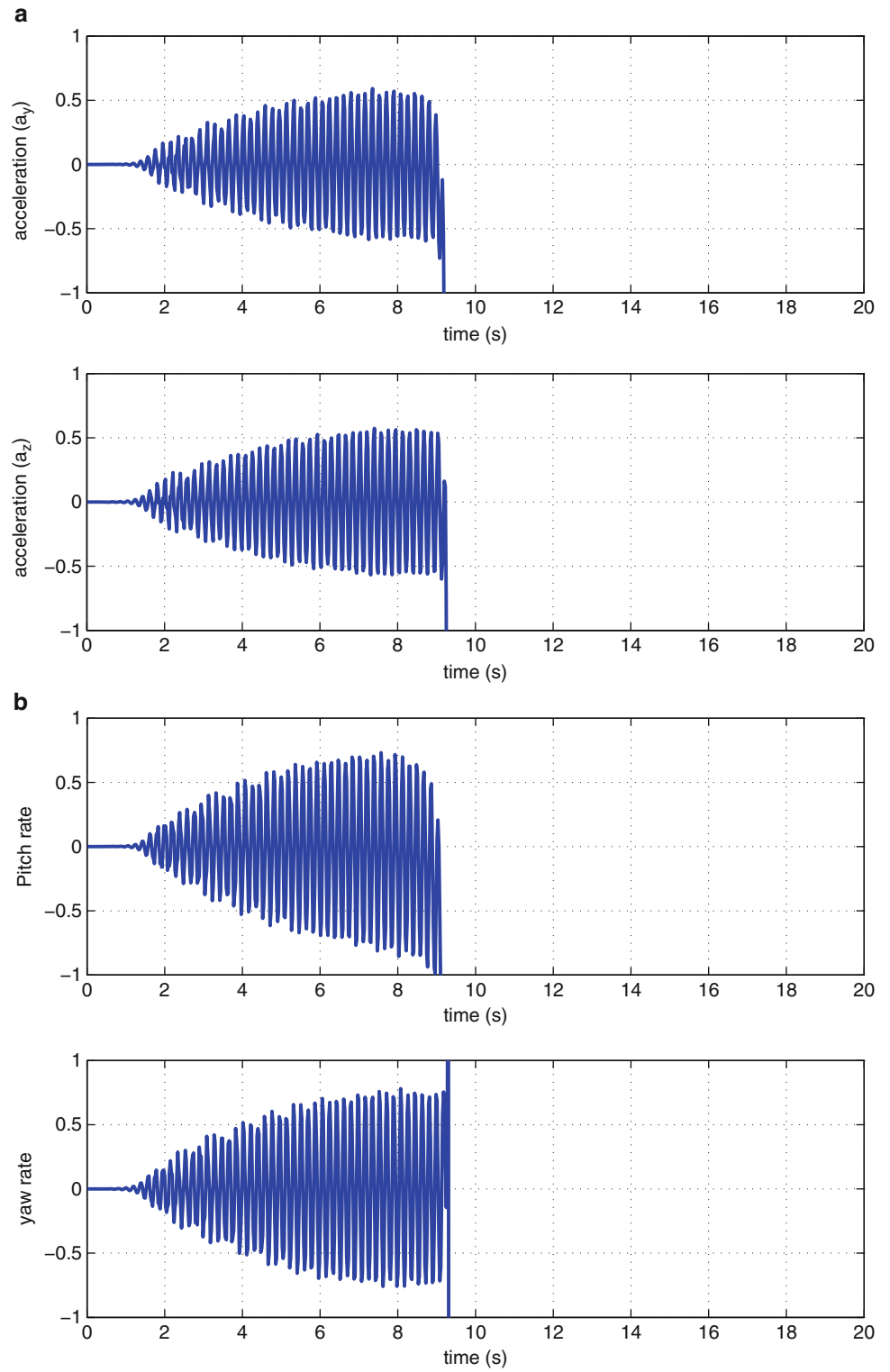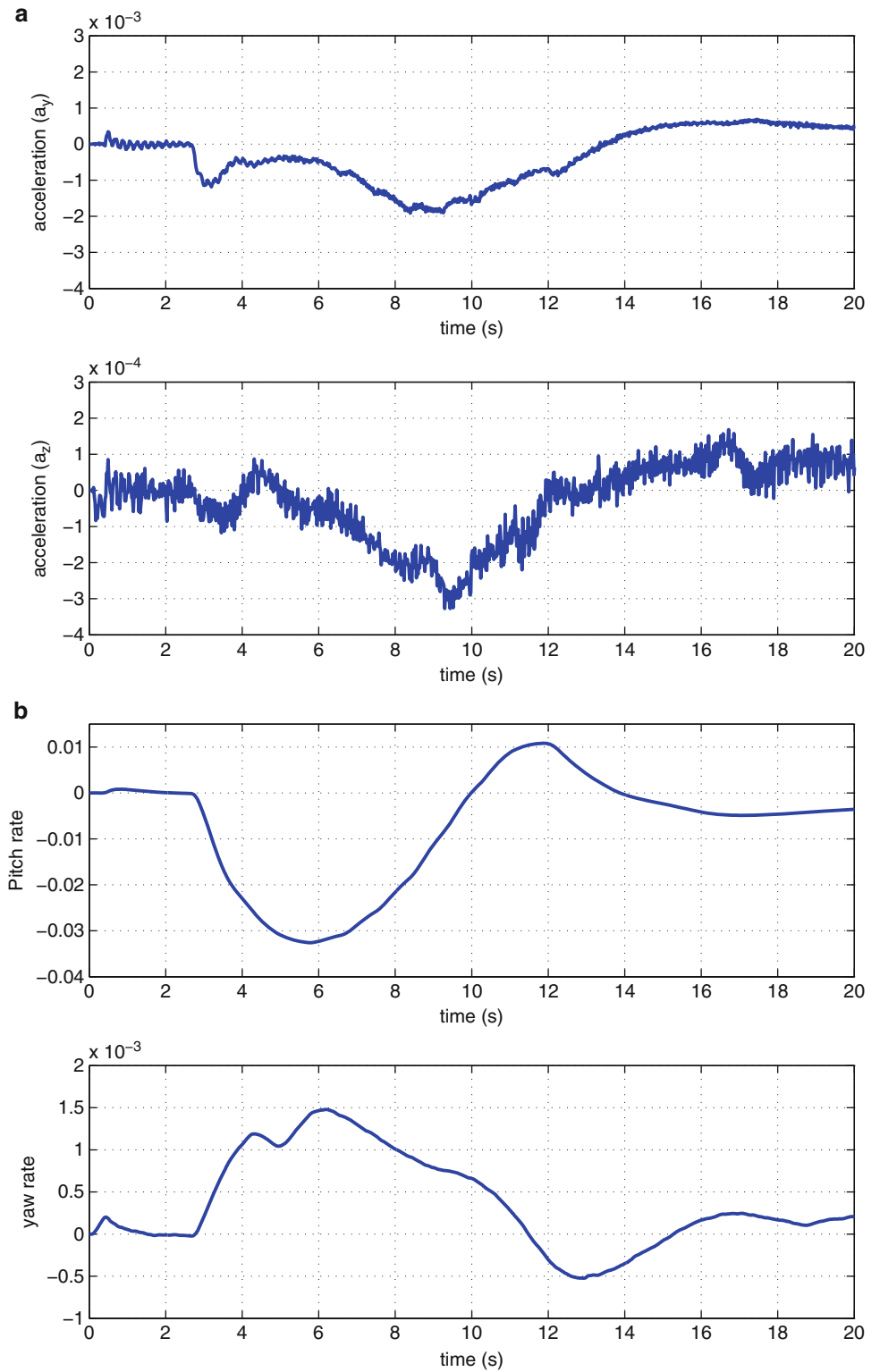
References

1. Effects of structural flexibility on launch vehicle control systems. NASA space vehicle design criteria (guidance and control), NASA SP-8036 (1970)
2. Karkee M, Steward B, Kelkar A, Kemp Z (2011) Modeling and real-time simulation architectures for virtual prototyping of off-road vehicles. J Virtual Real Spec Issue Virtual Manuf Constr 15(1):83–96
3. Elmqvist H, Mattsson S, Olsson H, Andreasson J et al (2004) Realtime simulation of detailed vehicle and powertrain dynamics. SAE Technical Paper 2004-01-0768. doi:10.4271/2004-01-0768
4. Schmidt D, Raney D (2001) Modeling and simulation of flexible flight vehicles. J Guid Control Dyn 24(3):539–546
5. Lester HC, Collins DF (1965) Determination of loads on a flexible launch vehicle during ascent through winds. NASA Technical Note, NASA TN D-2590, February 1965
6. Waszak M, Schmidt D (1988) Flight dynamics of aeroelastic vehicles. J Aircr 25(6):563–571
7. Tobbe P, Matras A, Wilson H, Modeling and simulation of variable mass, flexible structures. American institute of aeronautics and astronautics Dynamic Concepts, Inc., Huntsville, AL, 35806
8. Jafari AA, Khoshnood AM, Roshanian J (2010) Dynamic modelling and verification of a flexible clustered launch veehicle. Proc Inst Mech Eng Part K J Multibody Dyn 224:375. doi:10.1243/14644193JMBD280
9. Shabana AA (1997) Flexible multibody dynamics: review of past and recent developments. Multibody Syst Dyn 1:189–222
10. Wasfy TM, Noor AK (2003) Computational strategies for flexible multibody systems. Am Soc Mech Eng Appl Mech Rev 56(6):553–613
11. Meirovitch L (2001) Fundamentals of vibration. McGraw Hill International Edition McGraw Hill International Edition, Mechanical Engineering Series
12. Corben HC, Stehle P (1960) Classical mechanics, 2nd edn. Wiley, New York

Chapter 34
Modal Test of Six-Meter Hypersonic Inflatable Aerodynamic Decelerator

Nijo Abraham, Ralph Buehrle, Justin Templeton, Mike Lindell, and Sean Hancock

Abstract A modal test was performed on the six-meter Hypersonic Inflatable Aerodynamic Decelerator (HIAD) test article to gain a firm understanding of the dynamic characteristics of the unloaded structure within the low frequency range. The tests involved various configurations of the HIAD to understand the influence of the tri-torus, the varying pressure within the toroids and the influence of straps. The primary test was conducted utilizing an eletrodynamic shaker and the results were verified using a step relaxation technique. The analysis results show an increase in the structure's stiffness with respect to increasing pressure. The results also show the rise of coupled modes with the tri-torus configurations. During the testing activity, the attached straps exhibited a behavior that is similar to that described as fuzzy structures in the literature. Therefore extensive tests were also performed by utilizing foam to mitigate these effects as well as understand the modal parameters of these fuzzy sub structures. Results are being utilized to update the finite element model of the six-meter HIAD and to gain a better understanding of the modeling of complex inflatable structures.

Keywords Inflatable • Heat shield • Fuzzy structures • Toroids • Tri-Torus

34.1 Introduction

As part of NASA's concept of using inflatable technology for future planetary exploration, the Hypersonic Inflatable Aerodynamic Decelerator (HIAD) is a deployable entry, descent, landing (EDL) system currently in its development phase, consisting of a flexible thermal protection system (FTPS) over a stacked torus inflatable structure (IS) [1]. The tested six-meter diameter HIAD test article is used to measure the structural responses for comparison with finite element predictions. Over the course of design, the HIAD configuration has evolved from a simple structure of stacked toroids (fabricated from bias braided Technora® and a urethane liner and coating) paired using Kevlar webbing towards a complex structure with added Kevlar radial straps in a crow's-feet arrangement connected to multiple toroids [2]. Additionally, the six-meter test article incorporated removable, rigid buckles into the radial crow's-feet straps to facilitate easy testing of multiple strap configurations. A modified arrangement also includes an additional toroid, named tri-torus (described in Sect. 34.2). These additions were incorporated to prevent buckling, increase stiffness, and improve the distribution of aerodynamic load, all with a better performance to mass ratio. To understand the dynamic behavior of this complex structure during EDL phase, modal tests were performed on various configurations of this six-meter HIAD to understand the influence of the tri-torus, influence of straps and influence of varying pressure within the toroids.

This paper summarizes the results of the modal tests performed on the six-meter HIAD test article mounted to a fixed base in the high bay area of Building 1250 at the NASA Langley Research Center (LaRC). The frequency range of interest was 5–30 Hz and the targeted modes were the first four modes.

N. Abraham (✉) • R. Buehrle • J. Templeton
Systems Integration and Test Branch, NASA Langley Research Center, Hampton, VA 23681, USA
e-mail: nijo.a.abraham@nasa.gov

M. Lindell
Structural and Thermal Systems Branch, NASA Langley Research Center, Hampton, VA 23681, USA

S. Hancock
Mechanical Systems Branch, NASA Langley Research Center, Hampton, VA 23681, USA

34.2 Test Article Setup

The test article and support structure setup of the HIAD modal test can be seen in Fig. 34.1.

The HIAD structure which consists of eight toroids will be referred in descending order as Toroid 1 or T1 for the top most toroid to Toroid 8 or T8 for the bottom most toroid, from a nose up position. For the tri-torus configuration, the tri-torus will be referred as Toroid 6.5 or T6.5. The cross-sectional views of configurations with and without the tri-torus are shown in Figs. 34.2 and 34.3 respectively. Configurations were also tested with the straps and without the straps, as shown in Figs. 34.4 and 34.5 respectively. The configurations in the order they were tested are given in Table 34.1.
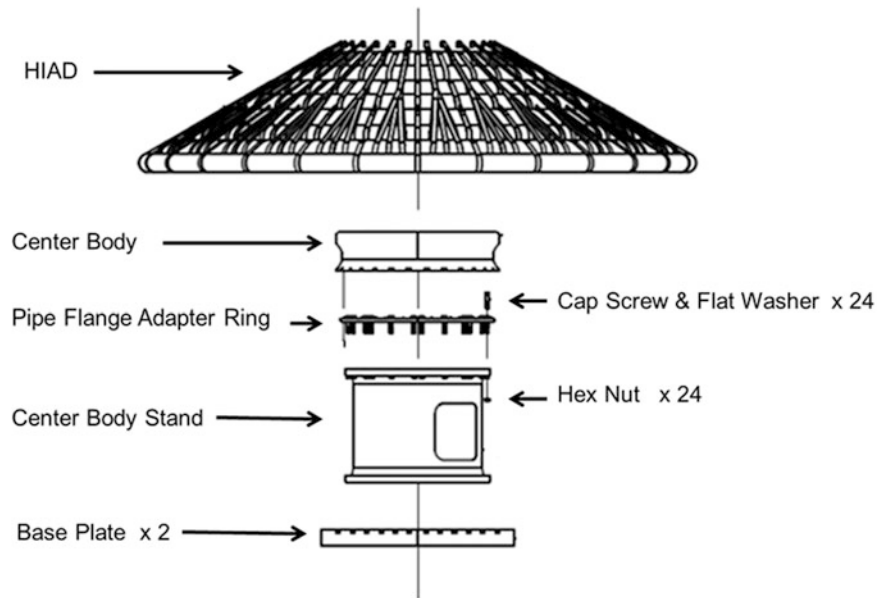
Fig. 34.1 Test article setup
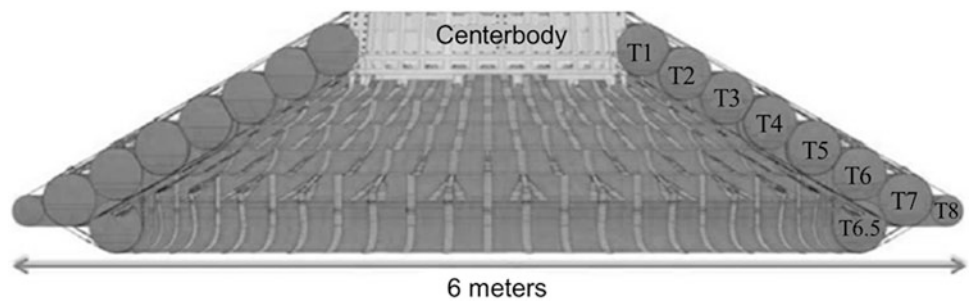
Fig. 34.2 Cross sectional view—with tri-torus configuration
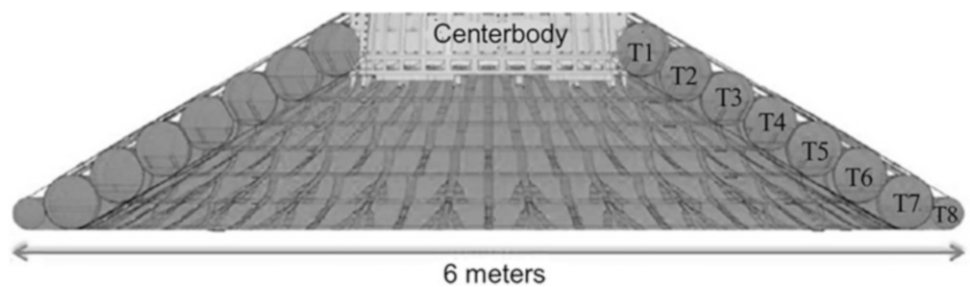
Fig. 34.3 Cross sectional view—without tri-torus configuration
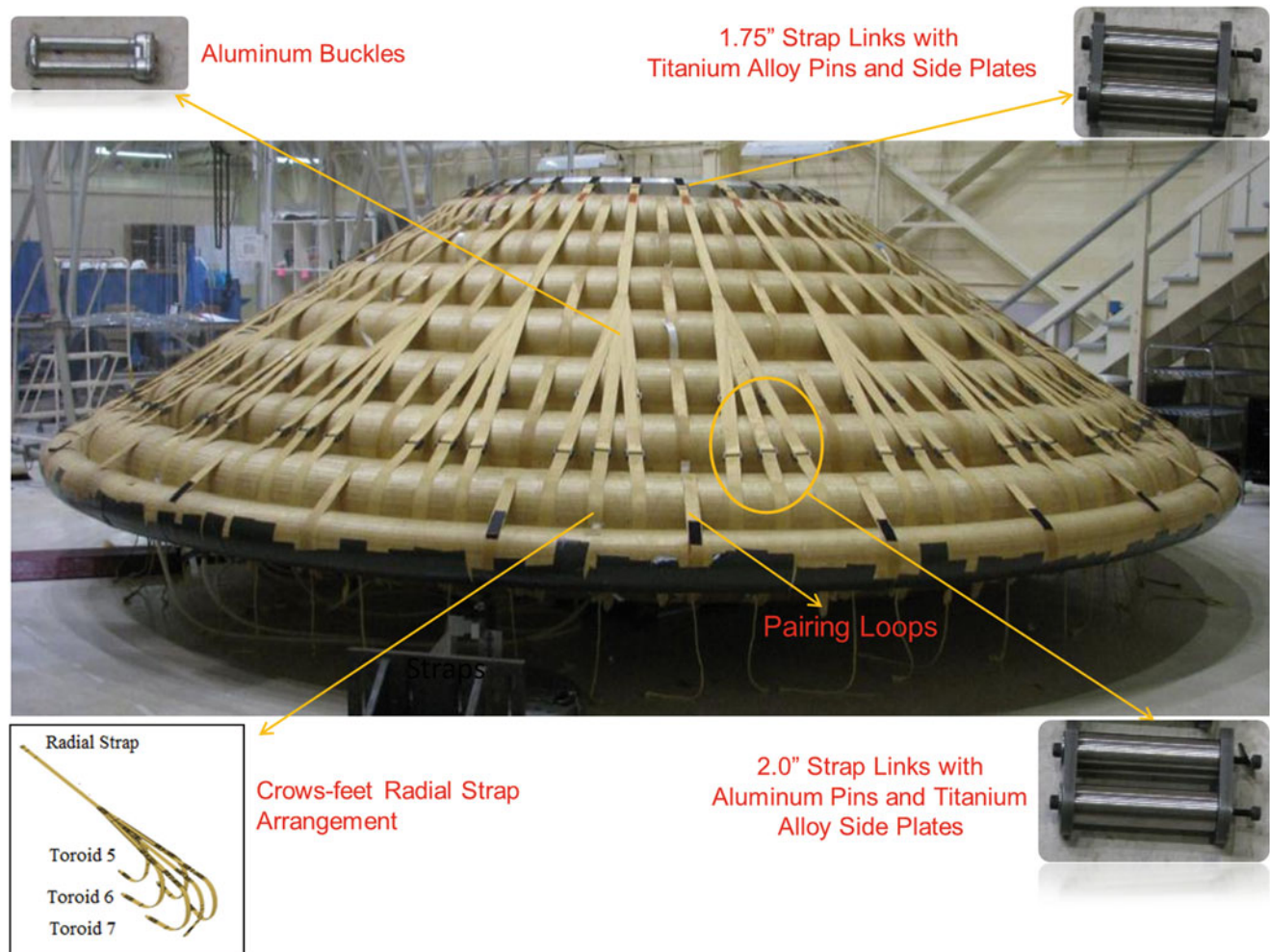
Fig. 34.4 HIAD configuration with straps

34.2.1 Test Instrumentation

The instrumentation consisted of 54 accelerometers, PCB series T333B accelerometers, glued with a urethane adhesive to 18 locations of the HIAD test article (shown in Fig. 34.6). Fourteen tri-axial accelerometer assemblies (Locations 1–14) were placed on the inflatable and four tri-axial accelerometer assemblies (Locations 15–18) on the center body. For each tri-axial accelerometer assembly, the first accelerometer pointed radially outward, the second accelerometer pointed tangential to the toroid and the third accelerometer pointed in the normal direction of Fig. 34.6. The transducers were placed on pre-determined locations to capture the desired first four modes.

34.2.2 Excitation Techniques

The excitation locations were under Toroid 7 beneath the accelerometer assemblies 2 and 6. The primary excitation of the structure was conducted using eletrodynamic shakers. The mounting block for each shaker was oriented at an angle of 30° from vertical to excite both the vertical and torsion modes (shown in Fig. 34.7).

   To verify that the modal parameters of this complex structure were not affected by the stiffness of the stinger rods, the shaker test results were compared with the results obtained using a step relaxation technique. The test setup for the step relaxation technique is shown in Fig. 34.8, where the load is released and the decaying responses were recorded. The modal parameters were obtained from the step relaxation techniques using the System/Observer/Controller Identification Toolbox

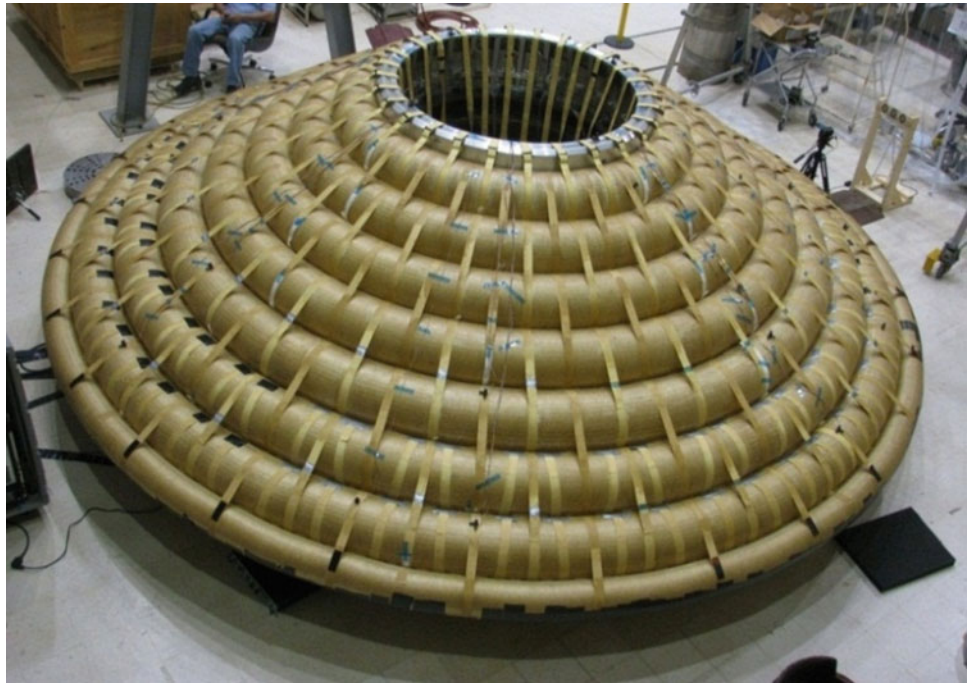**Fig. 34.5** HIAD configuration
without straps

Table 34.1 Test configuration
matrix

Test article	Configuration ID	Inflation pressure
Six-meter with Tri-Torus and Straps	1	8 psi all toroids
	2	15 psi all toroids
	3	20 psi all toroids
	4	15 psi T1/T2/T6.5, 8 psi all others
Six-meter without Tri-Torus and with Straps	5	8 psi all toroids
	6	15 psi all toroids
	7	20 psi all toroids
	8	15 psi T1/T2/T7, 8 psi all others
Six-meter without Straps and Tri-Torus	9	8 psi all toroids
	10	15 psi all toroids
	11	20 psi all toroids
	12	15 psi T1/T2/T7, 8 psi all others

(SOCIT) which utilizes a system identification process to calculate the mathematical representation of a physical system using experimental free decay time records [3]. The step relaxation technique was only performed for the configurations with the tri-torus (Configurations 1–4). The difference in the modal frequencies between the shaker and step relaxation test techniques were seen to range from 0.1 to 3 %, without any significant trends. This percent difference was acceptable for this study. It should be noted that all the results given in this paper are from the shaker tests.

34.3 Modal Test Results

The modes obtained from the experimental results are shown in their respective order in Fig. 34.9. With reference to Fig. 34.1, the brown quadrilateral represents the bottom plane of the center body assembly. The black quadrilateral represents the baseplate. The gray quadrilateral represents the four tri-axial accelerometer assembly locations for the center body. Finally, the joints of the orange quadrilaterals represent the 14 tri-axial accelerometer assembly locations on the inflatable.

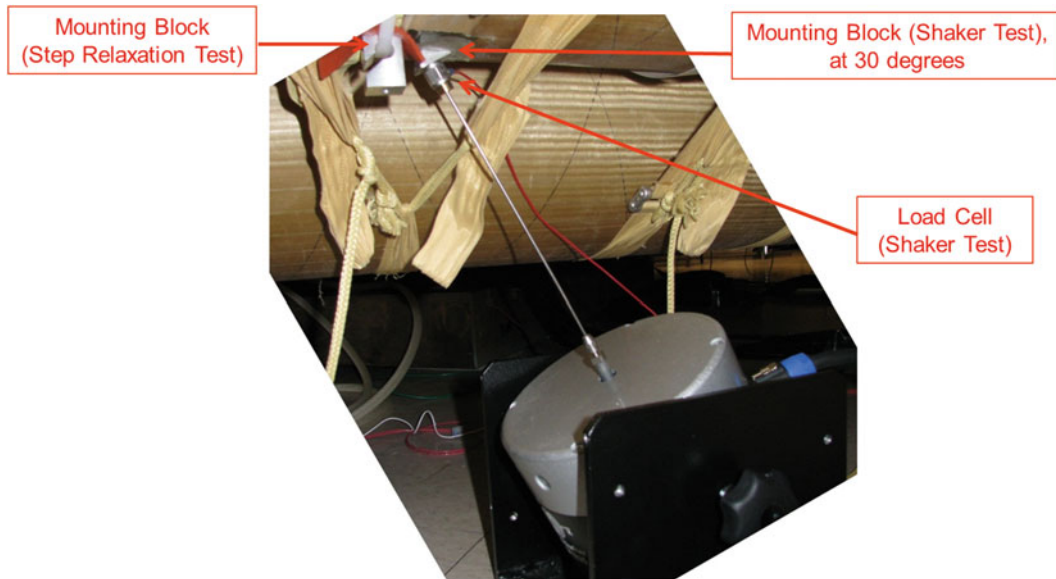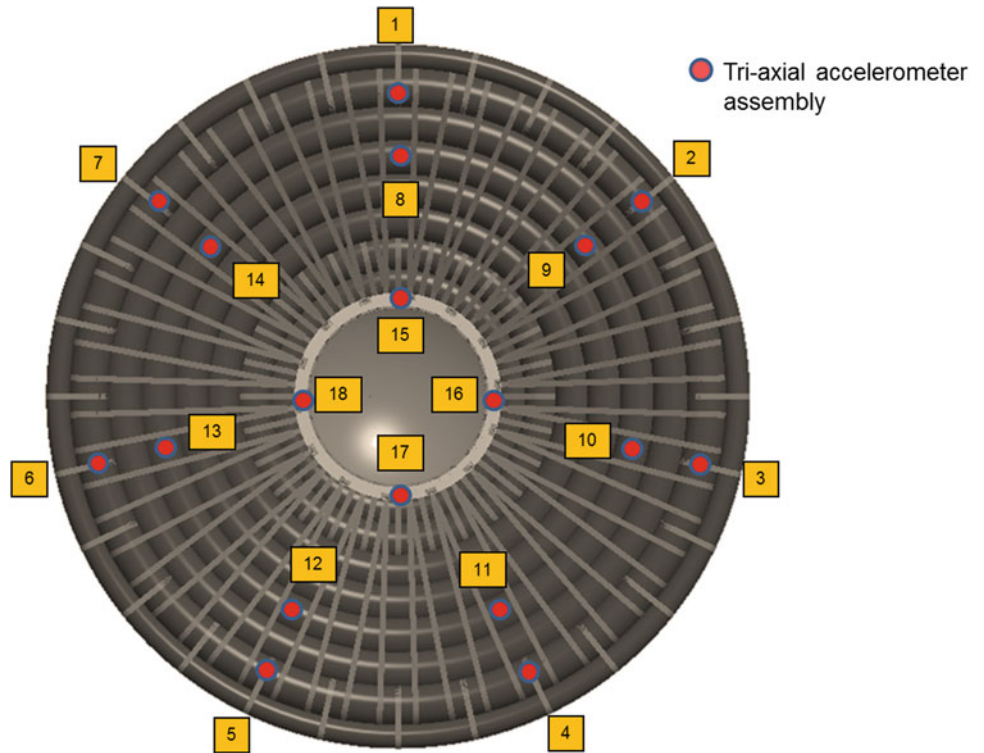**Fig. 34.6** Top view of the accelerometer assembly locations

Fig. 34.7 Shaker setup

34.3.1 Predicted vs. Experimental Results

Results from the experimental tests and its comparison with the predicted values are tabulated in Table 34.2. It was observed that the percentage difference between the frequencies of the first two modes was less than 4 % but between the third and fourth mode was 33–35 %. Data is currently being analyzed to determine the cause for this difference to obtain an accurate finite element model.
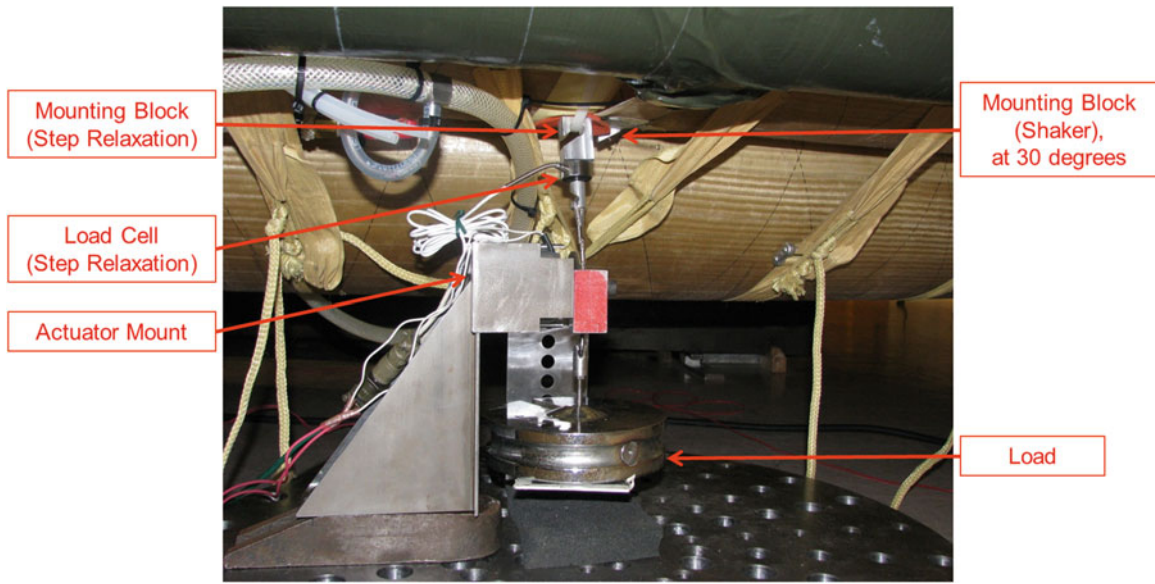
Fig. 34.8 Step relaxation setup
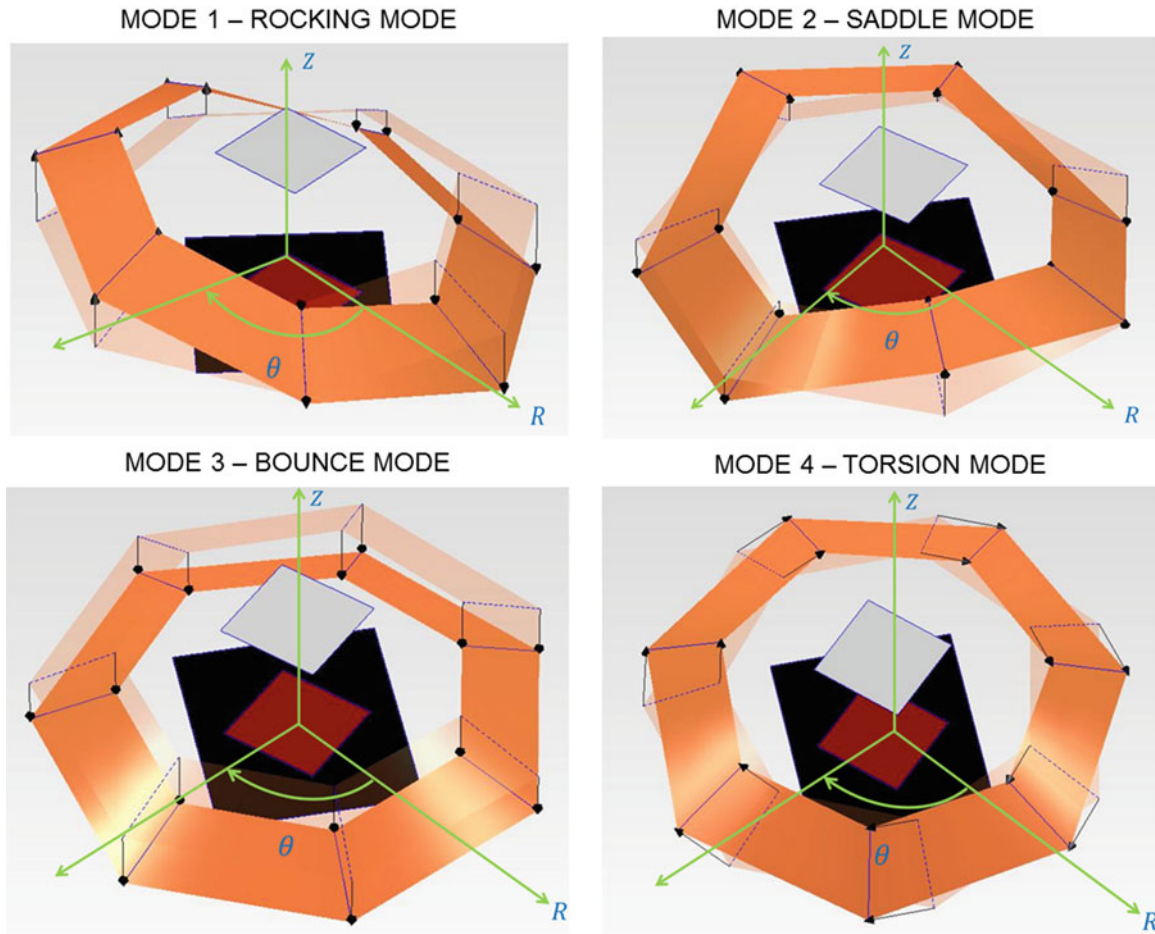
Fig. 34.9 Order of targeted modes

Table 34.2 Percentage difference between predicted and experimental modal frequencies

20 psi—with tri-torus, with straps and foam configuration				
Mode	Predicted (Hz)	Experimental (Hz)	% Difference $\dfrac{Experimental-Predicted}{Experimental}$	x 100 (%)
Rocking	8.50	8.77	3.07	
Saddle	12.30	12.26	−0.32	
Bounce	22.10	16.37	−35.00	
Torsion	14.50	21.68	33.11	
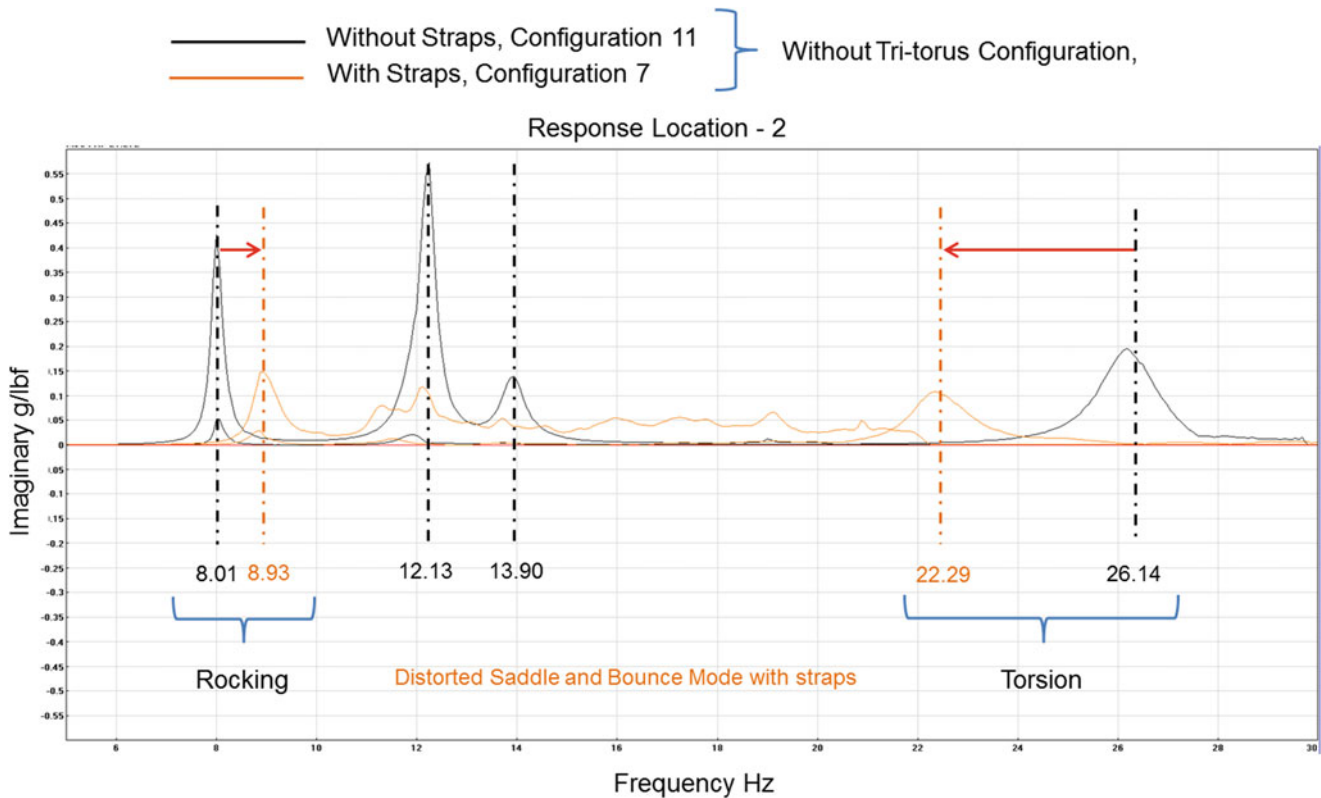
Fig. 34.10 FRFs highlighting influence of straps

34.3.2 *Influence of the Straps*

The function of the radial and crow's feet strap is to distribute the aerodynamic load from the outer toroids directly to the center-body to alleviate the loads carried by Toroid 1 and Toroid 2. Figure 34.10 shows a comparison of the imaginary portions of the frequency response functions for configurations with and without straps referred to as configuration 7 and 11 (see Table 34.1) respectively. Since the frequency response functions for the radial and vertical accelerometer locations resulted in modes at the same frequencies, only the responses from the vertical and tangential accelerometers will be plotted for all the figures within this paper.

It is observed that the straps caused an increase in the natural frequency for the rocking mode whereas it decreased the natural frequency for the torsion mode. The increase in the frequency of the rocking mode is due to the increase in the stiffness of the structure caused by the straps. For the torsion mode, the larger mass concentration of the strap links (shown in Fig. 34.4) located at a larger distance from the structure's center of mass is the likely cause for the decrease in the torsion mode's natural frequency resulted by the increase in the rotational moment of inertia.

One other observation is that the straps caused a distortion within the frequency range where the saddle and bounce modes were expected. Therefore, to find the dynamic characteristics of the straps, four PCB 352C22 teardrop accelerometers were placed on four locations within a radial (shown in Fig. 34.11). Nodes 1, 2 and 3 were the locations where most relative displacement of the straps was noticed during vibration. Figure 34.12 shows the imaginary part of the frequency response functions of the individual straps superimposed with that of the structure's response for configuration 7 (see Table 34.1).
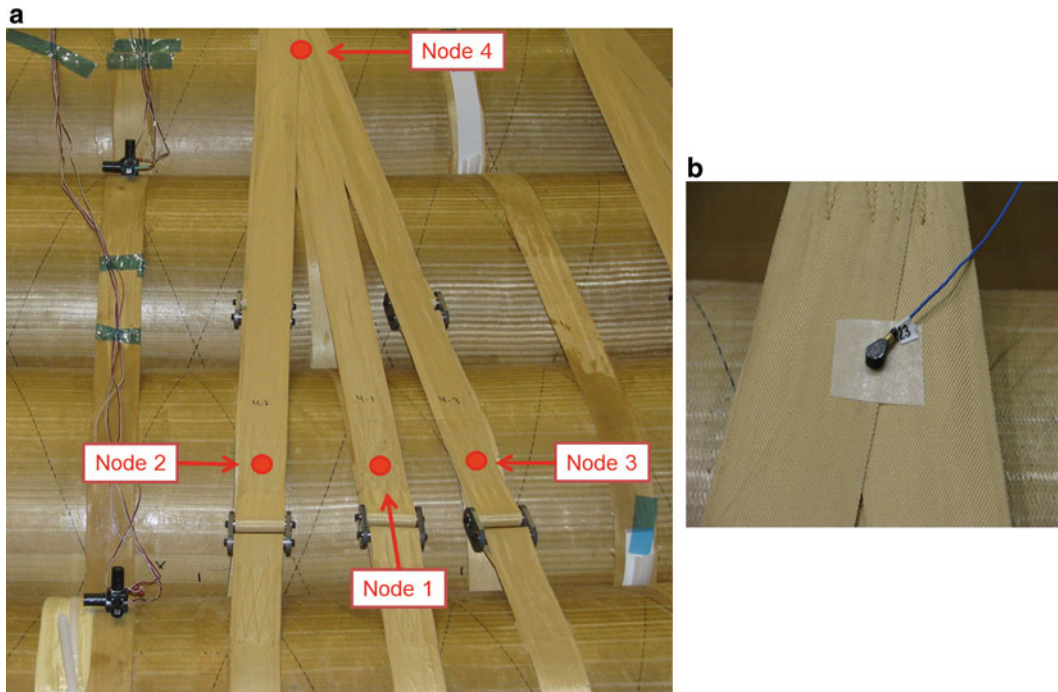
Fig. 34.11 Tear-drop accelerometer installations; (**a**) locations on the strap and (**b**) tear-drop accelerometer on the strap
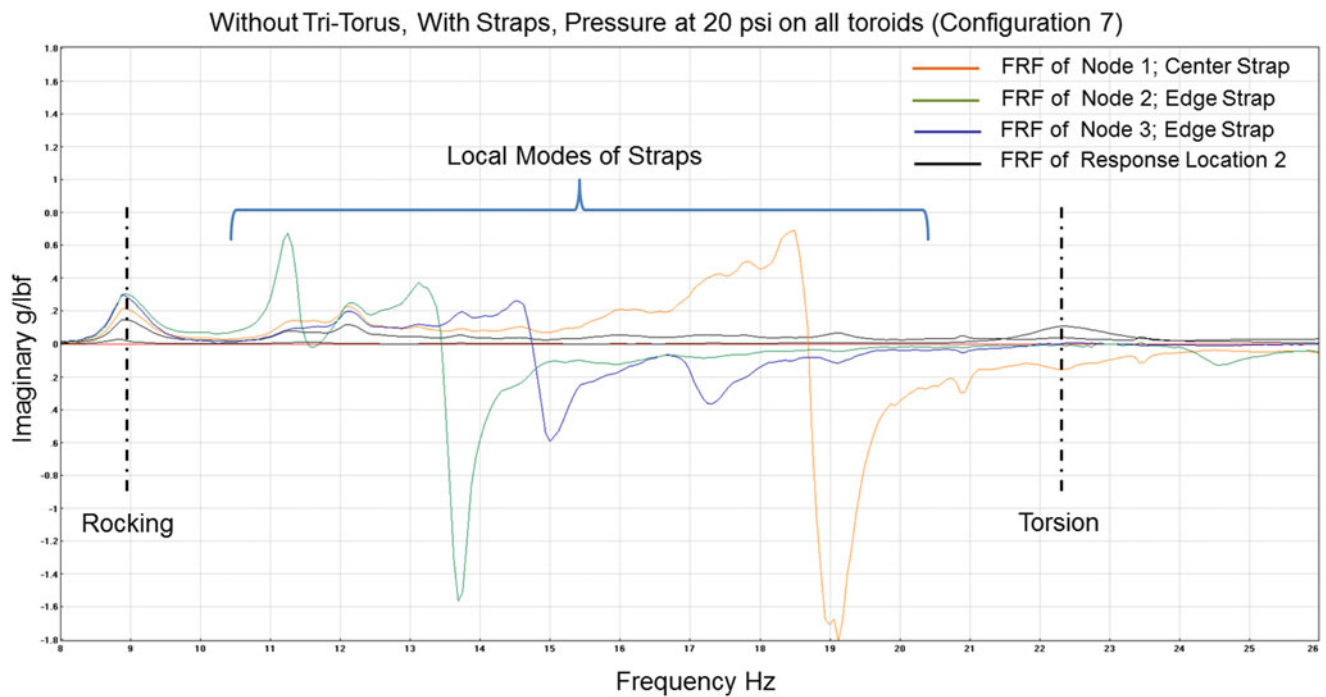

Fig. 34.12 FRFs highlighting local modes of straps

These modal results showed that the distortion of the structure's modes was caused by the local modes of the straps. Node 4 did not have any local modes within the frequency range of interest.

The distortion phenomenon caused by the straps can be explained by considering the inflatable structure with the straps as a fuzzy structure with the straps acting as fuzzy sub structures [4]. The inflatable by itself, can be considered as the master structure. The local modes are being excited as a result of energy transfer to fuzzy substructures through the common boundary between the master structure and fuzzy structure. This leads to dissipation at the global mode frequencies of the

Fig. 34.13 Foam locations per strap radial
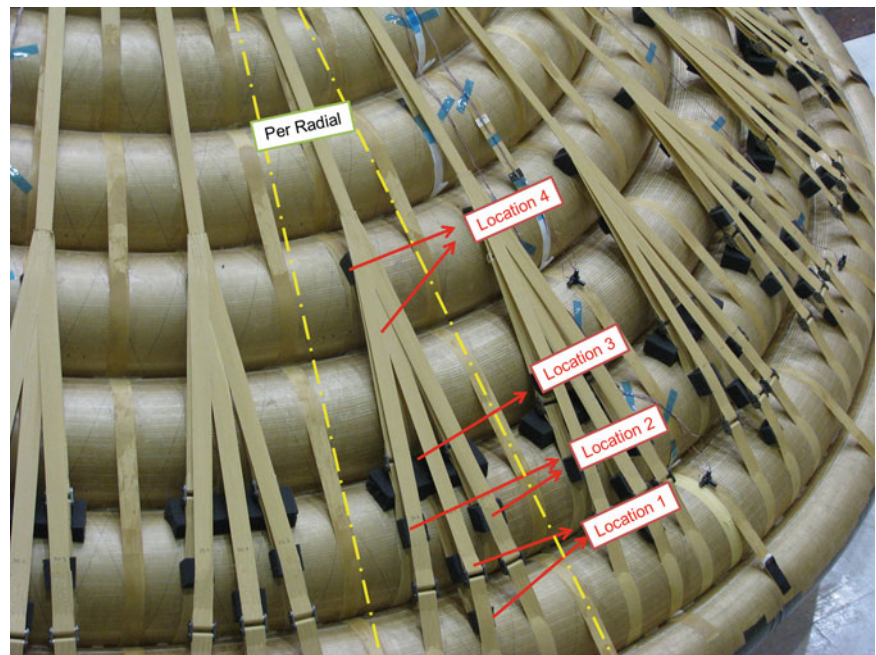
inflatable structure (master structure). Therefore, due to this fuzzy structure phenomenon, modeling the straps as discrete spring mass models will not capture the resulting local modes caused by the straps. One has to take into account the internal degrees of freedom of the straps during finite element modeling. One possible solution of capturing these effects of straps is by using probabilistic fuzzy boundary impedance elements [5] at the common boundary between the inflatable and straps.

Since modeling of straps as fuzzy structures can be challenging, another solution would be to increase the stiffness of the straps such that the frequencies of the distorting local modes would increase beyond the frequency range of interest. It was also desired to increase damping at these strap locations to decrease their vibration amplitude. These were achieved by placing foam blocks at selective locations such that the straps were isolated from the structure. Figure 34.13 shows the locations where the foam blocks were placed; Location 1 targets the central strap and its buckles attached to Toroid 7, Location 2 targets the targets the end straps and its buckles attached to Toroid 7, Location 3 targets the mid-strap assembly and its buckles attached to Toroid 6 and Location 4 isolates the strap assemblies attached to Toroid 7 from that of Toroid 6.

After placing the foam, no distortion of modes was observed within the targeted frequency range. The comparison of the imaginary part of the response functions between the strap configurations with and without foam (shown in Fig. 34.14) show an increase in the structure's stiffness at the bounce mode possibly caused due to tightening of the straps.

34.3.3 Influence of Tri-Torus

The function of the tri-torus is to increase the stiffness of the structure as well as prevent buckling of the toroids observed during static tests. Figure 34.15 shows a comparison of the imaginary part of the frequency response functions for configurations 3 and 7 (see Table 34.1), with and without the tri-torus respectively. One of the observations is that the tri-torus decreased the natural frequencies of the rocking, bounce and torsion modes when compared to the configuration without tri-torus. This is possibly due to the mass of the tri-torus, which is at a larger distance from the structure's center of mass resulting in a predominant mass effect for these three modes, causing a decrease in the natural frequency. On the other hand, the tri-torus was observed to cause an increase in stiffness affecting only the natural frequency of the saddle mode where the tri-torus would undergo bending deformation.

Another observation that can be made from Fig. 34.15 is that the tri-torus configuration resulted in the rise of coupled modes due to the combined stiffness and mass effect it had on the saddle and bounce modes respectively. At a higher pressure of 20 psi, the individual modes within the coupled mode could be distinctively identified contrary to the lower pressures where the modes were harder to distinguish. This is shown in Fig. 34.16 based on the tests conducted on configurations 4 and 8 (see Table 34.1).
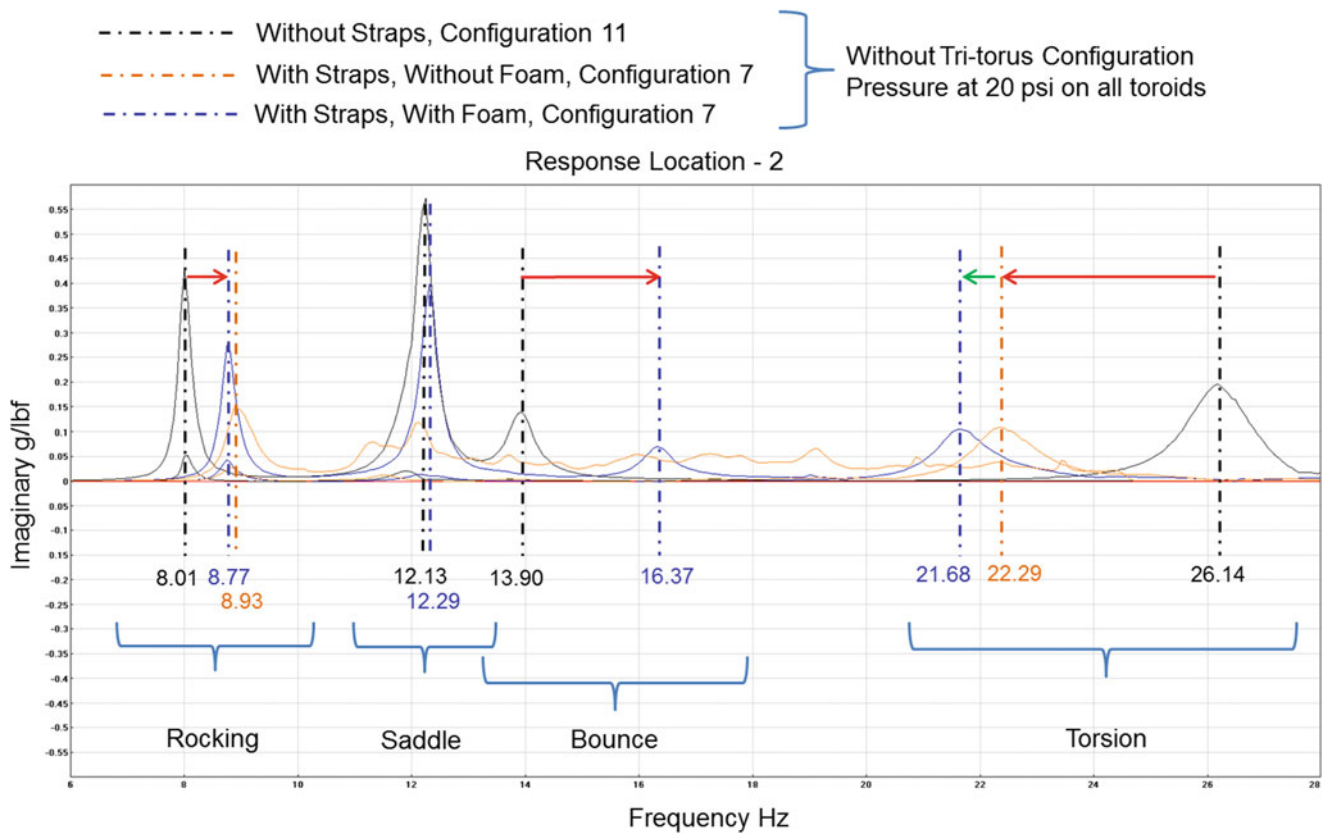
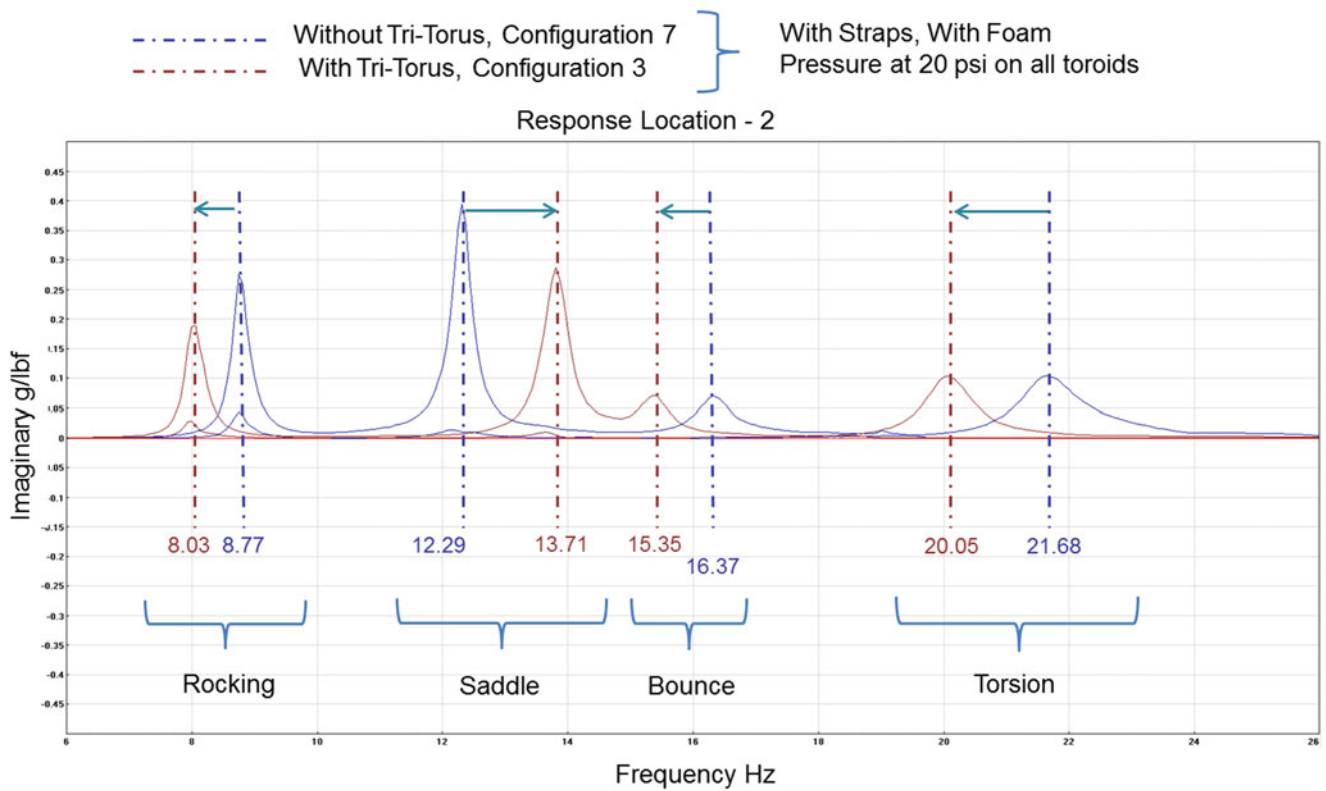**Fig. 34.14** FRFs highlighting influence of foam

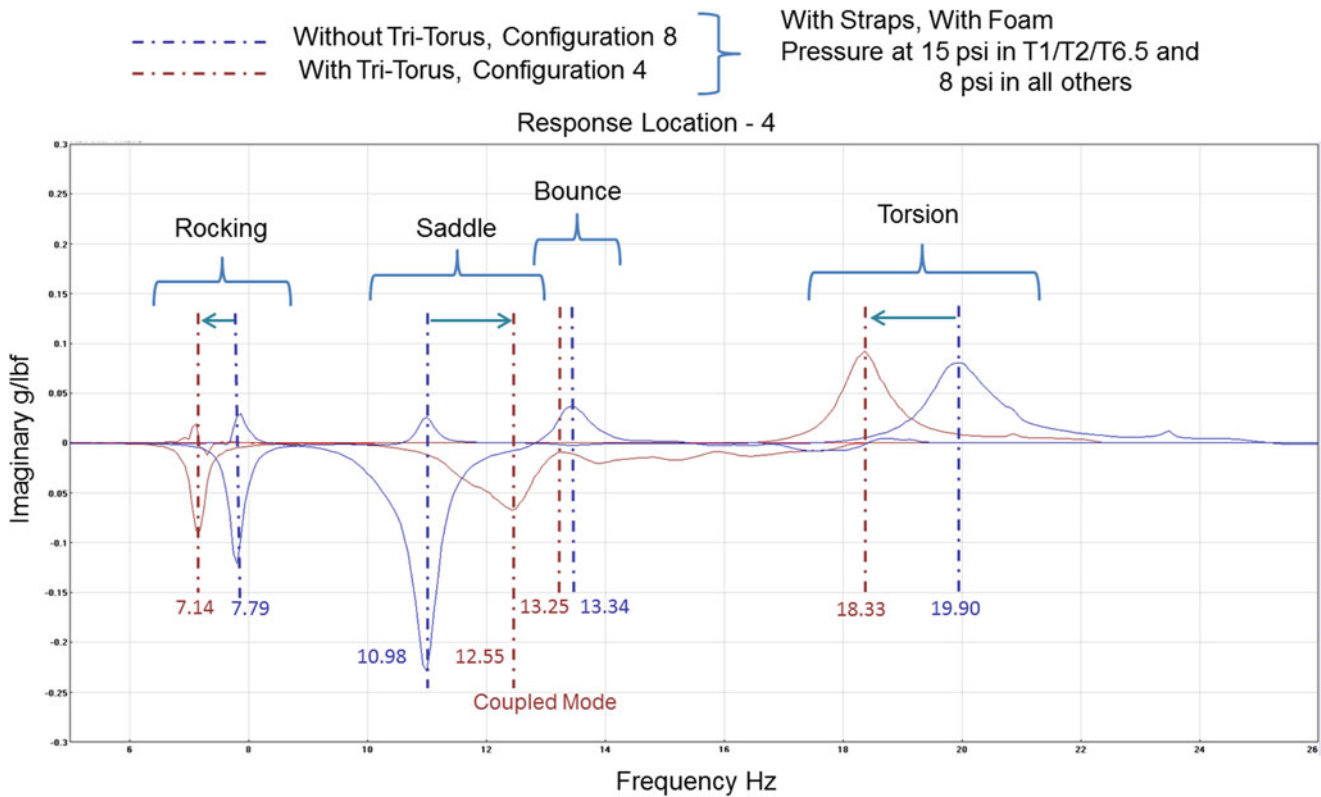**Fig. 34.15** FRFs highlighting influence of tri-torus at 20 psi pressure configuration

Fig. 34.16 FRFs highlighting coupled modes at 15/8 pressure configuration

34.3.4 Comparison of Tri-Torus and Straps Influences

Figure 34.17 shows the influences of the straps and tri-torus on frequency response functions at the 20 psi pressure configuration. Similar behavior was seen for all the other pressure configurations as well. It was observed that

1) The straps caused predominantly a stiffness effect, whereas the tri-torus resulted in a mass effect. In other words:

   a. straps caused an increase in natural frequency for three of the four target modes whereas
   b. tri-torus caused a decrease in natural frequency for three of the four target modes

2) The rocking mode was influenced by the stiffness effect of straps and almost equal mass effect of tri-torus, thereby causing no significant resultant effect
3) The saddle mode was primarily influenced by the stiffness effect of the tri-torus.
4) The bounce mode was influenced by the stiffness effect of the straps and the mass effect of the tri-torus, with the straps having a predominant influence
5) The torsion mode was influenced by the mass effects of both straps and tri-torus, with the straps having a predominant influence.

34.3.5 Influence of Varying Toroid Pressure

The effects of toroid pressure were examined with the configuration series 1–4, 5–8 and 9–12 (see Table 34.1). The behavior of the structure was similar across all these series. Figure 34.18 shows the imaginary portion of the frequency response functions for configuration series 1–4 with foam. It was observed that the natural frequencies of the structure increase with increasing pressure within the toroids. This is due to the fact that the pressure increases the stiffness of the structure, and since stiffness is directly proportional to the natural frequency squared, the natural frequency of the structure increases as well.
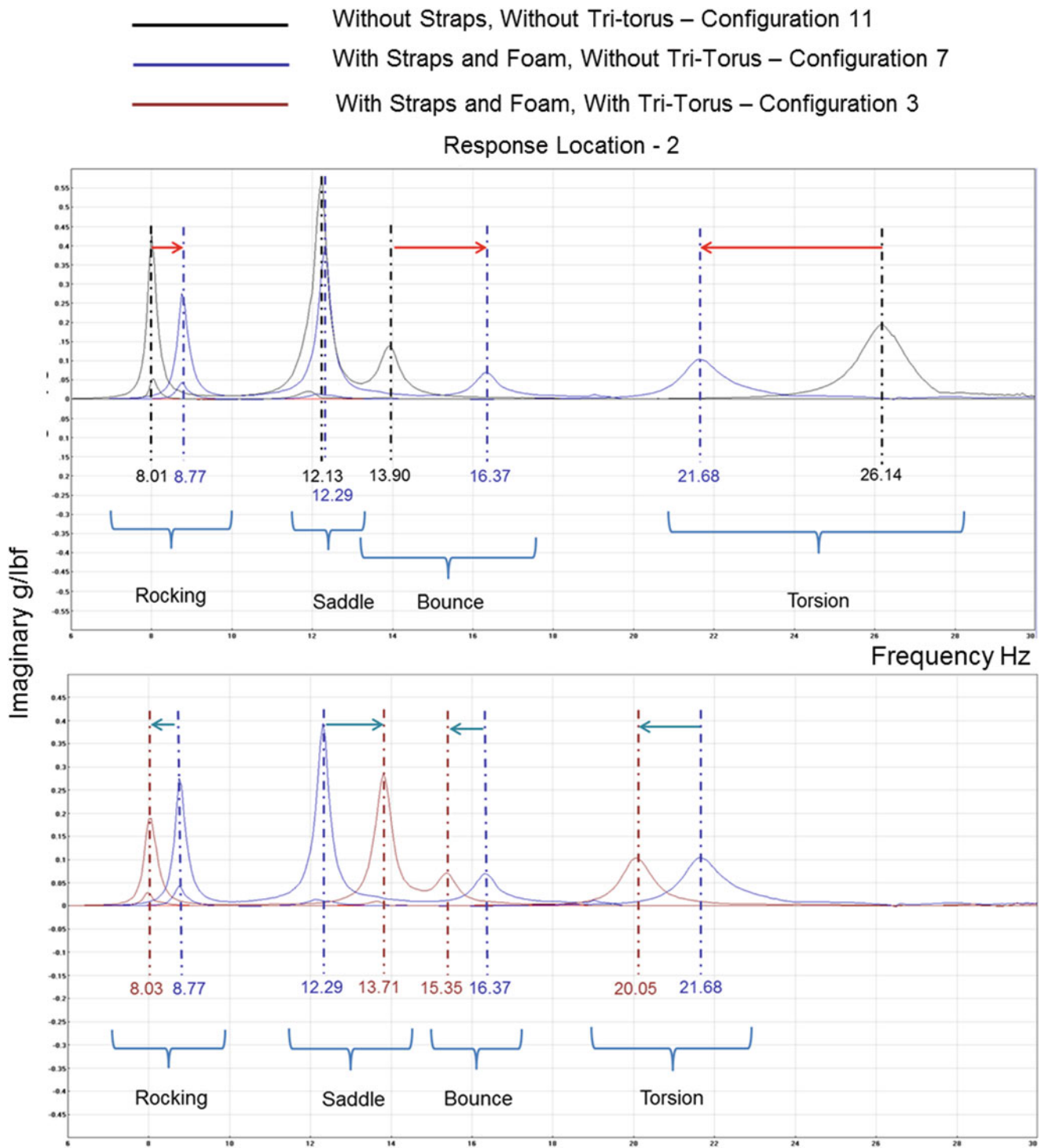
Fig. 34.17 Comparison of FRFs highlighting influence of straps and influence of tri-torus

This phenomenon is seen throughout all the modes. The natural frequency did not show any proportional increase with respect to the increase in pressure; however the percentage change in frequency between pressures remained approximately the same for all modes other than the bounce mode. Natural frequency squared is also inversely proportional to the mass. However, in this case, the increase in mass due to the increase in pressure is negligible compared to the increase in stiffness.
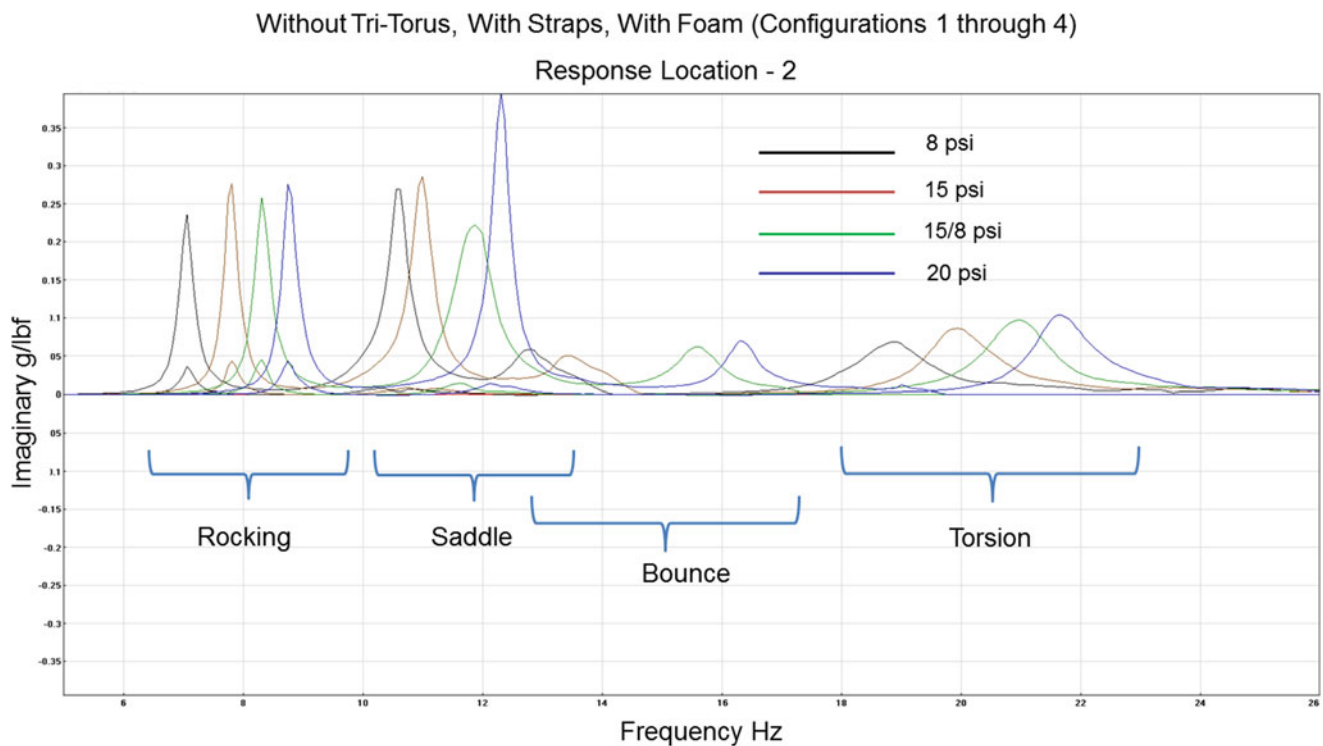
Fig. 34.18 FRFs highlighting influence of pressure

34.4   Conclusions

The modal test successfully identified the first four modes for the HIAD structure. The tests were able to identify the influence of the straps and tri-torus on the structure's modal parameters. It showed that the tri-torus predominantly results in a mass effect whereas the straps predominantly result in a stiffness effect on the modal frequencies of the structure. This is in tandem with the intent of the tri-torus to increase rigidity thereby preventing buckling as seen in the saddle mode. It was observed from the results that the stiffness of the structure increased with increasing toroid pressures. Also observed were the rise of coupled modes with the tri-torus configuration and the behavior of the unloaded straps as fuzzy substructures. To summarize, these tests provided substantial information on the dynamics of complex inflatable structures. These results are being used to verify and update the finite element modeling techniques for these HIAD systems. The data can also be used to aid controller design for the reentry trajectory control system of future HIAD flight articles. Future test plans include the investigation of dynamic effects of: scaling through testing of different size test articles, the addition of thermal protection systems, and simulated aerodynamic load.

References

1. Hughes SJ, Cheatwood MF, Calamino AM, Wright HS (2011) Hypersonic inflatable aerodynamic decelerator technology development overview. In: AIAA 2011–2524, 21st AIAA aerodynamic decelerator systems technology conference and seminar, Dublin, Ireland, 23–26 May 2011
2. Swanson GT, Cassell AM, Johnson KR, Hughes SJ, Calamino AM, Cheatwood MF (2013) Structural strap tension measurements of a 6 meter hypersonic inflatable aerodynamic decelerator under static and dynamic loading. In: AIAA aerodynamic decelerator system (ADS) conference, Daytona Beach, FL, 25–28 March 2013
3. Juang J-N (1994) Applied system identification. Prentice Hall, Englewood Cliffs, NJ
4. Soize C (1995) Vibration damping in low frequency range due to structural complexity. A model based on the theory of fuzzy structures and model parameters estimation. Comput Struct 58(5):901–915
5. Soize C (1986) Probabilistic structural modeling in linear dynamic analysis of complex mechanical systems. I - Theoretical elements. Rech Aerospatiale 5:23–48, English Edition

Chapter 35
Modal Testing of Space Exploration Rover Prototypes

Yvan Soucy and Frédérik Brassard

Abstract The Exploration Core program of the Canadian Space Agency (CSA) has developed a series of terrestrial prototypes of planetary rovers and payloads in view of future space exploration missions. This paper presents results and experience gained in performing modal testing on a JUNO rover, one of the families of the CSA rover fleet. The main objectives of these modal tests were to (1) develop efficient procedures for obtaining test-based modal parameters of rover-type structures, and (2) help develop a finite element model of a rover which could be used to predict the dynamic loads and responses the rover will have during its whole life. The test article configurations were (1) a rover and (2) the rover with a mast (to be used as support for scientific instrumentation and navigational equipment). Since this activity was the first experience of the group in modal testing of mobile type hardware such as rovers, the process for getting valid modal parameters of the test articles turned out of be more complicated than anticipated. This led to the performance of additional sensitivity studies whose interesting results will be accounted for in future testing of rovers. The paper includes some results of these studies and some lessons learned in testing the rover hardware.

Keywords Modal testing • Rover • Case study • Accelerometer mounting block • Lessons learned

35.1 Introduction

Robotics is one of the pillars of Canada's current role in space exploration. Future opportunities for Canadian space robotics capabilities lie in two main application areas. The first application area is space robotic servicing. The second application area, of relevance to the present paper, is planetary surface robotics for Mars and the Moon. Robotic technologies for such missions include manipulators, rovers, vision technologies, and specialized tools in support of scientific missions or to tend eventual surface infrastructure [1].

Thanks to the Government of Canada's economic action plan, the CSA has recently invested over $120M in technology development for space robotics in a period of 3 years. As part of this investment, under the Exploration Surface Mobility (ESM) project, the CSA has funded the development of several rover prototypes ranging from micro-rovers for lunar and Mars exploration to crew transport vehicles for the Moon.

Canada has a long history of developing and operating satellites and payloads to Earth orbits. It has also developed technologies and scientific instruments for missions to the Moon and Mars. However, Canada has never developed any large systems such as a rover for a planetary exploration mission. The CSA has recently started an internal study addressing the needs of the CSA Space Exploration program for the development of methodologies and technologies related to qualification, protection and optimization of planetary rovers. This project also meets the need of the CSA to develop in-house expertise in these areas.

One of the objectives of this project is to investigate and develop methods of structural qualification of a planetary flight rover at both system and component levels. The ultimate goal of the qualification aspect of this project is to help future Canadian planetary rover missions develop structural qualification requirements. This objective on rover qualification will be met through several activities including modeling and testing of prototype rovers. Since no Canadian flight rover or

Y. Soucy (✉) • F. Brassard
Engineering Development, Canadian Space Agency, 6767 route de l'Aéroport, St-Hubert, QC J3Y 8Y9, Canada
e-mail: yvan.soucy@asc-csa.gc.ca; frederik.brassard.1@ens.etsmtl.ca

mission exists presently, these test rovers are to be selected among the several terrestrial rovers composing the CSA fleet. The selection of the test rovers is to be made primarily on how closely their structural characteristics represent possible near future flight rovers and on their availability.

The structural testing to be performed and investigated in this project includes modal, vibration and field tests of the selected test rovers. Modal testing of the rover is to be performed on the rover structure to characterize its structural dynamic (or modal) parameters and to help understand its structural responses in operating conditions and under the various critical dynamic environments that occur during flight. These modal parameters will also be used to validate the finite-element (FE) model of the rover.

The rover selected for performing the first modal test campaign was one of the JUNO rovers. This type of rover was chosen for (1) its availability (several similar ones compose the JUNO fleet), (2) its structural characteristics are relatively close to a possible future flight rover and (3) its relative simplicity as opposed to some other types of rovers of the CSA fleet.

Under funding from the ESM project, the CSA fleet of JUNO rovers is composed of five terrestrial prototypes that were designed to CSA requirements to operate as a surface mobility platform for a variety of scientific payloads and instruments [1]. The JUNO rovers were developed by the Neptec Rover Team, which was composed of the following Canadian organizations: Neptec, Ontario Drive and Gear (Argo), COM DEV, NGC Aerospace, ProtoInnovations, Provectus Robotics Inc., Cross Chasm Inc., and McGill University. The JUNO rover can be set up with a number of different accessories, and in a variety of different configurations. The rover accommodates pneumatic and non-pneumatic wheels, as well as a set of custom-designed tracks.

This paper first describes the JUNO rover (and its mast) selected to be tested. It then presents some details and results of the modal testing of rover hardware. The test configurations were (1) the rover by itself and (2) the rover and its mast. It became apparent that testing the rover by itself was extremely helpful in characterizing the modes of the rover and mast assembly. The paper continues with a list of lessons learned from the first modal testing of the rover hardware; these lessons will be useful for future modal tests of rovers.

35.2   Description of Rover and Mast Assembly

Each rover of the JUNO fleet has a rectangular hollow "U"-shaped main body (referred to as MainBody in future sections) that encloses all of the batteries and required operating electronics. The main body has a length of 124 cm and a width of 87 cm. The main body is composed of three sections: an avionics box at the rear and a battery box on each side. On this main body are mounted the two parallel drive gearboxes on which the electric motors are mounted between the wheels and their respective spindles midway along the extended segments of the "U"-shaped rover. Figure 35.1 presents an overview of the rover (JUNO-005) that was tested.
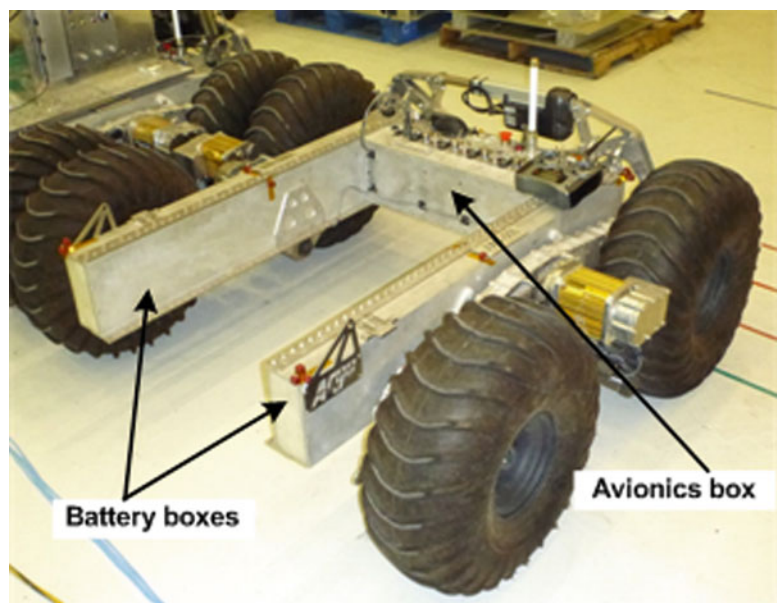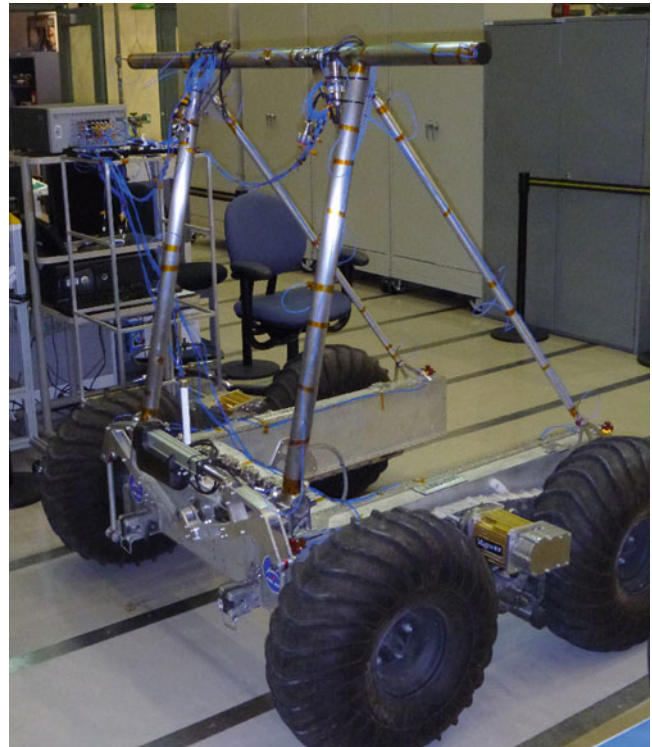

Fig. 35.1   Overview of the tested JUNO rover

Fig. 35.2 Overview of the rover and its mast assembly

A mast structure supporting navigational and scientific equipment can be attached to a JUNO rover (Fig. 35.2). The mast is composed of two main components: (1) the "Pi" shaped support beam (PiStrut), which is a 5.08 cm (2″) diameter hollow aluminum tubular structure leaning forward vertically from the back of the rover, and (2) the support structure (Struts) made up of two parallel 2.54 cm (1″) hollow aluminum tubes supporting the mass of the PiStrut from the forward extended segments of the "U" to the upper portion of the PiStrut. Figure 35.2 shows an overview of the rover with its mast assembly without any navigational or scientific payload.

35.3 Test Sequence

The initial plan was to perform modal testing on the rover by itself in various test configurations in order to obtain experimentally its modal parameters. These experiments were to include testing the rover sitting on its wheels and the rover supported (or suspended) from four hard points of the main body in order to eliminate the effects of the wheel subsystem. Theses test-based modal parameters were to provide a better understanding of the dynamic behaviour of this type of structure and possibly to be used to validate future finite-element models of the rover.

After performing these modal tests of the rover, the plan was to build up on the new knowledge of the rover and to perform some modal tests of the rover and mast assembly in order to measure the modal parameters of this more complex system.

While performing some preliminary testing of the rover, the planning of the test program was changed in order to perform modal testing of the rover and mast assembly first. The order of testing was changed for the following reasons. First, of the two mast presently existing, one was permanently used on another JUNO rover for telemetry testing and the other one could be made available to us only immediately and for a short period before departing for a deployment for an undefined period of time. Second, observation of the rover and mast assembly led to some concerns about the mast resonating while the rover was in motion; if such vibration of the mast was real, this could be detrimental for the operation of navigational and scientific payloads. Third, since the plan was to order three additional masts to equip the other JUNO rovers, it became necessary to establish the dynamic responses of the studied mast before the new ones were ordered.

The first real modal tests were then performed on the rover and mast assembly with the wheels sitting on the floor. First, some testing was performed with an impact hammer exciting the test article at several locations. For the sake of brevity, results of the impact hammer testing are not presented in this paper. Modal testing using simultaneously two portable exciters was performed next. As described in a subsequent section, over 50 accelerometers were mounted mainly on the mast (being

the principal structure under investigation) with some additional accelerometers fixed on the upper portion only of the rover main body. Preliminary data processing of the portable exciter and impact hammer testing led to the observation that there were some issues with the acquired data sets. The main issue was that several mode shapes associated with resonances at different frequencies resembled closely to each other, even for low order modes. This led to the conclusion that these modes, or at least some of them, were really associated with the dynamics of the rover itself and that not enough accelerometers were mounted on the rover in order to properly define these modes.

It was then decided to revert to the initial plan of performing some modal testing of the rover by itself before attempting further data processing for the rover and mast assembly. It turned out that this decision was beneficial since knowledge of the dynamics of the rover was crucial in order to properly process the data sets of the assembly, and to have a proper understanding of the real and apparent issues with these data that could then be resolved.

35.4 Developmental Activities

In the preliminary modal testing of the rover and mast assembly, characterization of the dynamic properties of the mast components, PiStrut and Struts, was first attempted by fixing 15 small three-axis accelerometers (PCB 356A01) onto the circular portions of the mast. This option was chosen due to the availability of the instrumentation hardware and to their small surface area easing their positioning on the tubular portions of the structure. Being developed mainly for vibration testing, these accelerometers had a sensitivity level too low, only 5 mV/g, to obtain clean data. The resulting frequency response functions (FRF) were too noisy in the low frequency range of interest to be of any value, therefore prohibiting the use of the small vibration accelerometers for the purpose of modal testing of the rover test article.

Two different types of modal accelerometers were available to conduct this testing; the Endevco 61-100 series with a nominal sensitivity of 100 mV/g and the PCB 336C series which has a nominal 1,000 mV/g sensitivity. These accelerometers had an increased nominal sensitivity by a factor of 20 and 200 times the sensitivity of the small three-axis vibration accelerometers. However, both types of accelerometers had a 1.5 cm^2 surface. Both types of accelerometers had to be mounted onto the tubular surface of both the Struts (Ø 2.54 cm) and the PiStrut (Ø 5.08 cm) components.

The standard procedure is to fabricate mounting blocks made from either aluminum or PMMA (Polymethyl methacrylate), which are both high density materials. Such high stiffness mounting blocks prevent any changes in measured data up to frequencies beyond the frequency range of interest. Since CSA's machine shop support was not available at that time, an alternative had to be found for manufacturing custom-made mounting blocks. Sending the blueprints of the designed mounting blocks to a local contractor would have been time consuming and expensive. It is with these constraints in mind that the idea was proposed of generating the conceived mounting blocks using the 3D printing machine while setting up the machine to its maximum density setting. The material used by the 3D printing machine is ABS (Acrylonitrile Butadiene Styrene) which has a density of 1.04 g/cm^3 as opposed to 2.70 g/cm^3 for aluminum. A picture of the generated 3D printed mounting block is shown in Fig. 35.3.

To validate the use of this alternative type of mounting blocks, two sets of three orthogonal accelerometers were assembled using the two different blocks; one set of accelerometers was mounted on a block of PMMA and the other set of accelerometers was mounted identically on a 3D printed ABS block. Both assemblies were positioned side by side on the rover. The test setup of the two sets of modal accelerometers can be seen in Fig. 35.4. The PMMA mounting block is on the right and the 3D printed ABS mounting block on the left with the orthogonally positioned accelerometers of similar sensitivity in the excitation axis. The excitation was impacted along the line joining the two blocks.

The FRF of the two accelerometers measuring in the direction of excitation are overlapped in Fig. 35.5. The red curve is from the accelerometer on the PMMA mounting block, and the green curve is from the 3D printed ABS mounting block. One can observe that the two curves are the same up to 225 Hz; this frequency was considered to be above the maximum frequency of interest for the rover test article. The overlap of these two curves confirms that the low density ABS block did not have any effect on the measurements in the frequency band of interest. It should be noted that these two plots are really the lower-frequency portion of the original FRF's taken up to 1,024 Hz. Some discrepancies in amplitude were observed between the two FRF's especially at higher frequencies beyond 400 Hz.
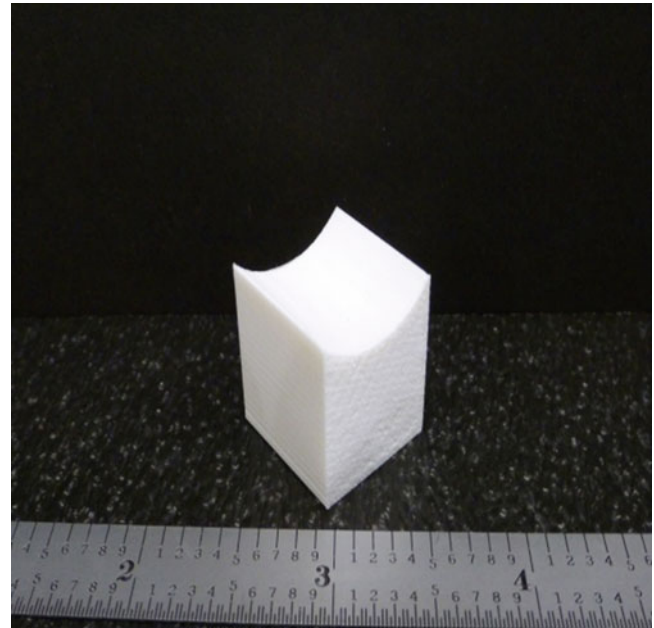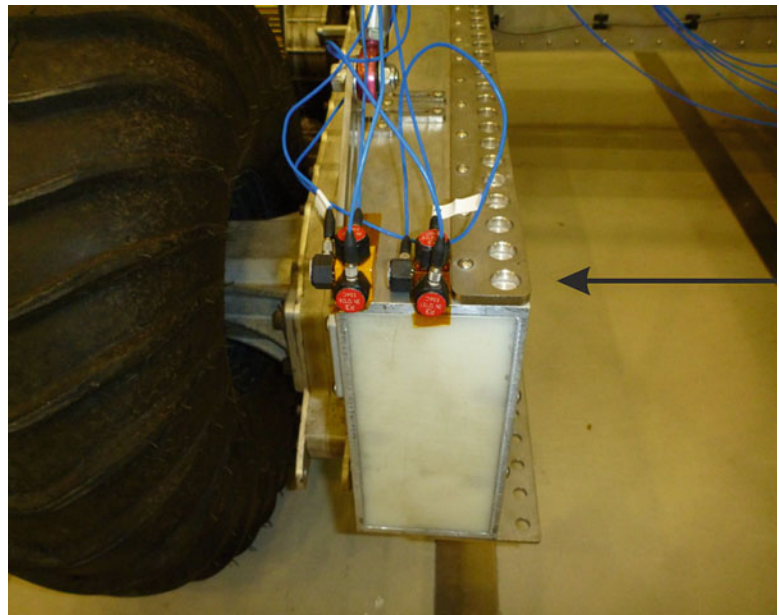
Fig. 35.3 3D printed ABS mounting block

Fig. 35.4 Set-up for validation of 3D printed ABS mounting block with excitation axis

35.5 Modal Testing of Rover with Portable Exciter

As mentioned in Sect. 35.3, it became clear in processing data from the modal tests of the rover and mast assembly that several modes were really rover modes and especially that not enough acceleration information on the rover itself had been captured in order to identify these modes. This section presents some details and results of the modal testing that was subsequently performed on the rover by itself.

35.5.1 Test Configuration and Instrumentation

The rover was instrumented with three orthogonal accelerometers at 20 different positions spread out at key points in order to identify modes of the main frame (Frame), the gear boxes (Gbox) and the motors; a total of 60 accelerometers was
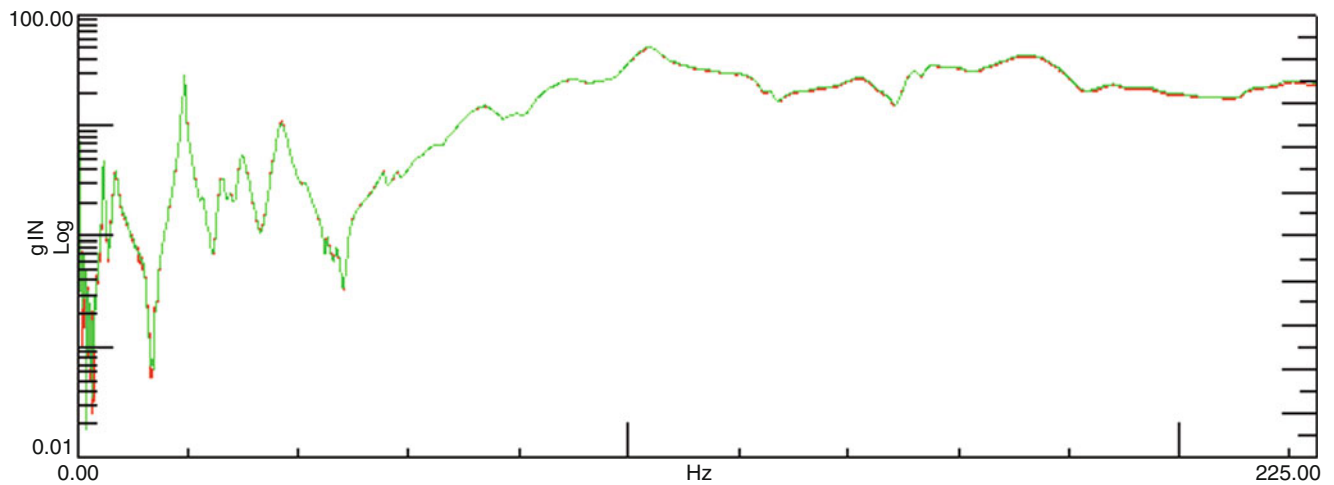
Fig. 35.5 Overlap of FRF's from accelerometers on 3D printed mounting block (*green*) and PMMA mounting block (*red*) (Color figure online)
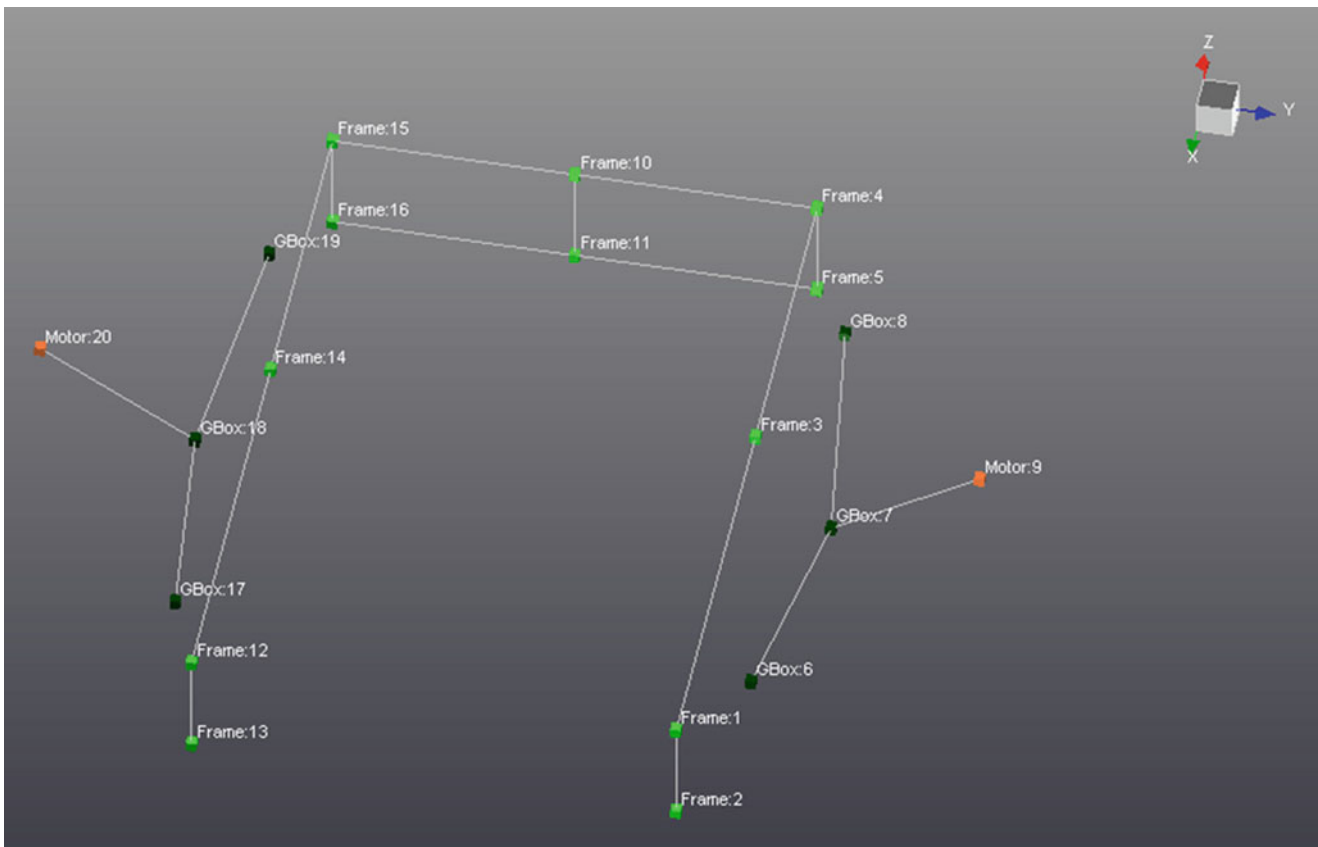

Fig. 35.6 Geometrical representation of the instrumented points for the tested rover

thus mounted on the rover. A geometric representation, generated by the LMS software, of these instrumented locations is presented in Fig. 35.6. As can be observed, this is significantly different than only monitoring the top portion of the main frame of the rover as was done in the earlier testing the rover and mast assembly.

The total number of accelerometers was selected based on the fact that the data acquisition system is equipped with a 32 channel front-end. Assuming two shakers are exciting the test article simultaneously requiring two channels for force measurement, 30 channels become available for acceleration measurement for each run. Consequently, instrumenting the rover with 60 accelerometers allowed the acquisition of all measurement data with only two different runs. Each run was to measure acceleration on one side of the rover (plus one of the two points at the centre of the avionics box).

Fig. 35.7 Overview of test setup
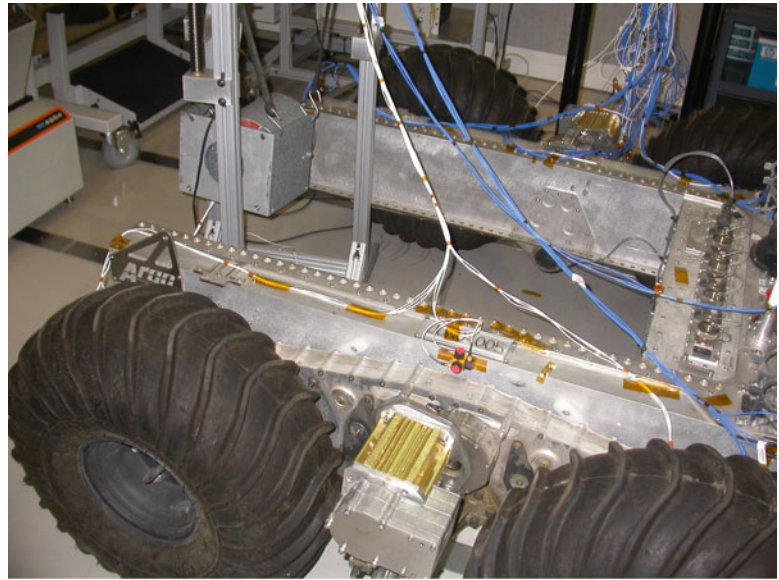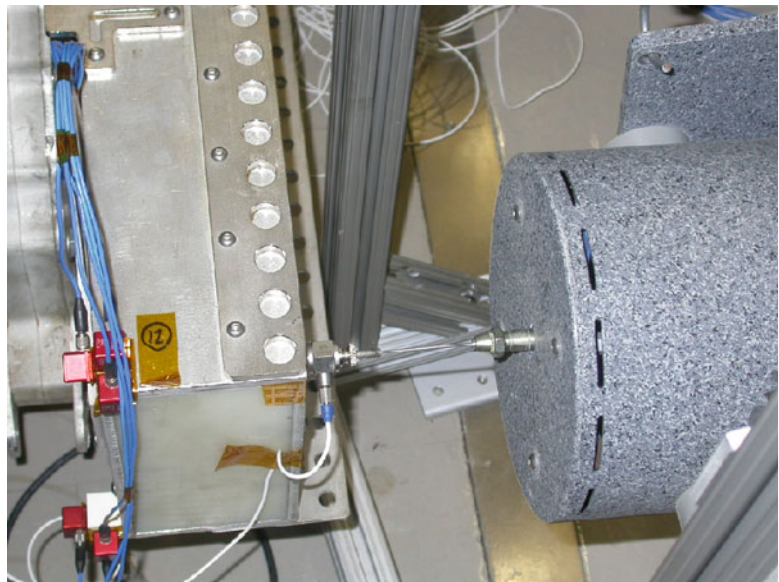for rover testing

Fig. 35.8 Close-up of portable
exciter

The original plan called for some preliminary runs with only the left side of the rover (i.e. from points 11 to 20 as shown in Fig. 35.6) being monitored. For these runs, the structure was excited with a single shaker attached to the top portion of the front extremity of the battery box; the rover was excited along the lateral Y axis (Frame:12 from Fig. 35.6 in the Y axis). An overview of the test setup is presented in Fig. 35.7. A close-up of the portable exciter with its stinger and force sensor mounted to the side of the battery box is shown in Fig. 35.8.

These preliminary runs were performed with the following test parameters:

– Frequency bandwidth: 512 Hz
– Number of spectral lines: 8,192
– Frequency resolution: 0.0625 Hz
– Excitation: Burst random (50 %)
– Number of averages: 25

It should be noted that the upper frequency was selected to be as high as 512 Hz simply because the large number of spectral lines available made it possible to still have very good resolution. For future modal testing of rovers, the frequency bandwidth will be reduced considering the large number of modes present even below 100 Hz.

Table 35.1 Test-based modal parameters of the rover

Mode no	Frequency (Hz)	Damping ratio (%)	Main axis of motion	Description
1	4.5	2.1	Y	Wheel mode: rigid body translation of rover in Y axis
2	5.1	8.1	X, Y	Wheel mode: most likely rigid body translation mode of rover in X axis, coupled with mode at 4.5 Hz
3	6.2	0.7	X, Y, Z	Mode not well defined and corresponding to small peaks appearing in FRF's in Z axis. Strongly coupled with mode at 5.4 Hz
4	8.8	4.3	X, Y, Z	Wheel mode: rigid body translation of rover in Z axis, strongly coupled with lower frequency modes
5	13.0	4.0	Z	Wheel mode: rigid body rocking mode of rover about X axis
6	19.0	1.3	X, Y	Bending mode of avionics box in X axis
7	22.0	1.7	X, Z	Torsion mode of avionics box, strongly coupled with mode at 19 Hz
8	24.7	3.0	Y, Z	Bending mode of gear box in Y axis
9	26.5	2.9	Z	Bending mode of avionics box in Z axis
10	27.8	2.2	X, Y, Z	Likely to be bending mode of battery box in Y axis, highly coupled with some other modes
11	29.2	2.4	X, Y, Z	Likely to be bending mode of shaft attaching the gear box to main frame of rover, highly coupled mode
12	30.2	1.7	Y	Bending mode of shaft
13	36.1	2.6	X, Y	Not clearly identified, but related to dynamics in gear box, or in the shaft
14	41.2	2.7	X, Y	Likely to be torsion mode of battery box
15	48.6	2.3	X, Y, Z	Second mode of battery box in Y axis or related to dynamics in the shaft
16	53.9	2.4	X, Y, Z	Appear to be a combination of bending and torsion modes of the shaft

After these preliminary runs, it was originally planned to perform other runs with different exciter configurations in order to eventually excite the rover in all three orthogonal directions. For each exciter configuration, two complementary runs were to be performed in order to get data for all 60 accelerometers; each run was to be done with two exciters to generate more uniform vibration within this nonlinear test article.

Finally, for logistic reasons, no other test was performed after the preliminary runs discussed earlier. It was decided from analysing the acquired data that complete mode shapes of the rover could be extrapolated from symmetry or, if required, from comparison with data already obtained by testing the rover and mast assembly. It turned out that the derivation of mode shapes for the rover was achieved for the first 16 modes using these two sources of information. This modal data base of the rover was more than what was required for this activity. However, with hindsight, considering the effort required for defining some of these modes, performing some complementary runs in the first place might have been a better decision.

35.5.2 Estimation of Modal Parameters

By curve fitting the FRF's for the left half of the rover obtained from the last preliminary run, the modal parameters of the rover for 16 modes were derived and are presented in Table 35.1. The mode description is as considered while looking at the rover data only, i.e. without comparing with the modes of the rover and mast assembly. The LMS PolyMAX curve fitting algorithm was used to perform these derivations.

35.6 Modal Testing of Rover and Mast Assembly with Portable Exciter

This section presents some details and results of modal testing performed on the rover and mast assembly. As mentioned earlier, one of the main reasons for testing the assembly at that time was to investigate possible resonance in the mast that could cause detrimental motion to the payloads supported on top of the mast.
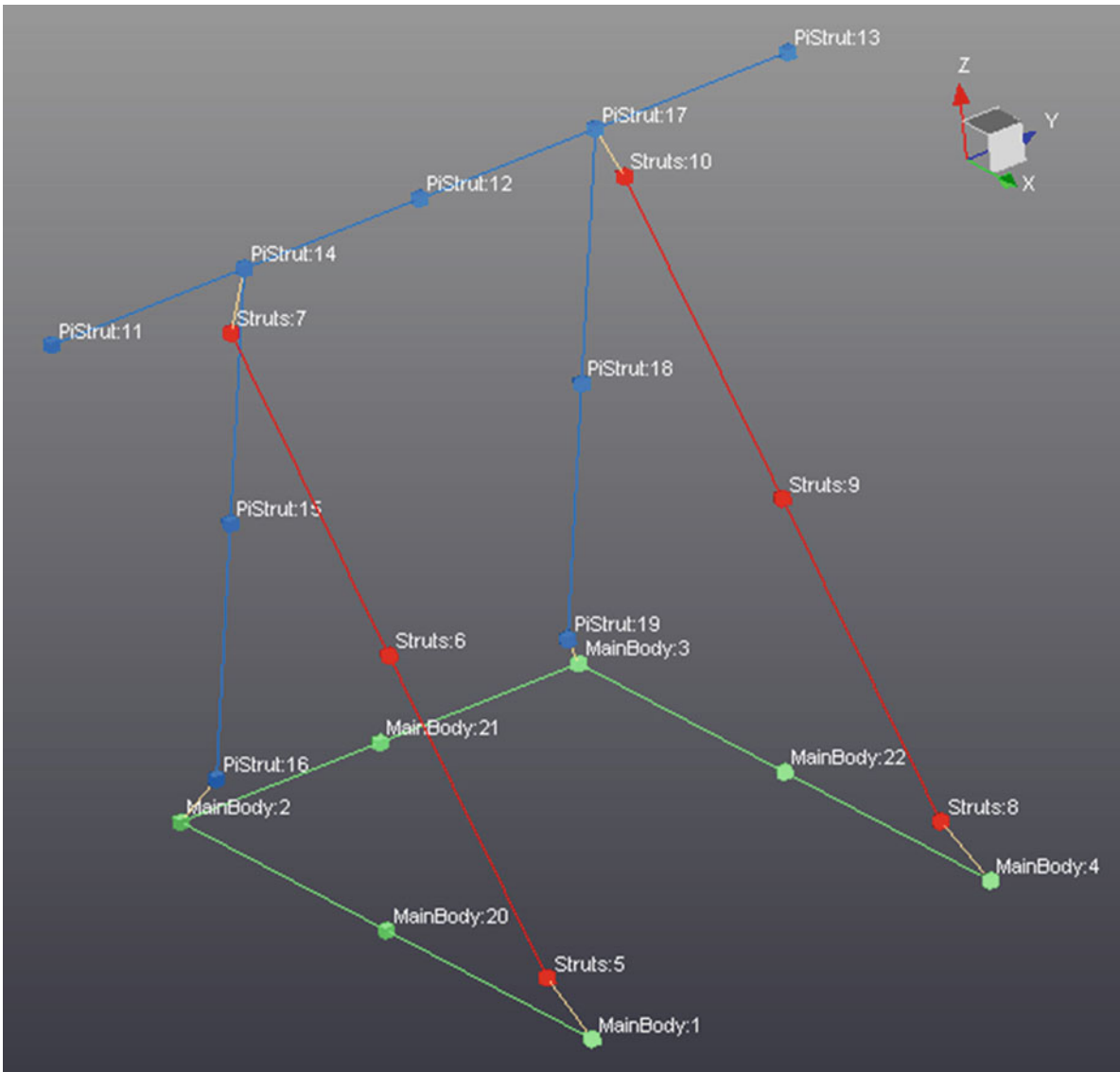
Fig. 35.9 Geometric representation of the instrumented points for rover and mast assembly testing

35.6.1 Test Configuration and Instrumentation

The assembly was instrumented with a total of 51 accelerometers mounted at 21 different locations. A geometric representation of these instrumented points is shown in Fig. 35.9. As can be observed from the figure, only the upper part of the main body was instrumented in order to monitor the motion of the rover. Of the 51 accelerometers, 16 were mounted on the main frame of the rover and the remaining 35 covered the mast.

Following are some details on instrumentation distribution on the test article and some comments regarding possible improvements for future rover assembly testing:

– Only 5 of the 15 instrumented locations on the mast had three orthogonal accelerometers; these point numbers were: 5, 8, 13, 16 and 19. For the other ten locations, only two accelerometers were mounted and measured orthogonal radial motion of the mast components. This decision of eliminating one accelerometer at these locations was made on the following considerations: (1) to reduce the total number of accelerometers and especially (2) only one accelerometer measuring motion along the length of the tubes was considered sufficient since clearly these components did not have any axial resonance in the frequency range of interest. For such 3-D structures for which the monitored motion was not aligned from one component to the other because of geometric consideration, not having three orthogonal accelerometers at each

Table 35.2 Portable exciter configurations for rover and mast assembly

	First exciter		Second exciter	
Configuration no	Location	Direction	Location	Direction
1	Strut:8	Y	MainBody:21	X
2	Strut:8	Y	PiStrut:16	X, Y, Z

Fig. 35.10 Overview of test setup for testing of rover and mast assembly, with exciters at Strut:8 and PiStrut:16
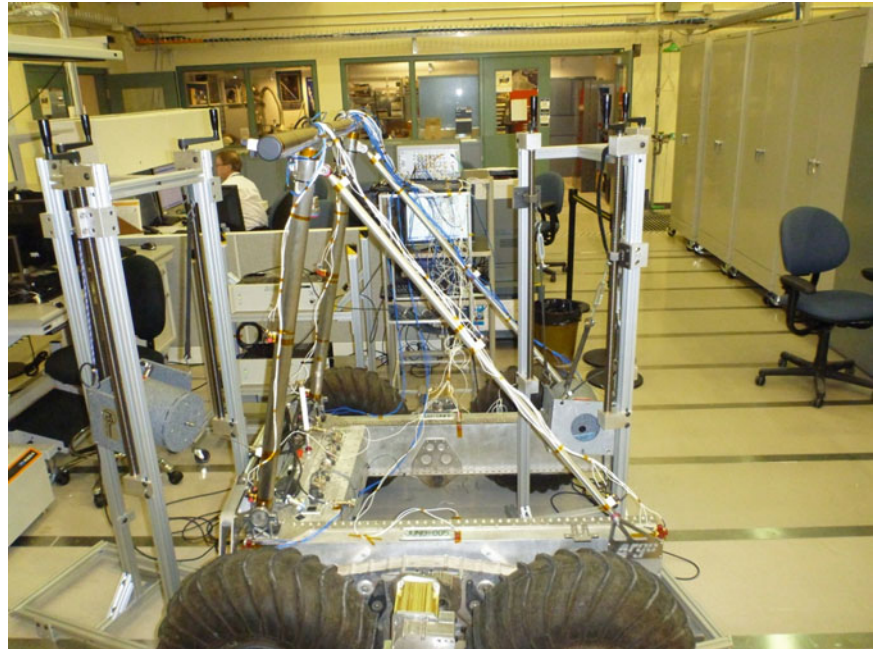
instrumented location turned out not to be the best decision. In fact, this situation resulted in the animated mode shapes showing artificial differential motion between adjacent points (for example, between Strut:10 and PiStrut:17), and between locations on the same member having different numbers of accelerometers.

– As explained in the previous section, up to 60 accelerometers could be monitored in performing two complementary test runs. Only 51 accelerometers were monitored for the portable exciter tests of the assembly. In fact, for an unclear reason, we 'lost' in the setup two additional accelerometers at point MainBody:21 measuring motion in the X and Z directions; these two accelerometers were used for the preceding impact hammer tests and would have been quite useful in monitoring bending modes of the avionics box. In future testing, the moment it is decided that the required number of measurements implies performing more than one run in order to have a complete data set, it might be a good idea to install additional accelerometers in order to use all available measurement channels of the data acquisition system. This comment obviously also applies in the case of only a single run being performed. It is more likely that, after the data acquisition phase is over and the test setup is possibly dismantled, one would prefer to have useful additional information than complain to have too many data. Data analysis with missing information can be more time consuming and costly than monitoring addition locations.

For the formal modal tests of the rover and mast assembly with portable exciters, two different exciter configurations were implemented. For each of these two configurations, two runs were performed in order to acquire data from the 51 accelerometers. The parameters of these exciter configurations are summarized in Table 35.2. Configuration 1 was the main configuration and turned out to be sufficient to excite all modes of interest. In a sense, this could be a bit surprising considering that several modes involve motion along the Z axis which is not excited by this exciter configuration. The fact that these exciters in the X and Y directions could generate motion along the vertical Z axis is attributed to the unsymmetrical U shape of the rover. Testing in the second configuration for which the second exciter was attached to the mast was more for properly exciting the modes of the mast structure. The orientation of the exciter at location PiStrut:16 was such that it was generating vibration along all three axes, although its main excitation direction was the X axis. A picture of the test set-up with this second exciter configuration is shown in Fig. 35.10.

These data acquisition runs were performed with the following test parameters:

– Frequency bandwidth: 1,024 Hz
– Number of spectral lines: 8,192

Table 35.3 Test-based modal parameters of the rover and mast assembly

Mode no	Freq. (Hz)	Damping ratio (%)	Main axis of motion	Freq. of rover mode (Hz)	Description
1	4.5	2.6	Y	4.5	Wheel mode: rigid body translation of rover in Y axis
2	5.4	0.7	X, Y, Z	6.2	Wheel mode: rigid body translation of rover in Z axis, coupled with rigid body modes in X and Y axes
3	6.7	4.7	X, Y	5.1	Wheel mode: rigid body rotation of rover in X-Y plane
4	8.5	3.0	Z	8.8	Wheel mode: rigid body translation of rover in Z axis
5	10.2	5.2	Z		Wheel mode: rigid body rocking mode of rover about Y axis
6	11.8	4.0	Z	13.0	Wheel mode: rigid body rocking mode of rover about X axis
7	19.1	1.2	X, Y	19.0	Bending mode of avionics box in X axis
8	20.9	2.1	X, Y	–	First mode of mast: in-phase bending mode of two Strut tubes in Y axis
9	27.1	1.1	Y	27.8	Bending mode of battery box in Y axis
10	29.3	2.9	Y	29.2	Likely to be bending mode of shaft attaching the gear box to main frame of rover
11	35.3	2.0	X, Y, Z	36.1	Mode in gear box or shaft, according to rover testing
12	40.7	2.3	X, Y	41.2	Torsion mode of battery box
13	43.0	1.3	X, Y	–	Second mode of mast: bending of top tube of PiStrut
14	44.8	1.4	X, Y	–	Third mode of mast: in-phase bending mode of two vertical tubes of PiStrut in Y axis

- Frequency resolution: 0.125 Hz
- Excitation: Burst random (50 %)
- Number of averages: 40

As for the rover testing, it should be noted that the upper frequency was selected quite high simply because the large number of spectral lines available made it possible to still have fairly good resolution. For future modal testing, the frequency bandwidth will be reduced considering the large number of modes present even below 100 Hz.

35.6.2 Estimation of Modal Parameters

Table 35.3 presents the parameters of the first 14 modes derived by curve fitting the FRF's obtained from the test configurations presented in the previous subsection. The fifth column includes the frequency, derived earlier, of corresponding mode of the rover tested by itself. The first six modes are related the wheel dynamics involving rigid body modes of the assembly. The first mode of the mast was measured at 20.9 Hz and is very strongly coupled with the rover mode at 19.1 Hz. The fact that only one mode of the mast occurs below 43 Hz explains the difficulty encountered in the first place in trying to identify the modal parameters of the rover and mast assembly, without any prior knowledge of the dynamics of the rover.

As seen in Table 35.3, the first resonance of the mast occurs only at 20.9 Hz. Consequently, resonance of the mast cannot be responsible for the observed motion on top of the mast while the rover is moving. Rigid body motion of the rover on the wheels is likely the primary cause of this observation.

Examples of four mode shapes of the rover and mast assembly are provided in Fig. 35.11. Rover modes associated to deformation of the main frame were not selected since they are best observed from animation.

35.7 Lessons Learned

This section contains some lessons learned from the activities presented in this paper. These will be used as guidelines of what to do (or not to do) in performing modal testing of rovers in the future.

- When having the choice between performing more tests or extrapolating results during data processing from partial testing, it might be better to spend more time in the first place in getting more test results and in saving time and effort in the subsequent data processing phase of the work.

Fig. 35.11 Examples of mode shapes for rover and mast assembly. (**a**) Mode at 4.5 Hz, (**b**) Mode at 6.7 Hz, (**c**) Mode at 11.8 Hz, (**d**) Mode at 43.0 Hz
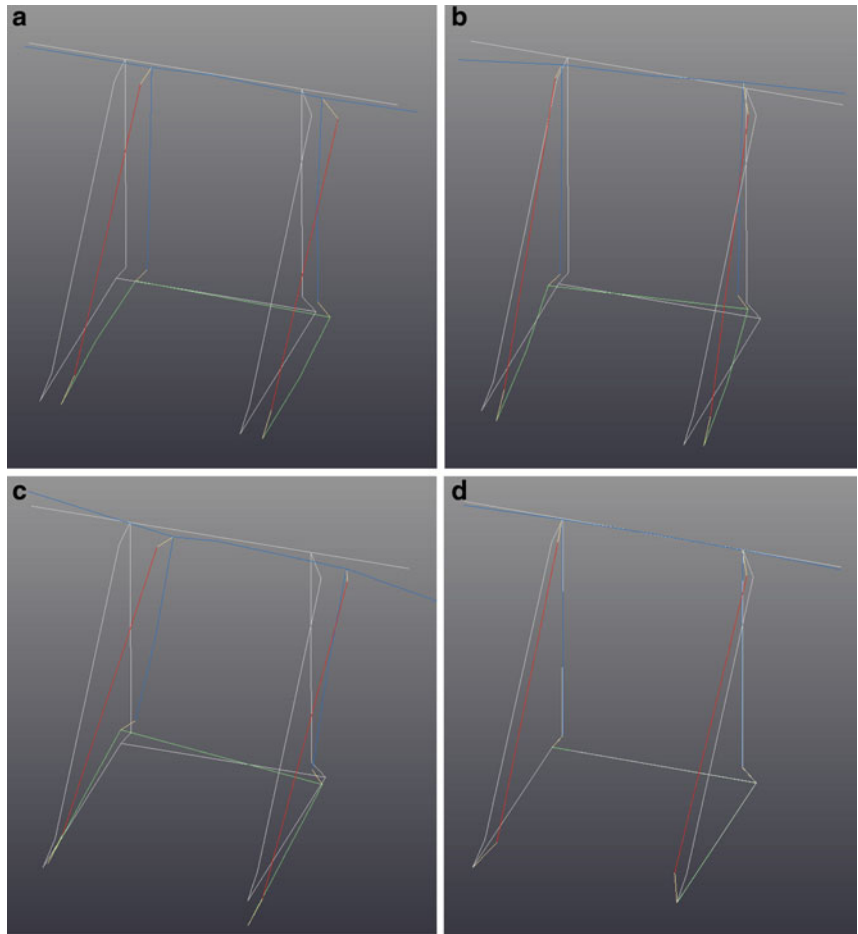
– For geometrically complex 3-D structures such as the rover and mast assembly, three orthogonal accelerometers (or a triaxial accelerometer) should be mounted at each instrumented location. This is to avoid having artificial deformation in the processed mode shapes that could be wrongly considered as being part of the mode.
– All available measurement channels allowed by the selected number of complementary runs to complete a full data set should be used for monitoring acceleration at different locations/directions. It is easy once the data acquisition phase is over to regret some missing information that could have been easily obtained.

35.8 Summary

The paper presents some details and results of modal testing activities performed on a terrestrial rover prototype developed in order to advance technology readiness in preparation for an eventual Canadian participation in future international space exploration missions.

The first set of tests was performed on the selected JUNO rover to which was attached a mast aimed at supporting navigational and scientific payload. In light of the difficulty in identifying the test-based modal parameters of the rover and mast assembly due to the limited amount of instrumentation mounted on the rover itself, subsequent modal tests on the rover without the mast were accomplished. These dedicated tests of the rover led to identification of several rover modes. These modes were critical in allowing the subsequent identification of the first 14 modes of the rover and mast assembly using already acquired data. The first six modes are related the wheel dynamics involving rigid body modes of the assembly. The first mode of the mast was measured at 20.9 Hz and is very strongly coupled with the rover mode at 19.1 Hz. The fact that only one mode of the mast occurs below 43 Hz explains the difficulty encountered in the first place in trying to identify the modal parameters of the rover and mast assembly, without any prior knowledge of the dynamics of the rover.

Reference

1. Dupuis E, Martin E (2012) An overview of recent Canadian Space Agency activities in space robotics. Proceedings of the 2012 international symposium on artificial intelligence, robotics and automation in space, Turin, Italy